

IntechOpen

Optoelectronics

Advanced Materials and Devices

Edited by Sergei L. Pyshkin and John M. Ballato



WEB OF SCIENCE™



OPTOELECTRONICS - ADVANCED MATERIALS AND DEVICES

Edited by **Sergei L. Pyshkin**
and **John M. Ballato**

Optoelectronics - Advanced Materials and Devices

<http://dx.doi.org/10.5772/3463>

Edited by Sergei L. Pyshkin and John M. Ballato

Contributors

Bruno Ullrich, Z. Xie, J.C. Fan, Meichun Huang, Guijiang Lin, Jingfeng Bi, Minghui Song, Jianqing Liu, Weiping Xiong, Gabriel Bernardo, David Bucknall, Abdelhakim Nafidi, Ayse Turak, Venkatachalam Shanmugam, Jin-Gang Liu, Yuan-Zheng Guo, Hai-Xia Yang, Shiyong Yang, Vladimir G. Krasilenko, Aleksandr Nikolsky, Alexander Lazarev, Sergei L. Pyshkin, John Ballato, Hiroki Kishikawa, Nobuo Goto, Moises Rivas-Lopez, Wendy Flores F., Marc Savanier, Filippo Ghiglieno, Xavier Lafosse, Aristide Lemaître, Ivan Favero, Sara Ducci, Giuseppe Leo, Cécile Ozanam, Loïc Lanco, Ulrich H.P. Fischer-Hirchert, Nibir Dhar, Ashok K. K Sood, Nuri Emanetoglu, Wang Zhang, Giulia Innocenti Bruni, Florin Stanculescu, Patrice Salzenstein

© The Editor(s) and the Author(s) 2013

The moral rights of the and the author(s) have been asserted.

All rights to the book as a whole are reserved by INTECH. The book as a whole (compilation) cannot be reproduced, distributed or used for commercial or non-commercial purposes without INTECH's written permission.

Enquiries concerning the use of the book should be directed to INTECH rights and permissions department (permissions@intechopen.com).

Violations are liable to prosecution under the governing Copyright Law.



Individual chapters of this publication are distributed under the terms of the Creative Commons Attribution 3.0 Unported License which permits commercial use, distribution and reproduction of the individual chapters, provided the original author(s) and source publication are appropriately acknowledged. If so indicated, certain images may not be included under the Creative Commons license. In such cases users will need to obtain permission from the license holder to reproduce the material. More details and guidelines concerning content reuse and adaptation can be found at <http://www.intechopen.com/copyright-policy.html>.

Notice

Statements and opinions expressed in the chapters are those of the individual contributors and not necessarily those of the editors or publisher. No responsibility is accepted for the accuracy of information contained in the published chapters. The publisher assumes no responsibility for any damage or injury to persons or property arising out of the use of any materials, instructions, methods or ideas contained in the book.

First published in Croatia, 2013 by INTECH d.o.o.

eBook (PDF) Published by IN TECH d.o.o.

Place and year of publication of eBook (PDF): Rijeka, 2019.

IntechOpen is the global imprint of IN TECH d.o.o.

Printed in Croatia

Legal deposit, Croatia: National and University Library in Zagreb

Additional hard and PDF copies can be obtained from orders@intechopen.com

Optoelectronics - Advanced Materials and Devices

Edited by Sergei L. Pyshkin and John M. Ballato

p. cm.

ISBN 978-953-51-0922-8

eBook (PDF) ISBN 978-953-51-4258-4

We are IntechOpen, the world's leading publisher of Open Access books Built by scientists, for scientists

4,000+

Open access books available

116,000+

International authors and editors

120M+

Downloads

151

Countries delivered to

Our authors are among the
Top 1%

most cited scientists

12.2%

Contributors from top 500 universities



WEB OF SCIENCE™

Selection of our books indexed in the Book Citation Index
in Web of Science™ Core Collection (BKCI)

Interested in publishing with us?
Contact book.department@intechopen.com

Numbers displayed above are based on latest data collected.
For more information visit www.intechopen.com



Meet the editors



Dr.Scie. Prof. Sergei L. Pyshkin is Principal Investigator of the Institute of Applied Physics, Academy of Sciences of Moldova, Adjunct Professor and Senior Fellow of Clemson University, SC, USA, member of The US Minerals, Metals & Materials Society (TMS), awarded the State Prize of Rep. Moldova for investigations in solid-state physics and microelectronics. The works deal with non-linear optics (multi-quantum absorption), electron and phonon transport phenomena, photoconductivity and light scattering, luminescence, crystal and thin film growth, molecular beam and laser assisted epitaxies, nanotechnology, lasers for medicine, scientific instrument making (boxcar-integrators and solid-state IR matrix photoreceivers). Biography of Prof. Pyshkin is included into the Marquis "Who's Who in America" (2008-2013) and "Who's Who in the World" (2009-2013).



Dr. John Ballato is a professor of materials science and engineering (MSE) at Clemson University where he also directs the Center for Optical Materials Science and Engineering Technologies (COMSET). He earned a B.S. in Ceramic Science and Engineering (1993) and the Ph.D. in Ceramic and Materials Engineering (1997) from Rutgers, The State University of New Jersey. Dr. Ballato has published more than 250 archival scientific papers, holds 25 U.S. and foreign patents, has given in excess of 140 invited lectures/colloquia, and has co-organized 25 national and international conferences and symposia. Among other honors, he is a Fellow of the Optical Society of America (OSA), the International Society of Optical Engineering (SPIE), and the American Ceramic Society (ACerS).

Contents

Preface XIII

- Chapter 1 **Advanced Light Emissive Device Structures 1**
Sergei L. Pyshkin and John Ballato
- Chapter 2 **ZnO-Based Light-Emitting Diodes 25**
J.C. Fan, S.L. Chang and Z. Xie
- Chapter 3 **Technological Challenges for Efficient AlGaAs Nonlinear Sources on Chip 59**
M. Savanier, C. Ozanam, F. Ghiglieno, L. Lanco, X. Lafosse, A. Lemaître, I. Favero, S. Ducci and G. Leo
- Chapter 4 **InP/InGaAs Symmetric Gain Optoelectronic Mixers 91**
Wang Zhang and Nuri W. Emanetoglu
- Chapter 5 **Preparation and Characterization of Nanostructured TiO₂ Thin Films by Hydrothermal and Anodization Methods 115**
S. Venkatachalam, H. Hayashi, T. Ebina and H. Nanjo
- Chapter 6 **Correlation Between Band Structure and Magneto-Transport Properties in n-type HgTe/CdTe Two-Dimensional Nanostructure Superlattice. Application to Far-Infrared Detection 137**
Abdelhakim Nafidi
- Chapter 7 **Advances in Infrared Detector Array Technology 149**
Nibir K. Dhar, Ravi Dat and Ashok K. Sood
- Chapter 8 **Theoretical Analysis of the Spectral Photocurrent Distribution of Semiconductors 191**
Bruno Ullrich and Haowen Xi

- Chapter 9 **Recent Progress in the Understanding and Manipulation of Morphology in Polymer: Fullerene Photovoltaic Cells** 207
Gabriel Bernardo and David G. Bucknall
- Chapter 10 **Dewetting Stability of ITO Surfaces in Organic Optoelectronic Devices** 229
Ayse Turak
- Chapter 11 **Organo-Soluble Semi-Alicyclic Polyimides Derived from Substituted-Tetralin Dianhydrides and Aromatic Diamines: Synthesis, Characterization and Potential Applications as Alignment Layer for TFT-LCDs** 269
Jin-gang Liu, Yuan-zheng Guo, Hai-xia Yang and Shi-yong Yang
- Chapter 12 **Aromatic Derivatives Based Materials for Optoelectronic Applications** 291
Florin Stanculescu and Anca Stanculescu
- Chapter 13 **Optoelectronic Oscillators Phase Noise and Stability Measurements** 337
Patrice Salzenstein
- Chapter 14 **Design and Modeling of Optoelectronic Photocurrent Reconfigurable (OPR) Multifunctional Logic Devices (MFLD) as the Universal Circuitry Basis for Advanced Parallel High-Performance Processing** 349
Vladimir G. Krasilenko, Aleksandr I. Nikolsky and Alexander A. Lazarev
- Chapter 15 **All-Optical Autonomous First-in–First-out Buffer Managed with Carrier Sensing of Output Packets** 375
Hiroki Kishikawa, Hirotaka Umegae, Yoshitomo Shiramizu, Jiro Oda, Nobuo Goto and Shin-ichiro Yanagiya
- Chapter 16 **A Method and Electronic Device to Detect the Optoelectronic Scanning Signal Energy Centre** 389
Moisés Rivas, Wendy Flores, Javier Rivera, Oleg Sergiyenko, Daniel Hernández-Balbuena and Alejandro Sánchez-Bueno
- Chapter 17 **Opto-Electronic Packaging** 419
Ulrich H. P. Fischer

- Chapter 18 **III-V Multi-Junction Solar Cells 443**
Gui jiang Lin, Jingfeng Bi, Minghui Song, Jianqing Liu, Weiping
Xiong and Meichun Huang
- Chapter 19 **Use of Optoelectronic Plethysmography in Pulmonary
Rehabilitation and Thoracic Surgery 471**
Giulia Innocenti Bruni, Francesco Gigliotti and Giorgio Scano

Preface

Optoelectronics, as the discipline devoted to the study and application of electronic devices that emit, detect, and otherwise control light, has widely proliferated around the world and enabled many of today's modern conveniences. Despite this ubiquity, new applications and novel optical phenomena continue to drive innovation. Accordingly, there is a need to compile advances and new achievements for specialists and all who are interested. Thus InTech – Open Access Publisher has developed this offering, Optoelectronics – Book II, as the second part of the InTech collection of international works on optoelectronics.

As with the first book Optoelectronics - Materials and Techniques, edited by Professor P. Predeep, this book covers recent achievements by specialists around the world. With pleasure we note the growing number of countries participating in this endeavor including Brazil, Canada, China, Egypt, France, Germany, India, Italy, Japan, Malaysia, Mexico, Moldova, Morocco, Netherlands, Portugal, Romania, Saudi Arabia, South Korea, Taiwan, Ukraine, USA, and Vietnam.

Our joint participation in this book and writing of one of its Chapters also testifies to the unifying effect of science. We started this book from the Chapter entitled "Advanced Light Emissive Device Structures" which highlights the progression in properties of a unique collection of aged GaP crystals grown over 50 years ago and now exhibit very interesting optoelectronics features and offer fundamental insights into solid state physics over such time scales.

We purposely do not divide the book into separate sections, as is common, because many of the Chapters are devoted to differing aspects of optoelectronics, including materials and their characterization, through device structures and applications. However, we tried to gather chapters of similar theme together. An interested reader will find in the book the description of properties and applications employing organic and inorganic materials, such as different polymers, oxides and semiconductors, as well as the methods of fabrication and analysis of operation and regions of application of modern optoelectronic devices.

We are grateful to the authors and hope that the contribution of authors and number of participating countries will continue to grow, while optoelectronics itself will be the object in permanent demand to further enhance human quality of life.

Editor:

Sergei L. Pyshkin

Professor, Principal Investigator
Institute of Applied Physics
Academy of Sciences of Moldova
Kishinev, Moldova
Adjunct-Professor, Senior Fellow
Clemson University
South Carolina, USA

Co-editor:

John M. Ballato

Professor, Director
Center for Optical Materials Science and Engineering Technologies
School of Engineering and Materials Science
Clemson University
South Carolina, USA

Advanced Light Emissive Device Structures

Sergei L. Pyshkin and John Ballato

Additional information is available at the end of the chapter

<http://dx.doi.org/10.5772/52416>

1. Introduction

This Chapter contains our latest achievements on organic and inorganic light emitters for display and waveguide applications. Two simultaneous efforts are described and analyzed. The first is the application of some transparent polymers to photoactive device structures. The second area focuses on the fabrication of optoelectronically-important structures based on GaP nanoparticles and their composites. The choice of materials are further complementary since they each are considered candidates for use in all optical circuits with commercial interest for light emitters, waveguides, converters, accumulators and other planar, fiber or discrete micro-optic elements.

Three objectives have been fulfilled and are reported here: 1) the development of new technologies for the preparation of nanocrystalline composite and GaP films; 2) the fabrication of novel optical planar light emissive structures for light emissive devices based on GaP/polymers nanocomposites; and 3) the generalization of experimental results from light emissive GaP bulk crystals, nanoparticles and nanocomposites.

Photoluminescence (PL), Raman light scattering (RLS), X-ray diffraction (XRD), atomic force and transmission electron microcopies (AFM and TEM) and other diagnostic methods have been used to characterize quality of GaP bulk and nanocrystals, GaP/polymers nanocomposites and to evaluate emissive efficiency of the obtained device structures. New solutions based on growth technique with use of modern analytical techniques were applied for growth and monitoring of semiconducting and composite films and fibers.

One of the main results described in the present Chapter is the creation and investigation of nanocomposite films based on GaP nanoparticles inserted into optically transparent polymers to prepare unique light emissive devices for optoelectronic applications. Different polymers were tested that combine the processability and durability of engineering

thermoplastics with suitable for GaP nanoparticles optical, electrical, thermal, and environment resistant properties.

Perfect single crystals from our unique collection of pure and doped GaP single crystals [1-25] compared with GaP nanoparticles prepared by us [26-31] serve as a standard yielding fundamental new knowledge and insights into semiconductor optical physics. Elaborating optimal methods of fabrication of GaP nanoparticles and their light emissive composites with compatible polymers [32-36] we use our own experience and literature data [37-39]. Due to considerable efforts in the past, including our contribution also, GaP has received significant attention as a material for use in a wide range of important modern optoelectronic devices including photodetectors, light emitters, electroluminescent displays and power diodes as well as being a model material with which to investigate the fundamental properties of semiconductors.

These two components of the composites, GaP and specially selected polymers, were unified based on their compatibility with the light emission spectral region as well as in their eventual integration into all optical circuits where bulk crystals or nanocrystals of GaP have been of commercial interest mainly for fiber and planar light emissive and micro-optic elements.

We hope our device structures obtained with application of accumulated for years results in their optics and technology [1-36, 41-43] will have significant commercial value because they present a new optical medium and product.

2. Development of technology for growth of GaP nanocrystals

While bulk and thin film GaP has been successfully commercialized for many years, its application in nanocomposites as a new optical medium has only received attention recently. This section reviews our recent efforts to advance the quality of GaP nanoparticles for light emissive devices based on polymer/GaP nanocomposites.

This activity is the important milestone in the creation of the nanocomposites for advanced light emissive device structures because GaP nanoparticles having the necessary luminescent and electroluminescent properties and compatible with a polymer matrix is a key element of these structures. We hope the described here some details and parameters of the technological processes used for fabrication of GaP nanocrystals with the improved and necessary for concrete application characteristics of luminescence will be useful in further elaboration of the relevant optoelectronic devices.

The quality of GaP nanoparticles was improved using mild aqueous synthesis and different colloidal reactions of Ga and P sources in toluene [26-38]. We used these methods taking into account that success of our activity depends on optimal choice of the types of chemical reactions, necessary chemicals and their purity, conditions of the synthesis (control accuracy, temperature, pressure, duration, etc.), methods and quality of purification of the nanocrystals, storage conditions for nanoparticles used in the further operations of fabrication of the GaP/nanocomposites.

Ultrasonication and ultracentrifugation have been applied during the synthesis and selection of nanoparticles to increase their quality and to select them on dimensions.

The relevant spectra of photoluminescence and Raman light scattering, X-ray diffraction and electron microscopy of the nanoparticles prepared under different conditions have been compared with each other as well as with those from bulk single crystals. Thoroughly-prepared powders and suspensions of the nanoparticles have been used for preparation of GaP film nanocomposites on the base of different polymers compatible with the nanoparticles on optical and mechanical properties.

2.1. Equipment for fabrication of nanoparticles, fluoropolymers and nanocomposites

The equipment for fabrication of fluoropolymers and polymer nanocomposites has been elaborated by the author (JB) from Clemson University during our joint activity on light emissive structures. This equipment and approaches were applied to our specific needs without any serious modification.

2.1.1. Equipment for sublimation of phosphorus

It was found the synthesis on the base of white phosphorus gives the best quality of GaP nanoparticles. Due to the known prohibition for free sale of white phosphorus we have elaborated the facilities for its preparation using sublimation of its red modification (see Figure 1).

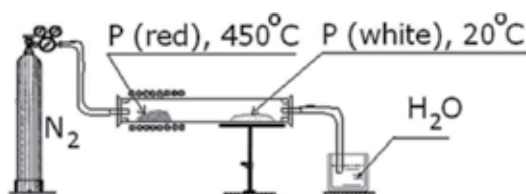


Figure 1. Preparation of white phosphorus.

The device is the silica tube, which is hermetic to the air, and is heated from one end while the P vapor is transferred by a neutral gas (nitrogen or argon) environment at the other cooled end of the tube where it is condensed there to form white phosphorus. After completion of the process the white phosphorus can be removed; the tube must be immersed into a water bath that to avoid inflammation of phosphorus in air.

The obtained white phosphorus must be stored as a water suspension. Then this suspension by melting in boiled water is turned into the substance using in the synthesis of GaP nanoparticles.

2.1.2. Equipment for hydrothermal and colloidal synthesis

A new model of autoclave for the hydrothermal synthesis of GaP nanoparticles from the appropriate chemical solutions has been established given the requisite high temperatures (up

to 500°C) for the organic solvents using $\text{GaCl}_3 \cdot 6\text{H}_2\text{O}$ and white phosphorus as precursors. Software for the process of synthesis at the temperature control and regulation with the accuracy of 0.1°C has been developed.

The key part of the method are the chemical reactions at high temperature and pressure. The reactor here is a hollow hermetic teflon cylinder. The necessary temperature (125°C, 200°C) inside the cylinder is obtained by its heating, while the pressure – by evaporation of water.

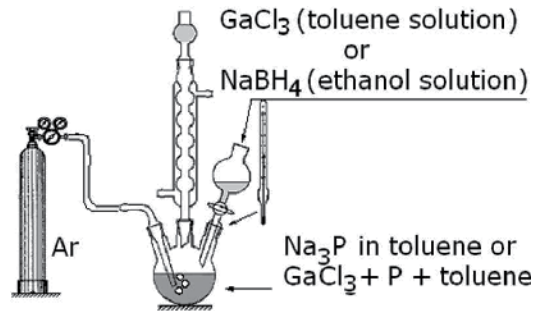


Figure 2. Equipment for preparation of GaP nanocrystals on the base of NaBH_4 or Na_3P .

The equipment for colloidal synthesis of GaP nanocrystals using NaBH_4 or Na_3P in toluene is shown in Figure 2.

2.2. Elaboration of technologies for fabrication of GaP nanoparticles

In 2005 the authors developed methods to fabricate GaP nanoparticles [26]. So, the technology and properties of the nanoparticles obtained in 2005-2006 and later [27, 28] are a good reference point for comparison to the new data provided herein.

More recently the authors [31] have concentrated on low temperature methods to synthesize GaP nanoparticles with improved luminescent characteristics. These methods are considerably different from those of other standard high temperature methods.

The first samples of GaP nanoparticles having a distinct luminescence at room temperature were obtained by hydrothermal method from aqueous solutions at relative low temperature (120-200°C). This method is discussed in Subsection 2.2.1. It was found that the composition of the nanoparticles corresponds to stoichiometric GaP.

The colloidal method provides a good opportunity to control the conditions of the synthesis, to decrease power inputs and to increase quality of nanoparticles concerning their purity and uniformity of their dimensions. In actuality, the single parameter, which may be controlled in the other methods, is the temperature, while using colloidal methods one can control nucleation of nanoparticles as well as velocity of their growth. The other important advantage of the colloidal method is the ability of so called “capping”; that is to isolate nanoparticles from each other, to prevent their agglomeration during storage, simultaneous-

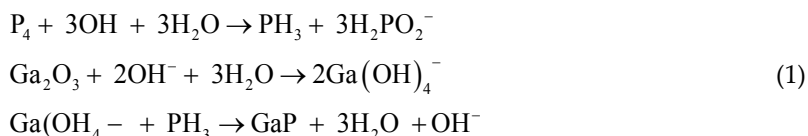
ly inhibiting their further growth. Therefore, we have elaborated the methods of GaP nanocrystals colloidal synthesis using NaBH_4 and Na_3P compounds (Subsections 2.2.2 and 2.2.3).

2.2.1. Hydrothermal method of synthesis of GaP nanocrystals

Noted here are only essential details of the aqueous syntheses of GaP nanoparticles prepared at different temperatures and reaction conditions.

Using the literature data noted above the first nanocrystalline samples of GaP [26] have been prepared. The first aqueous prepared, relatively monodisperse, well crystallized GaP nanocrystallites, exhibiting pronounced quantum confinement effect have been presented in [27]. The relevant reactions were carried out in an aqueous solution at 120-160°C. A typical synthesis was as follows: 35,0 ml H_2O , 1,0 g Ga_2O_3 , 1,0 g NaOH , 2,0 g white phosphorus were added to a 50 ml Teflon -lined autoclave, and 1,5 g I_2 then was added. The autoclave was kept at 120-160°C for 8 hrs and then cooled to room temperature.

GaP nanoparticles were obtained in an alkali solution, taking advantage of the reaction of $\text{Ga}(\text{OH})_4^-$ with PH_3 which was produced from white phosphorus dispersed in alkali solution:



The yield of GaP in alkali solution is only about 12%. In order to improve the yield of GaP iodine was added to induce the reaction with white phosphorus, based on follow process:



The X-ray powder diffraction patterns of the as-prepared products indicated to the zinc blend structure of GaP with $a = 5.43 \text{ \AA}$. Average crystallite size estimated by the Scherrer equation are about 5 nm for GaP nanocrystals [27].

Nanoparticles of GaP have been prepared by mild aqueous synthesis at different temperatures, modifications and compositions of the reacting components.

NaOH pellets were dissolved in distilled water. Ga_2O_3 , red or white phosphorus powder and I_2 were mixed and added to the NaOH solution. The mixed solution was then placed into an autoclave and heated in an oven for 8 hours at 125 or 200°C. After the completion of heating the autoclave was taken out of the oven and cooled. The obtained powder was filtered, washed with ethanol, HCl and distilled water and dried or ultrasonicated in the bath with a special solvent for separation in dimensions and preparation of a suspension for any nanocomposite. The dried powders were then characterized using standard methods of XRD, TEM, Raman scattering and photoluminescence. For comparison industrial and specially grown and aged GaP single crystals also were used [1, 24].

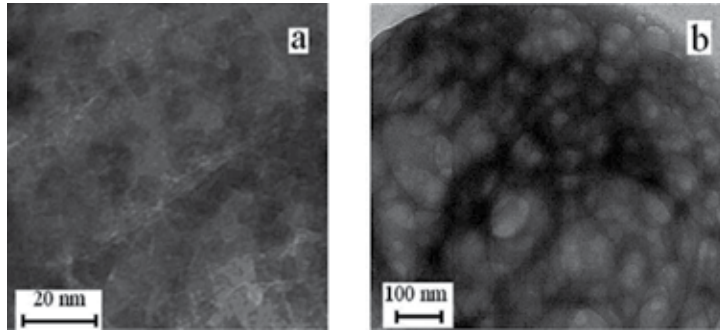


Figure 3. TEM images of GaP nanoparticles obtained by the aqueous synthesis. a. Thoroughly ultrasonicated and dried nanopowder. b. Initial clusters with the dimensions of the order of 100 nm.

The instruments employed for Raman light scattering and luminescence measurements included spectrographs interfaced to a liquid nitrogen-cooled detector and an argon ion laser or lamp excitation sources. Raman scattering spectra was obtained at room temperature by excitation with 514.5 nm radiation. Luminescence was excited by UV light of the lamps or the N_2 laser nanosecond pulses at wavelength 337 nm and measured at room temperature [25-28].

Figure 3 shows the TEM images of GaP nanoparticles obtained by the aqueous synthesis. The washed, thoroughly ultrasonicated and dried nanopowder contains mainly single 10nm nanoparticles (Figure 3a), obtained from the initial clusters with the dimensions of the order of 100 nm (Figure 3b).

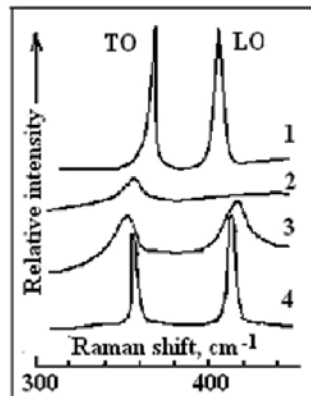


Figure 4. Raman light scattering from GaP nanoparticles of different treatment (spectra 2-4) in comparison with perfect GaP bulk crystals (spectrum 1).

Spectrum 2: Not thoroughly treated powder of nanoparticles prepared using red phosphorus at 200°C. Spectrum 3: Thoroughly treated GaP nanoparticles prepared using red phosphorus at 200°C. Spectrum 4: Nanoparticles prepared on the base of white P by low temperature syntheses.

Figure 4 shows the Raman light scattering spectra from GaP nanoparticles prepared using white or red P in mild aqueous synthesis at increased or low temperatures and ultrasonically treated.

In the colloidal method of the synthesis freshly prepared white phosphorus was used and ultrasonicated in toluene. Here the mixture for the reaction of the synthesis consists of $\text{GaCl}_3 \cdot n\text{H}_2\text{O}$ diluted in toluene and dry NaBH_4 . One of 2 fractions of different colors obtained in the synthesis was removed by rinsing in ethanol and water while the next one, containing the nanoparticles, was treated in an high-speed ultracentrifuge.

The characteristic GaP Raman lines from aged GaP single crystals (Figure 4, spectrum 1) and from the nanoparticles prepared using white P at low temperature (Figure 4, spectrum 4) were narrow and intense whereas, nanoparticles prepared from red P at higher temperatures (Figure 4, spectra 2 and 3) were weak and broad; the especially weak and broad spectrum exhibits not thoroughly washed powder (please see spectrum 2).

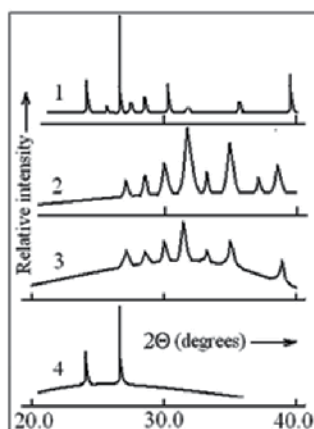


Figure 5. X-ray diffraction from GaP nanoparticles. 1. White phosphorus, using low temperature syntheses, well-treated powder. 2. White P, not the best performance and powder treatment. 3. Red phosphorus, the best result. 4. Perfect GaP bulk crystal.

In Figure 5 one can see x-ray diffraction from the GaP nanoparticles prepared at different conditions using red or white phosphorus (spectra 1-3) in comparison with the diffraction from perfect GaP single crystal (spectrum 4). The nanoparticles obtained by low temperature aqueous synthesis using white phosphorus exhibited clear and narrow characteristic lines like those obtained from perfect GaP bulk single crystals taken from our unique collection of long-term (app. 50 years) ordered GaP single crystals (Figure 5, spectra 1 and 4). Contrary to that, nanoparticles prepared using red phosphorus or less-than-optimum conditions showed broad and weak characteristic lines (Figure 5, spectra 2 and 3).

Any luminescence was absent in newly-made industrial and our freshly prepared crystals but it was bright in the same app. 50 years aged crystals (Figure 6, spectrum 1; the features of luminescence in the perfect aged crystals please see in [16-25]). Initial results on luminescent properties of GaP nanoparticles [26] confirmed the preparation of GaP nanoparticles

with dimensions of between 10-100 nm and clear quantum confinement effects but the luminescent spectrum was not bright enough and its maximum was only slightly shifted to UV side against the 2.24 eV forbidden gap at room temperature (Figure 6, spectrum 2). The nanoparticles obtained from the reaction with white P at low (125°C) temperature exhibit bright broad band spectra considerably shifted to UV side [27, 28, 36] (Figure 6, spectrum 3, 4). Note that the original powder contains only a part of GaP particles with nearly 10 nm dimension, which develop quantum confinement effect and the relevant spectrum of luminescence, so the spectrum of luminescence consists of this band with maximum at 3 eV and of the band characterizing big particles with the maximum close to the edge of the forbidden gap in GaP (Figure 6, spectrum 3), but thorough ultrasonic treatment gives an opportunity to get the pure fraction of nanoparticles with the spectrum 4 having the maximum at 3 eV.

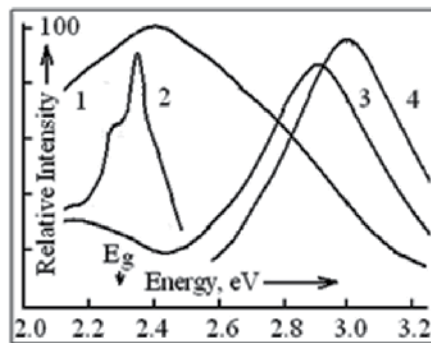


Figure 6. Luminescence of GaP nanoparticles prepared at different conditions (spectra 2-4) and in comparison with the luminescence of perfect GaP bulk single crystals (1). Please see explanations in the text below.

With these results, one can compare the properties of GaP nanoparticles with those of bulk single crystals grown in the 1960s or, approximately, 50 years ago [1-25]. The authors have investigated their optical and mechanical properties [16-25] in the 1960s, 1970s, 1980s and 1990s. Due to a significant number of defects and a highly intensive non-radiative recombination of non-equilibrium current carriers, initially luminescence from the freshly prepared undoped crystals could be observed only at the temperatures 80K and below. Today, luminescence is clearly detected in the region from 2.0 eV and until 3.0 eV at room temperature (see Figure 6, spectrum 1). Taking into account that the indirect forbidden gap is only 2.25 eV, it is suggested that this considerable extension of the region of luminescence to the high energy side of the spectrum as well as a pronounced increase of its brightness are connected with a very small concentration of defects, considerable improvement of crystal lattice, high transparency of perfect crystals, low probability of phonon emission at rather high temperature and participation of direct band-to-band electron transitions.

Our unique collection of long-term-ordered perfect GaP single crystals provides opportunities for deep fundamental analogies between perfect single crystals and nanoparticles [29-31] as well as to predict and to realize in nanoparticles and perfect bulk crystals new and interesting properties and applications as the advanced light emissive elements of relevant

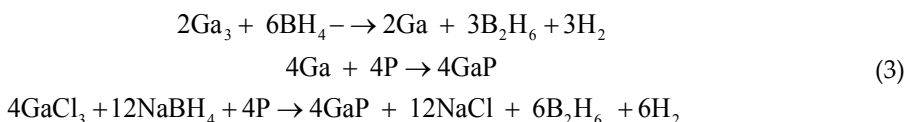
device structures. More detailed analyses and discussion of these results can be found in the references cited above and will be further published.

2.2.2. Synthesis of GaP nanocrystals on the base of NaBH₄ compound

In the method employed here, NaBH₄ was used as a deoxidizer during the synthesis in the solvent – toluene, where the sources of Ga and P (white phosphorus) have been dissolved (GaCl₃) or suspended. NaBH₄ can be used also due to its high solubility in ethanol. The ethanol solution of NaBH₄ was introduced into the process of the synthesis during 5 hours, controlling the velocity of its introduction at the moderate heating up to 70°C.

White-yellow precipitates were the result of the synthesis. The precipitate was rinsed multiple times in toluene, removing the remaining P and GaCl₃, and then in water, removing the water-soluble species such as NaCl. The centrifugal separation from the solvent has been used for extraction of the final precipitate having a lemon color.

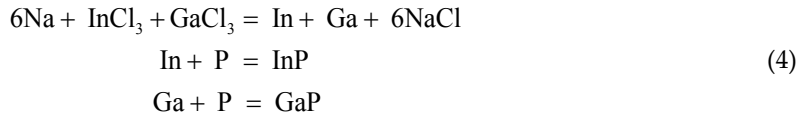
One can suppose the following scheme for the GaP synthesis:



The last reaction is the closing one, including creation of NaCl, which can be easily removed with deionized water. The main problem of the described synthesis is the exclusion of Ga metal particles in the precipitate. The problem is controlled via the rate of Ga ion deoxidation, depending on temperature, the types of solvent and deoxidizer. Using low (~1 mL/min) rate of introduction of NaBH₄ ethanol solution into the process helps to avoid the metal Ga creation.

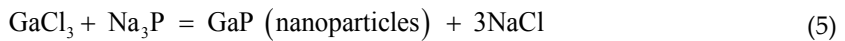
2.2.3. Synthesis of GaP nanocrystals on the base of Na₃P

For the preparation of Na₃P we used elementary Na, white P and the mixture of InCl₃/GaCl₃ (4 wt% InCl₃ + 96 wt% GaCl₃). The main experimental procedures can be described as follows: a 5.2 g mixture of GaCl₃ and InCl₃ was dissolved in 150 ml of xylene. Then, 2 g of sodium and 0.9 g of white phosphorus were added into the solution. The solution was stirred at 100°C for 10 hrs. After the reaction, the product was filtered for 3 times in xylene and 3 times in deionized water. The resultant powders were dried in vacuum at 60–80°C for 2 hrs. All the above mentioned manipulations were conducted in high purity nitrogen (99.999%) atmosphere in a glove box. Lastly, three equal parts of the product were heated respectively to 300°C, 480°C and 600°C for 1 hr in pure nitrogen (99.999%) flows. The reactions can be expressed as:



As the result the GaP nanoparticle aggregation was obtained. In a glove box, previously purged with dry nitrogen, 1.2 g of white phosphorus (P_4) and 1.7 g of sodium (Na) were placed in 100 mL of distilled dimethylbenzene in an Erlenmeyer flask. The mixture was then stirred, heated to 120°C and maintained at that temperature for 10 hrs. A black fragmented product, Na_3P , was obtained. About 10 g of gallium (Ga) pellets were added to a quartz tube with one sealed end. The tube was purged with dry nitrogen and then heated gently. A chlorine gas flow through the melting metal was put in place at a rate until all the gallium reacted. The product - gallium chloride (GaCl_3) was formed. In the glove box, 6.5 g of GaCl_3 was dissolved in 100 mL of distilled dimethylbenzene in an Erlenmeyer flask. The solution was stirred and heated to 100°C . Then 2.5 g of Na_3P was added to the Erlenmeyer flask and the mixture was heated at 100°C with continuous stirring for 2.5 hr. After cooling, the mixture was filtered and washed with water.

The alternative method for preparation of GaP nanocrystals is interaction of GaCl_3 and Na_3P :



In this method the stoichiometric ratio of Na (99,9%) and P (99,995%) is placed in the reactor with the Ar inert atmosphere. The reaction of preparation of Na_3P goes between melted Na and dispersed white P at 110°C in boiling toluene under intense stirring. This violent reaction must be supported at the necessary conditions (110°C and intense stirring) for 5 hrs. As the result we have the black suspension of Na_3P :

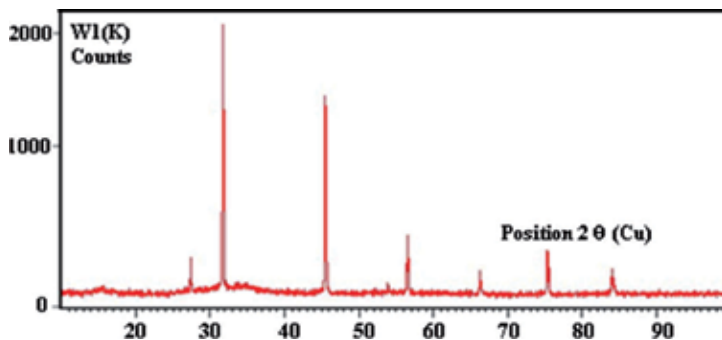


Figure 7. XRD spectrum of GaP nanocrystals prepared on the base of Na_3P and GaCl_3 .

According to elaborated by us technology [28, 31] the synthesis of GaP nanocrystals goes in the toluene solvent between dissolved (GaCl_3) and dispersed (Na_3P) initial chemicals at 80°C under ultrasonic machining for 5 hrs, creating a black-brown precipitate, which must be rinsed multiple times in toluene (removal of P and GaCl_3) and water (removal of the soluble matter like NaCl). A high speed centrifuge must be used for separation of the precipitate. The resultant material must not be cleaned; its purity depends only on the purity of the initial components.

The XRD spectrum of GaP nanocrystals prepared using Na_3P and GaCl_3 in toluene is presented in Figure 7. One can observe the characteristic (111), (220) and (311) reflections for GaP. However, there are some extraneous lines of the low intensity, probably, from NaCl, NaPO_3 and showing that purification of GaP nanoparticles was not enough. The extraneous lines of the other than GaP components can be seen also in the spectra of GaP nanoparticles obtained by the method of Energy Dispersion X-ray Analysis (EDAX).

In conclusion we note that the growth of GaP nanocrystals is the key element in the creation of nanocomposite for advanced device structures because, in spite of the lack of the concrete parameters and conditions of synthesis in the relevant literature sources, all the necessary data for the preparation of GaP nanoparticles are provided herein.

Thus, nanoparticles of GaP have been prepared using white P by mild aqueous low temperature synthesis and 2 methods of colloidal chemistry. The spectra of PL, RLS, and XRD together with TEM images of the nanoparticles prepared under different conditions have been compared with each other as well as with those from bulk single crystals, from hydrothermal and colloidal reactions in toluene were presented. Uniform GaP nanoparticles, following ultrasonic treatment yielded a bright luminescence at room temperature with a broad band with maximum at 3 eV and have been used to prepare GaP/polymer nanocomposites.

3. Development of methods of incorporation of the GaP nanoparticles into polymers

Polyglycidyl methacrylate (PGMA), polyglycidyl methacrylate-co-polyoligoethyleneglycol methacrylate (PGMA-co-POEGMA) and biphenyl vinyl ether (BPVE) polymers were used to synthesize GaP nanocomposites suitable for light emissive luminescent device structures. Some other polymers, dielectrics and with high electric conductivity, will be also investigated in the process of preparation of this Chapter and used for elaboration of light emissive device structures.

Film nanocomposites of good quality with very bright and broad-band luminescence have been prepared. Quality and surface morphology of the nanocomposite films was studied in ambient air using AFM in tapping mode on a Dimension 3100 (Digital Instruments, Inc.) microscope while luminescence of the nanocomposites films deposited by dip-coating from a suspension in water-ethanol mixture solution on the surface of a silica substrate was excited by the N_2 laser nanosecond pulses at wavelength 337 nm and measured at room temperature.

The nanocomposites on the base of the noted above polymers were used for preparation and test of film light emissive device structures.

Thickness of the polymer composite film was within 250-300 nm defined from AFM scratch experiment. The following procedures have been used in the fabrication of the nanocomposites:

1. GaP powder was ultrasonicated in methylethylketone (MEK) using Branson 5210 ultrasonic bath. Then, PGMA was added to the MEK solution. GaP to polymer ratio was less than 1:10.
2. GaP powder was dispersed in water-ethanol mixture (1:1 volume ratio) and ultrasonicated using Branson 5210 bath for 120 min. Then, PGMA-co- POEGMA was added in the form of water-ethanol mixture (1:1 volume ratio) solution. GaP to polymer ratio was less than 1:3. Nanocomposite films were deposited on quartz slides via dip-coating;
3. GaP powder was dispersed in the biphenyl vinyl ether/dichloromethane (BPVE/DCM) solution; the solution was stirred and filtered from the excess of the powder. A few mL drops of the settled solution were casted onto silicon wafer.

More details on preparation and characterization of our GaP/polymers nanocomposites can be found in [31-36].

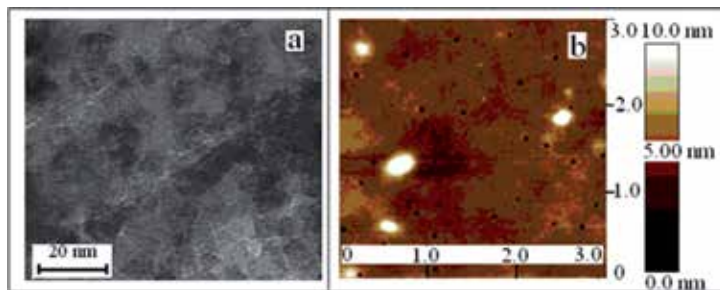


Figure 8. TEM image of GaP thoroughly ultrasonicated and dried nanoparticles obtained by mild aqueous synthesis (a) and AFM topography image of the GaP/PGMA nanocomposite (b).

Figure 8a shows the TEM images of GaP nanoparticles obtained by the aqueous synthesis. One can see GaP nanoparticles, having characteristic dimensions less than 10 nm. The washed, thoroughly ultrasonicated and dried nanopowder contains mainly single nanoparticles, while the same powder obtained without ultrasonic treatment consists of the clusters with the dimensions of the order of 100 nm.

Figure 8b shows the AFM topography images of the GaP/PGMA film nanocomposite deposited by dip-coating from a suspension in water-ethanol mixture solution on the surface of a silica substrate. The AFM images demonstrated that no significant aggregation was caused by the polymerization. In general, individual particles were observed.

The thoroughly washed, ultrasonicated and dried nanopowders obtained by mild low temperature aqueous synthesis from white P as well as their specially prepared suspensions

have been used for fabrication of blue light emissive GaP nanocomposites on the base of some optically and mechanically compatible with GaP polymers. The relevant luminescence spectra are presented in Figures 9 and 10.

Figure 9 shows the spectra for GaP/PGMA-co-POEGMA nanocomposites. Comparing the results for the nanocomposites prepared from GaP powder or suspension (Figure 9, spectra 1 and 2 respectively), it was established that the best quality have the nanocomposites obtained from the nanoparticles stored as a suspension in a suitable liquid (see spectrum 2).

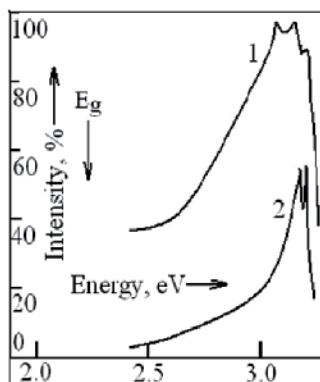


Figure 9. Spectra of luminescence from GaP/ PGMA-co-POEGMA nanocomposites. Nanoparticles have been prepared using white P by mild aqueous synthesis and stored as the dry powder (spectrum 1) or suspension in a liquid (spectrum 2).

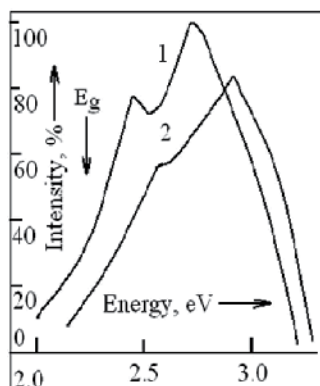


Figure 10. Luminescence spectra of 2 GaP/BPVE nanocomposites produced on the base of 2 parties of GaP nanoparticles prepared using different conditions.

According to our measurements, the matrix polymers PGMA-co-POEGMA or BPVE used in this work provide no contribution to the spectra of luminescence of the based on these matrixes GaP nanocomposites presented in Figures 9 and 10, so, the nanocomposite spectra co-

incide with those obtained from the relevant GaP powders or suspensions. We note that in the GaP/BPVE nanocomposite the position of the luminescent maximum can be changed between 2.5 – 3.2 eV and the brightness is 20-30 more than in the PGMA and PGMA-co-POEGMA matrixes. We explain the broadening of the luminescence band and the shift of its maximum to low photon energies in luminescence of the nanocomposite based on the GaP powder in Figure 9, spectrum 1, by the presence of the nanoparticles with the dimensions of 10-100 nm in the powder. Meanwhile, suspensions containing the 10 nm nanoparticles exhibit pronounced quantum confinement effects since this diameter equals the Bohr diameter of the bound exciton in GaP.

Figures 9 and 10 present a clear image of the quantum confinement effect in the GaP nanoparticles. In accord with our data [28-30] the shift is about a few tenths of eV and, obviously, it is impossible to explain only through this effect the dramatic 1 eV enhancement to the region of luminescence at 300 K on the high-energy side of the spectrum.

In order to explain this interesting phenomenon we postulate that the nanocrystals, much like the ideal long-term ordered bulk GaP single crystals, exhibit this huge increase in blue-shifted luminescence due to: (a) negligibly small influence of defects and non-radiative recombination of electron-hole pairs and very high efficiency of their radiative annihilation, (b) high perfection of nanocrystal lattice, and (c) high transparency of nanocrystals due to their small dimensions for the light emitted from high points of the GaP Brillouin zones, for instance, in the direct transitions $\Gamma^1_c - \Gamma^{15}_v$ between the conductive and valence bands with the photon energy at 300°K equal to 2.8 eV [40] and (d) high efficiency of this so called “hot” luminescence.

Our first attempts to prepare GaP nanoparticles [26] yielded room temperature luminescence with maximum shifted only to 2.4 eV in comparison with the new maximum at 3.2 eV. It confirms significant achievements in technology of GaP nanoparticles and GaP/polymers nanocomposites. On the base of these improved technologies for preparation of GaP nanoparticles and GaP/polymer nanocomposites we can change within the broad limits the main parameters of luminescence and expect to create a framework for novel light emissive device structures using dramatic 1 eV expansion of GaP luminescence to UV region.

The film device structures demonstrate broadband luminescence in the region from UV until yellow-red with controlled width and position of maximum with the luminous intensity up to 1 cd compared with industrial light emitting diodes.

4. Comparison of properties of the GaP nanocrystals and perfect bulk single crystals

Jointly with Refs. [1-31] this section is a generalization of the results on long-term observation of luminescence, absorption, Raman light scattering, and microhardness in bulk semiconductors in comparison with some properties of the best to the moment GaP nanocrystals. We show that the combination of these characterization techniques elucidates the evolution of these crystals over the course of many years, the ordered state brought about by pro-

longed room-temperature thermal annealing, and the interesting optical properties that accompany such ordering. We demonstrate that long-term natural stimuli improve the perfection of our crystals, which can lead to novel heterogeneous systems and new semiconductor devices with high temporal stability.

Our unique collection of long-term ordered perfect GaP single crystals gives opportunities to find deep fundamental analogies in properties of the perfect single crystals and nanoparticles as well as to predict and to realize in nanoparticles and perfect bulk crystals new interesting properties and applications.

The long-term ordering of doped GaP and other semiconductors has been observed as an interesting accompanying process, which can only be studied in the situation when one has a unique set of samples and the persistence to observe them over decade time scales.

Any attempt to accelerate the above noted processes, for instance, through annealing of GaP at increased temperatures cannot be successful because high-temperature processing results in thermal decomposition (due to P desorption) instead of improved crystal quality. Therefore successful thermal processing of GaP can only take place at temperatures below its sublimation temperature, requiring a longer annealing time. Evaluated within the framework of the Ising model the characteristic time of the substitution reaction during N diffusion along P sites in GaP:N crystals at room temperature constitutes 10 -15 years [5]. Hence, the observations of luminescence of the crystals made in the sixties and the nineties were then compared with the results obtained in 2009-2012 in closed experimental conditions.

The pure and doped GaP crystals discussed herein were prepared nearly 50 years ago. Throughout the decades they have been used to investigate electro- and photoluminescence (PL), photoconductivity, bound excitons, nonlinear optics, and other phenomena. Accordingly, it is of interest also to monitor the change in crystal quality over the course of several decades while the crystal is held under ambient conditions.

More specifically, since 2005, we have analyzed the optical and mechanical properties of single crystalline Si, some III-V semiconductors, and their ternary analog CdIn_2S_4 , all of which were grown in the 1960s. Comparison of the properties of the same crystals has been performed in the 1960s, 1970s, 1980s, 1990s [1-12], and during 2000s [13-25] along with those of newly made GaP nanocrystals [26-28] and freshly prepared bulk single crystals [19-23]. We improved in the preparation of GaP nanocrystals the known methods of hydrothermal and colloidal synthesis taking into account that success of our activity depends on optimal choice of the types of chemical reactions, necessary chemicals and their purity, conditions of the synthesis (control accuracy, temperature, pressure, duration, etc.), methods and quality of purification of the nanocrystals, storage conditions for nanoparticles used in the further operations of fabrication of the GaP/nanocomposites.

Single crystals of semiconductors grown under laboratory conditions naturally contain a varied assortment of defects such as displaced host and impurity atoms, vacancies, dislocations, and impurity clusters. These defects result from the relatively rapid growth conditions and inevitably lead to the deterioration of the mechanical, electric, and optical properties of the material, and therefore to rapid degradation of the associated devices.

Different defects of high concentration in freshly prepared GaP single crystals completely suppress any luminescence at room temperature due to negligible quantity of free path for non-equilibrium electron-hole pairs between the defects and their non-radiative recombination, while the quantum theory predicts their free movement in the field of an ideal crystal lattice. The long-term ordered and therefore close-to-ideal crystals demonstrate bright luminescence and stimulated emission repeating behavior of the best nanoparticles with pronounced quantum confinement effects. These perfect crystals due to their unique mechanical and optical properties are useful for application in top-quality optoelectronic devices as well as they are a new object for development of fundamentals of solid state physics, nanotechnology and crystal growth.

Continuing generalization of data on improvement of properties from semiconductor GaP:N crystals prepared nearly 50 years ago and their convergence to the behavior of GaP nanoparticles, here we discuss only the most interesting for fundamentals of solid state physics and application in optoelectronics and photonics data.

1. Over time, driving forces such as diffusion along concentration gradients, strain relaxation associated with clustering, and minimization of the free energy associated with properly directed chemical bonds between host atoms result in ordered redistribution of impurities and host atoms in a crystal.
2. We observe in the long-term ordered GaP:N single crystals a new type of the crystal lattice, where host atoms occupy their equilibrium positions, while impurities divide the lattice in the short chains of equal length in which the host atoms develop harmonic vibrations.
3. The nearly half-centennial evolution of the GaP:N luminescence and its other optical and mechanical properties are interpreted as the result of both volumetrically ordered N impurities and the formation of an ordered crystal-like bound exciton system. The highly ordered nature of this new host and excitonic lattices increases the radiative recombination efficiency and makes possible the creation of advanced non-linear optical media for optoelectronic applications.

Taking into account the above-mentioned results, a model for the crystal lattice and its behavior at a high level of optical excitation for 40-year-old ordered N-doped GaP have been suggested [3]. At relevant concentrations of N, the anion sub-lattice can be represented as a row of anions where N substitutes for P atoms with the period equal to the Bohr diameter of the bound exciton in GaP (approximately 10 nm). At some level of excitation, all the N sites will be filled by excitons, thereby creating an excitonic crystal which is a new phenomenon in solid-state physics and a very interesting object for application in optoelectronics and nonlinear optics [3, 30].

The perfect ordered GaP:N crystals demonstrate uniform luminescence from a broad excitonic band instead of the narrow zero-phonon line and its phonon replica in disordered and partly ordered (25-year-old) crystals due to the ordered crystals having no discrete impurity level in the forbidden gap. To the best of our knowledge, the transformation of a discrete level within the forbidden gap into an excitonic band is observed for the first time. In this

case, the impurity atoms regularly occupy the host lattice sites and affect the band structure of the crystals, which is now a dilute solid solution of GaP-GaN rather than GaP doped by occasionally located N atoms.

As noted previously, the luminescence of fresh doped and undoped crystals could be observed only at temperatures below about 80 K. The luminescence band and lines were always seen at photon energies less than the value of the forbidden gap (2.3 eV). Now, after 50 years, luminescence of the long-term-ordered bulk crystals similar to the GaP nanocrystals [27-31] is clearly detected in the region from 2.0 eV to 3.0 eV at room temperature [13-25]. We believe, in the long-term-ordered bulk crystals this considerable extension of the region of luminescence at 300°K to the high-energy side of the spectrum is due to: (a) a very small concentration of defects, (b) low contribution of nonradiative electron-hole recombination, (c) considerable improvement of crystal lattice, (d) high transparency of perfect crystals, and (e) low probability of phonon emission at indirect transition.

Earlier, in freshly prepared crystals we observed a clear stimulated emission from a GaP:N resonator at 80 K [4] as well as so called superluminescence from the GaP single crystals. Presently, our ordered crystals have a bright luminescence at room temperature that implies their perfection and very lower light losses. Currently we demonstrate [19, 20, 24, 29, 30] that the stimulated emission is developed even at room temperature by direct electron-hole recombination of an electron at the bottom of the conduction band with a hole at the top of the valence band and the LO phonon absorption.

We also have demonstrated the considerable improvement of quality of GaP nanocrystals as the result of elaboration of an optimal for them nanotechnology. Figure 11 compares the luminescence spectra of our long-term (up to 50 years) ordered GaP single crystals (spectrum 1) to that from high quality GaP nanoparticles [27-31] and their GaP nanoparticles/polymers nanocomposites [34-36].

The best quality GaP nanoparticles have been prepared by hydrothermal or colloidal synthesis from white phosphorus at decreased temperature (125°C) and intense ultrasonication.

Comparing the results for the nanocomposites prepared from GaP powder or suspension (Figure 11, spectra 2 and 3 respectively), it was established that the maximum shift to ultraviolet and the best quality in general have the nanocomposites obtained from the nanoparticles stored as a suspension in a suitable liquid.

Nanocrystals stored as dry powder demonstrate rather broad luminescent band with maximum at 2.8 eV (Figure 11, spectrum 2), while the nanocrystals of about 10 nm sizes, thoroughly separated and distributed in a suspension, that prevent their coagulation, mechanical and optical interaction, exhibit bright narrow-band luminescence with maximum at 3.2 eV, approximately 1 eV above the position of the absorption edge in GaP at 300°K (Figure 11, spectrum 3). The thoroughly washed, ultrasonicated and dried nanopowders as well as their specially prepared suspensions have been used for fabrication of blue light emissive GaP nanocomposites on the base of some optically and mechanically compatible with GaP polymers.

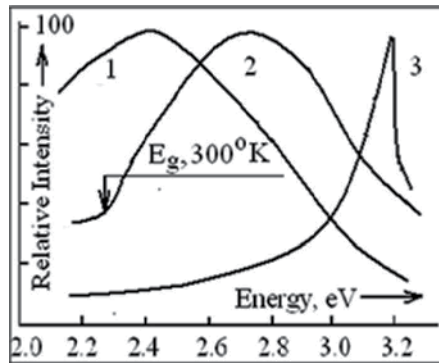


Figure 11. Luminescence of perfect bulk GaP single crystals (1) in comparison with the luminescence of GaP nanoparticles and GaP/polymers nanocomposites (2-3). Nanoparticles prepared from white P by mild aqueous or colloidal synthesis at decreased temperature, stored as the dry powder (spectrum 2) or suspension in a liquid (spectrum 3).

According to our measurements, the matrix polymers PGMA-co-POEGMA or BPVE used in this work provide no contribution to the spectra of luminescence of the based on these matrixes, so, the nanocomposite spectra coincide with those obtained from the relevant GaP powders or suspensions.

We note that in the GaP/BPVE nanocomposite the position of the luminescent maximum can be changed between 2.5 – 3.2 eV and the brightness is 20-30 more than in the PGMA and PGMA-co-POEGMA matrixes. We explain the broadening of the luminescence band and the shift of its maximum to low photon energies in luminescence of the nanocomposite based on the GaP powder by presence in the powder of the nanoparticles with the different dimensions between 10-100 nm. Meanwhile, the nanocomposites on the base of the suspensions containing only approximately 10 nm nanoparticles, exhibit bright luminescence with maximum at 3.2 eV due to high transparency of 10 nm nanoparticles for these high energy emitted photons and pronounced quantum confinement effects since this diameter equals the Bohr diameter of the bound exciton in GaP.

In accordance with previous data [27-31, 34-36] the shift due to the quantum confinement effects is about a few tenths of eV and, obviously, it is impossible to explain only through this effect the dramatic 1 eV expansion of the region of luminescence at 300 K to the high-energy side of the spectrum.

In order to explain this interesting phenomenon we postulate that the nanocrystals, much like the ideal long-term ordered bulk GaP single crystals, exhibit this huge increase in blue-shifted luminescence due to: (a) negligibly small influence of defects and non-radiative recombination of electron-hole pairs and very high efficiency of their radiative annihilation, (b) high perfection of nanocrystal lattice, and (d) high transparency of nanocrystals due to their small dimensions for the light emitted from high points of the GaP Brillouin zones, for instance, in the direct transitions $\Gamma_1^c - \Gamma_{15}^v$ between the conductive and valence bands with the photon energy at 300°K equal to 2.8 eV [40] and (e) high efficiency of this so called "hot" luminescence.

Our first attempts to prepare GaP nanoparticles [26] yielded room temperature luminescence with maximum shifted only to 2.4 eV in comparison with the new maximum at 3.2 eV. It confirms significant achievements in technology of GaP nanoparticles and GaP/polymers nanocomposites. On the base of these improved technologies for preparation of GaP nanoparticles and GaP/polymer nanocomposites we can change within the broad limits the main parameters of luminescence and expect to create a framework for novel light emissive device structures using dramatic 1 eV expansion of GaP luminescence to UV region.

Semiconductor nanoparticles were introduced into materials science and engineering mainly that to avoid limitations inherent to freshly grown semiconductors with a lot of different defects. The long-term ordered and therefore close to ideal crystals repeat behavior of the best nanoparticles with pronounced quantum confinement effect. These perfect crystals are useful for application in top-quality optoelectronic devices as well as they are a new object for development of fundamentals of solid state physics.

4.1. Conclusions

This study of long-term convergence of bulk- and nanocrystal properties brings a novel perspective to improving the quality of semiconductor crystals. The unique collection of pure and doped crystals of semiconductors grown in the 1960s provides an opportunity to observe the long term evolution of properties of these key electronic materials. During this almost half-centennial systematic investigation we have established the main trends of the evolution of their optoelectronic and mechanical properties. It was shown that these stimuli to improve quality of the crystal lattice are the consequence of thermodynamic driving forces and prevail over tendencies that would favor disorder. For the first time, to the best of our knowledge, we have observed a new type of the crystal lattice where the host atoms occupy their proper (equilibrium) positions in the crystal field, while the impurities, once periodically inserted into the lattice, divide it in the short chains of equal length, where the host atoms develop harmonic vibrations. This periodic substitution of a host atom by an impurity allows the impurity to participate in the formation of the crystal's energy bands. It leads to the change in the value of the forbidden energy gap, to the appearance of a crystalline excitonic phase, and to the broad energy bands instead of the energy levels of bound excitons. The high perfection of this new lattice leads to the abrupt decrease of non-radiative mechanisms of electron-hole recombination, to both the relevant increase of efficiency and spectral range of luminescence and to the stimulated emission of light due to its amplification inside the well arranged, defect-free medium of the crystal. The further development of techniques for the growth of thin films and bulk crystals with ordered distribution of impurities and the proper localization of host atoms inside the lattice should be a high priority.

This long-term evolution of the important properties of our unique collection of semiconductor single crystals promises a novel approach to the development of a new generation of optoelectronic devices. The combined methods of laser assisted and molecular beam epitaxies [41-43] will be applied to fabrication of device structures with artificial periodicity;

together with classic methods of crystal growth, can be employed to realize impurity ordering that would yield new types of nanostructures and enhanced optoelectronic device performance.

Our long-term ordered and therefore close to ideal crystals repeat behavior of the best nanoparticles with pronounced quantum confinement effect. These perfect crystals are useful for application in top-quality optoelectronic devices as well as they are a new object for development of fundamentals of solid state physics.

For the first time we also show that well-aged GaP bulk crystals as well as high quality GaP nanoparticles have no essential difference in their luminescence behavior, brightness or spectral position of the emitted light. The long-term ordered and therefore close to ideal crystals repeat behavior of the best nanoparticles with pronounced quantum confinement effect. These perfect crystals are useful for application in top-quality optoelectronic devices as well as they are a new object for development of fundamentals of solid state physics.

Especially important for application in new generation of light emissive devices is the discovered in framework of the Project [31] dramatic expansion of luminescence region in GaP perfect bulk single crystals as well as in the best prepared GaP nanocrystals and based on them composites with transparent polymers. The broad discussion and dissemination of our results will stimulate development of our further collaboration with reliable partners from the USA, Italy, Romania, France and other countries.

Acknowledgements

The authors are very grateful to the US Department of State, Institute of International Exchange, Washington, DC, The US Air Force Office for Scientific Research, the US Office of Naval Research Global, Civilian R&D Foundation, Arlington, VA, Science & Technology Center in Ukraine, Clemson University, SC, University of Central Florida, FL, Istituto di elettronica dello stato solido, CNR, Rome, Italy, Università degli studi, Cagliari, Italy, Joffe Physico-Technical Institute, St.Petersburg State Polytechnical University, Russia, Institute of Applied Physics and Academy of Sciences of Moldova for support and attention to this protracted (1963-present time) research.

Author details

Sergei L. Pyshkin^{1,2*} and John Ballato^{1,2}

*Address all correspondence to: spyshki@clemson.edu

1 Academy of Sciences of Moldova, Republic of Moldova

2 Clemson University, United States of America

References

- [1] Goryunova, N. A., Pyshkin, S. L., Borshchevskii, A. S., Radautsan, S. I., Kaliujnaya, G. A., Maximov, Yu. I., & Peskov, O. G. (July 1966). Influence of Impurities and Crystallisation Conditions on Growth of Platelet GaP Crystals. Paper presented at Proceedings of the Symposium on Crystal Growth at the 7th Int. Crystallography Congress, Moscow, published in ed. Sheftal NN, New York J. Growth of Crystals 1969, 8, 68-72.
- [2] Ashkinadze, B. M., Pyshkin, S. L., Bobrysheva, A. I., Vituu, E. V., Kovarsky, V. A., Lelyakov, A. V., Moskalenko, S. A., & Radautsan, S. I. (1968, July 23-29). Some non-linear optical effects in GaP. In: *Proceedings of the IXth International Conference on the Physics of Semiconductors*, 2-1189, Moscow.
- [3] Pyshkin, S., & Zifudin, L. (1974). Excitons in Highly Optically Excited Gallium Phosphide. *J. Lumin.*, 9-302.
- [4] Pyshkin, S.L. (1975). Stimulated Emission in Gallium Phosphide. *Sov. Phys. Dokl.*, 19-845, Presented by Nobel Prize Laureate Prokhorov AM.
- [5] Pyshkin, S. L., Radautsan, S. I., et al. (1990). Processes of Long-Lasting Ordering in Crystals with a Partly Inverse Spinel Structure. *Sov. Phys. Dokl.*, 35(4), 301-304.
- [6] Pyshkin, S. (1975). Luminescence of GaP:N:Sm Crystals. *J. Sov. Phys. Semicond.*, 8, 912-13.
- [7] Pyshkin, S., Radautsan, S., & Zenchenko, V. (1990). Raman Spectra of Cd-In-S with Different Cation-Sublattice Ordering. *Sov. Phys. Dokl.*, 35(12), 1064-67.
- [8] Pyshkin, S. L., & Anedda, A. (1993). Preparation and properties of GaP doped by rare-earth elements. In: Proceedings of the Materials Research Society (MRS) Spring Meeting, Symposium E, 301-192.
- [9] Pyshkin, S. L., Anedda, A., Congiu, F., & Mura, A. (1993). Luminescence of the GaP:N Ordered System. *J. Pure Appl. Opt.*, 2-499.
- [10] Pyshkin, S. L., & Anedda, A. (1998). Time-Dependent Behaviour of Antistructural Defects and Impurities in Cd-In-S and GaP. *ICTMC-XI (Salford, UK, 1997)*, Institute of Physics Conference Series, Ternary and Multinary Compounds, 152 Section E, 785-89.
- [11] Pyshkin, S.L. (invited, Indianapolis, 2001). Luminescence of Long-Time Ordered GaP:N. The 103rd ACerS Annual Meeting, ACerS Transaction series 2002; 126 3-10.
- [12] Pyshkin, S. L. (2002). Bound Excitons in Long-Time Ordered GaP:N. *Moldavian Journal of the Physical Sciences*, 1(3), 14-19.
- [13] Pyshkin, S. L., Zhitaru, R. P., & Ballato, J. (2007). Long-term evolution of optical and mechanical properties in Gallium Phosphide. In: Proceedings of the XVII St. Peters-

- burg Readings on the Problems of Durability, Devoted to the 90th Birthday of Prof. A.N. Orlov, 2-174.
- [14] Pyshkin, S. L., Zhitaru, R. P., & Ballato, J. (2007, Sept 16-20). Modification of crystal lattice by impurity ordering in GaP. Detroit, MI. Proceedings of the 2007 MS&T Conference, International Symposium on Defects, Transport and Related Phenomena, 303-310.
- [15] Pyshkin, S. L., Ballato, J., & Chumanov, G. (2007). Raman Light Scattering from Long-term Ordered GaP Single Crystals. *J. Opt. A: Pure Appl. Opt.*, 9-33.
- [16] Pyshkin, S. L., Ballato, J., Bass, M., & Turri, G. (2008). Luminescence of Long-Term Ordered Pure and Doped Gallium Phosphide (invited). *J. Electronic Materials*, 37(4), 388-395, TMS 2007 Annual Meeting & Exhibition, Orlando, FL, February - March 2007, Symposium "Recent Developments in Semiconductor, Electro Optic and Radio Frequency Materials".
- [17] Pyshkin, S., & Ballato, J. (2008). Long-term ordered crystals and their multi-layered film analogues. *The MS&T Conference, Pittsburgh, Symposium on Fundamentals & Characterization, Session "Recent Advances in Growth of Thin Film Materials"*, Proceedings, 889-900.
- [18] Pyshkin, S. L., Ballato, J., Bass, M., & Turri, G. (2008). New Phenomena in Luminescence of Gallium Phosphide (invited). *J. Electron. Mater.*, 37(4), 388-395, The 2007 TMS Annual Meeting and Exhibition, March 9-13, New Orleans, LA, Symposium: Advances in Semiconductor, Electro Optic and Radio Frequency Materials.
- [19] Pyshkin, S., Ballato, J., Bass, M., Chumanov, G., & Turri, G. (2009, Feb 15-19). Properties of the long-term ordered semiconductors. San Francisco. *The TMS Annual Meeting and Exhibition, Suppl. Proceedings*, 3, 477-484.
- [20] Pyshkin, S., Ballato, J., Bass, M., & Turri, G. (2009). Evolution of Luminescence from Doped Gallium Phosphide over 40 Years. *J. Electronic Materials*, 38(5), 640-646.
- [21] Pyshkin, S., Ballato, J., Chumanov, G., Bass, M., Turri, G., Zhitaru, R., & Tazlavan, V. (2008, Sept 23-26). Optical and Mechanical Properties of Long-Term Ordered Semiconductors. Paper presented at The 4th International Conference on Materials Science and Condensed Matter Physics, Kishinev. *Moldavian Journal of the Physical Sciences*, 8(3-4), 287-295.
- [22] Pyshkin, Sergei L., Ballato, John, Bass, Michael, Chumanov, George, & Turri, Giorgio. (2009, Sept 15-19, 2008). Time-Dependent Evolution of Crystal Lattice, Defects and Impurities in CdIn₂S₄ and GaP. Paper presented at The 16th Int Conference on Ternary and Multinary Compounds (ICTMC16), Berlin. *Phys. Status Solidi*, 6(5), 1112-1115.
- [23] Pyshkin, S., Zhitaru, R., Ballato, J., Chumanov, G., & Bass, M. (2009, October 24-29). Structural characterization of long-term ordered semiconductors. In: *The MS&T Con-*

- ference, Pittsburgh, Int. Symposium: "Fundamentals & Characterization", Session "Recent Advances in Structural Characterization of Materials", Proceedings, 698-709.
- [24] Pyshkin, Sergei, & Ballato, John. (2010). Evolution of Optical and Mechanical Properties of Semiconductors over 40 Years. *J. Electronic Materials*, 39(6), 635-641.
- [25] Pyshkin, Sergei, Ballato, John, Mura, Andrea, & Marceddu, Marco. (2010, February). Luminescence of the GaP:N long-term ordered single crystals. Seattle, WA, USA. In: *The 2010 TMS Annual Meetings*, Suppl. Proceedings, 3-47.
- [26] Pyshkin, S. L., Ballato, J., Chumanov, G., Di Maio, J., & Saha, A. K. (2006). Preparation and characterization of nanocrystalline GaP. Boston, MA. *The NSTI-Nanotech Conference*, www.nsti.org, 0-97679-858-1.
- [27] Pyshkin, S., Ballato, J., Chumanov, G., Tsyntsaru, N., & Rusu, E. (2010). Preparation and characterization of nanocrystalline GaP for advanced light emissive device structures. Anaheim, CA. In: *The 2010 NSTI-Nanotech Conference*, Proceedings, www.nsti.org, 978-1-43983-401-5, 1, 522-525.
- [28] Pyshkin, S. L., Ballato, J., Belevschii, S., Rusu, E., Racu, A., & Van Der Veer, D. (2011, June 13-16). Synthesis and characterization of GaP nanoparticles for light emissive devices. Boston, MA. *The 2011 NSTI-Nanotech Conference*, Proceedings, www.nsti.org, 978-1-43987-142-3, 327-330.
- [29] Pyshkin, S., & Ballato, J. (2011, October 17-21). Long-Term Convergence of Bulk- and Nanocrystal Properties. Paper presented at The 2010 Materials Science & Technology Conference, Symposium: Advances and Applications in Electroceramics, Houston, Texas. *Ceramic Transactions*, 226-77, 0002-7820.
- [30] Pyshkin, S., & Ballato, J. (2011). Long-Term Convergence of Bulk- and Nanocrystal Properties. In: *Chapter 19, InTech Open Access book "Optoelectronics- Materials and Technics"*, 978-9-53307-276-0.
- [31] Pyshkin, S. (2009-2012). *Project Manager. Moldova/US/Italy/France/Romania STCU*, www.stcu.int, Project 4610 "Advanced Light Emissive Device Structures".
- [32] Pyshkin, Sergei, & Ballato, John. (2005). Advanced Light Emissive Composite Materials for Integrated Optics. In: *MS&T Conference, Symposium: The Physics and Materials Challenges for Integrated Optics - A Step in the Future for Photonic Devices, Pittsburgh Proceedings*, 3-13.
- [33] Ballato, J., & Pyshkin, S. L. (2006). Advanced Light Emissive Materials for Novel Optical Displays, Lasers, Waveguides, and Amplifiers. *Moldavian J. of Physical Sciences*, 5(2), 195-208.
- [34] Pyshkin, S. L., Ballato, J., Luzinov, I., & Zdyrko, B. (2010, June 21-25). Fabrication and characterization of the GaP/ polymer nanocomposites for advanced light emissive device structures. Anaheim, CA. In: *The 2010 NSTI-Nanotech. Conference*, Proceedings, www.nsti.org, 978-1-43983-401-5, 1, 772-775.

- [35] Pyshkin, S. L., Ballato, J., Luzinov, I., & Zdyrko, B. (2011). Fabrication and Characterization of GaP/Polymer Nanocomposites for Advanced Light Emissive Device Structures. *Journal of Nanoparticle Research*, 13-5565.
- [36] Pyshkin, Sergei. L., & Ballato, John. (2012, March 11-15). Dramatic Expansion of Luminescence Region in GaP/Polymer Nanocomposites. Orlando, FL, USA. In: *The 2012 TMS Annual Meetings*, Supplemental Proc., 1Materials Processing and Interfaces, 353-359.
- [37] Shanmin, Gao, Jun, Lu, Nan, Chen, Yan, Zhao, & Yi, Xie. (2002). Aqueous Synthesis of III-V Semiconductor GaP and InP Exhibiting Pronounced Quantum Confinement. *Chem. Commun.*, 3064-3065.
- [38] Zhengang, Liu, Yujun, Bai, Deliang, Cui, & Qilong, Wang. (2003). Preliminary Insight into the Formation Process of InP and GaP Nanocrystals. *Solid State Sciences*, 5-1037.
- [39] Zhao-Chun, Zhang, & Bao-Ping, Wang. (2009). Diamond and Oxidized Disordered Graphite on the Surface of Gallium Phosphide. *Nanoparticles. Syst. Charact.*, 26-53.
- [40] Zallen, R., & Paul, W. (1964). Band Structure of Gallium Phosphide from Optical Experiments at High Pressure. *Phys. Rev.*, 134 A, 1628-1641.
- [41] Pyshkin, S. L. (1995). Heterostructures (CaSrBa)F₂ on InP for Optoelectronics. *Report to the US AFOSR/EOARD on the Contract* [SPQ-94-4098].
- [42] Pyshkin, S. L., Grekov, V. P., Lorenzo, J. P., Novikov, S. V., & Pyshkin, K. S. (1996). Reduced Temperature Growth and Characterization of InP/SrF₂/InP(100) Heterostructure, Physics and Applications of Non-Crystalline Semiconductors in Optoelectronics, NATO ASI Series. *High Technology*, 3(36), 468-471.
- [43] Pyshkin, S. (1997). CdF₂:Er/CaF₂/Si(111) Heterostructure for EL Displays. *Report to the US AFOSR/EOARD on the Contract* [SPQ-97-4011].

ZnO-Based Light-Emitting Diodes

J.C. Fan, S.L. Chang and Z. Xie

Additional information is available at the end of the chapter

<http://dx.doi.org/10.5772/51181>

1. Introduction

In the past decade, light-emitting diodes (LEDs) based on wideband gap semiconductor have attracted considerable attention due to its potential optoelectronic applications in illumination, mobile appliances, automotive and displays [1]. Among the available wide band gap semiconductors, zinc oxide, with a large direct band gap of 3.37eV, is a promising candidate because of characteristic features such as a large exciton binding energy of 60meV, and the realization of band gap engineering to create barrier layers and quantum wells with little lattice mismatch. ZnO crystallizes in the wurtzite structure, the same as GaN, but, in contrast, large ZnO single crystal can be fabricated [2]. Furthermore, ZnO is inexpensive, chemically stable, easy to prepare and etch, and nontoxic, which also make the fabrication of ZnO-based optical devices an attractive prospect. The commercial success of GaN-based optoelectronic and electronic devices trig the interest in ZnO-based devices [2-4].

Recently, the fabrication of *p*-type ZnO has made great progress by mono-doping group V elements (N, P, As, and Sb) and co-doping III-V elements with various technologies, such as ion implantation, pulsed laser deposition (PLD), molecular beam epitaxy (MBE) [2,3]. A number of researchers have reported the development of homojunction ZnO LEDs and heterojunction LEDs using *n*-ZnO deposited on *p*-type layers of GaN, AlGa_N, conducting oxides, or *p*-ZnO deposited on a *n*-type layer of GaN [1,3].

Figure1a shows the schematic structure of a typical ZnO homostructural *p*-*i*-*n* junction prepared by Tsukaza et al [5]. The I-V curve of the device displayed the good rectification with a threshold voltage of about 7V (Figure1b). The electroluminescence (EL) spectrum from the *p*-*i*-*n* junction (blue) and photoluminescence (PL) spectrum of a *p*-type ZnO film at 300K were shown in Figure1c, which indicated that ZnO was a potential material for making short-wavelength optoelectronic devices, such as LEDs for display, solid-state illumination and photodetector.

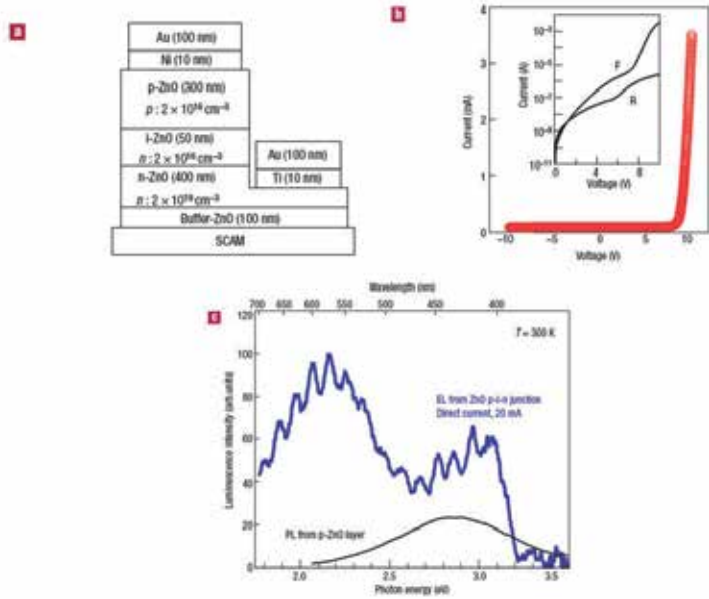


Figure 1. ZnO homostructural p-i-n junction shows rectifying current-voltage characteristics and electroluminescence (EL) in forward bias at room-temperature. (a), The structure of a typical p-i-n junction LED. (b), Current-voltage characteristics of a p-i-n junction. The inset has logarithmic scale in current with F and R denoting forward and reverse bias conditions, respectively. (c), Electroluminescence spectrum from the p-i-n junction (blue) and photoluminescence (PL) spectrum of a p-type ZnO film measured at 300 K. The p-i-n junction was operated by feeding in a direct current of 20 mA. From Ref.[5].

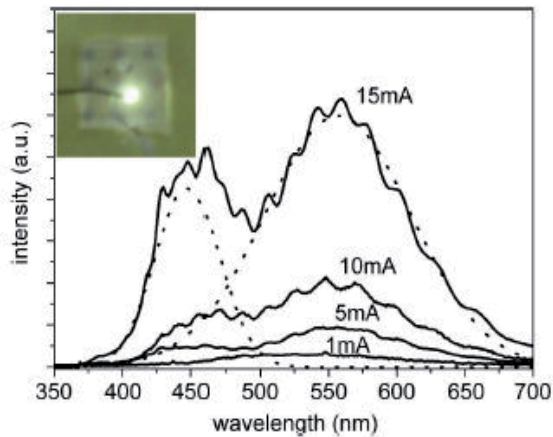


Figure 2. Room-temperature EL spectra of the n-ZnO/p-GaN heterojunction LED measured at various dc injection currents from 1 to 15mA at reverse breakdown biases. (Inset) EL image of the LED in a bright room. From Ref. [6].

White-light electroluminescence from n-ZnO/p-GaN heterojunction LED was reported [6]. The spectrum range from 400 to 700nm is caused by the carrier recombination at the interface between n-ZnO and p-GaN, as shown in Figure2, which makes ZnO as a strong candidates for solid-state light.

Currently, ZnO-based LEDs are leaping from lab to factory. A dozen or so companies are developing ultraviolet and white LEDs for market. The coloured ZnO-based LEDs have been produced by Start-up company MOXtronics, which shows its full-colour potential. Although the efficiency of these LEDs is not high, improvements are rapid and the emitters have the potential to outperform their GaN rivals. Figure3 shows some EL images of ZnO-based LEDs.

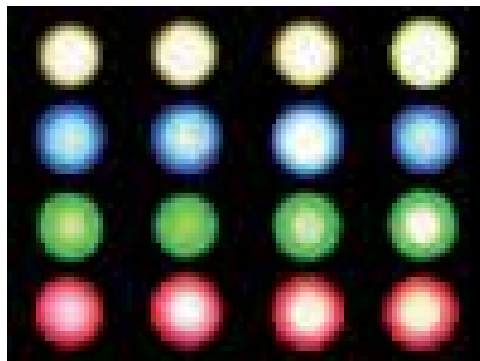


Figure 3. Some EL images of ZnO-based LEDs. From Ref. [7].

In this paper, based on the introduction of the band-gap engineering and doping in ZnO, we discuss the ZnO-based LEDs, comprehensively. We first discuss the band-gap engineering in ZnO, which is a very important technique to design ZnO-based LEDs. We then present the p- and n-types doping in ZnO. High quality n-type and/or p-type ZnO are necessary to prepare ZnO-based LEDs. Finally, we review the ZnO-based LEDs. In this part, we discuss homojunction ZnO LEDs and heterojunctions LEDs using *n*-ZnO deposited on *p*-type layers (GaN, AlGaN, conducting oxides, et al) or *p*-ZnO deposited on a *n*-type layer (GaN, Si, et al), comprehensively.

2. Band gap engineering in ZnO

Band gap engineering is the process of controlling or altering the band gap of a material by controlling the composition of certain semiconductor alloys. It is well known that tailoring of the energy band gap in semiconductors by band-gap engineering is important to create barrier layers and quantum wells with matching material properties, such as lattice constants, electron affinity for heterostructure device fabrication [2, 3].

Band-gap engineering in ZnO can be achieved by alloying with MgO, CdO or BeO. The energy band gap $E_g(x)$ of ternary semiconductor $A_xZn_{1-x}O$ ($A = \text{Mg, Cd or Be}$) can be calculated by the following equation:

$$E_g(x) = (1-x) E_{ZnO} + x E_{AO} - bx(1-x) \quad (1)$$

where b is the bowing parameter and E_{AO} and E_{ZnO} are the band-gap energies of compounds AO and ZnO, respectively. While adding Mg or Be to ZnO results in an increase in band gap, and adding Cd leads to a decrease in band gap [3, 8].

Both MgO and CdO have the rock-salt structure, which is not the same as the ZnO wurtzite structure. When Mg and Cd contents in ZnO are high, phase separation may be detected, while BeO and ZnO share the same wurtzite structure and phase separation is not observed in BeZnO [2, 8]. Ryu et al studied the band gap of BeZnO and did not observed any phase separation when Be content was varied over the range from 0 to 100mol%. Figure4 shows the a lattice parameter as a function of room-temperature E_g values in $A_xZn_{1-x}O$ alloy. Therefore, theoretically, the energy band gap of $A_xZn_{1-x}O$ can be continuously modulated from 0.9eV (CdO) to 10.6eV (BeO) by changing the A concentration [8]. Han et al reported the band gap energy of the $Be_xZn_{1-x}O$ can be tailored from 3.30eV ($x = 0$) to 4.13eV ($x = 0.28$) by alloying ZnO with BeO [9].

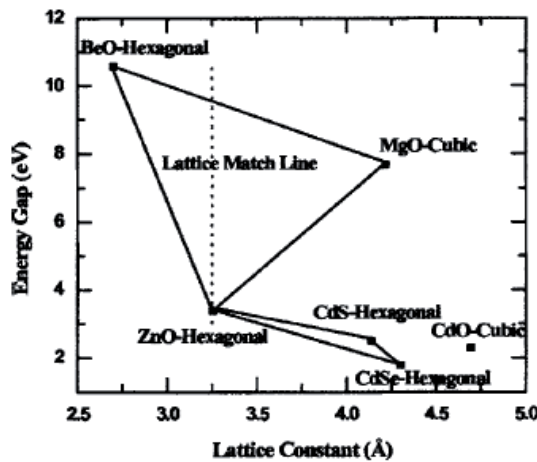


Figure 4. Energy band gaps, lattice constants and crystal structures of selected II-VI compounds. From Ref. [9].

Ohtomo et al investigated the band gap of $Mg_xZn_{1-x}O$ films grown on sapphire by PLD, where x is the atomic fraction [10]. The band gap of $Mg_xZn_{1-x}O$ could be increased to 3.99eV at room temperature as the content of Mg was increased upward to $x = 0.33$. Above 33%, the phase segregation of MgO impurity was observed from the wurtzite $MgZnO$ lattice. Takagi et al reported the growth of wurtzite $MgZnO$ film with Mg concentration of 51% on sapphire by molecular-beam epitaxy [11]. The band gap energy of $Mg_xZn_{1-x}O$ was successfully

turned from 3.3 to 4.5eV with the increase of Mg contents from 0 to 0.5. Tampo et al investigated excitonic optical transition in a $Zn_{1-x}Mg_xO$ alloy grown by radical source molecular beam epitaxy [12]. The strong reflectance peaks at room temperature were detected from 3.42eV ($x=0.05$) to 4.62eV ($x = 0.61$) from ZnMgO layers at room temperature. PL spectra at room temperature were also observed for energies up to 4.06eV ($x = 0.44$). Wassner et al studied the optical and structural properties of MgZnO films with Mg contents between $x = 0$ and $x = 0.37$ grown on sapphire by plasma assisted molecular beam epitaxy using a MgO/ZnMgO buffer layer [13]. In their experiments, the a -lattice parameter was independent from the Mg concentration, whereas the c -lattice parameter decreases from 5.20Å for $x = 0$ to 5.17Å for $x = 0.37$, indicating pseudomorphic growth. The peak position of the band edge luminescence blue shifted up to 4.11eV for $x = 0.37$.

Makino et al investigated the structure and optical properties of $Cd_xZn_{1-x}O$ films grown on sapphire (0001) and $ScAlMgO_4$ substrates by PLD [14]. The band gap of $Cd_xZn_{1-x}O$ films was estimated by $E_g(y) = 3.29 - 4.40y + 5.93y^2$. The band gap narrowing to 2.99eV was achieved by incorporating Cd^{2+} with Cd concentration of 7%. Both lattice parameters a and c increase with the increasing Cd content in ZnO, which was agreement with the larger atomic size of Cd compared with Zn. $Cd_xZn_{1-x}O$ films were also prepared on c -plane sapphires by metal-organic vapor-phase epitaxy. The fundamental band gap was narrowed up to 300meV for a maximum Cd concentration of ~5%, introducing a lattice mismatch of only 0.5% with respect to binary ZnO. Lai et al prepared the $Cd_xZn_{1-x}O$ alloy by conventional solid-state reaction over the composition range and found that CdO effectively decreased the electronic bandgap both in the bulk and near the surface ZnO [15].

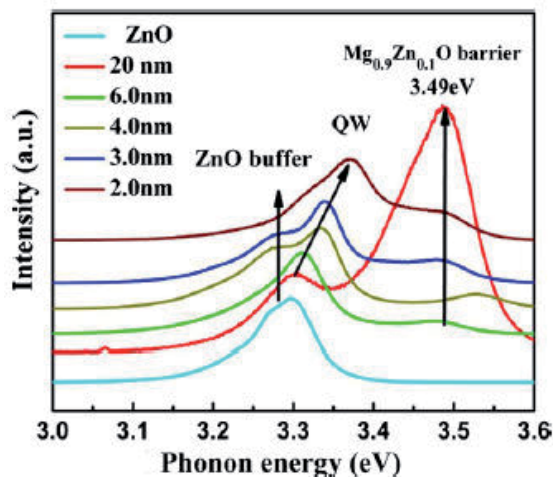


Figure 5. Room temperature PL spectra of ZnO/Zn_{0.9}Mg_{0.1}O SQW with different well width. From Ref. [17].

Using MgZnO as barrier layers, Chauveau et al prepared the nonpolar a -plane (Zn,Mg)O/ZnO quantum wells (QWs) grown by molecular beam epitaxy on r plane sapphire and a plane ZnO substrates [16]. They observed the excitonic transitions were strongly blue-shifted due to the

anisotropic strain state in heteroepitaxial QW and the reduction of structural defects and the improvement of surface morphology were correlated with a strong enhancement of the photoluminescence properties. Su et al investigated the optical properties of ZnO/ZnMgO single quantum well (SQW) prepared by plasma-assisted molecular beam epitaxy [17]. The photoluminescence peak of the SQW shifted from 3.31 to 3.37eV as the well layer thickness was decreased from 6 to 2nm (Figure5). ZnO/MgZnO superlattices were also fabricated by laser molecular-beam epitaxy and the excitonic stimulated emission up to 373K was observed in the superlattices. The emission energy could be tuned between 3.2 and 3.4eV, depending on the well thickness and/or the Mg content in the barrier layers.

3. Doping in ZnO

ZnO has a strong potential for various short-wavelength optoelectronic device applications. To realize these applications, the reliable techniques for fabricating high quality n-type and p-type ZnO need to be established. Undoped ZnO exhibits n-type conduction due to the intrinsic defects, such as the Zinc interstitial (Zn_i) and oxygen vacancy (V_o). It is easy to obtain the high quality n-type ZnO material by doping group-III elements. However, it is a major challenge to dope ZnO to produce p-type semiconductor due to self-compensation from native donor defects and/or hydrogen incorporation. To achieve p-type ZnO, various elements (N, P, As, Sb and Li) have been tried experimentally as p-type dopants with various techniques, such as pulse laser deposition, magnetron sputtering, chemical vapor deposition (CVD), molecular-beam epitaxy, hybrid beam deposition (HBD), metal organic chemical vapor deposition (MOCVD) and thermal oxidation of Zn_3N_2 [2, 3].

3.1. n-type ZnO

A number of researchers investigated the electrical and optical properties of n-type ZnO materials by doping III elements, such as Al, Ga and In, which can easily substitute Zn ions [1-3].

Kim et al reported the high electron concentration and mobility in AZO films grown on sapphire by magnetron sputtering [18]. AZO films exhibited the electron concentrations and mobilities were of the order of $10^{18}cm^{-3}$ and less than $8cm^2/Vs$, respectively, however, when annealed at $900^{\circ}C$, the films showed remarkably improved carrier concentrations and mobilities, e.g., about $10^{20}cm^{-3}$ and $45 - 65 cm^2/Vs$, respectively. Other researchers also reported the improved electrical properties in Al-doped zinc oxide by thermal treatment [19].

Bhosle et al investigated the electrical properties of transparent Ga-doped ZnO films prepared by PLD [20]. Temperature dependent resistivity measurements for the films showed a metal-semiconductor transition, which was rationalized by localization of degenerate electrons. The lowest value of resistivity $1.4 \times 10^{-4} \Omega cm$ was found at 5% Ga. Yamada et al reported the low resistivity Ga-doped ZnO films prepared on glass by ion plating with direct current arc discharge [21]. The ZnO:Ga film with a thickness of 98nm, exhibited a resistivity of $2.4 \times 10^{-4} \Omega cm$, a carrier concentration of $1.1 \times 10^{21}cm^{-3}$ and a Hall mobility of $23.5cm^2/Vs$. Liang et al reported the Ga-doped ZnO films prepared on

glass by magnetron sputtering and found that a carrier concentration exhibited only a slight change with the thickness variations [22].

Wang et al studied the properties of In-doped ZnO crystal by the hydrothermal technique [23]. The indium-doped ZnO crystals have a resistivity lower than $0.015\Omega\text{cm}$ with a free carrier concentration (mostly due to indium donors) of $1.09\times 10^{19}/\text{cm}^3$ at room temperature. Quang et al reported the In-doped ZnO films grown by hydrothermal [24]. The films had a mobility of $4.18\text{--}20.9\text{cm}^2/\text{Vs}$ and a concentration of $6.7\times 10^{18} - 3.2\times 10^{19}/\text{cm}^3$. The In-doped ZnO films with a carrier concentration of $3.22\times 10^{20}/\text{cm}^3$ were grown by sol-gel method [25].

VII elements such as F and Cl are also used as n-type dopants in ZnO, which substituted oxygen ions. Cao et al reported F-doped ZnO grown by PLD with a minimum resistivity of $4.83\times 10^{-4}\Omega\text{cm}$, with a carrier concentration of $5.43\times 10^{20}\text{cm}^{-3}$ and a mobility of $23.8\text{cm}^2/\text{Vs}$ [26]. Chikoidze et al grew Cl-doped ZnO films by MOCVD with a resistivity of $3.6\times 10^{-3}\Omega\text{cm}$ [27].

3.2. p-type ZnO

To realize ZnO-based LEDs, the most important issue is the fabrication of high quality p-type ZnO. However, undoped ZnO exhibits n-type conduction and the reliable p-type doping of the materials remains a major challenge because of the self-compensation from native donor defects (V_{O} and Z_{n}) and/or hydrogen incorporation. Considerable efforts have been made to obtain p-type ZnO by doping different elements (N, P, As, Sb, Li, Na and K) with various techniques [2, 3]. Here, we present the typical results of p-type ZnO materials.

Among all potential p-type dopants for ZnO, N is considered the most promising dopant due to similar ionic radius compared with oxygen. It substitutes O sites in ZnO structure, resulting in the shallow acceptors. N_2 , NO, N_2O , NH_3 and Zn_3N_2 are acted as N sources depended on growth techniques [2, 3]. Liu et al reported p-type ZnO:N films grown on c-sapphire by plasma-assisted molecular beam epitaxy [28]. The anomalous Raman mode at 275cm^{-1} was confirmed to be related to substitution of N for O site (N_{O}) in ZnO. The films exhibited a hole concentration of $2.21\times 10^{16}\text{cm}^{-3}$ and a mobility of $1.33\text{cm}^2/\text{Vs}$. Zeng et al investigated p-type ZnO films prepared on a-plane (11–20) sapphire by MOCVD [29]. The optimized result was achieved at the temperature of 400°C with a resistivity of $1.72\Omega\text{cm}$, a Hall mobility of $1.59\text{cm}^2/\text{Vs}$, and a hole concentration of $2.29\times 10^{18}\text{cm}^{-3}$. Wang et al prepared p-type ZnO films by oxidation of Zn_3N_2 films grown by direct current magnetron sputtering [30]. For oxidation temperature between 350 and 500°C , p-type ZnO:N films were achieved, with a hole concentration of $5.78\times 10^{17}\text{cm}^{-3}$ at 500°C . Kumar et al reported on the growth of p-type N,Ga-codoped ZnO films prepared by sputtering ZnO:Ga₂O₃ target in N_2O ambient [31]. The film deposited on sapphire at 550°C exhibited p-type conduction with a hole concentration of $3.9\times 10^{17}\text{cm}^{-3}$.

Beside N, other group V elements (P, As and Sb) are also used to be acceptor dopants to obtain p-type ZnO. However, first-principle calculations show that X_{O} (P_{O} , As_{O} and Sb_{O}) are deep acceptors and have high acceptor-ionization energies, owing to their large ionic radii as compared to O, which make it impossible for X_{O} to dop ZnO efficiently p-type [32]. We

could not contribute the p-type behaviour in X doped ZnO to X_{O} , simply. Recently, for the large-size-mismatched impurities in ZnO, Limpijumnong et al proposed $X_{\text{Zn}}-2V_{\text{Zn}}$ acceptor model [33]. In the model, X substitute Zn sites, forming a donor, then it induces two Zn vacancy acceptors as a complex form $X_{\text{Zn}}-2V_{\text{Zn}}$. The ionization energy of $As_{\text{Zn}}-2V_{\text{Zn}}$ complex was calculated to be 0.15eV (0.16eV for $Sb_{\text{Zn}}-2V_{\text{Zn}}$).

Xiu et al reported p-type P-doped ZnO films grown by MBE using a GaP effusion cell as a phosphorus dopant source [34]. PL spectra clearly indicated the existence of competitions between $D^0 X$ and $A^0 X$ for the phosphorus-doped ZnO films. The films exhibited a carrier concentration of $6.0 \times 10^{18} \text{ cm}^{-3}$, Hall mobility of $1.5 \text{ cm}^2/\text{Vs}$, and resistivity of $0.7 \Omega\text{cm}$. Kim et al achieved p-type ZnO:P films on a sapphire substrate using phosphorus doping and a thermal annealing process [35]. As-grown n-type ZnO:P prepared by radio-frequency sputtering were converted to p-ZnO:P by an rapid thermal annealing process under a N_2 ambient. The films had a hole concentration of $1.0 \times 10^{17} - 1.7 \times 10^{19}/\text{cm}^3$, a mobility of $0.53 - 3.51 \text{ cm}^2/\text{Vs}$ and a resistivity of $0.59 - 4.4 \Omega\text{cm}$. Pan et al prepared p-type ZnO:P films on the insulating quartz with a hole concentration of $1.84 \times 10^{18} \text{ cm}^{-3}$ by MOCVD [36]. Vaithianathan et al grew p-type ZnO:P films on $Al_2O_3(0001)$ by PLD [37]. The films exhibited a hole concentration of $5.1 \times 10^{14} - 1.5 \times 10^{17} \text{ cm}^{-3}$, a hole mobility of $2.38 - 39.3 \text{ cm}^2 / \text{Vs}$, and a resistivity of $17 - 330 \Omega\text{cm}$.

Ryu et al investigated the electrical properties of As-doped ZnO films on O-ZnO substrates by hybrid beam deposition [38]. The electrical behavior of ZnO:As films changed from intrinsic n-type to highly conductive p-type with increased As dopant concentration. They achieved p-type ZnO:As films with a hole concentration of $4 \times 10^{17} \text{ cm}^{-3}$ and a mobility of $35 \text{ cm}^2/\text{Vs}$. Vaithianathan et al reported As-doped p-type ZnO films using a Zn_3As_2/ZnO target by PLD [39]. As-grown ZnO:As showed n-type conductivity, however, ZnO:As films after annealed at 200°C in N_2 ambient for 2 min exhibited p-type conductivity with the hole concentrations varied between 2.48×10^{17} and $1.18 \times 10^{18} \text{ cm}^{-3}$. Kang et al grew ZnO films on GaAs by sputtering and annealed at 500°C in an oxygen gas pressure of 40 mTorr for 20 min. After annealing, ZnO film on GaAs showed p-type conductivity with a hole concentration of $9.684 \times 10^{19} \text{ cm}^{-3}$, a mobility of $25.37 \text{ cm}^2/\text{Vs}$, and a resistivity of $2.54 \times 10^{-3} \Omega\text{cm}$. The acceptor binding energy was calculated to be 0.1445eV, which was in good agreement with the ionization energy of $As_{\text{Zn}}-2V_{\text{Zn}}$ acceptor complex (0.15eV) [40].

Guo et al reported p-type ZnO:Sb films grown by PLD [41]. The films showed a resistivity of $4.2 - 60 \Omega\text{cm}$, a Hall mobility of $0.5 - 7.7 \text{ cm}^2/\text{Vs}$, and a hole concentration of $1.9 - 2.2 \times 10^{17} \text{ cm}^{-3}$. In the (HR) TEM images of p-type ZnO:Sb, they observed a high density of threading dislocations originating from the film/substrate interface and a large number of partial dislocation loops associated with small stacking faults. Xiu et al fabricated p-type ZnO:Sb films grown on n-Si (100) by MBE [42]. The film had a concentration of $1.7 \times 10^{18} \text{ cm}^{-3}$, and a high mobility of $20.0 \text{ cm}^2/\text{Vs}$ and a low resistivity of $0.2 \Omega\text{cm}$. The acceptor energy level of the Sb dopant was about 0.2eV above the valence band, which was agreement with the ionization energy of $Sb_{\text{Zn}}-2V_{\text{Zn}}$ (0.16eV).

Some researchers prepared p-type ZnO using Group I elements (Li, Na and K) as acceptor dopants. Yi et al fabricated p-type ZnO:Li films grown on quartz substrate by PLD

with a hole concentration of $5.4 \times 10^{18} \text{ cm}^{-3}$ [43]. p-type ZnO:Na films were fabricated on Si substrates by PLD [44]. The hole concentration ranged from 1.5×10^{18} to $1.1 \times 10^{19} \text{ cm}^{-3}$. Wu et al grew K-doped p-type ZnO films on (0001) Al_2O_3 substrates by radio frequency magnetron sputtering [45].

| Growth technique | Structure | Light emission (nm) | Reference |
|-----------------------------|---|---------------------|-----------|
| | n-ZnO/p-GaN | 570 | [46] |
| | n-ZnO/p-GaN | 450, 520 | [47] |
| MBE | n-ZnO:Ga/p-GaN:Mg | 430 | [48] |
| | n-MgZnO/CdZnO/p-GaN | 390, 410 | [49] |
| | n-MgZnO/n-ZnO/p-AlGaIn/p-GaN | 390 | [50] |
| | n-ZnO:Ga/p-GaN:Mg | 430, 440, 480 | [51] |
| Magnetron sputtering | n-ZnO /p-GaN | 400, 400-700 | [52] |
| | n-ZnO:Ga/i-ZnO/p-GaN:Mg | 405, 530, 620 | [53] |
| | n-ZnO/AlN/p-GaN:Mg | 392 | [54] |
| | n-ZnO:Er/p-GaN:Mg | 537, 538 | [55] |
| PLD | p-SrCu ₂ O ₂ /n-ZnO | 382 | [56] |
| | n-ZnO/p-GaN:Mg | 375 | [57] |
| | n-ZnO/p-GaN:Mg | 365.4, 384 | [58] |
| MOCVD | n-ZnO /p-Si | 580 | [59] |
| | n-ZnO /p-Si | 400-600 | [60] |
| CVD | n-ZnO/p-AlGaIn | 389 | [61] |
| | n-ZnO/p-GaN | 430 | [62] |
| HWEP sputtering | p-CuGaS ₂ /n-ZnO:Al | 496-775 | [63] |

Table 1. Structure and emission of n-ZnO based LEDs.

4. ZnO-based LEDs

4.1. Heterojunction LEDs

4.1.1. n-ZnO heterojunction LEDs

ZnO has attracted considerable attention because of its promising applications in UV LEDs and laser diodes. The fabrication of high-quality p-type ZnO remains great challenge. Many researchers reported on the heterojunction LEDs with n-type ZnO grown on p-type materials of Si, GaN and conducting oxides, as summarized in Table1.

Chang et al reported the MBE n-ZnO/MOCVD p-GaN heterojunction light-emitting diode [46]. They grew 1- μm -thick undoped GaN buffer layer on Al_2O_3 and a 500-nm-thick Mg-doped p-GaN layer by MOCVD, and grew 300-nm-thick n-ZnO by MBE on p-GaN layer. They observed a broad yellowish green emission peaked at around 570nm. The EL emission was attributed to the electron injection from n-ZnO to p-GaN. Hwang et al fabricated an n-ZnO:Ga/p-GaN:Mg heterostructure on Al_2O_3 substrate [51]. Undoped ZnO (buffer layer) and n-ZnO films doped with about 1% Ga were grown at 75W radio frequency (RF) power in 100% O_2 atmosphere, at 800°C and 700°C, respectively. I-V characteristics exhibited the typical rectifying behavior and the EL emissions from the n-ZnO:Ga/p-GaN:Mg heterostructure at room temperature show peaks at 430nm, 440nm and 480nm along with a broad band of yellow light.

Lee et al investigated the origin of emission of the annealed n-ZnO/p-GaN heterostructure LED [52]. They fabricated n-ZnO/p-GaN heterojunction LED on Al_2O_3 substrates by MOCVD (GaN layer) and RF sputtering (ZnO layer). After fabrication, ZnO films were annealed in a thermal furnace in air and nitrogen ambient at 800°C for 30–120min. For the LED annealed in N_2 , room-temperature EL in the blue region with peak wavelength 400nm was observed, and for the LED annealed in N_2 , a broad band from 400 to 700nm was detected in the EL emission spectrum, as shown in Figure 6. Alivov et al reported the n-ZnO/p-AlGaIn heterojunction light-emitting diodes on 6H-SiC substrates [61]. *n*-type ZnO layer with a thickness of 1 μm was deposited on *p*- $\text{Al}_{0.12}\text{Ga}_{0.88}\text{N}$ and I-V curve of the devices showed a rectifying diode-like behavior with threshold voltage ~ 3.2 V, a high reverse breakdown voltage of 30V and a small reverse leakage current of about 10^{-7} A. Under forward bias, UV EL with a peak emission near 389nm ($\sim 3.19\text{eV}$) and a full-width at half-maximum (FWHM) of 26nm was observed in the EL spectrum of the device. The emission was stable at temperatures up to 500K and was attributed to the recombination of the carriers within the ZnO. They also observed 430nm electroluminescence from ZnO/GaN heterojunction LEDs [62]. Yu et al reported ZnO/GaN heterostructure LEDs with a donor–acceptor pair emission band at 3.270eV [58]. In the EL spectrum of the device, two emission peaks, a strong emission peak (384.0nm), together with a weak emission (365.4nm) feature on the higher-energy side.

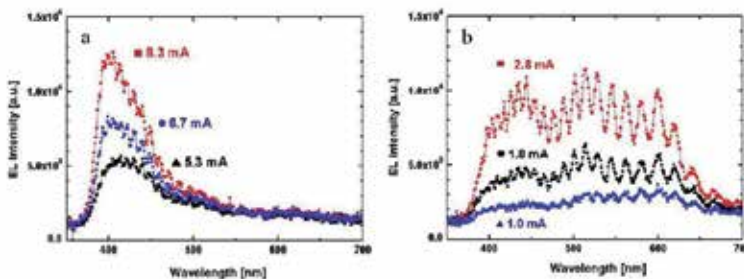


Figure 6. EL spectra of n-ZnO/p-GaN heterostructure LED annealed (a) in N_2 and (b) in air ambient. Inset: pictures of Light emission. From Ref. [52].

Chichibu et al fabricated p-CuGaS₂/n-ZnO:Al heterojunction LEDs by metal-organic vapor phase epitaxy (p-CuGaS₂) and helicon-wave-excited-plasma (HWEP) sputtering method (n-ZnO:Al) [63]. The EL spectra exhibited emission peaks and bands between 1.6 and 2.5eV. Ohta et al reported on p-SrCu₂O₂/n-ZnO heterojunction LEDs [56]. The I-V curve of the device exhibited nonlinear characteristics where the turn-on voltage was approximately 1.5V. An UV emission band centered at 382nm was observed at room temperature when a forward bias voltage greater than 3V was applied to the device, as shown in Figure7.

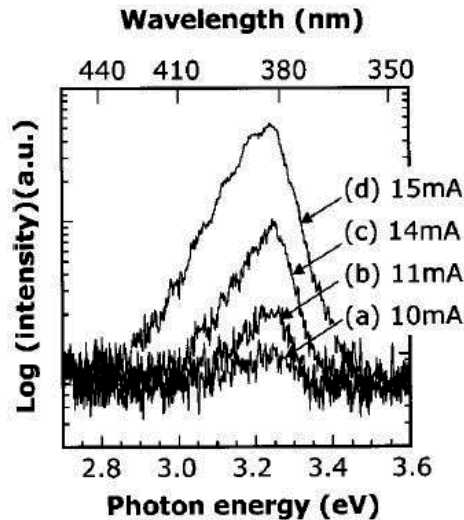


Figure 7. UV emission spectra of the p-SrCu₂O₂ /n-ZnO p – n junction LED for several currents. electric currents were (a) 10mA, (b) 11mA, (c) 14mA, and (d) 15mA, respectively. From Ref. [56].

Ye et al reported the distinct visible electroluminescence at room temperature from n-ZnO/p-Si heterojunction [59]. A high-quality ZnO layers were fabricated by metal organic chemical vapor deposition technique on p-type Si (111) substrate at 650°C. Before grew ZnO layer, a thin ZnO buffer layer (~25nm) was deposited to relieve the strains due to large lattice mismatch between Si and ZnO and to avoid the oxidation of Si surface. The EL peak energy coincided well with the deep-level photoluminescence of ZnO, indicating that the EL emission was originated from the radiative recombination via deep-level defects in n-ZnO layers.

To improve the emission of n-ZnO-based heterojunction LEDs, double and triple heterojunction LEDs were fabricated. Osinsky et al reported MgZnO/ZnO/AlGaIn/GaN triple heterostructures light-emitting diodes [50]. I-V curves of the device showed a rectifying characteristics with a turn-on voltage of ~3.2 V. Strong optical emission was observed at ~390nm. Mares et al prepared a hybrid n-MgZnO/CdZnO/p-GaN LEDs with a Cd_{0.12}Zn_{0.88}O quantum-well [49]. Under forward bias, visible electroluminescence was observed at room temperature in the EL spectrum of the device. The EL red shifted from 3.32 to 3.15eV as the

forward current was increased from 20 to 40mA. Zhang et al investigated the effects of the crystalline and thickness of AlN layer on the electroluminescent performance of n-ZnO/AlN/p-GaN [54]. They found that the better crystalline quality of AlN barrier layer may facilitate the improvement of EL performance of the device. For the thinner AlN layer, it was not enough to cover the whole surface of GaN, while in the thicker AlN layer, many of electrons were captured and nonradiatively recombined via the deep donors, indicating that AlN barrier layer played an important role on the performance of the device. In their experiments, AlN layer at the growth temperature of 700°C with an optimized thickness of around 10nm improved EL performance of the devices.

4.1.2. Heterojunction LEDs with ZnO nanomaterials

The optical devices using ZnO nanomaterials have attracted considerable attention due to their promising optical properties, such as enriched radiative recombination of carriers. Various ZnO nanomaterials have been grown by different methods. Based on the growth of n-type ZnO nanomaterials, some researcher reported the heterojunction LEDs with ZnO nanomaterials, as summarized in Table 2. Here, we only present the typical results on heterojunction LEDs with ZnO nanomaterials.

| Growth technique | Structure | Light emission (nm) | Reference |
|--------------------------|---|-------------------------|-----------|
| Solution method | n-ZnO nanowire/p-GaN film | 400-420 | [64] |
| | n-ZnO nanorods/PFO | 448, 469, 503, 541, 620 | [65] |
| | n-ZnO nanowire/i-polymer/p-GaN | 400 | [66] |
| | n-ZnO(nanowall, nanorod, nanoflower, nanotube) /p-GaN | White light | [67] |
| | n-ZnO nanorod/polymer | 420-800 | [68] |
| CVD | n-ZnO nanowire/p-GaN film | 370, 400- 440 | [69] |
| | n-ZnO nanowire in polystyrene /PEDOT:PSS | 383,430,640,748 | [70] |
| | n-ZnO nanowire/p-Si | 600 | [71] |
| | ITO/n-ZnO nanorod/p ⁺ -Si | 450 | [72] |
| MOCVD | n-ZnO nanorod/p-GaN film | 370, 440, 560 | [73] |
| | n-ZnO nanorod/p-GaN film | 440-560 | [74] |
| Electrodeposition | n-ZnO nanowire/p-GaN film | 397 | [75] |
| | n-ZnO nanorod/p-CuSCN | 390 | [76] |
| | p-NiO film /n-ZnO nanorod | UV-visible | [77] |
| PLD | n-ZnO nanowire/p-GaN film | 380 | [78] |

Table 2. Structure and emission of heterojunction LEDs with ZnO nanostructures.

Xu et al reported ordered ZnO nanowire array blue/near-UV LEDs [64]. The devices were fabricated by a conjunction of low temperature wet chemical methods and electron beam lithography. ZnO nanowire arrays were grown on Mg-doped p-type GaN films. $I - V$ curves of the devices exhibited the typical rectifying behavior. Under forward bias, each single nanowire was a light emitter. The EL spectra of the devices were shown in Figure 8. It can be seen that the contour of the EL spectrum does not change much with the biased voltage in the range of 4-10V and the dominant emission peak is slightly blue shifted in the range of 400nm– 420nm. By Gaussian deconvolution of the emission spectrum, the blue/near-UV emission is attributed particularly to three distinct electron-hole recombination processes. The LEDs give an external quantum efficiency of 2.5%, displaying great potential applications in high resolution electronic display, optical interconnect, and high density data storage.

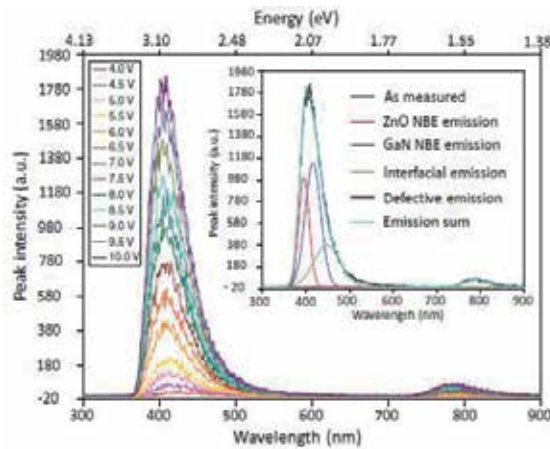


Figure 8. EL spectrum as a function of the forward biased voltage. Inset shows by Gaussian deconvolution analysis the blue/near-UV emission could be decomposed into three distinct bands that correspond to three different optoelectronic processes. From Ref. [64].

Zhang et al fabricated high-brightness blue-light-emitting diode using a ZnO-nanowire array grown on p-GaN thin film [69]. The EL spectrum of the device showed broad emission peaks from UV (370nm) to blue. When the forward bias increased from 10 to 35V, the emission peak was significantly enhanced and the main emission peak shifted from 440 to 400nm when the forward bias was increased (Figure 9), indicating that the modification of external voltage to the band profile in the depletion region. Lupan et al observed UV emission at 397nm with a low forward-voltage emission threshold of 4.4V and a high brightness above 5– 6V in ZnO-nanowire/p-GaN LEDs [75].

Alvi et al investigated the n-ZnO nanostructures (nanowalls, nanorods, nanoflowers and nanotubes)/p-GaN white-light-emitting diodes, systematically [67]. In their experiments, ZnO nanostructures were grown on p-GaN substrates using a low temperature aqueous chemical growth method (<100°C) forming p – n heterojunctions. The EL spectrum of ZnO-

nanowall LED exhibited three peaks centered at 420nm (violet emission), 450nm (violet–blue) and broad peak covering from 480 to 700nm (green, yellow, orange and red emissions). For ZnO nanoflowers LEDs, the emission peaks centered at 400nm (violet emission), 450nm (violet–blue) and a broad peak covering EL emissions from 480 to 700nm (green, yellow, orange and red emissions) were detected. ZnO nanorods and nanotubes LEDs showed the same EL spectra, and EL peaks centered at 400nm (violet emission), 450nm (violet–blue) and 540nm (green emission) were observed. For ZnO nanostructures (nanowalls, nanorods, nanoflowers and nanotubes)/p-GaN LEDs, the color rendering indices (CRI) were 95, 93, 87 and 88, and the correlated color temperatures were 6518, 5471, 4807 and 4801K, respectively.

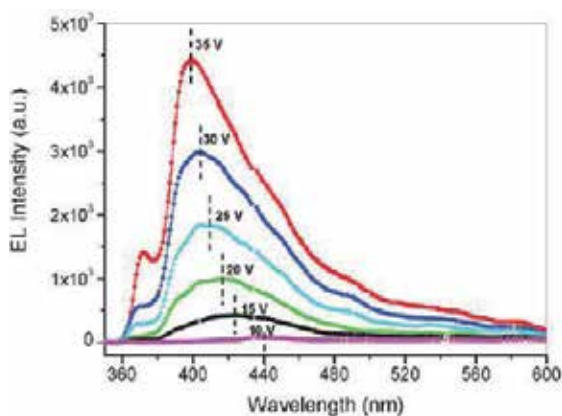


Figure 9. The electroluminescence spectrum of the (n-ZnO NWs)/(p-GaN film) LED device under various forward bias voltages (10, 15, 20, 25, 30, 35V), showing broad emission peaks from UV to blue and blue shift with increasing of bias voltage. From Ref. [69].

Xi et al fabricated heterojunction NiO/ZnO LEDs using low temperature solution-based growth method [77]. The devices exhibited room-temperature electroluminescence, and the steady increase of the UV-to-visible emission ratio was obtained for increased bias voltage, which was good agreement with some of the reported behavior of ZnO LEDs.

Klason et al reported the EL spectra obtained from ZnO nanodots/p-Si heterojunction LEDs [71]. The asymmetric EL emission peaked at around 600nm was observed and the emission from the devices having buffer layer were a bit blue shifted when compared to samples without the buffer layer. The buffer layer increased both the stability and efficiency of the devices.

Bano et al reported the ZnO-organic hybrid white LEDs grown on flexible plastic using low temperature aqueous chemical method [65]. Figure10 shows the structure of ZnO-organic hybrid white LEDs, schematically. I-V curve of the device exhibited the typical rectifying behaviors. The EL spectrum displayed a broad emission band covering the whole visible region and hence provided white light. The white light emission was the superposition of a violet line (448nm), blue line (469nm) from the PFO combined with green emissions (503 and 541nm), and a red emission (620nm) due to deep level defect emissions in ZnO nano-

rods (Figure11). The color rendering index and correlated color temperature of the white LEDs were calculated to be 68 and 5800K, respectively (Figure12).

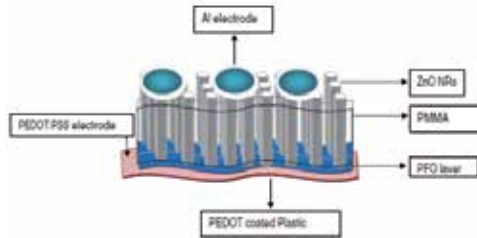


Figure 10. Schematic illustration of ZnO NRs/PFO hybrid device on PEDOT:PSS coated flexible plastic. From Ref. [65].

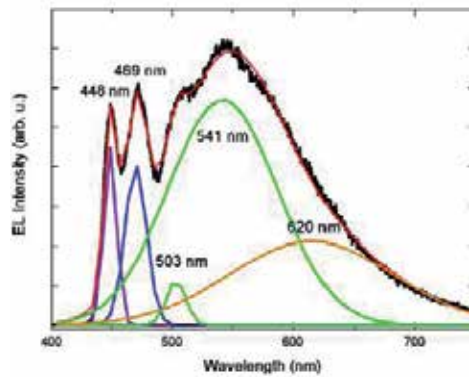


Figure 11. Room temperature EL spectrum and Gaussian fitting of the PFO/ZnO hybrid white LED. Inset: a photograph of white light emission from flexible device folded at a large angle during operation. From Ref. [65].

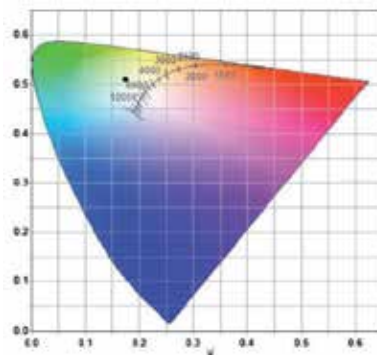


Figure 12. Typical color coordinates characteristics of the ZnO – PFO hybrid white LEDs. From Ref. [65].

4.1.3. *p-ZnO heterojunction LEDs*

Currently, the fabrication of p-type ZnO materials has made remarkable progress and some researchers attempted to prepare p-type ZnO based hereojunction LEDs by various methods, as summarized in Table3.

| Growth technique | Structure | Light emission (nm) | reference |
|----------------------|--|---------------------|-----------|
| MBE | p-ZnO:Sb/n-ZnO/n-Si | 381, 485, 612, 677 | [79] |
| | p-ZnO:Si/CuZnO/n-Si | 459, 391 | [80] |
| | p-MgZnO/n-ZnO bulk | 382 | [81] |
| MOCVD | p-ZnO:Si/n-GaN MQW/n-GaN | 465 | [82] |
| | p-ZnO:Ni/n-GaN/Si | 390 | [83] |
| Magnetron sputtering | p-ZnO:Pt/n-GaN | 409 | [84] |
| | p-ZnO:As/n-GaN film | 382, 601, 647 | [85] |
| | p-ZnO:In/n-Si | 550 | [86] |
| PLD | p-ZnO:P/Zn _{0.9} Mg _{0.1} O/ZnO/Ga | 385 | [87] |
| Solution method | p-ZnO:K/n-GaN | 372, yellow-orange | [88] |

Table 3. Structure and emission of p-type ZnO based heterojunction LEDs

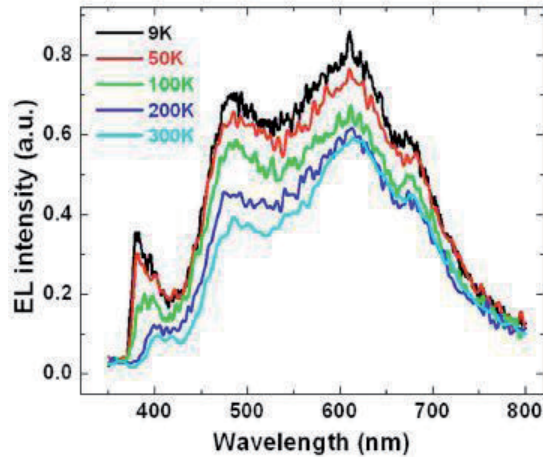


Figure 13. Temperature dependent EL spectra obtained at an injection current of 110 mA. EL from LED is obtained at 9, 50, 100, 200, and 300 K. From Ref. [79].

Mandalapu et al reported ultraviolet emission from Sb-doped *p*-type ZnO based heterojunction LEDs fabricated by growing p-type ZnO:Sb films on n-type Si substrates [79]. Thin un-

doped ZnO film(50nm) was grown at low temperature on *n*-Si(100) substrate as a buffer layer, followed by p-type ZnO:Sb layer (370nm) at a higher temperature by MBE. After the growth, thermal activation of Sb dopant was carried out in *in situ* in vacuum at 800°C for 30 min. The I-V curves of the heterojunction LEDs displayed a typical rectifying behavior with higher leakage current at both higher temperatures and higher biases, which may origin from the band alignment of wide-band-gap *p*-ZnO and narrow-band-gap *n*-Si. Figure13 shows the EL spectra obtained at different temperatures for an injection current of 110mA. Four emission peaks at 381, 485, 612 and 671nm were detected from the spectra at 9 K. The peak at 381nm was the near-band edge emission and the other peaks were attributed to intrinsic defects in ZnO. A small UV peak at 396nm was also observed in the EL spectra at 9K, which was related to Zn vacancies. With increasing temperature in the range from 9 to 300K, both the small UV peak and the near band edge emission redshifted and became a single peak at higher temperatures. The intensity of emissions decreased throughout the spectra with increasing temperature, which was due to the increase in nonradiative recombinations at higher temperatures.

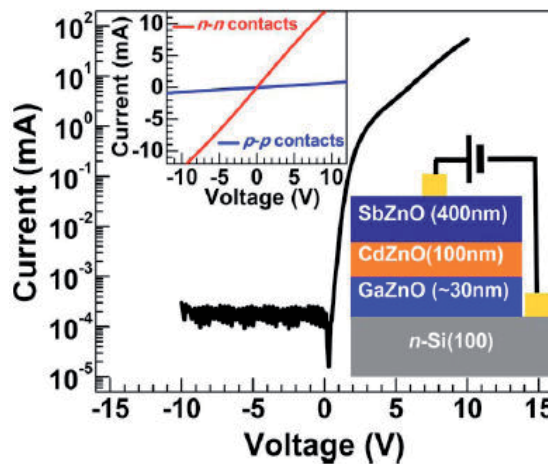


Figure 14. I-V curve of the device, showing rectifying characteristics. Top inset shows the linear I-V of *n*-contacts (red line) and *p*-contacts (blue line), respectively. Bottom inset shows device structure of the sample: SbZnO/CdZnO/GaZnO/Si. From Ref. [80].

Li et al reported on the blue electroluminescence from ZnO based heterojunction LEDs with CdZnO active layers [80]. *p*-ZnO:Sb/*i*-CdZnO/*n*-ZnO was grown on *n*-type Si substrates by plasma-assisted molecular-beam epitaxy. Figure14 shows the typical rectifying characteristics of the heterojunction LEDs, and the top inset of Figure14 reveals the I-V curves of Au/Ni and Au/Ti metal contacts on *p*-type ZnO:Sb and *n*-type Si, respectively, indicating that good ohmic contacts were formed on both electrodes. The PL spectra showed ZnO near band edge (NBE) emission of *p*-type ZnO:Sb at 378nm and NBE emission of CdZnO active layer at 445nm. Figure15 shows EL spectra of a hereojunction under different injection currents. The blue EL emissions at around 459nm were observed and the emission intensity increased

with the increase of the injection current. A comparison of PL and EL spectra of the device shows that the EL emission of the device originated from the radiative recombinations in CdZnO active layers in the film.

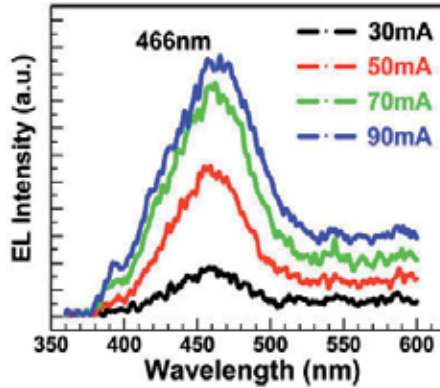


Figure 15. Room temperature EL characteristics of the LEDs under different injection currents. From Ref. [80].

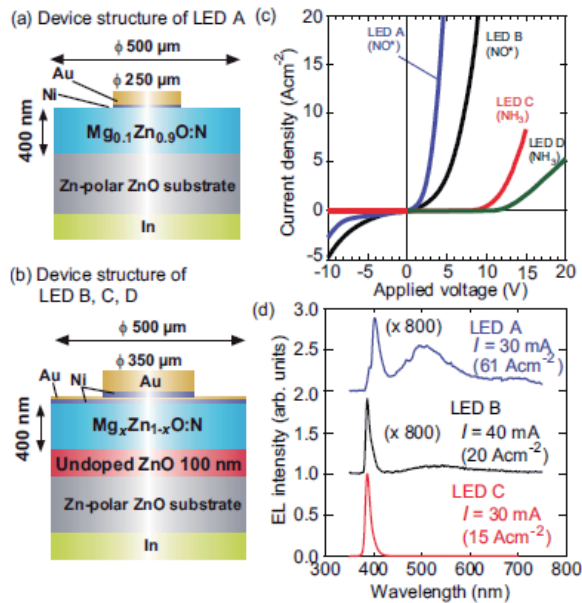


Figure 16. a) and (b) depict cross-sectional schematics for LED A and those of B–D, respectively. The device was 500 μm in diameter and the back side of the ZnO substrates was bonded to a metal plate with In. The top electrode in (a) was formed as Au(200nm)/Ni(10nm) with a diameter of 250 μm . That of (b) consists of a semitransparent electrode of Au (4nm)/Ni (2nm) with a diameter of 500 μm and a contact pad of Au (500nm)/Ni (2nm) with a diameter of 350 μm . (c) The rectifying I - V curve measured for LEDs A, B, C, and D. (d) EL spectra from LEDs A–C. All spectra were measured at room temperature. Forward bias operation conditions are also shown. From Ref. [81].

Nakahara et al fabricated heterostructure LEDs by growing N-doped p-type $\text{Mg}_x\text{Zn}_{1-x}\text{O}$ layer by MBE on Zn face ZnO crystal using NO and NH_3 as N source [81]. The structures of the LEDs were shown in Figures 16(a) and (b). The I-V curves of the LEDs exhibited a rectifying property [Figure 16(c)]. LEDs A and B (NO as N source) had a turn-on voltage of approximately 3V, LEDs C and D (NH_3 as N source) showed a turn-on voltage of 10V. In the EL spectra of LEDs A and B, a sharp EL peak at the near band edge ($\lambda = 380 - 400\text{nm}$) was seen, indicating an effective blocking of electrons by the wide band gap $\text{Mg}_{0.1}\text{Zn}_{0.9}\text{O}:\text{N}$ layers and efficient exciton recombination in the *n*-type ZnO layers [Figure 16(d)]. The EL of LED C was much more intense by a factor of 800 than those of LEDs A and B.

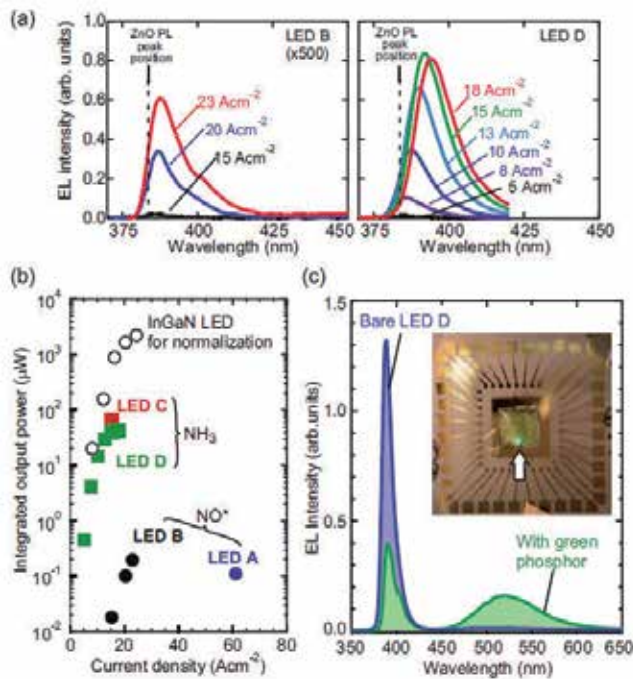


Figure 17. a) EL spectra of the LEDs B and D operated with various current densities. (b) Integrated EL intensity for the spectra shown in (a) (LEDs B and D) as a function of applied current density. The data for LEDs A and C are also shown. The integration was conducted in a wavelength range from 350 to 450 nm. (c) EL spectra for bare and with a green phosphor coating for LED D at an operation current of 40 mA. Inset is a picture taken under standard laboratory illumination. Emission from the phosphor can be clearly seen as indicated by an arrow. From Ref. [81].

The EL peak energies of the LEDs were slightly lower than the PL peak energy of ZnO, which were due to the self-absorption of the ZnO emission in the thick ZnO substrate and the heating effect during the operation [Figure 17(a)]. The outpower of the LEDs ranged from 0.1 to $70\mu\text{W}$ at the maximum attainable operation current (typically 30–40mA)[Figure 17(b)]. Interestingly, when LED was coated with a 0.1-mm-thick epoxy resin containing 5wt % (BaEu)(MgMn) $\text{Al}_{10}\text{O}_{17}$ green phosphor, a part of ultraviolet NBE in the EL spectrum of the LED was converted into green, indicating that the UV emission may excite many existing phosphors developed for fluorescent tube and enable better color rendering [Figure 17(c)].

| Growth technique | Structure | Light emission (nm) | Reference |
|-------------------------------|---|---------------------|-----------|
| MBE | p-ZnO:N/i-ZnO/n-ZnO | Violet-green | [5] |
| | p-ZnO:N/n-ZnO | 420 | [89] |
| | p-ZnO:Sb/n-ZnO:Ga | 383.3, 490, 605 | [90] |
| | p-ZnO:Sb/n-ZnO:Ga | 385-393 | [91] |
| MOCVD | p-ZnO:N/n-ZnO/ZnO bulk | 372, 435, 520 | [92] |
| | n-ZnO/p-ZnO:As/GaAs | 388, 496 | [93] |
| | n-ZnO:Ga/p-ZnO:N | 388, 516 | [94] |
| Ion implantation | p-ZnO:N/n-ZnO bulk | 530, 740 | [95] |
| | p-ZnO:As nanorod /n-ZnO nanorod | 380, 630 | [96] |
| | p-ZnO:P nanorod /n-ZnO nanorod | UV, 510, 800 | [97] |
| Magnetron sputtering | p-ZnO:P /n-ZnO | 380, 640 | [98] |
| Solution method | p-ZnO:P nanorod / n-ZnO film | 415, 450-650 | [99] |
| Hybrid beam deposition | p-ZnO:As /p-Be _{0.3} Zn _{0.7} O / (ZnO/Be _{0.2} Zn _{0.8} O)MQW/ n-Be _{0.3} Zn _{0.7} O/n-ZnO | 363, 388, 550, | [100] |

Table 4. Structure and emission of ZnO based homojunction LEDs.

Park et al reported on the growth and device properties of *p*-ZnO/(InGaN/GaN) multiquantum well (MQW)/*n*-GaN heterojunction LEDs [82]. A GaN buffer layer (30nm) was deposited on a sapphire substrate. After high temperature annealing of the buffer layer, undoped GaN(5μm), *n*-type GaN:Si(2μm) and InGaN/GaN MQW were grown by MOCVD, then, *p*-type ZnO:Sb layer was deposited on InGaN/GaN MQW. Finally, to active *p*-type dopant, a rapid thermal annealing was performed in an N₂ ambient for 1min. The emission peak at 468nm was observed at room temperature, and the emission intensity of the LEDs increased as injection current increased, indicating that *p*-ZnO:Sb layer acted as a hole supplying layer in the hybrid LEDs. The emission peak red shifted as injection current increased due to the decrease in strain-induced piezoelectric field in the InGaN well by Sb-doped *p*-ZnO and Joule heating. Similarly, Hwang et al prepared *p*-ZnO:P/*n*-GaN heterostructure LEDs [84]. The PL spectra of the *p*-ZnO and *n*-GaN films exhibited the emission peaks at 365nm and 385nm, corresponding to NBE emissions of *n*-type GaN and *p*-type ZnO, respectively. Under forward bias, an EL emission at 409nm at room temperature were observed, which was attributed to the band gap of *p*-ZnO:P grown on *n*-GaN.

4.1.4. Homojunction LEDs

Based on the fabrication of p-type ZnO materials, some researchers reported on ZnO-homojunction LEDs. Table 4 is a survey of structure, method and emission peak of ZnO-homojunction LEDs.

Tsukaza et al fabricated ZnO p-i-n homojunction LEDs by laser MBE using N as acceptor dopant [5]. The structure of the device was shown in Figure 1(a). To realize an automatically flat interface, the homojunction structure was grown in layer-by-layer. The I-V curve of the LED exhibited a rectifying behavior with a threshold voltage of 7V [Figure 1(b)]. The threshold voltage was higher than the bandgap of ZnO (3.3eV), which was mainly attributed to the high resistivity of the p-type ZnO layer. The EL spectrum of the homojunction LED showed luminescence from violet to green regions with multi-reflection interference fringes. Compared PL spectrum of p-type ZnO and EL spectrum obtained from the LED, the higher energy side peak around 430nm in the EL spectrum matches well with the PL spectrum [Figure 1(c)].

Chu et al reported on homojunction UV LEDs based on p-type Sb-doped ZnO/n-type Ga-doped ZnO films. ZnO homojunction was grown on n-type Si(100) substrates by MBE [90]. A thin MgO/ZnO buffer layer was deposited to reduce the lattice mismatch between Si and ZnO, then, the two layer structured Sb-doped p-type ZnO (420nm)/Ga-doped n-type ZnO (420nm) homojunction was grown on this MgO/ZnO buffer. After the growth, *in situ* thermal annealing was performed to active Sb dopant in ZnO:Sb films. The I-V curve p-ZnO:Sb/n-ZnO:Ga homojunction exhibited rectifying characteristics with a threshold voltage of 6V. Figure 18 shows room temperature EL of the homojunction LEDs under different injection currents. The NBE emission at ~383 nm was observed, the other peaks around 490 and 605nm related to intrinsic defects were also detected. With the increase of the injection current, the NBE emission redshifted from 383.3nm (30mA) to 390.9nm (100mA), which was induced by the band gap variations due to the increased heating effects during the operation of LEDs.

Similarly, Kong et al fabricated Sb-doped p-type ZnO/Ga-doped n-type ZnO homojunction on Si (100) substrate [91]. I-V and C-V curves presented typical electrical properties of a diode. The EL emission of the homojunction LEDs demonstrated dominant UV emissions. A NBE emission at 3.2eV started to appear when the current is 60mA. When the injection current increases from 60 to 100mA. The intensity of the UV emission increased and the emission peak slightly redshifted from 385 to 393nm. The output power of this LED was estimated to be only 1nW at drive current of 100mA.

Wei et al prepared ZnO homojunction LEDs on c-plane Al₂O₃ substrates by plasma-assisted MBE using a gas mixture of N₂ and O₂ as the p-type dopant [89]. At low temperature (100K), the I-V curve of the LEDs exhibited a typical rectifying behavior with a threshold voltage of 4.0V at forward bias and a low leak current at reversed bias voltage. The LED keeps a good rectifying characteristic even as increasing temperature up to 300K. A emission at 2.83eV started to appear when the current was 2.42mA. The emission peak blue shifted from 2.83 to 2.95eV as the injection current changed from 2.42 to 3.31mA, indicating that the EL emission

originated from the donor-acceptor pair recombination in the *p*-type ZnO layer. The LED can even emit intensive EL in the blue-violet region at the temperature of 350K.

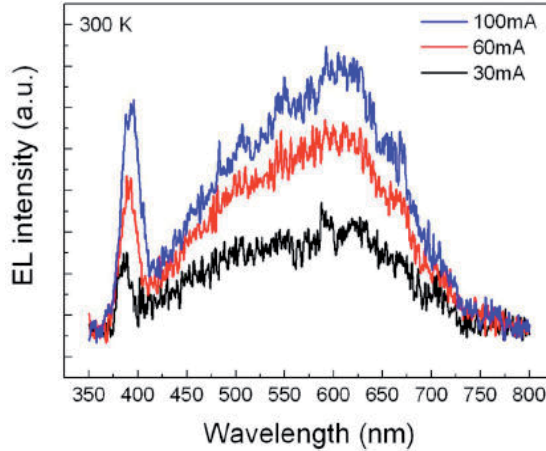


Figure 18. Room temperature EL spectra at different injection current from 30 to 100mA. From Ref.[90].

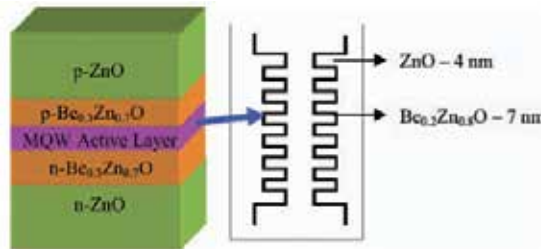


Figure 19. Schematic illustration of the structure of the ZnO-based UV LED devices that employ a BeZnO/ZnO active layer comprised of MQWs. From Ref. [100].

Sun et al reported on the ultraviolet electroluminescence from ZnO homojunction with *n*-ZnO/*p*-ZnO:As/GaAs structure [93]. To obtain *p*-type ZnO film, firstly, a 400nm ZnO layer was deposited on *p*-GaAs (100) substrate at 450°C by MOCVD, followed by a thermal annealing at 550°C in 20Pa oxygen ambient for 30min to enhance the diffusion of arsenic and activate the acceptor impurities. After the thermal annealing, a 300nm undoped *n*-type ZnO layer was grown on the ZnO:As film at 350°C. The ZnO homojunction had a rectifying behavior with a turn-on voltage of about 4V and a reverse breakdown voltage of higher than 6V. Under forward injection current of 30mA, the EL emission exhibited two independent bands centered at 3.2 and 2.5eV, which could be assigned to the NBE emission and deep-level emission, respectively.

Ryu et al reported on ZnO-based UV LEDs fabricated by the hybrid beam deposition [100]. The LEDs employed a BeZnO/ZnO active layer between *n*-type and *p*-type ZnO and Be_{0.3}Zn_{0.7}O layers, as shown in Figure 19. The active layer is composed of seven quantum wells for which undoped Be_{0.2}Zn_{0.8}O (7nm) and ZnO (4nm) form barrier and well layers, respectively. The *p*-type ZnO and BeZnO layers were prepared with As as the acceptor dopant and *n*-type ZnO and BeZnO layers were formed with Ga as the dopant. The I-V curve of the LEDs exhibited a typical rectifying behavior with a high threshold voltage and a low reverse bias current.

Figure 20 shows the EL spectra of the LEDs at room temperature. The peaks centered 388nm (bound exciton – BE) and 550nm (green band – GB) were the dominant features at low forward currents (≤ 20 mA), which were attributed to the impurity (donor or acceptor)-bound exciton emission and donor-acceptor pair recombination. As the current injection levels were above 20mA, the peak at 363nm becomes the prominent spectral feature and the peaks at 388 and 550nm have become saturated. The peak at 363nm could be assigned to band-to-band recombination, such as from localized-exciton peaks in the active layer of the QWs.

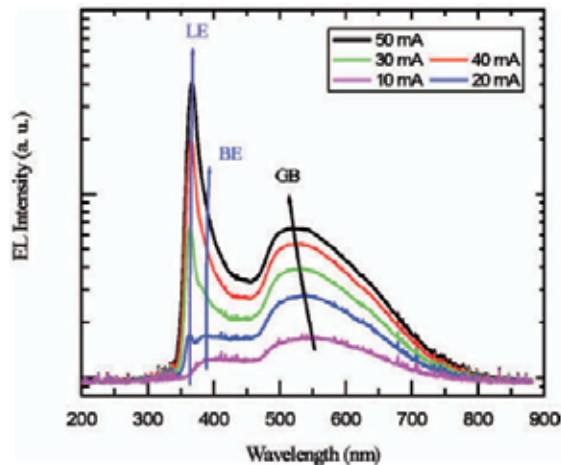


Figure 20. EL spectrum measured at room temperature in continuous current mode of a *p-n* junction ZnO-based LED having a BeZnO active layer. The primary spectral emission peak is located near 363 nm and arises from localized-exciton emissions in the QWs. The secondary peak centered near 388 nm is from impurity-bound exciton emissions in ZnO. From Ref. [100].

Lim et al fabricated UV LEDs based on ZnO *p-n* homojunction [98]. A Ga-doped ZnO layer (1.5 μ m) were grown on a c-Al₂O₃ substrates at 900°C by sputtering a ZnO target mixed with 1 wt% Ga₂O₃. A *p*-type ZnO layer (0.4 μ m) was grown in situ on the *n*-type ZnO layer at 900°C by sputtering a ZnO target mixed with 1 wt% P₂O₅. A rapid thermal annealing process was performed to the LEDs for 5min at 800°C in a nitrogen atmosphere in order to activate the *p*-type ZnO layers. The I-V curve of the device showed clear rectification with a threshold voltage of 3.2V, which was in good agreement with the ZnO bandgap energy (3.37eV). The EL spectra of the ZnO homojunction LED is shown in Figure 21. A NBE emission at 380nm and broad deep-level emissions at approximately 640nm were observed. The

EL spectra of the LED matched well with the PL spectrum of the p-type ZnO film, indicating that the recombination of electrons and holes occurred mostly in p-type ZnO layer.

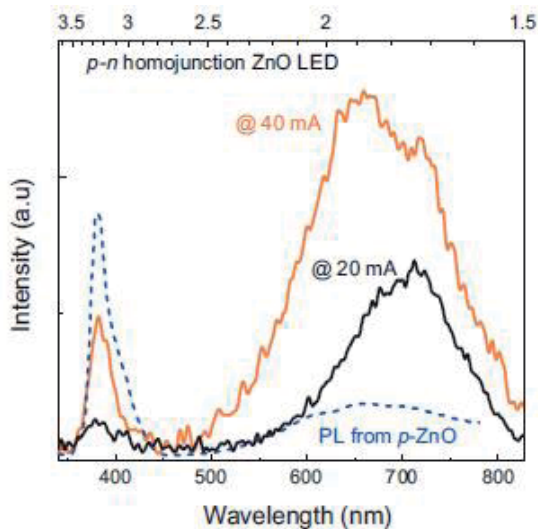


Figure 21. EL spectra of p-n homojunction ZnO LED operated at forward currents of 20 and 40 mA; PL spectrum of p-type ZnO obtained at room temperature. From Ref. [98].

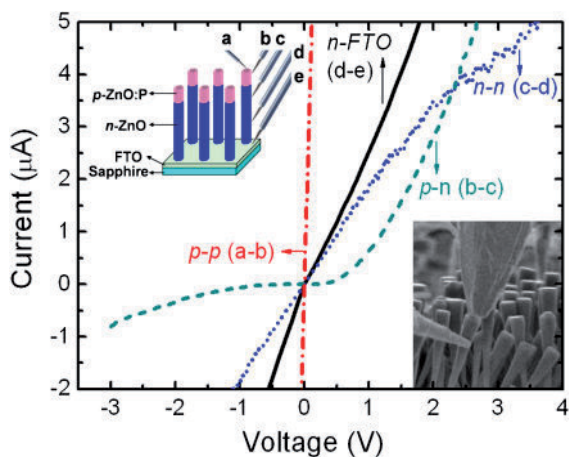


Figure 22. I - V characteristics of p - p , p - n , n - n , and n -FTO regions in a single ZnO rod. The upper left and lower right insets show the schematic diagram and a SEM image of probing by Zyvex nanomanipulator, respectively. From Ref. [97].

Sun et al reported on UV emission from a ZnO rod homojunction LED [97]. Vertically aligned ZnO rods (Diameters: 200–500nm; Length:3.5 μ m) were uniformly grown on fluo-

rine-doped tin oxide (FTO) coated sapphire *c*-plane substrates by a vapor phase transport method. After the growth, ZnO rod arrays were implanted with P⁺ ions with 50keV (device I) and 100keV (device II) at a dosage of $1 \times 10^{14} \text{ cm}^{-2}$ perpendicular to the aligned rods. The implanted ZnO rods were annealed at 900°C for 1 h with an O₂ flow rate of 100 SCCM at 1 Torr to active p-type dopant. Figure 22 exhibits the typical *I-V* characteristics of different regions in a single vertically aligned *p*-ZnO:P/*n*-ZnO rod. The rectifying behavior with a threshold voltage of 0.8V was observed for *p-n* junction. The near-linear relationship was also detected for *p-p*, *n-n*, and *n*-FTO curves, indicating an Ohmic behavior.

Figure 24 displays the EL spectra of ZnO rod homojunction LEDs at various injection currents. Strong UV emission was observed from both devices, corresponding to the NBE emission of ZnO. The UV light output intensities increased linearly as injection current was above a threshold current (Figure 23 insets). In addition, device I shows a relatively weak and broad emission band in the visible range, indicating a low density of deep-level defects, and the broad emission consisted of one green emission (~510nm) and one nearinfrared peak (~800nm) became stronger for device II. Similarly, Yang et al fabricated ZnO nanorod *p-n* homojunction LEDs with As implantation [96]. The EL spectrum of the device exhibited a strong UV band centered at ~380 nm and a weak broad red band peaking at ~630nm.

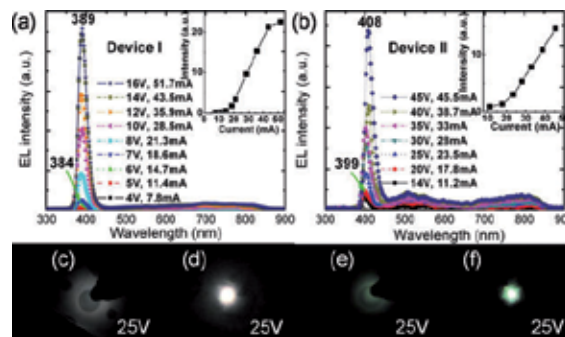


Figure 23. EL spectra of (a) device I and (b) device II under various injection currents, respectively. The insets show the UV light output intensities as a function of forward injection current. The photographs of corresponding light emissions collected from both (c) and (e) front side (Au anode) and (d) and (f) back side single-sided polished sapphire substrate in these two devices under the same bias voltage of 25 V. From Ref. [97].

5. Conclusion and outlook

With a large direct band gap of 3.37eV and a large exciton binding energy of 60meV, ZnO has attracted much attention for its application in optoelectronics applications, such as LEDs, photodetector and laser diodes. In the paper, based on the introduction of the band-gap engineering and doping in ZnO, we presented a comprehensive review of ZnO-based LEDs. Band-gap engineering in ZnO can be achieved by alloying with MgO, CdO or BeO. Theoretically, the energy band gap of $A_xZn_{1-x}O$ can be continuously modulated from 0.9eV

(CdO) to 10.6eV (BeO) by changing the A concentration. As a n-type semiconductor, high quality n-type ZnO materials can be obtained by doping III elements (Al, Ga and In). Although the fabrication of p-type ZnO remain great challenges due to the self-compensation, p-type ZnO have been prepared by doping different elements (N, P, As, Sb, Li, Na and K) with various techniques. ZnO based heterojunction and homojunction LEDs have been achieved, which makes ZnO as a strong candidates for solid-state light. Although the efficiency of ZnO-based LEDs is not high, improvements are rapid and the emitters have the potential to outperform their GaN rivals.

ZnO-based LEDs show great promise for the future, however, there are some severe issues that are in need of further investigation to transition ZnO-based LEDs to commercial use from the current stage. One problem is that the usable, reproducible p-type ZnO are not easy to fabricate, although some researchers have been successful. Another is the achievement of high quality p-n junction based ZnO. The p-n junction with good threshold and breakdown voltages is necessary for the LEDs. In addition, diode-like behavior and light emission have been observed, however, the mechanism of the properties remain unclear.

6. Acknowledgements

The work was supported by the Fundamental Research Funds for the Central Universities (Contract No: 531107040334) and the Aid Program for exploring investigation (Contract No: 513280501).

Author details

J.C. Fan¹, S.L. Chang² and Z. Xie¹

1 College of Physics and Microelectronics Science, Key Laboratory for Micro-Nano Physics and Technology of Hunan Province, Hunan University, Changsha 410082, People's Republic of China

2 Center of Materials Science, College of Science, National University of Defense Technology, Changsha, 410073, People's Republic of China

References

- [1] Choi Y-S, Kang J-W, Hwang D-K, Park S-J. Recent advances in ZnO-based light-emitting diodes, *IEEE Trans. Electr. Dev.* 2010; 57,26-41.
- [2] Janotti A, Van de Walle CG. Fundamentals of zinc oxide as a semiconductor, *Rep.Prog.Phys.*2009; 72, 126501 (29pages).

- [3] Özgür Ü, Alivov C, Liu C, Teke A, Reshchikov A, Doğan S, Avrutin V, Cho S-J, Morkoç H. A comprehensive review of ZnO materials and devices, *J.Appl.Phys.*2005; 98, 041301(103pages).
- [4] Look D.C., Recent advances in ZnO materials and devices, *Mater.Sci.and Eng. B* 2001; 80,383-387.
- [5] Tsukazaki A, Ohtomo A, Onuma T, Ohtani M, Makino T, Sumiya M, Ohtani K, Chichibu SF, Segawa Y, Ohno H, Koinuma H, Kawasaki M. Repeated temperature modulation epitaxy for p-type doping and light-emitting diode based on ZnO. *Nat.Mater.* 2005; 4,42-46.
- [6] Chen SC, Chen MJ, Huang YH, Sun WC, Li W C, Yang J R, Kuan H, Shiojiri M. White-light electroluminescence from n-ZnO/p-GaN heterojunction light-emitting diodes at reverse breakdown bias. *IEEE Trans. Electron Devices* 2011; 58,3970-3975.
- [7] <http://optics.org/article/26093>
- [8] Ryu YR, Lee TS, Lubguban J A, Corman A B, White H W, Leem J H, Han M S, Park YS, Youn C J, Kim WJ. Wide-band gap oxide alloy: BeZnO. *Appl.Phys.Lett.*88, 052103(3pages).
- [9] Han MS, Kima JH, Jeonga TS, Parka JM, Youn CJ, Leem JH, Ryu YR. Growth and optical properties of epitaxial $\text{Be}_x\text{Zn}_{1-x}\text{O}$ alloy films. *J.Cryst.Growth* 2007; 303, 506–509.
- [10] Ohtomo A, Kawasaki M, Koida T, Masubuchi K, Koinuma H, Sakurai Y, Yoshida Y, Yasuda T, Segawa Y. $\text{Mg}_x\text{Zn}_{1-x}\text{O}$ as a II–VI wide-gap semiconductor alloy. *Appl.Phys.Lett.*1998;72, 2466-2468 (3pages).
- [11] Takagi T, Tanaka H, Fujita S, Fujita S. Molecular beam epitaxy of high magnesium content single-phase wurtzite $\text{Mg}_x\text{Zn}_{1-x}\text{O}$ alloys (x similar or equal to 0.5) and their application to solar-blind region photodetectors. *Jpn. J.Appl. Phys.*2003;42, L401–L403.
- [12] Tampo H, Shibata H, Maejima K, Yamada A, Matsubara K, Fons P, Niki S, Tainaka T, Chiba Y, Kanie H. Strong excitonic transition of $\text{Zn}_{1-x}\text{Mg}_x\text{O}$ alloy. *Appl.Phys.Lett.* 91, 261907(3pages).
- [13] Wassner T A, Laumer B, Maier S, Laufer A, Meyer B K, Stutzmann M, Eickhoff M. (2009), Optical properties and structural characteristics of ZnMgO grown by plasma assisted molecular beam epitaxy. *J. Appl.Phys.*2009; 105, 023505 (6pages).
- [14] Makino T, Segawa Y, Kawasaki M, Ohtomo A, Shiroki R, Tamura K, Yasuda T, Koinuma H. Band gap engineering based on $\text{Mg}_x\text{Zn}_{1-x}\text{O}$ and $\text{Cd}_y\text{Zn}_{1-y}\text{O}$ ternary alloy films. *Appl.Phys.Lett.*2001; 78, 1237-1239.
- [15] Lai H H-C, Kuznetsov V, Egdell RG, Edwards PP. Electronic structure of ternary $\text{Cd}_x\text{Zn}_{1-x}\text{O}$ ($0 \leq x \leq 0.075$) alloy. *Appl.Phys.Lett.*100, 072106 (4 pages).
- [16] Chauveau J-M, Teisseire M, Kim-Chauveau H, Morhain C, Deparis O, Vinter B. Anisotropic strain effects on the photoluminescence emission from heteroepitaxial and

- homoepitaxial nonpolar (Zn,Mg)O/ZnO quantum wells. *J.Appl.Phys.*109,102420 (6pages).
- [17] Su SC, Lu Y M, Zhang Z Z, Shan C X, Yao B, Li B H, Shen D Z, Zhang J Y, Zhao D X, Fan XW. The optical properties of ZnO/ZnMgO single quantum well grown by P-MBE. *Appl. Surf. Sci.*2008; 254, 7303–7305.
- [18] Kim K-K, Niki S, Oh J-Y, Song J-O, Seong T-Y, Park S-J, Fujita SZ, Kim S-W. High electron concentration and mobility in Al-doped n-ZnO epilayer achieved via dopant activation using rapid-thermal annealing. *J.Appl.Phys.*97,066103 (6pages).
- [19] Kim Y M, Lee W J, Jung D-R, Kim J M, Nam SH, Kim H C, Park BW. Optical and electronic properties of post-annealed ZnO:Al thin films. *Appl. Phys. Lett.* 2010; 96, 171902 (3pages).
- [20] Bhosle V, Tiwari A, Narayan J. Electrical properties of transparent and conducting Ga doped ZnO. *J. Appl. Phys.*2006; 100, 033713 (6pages).
- [21] Yamada T, Miyake A, Kishimoto S, Makino H, Yamamoto N, Yamamoto T. Low resistivity Ga-doped ZnO thin films of less than 100 nm thickness prepared by ion plating with direct current arc discharge. *Appl. Phys. Lett.* 2007;91,051915(3pages).
- [22] Liang S, Bi X F. Structure, conductivity, and transparency of Ga-doped ZnO thin films arising from thickness contributions. *J.Appl.Phys.*2008;104,113533 (5pages).
- [23] Wang B G, Callahan MJ, Xu CC, Bouthillette LO, Giles NC, Bliss DF. Hydrothermal growth and characterization of indium-doped-conducting ZnO crystal. *J. Cryst. Growth.*2007; 304, 73-79.
- [24] Quang LH, Kuan LS, Liang GGK. Structural and electrical properties of single crystal indium doped ZnO films synthesized by low temperature solution method. *J.Cryst.Growth*2010; 312, 437-442.
- [25] Chen KJ, Hung FY, Chang SJ, Hu ZS. Microstructures, optical and electrical properties of In-doped ZnO thin films prepared by sol-gel method. *Appl. Surf. Sci.*2009; 255, 6308-6312.
- [26] Cao L, Zhu LP, Jiang J, Zhao R, Ye ZZ, Zhao BH. Highly transparent and conducting fluorine-doped ZnO thin films prepared by pulsed laser deposition. *Sol. Energ. Mat.Sol. C.*2011; 95, 894-898.
- [27] Chikoidze E, Modreanu M, Sallet V, Gorochoy O, Galtier P. (2008), Electrical properties of chlorine-doped ZnO thin films grown by MOCVD, *Phys. Stat. Sol. (A)*2008; 205, 1575–1579.
- [28] Liu W W, Yao B, Zhang ZZ, Li WF, Li BH, Shan CX, Zhang J Y, Shen D Z, Fan XW. Doping efficiency, optical and electrical properties of nitrogen-doped ZnO films. *J. App. Phys.*2011; 109,093518 (5pages).
- [29] Zeng YJ, Ye ZZ, Xu WZ, Liu B, Che Y, Zhu LP, Zhao BH. Study on the Hall-effect and photoluminescence of N-doped p-type ZnO thin films. *Mater.Lett.*2007; 61, 41-44.

- [30] Wang C, Ji ZG, Xi JH, Du J, Ye Z Z. Fabrication and characteristics of the low-resistive p-type ZnO thin films by DC reactive magnetron sputtering. *Mater. Lett.* 2006; 60, 912-914.
- [31] Kumar M, Kim T-H, Kim S-S, Lee B-T. Growth of epitaxial p-type ZnO thin films by codoping of Ga and N. *Appl. Phys. Lett.* 2006; 89, 112103 (3 pages).
- [32] Park CH, Zhang SB, Wei S-H. Origin of p-type doping difficulty in ZnO: The impurity perspective. *Phys. Rev. B* 2002; 66, 073202 (3 pages).
- [33] Limpijumngong S, Zhang S B, Wei S-H, Park CH. Doping by large-size-mismatched impurities: the microscopic origin of Arsenic or Antimony-doped p-type Zinc Oxide. *Phys. Rev. Lett.* 2004; 92, 15504 (4 pages).
- [34] Xiu FX, Yang Z, Mandalapu L J, Liu J L. Donor and acceptor competitions in phosphorus-doped ZnO. *Appl. Phys. Lett.* 2006; 88, 152116 (3 pages).
- [35] Kim K K, Kim H-S, Hwang DK, Lim J-H, Park S-J. Realization of p-type ZnO thin films via phosphorus doping and thermal activation of the dopant. *Appl. Phys. Lett.* 2003; 88, 152116 (3 pages).
- [36] Pan X H, Jiang J, Zeng Y J, He H P, Zhu L P, Ye Z Z, Zhao B H, Pan X Q. Electrical and optical properties of phosphorus-doped p-type ZnO films grown by metalorganic chemical vapor deposition. *J. Appl. Phys.* 2008; 103, 023708 (4 pages).
- [37] Vaithianathan V, Lee B-T, Kim S S. Pulsed-laser-deposited p-type ZnO films with phosphorus doping. *Appl. Phys. Lett.* 2005; 98, 043519 (3 pages).
- [38] Ryu Y R, Lee T S, Leem J H, White H W. Fabrication of homostructural ZnO p-n junctions and ohmic contacts to arsenic-doped p-type ZnO. *Appl. Phys. Lett.* 2003; 83, 4032-4034.
- [39] Vaithianathan V, Lee B-T, Kim S S. Preparation of As-doped p-type ZnO films using a Zn₃As₂/ZnO target with pulsed laser deposition. *Appl. Phys. Lett.* 2005; 86, 062101 (3 pages).
- [40] Kang HS, Kim GH, Kim DL, Chang HW, Ahn BD, Lee SY. Investigation on the p-type formation mechanism of arsenic-doped p-type ZnO thin films. *Appl. Phys. Lett.* 2006; 89, 181103 (3 pages).
- [41] Guo W, Allenic A, Chen YB, Pan XQ, Che Y, Hu Z D, Liu B. Microstructure and properties of epitaxial antimony-doped p-type ZnO films fabricated by pulsed laser deposition. *Appl. Phys. Lett.* 2007; 90, 242108 (3 pages).
- [42] Xiu FX, Yang Z, Mandalapu L J, Zhao DT, Liu JL, Beyermann YP. High-mobility Sb-doped p-type ZnO by molecular-beam epitaxy. *Appl. Phys. Lett.* 2005; 87, 152101 (3 pages).
- [43] Yi JB, Lim CC, Xing GZ, Fan HM, Van LH, Huang SL, Yang KS, Huang XL, Wang BY, Wu T, Wang L, Zhang HT, Gao XY, Liu T, Wee ATS, Feng Y.P, Ding J. (2010),

- Ferromagnetism in dilute magnetic semiconductors through defect engineering: Li-doped ZnO. *Phys.Rev.Lett.*2010;104,137201 (4pages).
- [44] Lin SS, He HP, Lu YF, Ye ZZ. Mechanism of Na-doped p-type ZnO films: Suppressing Na interstitials by codoping with H and Na of appropriate concentrations. *J.Appl.Phys.*2009;106, 093508(5pages).
- [45] Wu J, Yang YT. Deposition of K-doped p type ZnO thin films on (0001) Al₂O₃ substrates. *Mater.Lett.*2008; 62, 1899-1901.
- [46] Chang SP, Chuang RW, Chang SJ, Chiou YA, Lu CY. MBE n-ZnO/MOCVD p-GaN heterojunction light-emitting diode. *Thin Solid Films* 2009; 517, 5054-5056.
- [47] Wang SP, Shan CX, Zhu H, Li B H, Shen D Z, Liu XY, Tang Z K. Phosphor-converted light-emitting diode based on ZnO-based heterojunction. *J. Lumin.*2010;130, 2215-2217.
- [48] Zheng H, Mei ZX, Zeng Z Q, Liu Y Z, Guo LW, Jia JF, Xue Q K, Zhang Z, Du X L. Fabrication and characterization of high quality n-ZnO/p-GaN heterojunction light-emission diodes. *Thin solid films*2011; 520, 445- 447.
- [49] Mares J W, Falanga M, Thompson AV, Osinsky A, Xie J Q, Hertog B, Dabiran A, Chow PP, Karpov S, Schoenfeld W V. Hybrid CdZnO/GaN quantum-well light emitting diodes. *J.Appl.Phys.*2008; 104,093107 (5pages).
- [50] Osinsky A, Dong GW, Kauser MZ, Hertog B, Dabiran AM, Chow PP, Pearton SJ, Lopatiuk O, Chernyak L. MgZnO/AlGaN heterostructure light-emitting diodes. *Appl.Phys.Lett.*2004; 85,4272-4274.
- [51] Hwang S-H, Chung TH, Lee BT. Study on the interfacial layer in ZnO/GaN heterostructure light-emitting diode. *Mater.Sci.Eng.B*2009;157, 32-35.
- [52] Lee JY, Lee JH, Kim HS, Lee CH, Ahn H-S, Cho HK, Kim YY, Kong BH, Lee HS. A study on the origin of emission of the annealed n-ZnO/p-GaN heterostructure LED. *Thin Solid Films*2009;517, 5157-5160.
- [53] Han W S, Kim Y Y, Kong BH, Cho H K. Ultraviolet light emitting diode with n-ZnO:Ga/i-ZnO/p-GaN:Mg heterojunction. *Thin solid films*2009; 517, 5106-5109.
- [54] Zhang SG, Zhang XW, Yin ZG, Wang JX, Dong JJ, Wang ZG, Qu S, Cui B, Wowchak AM, Dabiran AM, Chow P P. Improvement of electroluminescent performance of n-ZnO/AlN/p-GaN light-emitting diodes by optimizing the AlN barrier layer. *J. Appl.Phys.*2011; 109, 093708 (6pages).
- [55] Iwan S, Bambang S, Zhao JL., Tan ST, Fan HM, Sun L, Zhang S, Ryu HH, Sun XW. Green electroluminescence from an n-ZnO: Er/p-Si heterostructured light-emitting diode. *Physica B*, <http://dx.doi.org/10.1016/j.physb.2012.03.072> .
- [56] Ohta H, Kawamura K-I, Orita M, Hirano M, Sarukura N, Hosono H. Current injection emission from a transparent p-n junction composed of p-SrCu₂O₂/n-ZnO. *Appl.Phys.Lett.*2000;77, 475-477.

- [57] Rogers DJ, Teherani F H, Yasan A, Minder K, Kung P, Razeghi M. Electroluminescence at 375 nm from a ZnO/GaN:Mg/c-Al₂O₃heterojunction light emitting diode. *Appl.Phys.Lett.*2006; 88,14198 (3pages).
- [58] Yu QX, XuB, Wu Q H, Liao Y, Wang GZ, Fang RC. Optical properties of ZnO/GaNheterostructure and its near-ultravioletlight-emitting diode. *Appl. Phys. Lett.* 2003; 83, 4713-4715.
- [59] Ye J D,Gu S L ,Zhu S M, Liu W, Liu SM, Zhang R, Shi Y, Zheng Y D. Electroluminescent and transport mechanisms of n-ZnO/p-Siheterojunctions. *Appl.Phys.Lett.*2006; 88, 182112 (3pages).
- [60] Li XP, Zhang BL, Zhu HC, Dong X, Xia XC, Cui YG, Ma Y, Du GT. Study on the luminescence properties of n-ZnO/p-Si hetero-junction diode grown by MOCVD. *J. Phys. D: Appl. Phys.* 2008; 41, 035101(5pages).
- [61] Alivov YI, Kalinina EV, Cherenkov AE, Look DC, Ataev BM, Omaev AK, Chukichev MV, Bagnall DM. Fabrication and characterization of n-ZnO/p-AlGaNHeterojunction-light-emitting diodes on 6H-SiC substrates. *Appl. Phys.Lett.*2003; 83, 4719-4721.
- [62] Alivov Y I, Nostrand JEV, Look DC, Chukichev MV, Ataev BM. Observation of 430nm electroluminescence from ZnO/GaNheterojunctionlight-emitting diodes. *Appl.Phys.Lett.*2003; 83, 2943-2945.
- [63] Chichibu SF, Ohmori T, Shibata N, Koyama T, Onuma T. Fabrication of p-CuGaS₂/n-ZnO: Alheterojunction light-emitting diode grown by metalorganic vapor phase epitaxy and helicon-wave-excited-plasma sputtering methods. *J. Phys. Chem.Solids*2005; 66, 1868-1871.
- [64] Xu S, Xu C, Liu Y, Hu YF, Yang RS, Yang Q, Ryou J-H, Kim HJ, Lochner Z, Choi S, Dupuis R, Wang ZL. Ordered nanowire array blue/near-UV light emitting diodes. *Adv.Mater.*2010;22, 4749-4753.
- [65] Bano N, Zaman S, Zainelabdin A, Hussain S, Hussain I, Nur O, Willander M. (2010), ZnO-organic hybrid white light emitting diodes grown on flexible plastic using low temperature aqueous chemical method. *J. Appl.Phys.*2010;108, 043103 (5pages).
- [66] Guo Z, Zhang H, Zhao D X, Liu YC, Yao B, Li B H, Zhang Z Z, Shen D Z. The ultra-low driven current ultraviolet-blue light-emitting diode based on n-ZnO nanowires/i-polymer/p-GaN heterojunction. *Appl. Phys. Lett.*2010; 97, 173508 (3pages).
- [67] Alvi NH, Usman Ali SM, Hussain S, Nur O, Willander M. Fabrication and comparative optical characterization of n-ZnO nanostructures (nanowalls, nanorods, nanoflowers and nanotubes)/p-GaN white-light-emitting diodes. *Scripta.Mater.* 2011; 64, 697-700.
- [68] Willander M, Nur O, Zaman S, Zainelabdin Z, Banon, Hussain I. (2011), Zinc oxide nanorods/polymer hybrid heterojunctions for white light emitting diodes. *J. Phys. D: Appl. Phys.* 2011; 44 , 224017(6pages).

- [69] Zhang X M, Lu M-Y, Zhang Y, Chen L-J, Wang Z L. Fabrication of a high-brightness blue-light-emitting diode using a ZnO-nanowire array grown on p-GaN thin film. *Adv. Mater.* 2009; 21, 2767-2770.
- [70] Chang C-Y, Tsao F-C, Pan C-J, Chi G-C, Wang H-T, Chen J-J, Ren F, Norton D P, Pearton S J, Chen K-H, Chen L-C. Electroluminescence from ZnO nanowire/polymer composite p-n junction. *Appl. Phys. Lett.* 2006; 88, 173503 (3 pages)
- [71] Klason P, Rahman MM, Hu Q-H, Nur O, Turan R, Willander M. Fabrication and characterization of p-Si/n-ZnO heterostructured junctions. *Microelectronics Journal* 2009; 40, 706-710.
- [72] Lee S W, Cho H D, Panin G, Kang T W, Vertical ZnO nanorod/Si contact light-emitting diode. *Appl. Phys. Lett.* 2011; 98, 093110 (3 pages)
- [73] Park W I, Yi G C. Electroluminescence in n-ZnO nanorod arrays vertically grown on p-GaN. *Adv. Mater.* 2004; 16, 87-90.
- [74] Park S H, Kim S H, Han S W. Growth of homoepitaxial ZnO film on ZnO nanorods and light emitting diode applications. *Nanotech.* 2007; 18, 055608 (6 pages).
- [75] Lupan O, Pauporté T, Viana B. Low-voltage UV-electroluminescence from ZnO-nanowire array/p-GaN light-emitting diodes. *Adv. Mater.* 2010; 22, 3298-3302.
- [76] Zhang Q B, Guo H H, Feng Z F, Lin L L, Zhou J Z, Li Z H. n-ZnO nanorods/p-CuSCN-heterojunction light-emitting diodes fabricated by electrochemical method. *Electrochim. Acta* 2010; 55, 4889 - 4894.
- [77] Xi Y Y, Hsu Y F, Djurić AB, Ng A M C, Chan W K, Tam H L, Cheah K W. NiO/ZnO light emitting diodes by solution-based growth. *Appl. Phys. Lett.* 2008; 92, 113505 (3 pages).
- [78] Guo R, Nishimura J, Matsumoto M, Higashihata M, Nakamura D, Okada T. Electroluminescence from ZnO nanowire based p-GaN/n-ZnO heterojunction light-emitting diodes. *Appl. Phys. B, Photophys. Laser Chem.* 2009; 94, 33-38.
- [79] Mandalapu L J, Yang Z, Chu S, Liu J L. Ultraviolet emission from Sb-doped p-type ZnO based heterojunction light-emitting diodes. *Appl. Phys. Lett.* 2008; 92, 122101 (3 pages).
- [80] Li L, Yang Z, Kong J Y, Liu J L. Blue electroluminescence from ZnO based heterojunction diodes with CdZnO active layers. *Appl. Phys. Lett.* 2009; 95, 232117 (3 pages)
- [81] Nakahara K, Akasaka S, Yuji H, Tamura K, Fujii T, Nishimoto Y, Takamizu D, Sasaki A, Tanabe T, Takasu H, Amaike H, Onuma T, Chichibu S F, Sukazaki A, Ohtomo A, Kawasaki M. Nitrogen doped $\text{Mg}_x\text{Zn}_{1-x}\text{O}/\text{ZnO}$ single heterostructure ultraviolet-light-emitting diodes on ZnO substrates. *Appl. Phys. Lett.* 2010; 97, 013501 (3 pages).
- [82] Park T-Y, Choi Y-S, Kim S-M, Jung G-Y, Park S-J, Kwon B-J, Cho Y-H. Electroluminescence emission from light-emitting diode of p-ZnO/(InGaN/GaN) multi-quantum well/n-GaN. *Appl. Phys. Lett.* 2011; 98, 251111 (3 pages)

- [83] Sun J C, Feng Q J, Bian JM, Yu DQ, Li MK, Li CR, Liang HW, Zhao JZ, Qiu H, Du GT. Ultraviolet electroluminescence from ZnO-based light-emitting diode with p-ZnO:N/n-GaN:Si heterojunction structure. *J. Lumin.* 2011; 131, 825-828.
- [84] Hwang D-K, Kang S-H, Lim J-H, Yang E-J, Oh J-Y, Yang J-H, Park S-J. p-ZnO/n-GaN-heterostructure ZnO light-emitting diodes. *Appl. Phys. Lett.* 2005; 86, 222101 (3pages).
- [85] Choi H-K, Park J-H, Jeong S-H, Lee B-T. Realization of As-doped p-type ZnO thin-films using sputter deposition. *Semicond. Sci. Technol.* 2009; 24, 105003 (4pages).
- [86] Kim YY, Han WS, Cho HK. Determination of electrical types in the P-doped ZnO thin films by the control of ambient gas flow. *Appl. Surf. Sci.* 2010; 256, 4438-4441.
- [87] Kim HS, Lugo F, Pearton S J, Norton D P, Wang Y-L, Ren F. Phosphorus doped ZnO light emitting diodes fabricated via pulsed laser deposition. *Appl. Phys. Lett.* 2008; 92, 112108 (3pages).
- [88] Tay C B, Chua S J, Loh K P. Stable p-type doping of ZnO film in aqueous solution at low temperatures. *J. Phys. Chem. C* 2010; 114, 9981-9987.
- [89] Wei ZP, Lu YM, Shen DZ, Zhang ZZ, Yao B, Li BH, Zhang JY, Zhao DX, Fan XW, Tang ZK. Room temperature p-n ZnO blue-violet light-emitting diodes. *Appl. Phys. Lett.* 2007; 90, 042113 (3pages).
- [90] Chu S, Lim JH, Mandalapu LJ, Yang Z, Li L, Liu J L. (2008), Sb-doped p-ZnO/Ga-doped n-ZnO homojunction ultraviolet light emitting diodes. *Appl. Phys. Lett.* 2008; 92, 152103 (3pages).
- [91] Kong JY, Chu S, Olmedo M, Li L, Yang Z, Liu J L. Dominant ultraviolet light emissions in packed ZnO columnar homojunction diodes. *Appl. Phys. Lett.* 2008; 93, 132113 (3pages).
- [92] Liu W, Gu SL, Ye J D, Zhu SM, Liu S M, Zhou X, Zhang R, Shi Y, Zheng YD, Hang Y, Zhang CL. (2006), Blue-yellow ZnO homojunction light-emitting diode realized by metalorganic chemical vapor deposition technique. *Appl. Phys. Lett.* 2006; 88, 092101 (3pages).
- [93] Sun J C, Zhao J Z, Liang H W, Bian J M, Hu L Z, Zhang H Q, Liang X P., Liu W F, Du GT. Realization of ultraviolet electroluminescence from ZnO homojunction with n-ZnO/p-ZnO:As/GaAs structure. *Appl. Phys. Lett.* 2007; 90, 121128 (3pages).
- [94] Sun J C, Liang H W, Zhao J Z, Bian J M, Feng Q J, Hu L Z, Zhang H Q, Liang X P., Luo Y M, Du GT. Ultraviolet electroluminescence from n-ZnO:Ga/p-ZnO:N homojunction device on sapphire substrate with p-type ZnO:N layer formed by annealing in N₂O plasma ambient. *Chem. Phys. Lett.* 2008; 460, 548-551.
- [95] Gu Q L, Ling C C, Brauer G, Anwand W, Skorupa W, Hsu Y F, Djurišić AB, Zhu C Y, Fung S, Lu L W. Deep level defects in a nitrogen-implanted ZnO homogeneous p-n junction. *Appl. Phys. Lett.* 2008; 92, 222109 (3pages).

- [96] Yang Y, Sun X. W, Tay B K, You G F, Tan S T, Teo KL. (2008), A p-n homojunction ZnO nanorod light-emitting diode formed by As ion implantation. *Appl.Phys.Lett.* 2008;93,253107 (3pages).
- [97] Sun X W, Ling B, Zhao J L, Tan ST, Yang Y, Shen YQ, Dong Z L, Li CX. Ultraviolet emission from a ZnO rod homojunction light-emitting diode. *Appl.Phys.Lett.* 2009; 95,133124 (3pages).
- [98] Lim J H, Kang C K, Kim K K, Park I K, Hwang D K, Park S J. UV electroluminescence emission from ZnO light-emitting diodes grown by high-temperature radio frequency sputtering. *Adv.Mater.* 2006; 18, 2720–2724.
- [99] Fang X, Li JH, Zhao D X, Shen DZ, Li B H, Wang X H. Phosphorus-doped p-type ZnO nanorods and ZnO nanorod p-n homojunction LED fabricated by hydrothermal method. *J. Phys. Chem. C* 2009; 113, 21208–21212.
- [100] Ryu Y R, Lee T-S, Lubguban J A, White H W, Kim B J, Park Y S, Youn C J. (2006), Next generation of oxide photonic devices: ZnO-based ultraviolet light emitting diodes. *Appl.Phys.Lett.* 2006; 88, 241108 (3pages).

Technological Challenges for Efficient AlGaAs Nonlinear Sources on Chip

M. Savanier, C. Ozanam, F. Ghiglieno, L. Lanco,
X. Lafosse, A. Lemaître, I. Favero, S. Ducci and G. Leo

Additional information is available at the end of the chapter

<http://dx.doi.org/10.5772/52201>

1. Introduction

Photonics puts at stake a wide variety of applications, from applied fields of physics, such as ultrafast all-optical signal processing [1] or pollutant monitoring [2], to more fundamental ones, *e.g.* quantum information [3], and its convergence with electronics at chip-scale level is one of today's great scientific and technological challenges. As a consequence, the full integration of optoelectronics devices on existing developed platforms is expected to be the next technological leap, with major breakthroughs in telecommunications, industry and health. While the main building blocks of optical integrated circuitry have been reported in the standard SOI platform [4], coherent light sources still markedly lack to achieve this transition of paradigm. To date, the hybrid conjunction of silicon photonics and direct-gap III-V compounds appears to be one of the most promising key technologies towards large-scale photonic integration and scalability [5]. In particular, such photonics platform could capitalize advanced functionalities enabled by guided-wave quadratic nonlinear optics. Thus, the demonstration of the electrically pumped versions of an optical parametric oscillator (OPO) or of a telecom twin-photon source (TTPS) would have a great impact on applications requiring room-temperature operation and wide tunability.

In this context, the Aluminum Gallium Arsenide (AlGaAs) system is an ideal candidate for the nonlinear photonic design, because of its numerous advantages: high second order susceptibility, wide transparency window, good thermal conductivity and monolithic integration.

In order to design efficient frequency converters, the key issue is to keep a constant phase relation between the three interacting waves. In general, this is not a trivial task because of the phase-velocity mismatch induced by the material chromatic dispersion [6]. While few phase-

matching strategies have been investigated, an original modal phase-matching scheme based on Bragg reflector waveguides has been recently addressed, reviving the interest for spontaneous parametric down-conversion (SPDC) in AlGaAs-based waveguides [7,8].

In this chapter we will focus on AlGaAs-based nonlinear waveguides in which phase-matching is achieved through form birefringence, artificially induced in optical heterostructures by selective oxidation of Al-rich layers into Aluminum Oxide (referred to as AlOx thereafter). Despite recent technological improvement and promising performances for frequency conversion in the near [9] and mid-infrared regions [10], neither the OPO nor the TTPS has been demonstrated yet on chip, because of technological issues, mainly excessive propagation losses and absence of appropriate built-in cavity. In the second section we present the scientific context of this work, focusing on AlGaAs integrated nonlinear devices exploiting the so-called form birefringence phase-matching scheme. Section three is devoted to the design procedure and the optimization of the fabrication process of two types of partially oxidized waveguides, while their experimental performances are summarized in section four. A comprehensive study of the different loss mechanisms involved is presented in section five, and the design and fabrication of built-in cavity mirrors is described in the sixth section.

2. Integrated frequency converters in the infrared

2.1. Key importance of the near and mid-infrared ranges

Near and mid-infrared radiation corresponds to the region of the electromagnetic spectrum with wavelengths spanning between 1 and 20 μm . It contains two telecom windows (around 1.3 and 1.5 μm) as well as strong characteristic roto-vibrational lines of many molecules (pollutants, toxins, etc.) and two atmospheric transmission windows (3-5 μm and 8-13 μm), which makes it essential for civilian and military applications such as spectroscopy, material processing, molecular sensing, thermal imaging and defense.

The current state-of-the-art sources developed for these applications can be categorized in three main groups: solid-state and fiber lasers, semiconductor lasers, and parametric sources. Although the former include a wide variety of well-known and established emitters, they still remain macroscopic objects falling out of the scope of on-chip integration, and their tunability is severely limited by the discrete energy transitions of the active media [11]. On the contrary, since their first demonstration respectively 50 and almost 20 years ago [12,13], laser diodes and quantum cascade lasers (QCLs) have greatly benefited from the flexibility enabled by the engineering of energy band structure and from clean-room fabrication technologies. Yet, these two technological streams hardly overlap in the wavelength range around 3 μm . So far, room temperature operation has only been demonstrated for III-V antimonide laser diodes operating in continuous-wave (CW) regime up to 3.0 μm [14]; and for QCLs (either grown on InP substrate or in the III-V antimonide system) with emission wavelength extended down to 3.1 μm in pulsed regime, and to 3.6 μm CW [15,16]. However, because of its controllability and re-growth constraints, commercial producers tend to avoid the use of antimony. That is why antimonide laser diodes are not yet standard

off-the-shelf products, whereas QCLs, thanks to a mature and possibly Sb-free technology, are now finding commercial applications and increasingly replace the outdated lead-salt laser diodes. Nevertheless, integrated semiconductor sources are still lacking around 3 μm , and apart from few QCL products (*e.g.* $\lambda \sim 3.3 \mu\text{m}$ by Daylight Solutions), solid state and nonlinear optics-based sources represent the majority of commercially available sources [17]. Recently, intra-cavity second harmonic generation (SHG) has been reported in QCLs, extending their emission range to wavelengths as small as 2.7 μm , at the price of poor conversion efficiency though [18].

Nonlinear optics, by means of difference frequency generation (DFG) and optical parametric oscillation, is a well-known alternative to cover the whole 1-10 μm span. The wide variety of spectral/temporal formats allowed by nonlinear $\chi^{(2)}$ processes in transparent materials, endows parametric sources with a high level of flexibility. Moreover, SPDC is currently the most widely used process to generate quantum photon pairs, which have become one of the building blocks of quantum information. To date, room-temperature SPDC has been reported in passive AlGaAs waveguides designed to perform 0.775-to-1.55 μm down-conversion [7,8], while entanglement has been demonstrated in light emitting diodes only at cryogenic temperature [19]. Thus, the fabrication of an electrically-pumped version of such light source operating at room temperature in the telecom range also constitutes a high-potential and challenging goal.

2.2. Integration of nonlinear devices

Fulfilling the phase-matching condition is crucial for efficient three-wave mixing. The classical approach to cancel out the phase-velocity mismatch between the interacting waves is to rely on the birefringence of the nonlinear medium. The limited choice of suitable materials led to quasi-phase matching (QPM), well established in ferroelectric crystals, with a great impact on the fabrication of infrared parametric sources. QPM consists in a periodic inversion of nonlinearity along the propagation direction, minimizing the phase-mismatch to allow the nonlinear interaction to build constructively. In this context, the development of bulk dielectric crystals like periodically-poled LiNbO_3 (PPLN) has made them the workhorse materials of $\chi^{(2)}$ optics. Besides, by implementing a guided-wave configuration in which the three optical modes are confined and can interact over several centimeters, normalized conversion efficiencies up to $\sim 150 \text{ \%W}^{-1}\text{cm}^{-2}$ have been demonstrated [20], yielding to the demonstration of compact and efficient photon pairs sources [21] and OPOs [22]. Nonetheless, such setups are composed of discrete optical components with critical alignment and do not lend themselves to optoelectronic integration. That is why direct-gap semiconductor compounds, provided that they have significant second-order nonlinearity, are an attractive platform for the coming years' photonics, thanks to mature nano-fabrication technology. Indeed they promise on-chip integration of both efficient frequency converters and laser pumps. Gallium arsenide (GaAs), or more generally the AlGaAs system, is particularly interesting because it exhibits a huge second-order nonlinearity ($d_{14} \sim 100 \text{ pm/V}$), a broad transparency window (from 0.9 to 17 μm), and a large variety of design and fabrication solutions [23]. Because AlGaAs is neither birefringent nor ferroelectric, phase matching

is not a trivial task, especially if the frequencies involved lie close to the material bandgap, where the dispersion is strong. Similarly to lithium niobate, the demonstration of QPM in bulk orientation-patterned GaAs (OP-GaAs) [24] enabled the demonstration of efficient tunable infrared sources, including the first GaAs-based OPO in 2004 [25]. Regarding OP-GaAs waveguides, in addition to their complex fabrication process, their performances are limited by high optical losses due to scattering in the corrugated waveguide core, resulting in modest normalized conversion efficiencies of $\sim 90\%W^{-1}cm^{-2}$ [24]. Another approach, based on the engineering of modal dispersion, enabled the implementation of two additional phase-matching strategies:

1. modal phase-matching, involving transverse modes of different order at the price of a worse nonlinear overlap integral [8]; and
2. form-birefringent phase matching.

The latter relies on optical heterostructures, in which thin low-index non-stoichiometric AlOx layers are intertwined with AlGaAs layers, so to artificially induce the necessary birefringence to compensate for the chromatic dispersion [10]. For these two schemes, normalized conversion efficiencies of $\sim 250\%W^{-1}cm^{-2}$ and $\sim 1000\%W^{-1}cm^{-2}$ have been reported respectively, confirming that nonlinear integrated GaAs-based devices are a credible and promising alternative to standard LiNbO₃.

2.3. Form birefringence phase matching scheme

Since AlGaAs is optically isotropic, the standard birefringent phase-matching scheme cannot be implemented. Nevertheless, in a guided-wave configuration, a small anisotropy appears as the TE₀₀ and TM₀₀ solutions of the Maxwell equations experience different boundary conditions, hence leading to a non-zero birefringence $|n(TE_{00})-n(TM_{00})|$. The latter can then be tailored for fundamental, orthogonally polarized eigen modes. However this quantity is in general much smaller than the dispersion, so that this technique remains unsuitable to phase match any nonlinear interaction.

In order to boost this effect and artificially induce a significant amount of birefringence, one can pattern the waveguide core at sub-wavelength scale, by repeatedly breaking the refractive index continuity with a two-material multilayer. The resulting metamaterial behaves as a macroscopic uniaxial crystal, whose birefringence is fully determined by the index contrast and the filling factors of the materials [27]. In particular, this so-called form birefringence phase-matching scheme has been developed in the AlGaAs platform during the late 90's at Thomson CSF laboratory (today Alcatel Thales III-V Lab) [26]. Thanks to the wide variety of index profile designs enabled by the dependence of refractive index with the aluminum fraction, the phase-matching condition can be engineered at will.

The first phase-matched interaction of this type dates back to the seventies, with the doubling of a CO₂ laser emitting at 10.6 μm [27]. In that case, given the weak material dispersion in the mid-infrared (few 10^{-2}) an AlAs/GaAs heterostructure suffices to meet the phase-matching condition. However, since the material dispersion strongly increases when the frequencies of the interacting waves lie close to the bandgap of the material, nonlinear

interactions between the visible and the mid-infrared are then prevented for the simple Al-GaAs platform.

In 1990, the discovery of selective wet oxidation of Al-rich AlGaAs layers drastically broadened the potential of form-birefringent phase-matching, thanks to the density, homogeneity and stability of a new type of aluminum oxide [28]. This material exhibits nice optical properties, such as a wide transparency window and a low refractive index of ~ 1.6 , and is electrically insulating. A few engineering domains rapidly took advantage of these physical properties: electronics, with field effect transistors [29]; optics, with broadband Bragg mirrors [30]; and optoelectronics, by combining optical and electrical confinement in vertical-cavity surface-emitting lasers (VCSELs) to improve their yield and ensure single-mode emission [31].

In the case dealt with in this chapter, the GaAs/AlOx system allows accessing birefringence of several 10^{-1} , *i.e.* up to one order of magnitude higher than in a GaAs/AlAs heterostructure. This in turn enables to phase-match any nonlinear quadratic interaction with wavelengths spanning from the visible to the mid-infrared region [9,10,32]. Despite this substantial advantage, this material is not yet completely mature for demanding photonics applications, and its fine understanding is a matter at the intersection of photonics and materials science.

3. Design and fabrication of the devices

3.1. Design guidelines of partially oxidized AlGaAs waveguides

To demonstrate the high potential of the form birefringence phase-matching scheme, we have implemented it into two multi-layered structures designed for the down-conversion of pumps with respective wavelength $1.06 \mu\text{m}$ and $0.775 \mu\text{m}$. The first device is intended to perform as an OPO in the near and mid-infrared regions, while the second one is meant to operate as a TTPS.

For each structure, the design's objective is to balance the combined material and waveguide dispersions with enough induced birefringence, taking into account the following criteria:

- the transverse dimensions of the waveguide should favor zero-order modes to maximize their nonlinear overlap integral and avoid injecting power into non phase-matched higher order modes,
- the aluminum fraction in the guiding core should be low to optimally exploit the $\chi^{(2)}$ non-linearity of the material, which must also be transparent at every frequency involved in the three-wave mixing,
- the aluminum fraction in the claddings should be high enough for a good confinement of the waves, but also guarantee the stability of the material, with no parasitic spontaneous oxidation,
- the number of AlOx layers should be kept as small as possible as their second order susceptibility is zero and their quality is expected to be worse than crystalline lattice-matched AlGaAs.

Moreover, our choice is for type I phase-matching, rather than type II, as it requires a smaller amount of birefringence (and therefore of AlOx). According to this configuration and the non-zero elements of the second order susceptibility tensor of GaAs, quadratic interactions are only possible between a combination of two low frequency TE modes (*i.e.* with polarization in the layers plane) and a higher frequency TM mode (*i.e.* with polarization perpendicular to the layers plane).

For technological reasons, the thickness of the Al-rich layers to be oxidized must be comprised between few nanometers and few microns. Indeed, the diffusion of oxidant species along very thin layers is impeded, and the overall mechanical stability of thick oxidized layers is critical. However, this mechanical instability can be mitigated by adding a small amount of gallium to the thin AlAs layers [33]. As a result, we have chosen to deal with ~30 nm layers of $\text{Al}_{0.98}\text{Ga}_{0.02}\text{As}$ (basically AlAs). Note that all the thicknesses of the oxidized layers are fixed to be the same throughout the whole structure, so to optimally calibrate the oxidation process and benefit from the best experimental conditions.

While for the first “OPO structure”, the fulfillment of the phase-matching condition requires the insertion of only five AlOx layers in the GaAs core, the situation differs in two aspects for the “TTPS structure”:

1. the guiding core material must be switched to $\text{Al}_{0.25}\text{Ga}_{0.75}\text{As}$ to ensure its transparency at $0.775\ \mu\text{m}$, and
2. due to the higher dispersion generated by the proximity of the material bandgap, the number of AlOx layers must be significantly increased, leading to their insertion into the waveguide claddings as well.

In both cases, the thickness of the (Al)GaAs layers surrounded by oxide layers is set to tune the degeneracy wavelength. The two final designs are given in Tables 1 and 2, whereas the corresponding refractive index profiles and the intensity distributions of the phase-matched modes at degeneracy are shown in Figures 1 and 2.

| Layer | Composition | Thickness (nm) | Repetition |
|-----------|---|----------------|------------|
| Cap | GaAs | 30 | |
| Cladding | $\text{Al}_{0.7}\text{Ga}_{0.3}\text{As}$ | 1000 | |
| Core | $\text{Al}_{0.98}\text{Ga}_{0.02}\text{As}$ | 37.5 | × 4 |
| | GaAs | 273 | |
| | $\text{Al}_{0.98}\text{Ga}_{0.02}\text{As}$ | 37.5 | |
| Cladding | $\text{Al}_{0.7}\text{Ga}_{0.3}\text{As}$ | 1000 | |
| Buffer | $\text{Al}_{0.92}\text{Ga}_{0.08}\text{As}$ | 1000 | |
| Substrate | GaAs | - | |

Table 1. Multilayer sequence for $1.06\ \mu\text{m}$ to $2.12\ \mu\text{m}$ frequency conversion.

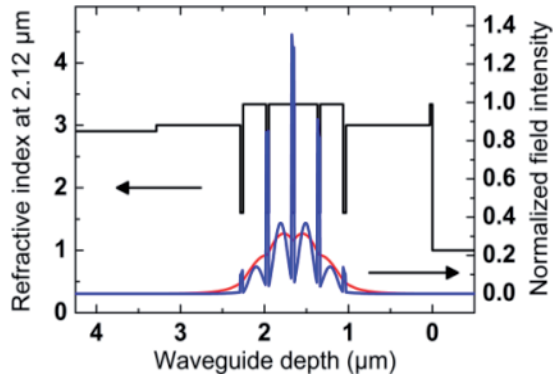


Figure 1. Refractive index profile (black line), phase-matched TE₀ (red line), and TM₀ (blue line) modes at 2.12 μm and 1.06 μm respectively, represented along the growth direction.

| Layer | Composition | Thickness (nm) | Repetition |
|-----------|--|----------------|------------|
| Cap | GaAs | 30 | |
| Cladding | Al _{0.8} Ga _{0.2} As | 166 | × 4 |
| | Al _{0.98} Ga _{0.02} As | 37.5 | |
| Core | Al _{0.25} Ga _{0.75} As | 166 | × 8 |
| | Al _{0.98} Ga _{0.02} As | 37.5 | |
| Cladding | Al _{0.8} Ga _{0.2} As | 166 | × 4 |
| | Al _{0.98} Ga _{0.02} As | 37.5 | |
| Buffer | Al _{0.8} Ga _{0.2} As | 100 | |
| Substrate | GaAs | - | |

Table 2. Multilayer sequence for 0.775 μm to 1.55 μm frequency conversion.

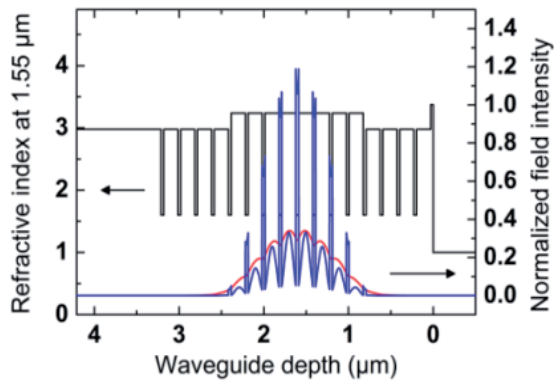


Figure 2. Refractive index profile (black line), phase-matched TE₀ (red line), and TM₀ (blue line) modes at 1.55 μm and 0.775 μm respectively, represented along the growth direction.

3.2. Waveguide fabrication steps

The main advantage of the form birefringence phase-matching scheme with respect to competing techniques is the inherently high nonlinear overlap integral between very look-alike fundamental modes. Thereby, nonlinear partially oxidized AlGaAs waveguides are expected to give interestingly high conversion efficiencies. However, their performances rely on the quality of their fabrication, for optical propagation losses heavily affect the phase-matching.

Fabrication improvements

Thanks to the well-developed clean-room techniques and equipments (*e.g.* epitaxial growth, lithography and cleaving) the AlGaAs platform is readily mature and compatible with the fabrication of high quality integrated devices. Furthermore, over the last fifteen years GaAs/AlOx waveguides have significantly benefited from the efforts and technological improvements achieved in terms of etching and oxidation [34].

The first mid-infrared DFG results have been reported in RIE-etched double mesa waveguides consisting in a 3 μm wide ridge (for lateral confinement of the guided modes) on top of a 100 μm wide mesa (to access the buried AlAs layers), with high propagation losses of $\sim 2 \text{ cm}^{-1}$ in the near infrared, and a 3 $\%W^{-1}\text{cm}^{-2}$ normalized conversion efficiency [35]. This high attenuation coefficient was assumed to stem from

1. the poor quality of the etched sidewalls responsible for significant scattering losses and
2. long oxidation times (1h20min) during which the oxide quality was degraded.

After optimization of the design, dry etching has then been replaced with $\text{H}_2\text{SO}_4:\text{H}_2\text{O}_2:\text{H}_2\text{O}$ (3:1:1) chemical wet etching to obtain smoother sidewalls. The resulting losses of oxidized samples were reduced to $\sim 1.5 \text{ cm}^{-1}$, and a normalized conversion efficiency of 1000 $\%W^{-1}\text{cm}^{-2}$ was estimated through SPDC around 2 μm [36]. Then, always in the same group, the waveguide geometry has been switched to single ridges (3 $\mu\text{m} \times 3\mu\text{m}$) to shorten the oxidation time to several minutes, hence low losses of $\sim 0.7 \text{ cm}^{-1}$ and a 1500 $\%W^{-1}\text{cm}^{-2}$ normalized conversion efficiency [10]. However, the slight etchant selectivity led to peculiar saw-tooth transverse profiles with mediocre process uniformity. Finally, sample homogeneity has been improved by using the non selective $\text{CH}_3\text{COOH}:\text{HBr}:\text{K}_2\text{Cr}_2\text{O}_7$ etchant (1:1:1) [37].

Two scanning electron microscopy images of finalized samples are presented in Figure 3. Despite the poor control on the waveguide transverse profile, chemical etching is still relevant compared to dry etching techniques such as ICP-RIE, whose development in terms of sidewalls roughness and chemical state is not yet satisfactory for low-loss integrated frequency converters [38].

Growth and processing

The epitaxial structures reported in Tables 1 and 2 have been grown on semi-insulating (001) GaAs substrates by means of molecular beam epitaxy (MBE). This technique enables the growth of high purity layers with a sharp control of their compositions and thicknesses, with abrupt interfaces. The former accuracy is important to meet the phase-matching condi-

tion at the desired wavelength, whereas the latter is essential to keep the scattering losses to a minimum.

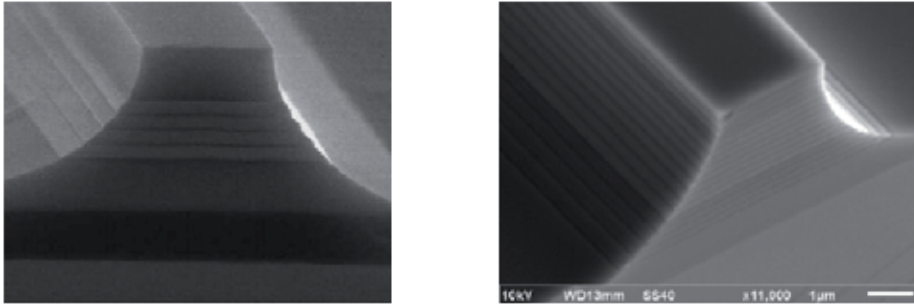


Figure 3. Scanning Electron Microscopy pictures of etched and oxidized waveguide facets (Left: “OPO Structure”– Right: “TTPS Structure”).

A thin film of positive photoresist is spin coated on the wafer and binary ridge patterns are defined with standard photolithography technique. Waveguides are oriented along the [110] crystalline direction in order to exploit the maximum $\chi^{(2)}_{xyz}$ element of the GaAs nonlinear susceptibility tensor and the {110} cleavage plane to define the waveguide facets. Typical $3\mu\text{m} \times 3\mu\text{m}$ ridges, are then etched using the $\text{CH}_3\text{COOH}:\text{HBr}:\text{K}_2\text{Cr}_2\text{O}_7$ solution. The resulting waveguide sidewalls are extremely smooth (roughness RMS value of 2 nm), which prevents the scattering of guided modes and favors the diffusion of the oxidant species during the oxidation step. The whole process is quite reproducible and easily homogeneous over several millimeters.

Samples are then cleaved in mm-long devices and the Al-rich layers are selectively oxidized. Oxidation is held in a quartz tube where samples are heated up to high temperatures in the 400°C - 500°C range, in a wet atmosphere. The latter is obtained using a 2L/min nitrogen flux flowing through a water bubbler stabilized at 70°C .

3.3. Optimization of the oxidation process

Optical propagation losses clearly originate from the oxidation process, for they are much lower before this fabrication step (respectively around 0.1 and 0.4 cm^{-1} in the near infrared for the best waveguides of the reported structures). Since the former demonstration of AlAs oxidation, such process has undergone a considerable progress in the last two decades, leading to reliable parameters for the kinetics of the reaction [34]. Thus, using the above mentioned processing technique and oxidation apparatus, this fabrication step has been carefully calibrated and optimized.

Furnace calibration

The kinetics of the oxidation depends on several parameters: the thickness and composition of the Al-rich layers, the furnace temperature, the carrier gas flux, and the bubbler tempera-

ture [33]. We have chosen here to focus only upon temperature, the carrier gas flux and the bubbler temperature being fixed to have an excess of reactants in the wet atmosphere. Figure 4 represents, for our grown AlAs layers, the log-log representation of lateral oxidation depth versus process duration, for different temperatures ranging from 400°C to 500°C. The linear progression of the oxide front with time is pointed out by the unitary slope of the dashed lines fitting the data, meaning that the process is reaction limited. From the y-intercept we can estimate the indicated oxidation rates, varying from fractions of microns to several microns per minute. Since the reaction is thermally-activated, they follow an Arrhenius law $r = r_0 \cdot \exp(-E_a/k_B T)$, where r is the oxidation rate (in $\mu\text{m}/\text{min}$), r_0 the reaction constant (in $\mu\text{m}/\text{min}$), E_a the activation energy (in eV), k_B the Boltzmann constant, and T the process temperature (in Kelvin). According to Figure 4 we obtain $E_a = 1.7\text{eV}$ in fair agreement with the literature [33].

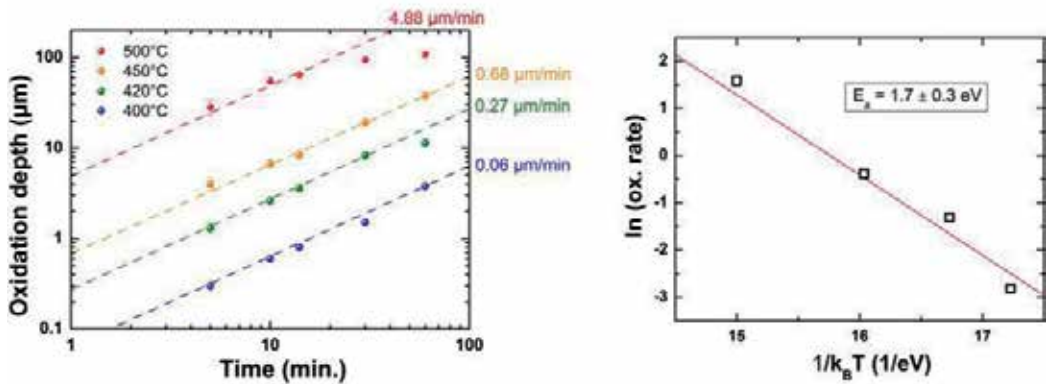


Figure 4. (Left) Lateral oxidation depth of 37.5nm thick $\text{Al}_{0.98}\text{Ga}_{0.02}\text{As}$ layers vs. Time, for several temperatures; (Right) Arrhenius plot of the oxidation rate.

Optimization of the oxidation parameters

Knowing the width of our ridge waveguides, the previous calibration allows us to estimate the nominal process duration required to complete the oxidation (*i.e.* when the oxidation fronts merge at the centre of the structure). Systematic loss measurements have been performed on several waveguides oxidized at 410°C, 420°C and 430°C, with oxidation durations around the estimated nominal values. In Figure 5 we report the average value and standard deviation of TE_{00} modal losses, conveniently measured around 1.55 μm . Data are normalized to the reference loss level obtained for a 14 minutes long oxidation at 420°C. Two conclusions can be drawn:

1. the average loss level suffers from slow oxidation kinetics, and
2. the process must be stopped at the exact moment when all the AlAs has been converted into oxide.

As we can see from the graph, this last condition is particularly difficult to meet at high temperature where losses are highly sensitive to any imprecision on the oxidation time. Consequently the set of parameters {14 min., 420°C} has been chosen as the best reasonable trade-off.

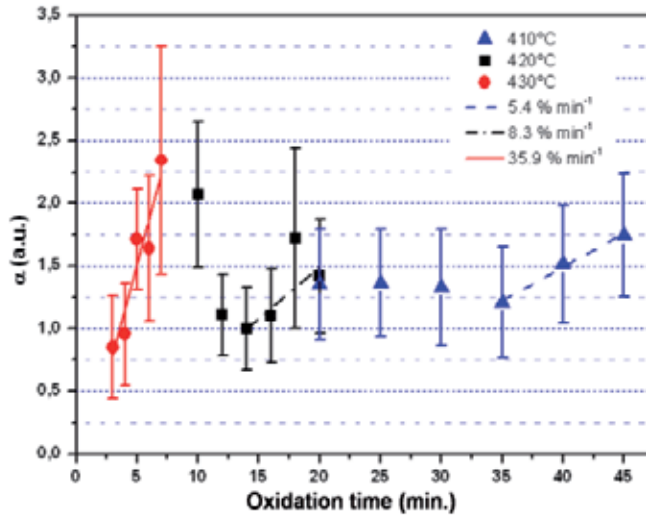


Figure 5. Normalized losses vs. Oxidation time for three different process temperatures.

4. Nonlinear optics experimental performances

4.1. Nonlinear optics characterization

Nonlinear characterization of a frequency converter is achieved through three-wave mixing experiments for which the nonlinearity of the material couples fields of angular frequency ω_i ($i=1,2,3$) such as $\omega_1+\omega_2=\omega_3$ [6]. Different setup configurations can be implemented depending on the modes injected at the guiding structure input, and several figures of merit can be inferred. Second harmonic generation ($\omega+\omega\rightarrow 2\omega$) is the simplest to achieve, as the output power of the generated beam scales quadratically with the input power. It enables the estimation of normalized conversion efficiency $\eta_{\text{norm}}=P_{2\omega}/(P_{\omega}^2L^2)$. The inverse process (at least at degeneracy) that is SPDC ($\omega_3\rightarrow\omega_1+\omega_2$) is more subtle to detect as the pump wave interacts with weak vacuum quantum fluctuations. It gives access to the device tuning curve and to the off-degeneracy conversion efficiency. Finally, seeded down-conversion ($\omega_3-\omega_1\rightarrow\omega_2$) can alternatively be described as DFG or parametric amplification. Normalized parametric gain $g/P^{1/2}=\eta_{\text{norm}}^{1/2}$ is crucial when it comes to optical parametric amplifiers (OPAs) and OPOs.

Since the first experimental demonstration of mid-infrared DFG in form birefringent waveguides in 1997 [35], the performances of such device have been significantly improved in terms of optical losses and conversion efficiency. Thereby, this phase-matching scheme has been successfully extended to visible and near infrared spectral ranges [9,10]. Concerning the first structure discussed here, designed for 1.06-to-2.12 μm parametric down-conversion, three-wave mixing experiments have been extensively carried out, and their results have already been published. A normalized conversion efficiency of $\eta_{\text{norm}} = 1500 \text{ \%W}^{-1}\text{cm}^{-2}$, corresponding to a normalized parametric gain of $3.9 \text{ cm}^{-1}\text{W}^{-1/2}$ at degeneracy, was estimated by parametric fluorescence measurements, and confirmed by SHG [10]. Direct parametric amplification measurements have been performed, and a maximum single-pass parametric gain of 4.5% has been obtained with 30 mW in-coupled pump power [37]. This the highest value ever reported in semiconductor waveguide. Furthermore, tunability for signal and idler beams in the 1.7 – 2.7 μm range has been established. The only limitation to this span was shown to stem from the O-H absorption band around 3 μm , due to the presence of hydroxide AlO(OH) [32]. Nevertheless, this band can be recovered, extending the tunability between 1.3 and 4.2 μm , after dehydroxylation of the sample (*i.e.* decomposing AlO(OH) into $\gamma\text{-Al}_2\text{O}_3$) by thermal annealing [39]. These main figures reflect the competitiveness of integrated GaAs-based frequency converter in the mid-infrared with respect to standard PPLN. However, the excessive propagation losses still prevent the use of cm-long waveguides in which the oscillation threshold would be at reach.

Shortly after the demonstration of SHG of a $\lambda = 1.6 \mu\text{m}$ pump in AlGaAs/AlOx waveguides as early as 1998 [40], the interest in the telecom band faded because of propagation loss issues. During the following decade, up and down-conversion between 0.775 μm and the telecom band remained out of reach for the form birefringent phase-matching scheme as the fabrication and oxidation steps were not fully optimized. In the following, we present our latest results obtained in the most recent generation of partially oxidized AlGaAs waveguides. State-of-the-art conversion efficiency is estimated *via* SHG experiment, and off-degeneracy dispersion is assessed by DFG experiment. A tunability greater than 500 nm is reported.

4.2. Second Harmonic Generation

In the experiment we report here, a CW single mode external cavity laser diode, largely tunable in the telecom band, was used to generate the pump beam at the fundamental frequency. The laser beam was TE-polarized then injected into a 500 μm long waveguide by end-fire coupling through a $\times 60$ (0.85 N.A.) microscope objective. The internal fundamental harmonic input power was estimated using the in-coupling efficiency of 37% assessed by taking into account the objective transmission (75%), the 28% facet reflectivity calculated accurately by finite-difference time domain (FDTD) method, and the overlap integral between the laser beam and the guided mode (69%). The second harmonic radiation was collected at the output facet by a similar microscope objective, filtered by a TM polarizer to get rid of the pump beam then focused onto a silicon photodiode connected to a lock-in amplifier.

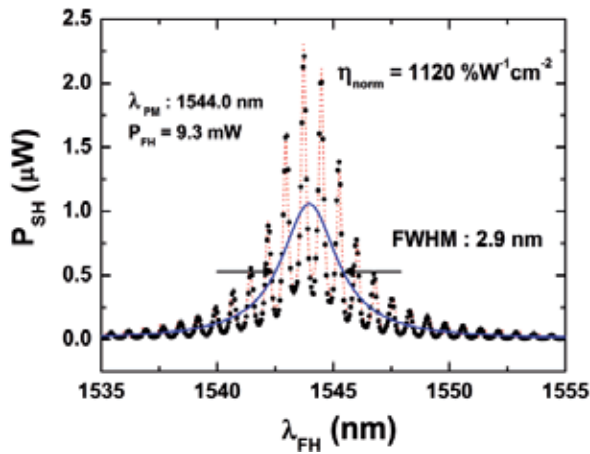


Figure 6. Second harmonic power vs. Fundamental harmonic wavelength. The photodiode signal (black dots) is theoretically fitted (red dotted line), and the Lorentzian single-pass phase-matching curve is extracted (solid blue line).

A typical phase-matching spectrum is shown in Figure 6. It was obtained by monitoring the second harmonic output power while scanning the fundamental harmonic input wavelength at constant 9.3 mW power. The experimental data exhibit a smooth phase-matching resonance modulated by Fabry-Perot fringes and can be nicely fitted after [41]. This high frequency feature corresponds to the interference pattern arising from the multiple reflections of the pump beam on the waveguide facets. Once the cavity fringes are filtered, the single-pass phase-matching curve is extracted and fitted by a Lorentzian curve with a 2.9 nm full width at half maximum (FWHM). The phase-matching condition is met at 1544 nm instead of the designed nominal value of 1550 nm. This slight discrepancy is a combined effect of the small systematic deviation of our MBE reactor on the layer thicknesses (typically 1 to 2 percents), the shift of the phase-matching wavelength induced by the 2D transverse confinement whereas the design procedure is 1D, and the temperature dependence of the structure refractive indices [42]. The broadening of the envelope shape and its deviation from the ideal *sinc* function are generally ascribed to waveguide inhomogeneities along propagation or to optical losses. In our case, however, the relatively large width and the high quality of the waveguide ridge suggest that we can assume waveguide invariance along propagation. Using the Fabry-Perot fringes method, TE optical losses, α_{FH} , were measured to be 0.4 cm^{-1} and 1.2 cm^{-1} in the $1.55 \text{ }\mu\text{m}$ region, respectively before and after oxidation of the thin AlAs barriers. TM losses, α_{SH} , were assessed *via* transmission measurement of a Ti:Sapphire laser at 775 nm, yielding a value of 151 cm^{-1} . Consistently, losses of 140 cm^{-1} were inferred for the second harmonic from the FWHM of the lorentzian curve according to the textbook equation [6]:

$$\eta \propto \exp\left[-(\alpha_{FH} + \alpha_{SH}/2)L\right] \times \frac{\sin^2(\Delta k L/2) + \sinh^2\left[(\alpha_{FH} - \alpha_{SH}/2)L/2\right]}{(\Delta k L/2)^2 + \left[(\alpha_{FH} - \alpha_{SH}/2)L/2\right]^2} \quad (1)$$

The evolution of the second harmonic power with the fundamental harmonic power at degeneracy is given in log-log scale in Figure 7. The quadratic law is confirmed by the slope of the line fitting the experimental data, and a SHG efficiency of $2.8 \%W^{-1}$ is estimated. The normalized conversion efficiency is found to be $1120 \%W^{-1}cm^{-2}$ *i.e.* comparable to the best value reported in AlGaAs waveguides [38], and which corresponds to a $3.3 cm^{-1}W^{-1/2}$ normalized parametric gain at degeneracy. Furthermore, no sublinear deviation is observed for pump power up to 50 mW, whereas such an onset occurs at 10 mW and is ascribed to two-photon absorption in [43]. Finally a maximum second harmonic power of $267 \mu W$ is reported, only limited by our source power at fundamental harmonic. This is the highest value reported for integrated AlGaAs waveguides.

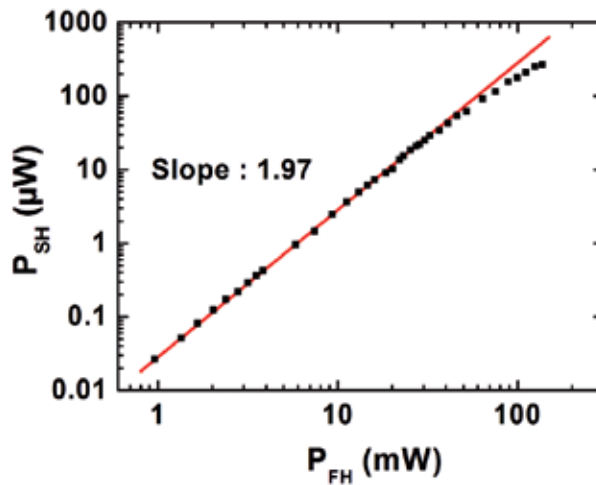


Figure 7. Log-log representation of second harmonic power vs. Fundamental harmonic power. The slope of the linear fit highlights the expected quadratic behavior.

4.3. Difference Frequency Generation

DFG was achieved on the same sample in order to investigate its performance out of degeneracy. In our case, this three-wave mixing process required a TM-polarized pump mode at visible wavelength λ_P , interacting with a TE-polarized infrared seed at wavelength λ_S , so to generate a TE-polarized difference frequency beam whose wavelength λ_{DF} is set by energy conservation $1/\lambda_{DF} = 1/\lambda_P - 1/\lambda_S$. The pump and seed beams were provided respectively by a linearly polarized CW Ti:Sapphire laser tunable around 775 nm, and an external cavity laser diode tunable between 1490 and 1600 nm. Both beams were combined using a 50/50 beam splitter then collinearly coupled in, and out of, a waveguide by two $\times 40$ (0.65 N.A.) microscope objectives. Its collimated output was either visualized on a camera or passed through a spectrometer before being filtered by a TE polarizer then detected using a strained InGaAs photodiode and a lock-in amplifier.

Typical spectra are shown in Figure 8, where the central peaks are unambiguously attributed to the second order of the residual pump beam diffracted by the monochromator grating. They were obtained for three different pump wavelengths below degeneracy ($\lambda_P = 773.2$ nm), after adjustment of the seed wavelength to optimize the difference frequency power. All the $(\lambda_P, \lambda_S, \lambda_{DF})$ sets verify energy conservation at phase-matching and are reported in Figure 9 along with the simulated tuning curve, with a good agreement. The spread of the dark line corresponds to the spectral acceptance of the DFG around phase-matching and its width accounts for the losses experienced by the three fields. Regarding the tunability of the device, we can see that a shift of the pump wavelength as small as 5.2 nm requires a spectral separation for the seed and difference frequency waves of 570 nm. This is due to the strong dispersion in the vicinity of material bandgap [44], and it turns out to be a great advantage regarding the fabrication of integrated source tunable in the near infrared for instance.

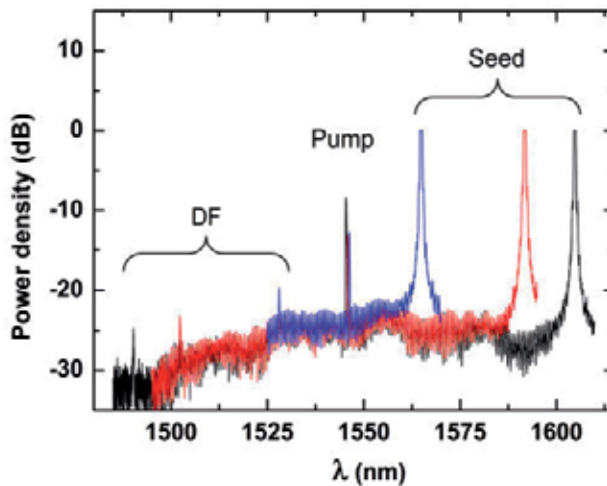


Figure 8. Normalized DFG spectra obtained for three different pump wavelengths (the seed peaks are clipped due to the lock-in finite dynamic range).

The combined study of SHG and DFG allowed us to fully characterize our form birefringent partially oxidized AlGaAs waveguides in terms of tunability and parametric gain. While this device strongly benefited from technologic improvements in terms of design, etching and oxidation, its performances compare favorably with respect to other alternative phase-matching approaches, but they are still limited by optical losses, which prevented so far the observation of SPDC. However, the reported figures are strongly motivating in view of the fabrication of a telecom source of quantum light. Indeed, for a 2 mm long waveguide, we theoretically estimate a parametric fluorescence efficiency of $\eta_{PF} \sim 1.7 \times 10^{-8}$ pairs/pump photon, whereas a significant reduction of optical losses to $\sim 1 \text{ cm}^{-1}$ would lead to $\eta_{PF} \sim 3 \times 10^{-7}$ pairs/pump photon, *i.e.* comparable with cm-long PPLN waveguides values [3].

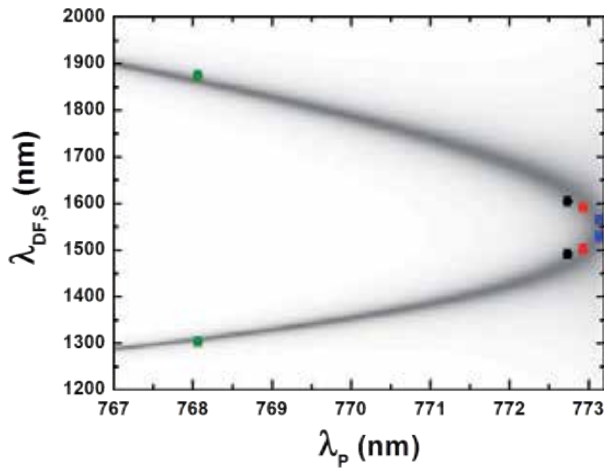


Figure 9. Tuning curve: experimental data (colored dots) and theoretical prediction (grayscale).

5. Phenomenological study of loss mechanisms

5.1. Structural and chemical characterization of the oxide

To date, the performances of partially oxidized AlGaAs waveguides are mitigated by high propagation losses ($\sim 1 \text{ cm}^{-1}$ in the infrared). As a comparison, typical PPLN waveguide losses are in the range of few 0.01 cm^{-1} , enabling the fabrication of several cm-long devices. Since optical propagation losses play a major role in all guided-wave phase-matching schemes proposed so far in the AlGaAs platform, their reduction is a critical issue.

Promising results have already been obtained by decreasing the losses after optimization of the waveguides design and the oxidation parameters, but today, a better understanding of the propagation losses origins is necessary if we want to lower them even more. Indeed, many aspects of the oxidation process are still not clearly established, including the exact formation mechanisms and the fine chemical and structural properties of the oxide. Therefore a transmission electron microscopy characterization of oxidized layers has been carried out [45] to assess the quality of the material at microscopic scale.

Chemical and structural characterization

The fabrication of cross-section samples has been carried out with an ion slicer used to perform the thinning of a waveguide oxidized guiding core. Based on high resolution transmission electron microscopy pictures combined with power spectrum analysis and energy filtered transmission electron microscopy images, it has been shown that:

- GaAs surrounding AlOx becomes amorphous in the close vicinity of the oxidized layers (~20 nm from the interface) and remains mono-crystalline beyond.
- Residual oxidation of the neighboring GaAs and Al_{0.7}Ga_{0.3}As layers occurs through the interfaces, over 3 to 9 nm. The richer in aluminum the deeper an AlGaAs layer gets oxidized.
- The oxidation of Al_{0.98}Ga_{0.02}As results in a 12% contraction of the layers thicknesses.
- AlOx layers are composed of γ -Al₂O₃ polycrystalline grains, with size between 10 and 20 nm, embedded in an amorphous AlOx matrix.

Interface roughness

Additionally, the internal interfaces were investigated by high-angle annular dark-field (HAADF) scanning transmission electron microscopy. Figure 10 shows two images of the same waveguide core area acquired before and after oxidation. Oxidation is obviously responsible for the deterioration of the multilayer morphology, as rough interfaces are clearly visible afterwards, especially at the bottom interface. The acquisition of several of such pictures contiguous over about 700 nm allowed us to reconstruct the respective roughness profiles. Gaussian fits of their autocorrelation functions have been performed in order to reliably extract their stochastic parameters: the RMS amplitude σ and the coherence length L_c . The results are summarized in Table 3 for the different types of interfaces.



Figure 10. HAADF images of an Al_{0.98}Ga_{0.02}As layer (in dark) embedded in GaAs (Top) and Al_{0.7}Ga_{0.3}As (Bottom), before (Left) and after oxidation (Right).

| Interface | GaAs/Al _{0.98} Ga _{0.02} As | Al _{0.7} Ga _{0.3} As/Al _{0.98} Ga _{0.02} As | GaAs/AlOx | Al _{0.7} Ga _{0.3} As/AlOx |
|---------------------|---|---|-----------|---|
| σ (nm) | 0.37 | 0.37 | 0.53 | 0.69 |
| $\Delta\sigma$ (nm) | 0.08 | 0.08 | 0.08 | 0.06 |
| L_c (nm) | 4 | 4 | 53 | 30 |
| ΔL_c (nm) | 0 | 0 | 14 | 7 |

Table 3. Measured RMS amplitudes and coherence lengths for two types of interface, before and after oxidation.

For such step index waveguides with high index contrasts, optical modes are highly sensitive to any irregularities. We remind that the devices presented here are passive, and consequently the semiconductor alloys are chosen to be transparent for the wavelengths involved in the nonlinear process. Hence, assuming a good confinement by design, *i.e.* no substrate optical leakage, losses can only arise from scattering (rough sidewalls and layers interfaces, volume inhomogeneities) or absorption (defects).

Since the index contrast between AlOx and γ -Al₂O₃ is negligible, the polycrystalline grains are not expected to contribute significantly to scattering losses. Based on the previous observations, our work hypothesis was then to ascribe the optical propagation losses of the guided modes to scattering by the rough AlGaAs/AlOx boundaries.

5.2. Modeling the scattering by rough interfaces

The study of scattering losses in semiconductor waveguides is of great practical interest in the field of integrated optics, and since Marcuse's early work [46] a large amount of research has been done in this area. Most of the recent roughness studies in dielectric waveguides are now based on the convenient Lacey and Payne model [47,48], which offers the advantage to provide a semi-analytical expression for TE-mode losses, quite simply expressed in terms of fundamental waveguide parameters and statistics of the surface roughness.

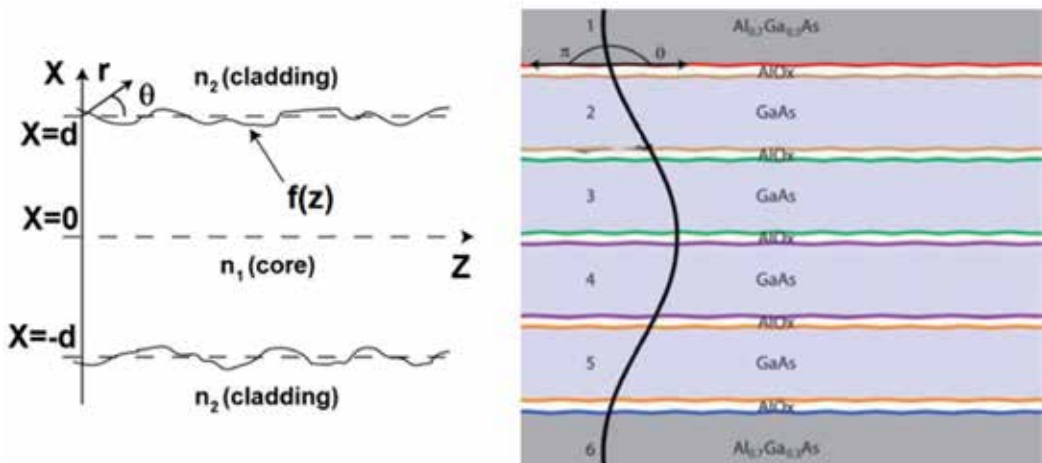


Figure 11. (Left) Schematics of rough interfaces in a slab waveguide. (Right) Schematics of the adaptation to our multilayer selectively oxidized waveguide.

The Lacey and Payne model deals with a three-layer slab core/cladding waveguide with rough interfaces as shown in Figure 11. It provides the scattering contribution to the propagation losses via the direct computation of the radiated far field, with the equivalent-current method [49]. Within this approach, it is possible to derive an expression for the exponential radiation loss coefficient due to scattering by the roughness, in a symmetric single mode waveguide of thickness $2d$:

$$\alpha_r = \phi^2(d) (n_1^2 - n_2^2)^2 \frac{k_0^3}{4\pi n_{eff}} \int_0^\pi \left[(1+r(\theta))^2 + t(\theta)^2 \right] \tilde{R}(\beta - n_2 k_0 \cos(\theta)) d\theta \quad (2)$$

Where $\phi(d)$ is the modal field evaluated at the waveguide core/cladding interface, normalized following:

$$\int_{-\infty}^{+\infty} \phi^2(x) dx = 1 \quad (3)$$

n_1 and n_2 are the core and cladding refractive indices respectively, k_0 is the free-space wave vector, β is the modal propagation constant associated to the effective index n_{eff} , r and t are the respective reflection and transmission Fresnel coefficients and θ is the photon scattering angle with respect to the interface. The surface roughness of the waveguide walls is described by the spectral density function, which is obtained from the autocorrelation function $R(u)$ of the surface roughness via the Wiener-Khinchine theorem:

$$\tilde{R}(\Omega) = \int_{-\infty}^{+\infty} R(u) \exp(i\Omega u) du \quad (4)$$

This model requires two input parameters: the mean square deviation from a flat surface σ^2 and the correlation length L_c . The parameter σ^2 is related to the autocorrelation function by $R(0)=\sigma^2$, and the coherence length L_c of the interface profile corresponds to the half-width at half maximum of the Gaussian fit of the interface profile autocorrelation function.

To adapt this model to our multilayer structures, we ideally separate the waveguide in several microstructures. In Figure 11 we also show a scheme of one of our device, for which the interfaces are bunched in groups of two, in order to mark off regions with refractive index n_1 higher than the two adjacent ones n_2 . The core of each of these six microstructures, sandwiched between AlOx layers and bounded by rough interfaces, is identified and numbered from 1 to 6. Its refractive index is the one of the appropriate alloy (GaAs or $Al_{0.7}Ga_{0.3}As$).

In order to infer a rough estimate of the optical losses for the fundamental optical TE_0 mode, we compute α_i ($i=1,6$) the losses of each microstructure, then we simply convert the equation (2) under the assumption that each contribution adds up incoherently with the others:

$$\alpha_{tot} = \sum_{i=1}^6 \alpha_i \quad (5)$$

At this point, we should stress that our adaptation is very simplistic and its derivation is only qualitative.

5.3. Spectral study of propagation losses

Among the several different ways to measure optical losses, the Fabry-Perot fringes measurement is the most suitable technique for low-loss waveguides [50]. Unlike the cut-back method, it has the advantage of not being destructive, and contrary to transmission measurement, it is independent of coupling and collection efficiencies estimations. In this frame, we can picture the waveguide as a resonator in which guided modes are reflected by the cleaved facets and travel in both directions. By scanning the wavelength of the input wave, we observe a multiple wave interference pattern at the output, namely the Airy function of the cavity. The contrast and finesse of the resonances are straightforwardly linked to the number of waves participating to the total interference, therefore to the reflection (estimated by FDTD simulations) and propagation losses experienced by the traveling modes.

In order to test our hypothesis and investigate the optical loss mechanisms, we carried out a study on their spectral dependence. The results are reported in Figure 12, for both the structures presented previously. According to our phase-matching scheme, the data around λ_p represent the TM_{00} losses, whereas the data at wavelength close to degeneracy represent the TE_{00} losses.

The data were obtained by using external cavity diode lasers tunable in the telecom band from 1.3 to 1.6 μm , and a slightly tunable DFB laser around 2.12 μm . However we resorted to transmission measurements of a CW Ti:Sapphire laser around 1 μm and below, where losses were found to be too high to be reliably inferred from Fabry-Perot fringes.

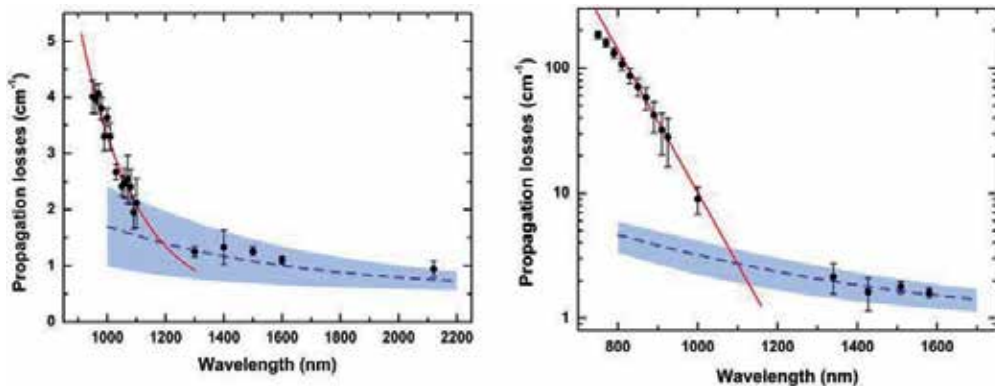


Figure 12. Propagation losses vs. Wavelength, fitted by decaying exponential (red curves) for short wavelengths, and inverse-power law (blue curves) for long wavelengths. The left (resp. right) figure corresponds to the OPO (resp. TTPS) structure.

Two different regimes are apparent: for wavelengths below $\sim 1.1 \mu\text{m}$, data are well fitted by decaying exponential curves (red lines), whereas their decays follow inverse power laws above $\sim 1.1 \mu\text{m}$.

For the longest wavelengths involved, losses are fairly low (around 1 cm^{-1} and less) and can be ascribed to the interfaces roughness that appears during oxidation. Indeed, the reasonable agreement between the experimental data (black dots) and the prediction band derived from our simple semi-analytical model (blue bands) confirms that, in this spectral range, losses are dominated by the scattering contribution in a Rayleigh-like regime. Note that this result is consistent with previous work achieved on an older generation of similar waveguides [51], in which losses were probed by scattered light measurements, and they were also found to decrease between 1.3 and 2.1 μm .

For shorter wavelengths, our previous assumption is inadequate and a new loss mechanism must be considered. The very high losses and their exponential decay with wavelength suggest an Urbach's tail absorption, highlighting the fact that not only surface imperfections but also volume defects at the oxide interfaces play a critical role. As was already noticed several years ago [40], these additional losses are likely to be ascribed to arsenic antisites formed during oxidation at the oxide-semiconductor interface [52]. Trapped reaction products (*e.g.* elemental As and AsH_3) could explain this excess of arsenic and the resulting EL2-like crystalline defects, with donor levels in the gap of AlGaAs. Indeed, the transition between the two regimes occurs at photon energy corresponding to 65 to 70% of the bandgap of the waveguide core material (respectively GaAs and $\text{Al}_{0.25}\text{Ga}_{0.75}\text{As}$).

These levels of pump losses are currently the limiting factor for the efficiency of our AlGaAs integrated devices. Nevertheless, as shown by existing research on quantum-well luminescence close to oxidized layers [52] hydrogenation can be effectively used to remove absorbing species trapped at the oxide interfaces. Thermal annealing cycles are also expected to improve the crystallinity of spoiled materials. Moreover, a study on the spatial distribution of the mechanical strains arising from the volume shrinkage of oxidized thin AlAs layers showed that a critical overstrained zone appears at the merging point of the two counter-propagative oxidation fronts [53]. In our case, this could be an additional source of concern since the maximum intensity of the optical modes is at the confluence of the oxidation fronts. In order to circumvent such over-oxidation issue, new innovative designs are being tested (*e.g.* oxidation unidirectionally launched from one side of the ridge).

Despite the fact that propagation losses have prevented the use of form birefringent phase-matching scheme at its full potential, we are able to design and fabricate reasonably low-loss integrated waveguides. At the moment, aluminum oxide remains very promising for our photonic applications but its quality is not yet compatible with the most demanding nonlinear devices. Various investigations of its fine properties allowed us to better understand the loss mechanisms involved, and they gave us clues for their minimization. Improvement of the oxide quality is necessary for further significant progress, and will only occur after a specific technological development of the oxidation process, starting with the solutions evoked above which are currently under exploration.

6. Implementation of an integrated cavity

6.1. Design and fabrication of the cavity mirrors

A standard way to enhance nonlinear optical interactions consists in the insertion of the $\chi^{(2)}$ parametric gain medium into an optical resonator. The large amount of energy resulting from the light confinement inside the cavity enables to trigger nonlinear processes with lower input powers and larger efficiency. To this purpose, we have been focusing on the fabrication of an integrated resonant cavity. Indeed, regarding the realization of an OPO, the modest single-pass parametric gain in our waveguides makes the quality of the cavity mirrors critically important towards the reach of the oscillation threshold. One should stress that, in a 2 mm-long cavity, the mirror losses $\alpha_M = -\ln(R_1 R_2)/2L$ becomes of the order of the typical 1 cm^{-1} propagation losses as soon as their reflectivity reaches 82%.

As a trade-off between the pump power threshold and the spectral stability and tunability of the oscillator, we opted for a symmetric doubly resonant configuration (DROPO) with single pass of the pump, in which case the steady-state pump threshold at degeneracy P_p^{th} reads [54]:

$$P_p^{\text{th}} = \frac{1}{\eta_{\text{norm}}} \left(\frac{-\alpha_p \ln(R_{s,i} \exp(-\alpha_{s,i} L))}{2(1 - \exp(-\alpha_p L/2))} \right)^2 \quad (6)$$

With η_{norm} the waveguide normalized conversion efficiency, α_p the pump losses, $\alpha_{s,i}$ the signal and idler losses, L the waveguide length and $R_{s,i}$ the modal reflectivity at signal and idler wavelength. Consequently, for a 2 mm-long device, by plugging in our typical values of parametric gain and losses we can see that mirrors with reflectivity as high as 98.3% are required to have a threshold power of 100 mW, which is the maximum power that we can safely couple into the waveguide. The fabrication of such a demanding integrated cavity is all the more challenging that the adhesion of coating is made tricky, due to AIAs layers shrinkage during oxidation [55] producing non-ideal facets with possible irregular surface and mechanical stress. The high quality of the sample surface and waveguide sidewalls must also be preserved since the slightest deterioration would lead to additional scattering losses.

The solution we adopted to place our nonlinear waveguide in a DROPO resonator is the fabrication of integrated $\text{SiO}_2/\text{TiO}_2$ Bragg mirrors. The choice of these two materials has been dictated by the need to keep the thickness of the dielectric stack to a minimum thanks to their high-index contrast. The multilayer structures corresponding to the chosen cavity configuration are designed using commercial software [56] by implementing 1D transfer matrix algorithm along with optimization routines. They are then deposited by Ion beam Assisted Deposition (IAD) onto the cleaved facets of a sample, whose surface is protected from dielectric material overspray with a photoresist film lifted afterwards.

Figure 13a shows an experimental FTIR spectrum of a 6 bi-layers dielectric stack deposited on silicon substrate along with data acquired by focusing lasers with different wavelengths below a waveguide facet. The fair agreement between the experimental sets of data acquired on both the silicon and the sample substrates shows that the adhesion of the coating is satisfactory. The cleanliness of the sample surface can be appreciated on the scanning electron microscopy pictures provided in Figures 13b-c, where the dotted line highlights the edge of the waveguide.

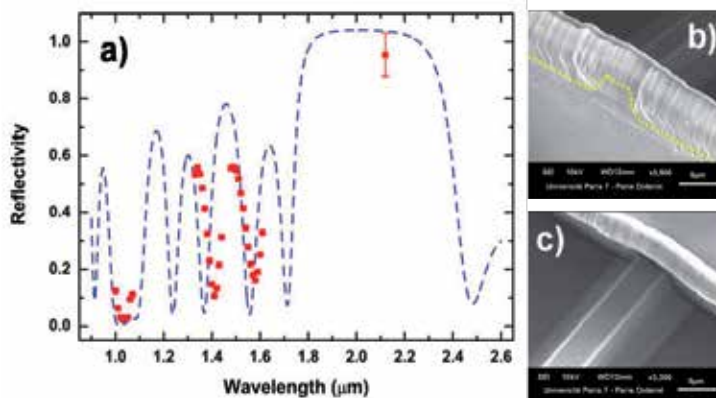


Figure 13. a) Experimental FTIR reflectivity spectrum of a cavity mirror, measured on a silicon substrate (dashed blue line) and below waveguide facet (red squares). b) and c) Bird's views of a mirror deposited on a waveguide facet.

6.2. Optical characterization

In order to quantitatively evaluate the coating optical quality, the modal reflectivity of the deposited mirrors was inferred from the study of the Fabry-Perot fringes. The Airy functions, presented in Figure 14 were acquired with a DFB laser diode slightly tunable around 2.12 μm injected in a waveguide respectively without and with one coating. From the modification of the cavity finesse, increasing from 1.7 to 3.9, we can deduce a modal reflectivity of ~85% at this wavelength. The significant discrepancy from the designed nominal value of 98.5% can be explained by the simplicity of the design procedure that only considers plane waves perpendicularly impinging on an infinite surface mirror. Indeed, the effects of the guided-mode numerical aperture and the finite transverse dimensions of the mirror are not taken into account.

Finally, SPDC experiment has been achieved in those integrated cavities. The TM-polarized pump beam of a CW Ti:Sapphire laser, tunable around 1 μm, was injected through a ×60 (0.85 N.A.) microscope objective into a 2-mm long waveguide with both facets coated. The device output was collected and collimated by an identical objective. Then it was passed through a germanium window to filter out the pump beam. Finally, the TE-polarized parametric fluorescence signal around 2 μm was focused on a strained InGaAs photodiode and detected with a lock-in amplifier. In Figure 15 we have plotted the external signal power

measured after the exit mirror as a function of the external pump power focused onto the entrance mirror, while the pump wavelength was set at degeneracy. The nonlinear trend at high pump powers may be evidence that the nonlinear process tends to go beyond the low-gain regime. However, given the estimation of modal reflectivity, the oscillation threshold is currently out of reach. But beyond the demonstration of an integrated OPO, the scope of these technological results is very broad and could concern various types of integrated Al-GaAs-based nonlinear devices.

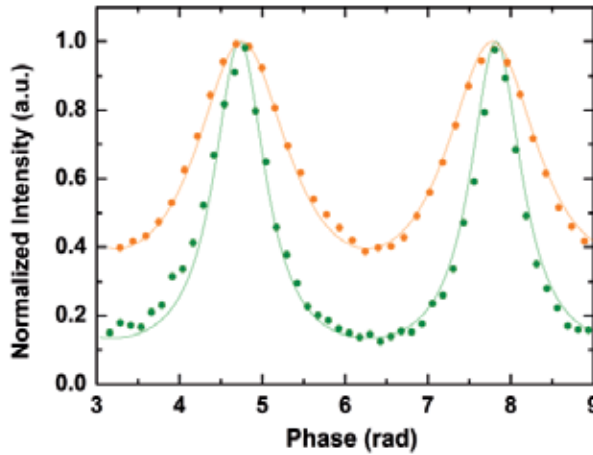


Figure 14. Fabry-Perot fringes of bare waveguide (orange) and semi-cavity (green) acquired around 2.12 μm .

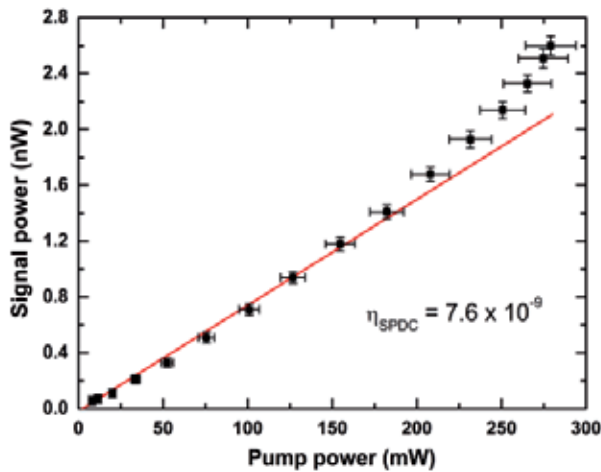


Figure 15. Generated output signal power vs. Input pump power (external values). The linear fit at low power (red solid line) points out the superlinear trend at high power.

7. Conclusion and perspectives

In this chapter we have shown that the field of semiconductor sources would largely benefit from the development of integrated AlGaAs nonlinear devices. Indeed, the demonstrations of an integrated OPO or a TTPS, for example, would have a great impact on applications such as optical spectroscopy and quantum telecommunications. The work presented in this chapter is part of the sustained research activity led on these two fronts.

Different technological solutions have been realized to fulfill the phase-matching condition necessary for efficient AlGaAs-based frequency converters. Thus it is interesting to compare their respective characteristics and performances.

It should first be noted that our “OPO structure”, designed for guided-wave parametric down-conversion of a 1.06 μm CW pump, cannot be straightforwardly be compared to any other AlGaAs device. Indeed, the closest existing research, which is on OP-GaAs OPOs, is not focusing at the moment on monolithic integration but rather on applications such as metrology or gas spectroscopy. Furthermore, because these setups have been operated in pulsed regime at first, the pump wavelength is fixed above 1.8 μm to avoid two-photon absorption in GaAs. Consequently, these crystals are optically pumped around 2 μm , and their degeneracy is typically between 4 and 5 μm .

The “TTPS structure” however is topical, as confirmed by the continuous track record of design and experimental results on 0.775-to-1.55 μm frequency conversion in semiconductor devices. An overview of the current state-of-the-art is given by Table 4, in which we reported the loss values, generated power, normalized conversion efficiency and spectral acceptance of type I CW SHG experiment for several phase-matching schemes. The figures in bold (resp. in italics) correspond to the best (resp. second best) value of each column.

This provides us with a synoptic vision of the strength and weakness of respectively modal phase-matching [57], QPM [24] and form birefringence phase-matching [9,38]. It is then quite clear that, regarding conversion efficiency, form birefringence phase-matching compare favorably with respect to modal phase-matching and QPM. Moreover, low infrared losses and high generated powers are enabled by optimized design and fabrication processes. The very high losses in the visible are caused by the presence of AlOx layers, and they are the current limiting factor of this phase-matching strategy. The resulting broadening of the $\chi^{(2)}$ process spectral acceptance may in turn be an issue for experimental protocols requiring spectrally narrow and pure sources of telecom twin-photons.

| Ref. | $\alpha(1.55 \mu\text{m}) [\text{cm}^{-1}]$ | $\alpha(775 \text{ nm}) [\text{cm}^{-1}]$ | $P_{\text{SH}}[\mu\text{W}]$ | $\eta_{\text{norm}}[\% \text{W}^{-1} \text{cm}^{-2}]$ | $\Delta\lambda [\text{nm}]$ |
|------|---|---|------------------------------|---|-----------------------------|
| [57] | 7.8 | 41 | 0.023 | 6.8×10^{-3} | 0.9 |
| [24] | 1.7 | 2.2 | 6.6 | 92 | 0.3 |
| [38] | 5.3 | 70 | 10^{-4} | 1250 | 10 |
| [9] | 1.1 | 140 | 267 | 1120 | 3 |

Table 4. Summarize of the characteristics and performances of devices implementing different phase-matching schemes.

In conclusion, we have shown that, although the choice of AlGaAs/AlOx nonlinear waveguides is relevant to fabricate highly efficient integrated frequency converters, losses remain the main bottleneck and prevent further breakthrough. Nevertheless, progress has been made by investigating the different loss mechanisms, and a specific technological development of the AlAs oxidation process is expected to reduce further optical losses. Finally, we have demonstrated the feasibility of monolithic integrated Fabry-Perot cavity, by depositing highly reflective dielectric mirrors on the waveguide facets.

Acknowledgements

The authors warmly acknowledge Alessio Andronico for help in the simulations, and Guilhem Almuneau for experimental help.

Author details

M. Savanier¹, C. Ozanam¹, F. Ghiglieno¹, L. Lanco², X. Lafosse², A. Lemaître², I. Favero¹, S. Ducci¹ and G. Leo¹

¹ Université Paris Diderot, Sorbonne Paris Cité, Laboratoire Matériaux et Phénomènes Quantiques, CNRS-UMR 7162, France

² Laboratoire de Photonique et de Nanostructures, CNRS-UPR 20, France

References

- [1] Langrock, C., Kumar, S., Mc Geehan, J. E., Willner, A. E., & Fejer, M. M. (2006). All-optical signal processing using $\chi^{(2)}$ nonlinearities in guided-wave devices. *IEEE Journal of Lightwave Technology*, 24(7), 2579.
- [2] Werle, P. (1998). A review of recent advances in semiconductor laser based gas monitors. *Spectrochimica Acta Part A: Molecular and Biomolecular Spectroscopy*, 54(2), 197.
- [3] Tanzilli, S., Tittel, W., De Riedmatten, H., Zbinden, H., Baldi, P., De Micheli, M., Ostrowsky, D. B., & Gisin, N. (2002). PPLN waveguide for quantum communication. *The European Physical Journal D Atomic, Molecular, Optical and Plasma Physics*, 18(2), 155.
- [4] Pavesi, L. (2003). Will silicon be the photonic material of the third millennium? *Journal of Physics: Condensed Matter*, 15(26), R1169.

- [5] Roelkens, G., Liu, L., Liang, D., Jones, R., Fang, A., Koch, B., & Bowers, J. (2010). III-V/silicon photonics for on-chip and intra-chip optical interconnects. *Laser & Photonics Reviews*, 4(6), 751.
- [6] Sutherland, R. L. (2003). Handbook of nonlinear optics. *New York: Marcel Dekker*.
- [7] Lanco, L., Ducci, S., Likforman, J. P., Marcadet, X., van Houwelingen, J. A. W., Zbinden, H., Leo, G., & Berger, V. (2006). A semiconductor waveguide source of counter-propagating twin photons. *Physical Review Letters*, 97(17), 173901.
- [8] Horn, R., Abolghasem, P., Bijlani, B. J., Kang, D., Helmy, A. S., & Weihs, G. (2012). Monolithic source of photon pairs. *Physical Review Letters*, 108(15), 153605.
- [9] Savanier, M., Andronico, A., Lemaître, A., Galopin, E., Manquest, C., Favero, I., Ducci, S., & Leo, G. (2011). Large second-harmonic generation at 1.55 μm in oxidized AlGaAs waveguides. *Optics Letters*, 36(15), 2955.
- [10] Ravaro, M., Le Dû, M., Likforman, J. P., Ducci, S., Berger, V., Marcadet, X., & Leo, G. (2007). Estimation of parametric gain in GaAs/AlOx waveguides by fluorescence and second harmonic generation measurements. *Applied Physics Letters*, 91(19), 191110.
- [11] Siegman, A. E. (1986). Lasers, Mill Valley, Calif. *University Science Books*.
- [12] Hall, R. N., Fenner, G. E., Kingsley, J. D., Soltys, T. J., & Carlson, R. O. (1962). Coherent light emission from GaAs junctions. *Physical Review Letters*, 9(9), 366.
- [13] Faist, J., Capasso, F., Sivco, D. L., Sirtori, C., Hutchinson, A. L., & Cho, A. Y. (1994). Quantum cascade laser. *Science*, 264(5158), 553.
- [14] Lehnhardt, T., Hümmer, M., Rößner, K., Müller, M., Höfling, S., & Forchel, A. (2008). Continuous wave single mode operation of GaInAsSb/GaSb quantum well lasers emitting beyond 3 μm . *Applied Physics Letters*, 92(18), 183508.
- [15] Laffaille, P., Moreno, J. C., Teissier, R., Bahriz, M., & Baranov, A. N. (2012). High temperature operation of short wavelength InAs-based quantum cascade lasers. *AIP Advances*, 2(2), 022119.
- [16] Feng, X., Caneau, C., Le Blanc, H. P., Visovsky, N. J., Chaparala, S. C., Deichmann, O. D., Hughes, L. C., Chung-en, Z., Caffey, D. P., & Day, T. (2011). Room temperature CW operation of short wavelength quantum cascade lasers made of strain balanced $\text{Ga}_x\text{In}_{1-x}\text{As}/\text{Al}_y\text{In}_{1-y}\text{As}$ material on InP substrates. *IEEE Journal of Selected Topics in Quantum Electronics*, 17(5), 1445.
- [17] The Scott Partnership. (2010). Mid-infrared lasers. *Nature Photonics*, 4(8), 576.
- [18] Vizbaras, A., Anders, M., Katz, S., Grasse, C., Boehm, G., Meyer, R., Belkin, M. A., & Amann, M. C. (2011). Room-temperature $\lambda \approx 2.7 \mu\text{m}$ quantum cascade laser sources based on intracavity second-harmonic generation. *IEEE Journal of Quantum Electronics*, 47(5), 691.

- [19] Salter, C. L., Stevenson, R. M., Farrer, I., Nicoll, C. A., Ritchie, D. A., & Shields, A. J. (2010). An entangled-light emitting diode. *Nature*, 465(7298), 594.
- [20] Parameswaran, K. R., Route, R. K., Kurz, J. R., Roussev, R. V., Fujimura, M., & Fejer, M. M. (2002). Highly efficient second-harmonic generation in buried waveguides formed by annealed and reverse proton exchange in periodically poled lithium niobate. *Optics Letters*, 27(3), 179.
- [21] Pomarico, E., Sanguinetti, B., Gisin, N., Thew, R., Zbinden, H., Schreiber, G., Thomas, A., & Sohler, W. (2009). Waveguide-based OPO source of entangled photon pairs. *New Journal of Physics*, 11(11), 113042.
- [22] Orlov, S., Grundkötter, W., Hofmann, D., Quiring, V., Ricken, R., Suche, H., & Sohler, W. (2008). Mid-infrared integrated optical parametric generators and oscillators with periodically poled Ti:LiNbO₃ waveguides. *Ebrahimzadeh M., Sorokina I. T. (eds.) Mid-Infrared Coherent Sources and Applications. Dordrecht, The Netherlands: Springer*, 377.
- [23] Stegeman, G. I., Villeneuve, A., Kang, J., Aitchison, J. S., Ironside, C. N., Al-Hemyari, K., Yang, C. C., Lin, C., H., Lin, H., H., Kennedy, G. T., Grant, R. S., & Sibbett, W. (1994). AlGaAs below half bandgap: the silicon of nonlinear optical materials. *Journal of Nonlinear Optical Physics & Materials*, 3(3), 347.
- [24] Yu, X., Scaccabarozzi, L., Lin, A. C., Fejer, M. M., & Harris, J. S. (2007). Growth of GaAs with orientation-patterned structures for nonlinear optics. *Journal of Crystal Growth*, 301(1), 163.
- [25] Vodopyanov, K. L., Levi, O., Kuo, P. S., Pinguet, T. J., Harris, J. S., Fejer, M. M., Gerard, B., Becouarn, L., & Lallier, E. (2004). Optical parametric oscillation in quasi-phase matched GaAs. *Optics Letters*, 29(16), 1912.
- [26] Fiore, A., Berger, V., Rosencher, E., Bravetti, P., & Nagle, J. (1998). Phase-matching using an isotropic nonlinear material. *Nature*, 391(6666), 463.
- [27] Van der Ziel, J. P. (1975). Phase-matched harmonic generation in a laminar structure with wave propagation in the plane of the layers. *Applied Physics Letters*, 26(2), 60.
- [28] Dallesasse, J. M., Holonyak, N., Sugg, A. R., Richard, T. A., & El-Zein, N. (1990). Hydrolyzation oxidation of Al_xGa_{1-x}As-AlAs-GaAs quantum-well heterostructures and superlattices. *Applied Physics Letters*, 57(26), 2844.
- [29] Chen, E. I., Holonyak Jr, N., & Maranowski, S. A. (1995). Al_xGa_{1-x}As-GaAs metal-oxide semiconductor field effect transistors formed by lateral water vapor oxidation of AlAs. *Applied Physics Letters*, 66(20), 2688.
- [30] Mac, Dougal. M. H., Dapkus, P. D., Pudikov, V., Zhao, H., & Yang, G. M. (1995). Ultralow threshold current vertical-cavity surface-emitting lasers with AlAs oxide-GaAs distributed Bragg reflectors. *IEEE Photonics Technology Letters*, 7(3), 229.
- [31] Huffaker, D. L., Deppe, D. G., Kumar, K., & Rogers, T. J. (1994). Native oxide defined ring contact for low threshold vertical cavity lasers. *Applied Physics Letters*, 65(1), 97.

- [32] Bravetti, P., Fiore, A., Berger, V., Rosencher, E., & Nagle, J. (1998). 5.2-5.6 μm source tunable by frequency conversion in a GaAs-based waveguide. *Optics Letters*, 23(5), 331.
- [33] Choquette, K. D., Geib, K. M., Ashby, C. I. H., Twesten, R. D., Blum, O., Hou, H. Q., Follstaedt, D. M., Eugene, Hammons. B., Mathes, D., & Hull, R. (1997). Advances in selective wet oxidation of AlGaAs alloys. *IEEE Journal of Selected Topics in Quantum Electronics*, 3(3), 916.
- [34] Suárez, I., Almuneau, G., Condé, M., Arnoult, A., & Fontaine, C. (2009). Optimal control of AlAs oxidation via digital alloy heterostructure compositions. *Journal of Physics D: Applied Physics*, 42(17), 175105.
- [35] Fiore, A., Berger, V., Rosencher, E., Bravetti, P., Laurent, N., & Nagle, J. (1997). Phase-matched mid-infrared difference frequency generation in GaAs-based waveguides. *Applied Physics Letters*, 71(25), 3622.
- [36] De Rossi, A., Berger, V., Calligaro, M., Leo, G., Ortiz, V., & Marcadet, X. (2001). Parametric fluorescence in oxidized aluminum gallium arsenide waveguides. *Applied Physics Letters*, 79(23), 3758.
- [37] Guillotel, E., Ravaro, M., Ghiglieno, F., Langlois, C., Ricolleau, C., Ducci, S., Favero, I., & Leo, G. (2009). Parametric amplification in GaAs/AlO_x waveguide. *Applied Physics Letters*, 94(17), 171110.
- [38] Scaccabarozzi, L., Fejer, M. M., Huo, Y., Fan, S., Yu, X., & Harris, J. S. (2006). Enhanced second-harmonic generation in AlGaAs/Al_xO_y tightly confining waveguides and resonant cavities. *Optics Letters*, 31(24), 3626.
- [39] Ravaro, M., Guillotel, E., Le Dû, M., Manquest, C., Marcadet, X., Ducci, S., Berger, V., & Leo, G. (2008). Nonlinear measurement of mid-infrared absorption in AlO_x waveguides. *Applied Physics Letters*, 92(15), 151111.
- [40] Fiore, A., Janz, S., Delobel, L., van der Meer, P., Bravetti, P., Berger, V., Rosencher, E., & Nagle, J. (1998). Second-harmonic generation at $\lambda \sim 1.6 \mu\text{m}$ in AlGaAs/Al₂O₃ waveguides using birefringence phase matching. *Applied Physics Letters*, 72(23), 2942.
- [41] Ota, J., Narita, W., Ohta, I., Matsushita, T., & Kondo, T. (2009). Fabrication of periodically-inverted AlGaAs waveguides for quasi-phase-matched wavelength conversion at 1.55 μm . *Japanese Journal of Applied Physics*, 48(4), 04C110.
- [42] Gehrsitz, S., Reinhart, F. K., Gourgon, C., Herres, N., Vonlanthen, A., & Sigg, H. (2000). The refractive index of Al_xGa_{1-x}As below the band gap: Accurate determination and empirical modelling. *Journal of Applied Physics*, 87(11), 7825.
- [43] Abolghasem, P., Han, J., Bijlani, B. J., Arjmand, A., & Helmy, A. S. (2009). Highly efficient second-harmonic generation in monolithic matching layer enhanced Al_xGa_{1-x}As Bragg reflection waveguides. *IEEE Photonics Technology Letters*, 21(19), 1462.

- [44] De Rossi, A., Berger, V., Leo, G., & Assanto, G. (2005). Form birefringence phase-matching in multilayer semiconductor waveguides: tuning and tolerances. *IEEE Journal of Quantum Electronics*, 41(10), 1293.
- [45] Guillotel, E., Langlois, C., Ghiglieno, F., Leo, G., & Ricolleau, C. (2010). TEM characterization of oxidized AlGaAs/AlAs nonlinear optical waveguides. *Journal of Physics D: Applied Physics*, 43(38), 385302.
- [46] Marcuse, D. (1969). Mode conversion caused by surface imperfections of a dielectric slab waveguide. *Bell System Technical Journal*, 48(10), 3197.
- [47] Lacey, J. P. R., & Payne, F. P. (1990). Radiation loss from planar waveguides with random wall imperfections. *IEE Proceedings Optoelectronics*, 137(4), 282.
- [48] Schmid, J. H., Del age, A., Lamontagne, B., Lapointe, J., Janz, S., Cheben, P., Densmore, A., Waldron, P., Xu, D. X., & Yap, K. P. (2008). Interference effect in scattering loss of high-index contrast planar waveguides caused by boundary reflections. *Optics Letters*, 33(13), 1479.
- [49] Snyder, A. W., & Love, J. D. (1983). *Optical waveguide theory*. London: Chapman and Hall.
- [50] De Rossi, A., Ortiz, V., Calligaro, M., Lanco, L., Ducci, S., Berger, V., & Sagnes, I. (2005). Measuring propagation loss in a multimode semiconductor waveguide. *Journal of Applied Physics*, 97(7), 073105.
- [51] Rao, S. V., Moutzouris, K., Ebrahimzadeh, M., De Rossi, A., Gintz, G., Calligaro, M., Ortiz, V., & Berger, V. (2003). Influence of scattering and two-photon absorption on the optical loss in GaAs/Al₂O₃ nonlinear waveguides measured using femtosecond pulses. *IEEE Journal of Quantum Electronics*, 39(3), 478.
- [52] Shi, S. S., Hu, E. L., Zhang, J. P., Chang, Y. L., Parikh, P., & Mishra, U. (1997). Photoluminescence study of hydrogenated aluminum oxide-semiconductor interface. *Applied Physics Letters*, 70(10), 1293.
- [53] Chouchane, F., Almuneau, G., Gauthier-Lafaye, O., Monmayrant, A., Arnoult, A., Lacoste, G., & Fontaine, C. (2011). Observation of overstrain in the coalescence zone of AlAs/AlOx oxidation fronts. *Applied Physics Letters*, 98(26), 261921.
- [54] Bava, G., Montrosset, I., Sohler, W., & Suche, H. (1987). Numerical modeling of Ti:LiNbO₃ integrated optical parametric oscillators. *IEEE Journal of Quantum Electronics*, 23(1), 42.
- [55] Durand, O., Wyckzisk, F., Olivier, J., Magis, M., Galtier, P., De Rossi, A., Calligaro, M., Ortiz, V., Leo, G., & Assanto, G. (2003). Contraction of aluminum oxide thin layers in optical heterostructures. *Applied Physics Letters*, 83(13), 2554.
- [56] Thin film center Inc. Essential MacLeod. <http://www.thinfilmcenter.com/essential.html>.

- [57] Abolghasem, P., Han, J., Bijlani, B. J., Arjmand, A., & Helmy, A. S. (2009). Continuous-wave second harmonic generation in Bragg reflection waveguides. *Optics Express*, 17(11), 9460.

InP/InGaAS Symmetric Gain Optoelectronic Mixers

Wang Zhang and Nuri W. Emanetoglu

Additional information is available at the end of the chapter

<http://dx.doi.org/10.5772/51461>

1. Introduction

Optoelectronic mixers (OEM) are photodetectors which detect an optical signal and internally mix it with an electrical signal to obtain an electrical base-band (low frequency) signal. OEM devices have applications in optical communications and sensors such as laser assisted detection and ranging (LADAR) systems. Optoelectronic mixers can simplify signal processing in an optoelectronic system by combining the photodetection and mixing functions, leading to reduced component count. An optoelectronic mixing device which also amplifies the detected signal would further benefit the system.

In this work, a symmetric gain optoelectronic mixer based on a lattice-matched indium gallium arsenide ($\text{In}_{0.53}\text{Ga}_{0.47}\text{As}$) / indium phosphide (InP) symmetric heterojunction phototransistor structure is investigated for chirped-AM laser detection and ranging systems (LADAR) operating in the “eye-safe” 1.55 μm wavelength range. The symmetric current-voltage (I-V) characteristics of this device allows for it to be operated without the application of a DC bias voltage.

1.1. LADAR and the need for optoelectronic mixing devices

The requirements and constraints of the application, LADAR, determine the specifications of the SG-OEM device. Therefore, a basic review of the application is necessary.

Two types of LADAR systems exist, pulse and continuous wave systems, both of which operate in similar manner to their RADAR equivalents [1]. In pulsed LADAR, a laser pulse is transmitted, and the time-of-flight of the return signal is measured. The alternative is to modulate the intensity of a continuous-wave laser with a chirped-FM signal. In order to avoid confusion with optical wavelength modulation, this method has also been called chirped-AM LADAR [2]. The frequency difference (f_{IF}) between the reference (LO) and return (RF) signals is related to target distance by:

$$f_{IF} = 2\Delta F \frac{D}{cT} \quad (1)$$

where ΔF the difference between the start and end frequencies of the chirp, T the chirp period, c the speed of light and D the distance to target. The chirp may cover frequencies ranging from hundreds of MHz to several GHz. In contrast, the mixing product is in the range of tens of kHz to several MHz, as a function of the chirp period T and distance D .

The primary advantage of chirped LADAR over pulsed LADAR is the ability to use semiconductor lasers as the transmitter source, leading to lower cost, power and weight. An additional advantage for a LADAR-on-chip implementation is that by using an optoelectronic mixer device, as described below, the microwave bandwidth return signal can be converted into a low frequency electrical signal that can be read-out using CMOS technology.

A typical photodetector in an optoelectronic system would be DC biased, and convert the RF modulation of the optical signal to an electrical signal at the RF frequency. In a chirped-AM LADAR system this RF signal output is then electronically mixed with LO signal. Due to the small available optical power, below 1 nW in some applications, the RF signal output of the detector may need to be amplified with a wide band amplifier before the electronic mixing. This amplifier can only have a low gain, due to the wide bandwidth nature of the RF signal. An alternative is to mix the photodetector output with the LO signal, then amplify the low frequency signal.

Signal processing of a chirped-AM LADAR system is simplified if the photodetector is used as an optoelectronic mixer (OEM) [2]. An optoelectronic mixer is a photodetector whose responsivity is modulated with the LO signal. The OEM output contains the difference (IF), sum, LO and RF signals. The mixed output signal is low-pass filtered to isolate the IF signal, which is then amplified. Due to the frequency difference, tens to hundreds of kHz vs. hundreds of MHz, much higher gains are possible in the following transimpedance amplifier.

A symmetric I-V characteristic photodetector can be used as an optoelectronic mixer. Symmetric I-V characteristics refer to having equal absolute magnitude current for equal absolute magnitude voltage, $I(-V) = -I(V)$, with $I(0) = 0$. This allows driving the OEM directly with the LO signal, without a DC bias. The output of the detector will thus contain the LO, RF, IF and sum frequencies. This output can be low pass filtered and the IF signal amplified. As this IF signal's bandwidth can be up to six orders of magnitudes smaller than the carrier frequencies, much higher gains can be used at the trans-impedance amplifier (TZA) following the OEM. Due to the lack of a DC bias, sensitivity to background light is reduced, as the response from background light averages to zero. An additional 3 dB signal processing gain is also obtained. The metal-semiconductor-metal (MSM) Schottky photodetector is such a symmetric device [2-5]. Chirped-FM LADAR with GaAs MSM optoelectronic mixers, operating in the 800-850 nm wavelength range, have been reported [2,3]. Eye-safe operation requires operating wavelengths in the 1.3 μm to 1.55 μm . This has motivated to development of InGaAs MSM optoelectronic mixers for operation at 1550 nm [4,5]. These InGaAs MSMs have been reported to have dark currents two orders of magnitude larger than GaAs MSMs [5], affecting noise level, and require larger RF power to achieve similar performance to GaAs

MSMs. The DC responsivity of the InGaAs MSM optoelectronic mixers was reported to be approximately 0.34 A/W [4,5].

The symmetric MSM Schottky photodetectors do not have a gain mechanism. Incorporating gain to the optoelectronic mixer would allow the following transimpedance amplifier's gain to be reduced, increasing bandwidth and improving the system's noise performance.

1.2. Phototransistors as optoelectronic mixing devices

There are three possible candidate structures, based on the avalanche photodiode (APD), the heterojunction phototransistor (HPT) and the modulated barrier diode (MBD). The avalanche photodiode suffers from several drawbacks, including excess noise, and high sensitivity to temperature, voltage bias and defects in the semiconductor material. HPTs and MBDs, on the other hand, can provide high gain with low noise. The basic HPT and MBD structures are shown in Figure 1. MBDs in particular are low noise devices, which have higher gain for lower incident optical powers. A standard asymmetric heterojunction HPT or MBD requires a DC bias to achieve the associated high gain. In a typical system, the DC biased device is used to detect the incoming optical signal at RF frequency. This signal may need to be amplified electronically. However, only low gains are possible due to the frequency. The next stage employs a mixer circuit to obtain the IF signal from the difference of the RF and LO signals. The IF signal may need further amplification.

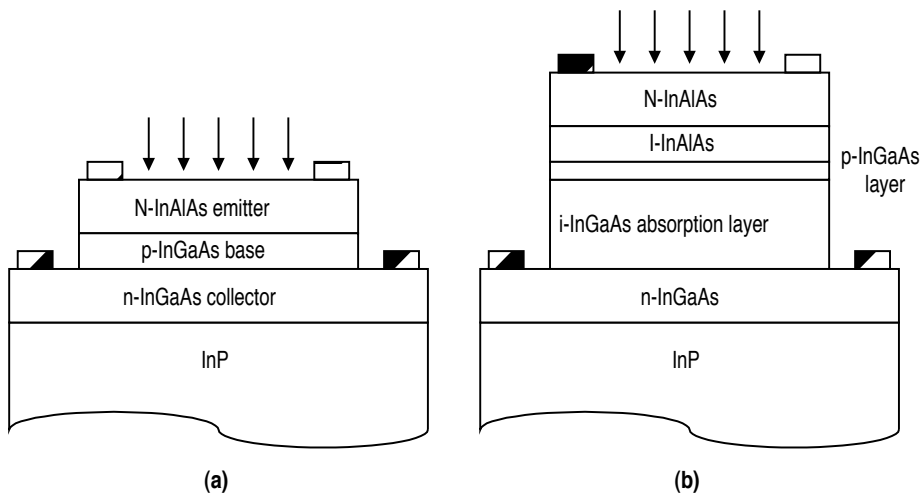


Figure 1. Basic structures of (a) heterojunction phototransistor; and (b) modulated barrier diode.

The heterojunction phototransistor is a transistor with its emitter made of a wider bandgap material than the base. This improves carrier injection efficiency, and also ensures absorption is limited to the base and the base-collector depletion region. The basic HPT is a two terminal device. A number of modifications to the basic HPT structure have been investigated to improve performance. A base bias can be provided, either optically or by an electrical

contact [6]. The base composition can be graded to establish an electric field which enhances electron transport [7,8]. It was demonstrated that symmetric-area heterojunction phototransistors have a larger bandwidth than asymmetric area HPTs [9]. It should be noted that while Milano *et al* predicted a rather pessimistic bandwidth, improvements in material growth, device design and fabrication techniques have improved the maximum bandwidth of HPTs to the tens of GHz range [10,11].

HPT responsivity typically increases with increasing optical power. This has been attributed to recombination at the base-emitter heterojunction. It is desirable to have gain independent from the optical power, or have larger gain at lower optical power levels. Leu *et al* have demonstrated an approach to improve the gain dependence on optical power, by adjusting the doping profile of the emitter and base layers of InP emitter/InGaAs base HPTs [12]. By using a high-low emitter doping, that is reducing the emitter doping in a thin layer at the emitter-base junction, they eliminated the quantum well trapping the electrons at this interface. Thus, the recombination currents were reduced, and the ideality factor of the transistor improved, leading to a flattening of the gain vs. incident power characteristics.

HPTs have been demonstrated for optoelectronic mixing applications, where the LO signal was provided electrically [10,13] or optically [14].

The modulated barrier diode, also known as the Camel diode, is a non-Schottky majority carrier diode in which the carrier transport is controlled by a potential barrier in the bulk of the semiconductor. The application of MBDs as photodetectors was first demonstrated by A.Y. Cho and co-workers [15,16], who also showed its application in a picosecond sampling system [17]. The gain of the MBD is due to the hole trapping at the heterostructure interface. As holes accumulate in this quantum well, the barrier height will be lowered, resulting in an increased electron current, thus providing gain. As a majority carrier device, the MBD has fast intrinsic response [15,17]. In contrast with the HPT, the MBD device has higher responsivity at lower optical power levels [15,16]. The MBD has been used in a front-end photoreceiver, integrated with an FET [18], and a monolithically integrated phototransceiver in which it was integrated with an LED [19]. In the first case, the MBD and FET shared a common structure, and circuit utilized the MBD's gain and response speed. In the second case, the MBD's increasing gain with lower optical power was utilized to improve optical transceiver performance.

1.3. Symmetric gain optoelectronic mixers

Symmetric Gain OptoElectronic Mixers (SG-OEMs) for chirped-AM LADAR operating in the "eye-safe" 1.55 μm wavelength have been investigated by our research group at the University of Maine. These devices are based on symmetric heterojunction phototransistors.

The first generation SG-OEMs used indium aluminum arsenide ($\text{In}_{0.52}\text{Al}_{0.48}\text{As}$)/ indium gallium arsenide ($\text{In}_{0.53}\text{Ga}_{0.47}\text{As}$) heterostructures grown on InP substrates [20,21]. The device structures were designed and simulated using the TCAD-Sentaurus tools from Synopsys. These simulations predicted mixing responsivities up to 100 A/W for these devices.

The heterostructures were grown using molecular beam epitaxy at the US Army Research Laboratory, Adelphi, MD. Cracking defects in the thin films were revealed during device fabrication, leading to an investigation into an alternative device structure with indium phosphide (InP) layers to improve the growth quality [22,23].

2. Device Structure and Simulation

A schematic of the InP based symmetric gain optoelectronic mixer is shown in Figure 2. The targeted operating wavelength is 1.55 μm , therefore the base is $\text{In}_{0.53}\text{Ga}_{0.47}\text{As}$, which has a bandgap of approximately 0.74eV at 300K and is lattice matched to the InP substrate. The base is doped with acceptor atoms to obtain a p-type region. The n-type emitter/collector layers in the structure are made of InP. Highly doped n-type InP/ $\text{In}_{0.53}\text{Ga}_{0.47}\text{As}$ layers are used for ohmic contact formation with the metal electrodes. The schematic in Figure 2 also shows highly doped interface layers at the emitter-base and collector-base interfaces. The device, as shown, is configured for top illumination.

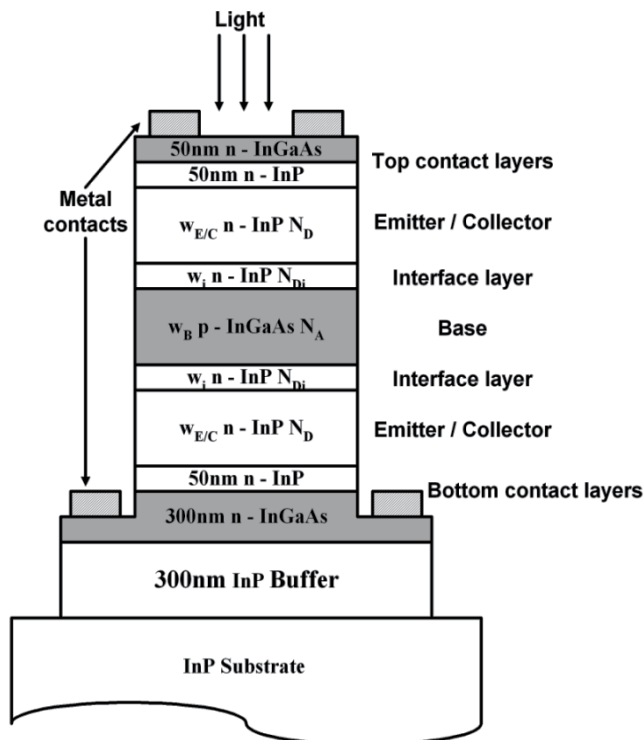


Figure 2. Schematic of an InP/ InGaAs symmetric gain optoelectronic mixer, top illumination configuration.

The design parameters investigated in this work are the base and emitter/collector layer thicknesses and doping levels, as identified in Table 1. The base width w_B is the primary pa-

parameter that will determine the responsivity of the optoelectronic mixer. Increasing the base thickness will extend the carrier path and decrease transistor gain. This will lead to a decrease in the dark and optical currents. However, a trade off has to be made between light absorption, which is directly proportional to base thickness, and the recombination of light generated carriers in the base, which is inversely proportional to base thickness. The responsivity, R , is proportional to:

$$R \propto \frac{(1 - e^{-\alpha w_B})}{d^2} \quad (2)$$

where w_B is the thickness of the base region and α is the absorption coefficient. The base thickness and doping will also impact the base narrowing due to the growth of the reverse biased collector-base junction depletion region with increasing reverse bias, known as the Early effect. When the device is sufficiently reverse biased, the collector-base depletion region will reach the base-emitter depletion region, shorting the device. This is known as punch-through breakdown, and should be avoided.

| Symbol | Parameter |
|-----------|---|
| w_B | In _{0.53} Ga _{0.47} As base thickness |
| N_A | In _{0.53} Ga _{0.47} As base acceptor doping density, p-type |
| $w_{E/C}$ | InP emitter/collector thickness |
| N_D | InP emitter/collector donor doping density, n-type |
| w_i | InP emitter/collector-base interface layer thickness |
| N_{Di} | InP emitter/collector-base interface layer donor doping density, n-type |

Table 1. Design parameters investigated for the symmetric gain optoelectronic mixer

Emitter/collector doping impact device performance in several ways. If they are highly doped, most of the depletion region will be in the base, significantly reducing the effective base thickness. This will provide higher transistor gain, but will also result in punch through breakdown of the device at low voltages. If these layers are lightly doped, then the series resistance will increase, reducing the available current from the device. The effect of the interface layers on device performance are also investigated in this work.

The work reported here covers device design, simulation and optimization using the 2D/3D TCAD-Sentaurus device simulator package from Synopsys, and device modeling. Parameters investigated for device optimization include the highly doped emitter-base interface layers, the base thickness and the doping of each layer. The horizontal dimensions of the standard device are summarized in Table 2. The simulation results are discussed in section 3 and the device model is presented in section 4.

| Parameter | Size [μm] |
|-----------------------------|------------------------|
| Inner mesa width | 16 |
| Outer mesa width | 30 |
| Top contact window width | 12 |
| Top contact metal width | 14 |
| Bottom contact window width | 2 |
| Bottom contact metal width | 4 |

Table 2. SG-OEM horizontal dimensions

3. DC Simulations: Dark Current and Responsivity

3.1. Comparison of InAlAs/InGaAs and InP/InGaAs SG-OEMs

The switch to InP layers was proposed due to the film stoichiometry and resulting lattice mismatch issues experienced with InAlAs films [20]. The first task in this project was to determine how the switch to InP would impact predicted device performance. Figure 3 compares the simulated I-V characteristics for two structures based on Figure 2. The layer thicknesses and doping densities are given in Table 3. InP_A is the structure shown in the figure, while in InAlAs_A all of the InP film layers are replaced by InAlAs, as reported in [20,21]. Both the dark current (i.e., no incident light) and the current with an incident optical power density of 1 mW/cm^2 are displayed. The light is set to be incident on the device's inner mesa and has the same width, $16 \mu\text{m}$. A transparent electrode was assumed. The incident optical power on the detector is $160 \text{ pW}/\mu\text{m}$. The figure illustrates the behavior of a device for a bias voltage sweep from 0 V to 5V.

| Parameter | Value |
|-----------|--------------------------------------|
| w_B | 800 nm |
| N_A | $2.5 \times 10^{16} \text{ cm}^{-3}$ |
| $w_{E/C}$ | 390 nm |
| N_D | $1 \times 10^{16} \text{ cm}^{-3}$ |
| w_i | 10 nm |
| N_{Di} | $5 \times 10^{-18} \text{ cm}^{-3}$ |

Table 3. Layer thickness and doping values for the simulations presented in Figure 3.

The simulation predicts that the $\text{In}_{0.52}\text{Al}_{0.48}\text{As}/\text{In}_{0.53}\text{Ga}_{0.47}\text{As}$ based device will have larger dark and optical currents than the $\text{InP}/\text{In}_{0.53}\text{Ga}_{0.47}\text{As}$ one over the bias range. The optical current of the $\text{In}_{0.52}\text{Al}_{0.48}\text{As}/\text{In}_{0.53}\text{Ga}_{0.47}\text{As}$ based structure is $2.19 \text{ nA}/\mu\text{m}$ at 2 V, compared to 1.64

nA/ μm at 2 V for the InP/ $\text{In}_{0.53}\text{Ga}_{0.47}\text{As}$ based structure. The dark current is also larger for the InAlAs based device. This latter result initially seems counter-intuitive, as $\text{In}_{0.52}\text{Al}_{0.48}\text{As}$ has a larger bandgap than InP, as indicated in Table 4. Table 4 lists the material parameters for the three semiconductor materials, as calculated by TCAD Sentaurus for these compositions at 300K. This behavior can be attributed to two separate mechanisms. First, InP and InAlAs have different conduction band offsets with InGaAs. Second, the Early effect, i.e. base narrowing, is more prominent in the InAlAs based devices.

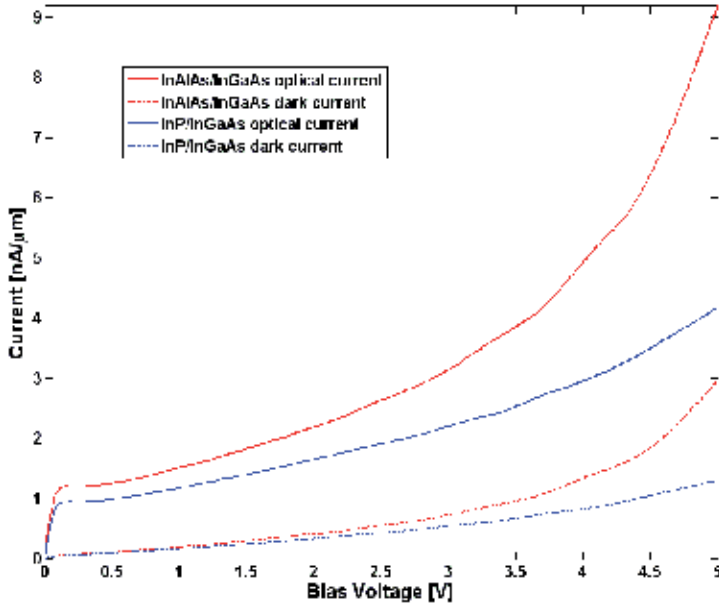


Figure 3. Dark and optical currents versus bias voltage for InP/ $\text{In}_{0.53}\text{Ga}_{0.47}\text{As}$ and $\text{In}_{0.52}\text{Al}_{0.48}\text{As}/\text{In}_{0.53}\text{Ga}_{0.47}\text{As}$ based symmetric gain optoelectronic mixers with the same layer thickness and doping.

| | $\text{In}_{0.53}\text{Ga}_{0.47}\text{As}$ | InP | $\text{In}_{0.52}\text{Al}_{0.48}\text{As}$ |
|----------------------------|---|-----------------------|---|
| E_g [eV] | 0.718721 | 1.33587 | 1.48159 |
| χ_0 [eV] | 4.5472 | 4.4 | 4.2711 |
| ϵ_r | 13.9061 | 12.4 | 12.3948 |
| N_c [cm^{-3}] | 2.5396×10^{17} | 5.66×10^{17} | 5.7814×10^{17} |
| N_v [cm^{-3}] | 7.5107×10^{18} | 2.03×10^{19} | 9.4152×10^{18} |

Table 4. Material parameters used by TCAD Sentaurus in the device simulations

The different conduction band offsets results in a significantly larger two-dimensional electron gas (2DEG) concentration at the InGaAs side of the InP/InGaAs/ contact layer $n^{++}\text{-N}^{++}$

isotype heterojunction compared to that in the InAlAs/InGaAs case, as predicted by TCAD Sentaurus simulations. The electron concentrations at this interface for both structures is shown in Figure 4. The InP based device is on the left, and the InAlAs based device is on the right. The top layer (above the line at 2.3 μm) is the InGaAs contact layer, and below it is the wider bandgap layer. In the InP/InGaAs structure, the 2DEG induces a depletion layer on either side of it (denoted by the white lines), about 7.5 nm in total, larger than that in the InAlAs based device, which is about 2 nm.

Base width narrowing also contributes to the larger InAlAs/InGaAs SG-OEM current. The effective base width is defined as:

$$x_B = w_B - x_{df} - x_{dr} \quad (3)$$

where x_B is the effective base width, x_{df} is the depletion region width of the forward biased heterojunction and x_{dr} is the depletion region width of the reverse biased heterojunction. The change of the forward biased junction width due to the bias voltage is relatively small compared to the reverse biased junction, and can be considered to be its 0V bias value. From TCAD Sentaurus simulations, the effective base width at 1V for the InP based structure is predicted to be 719.17 nm, and 710.19 nm for the InAlAs based structure. Considering the magnitude of this difference, it can be concluded that the dominant reason for the smaller dark current in the InP based devices is the conduction band edge discontinuity.

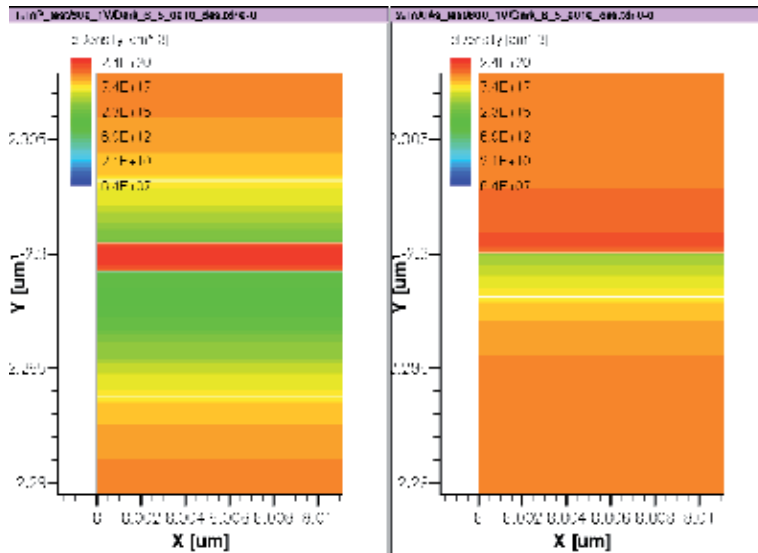


Figure 4. Comparison of the electron concentration in the InP/InGaAs contact layer n^+/N^+ isotype heterojunction (left) with that in the InAlAs/InGaAs contact layer n^+/N^+ isotype heterojunction (right). The black line at 2.3 μm designates the metallurgical boundary between the n^+ InGaAs layer (top in the figure) and the wider bandgap N^+ layer.

A photodetector's noise current is proportional to its dark current. Therefore, the InP based SG-OEM should have better noise performance. The I-V curves in Figure 3 also show that the InP/ $\text{In}_{0.53}\text{Ga}_{0.47}\text{As}$ based structure is less susceptible to the Early effect and punch-through breakdown. This is illustrated by the fact that the InP/ $\text{In}_{0.53}\text{Ga}_{0.47}\text{As}$ based structure has a flatter current curve and does not have the sudden current increase of the $\text{In}_{0.52}\text{Al}_{0.48}\text{As}/\text{In}_{0.53}\text{Ga}_{0.47}\text{As}$ based structure at 4.5 V, which is due to the device approaching punch-through breakdown as the base width decreases with the Early effect.

3.2. Base – Emitter/Collector Interface Layers

Our prior work on InAlAs/InGaAs SG-OEMs predicted that using a highly doped interface layer in InAlAs based devices would improve their performance [20,21]. This phenomenon was investigated for InP based devices as well. Figure 5 shows two nearly identical device structures, where the only difference is the presence or absence of the said highly doped interface layers. The structure InP_A has the interface layers while structure InP_B does not. Figure 6 shows the predicted performance of the two structures.

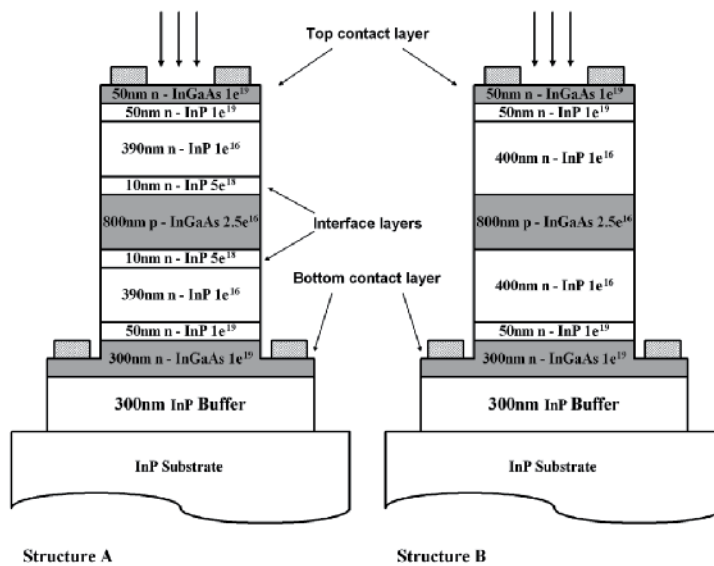


Figure 5. Schematic of the InP / $\text{In}_{0.53}\text{Ga}_{0.47}\text{As}$ heterostructure based symmetric gain optoelectronic mixers for investigating the effect of base-emitter interface layers. Structure InP_A has the interface layers while structure InP_B does not.

Structure InP_B, without the interface layer, is predicted to have a larger optical current than structure InP_A at low bias voltages. Figure 6 also shows that structure B is less susceptible to the Early effect, and has lower dark current. The larger optical current and the lower dark current of structure InP_B is due to structure InP_B having a larger effective base thickness than structure InP_A. In structure InP_A, the highly doped (10 nm, 10^{18} cm^{-3}) emitter interface layers force practically all of the depletion region to extend into the base. The emit-

ter/collector layers of structure InP_B are doped slightly lower than the base layer, therefore most of the depletion region extends into these layers instead of the base. Thus, the InP_B device has a larger effective base width, which increases the optical current by allowing more electron-hole pairs to be generated, and decreases the dark current by inducing more recombination at the base.

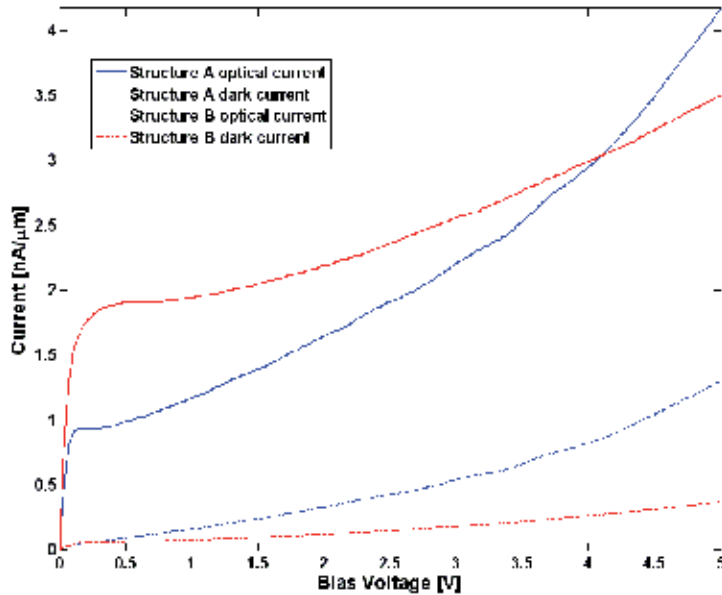


Figure 6. Dark and optical currents versus bias voltage for two InP/ In_{0.53}Ga_{0.47}As based symmetric gain optoelectronic mixers with the same layer thickness and doping. Structure InP_A (with the interface layer) and structure InP_B (without the inter face layer).

Figure 7 shows the responsivity versus the bias voltage for structure InP_A and structure InP_B. Structure InP_B is predicted to have larger responsivity than structure InP_A throughout the bias range. This agrees reasonably well with the dark and optical currents plotted in Figure 6, as the responsivity is directly proportional to the difference of optical and dark currents. Structure B has a responsivity of 12.95 A/W at 2 V. This value is about 1.5 times of the one of structure A, which is 8.194 A/W at 2 V. The currents and responsivity plots displayed above illustrate the fact that structure B (without the interface layers) is a better candidate for the symmetric gain optoelectronic mixer design.

SG-OEM structures with base widths ranging from 500 nm to 1 μm were simulated with and without the highly doped interface layers. Structure A devices, with the interface layers, are more susceptible to punch-through breakdown, as can be seen from their dark current characteristics shown in Figure 8. In contrast, the structure B devices were better behaved, as shown in Figure 9. The highly doped emitter/base interface layer in the Structure A devices forces the depletion region to extend mostly into the base layer, resulting in an early punch-through breakdown.

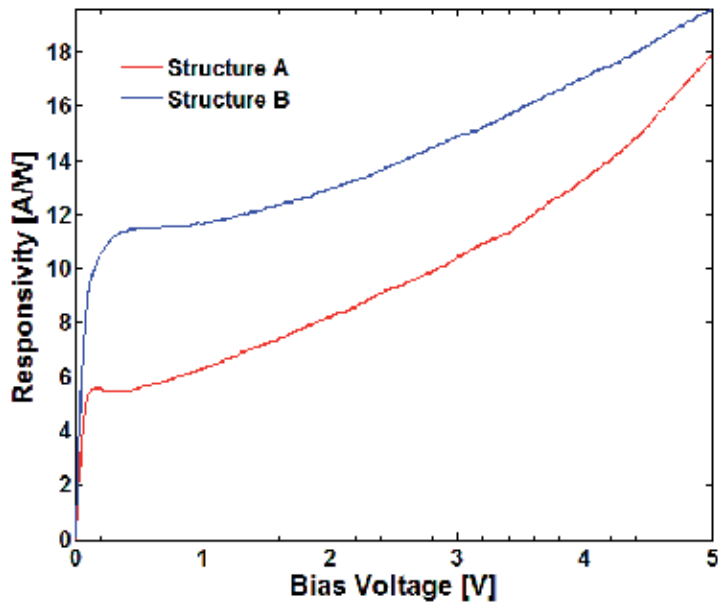


Figure 7. Responsivity versus bias voltage for two InP/ In_{0.53}Ga_{0.47}As based symmetric phototransistors with the same layer thickness and doping. Structure InP_A (with the interface layer) and structure InP_B (without the interface layer).

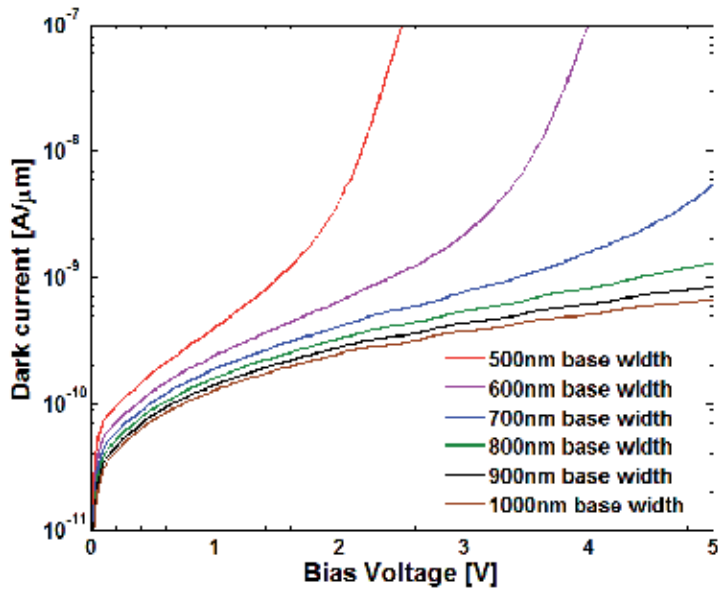


Figure 8. Dark current of structure InP_A as a function of base thickness. The base thickness ranges from 500 nm to 1000 nm.

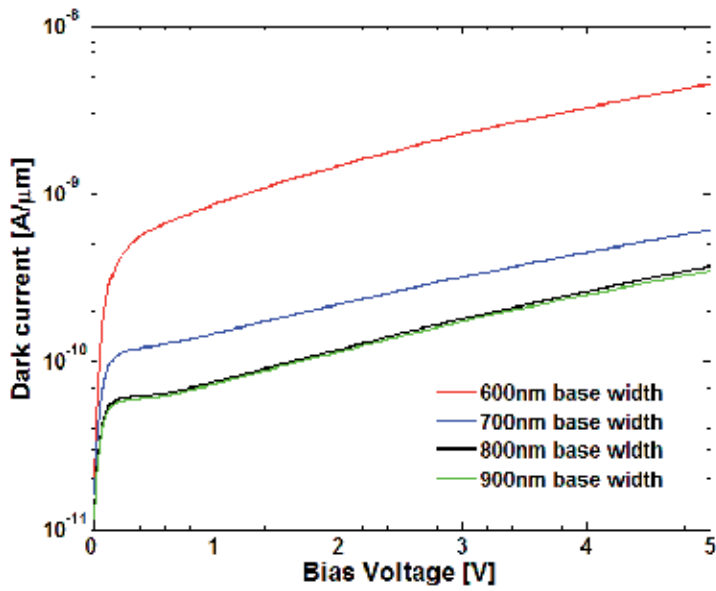


Figure 9. Dark current of structure InP_B as a function of the base thickness. The base thickness ranges from 600 nm to 900 nm.

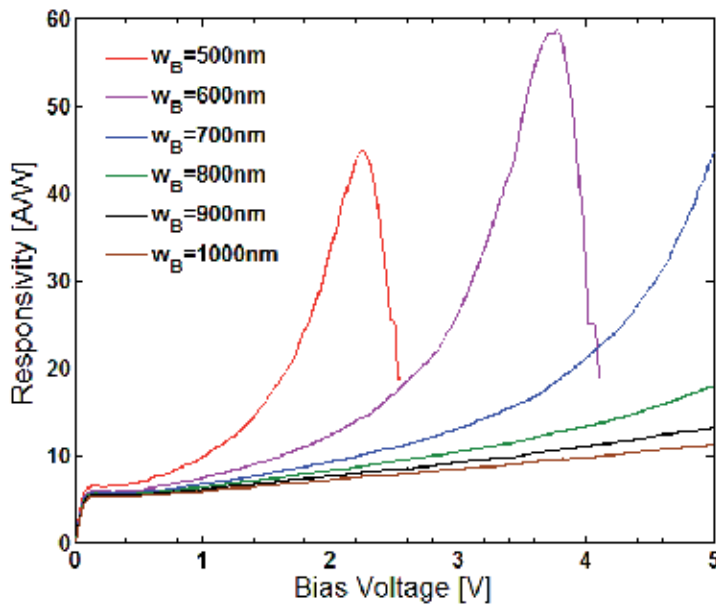


Figure 10. Responsivity of structure InP_A as a function of the base thickness. The base thickness ranges from 500 nm to 1000 nm.

The responsivities of the devices were extracted using simulations with an incident light power of 1 mW/cm^2 , corresponding to an incident optical power of $1.6 \text{ nW}/\mu\text{m}$. Figure 10 shows the DC responsivity of Structure InP_A devices with bases thickness ranging from 500 nm to 1000 nm, with steps of 100 nm. Devices with base thickness below 800 nm show punch-through breakdown effects, where the responsivity increases rapidly as the base narrows, then falls down rapidly when the device punches through.

Figure 11 shows the DC responsivity of four InP/ $\text{In}_{0.53}\text{Ga}_{0.47}\text{As}$ SG-OEMs based on structure InP_B, with base thickness from 600 nm to 900 nm. Similar to structure InP_A devices, the responsivity decreases with increasing base thickness. However, the punch-through behaviour does not occur under 5 V, which agrees with the dark current curves presented in Figure 9.

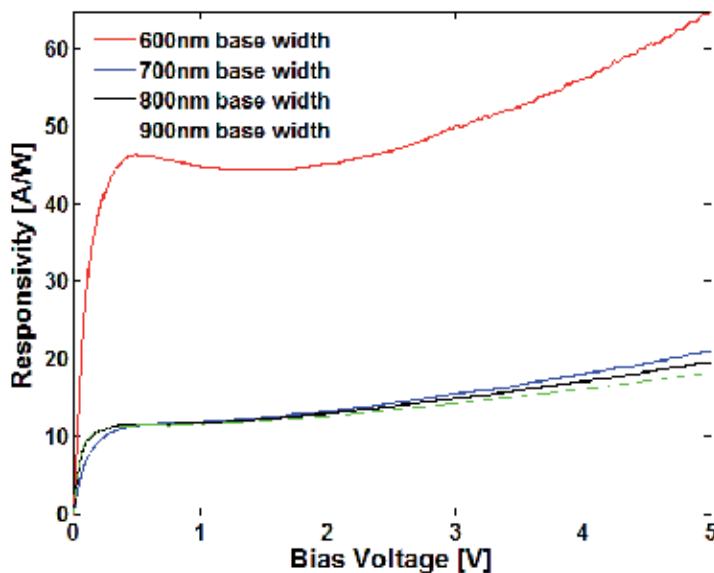


Figure 11. Responsivity of structure InP_B as a function of the base thickness. The base thickness ranges from 600 nm to 900 nm.

The doping dependence of the responsivity was investigated using a matrix of emitter/collector and base layer doping densities. The two extremes and the best case scenario are summarized below, in table 5. Doping profile 1 results in rapid punch-through of the SG-OEM. While a traditional homojunction bipolar junction transistor (BJT) has an emitter layer that is heavily doped compared to the base, the wider bandgap of the InP layer compared to InGaAs results in increased injection efficiency. Therefore, the collector / emitter layer doping levels can be reduced in comparison to the base, making doping profiles 2 and 3 practical.

Figure 12 shows responsivity as a function of doping profile for structure B devices,. These devices were simulated for a base width of 800 nm. The device with doping profile 1 exhibits its punch-through effects rapidly, reaching its peak responsivity of 81.25 A/W at 3V. The rapid decline in responsivity past 3V is due to punch-through breakdown. The device with

doping profile 3 shows no improvement over the InGaAs MSMs [4,5], having an average responsivity of 0.36 A/W over the bias range. The device with doping profile 2 presents a good compromise for the end application, with responsivities above 10 A/W for most of the bias range. For example, the predicted responsivity at 2V is 12.95 A/W. This represents a factor of 38 improvement over the InGaAs MSMs.

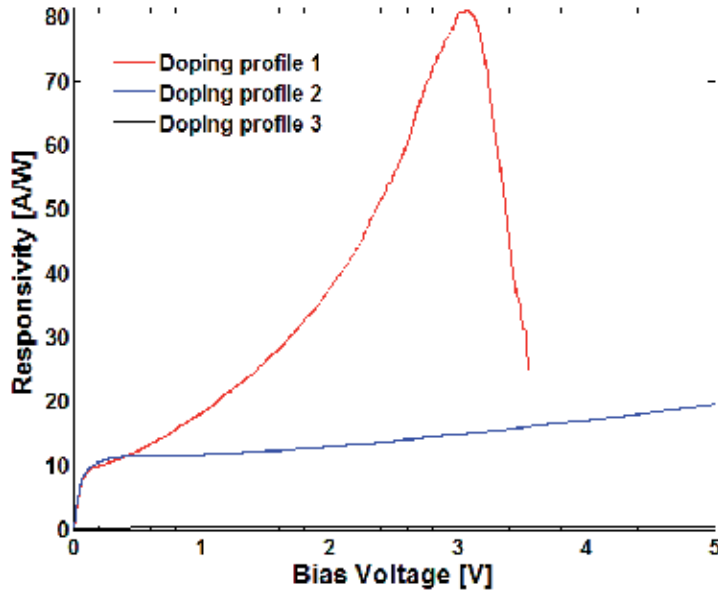


Figure 12. Responsivity of structure InP_B as a function of the doping profiles given in table 5. Base thickness is 800 nm.

4. Device Model

The equivalent circuit model of the SG-OEM is based on the equivalent circuit model of a heterojunction phototransistor. The equivalent circuit model is shown in Figure 13. This model is based on the conventional hybrid- π model. The resistance r_T represents the equivalent series resistance of the top metal-semiconductor contact, the contact layers and the top emitter/collector layer. The resistance r_B represents the equivalent series resistance of the bottom metal-semiconductor contact, the contact layers and the bottom emitter/collector layer. C_μ and C_π represent the junction diffusion capacitances of the base – emitter and base – collector junctions, respectively. r_μ and r_π are the diffusion resistances of these two junctions. The resistance r_o represents the Early effect. The current source I_{dark} represents the dark current of the optoelectronic mixer. I_{opt} represents the photocurrent due to absorption in the base, which is amplified by transistor action. Photon absorption in the InGaAs contact layers is ignored in this analysis as it is substantially smaller than in the base layer. This model can be used for both DC analysis and AC small signal analysis of the device performance. The

circuit parameters were calculated theoretically and extracted from Sentaurus TCAD two-dimensional simulations.

| | Base Doping | Collector / Emitter Doping |
|-----------|--------------------------------------|------------------------------------|
| Profile 1 | $1 \times 10^{16} \text{ cm}^{-3}$ | $5 \times 10^{16} \text{ cm}^{-3}$ |
| Profile 2 | $2.5 \times 10^{16} \text{ cm}^{-3}$ | $5 \times 10^{15} \text{ cm}^{-3}$ |
| Profile 3 | $5 \times 10^{16} \text{ cm}^{-3}$ | $5 \times 10^{15} \text{ cm}^{-3}$ |

Table 5. The base and emitter/ collector doping profiles for the responsivity doping dependence study

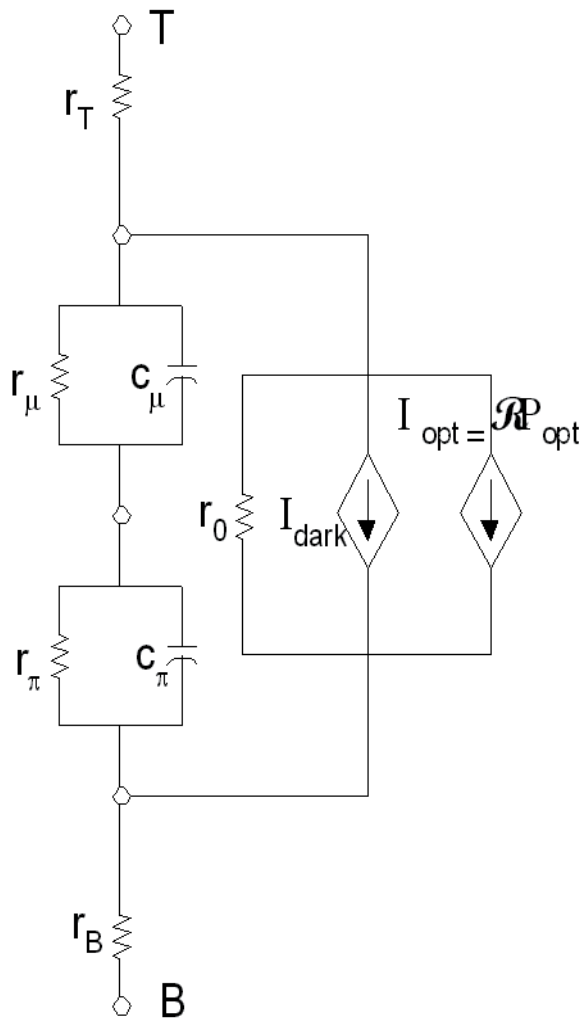


Figure 13. (a) Equivalent circuit model of the SG-OEM device structure.

The equivalent resistances r_T and r_B model the metal-semiconductor junction, the degenerately doped InP and InGaAs contact layers, the isotype heterojunction between these contact layers and the quasi-neutral regions (QNRs) of the emitter and collector. Of these components, the quasi-neutral region resistance and the isotype heterojunction dominate r_T and r_B . The resistance of the contact layers and the quasi-neutral region can be predicted by using the conductivity of the semiconductor layers, and can be formulated as:

$$r = \frac{w_{\text{layer}}}{q\mu_n n d} [\Omega.\text{cm}] \quad (4)$$

where w_{layer} is the layer thickness, d the width of the layer, q elemental charge, n the free electron density, and μ_n the mobility of electrons in the layer. The unit of the contact resistance as defined by Equation 4 is $\Omega.\text{cm}$.

The second contributor to the voltage drop at the contact layers is the highly doped InP/InGaAs isotype heterojunction interface. The carrier conduction at the highly doped InP/InGaAs isotype heterojunction interface can be analyzed based on the band diagram shown in Figure 14. The conduction band edge is similar to that of a rectifying metal – semiconductor contact. Such a contact can have one of three conduction mechanisms: thermionic emission, thermionic-field emission and field emission. It was determined that field emission dominated the current conduction between the InP and InGaAs layers, due to the very high doping densities of both layers.

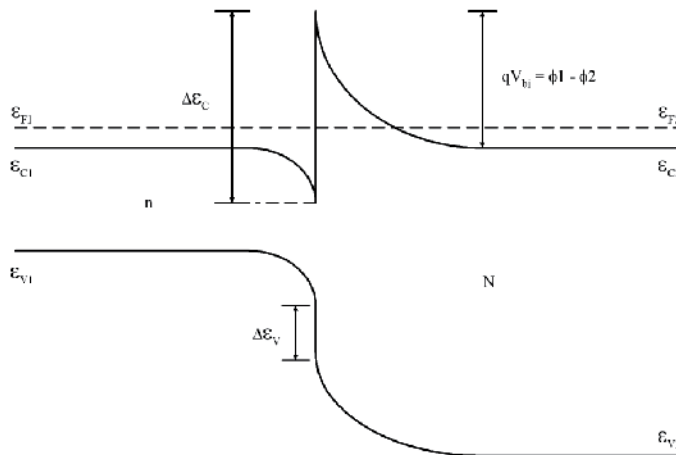


Figure 14. Band diagram of the isotype heterojunction formed by the highly doped InP and InGaAs contact layers.

In order to verify the assumptions made above, the contact regions of the original device were modeled separately in TCAD-Sentaurus and a set of simulations were carried out. The results were then compared with the theoretical calculations. The structures shown in Figure 15 were simulated to verify the calculations for the top and bottom contact resistances. Fig-

ure 16 shows the simulated I-V characteristics for the top and bottom emitter/collector quasi-neutral region and contact layer models depicted in Figure 15. The simulation was done under dark conditions, with the bias voltage being swept from 0 to 5 V.

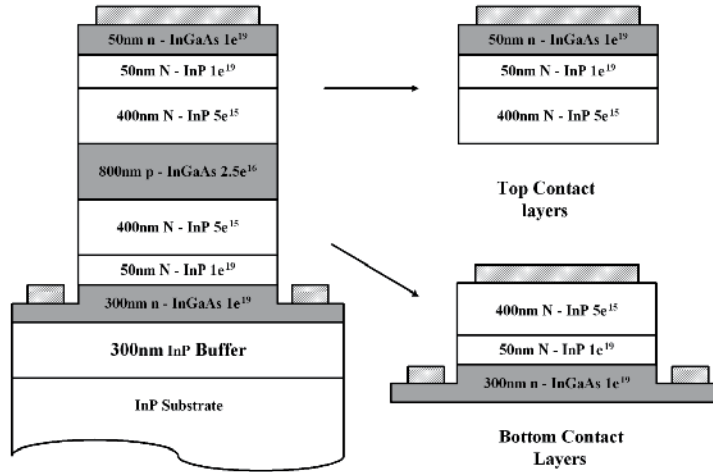


Figure 15. Structures for series resistance extraction of InP / $\text{In}_{0.53}\text{Ga}_{0.47}\text{As}$ HPT based SG-OEMs. Original structure is on the left, top contact layers are on the right top and bottom contact layers are on the right bottom.

The dark current of the top emitter/collector region shows a linear trend with increasing bias voltage and the top contact layer series resistance r_T can be calculated from the I-V data presented in Figure 16 using:

$$r_{eq} = \frac{\Delta V}{\Delta I} \quad (5)$$

where r_{eq} is the equivalent resistance (r_T or r_B), ΔV is the voltage difference between two points and the ΔI is the corresponding current difference on the I-V curve shown in Figure 16. The value of r_T for this structure, is calculated to be $2.97 \times 10^{-2} \Omega\text{-cm}$. This value is close to the sum of the theoretically calculated quasi-neutral region resistance ($6.9 \times 10^{-3} \Omega\text{-cm}$) and isotype heterojunction field emission equivalent resistance ($1.03 \times 10^{-2} \Omega\text{-cm}$). Therefore, it can be concluded that the top contact series resistance is dominated by the quasi-neutral layer resistance and the field emission equivalent resistance of the isotype heterojunction formed by the InGaAs/InP contact layers. The I-V curve of the bottom contact layer, on the other hand, shows a non-linear saturating trend as the voltage increases. The current saturation is induced by the narrowing of the contact layer after the mesa etch step. The increase of the current is limited by the narrow corner region of the InGaAs contact layer. The equivalent resistance is predicted to be approximately $0.57 \Omega\text{-cm}$, assuming the contact layer is etched mid-way and the current starts to crowd in the narrowing contact layer. This resistance will depend on accurate control of the inner mesa etch step in the device fabrication process and can be an issue at high current levels.

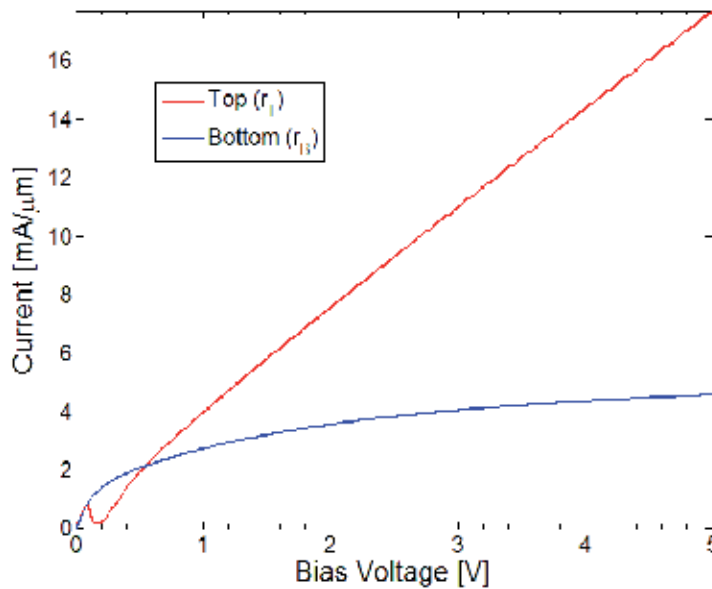


Figure 16. Dark current versus bias voltage for top and bottom contact layers of InP / In_{0.53}Ga_{0.47}As HPT based SG-OEMs.

The frequency response related parameters are the junction capacitances C_{μ} and C_{π} . These can be calculated from the junction capacitance formula for a heterostructure:

$$C = \sqrt{\frac{qN_A N_{D,base,E/C}}{2(N_{A',base} + N_{D',E/C})(V_{bi} + V_R)}} \quad (6)$$

where N_A and N_D are the doping densities of base and emitter/collector, respectively, $\epsilon_{r,base}$ is the relative permittivity of the InGaAs base and $\epsilon_{r,E/C}$ that of the InP emitter/collector, V_{bi} is the built-in barrier, V_R is the bias voltage and q is unit charge. The total capacitance of the SG-OEM device is dominated by the junction capacitance of the reverse biased junction.

Equivalent capacitance of the SG-OEM was extracted for both the full structure and a single base-emitter/collector heterojunction, as shown in Figure 17. The device total capacitance is the capacitance seen between the two terminals of the SG-OEM, which includes the two base-emitter/collector junction capacitances in series and the base transit time.

A set of AC bias simulations were carried out on the two structures displayed in Figure 17. The simulations were set at dark condition and the bias voltage was swept from 0 to 5V. A small signal simulation was applied at each voltage point and the corresponding capacitance was modeled and calculated. The simulated total capacitance of the original structure and the junction capacitance of the base-emitter heterojunction are plotted in Figure 18 as a function of the bias voltage.

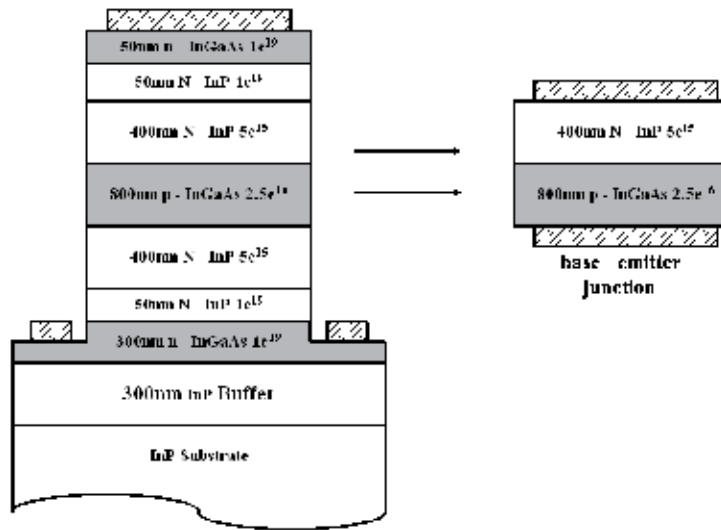


Figure 17. Structures used for extracting the equivalent capacitances of InP / $\text{In}_{0.53}\text{Ga}_{0.47}\text{As}$ HPT based SG-OEMs. The full SG-OEM structure is on the left, and a single base-emitter junction is on the right.

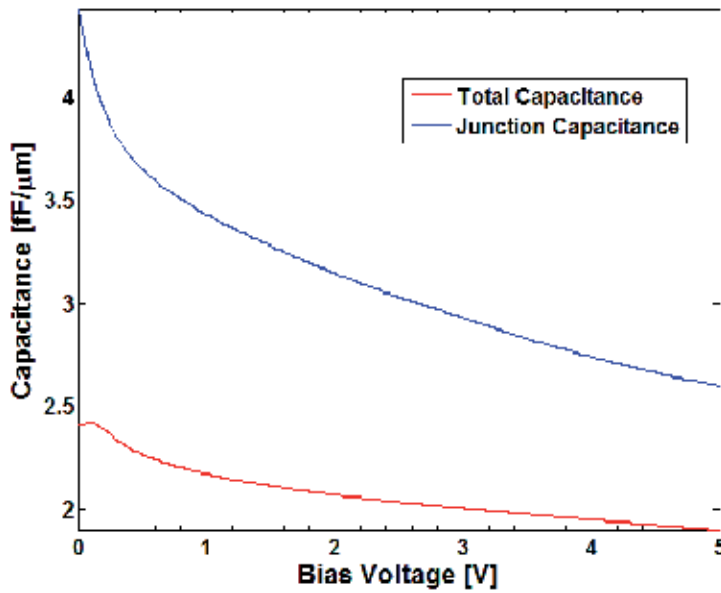


Figure 18. Total device capacitance and capacitance of a single reverse-biased base-emitter/collect junction of InP / $\text{In}_{0.53}\text{Ga}_{0.47}\text{As}$ HPT based SG-OEMs.

A set of AC simulations were carried out on the two structures displayed in Figure 17, with $N_A = 2.5 \times 10^{16} \text{ cm}^{-3}$ and $N_D = 5 \times 10^{15} \text{ cm}^{-3}$. The simulations were carried out for dark conditions and the DC bias voltage was swept from 0 to 5V, with a small signal perturbation applied to the bias

voltage. The simulated total capacitance of the SG-OEM structure and that of a single base-emitter/collector heterojunction are plotted in Figure 18 as a function of the bias voltage.

The AC simulation results show that both the device total capacitance and the base-emitter junction capacitance decrease with increasing bias voltage, as would be expected. The capacitance of the reverse biased heterojunction decreases with increasing V_R as given in Equation 6. This is due to the increase of the depletion region width with increasing reverse bias voltage, which leads to a decrease in the junction capacitance. The total capacitance is dominated by the reverse-biased junction capacitance, which has a smaller value than the forward biased junction. At 0V bias, the capacitance of a single heterojunction was calculated to be 4 fF/ μm using Equation 6, with $\epsilon_{r,\text{base}} = 13.906$ for the InGaAs layer and $\epsilon_{r,E/C} = 12.4$ for the InP layer. The TCAD Sentaurus simulation gives 4.434 fF/ μm , as shown in Figure 18. At 0V bias, both heterojunction capacitances are equal. Therefore, the equivalent capacitance seen looking into the SG-OEM device, which is the series equivalent capacitance of the two heterojunctions, is half of the capacitance of a single heterojunction.

5. Conclusion

Symmetric gain optoelectronic mixers based on InP/ $\text{In}_{0.53}\text{Ga}_{0.47}\text{As}$ heterostructures are promising candidates use in the receivers of chirped-AM LADAR systems. These devices can reduce LADAR system component count and complexity, and improve their performance. Two dimensional device simulations were used to optimize device structure parameters, including base width and doping density, and emitter/collector layer doping density. It was determined that highly doped interface layers caused an increase in dark current and device capacitance and also lowered the base punch through breakdown voltage. Therefore, the optimized device design does not contain such an interface layer.

Acknowledgements

This work was partially supported by the US Army Research Laboratory (Dr. Neal Bambha) under the auspices of the U.S. Army Research Office Scientific Services Program administered by Battelle (Delivery Order 0812, Contract No. W911NF-07-D-0001)

Author details

Wang Zhang and Nuri W. Emanetoglu*

Electrical and Computer Engineering, University of Maine, Orono, Maine, USA

References

- [1] Jelalian, AV. (1992). *Laser Radar Systems*. London: Artech House.
- [2] Ruff, W., Bruno, J., Kennerly, S., Ritter, K., Shen, P., Stann, B., Stead, M., Sztankay, G., & Tobin, M. (2000). Self-mixing Detector Candidates for an FM/cwLadarArchitecture. *Laser Radar Technology and Applications V*, Proc. SPIE, 4035.
- [3] Shen, H., & Aliberti, K. (2002). Theoretical analysis of an anisotropic metal-semiconductor-metal optoelectronic mixer. *Journal of Applied Physics*, 91(6), 3880-3890.
- [4] Shen, H., Aliberti, K., Stann, B., Newman, P. G., Mehandru, R., & Ren, F. (2004). Analysis of InGaAs metal-semiconductor-metal OE mixers. *Physics and Simulation of Optoelectronic Devices XII*, Proc. SPIE, 5349.
- [5] Shen, H., Aliberti, K., Stann, B., Newman, P., Mehandru, R., & Ren, F. (2003). Mixing characteristics of InGaAs metal-semiconductor-metal photodetectors with Schottky enhancement layers. *Applied Physics Letters*, 82(22), 3814-3816.
- [6] Chandrasekhar, S., Hoppe, M. K., Dentai, A. G., Joyner, C. H., & Qua, G. J. (1991). Demonstration of enhanced performance of an InP/InGaAs heterojunction phototransistor with a base terminal. *IEEE Electron Device Letters*, 12(12), 550-552.
- [7] Capasso, F., Tsang, W. T., Bethea, C. G., Hutchinson, A. L., & Levine, B. F. (1983). New graded band-gap picosecond phototransistor. *Applied Physics Letters*, 42(1), 93-95.
- [8] Thuret, J., Gonzalez, C., Benchimol, J. L., Riet, M., & Berdager, P. (1999). High-speed InP/InGaAs heterojunction phototransistor for millimeter-wave fibre radio communications. *Proc. 11th Int. Conference on Indium Phosphide and Related Materials*, 389-392.
- [9] Milano, R. A., Dapkus, P. D., & Stillman, G. E. (1982). An analysis of the performance of heterojunction phototransistors for fiber optic communications. *IEEE Transactions on Electron Devices*, 29(2), 266-274.
- [10] Choi, C. S., Seo, J. H., Choi, W. Y., Kamitsuna, H., Ida, M., & Kurishima, K. (2005). GHz Bidirectional Radio-on-Fiber Links Based on InP-InGaAs HPT Optoelectronic Mixers. *IEEE Photonic Technology Letters*, 17(12), 2721-2723.
- [11] Polleux, J. L., Paszkiewicz, L., Billabert, A. L., Salset, J., & Rumelhard, C. (2004). Optimization of InP-InGaAs HPT Gain: Design of an Opto-Microwave Monolithic Amplifier. *IEEE Transactions on Microwave Theory and Technology*, 52(3), 871-881.
- [12] Leu, L. Y., Gardner, J. T., & Forrest, S. R. (1991). A high-gain high-bandwidth In_{0.53}Ga_{0.47}As/InP heterojunction phototransistor for optical communications. *Journal of Applied Physics*, 69(2), 1052-1062.
- [13] Liu, , Seeds, A. J., & Wake, D. (1997). Two-terminal edge-coupled InP/InGaAs heterojunction phototransistor optoelectronic mixer. *IEEE Microwave and Guided Wave Letters*, 7(3), 72-74.

- [14] Van de Castele, J., Vilcot, J. P., Gouy, J. P., Mollot, F., & Decoster, D. (1996). Electro-optical mixing in an edge-coupled GaInAs/InP heterojunction phototransistor. *Electronics Letters*, 32(11), 1030-1032.
- [15] Chen, C. Y., Cho, A. Y., Garbinski, P. A., Bethea, C. G., & Levine, B. F. (1981). Modulated barrier photodiode: A new majority-carrier photodetector. *Applied Physics Letters*, 39(4), 340-342.
- [16] Chen, C. Y. (1981). Theory of a modulated barrier photodiode. *Applied Physics Letters*, 39(12), 979-981.
- [17] Bethea, C. G., Chen, C. Y., Cho, A. Y., & Garbinski, P. A. (1982). Opto-electronic picosecond sampling system utilizing a modulated barrier photodiode. *Applied Physics Letters*, 40(7), 591-594.
- [18] Li, W. Q., & Bhattacharya, P. K. (1989). Integration of a modulated barrier photodiode with a doped-channel quasi-MISFET. *IEEE Electron Device Letters*, 10(9), 415-416.
- [19] Qasaimeh, O., Zhou, W. D., Bhattacharya, P., Huffaker, D., & Deppe, D. G. (2000). Monolithically integrated low-power phototransceiver incorporating InGaAs/GaAs quantum-dot microcavity LED and modulated barrier photodiode. *Electronics Letters*, 36(23), 1955-1957.
- [20] Emanetoglu, N. W., Drew, S., Bambha, N., & Bickford, J. R. (2008). Symmetric Gain Optoelectronic Mixers for LADAR. *Proceedings of the 2008 US Army Science Conference*, NP-11.
- [21] Drew, S. (2009). Symmetric Gain Optoelectronic Mixers for LADAR Applications. *MS thesis. University of Maine Orono*.
- [22] Zhang, W., Emanetoglu, N. W., Bambha, N., & Bickford, J. R. (2010). Design and Analysis of In_{0.53}Ga_{0.47}As/InP Symmetric Gain Optoelectronic Mixers. *Solid State Electronics*, 54(12), 1549-1553.
- [23] Zhang, W. (2010). InP/In_{0.52}Ga_{0.47}As Symmetric Gain Optoelectronic Mixers for LADAR Applications. *MS thesis. University of Maine Orono*.

Preparation and Characterization of Nanostructured TiO₂ Thin Films by Hydrothermal and Anodization Methods

S. Venkatachalam, H. Hayashi, T. Ebina and H. Nanjo

Additional information is available at the end of the chapter

<http://dx.doi.org/10.5772/51254>

1. Introduction

In recent years, metal oxide materials such as TiO₂ and ZnO thin films have been extensively studied for various applications such as solar cells, gas sensors and protective coating [1-2]. Among them, TiO₂ is a very suitable oxide material for dye-sensitized solar cell (DSC) applications, because of its extraordinary oxidizing ability of photogenerated holes. TiO₂ thin films are prepared by various preparation methods, but the efficiency of the DSC solar cell is strongly enhanced by the increased dye absorption capacity of the photoelectrode. The most important factors which strongly affect the device performance are series resistance, charge carrier-recombination, electron injection from a photoexcited dye into the conduction band of an oxide semiconductor and hole transportation to the counter. Adachi et al. [3] reported that the dye absorption capacity of TiO₂ nanowires was about 4-5 times higher than that of P25 film, which is made of TiO₂ nanoparticles. It means that the electron collection efficiency in P25 film is lower than that of TiO₂ nanowires. The electron collection efficiency is determined by trapping/detrapping events along the site of the electron traps (grain boundaries and defects). All these problems can be resolved using nanostructured TiO₂ films such as nanoholes, nanotubes, nanorods and nanowires. Nanostructured TiO₂ thin films have been prepared by sol-gel, anodization and hydrothermal methods [1, 4]. Very suitable methods to prepare the TiO₂ nanorod and nanotube are hydrothermal and electrochemical anodization. In the present work, TiO₂ nanowires, nanorods, nanoporous and nanotubes were prepared using hydrothermal and anodization methods. In this paper, we report the surface morphological, optical, structural and electrical properties of TiO₂ nanowires, nanorods, nanoporous and nanotubes. The fabrication procedure of dye-sensitized solar cells and the factors which affect the device performance will be discussed. Finally, photovoltaic parameters (I_{sc} , V_{oc} , FF

and η) of DSC based on rutile and anatase TiO_2 films will be compared with TiO_2 nanoporous, nanoholes, nanotube array films based DSC.

2. Experimental methods

TiO_2 nanowires (TNWs), nanorods (TNRs) and nanoporous films were grown on ITO glass substrates using hydrothermal method. The hydrothermal synthesis of TNWs, TNRs and nanoporous was carried out in a Teflon-lined stainless steel autoclave. Titanium n-butoxide (TNB) solution was used as precursor for the production of TiO_2 films. In a typical synthesis process, TNB (0.5 – 1.0 ml) was used with different amounts of HCl (15 - 23 ml), HNO_3 (5 – 15 ml) and deionized water (DI=35-45 ml). Finally, the resulting solution was transferred into an autoclave. Here ITO-coated glass was used as a substrate. The autoclave was sealed and then placed into an electric oven. The synthesis process was carried out for different reaction times as well as temperatures. After completion of the reaction, the autoclave was cooled down to room temperature. Finally, the substrates were thoroughly washed with deionized water, followed by drying overnight at ambient temperature. Nanocrystalline indium tin oxide (ITO) thin films were prepared on glass substrates by ion beam sputter deposition method. The deposition procedure of nanocrystalline ITO thin films can be found elsewhere [5]. The TiO_2 films were characterized by X-ray diffraction (XRD) using $\text{Cu K}\alpha$ radiation ($\lambda=1.54056 \text{ \AA}$) at 40 kV and 30 mA, with a Rigaku; RINT 2200VK/PC diffractometer. Transmission through the films was measured using an UV-VIS-NIR spectrophotometer (UV-3150, Shimadzu). The surface morphologies of the TiO_2 films were observed by field emission scanning electron microscopy (FE-SEM, S4800, Hitachi). In order to prepare the DSC devices, the TiO_2 electrodes were immersed in ethanol solution containing N-719 dye. Then the dye-anchored TiO_2 electrodes were rinsed with ethanol solution and dried in air. The liquid electrolyte was prepared by dissolving 0.05 M of iodine (I_2) and 0.5 M of potassium iodide (KI) in 10 ml of ethylene glycol. Meanwhile, platinum film was prepared by ion-beam sputter deposition method and the Pt-sputtered ITO/Glass was used as a counter-electrode. Surlyn spacer film with a thickness of 60 μm was used as a spacer. I-V measurements were performed using Keithley High Resistance Meter/Electrometer 6517A at room temperature.

3. Results and discussion

3.1. Preparation and characterization of TiO_2 thin film by hydrothermal method

The effects of reaction temperature, HCl and titanium n-butoxide (TNB) volume on the structural properties of TiO_2 films are discussed in this section. Here, the volume of titanium n-butoxide (TNB= 1 ml) is fixed and the volume of deionized water (45-30 ml) and HCl (15-23 ml) are varied. The reaction time and temperature are fixed at 17 h and 160° C, respectively.

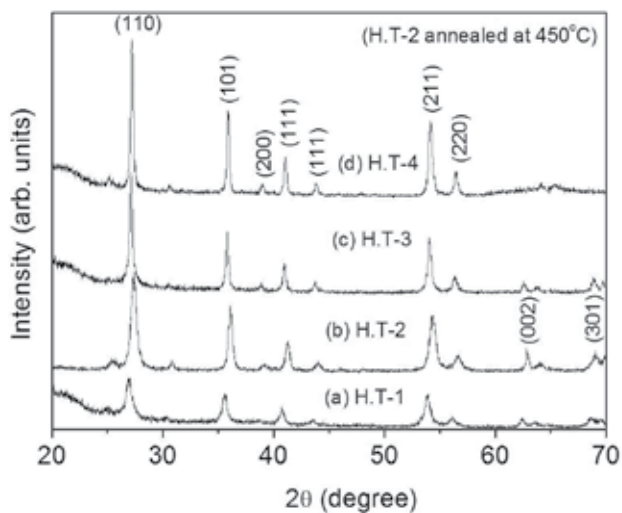


Figure 1. XRD patterns of TiO₂ films prepared using different volume of HCl. (a) H.T-1 [HCl=15 ml; DI=45 ml], (b) H.T-2 [HCl=20 ml; DI=40 ml], (c) H.T-3 [HCl=23 ml; DI=30 ml] and (d) H.T-4 [H.T-2 annealed at 450°C for 30 min]. Here TNB (1 ml), reaction time (17 h) and reaction temperature (160°) were kept constant.

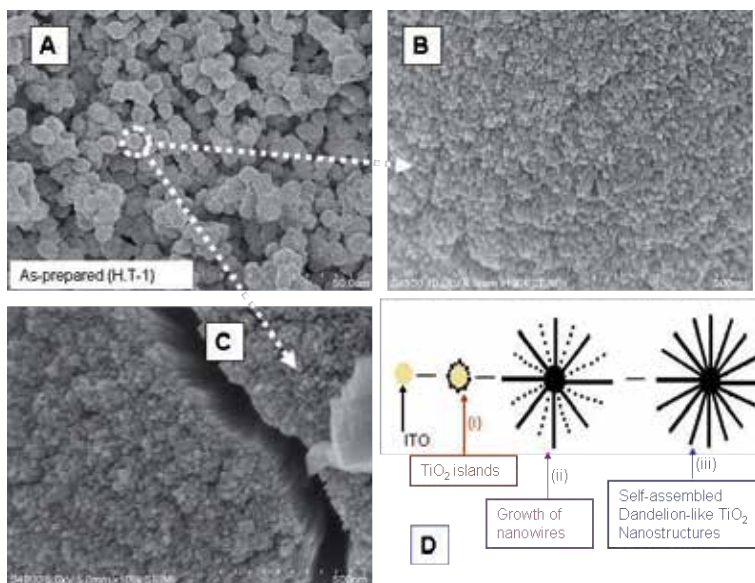


Figure 2. SEM images of TiO₂ films prepared with TNB of 1 ml, HCl of 15 ml, DI of 45 ml, reaction time of 17 h and at a reaction temperature of 160°C.

Figure 1 shows the XRD patterns of TiO₂ films prepared using different volumes of HCl. A very strong rutile peak is observed at 2θ of 27.37°, assigned to (110) plane (see Fig.1). Other

rutile peaks are observed at 2θ of 36.10° (101), 39.16° (200), 41.26° (111), 44.01° (210), 54.36° (211), 56.59° (220), 62.92° (002), 64.10° (310) and 68.91° (301). The (110) peak intensity increases as the volume of HCl is increased from 15 to 23 ml. The positions of all diffraction peaks correspond to rutile TiO_2 and they coincide well with the reported value [6]. However, a weak anatase peak is observed at 2θ of 25.46° , assigned to (101) plane. The TiO_2 sample (H.T-2) is annealed in air at 450°C for 30 min and the XRD pattern of annealed TiO_2 sample is shown in Figure 1(d). The position of these diffraction peaks is the same as those observed in Fig.1 (b). However, the relative intensity of these diffraction peaks increases after annealing at 450°C . This result shows that the increase in HCl volume enhances the growth of the films along (110) direction. This result agrees well with the previous result reported by Wu et al. [7]. Meanwhile, TiO_2 nanorods did not grow on the substrate surface when the volume of HCl is either increased from 23 to 30 ml or decreased from 15 to 10 ml. These data of 10 and 30 ml are not shown in Fig.1. This is attributed that the moderate hydrolysis of titanium n-butoxide (TNB) is important to grow the growth oriented TiO_2 nanorods.

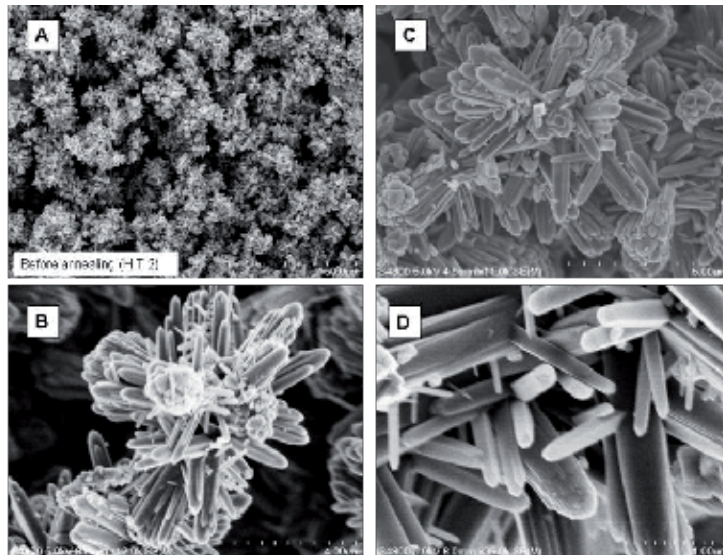


Figure 3. SEM images of TiO_2 films (H.T-2) prepared using TNB of 1 ml, HCl of 20 ml and DI of 40 ml.

Figure 2 shows the SEM images of TiO_2 films prepared on ITO-coated glass substrates with TNB of 1 ml, HCl of 15 ml and DI of 45 ml. The overall morphology indicates the existence of many uniform, dandelion-like TiO_2 nanostructures with diameters in the range of 4 - 6 μm . A selected area of high magnification SEM images [Top (Fig.2B) and side view (Fig.2C)] show that each dandelion-like nanostructure is composed of ordered nanowires with an average diameter of 17 nm. Similar nanowire-structured TiO_2 surface has been observed by Feng et al. [1]. This is attributed that if there is no lattice match between the TiO_2 film and substrate, the TiO_2 firstly nucleated as islands and then nanowires grow from these islands to form dandelion-like morphologies (see the Fig.2d). SEM images of as-prepared TiO_2 films are shown in Fig. 3 which

is prepared by adding HCl volume of 20 ml in the reaction solution. At low and high magnifications (Figs. 3A and B), the whole surface is composed of flower-like structures, which are composed of nanorods and nanorod bundles (see Fig.3C). The nanorod size is in the range of ~150-200 nm (Fig.3D). The as-prepared sample is then annealed at 450°C for 30 min in order to check the robustness of the morphology of the TiO₂ nanorod arrays. The low and high magnification SEM images of annealed TiO₂ films are shown in Figs. 4A and B, respectively. Upon annealing at 450°C, the nanorod array remains unchanged, but the size of the nanorod and nanorod bundles increase after annealing at 450°C (see Fig.4C). After annealing, the size of the nanorod is in the range of 200-300 nm (Fig. 4D). It is apparent that the conversion of nanostructure from nanowires to nanorods is realized by increasing the volume of HCl in the synthesis solution. TiO₂ nanorods did not grow on glass substrates. It seems that the nucleation and growth of the crystals could be promoted by ITO.

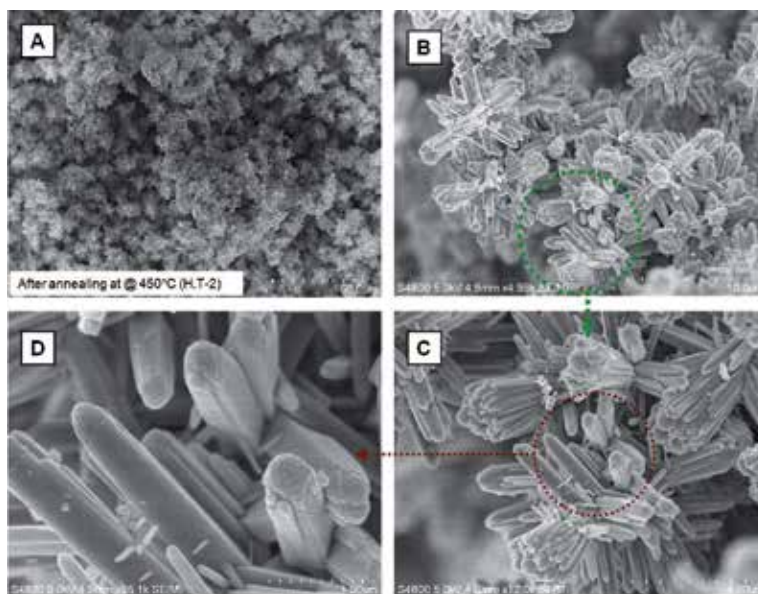


Figure 4. SEM images of TiO₂ films (H.T-2) annealed at 450°C for 30 min.

Figure 5 shows the photocurrent density-voltage characteristics of DSC based on TiO₂ nanowire, nanorod and P25 films. The photovoltaic parameters are given in Table 1. The short-circuit current density and fill factor of nanowire based DSC is higher than that of nanorod based DSC. The optical absorption study shows that the dye absorption capacity of TiO₂ nanowire is much better than that of TiO₂ nanorods (Figure not shown). As a result, the power conversion efficiency of nanowire based DSC is higher than that of nanorod based DSC. However, the power conversion efficiency of rutile TiO₂ based DSC is lower than that of anatase TiO₂ (P25) nanoparticles based DSC. Similar results have been observed by Lin et al. [8]. The power conversion efficiency could also be increased by increasing the TiO₂ film thickness [9].

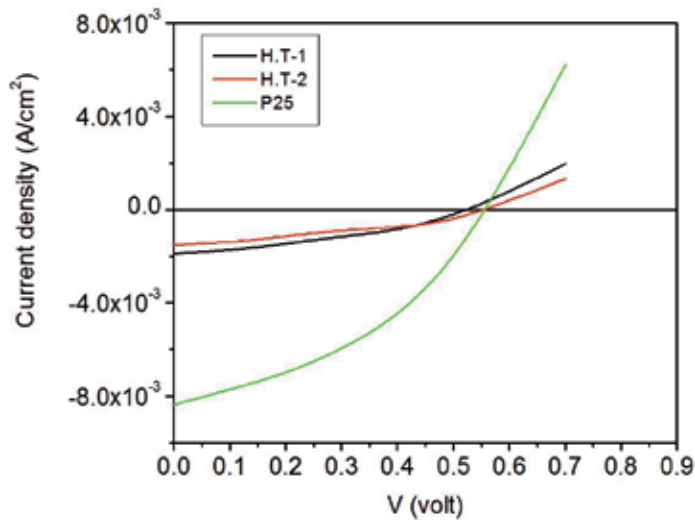


Figure 5. Photocurrent density - Voltage characteristics of TiO₂ nanowires (H.T-1), nanorods (H.T-2) and P25 based DSC for film thicknesses of 4.2 μm (H.T-1), 4.5 μm (H.T-2) and 4.0 μm, respectively.

| Photoelectrodes | Film Thicknesses (μm) | V _{oc} (V) | J _{sc} (mA/cm ²) | FF | η (%) |
|-------------------------------|-----------------------|---------------------|---------------------------------------|------|-------|
| TiO ₂ /ITO (H.T-1) | 4.2 | 0.53 | 1.88 | 0.35 | 0.35 |
| TiO ₂ /ITO (H.T-2) | 4.5 | 0.56 | 1.52 | 0.30 | 0.25 |
| TiO ₂ (P25) | 4.0 | 0.56 | 8.39 | 0.41 | 1.93 |

Table 1. Photovoltaic parameters of DSC based on TiO₂ nanowires, nanorods and P25 films.

In the above section; effect of HCl concentration on growth rate, surface morphological and structural properties of TiO₂ films is studied. In this section, effect of reaction temperature on the surface morphological and structural properties of TiO₂ films is studied. Figure 6 shows the XRD patterns of TiO₂ films prepared at various reaction temperatures (120 and 160°C). It shows that the rutile phase is dominant ($2\theta = 27.19^\circ$), with weak peaks arising from 2θ values of 35.78° (101), 40.90° (111), 54.03° (211), 56.20° (220) and 62.64° (002) for sample H.T-5. Figure 6b shows the XRD patterns of TiO₂ film prepared at a reaction temperature of 160°C. The XRD intensity of rutile peaks increases as the reaction temperature is increased from 120 to 160°C. This is attributed to the solid state phase transformation [10]. Figure 7 shows the surface morphologies of TiO₂ films prepared at various reaction temperatures. The average diameter and length of TiO₂ nanorod prepared at 120°C are calculated as 125 and 480 nm, respectively. The TiO₂ nanorod length and diameter gradually increases as the reaction temperature is increased from 120 to 160°C. At 160°C, the average diameter and length of TiO₂ nanorods are calculated as 310 nm and 2.6 μm, respectively.

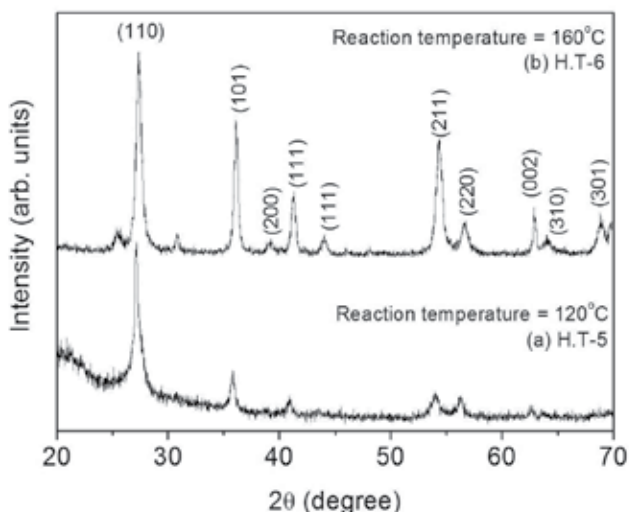


Figure 6. XRD patterns of TiO₂ films prepared at various reaction temperatures (R_T). (a) H.T-5; [$R_T=120^\circ\text{C}$; HCl=20 ml and DI=40 ml] and (b) H.T-6 [$R_T=160^\circ\text{C}$; HCl=20 ml and DI=40 ml]. Here the TNB and reaction time were 1 ml and 17 h, respectively.

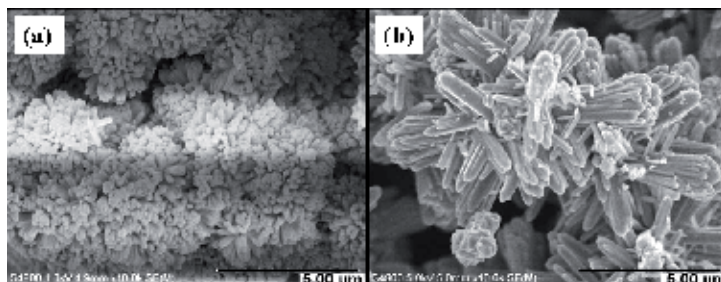


Figure 7. SEM images of TiO₂ films prepared at various reaction temperatures (R_T). (a) H.T-5; [$R_T=120^\circ\text{C}$; HCl=20 ml and DI=40 ml] and (b) H.T-6 [$R_T=160^\circ\text{C}$; HCl=20 ml and DI=40 ml]. Here the TNB and reaction time were 1 ml and 17 h, respectively.

XRD patterns of TiO₂ films prepared using different volume of TNB are shown in Fig. 8. The rutile phase appears to be the dominant phase, with peaks appearing at 2θ values of 27.16° (110), 35.89° (101), 38.94° (200), 41.02° (111) and 43.87° (210) for sample H.T-7 which is prepared at 0.5 ml of TNB. A very small weak anatase phase is also observed at 25.1° , assigned to (101) (see inset of Fig.8). The peak position and FWHM are measured by curve fitting using Gaussian line shape analysis. As the TNB volume is increased to 0.75 ml, a significant change is observed in the XRD pattern of sample H.T-8. But rutile is the dominant phase (Fig.8b). At TNB volume of 1 ml (Fig.8c), two anatase peaks are observed at 25.16° (101) and 53.81° (105). The anatase peak (101) intensity increases as the volume of TNB is increased from 0.5 to 1.0 ml. TiO₂ is grown as a mixture of anatase and rutile, but the rutile phase is

dominant with peaks arising from the (110), (101) and (111) planes. The fraction of anatase can be calculated from the following relation [11]

$$f_a = \left(1 + 1.26 \frac{I_r}{I_a}\right)^{-1} \quad (1)$$

where I_a and I_r are the peak intensities of the strongest (101) and (110) reflections of anatase (I_a) and rutile (I_r), respectively. The variations of anatase fractions is shown in Table 2.

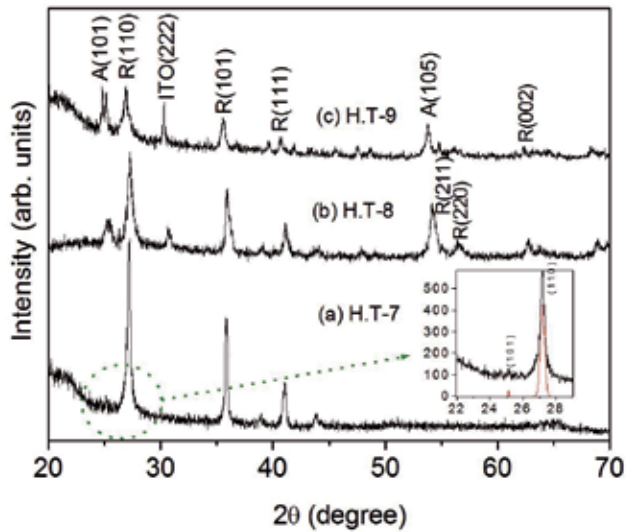


Figure 8. XRD patterns of TiO_2 films grown with three different volume of titanium precursor. (a) H.T-7; [TNB=0.5 ml; HCl=20 ml and DI=40 ml] and (b) H.T-8 [TNB=0.75 ml; HCl=20 ml and DI=40 ml] and H.T-9 [TNB=1.0 ml; HCl=20 ml and DI=40 ml]. Here the reaction time (17 h) and reaction temperature (150°C) were kept constant.

| Sample Code | TNB (ml) | HCl (ml) | Di (ml) | I_{101} (a. u) | I_{110} (a. u) | f_a | 2θ (degree) | β_{110} | a_{110} (Å) | Stress (%) |
|-------------|----------|----------|---------|------------------|------------------|-------|--------------------|---------------|---------------|------------|
| H.T-7 | 0.50 | 40.0 | 20.0 | 13.78 | 531.72 | 0.02 | 27.166 | 0.23 | 4.6368 | 0.89 |
| H.T-8 | 0.75 | 40.0 | 20.0 | 52.57 | 207.45 | 0.17 | 27.268 | 0.33 | 4.6210 | 0.56 |
| H.T-9 | 1.00 | 40.0 | 20.0 | 99.30 | 102.61 | 0.43 | 26.906 | 0.45 | 4.6826 | 1.90 |

Note: TNB – titanium butoxide; HCl– Hydrochloric acid; DI– deionized water; I_{101} -XRD intensity of (101) plane; I_{110} -XRD intensity of (110) plane; f_a -anatase fraction ratio; β_{110} -FWHM of (110) plane; a_{110} -lattice constant.

Table 2. Growth and structural parameters of TiO_2 films.

As shown in Table 2, the fraction of anatase phase increases as the TNB volume is increased from 0.5 to 1.0 ml. It is clear that the phase transformation occurs more easily at low volume of

TNB [10]. The lattice constant of TiO₂ films (Table 2) is greater than that of bulk TiO₂ (4.59 Å) [12]; it is due to the internal stress in the film. The stress in the film is also calculated [5] and is given in Table 2; it shows that all the TiO₂ films prepared under the above mentioned deposition conditions are under tensile stress (Table 2). Surface morphologies of TiO₂ films prepared using different volume of TNB are shown in Fig. 9. SEM images of TiO₂ films prepared under the above mentioned preparation conditions show similar surface morphology. The diameter of the TiO₂ nanorod prepared at 0.5 ml of TNB volume is calculated as 340 nm. The diameter of TiO₂ nanorod is calculated as 240 and 205 nm for 0.75 and 1.0 ml of TNB, respectively.

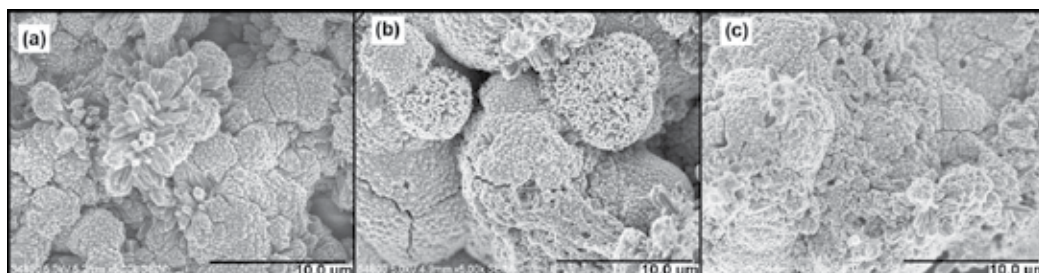


Figure 9. SEM images of TiO₂ films grown with three different volume of titanium precursor. (a) H.T-7, (b) H.T-8 and (c) H.T-9. Here the reaction time (17 h) and reaction temperature (150°C) were kept constant.

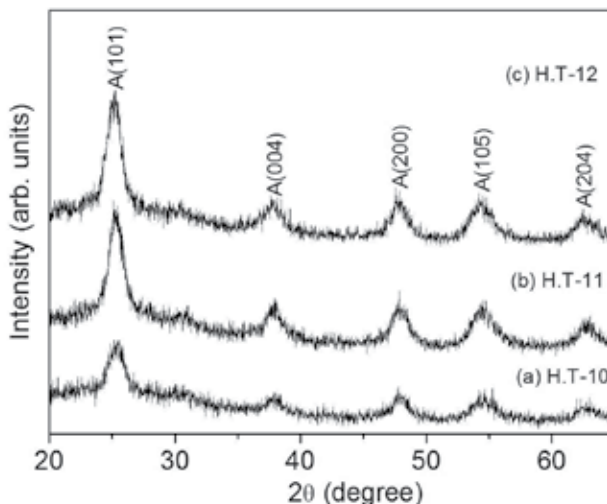


Figure 10. XRD patterns of TiO₂ films prepared using various amounts of HNO₃. (a) HT-10 [HNO₃ =5 ml], (b) H.T-11 [HNO₃=10 ml] and (c) H.T-12 [HNO₃=15 ml]. Here TNB (1 ml), DI (45 ml), reaction time (16 h) and reaction temperature (150°C) were kept constant.

Figure 10 shows the XRD patterns of nanoporous TiO₂ films prepared at various volumes of HNO₃. Here the volume of DI and TNB were fixed at 45 and 1 ml, respectively. Anatase is

the dominant phase in this sample. The TiO_2 sample shows a preferred orientation in the (101) direction, as indicated by strong characteristic peak at $2\theta = 25.34^\circ$. Some anatase peaks appear at 2θ of 37.92° (004), 47.90° (200), 54.55° (105) and 62.4° (204). The anatase phase remains as the dominant phase in HNO_3 volume of 5, 10 and 15 ml. In all the cases, a pure anatase phase is observed with characteristic peaks at 25.14° (101), 37.78° (004), 47.86° (200), 54.42° (105) and 62.62° (204). This result shows that HNO_3 is very suitable to grow anatase TiO_2 on ITO coated glass substrates. It is concluded that the addition of HCl strongly enhances the growth of the film along (110) direction. In contrast, HNO_3 solution enhances the film growth in (101) direction. In the hydrothermal process, Cl^- and NO_3^- anions play an important role in the formation of rutile and anatase TiO_2 films, respectively. Because NO_3^- anions show stronger affinity to titanium than Cl^- , the pure anatase TiO_2 could be easily obtained in HNO_3 medium.

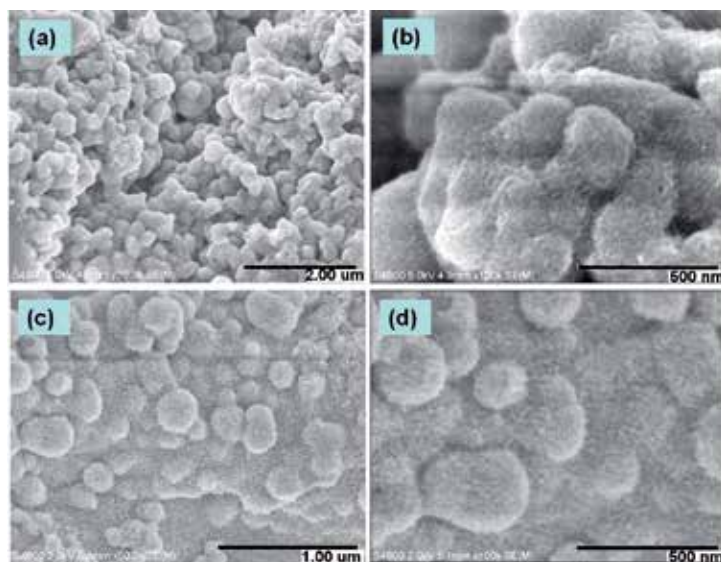


Figure 11. Low and high magnification SEM images of TiO_2 films prepared using various amounts of HNO_3 . (a) HT-10 [$\text{HNO}_3 = 5$ ml] and (b) H.T-11 [$\text{HNO}_3 = 10$ ml]. Here TNB (1 ml), DI (45 ml), reaction time (16 h) and reaction temperature (150°C) were kept constant.

Figure 11 shows the surface morphologies of nanoporous TiO_2 films prepared at various volumes of HNO_3 . Here the volume of DI and TNB were fixed at 45 and 1 ml, respectively. SEM images clearly show the formation of nanoporous TiO_2 films on ITO coated glass substrates. For DSC applications, the TiO_2 coated ITO sample was annealed at 270°C for 1 h under a vacuum of 90 kPa. The nanoporous TiO_2 film thicknesses are calculated as ~ 3 and 3.2 μm for HNO_3 volume of 5 and 10 ml. Finally, the TiO_2 electrodes were immersed into the ethanol solution containing N-719 dye. Then the dye-anchored TiO_2 electrodes were rinsed with ethanol solution and then dried in air. Figure 12 shows the photocurrent density-voltage characteristics of DSC based on nanoporous TiO_2/ITO . The short circuit density of TiO_2

electrode based DSC increases from 4.02 to 5.9 mA/cm² as the nanoporous TiO₂ film thickness is increased from 3 to 3.2 μm. The fill factor and power conversion efficiency also increase with increasing nanoporous TiO₂ film thickness (see Table 3).

| Photoelectrode | Film Thickness (μm) | V _{oc} (V) | J _{sc} (mA/cm ²) | FF | η (%) |
|--------------------------------|---------------------|---------------------|---------------------------------------|-------|-------|
| TiO ₂ /ITO (H.T-10) | 3.0 | 0.40 | 4.02 | 0.512 | 0.82 |
| TiO ₂ /ITO (H.T-11) | 3.2 | 0.38 | 5.90 | 0.534 | 1.20 |

Table 3. Photovoltaic parameters of DSC based on TiO₂ nanoporous films.

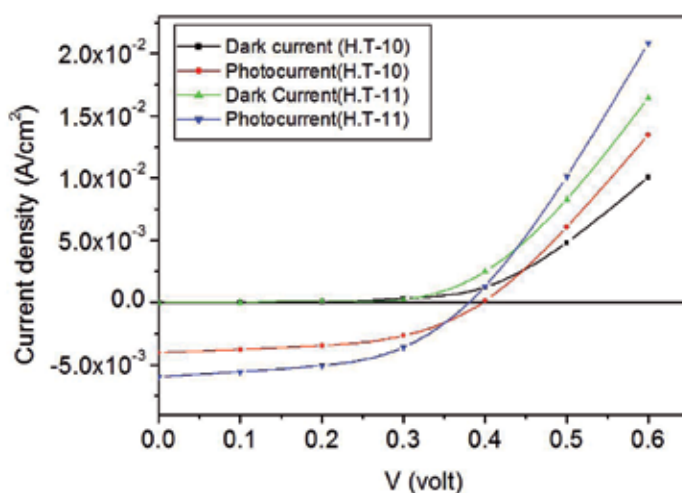


Figure 12. Photocurrent density –voltage characteristics of TiO₂ nanoporous based DSC for different film thickness (3.0 μm (H.T-10) and 3.2 μm (H.T-11)).

3.2. Preparation and characterization of TiO₂ thin films by electrochemical anodization method

Nanocrystalline ITO thin films were deposited on glass substrates by ion beam sputter deposition method at room temperature. The applied acceleration voltage was 2500 V. The sputtering process was performed in 3%O₂ + Ar gas. The gas flow rate was controlled by mass flow meter. Ti thin films were deposited on ITO coated glass substrate by ion beam sputter deposition method at room temperature. The acceleration voltage supplied to the main gun was fixed at 2500 V. Pure Ar was employed as the sputtering gas. The electrochemical anodization was performed in 1M H₂SO₄+0.15 wt. % HF at an applied potential of 10 V for different anodization time (30, 60 and 120 min). Nanostructured TiO₂ films were formed by anodization using a two-electrode configuration with Ti film as an anode and platinum electrode as a cathode. The anodized Ti sample was then annealed in air at 450°C for an hour.

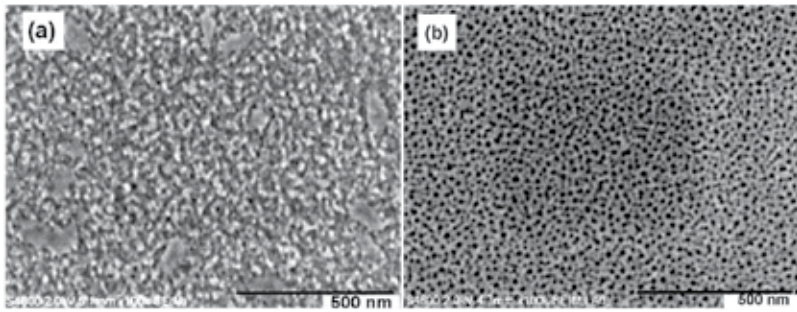


Figure 13. SEM images of TiO₂ films; a) 30 min (T-1) and (b) 60 min (T-2).

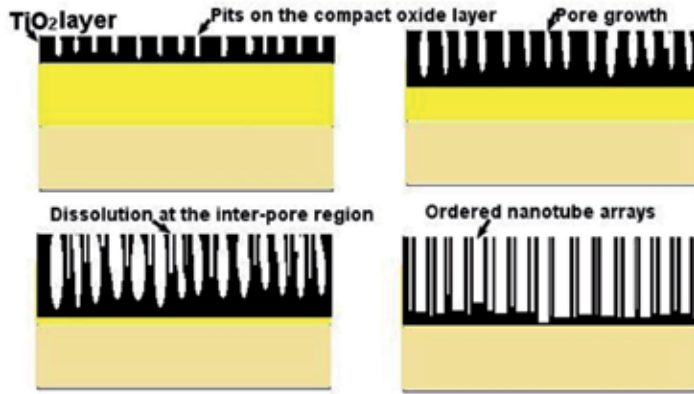


Figure 14. Schematic diagram of the growth stages of TiO₂ nanotube arrays by anodization.

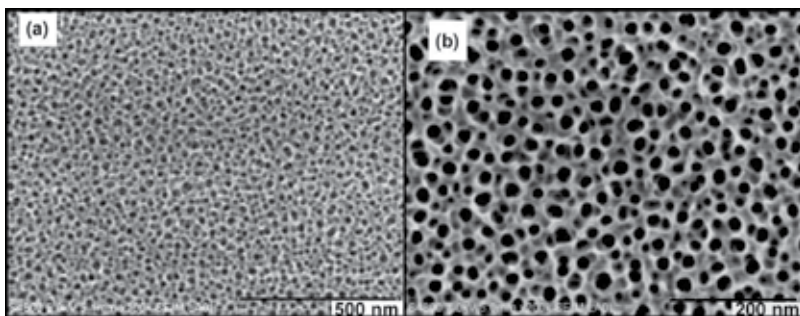


Figure 15. Low (a) and high (b) magnification SEM images of Ti plate anodized at an applied potential of 10 V.

Figure 13 shows the top-view SEM images of anodized Ti films in H₂SO₄/HF electrolytes at an applied potential of 10 V for anodization time of 30 min (Fig.13a) and 60 min (Fig.13b),

respectively. It can be seen that TiO₂ nanoporous were formed when the anodization time was fixed at 30 min (see Fig.13a). When the anodization time was increased to 60 min, highly ordered TiO₂ nanoporous arrays were formed (see Fig.13b). Similar results have been observed by Huang et al. [13]. Generally, the formation mechanism of the TiO₂ nanoporous arrays is proposed as two competitive processes; electrochemical oxidation and chemical dissolution. From these results, we observed that no TiO₂ nanotubes, but TiO₂ nanoporous were formed at the anodization time of 60 min. It shows that the TiO₂ porous layer is easily formed during the short-time of anodization. TiO₂ nanotube arrays can also be prepared on the Ti film surface, but this can be accomplished by increasing the anodization time; this is due to the high chemical dissolution at the inter-pore region (see Fig.14c& d). Because of the limitation of Ti film thickness, Ti metal was used in order to check this effect. Figure 15 shows surface morphology of anodized Ti plate for 120 min. It can be seen that the pore growth and formation on the Ti surface were uniformly distributed (Fig. 15a). It clearly shows the formation of pore growth and small opening at the inter-pore region (Fig. 15b). Similar results have been observed by Yang et al. [14] and Kaneco et al. [15]. Figure 14c can be correlated with Fig.15b. These results clearly show that high dissolution rate at the inter-pore region is very important in order to get the ordered nanotube arrays (see Fig. 14d).

Figure 16 shows the current density-time transient curve recorded during the anodization of Ti sample at an applied potential of 10 V for 30 min. Initially, the current density gradually increases (see inset of Fig.16) because of the electrochemical treatment which consists of a potential ramp from 0 to 10V with a sweep rate of 50 mV/sec followed by a constant potential at 10 V for 30 min. Once the oxide layer is formed, the impedance between the electrodes increases; which results in a drastically reduced current between the electrodes. Furthermore, there is no change in impedance.

Figure 17 shows the optical transmittance spectrum of titania films after annealing at 450°C for an hour. The optical transmittance of annealed nanoporous TiO₂ film in the visible range is estimated as 60%. The thickness of nanoporous TiO₂ film can be calculated from the following relation:

$$d = \frac{\lambda_1 \lambda_2}{2[\lambda_2 n(\lambda_1) - \lambda_1 n(\lambda_2)]} \quad (2)$$

where $n(\lambda_1)$ and $n(\lambda_2)$ are the refractive indices of the two adjacent maxima (or minima) at λ_1 and λ_2 . The film thickness of TiO₂ is calculated as 250 nm. The relation between absorption coefficient α and incident photon energy $h\nu$ can be written as [16].

$$\alpha h\nu = C(h\nu - E_g^d)^{1/2} \quad (3)$$

for a direct allowed transition, where C is constant and E_g^d is direct band gap. The plot of $h\nu$ vs. $(\alpha h\nu)^2$ is shown in Fig.18. The optical band gap is calculated as 3.25 eV. The optical band gap of nanoporous TiO₂ film is little bit greater than that of bulk anatase TiO₂ (3.2 eV). Similar band tail (2.66 eV) at the low energy side has been observed by Mor et al. [17]. The refractive index

was calculated from the measured transmittance spectrum. Figure 19 shows the variation refractive index versus wavelength of nanoporous TiO₂ film after annealing at 450°C for an hour. It shows that the refractive index gradually decreases with increasing wavelength. The porosity of nanoporous TiO₂ films can be calculated from the following relation [17]

$$\text{Porosity}(\%) = \left[1 - \frac{n^2 - 1}{n_d^2 - 1} \right] \times 100 \quad (4)$$

where n and n_d are the refractive indices of the nanoporous film (2.2) and non-porous anatase film (2.5), respectively. The porosity of nanoporous structure is calculated as 27 %.

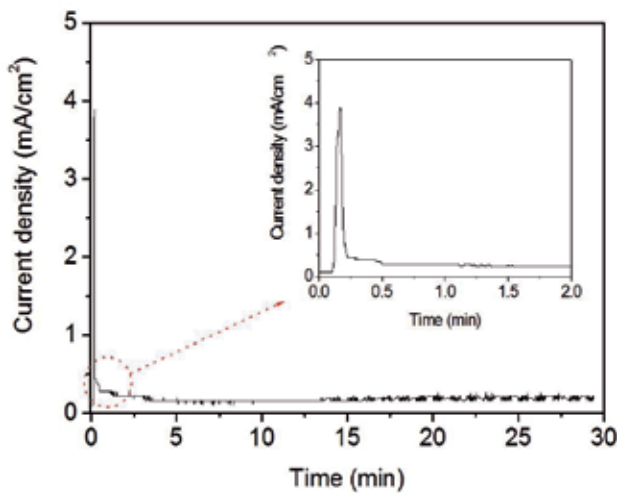


Figure 16. The current density vs. time transient curve which was recorded during the anodization of Ti film for an anodization time of 30 min.

Figure 20 shows the dark and photocurrent density versus voltage characteristics of DSC solar cells based on nanoporous titania films. The power conversion efficiencies of device-1 (T-1) and 2 (T-2) are calculated as 0.25 and 0.17 %. Similar results have been observed by Yang et al. [14]. The short-circuit current density of device-2 is higher than that of device-1. SEM images (T-1 and T-2) show that the TiO₂ films have different surface morphology; due to this, the DSC devices show difference in performance; because the amount of dye adsorption can be increased by large internal surface area of the films. The fill factor and open circuit voltage of device-1 are higher than that of device-2. It shows that the fill factor can be affected by resistance of the substrate and quality of the counter electrode. In the present work, Pt coated ITO films were used as counter electrodes. The low value of fill factor is attributed to large large value of series resistance at the interface between TiO₂ and ITO films. Figure 21 shows the dark and photocurrent density-voltage characteristics of TiO₂/Ti plate. The power conversion efficiency of device-3 is estimated as 0.01% (see Table 4). This result agrees well with the previous results

reported by Ok et al. [18]. The power conversion efficiency of device-3 is much lower than that of device-1 and device-2 (see Table 4). Particularly, the short-circuit current for device-3 is much lower than that of device-1 and 2. It is attributed that the backside illumination affects the light absorption capacity of the dyes, because the I₃⁻ electrolyte cuts the incident light in the wavelength range from 400 – 650 nm. But the fill factor for device-3 is higher than that of device-1 and device-2. It shows that the high value of FF is attributed to the small value of series resistance at TiO₂/substrate interface.

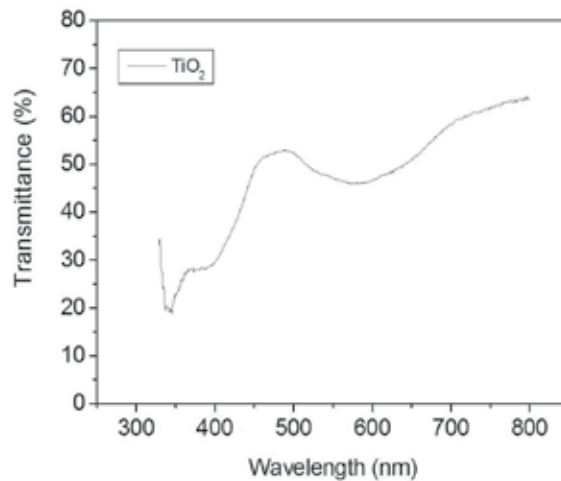


Figure 17. Optical transmittance spectrum of nanoporous TiO₂ film after annealing at 450°C.

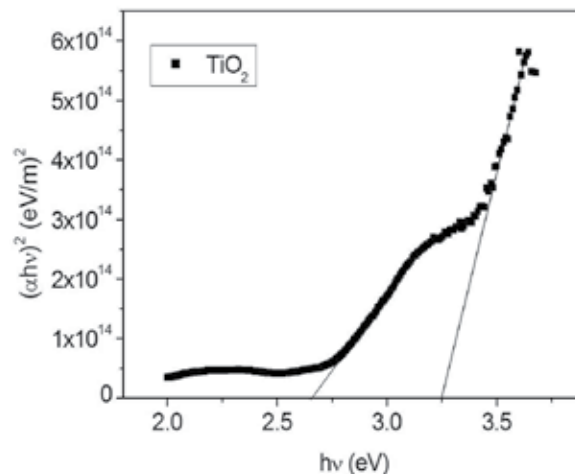


Figure 18. Plot of hv vs. (αhv)² of nanoporous TiO₂ film after annealing at 450°C.

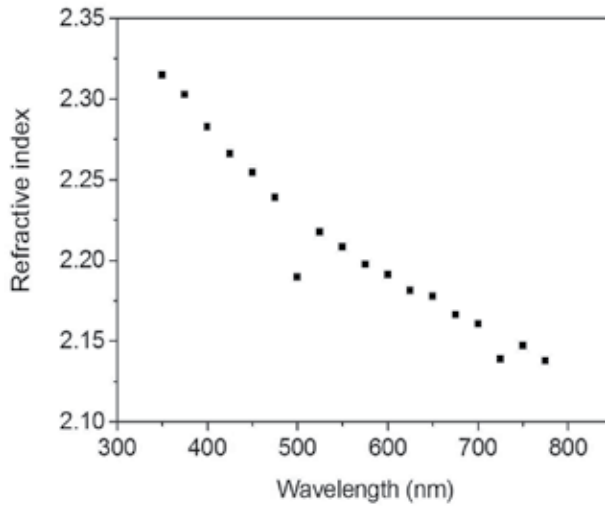


Figure 19. Variation of refractive index of annealed nanoporous TiO₂ film. The average refractive index of nanoporous structure in the visible range is 2.2.

| Photoelectrode | Film Thickness (nm) | Voc (V) | Jsc (mA/cm ²) | FF | η (%) |
|-----------------------------|---------------------|---------|---------------------------|------|-------|
| TiO ₂ /ITO/Glass | 250 | 0.432 | 1.58 | 0.36 | 0.25 |
| TiO ₂ /ITO/Glass | 350 | 0.358 | 1.72 | 0.28 | 0.17 |
| TiO ₂ /Ti plate | - | 0.482 | 0.07 | 0.39 | 0.01 |

Table 4. Photovoltaic parameters of DSC based on TiO₂ nanoporous films.

Nanostructured TiO₂ was prepared by anodization of Ti foil at room temperature. The anodization was performed in ethylene glycol containing 2 vol.% H₂O+ 0.3 wt.% NH₄F for an anodization of 180 min at 30 V. The anodized Ti sample was then annealed in air at 400°C for an hour. Figure 22 shows surface morphologies of anodized Ti foil. It clearly shows the formation of well ordered TiO₂ nanotube arrays on Ti foil (Fig. 22a). At the bottom, the nanotubes are closely packed together (Fig. 22b). The diameter and wall thickness of TiO₂ nanotube arrays are calculated as 45 nm and 25 nm, respectively. The length of TiO₂ nanotube arrays is estimated as 4.5 μm (Fig. 22c). The side-view of the tube layer (Fig. 22d) reflects an uneven morphology. Figure 23 shows the XRD patterns of anodized Ti foil before and after annealing. In Fig. 23a, the XRD peaks at 35.3, 38.64, 40.4, 53.2 and 63.18 correspond to Ti. This is attributed that the as-prepared TiO₂ is amorphous before annealing; only Ti peaks are seen (Fig. 23a). In order to change the amorphous TiO₂ into anatase TiO₂, anodized Ti sample was annealed in air at 400°C for an hour. After annealing, the amorphous TiO₂ has been changed into crystalline with a more preferred orientation along (101) direction.

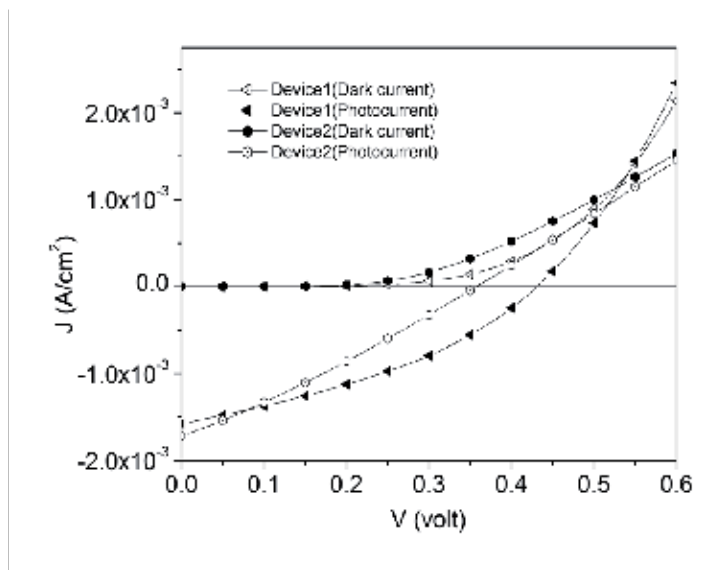


Figure 20. Dark and photocurrent density versus voltage characteristics of DSC based on nanoporous titania films.

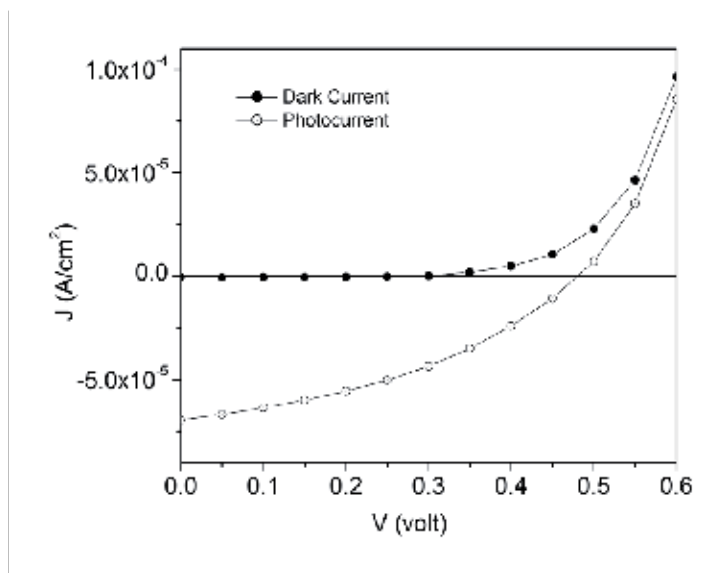


Figure 21. Dark and photocurrent density– voltage characteristics of TiO₂/Ti plate (Device 3).

Figure 24 shows the photocurrent density–voltage characteristics of DSC based on TiO₂ nanotubes arrays. Under back-side illumination, the open circuit voltage, short-circuit current density, fill-factor and power conversion efficiency of DSC based on TiO₂ nanotube arrays are estimated as 0.55 V, 8.27 mA/cm², 0.39 and 1.78 %, respectively. Similar results have

been observed by Tao et al. [19]. This result shows that the main factor responsible for enhancement of short circuit current is improvement of electron transport and electron lifetime in TiO_2 nanotube arrays. This increased light-harvesting efficiency in TiO_2 nanotube-based DSC could be a result of stronger light scattering effects that leads to significantly higher charge collection efficiencies of nanotube-based DSC.

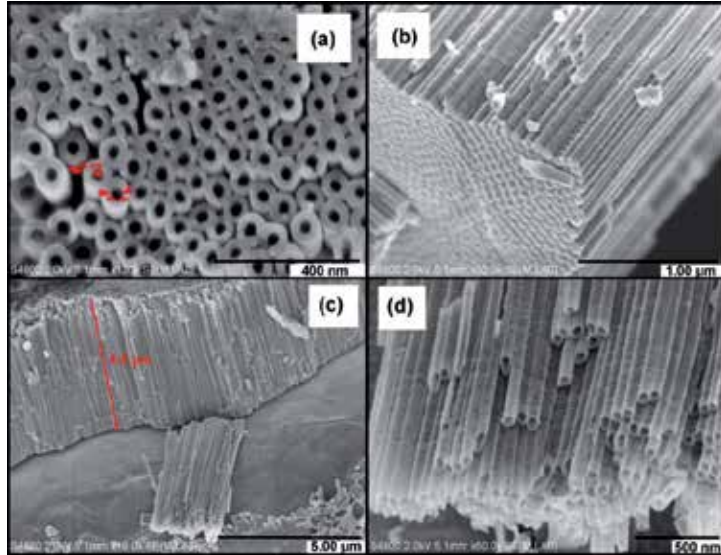


Figure 22. SEM images of Ti foil anodized at an applied potential of 30 V.

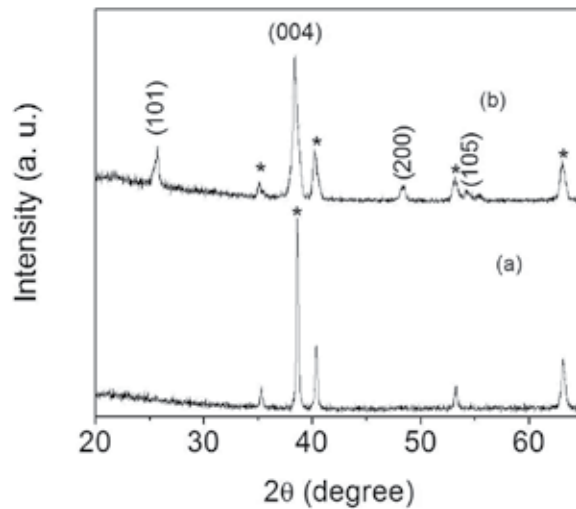


Figure 23. XRD patterns of as-prepared (a) and annealed (400°C) TiO_2 nanotube arrays.

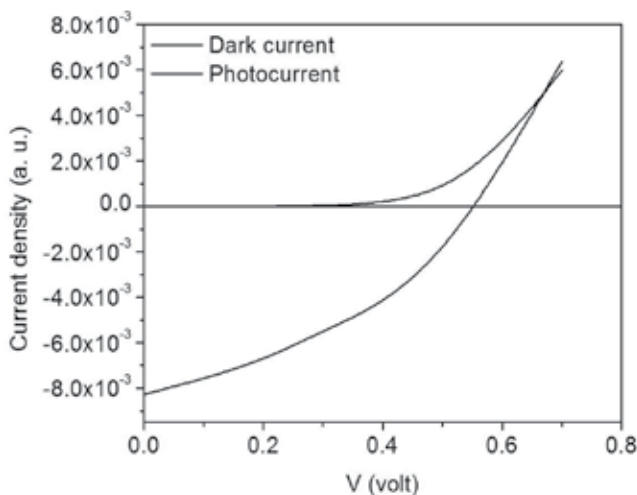


Figure 24. Dark and photocurrent density-voltage characteristics of TiO₂ nanotube arrays.

4. Conclusions

TiO₂ nanowires, nanorods and nanoporous films were successfully prepared using hydrothermal method. The nanorod size increased as the volume of HCl in the reaction solution was increased. Annealing at 450°C for 30 min produced no substantial change in the structure. A rutile to anatase phase transition was observed when the TNB volume increased from 0.5 to 1.0 ml. From the XRD patterns, no rutile structure peaks was detected for the films grown in HNO₃ medium. In this case, anatase was the dominant phase. XRD clearly showed that the crystal quality and orientation of final products were strongly dependent on the experimental parameters, such as volume of TNB, HCl and HNO₃ solution and the reaction temperature. The shape and size of the nanowires and nanorods could be perfectly generated by controlling the volume of HCl and the annealing temperature. Photovoltaic parameters showed that the power conversion efficiency of DSC based on anatase TiO₂ was higher than that of rutile TiO₂ based DSC. TiO₂ nanoporous, nanoholes and nanotubes were successfully fabricated by anodization method. The power conversion efficiency of TiO₂ nanoporous and nanotube arrays based DSC was higher than of TiO₂ nanohole based DSC. The device performance of nanoporous TiO₂ films prepared on transparent conducting substrate was higher than that of TiO₂ nanoholes on Ti plate. The front-side illumination was very suitable in increasing the light harvesting efficiency of the solar cell device.

Author details

S. Venkatachalam*, H. Hayashi, T. Ebina and H. Nanjo

*Address all correspondence to: svchalam23@gmail.com

National Institute of Advanced Industrial Science and Technology (AIST), Sendai, Japan

References

- [1] Feng, X., Shankar, K., Varghese, O. K., Paulose, M., Latempa, T. J., & Grimes, C. A. (2008). Vertically Aligned Single Crystal TiO₂ Nanowire Arrays Grown Directly on Transparent Conducting Oxide Coated Glass: Synthesis Details and Applications. *Nano. Lett.* . <http://pubs.acs.org/doi/abs/10.1021/nl802096a> , 8, 3781-3786.
- [2] Baxter, J. B., Walker, A. M., Van Ommering, K., & Aydil, E. S. (2006). Synthesis and characterization of ZnO nanowires and their integration into dye-sensitized solar cells. *Nanotechnology*, 17, S304, <http://iopscience.iop.org/0957-4484/17/11/S13/>.
- [3] Adachi, M., Murata, Y., Takao, J., Jiu, J., Sakamoto, M., & Wang, F. (2004). Highly Efficient Dye-Sensitized Solar Cells with a Titania Thin-Film Electrode Composed of a Network Structure of Single-Crystal-like TiO₂ Nanowires Made by the "Oriented Attachment" Mechanism. *J. Am. Chem. Soc.* . <http://pubs.acs.org/doi/abs/10.1021/ja048068s> , 126, 14943-14949.
- [4] Yuxiang, L., Mei, Z., Min, G., & Xidong, W. (2010). Hydrothermal growth of well-aligned TiO₂ nanorod arrays: Dependence of morphology upon hydrothermal reaction conditions. *Rare metals*, 29, 286-291, <http://www.springerlink.com/content/9433284w0142tt58/>.
- [5] Venkatachalam, S., Nanjo, H., Hassan, F. M. B., Kawasaki, K., Kanakubo, M., Aizawa, T., Aida, T., & Ebina, T. (2010). Characterization of nanocrystalline indium tin oxide thin films prepared by ion beam sputter deposition method. *Thin Solid Films*, 518, 6891-6896, <http://dx.doi.org/10.1016/j.tsf.2010.07.034>.
- [6] Kumar, A., Madaria, A. R., & Zhou, C. Growth of Aligned Single-Crystalline Rutile 2 Nanowires on Arbitrary Substrates and Their Application in Dye-Sensitized Solar Cells. *J. Phys. Chem. C* . <http://pubs.acs.org/doi/abs/10.1021/jp100491h> , 114, 7787-7792.
- [7] Wu, M., Long, J., Huang, A., & Luo, Y. (1999). Microemulsion-Mediated Hydrothermal Synthesis and Characterization of Nanosize Rutile and Anatase Particles. *Langmuir* . <http://pubs.acs.org/doi/abs/10.1021/la990514f> , 15, 8822-8825.
- [8] Lin, C.-J., Tu, W.-K., C.-K., Kuo, & Chien, S.-H. Single-step fabrication of phase-controllable nanocrystalline 2 films for enhanced photoelectrochemical water splitting

- and dye-sensitized solar cells. *J. Power Sources*. <http://dx.doi.org/10.1016/j.jpowsour.2010.12.077>, 196, 4865-4869.
- [9] Tang, X., Qian, J., Wang, Z., Wang, H., Feng, Q., & Liua, G. (2009). Comparison of low crystallinity TiO₂ film with nanocrystalline anatase film for dye-sensitized solar cells. *J. Colloid Interf. Sci.*, 330, 386-391, <http://www.sciencedirect.com/science/article/pii/S0021979708013994>.
- [10] Wu, M., Lin, G., Chen, D., Wang, G., He, D., Feng, S., & Xu, R. (2002). Sol-Hydrothermal Synthesis and Hydrothermally Structural Evolution of Nanocrystal Titanium Dioxide. *Chem. Mater.*, 14, 1974-1980, <http://pubs.acs.org/doi/full/10.1021/cm0102739>.
- [11] Spurs, R. A., & Myers, H. (1957). Quantitative Analysis of Anatase-Rutile Mixtures with an X-Ray Diffractometer. *Anal. Chem.*, 29, 760-762, <http://pubs.acs.org/doi/abs/10.1021/ac60125a006>.
- [12] Tanemura, S., Miao, L., Wunderlich, W., Tanemura, M., Mori, Y., Toh, S., & Kaneko, K. (2005). Fabrication and characterization of anatase/rutile-TiO₂ thin films by magnetron sputtering: a review. *Sci. Tech. Adv. Mater.*, 6, 11-17, <http://iopscience.iop.org/1468-6996/6/1/A03>.
- [13] Huang, L., Peng, F., Yu, H., Wang, H., Yang, J., & Li, Z. (2010). The influence of ultrasound on the formation of TiO₂ nanotube arrays. *Material Research Bulletin*, 45, 200, <http://dx.doi.org/10.1016/j.materresbull.2009.09.018>.
- [14] Yang-J, D., Park, H., Cho-J, S., Kim-G, H., & Choi-Y, W. (2008). TiO₂-nanotube-based dye-sensitized solar cells fabricated by an efficient anodic oxidation for high surface area. *J. Phys. Chem. Solids*, 69, 1272-1275, <http://www.sciencedirect.com/science/article/pii/S0022369707006361>.
- [15] Kaneko, S., Chen, Y., Westerhoff, P., & Crittenden, J. C. (2007). Fabrication of uniform size titanium oxide nanotubes: Impact of current density and solution conditions. *Scripta Mater.*, 56, 373-376, <http://www.sciencedirect.com/science/article/pii/S1359646206008025>.
- [16] Venkatachalam, S., Mangalaraj, D., & Narayandass, Sa. K. (2007). Characterization of vacuum-evaporated ZnSe thin films. *Physica B*, 393, 47-55, <http://www.sciencedirect.com/science/article/pii/S0921452606019466>.
- [17] Mor, G. K., Varghese, O. K., Paulose, M., Ong, K. G., & Grimes, C. A. (2006). Fabrication of hydrogen sensors with transparent titanium oxide nanotube-array thin films as sensing elements. *Thin Solid Films*, 496, 42-48, <http://www.sciencedirect.com/science/article/pii/S0040609005014264>.
- [18] k, S.-Y., Cho, K.-K., Kim, K.-W., & Ryu, K.-S. (2010). Structure and dye-sensitized solar cell application of TiO₂ nanotube arrays fabricated by the anodic oxidation method. *Phys. Scr.*, T139, 014052, <http://iopscience.iop.org/1402-4896/2010/T139/014052>.
- [19] Tao, R.-H., Wu, J.-M., Xue, H.-X., Song, X.-M., Pan, X., Fang, X. G., Fang, X. Q., & Dai, S. Y. (2010). A novel approach to titania nanowire arrays as photoanodes of back-illu-

minated dye-sensitized solar cells. *J. Power Sources*, 195, 2989-2995, <http://www.sciencedirect.com/science/article/pii/S0378775309020837>.

Correlation Between Band Structure and Magneto-Transport Properties in n-type HgTe/CdTe Two-Dimensional Nanostructure Superlattice. Application to Far-Infrared Detection

Abdelhakim Nafidi

Additional information is available at the end of the chapter

<http://dx.doi.org/10.5772/52101>

1. Introduction

The work of Essaki & Tsu [1] caused a big interest to the study of superlattices made from alternating layers of two semiconductors. The development of molecular beam epitaxy (MBE) was successfully applied to fabricate different quantum wells and superlattices. Among them III-V superlattices [$\text{Ga}_{1-x}\text{Al}_x\text{As-GaAs}$ [1-2] - type I], III-V superlattices [InAs/GaSb [3] - type II] and later II-VI superlattice [HgTe/CdTe [4] - type III]. The latter is a stable alternative for application in infrared optoelectronic devices than the $\text{Hg}_{1-x}\text{Cd}_x\text{Te}$ alloys. Especially in the region of second atmospheric window (around 10 μm) which is of great interest for communication.

HgTe and CdTe crystallize in zinc-blend lattice respectively. The lattice-matching within 0.3 % yield to a small interdiffusion between HgTe and CdTe layers at low temperature near 200 °C by MBE. HgTe is a zero gap semiconductor (due to the inversion of relative positions of Γ_6 and Γ_8 edges [5]) when it is sandwiched between the wide gap semiconductor CdTe (1.6 eV at 4.2 K) layers yield to a small gap HgTe/CdTe superlattice which is the key of an infrared detector.

A number of papers have been published devoted to the band structure of this system [6] as well as its magneto-optical and transport properties [7]. The aim of this work is to show the correlation between calculated bands structures and magneto-transport properties in n type HgTe/CdTe nanostructures superlattices. The interpretation of the experimental data is consistent with the small positive offset $\Lambda=40$ meV between the HgTe and CdTe valence bands.

Theoretical calculations of the electronic properties of n-type HgTe/CdTe superlattices (SLs) have provided an agreement with the experimental data on the magneto-transport behaviour. We have measured the conductivity, Hall mobility, Seebeck and Shubnikov-de Haas effects and angular dependence of the magneto-resistance [8]. Our sample, grown by MBE, had a period $d=d_1+d_2$ (124 layers) of $d_1=8.6$ nm (HgTe) / $d_2=3.2$ nm (CdTe). Calculations of the spectra of energy $E(d_z)$, $E(k_z)$ and $E(k_p)$, respectively, in the direction of growth and in plane of the superlattice; were performed in the envelope function formalism. The energy $E(d_z, \Gamma, 4.2$ K), shown that when d_2 increase the gap E_g decrease to zero at the transition semiconductor to semimetal conductivity behaviour and become negative accusing a semimetallic conduction. At 4.2 K, the sample exhibits n type conductivity, confirmed by Hall and Seebeck effects, with a Hall mobility of $2.5 \cdot 10^5$ cm²/Vs. This allowed us to observe the Shubnikov-de Haas effect with $n = 3.20 \cdot 10^{12}$ cm⁻². Using the calculated effective mass ($m_{E_1}^*(E_F) = 0.05 m_0$) of the degenerated electrons gas, the Fermi energy (2D) was $E_F=88$ meV in agreement with 91 meV of thermoelectric power α . In intrinsic regime, $\alpha T^{-3/2}$ and $R_H T^{3/2}$ indicates a gap $E_g = E_1 - HH_1 = 101$ meV in agreement with calculated $E_g(\Gamma, 300$ K) = 105 meV. The formalism used here predicts that the system is semiconductor for $d_1/d_2 = 2.69$ and $d_2 < 100$ nm. Here, $d_2=3.2$ nm and $E_g(\Gamma, 4.2$ K) = 48 meV so this sample is a two-dimensional modulated nano-semiconductor and far-infrared detector ($12 \mu\text{m} < \lambda_c < 28 \mu\text{m}$).

In conclusion, we will show that the HgTe/CdTe nano-superlattice is a stable alternative for application in infrared optoelectronic devices than the alloys $\text{Hg}_{1-x}\text{Cd}_x\text{Te}$.

2. Experimental techniques

The HgTe/CdTe superlattice was grown by molecular beam epitaxy (MBE) on a [111] CdTe substrate at 180 °C. The sample (124 layers) had a period $d=d_1+d_2$ where $d_1(\text{HgTe})=8.6$ nm and $d_2(\text{CdTe})= 3.2$ nm. It was cut from the epitaxial wafer with a typical sizes of $5 \times 1 \times 1$ mm³. The ohmic contacts were obtained by chemical deposition of gold from a solution of tetrachloroauric acid in methanol after a proper masking to form the Hall crossbar. Carriers transport properties were studied in the temperature range 1.5-300K in magnetic field up to 17 Tesla. Conductivity, Hall Effect, Seebeck effect and angular dependence of the transverse magnetoresistance were measured. The measurements at weak magnetic fields (up to 1.2 T) were performed into standard cryostat equipment. The measurements of the magnetoresistance were done under a higher magnetic field (up to 8 T), the samples were immersed in a liquid helium bath, in the centre of a superconducting coil. Rotating samples with respect to the magnetic field direction allowed one to study the angular dependence of the magnetoresistance.

3. Theory of structural bands

Calculations of the spectra of energy $E(k_z)$ and $E(k_p)$, respectively, in the direction of growth and in plane of the superlattice; were performed in the envelope function formalism [6-7])

with a valence band offset Λ between heavy holes bands edges of HgTe and CdTe of 40 meV determined by the magneto-optical absorption experiments [9].

The general dispersion relation of the light particle (electron and light hole) subbands of the superlattice is given by the expression [6]:

$$\cos k_z(d_1+d_2) = \cos(k_1d_1) \cos(k_2d_2) - \frac{1}{2} \left[\left(\xi + \frac{1}{\xi} \right) + \frac{k_p^2}{4k_1k_2} \left(r + \frac{1}{r} - 2 \right) \right] \sin(k_1d_1) \sin(k_2d_2) \quad (1)$$

where the subscripts 1 and 2 refer to HgTe and CdTe respectively. k_z is the superlattice wave vector in the direction parallel to the growth axis z . The two-dimensional wave vector $k_p(k_x, k_y)$ describes the motion of particles perpendicular to k_z . Here,

$$\xi = \frac{k_1}{k_2} \quad \text{and} \quad r = \frac{E - \varepsilon_2}{E + |\varepsilon_1| - \Lambda} \quad (2)$$

E is the energy of the light particle in the superlattice measured from the top of the Γ_8 valence band of bulk CdTe, while ε_i ($i=1$ or 2) is the interaction band gaps $E(\Gamma_6) - E(\Gamma_8)$ in the bulk HgTe and CdTe respectively. At given energy, the two-band Kane model [10] gives the wave vector $(k_i^2+k_p^2)$ in each host material:

$$\left. \begin{aligned} \frac{2}{3} P^2 \hbar^2 (k_1^2 + k_p^2) &= (E - \Lambda) (E - \Lambda + |\varepsilon_1|) && \text{for HgTe} \\ \frac{2}{3} P^2 \hbar^2 (k_2^2 + k_p^2) &= E (E - \varepsilon_2) && \text{for CdTe} \end{aligned} \right\} \quad (3)$$

P is the Kane matrix element given by the relation:

$$\frac{2P^2}{3|\varepsilon_1|} = \frac{1}{2m^*} \quad (4)$$

where $m^* = 0.03 m_0$ is the electron cyclotron mass in HgTe [5]. For a given energy E , a superlattice state exists if the right-hand side of Eq. (1) lies in the range $[-1,1]$. That implies $-\pi/d \leq k_z \leq \pi/d$ in the first Brillion zone.

The heavy hole subbands of the superlattice are given by the same Eq. (1) with :

$$\xi = \frac{k_1}{k_2} r, \text{ and } r=1 \quad \text{with} \quad \left\{ \begin{aligned} -\frac{\hbar^2(k_1^2+k_p^2)}{2 m_{HH}^*} &= E - \Lambda && \text{for HgTe} \\ -\frac{\hbar^2(k_2^2+k_p^2)}{2 m_{HH}^*} &= E && \text{for CdTe} \end{aligned} \right. \quad (5)$$

$m_{HH}^* = 0.3 m_0$ [5] is the effective heavy hole mass in the host materials.

The band structure computation consists of solving Eq. (1) which represents the dispersion relations (i.e. finding the values of energy E which are roots of the Eq. (1) for a given value

of the carrier wave vector). Here, we are interested in studying the states of energy of light particles and heavy holes in HgTe/CdTe superlattice as function of k_z when $k_p=0$ and as function of k_p when $k_z=0$ and when $k_z=\pi/d$. The solving procedure used for studying E as function k_z in the case where $k_p=0$ consists of going, with a steep E , through the studied range of energy E and then finding, for each value of E ,

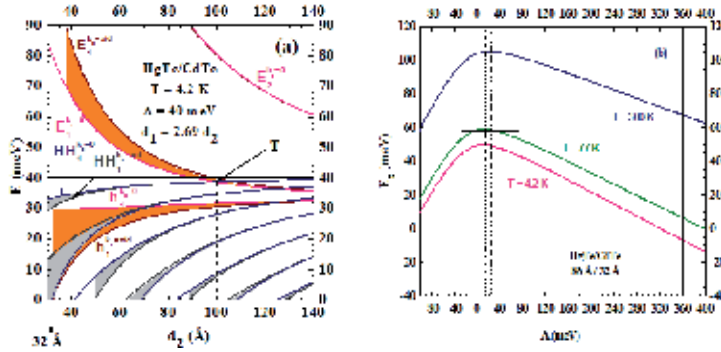


Figure 1. a) Energy position and width of the conduction (E_i), heavy-hole (HH_i), and the first light-hole (h_1) subbands calculated at 4,2 K in the first Brillion zone as a function of layer thickness for HgTe/CdTe superlattice with $d_1=2.69 d_2$, where d_1 and d_2 are the thicknesses of the HgTe and CdTe layers, respectively. T is the point of the transition semiconductor- semimetal. (b) the band gap E_g (Γ) at Γ , as function of temperature and valence band offset Δ between heavy holes bands edges of HgTe and CdTe for the investigated HgTe/CdTe superlattice.

the value of k_z which satisfies the dispersion relations. The same procedure is used for studying E as function k_p in the case where $k_z=0$ and $k_z=\pi/d$. It is noteworthy that, for a given value of E , Eq. (1) may have more than one root in k_p . It appears, from Eq. (3)-(5), that the carrier wave vectors k_x , k_y , and k_p are either real or imaginary (i.e. complex) and then using complex numbers in the calculation seems to be more adequate.

4. Theoretical results and discussions

The energy E as a function of d_2 , at 4.2 K, in the first Brillion zone and for $d_1 = 2.69 d_2$, is shown in “Figure 1 (a)”. The case of our sample ($d_2 = 32$ Å) is indicated by the vertical solid line. Here the cross-over of E_1 and HH_1 subbands occurs. d_2 controls the superlattice band gap $E_g = E_1 - HH_1$. For weak d_2 the sample is semiconductor with a strong coupling between the HgTe wells. At the point T($d_2 = 100$ Å, $E = 38$ meV) the gap goes to zero with the transition semiconductor- semimetal. When d_2 increases, E_1 and h_1 states drops in the energy gap $[0, \Delta]$ and become interface state with energy

$$E_I = \frac{\Delta \epsilon_2}{|\epsilon_1| + \epsilon_2} = 34 meV \tag{6}$$

for infinite d_2 obtained from Eq. (1). Then the superlattice has the tendency to become a layer group of isolated HgTe wells and thus assumes a semimetallic character. The ratio d_1/d_2 governs the width of superlattice subbands (i.e. the electron effective mass). A big d_1/d_2 , as in the case of 4.09 in Fig. 2, moves away the material from the two-dimensional behaviour.

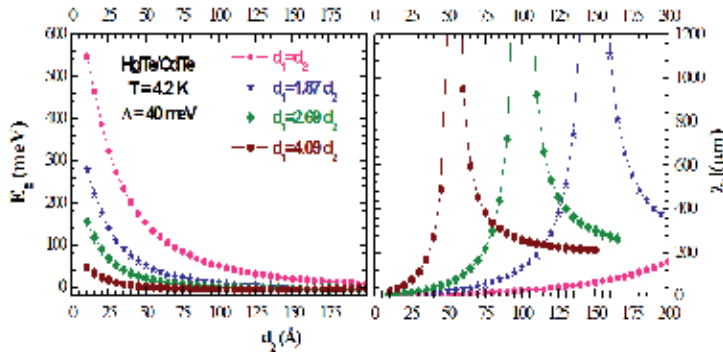


Figure 2. $E_g(\Gamma)$ and $|\lambda_c|$ as function of d_2 for various d_1/d_2 at 4.2 K.

In “Figure 1 (b)” we can see that the band gap $E_g(\Gamma)$ increases, presents a maximum at 10, 15 and 25 meV respectively for 4.2, 77 and 300K, near $\Lambda=40$ meV and decreases when the valence band offset Λ between heavy hole band edges of HgTe and CdTe increase. For each Λ , $E_g(\Gamma)$ increases with T . Our chosen value of 40 meV is indicated by a vertical solid line. This offset agrees well with our experimental results and 0 meV used by [4] for all temperatures, indicated by a horizontal solid line in “Figure 1 (b)”, contrary to 360 meV given by [11]. The later offset give $E_g = -8$ meV in “Figure 1 (b)” whereas, in intrinsic regime, $R_H T^{3/2}$ indicates a measured gap $E_g \approx 98$ meV in agreement with our calculated $E_g(\Gamma, 300\text{ K}) = 105$ meV.

“Figure 2” shows that, for each d_2 , $E_g(\Gamma)$ decreases when d_1/d_2 increases. For each d_1/d_2 , when d_2 increases $E_g(\Gamma)$ decreases, go to zero at the transition point T and became negative for a semimetal conductivity. In the right of “Figure 2”, the cut-off wavelength $|\lambda_c|$ diverge at T with $d_2=54 \text{ \AA}$, 100 \AA , 150 \AA ,... respectively for $d_1/d_2=4.09, 2.69, 1.87, \dots$. So, the transition goes to high d_2 when d_1/d_2 decreases. In the case of our sample the transition occur at $d_2 = 100 \text{ \AA}$.

Using the value of ϵ_1 and ϵ_2 at different temperatures between 4.2 K and 300 K [12] and taking P temperature independent, this is supported by the fact that from eq.(4) $P \approx \epsilon_c(T)/m^*(T) \approx \text{Cte}$, we get the temperature dependence of the band gap E_g , in the centre Γ of the first Brillouin zone in “Figure 3”. Note that E_g increases from 48 meV at 4.2 K to 105 meV at 300 K. We calculated the detection cut-off wave length by the relation

$$\lambda_c(\mu m) = \frac{1240}{E_g(\text{meV})} \quad (7)$$

In the investigated temperature range $12 \mu\text{m} < \lambda_c < 28 \mu\text{m}$ situates our sample as a far infra-red detector.

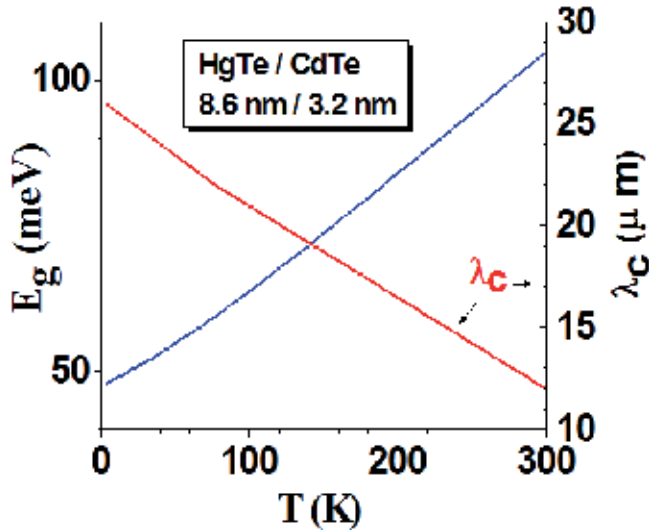


Figure 3. Temperature dependence of the band gap E_g and the cut-off wavelength λ_c , at the center Γ of the first Brillouin zone.

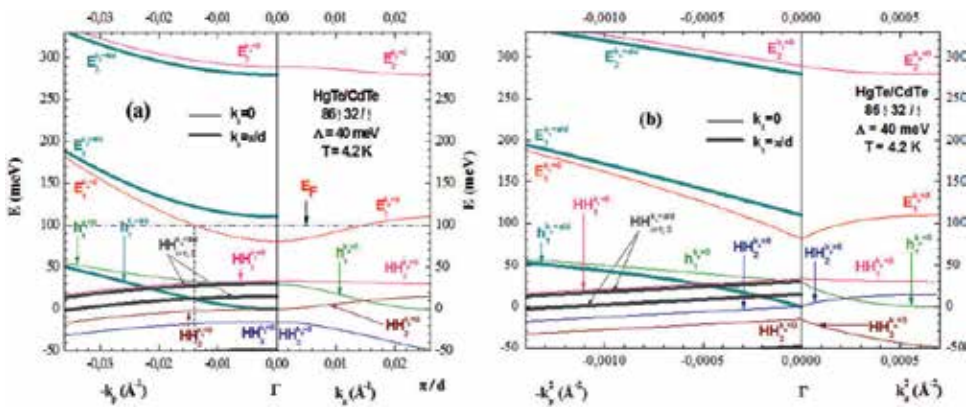


Figure 4. a) Calculated bands along the wave vector k_z in the right and in plane $k_p(k_x, k_y)$ for $k_x=0$ and π/d in the left, E_F is the energy of Fermi level. (b) Calculated bands along the k_z^2 in the right and k_p^2 for $k_x=0$ and π/d in the left, of the HgTe/CdTe superlattice at 4.2 K.

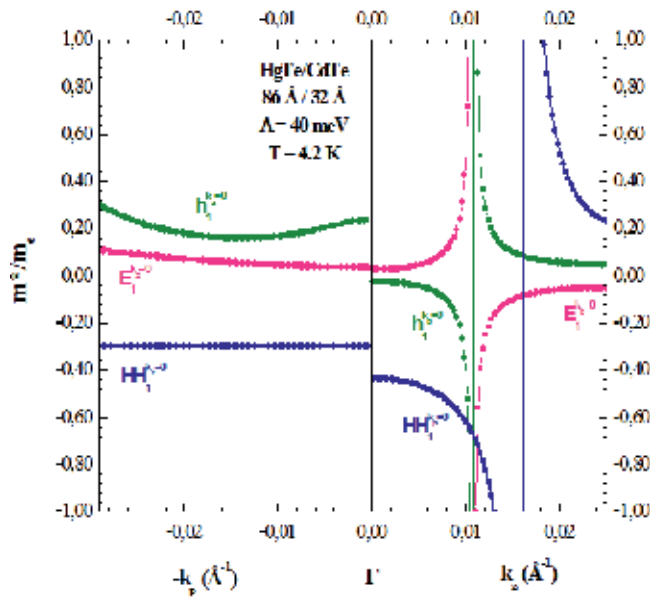


Figure 5. Calculated relative effective mass bands along the wave vector k_z and in plane k_p of the HgTe/CdTe superlattice at 4.2 K

In “Figure 4 (a)” we can see the spectres of energy $E(k_z)$ and $E(k_p)$, respectively, in the direction of growth and in plane of the superlattice at 4.2 K. Along k_z the subbands E_1 and h_1 are large and non-parabolic as shown in “Figure 4. (b)”. Along k_p , E_1 and h_1 increase with k_p whereas the parabolic HH_n decreases in “Figure 4. (b)”. This yield to an anti-crossing of HH_1 and h_1 at $k_p=0.0139 \text{ \AA}^{-1}$ near the middle of the first Brillouin zone ($\pi/2d$).

For an anisotropic medium, such as the HgTe/CdTe superlattices, the effective mass is a tensor and its elements along μ and ν directions are given by the following expression [12].

$$\left(\frac{1}{m^*}\right)_{\mu\nu} = \frac{1}{\hbar^2} \frac{\partial^2 E_{k_{\mu\nu}}}{\partial k_\mu \partial k_\nu} \tag{8}$$

By carrying out second derivative of the energy E_1 , h_1 and HH_1 along k_z and k_p in “Figure 4 (a)”, we calculated the effective mass bands in “Figure 5”. Along k_p , the effective mass of heavy holes $m_{HH1}^* = -0.30 m_0$ and the effective mass of electrons m_{E1}^* increases from $0.04 m_0$ to $0.11 m_0$. In “Figure 4 (a)”, the Fermi level across the conduction band E_1 at $k_p=0.014 \text{ \AA}^{-1}$ corresponding to

$$\left(m_{E_1}^*\right)_{E_F} = 0.05 m_0 \tag{9}$$

from “Figure 5”. Whereas, the effective mass of the light holes h_1 decreases from $0.24 m_0$, to a minimum of

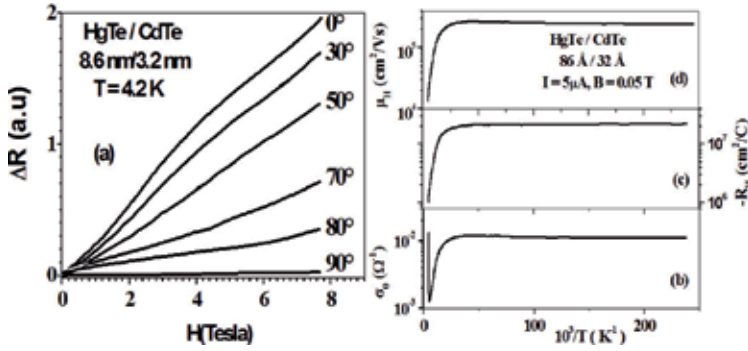


Figure 6. Variation of magnetoresistance of the sample with various angles between the magnetic field and the normal to the HgTe/CdTe superlattice surface (a). Temperature dependence of the conductivity (b), weak-field Hall coefficient (c) and Hall mobility (d) in the investigated HgTe/CdTe superlattice

$$\left(m_{h_1}^*\right)_{\min} = 0.16 m_0 \quad (10)$$

at $k_p = 0.14 \text{ \AA}^{-1}$, and increase to $0.30 m_0$ assuming an electronic conduction.

5. Experimental results and discussions

In “Figure 6.(a)” we can see that the angular dependence of the magnetoresistance vanishes, when the field is parallel to the plane of the SL (at 90°), indicating a two dimensional (2D) behaviour supported by the observation of SDH oscillations in “Figure 8 (a)”.

We have also measured the conductivity, Hall mobility and Seebeck effect. At low temperatures, the sample exhibits n type conductivity ($R_H < 0$) with a concentration $n = 1/e R_H = 3.24 \times 10^{12} \text{ cm}^{-2}$ from “Figure 6 (c)” and in “Figure 7. (a)” and a Hall mobility $\mu_n = 2.5 \times 10^5 \text{ cm}^2/\text{Vs}$ in “Figure 6 (d)”. The plot $\log(\mu_n) - \log(T)$ in the “Figure 7.(b)” of the Hall mobility shows a scattering of electrons by phonons in the intrinsic regime with $\mu_H T^{1.58}$ and weak activation energy at low temperature with $\mu_H T^{0.05}$.

This relatively electrons high mobility allowed us to observe the Shubnikov-de Haas effect until 8 Tesla in “Figure 8 (a)”. Its well knows that the oscillations of the magnetoresistance are periodic with respect to $1/B$ [14]. The period ($1/B$) is related to the concentration n of the electrons by the relation:

$$n = \frac{e}{\pi \hbar \Delta \left(\frac{1}{B} \right)} \quad (11)$$

In the insert of “Figure 8(a)” we have plotted the inverse of the minima’s $1/B_m$ as a function of the entire n' following the formula:

$$\frac{1}{B_m} = \Delta \left(\frac{1}{B} \right) \left(n' + \frac{1}{2} \right) \quad (12)$$

The linear line slope gives $(1/B)$ and $n = 3.20 \times 10^{12} \text{ cm}^{-2}$ in good agreement with that measured by weak field Hall effect ($H=0.5 \text{ KOe}$, $I=5 \mu\text{A}$) from “Figure 6(c)”.

At low temperature, the superlattice electrons dominate the conduction in plane. The E_1 band is not parabolic with respect to k_p^2 in “Figure 4 (b)”. That permits us to estimate the Fermi energy (2D) at 4.2K

$$E_F = n\pi h^2 / (m_{E_1}^*)_{E_F} = 88 \text{ meV} \quad (13)$$

The thermoelectric power ($\alpha < 0$) measurements shown in “Figure 8(b)” indicate n-type conductivity, confirmed by Hall Effect measurements ($R_H < 0$) in “Figure 6(c)”. At low temperature, $\alpha \propto T^{0.96}$ (in the top insert of “Figure 8(b)”) is in agreement with Seebeck effect theory deduced from the relaxation time resolution of the Boltzmann equation [15].

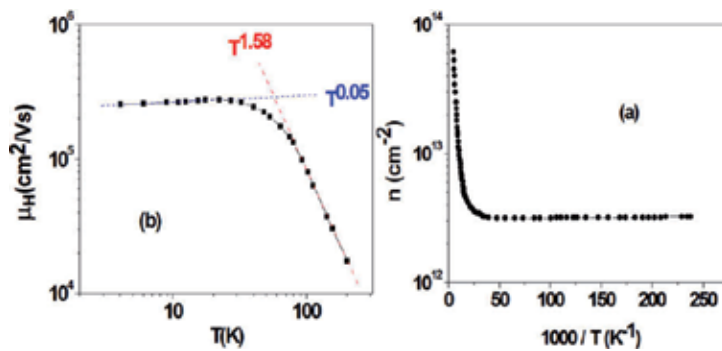


Figure 7. a) Variation with $1/T$ of weak-field Hall concentration and (b) Variation with T of Hall mobility in the investigated HgTe/CdTe superlattice

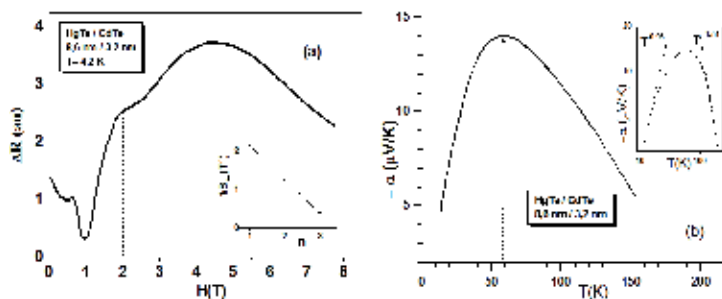


Figure 8. a) Variation of transverse magneto-resistance with magnetic field at 4.2 K, (b) Measured thermoelectric power as a function of temperature in the investigated HgTe/CdTe superlattice.

For our degenerate electrons gas the Seebeck constant is described by the formula:

$$\alpha = \frac{[(\pi k_B)^2 T (s + 1)]}{3eE_F} \quad (14)$$

where the collision time $\tau \propto E^{-(1/2)}$. This permits us to estimate the Fermi energy at $E_F = 91$ meV (in "Figure 4(a)"), with $s = 2.03$ corresponding to electrons diffusion by ionized impurities, in agreement with the calculated $E_F = 88$ meV in formula (13). In intrinsic regime for $T > 150$ K, the measure of the slope of the curve $R_H T^{3/2}$ indicates a gap $E_g = 98$ meV which agree well with calculated $E_g(\Gamma, 300 \text{ K}) = E_1 - HH_1 = 105$ meV. Here $\alpha T^{-3/2}$ indicates electrons scattering by phonons.

This HgTe/CdTe superlattice is a stable alternative for application in far infrared optoelectronic devices than the random alloys $\text{Hg}_{0.99}\text{Cd}_{0.01}\text{Te}$ because the small composition $x = 0.01$, with $E_g(\Gamma, 300 \text{ K}) = 100$ meV given by the empiric formula for $\text{Hg}_{1-x}\text{Cd}_x\text{Te}$ [16]

$$E_g(x, T) = -0,302 + 1,93x - 0,810x^2 + 0,832x^3 + 5,035 \times 10^{-4}(1-2x) T \quad (15)$$

is difficult to obtain with precision while growing the ternary alloys and the transverse effective masse in superlattice is two orders higher than in the alloy. Thus the tunnel length is small in the superlattice [17].

6. Conclusions

The fundamental main ideas of this work are:

- HgTe is a zero gap semiconductor (or semimetal) when it is sandwiched between the wide gap semiconductor CdTe (1.6 eV at 4.2 K) layers yield to a narrow gap HgTe/CdTe superlattice which is the key of an infrared detector.

- Before growing our superlattice, we calculated the bands structures $E(d_z)$ and the gap for each ratio thickness d_1/d_2 . After we choosed the SL in the semiconductor conductivity zone.

We reported here remarkable correlations between calculated bands structures and magneto-transport properties in HgTe/CdTe nanostructures superlattices. Our calculations of the specters of energy $E(d_z)$, $E(k_z)$ and $E(k_p)$, respectively, in the direction of growth and in plane of the superlattice; were performed in the envelope function formalism.

The formalism used here predicts that the system is semiconductor, for our HgTe to CdTe thickness ratio $d_1/d_2 = 2.69$, when $d_2 < 100$ nm. In our case, $d_2 = 3.2$ nm and $E_g(\Gamma, 4.2 \text{ K}) = 48$ meV. In spite of it, the sample exhibits the features typical for the semiconductor n-type conduction mechanism. In the used temperature range, this simple is a far-infrared detector, narrow gap and two-dimensional n-type semiconductor. Note that we had observed a semi-metallic conduction mechanism in the quasi 2D p type HgTe/CdTe superlattice [18].

In conclusion, the HgTe/CdTe superlattice is a stable alternative for application in infrared optoelectronic devices than the alloys $\text{Hg}_{1-x}\text{Cd}_x\text{Te}$.

Measurements performed by us on others' samples indicate an improvement of quality of the material manifested by higher mobility.

Author details

Abdelhakim Nafidi

Laboratory of Condensed Matter Physics and Nanomaterials for Renewable Energy University Ibn-Zohr 80000 Agadir, Morocco

References

- [1] Esaki, L., & Tsu, R. (1970). Superlattice and negative differential conductivity in Semiconductors. *IBM J. Res. Development*, 1970(14), 61-65, 0018-8646.
- [2] Dingle, R., Gossard, A. C., & Wiegmann, W. (1975). Direct Observation of Superlattice Formation in a Semiconductor Heterostructure. *Phys. Rev. Lett.*, 34, 1327-1330, 10.1103/PhysRevLett.34.1327.
- [3] Sakaki, H., Chang, L. L., Sai-Halasz, G. A., Chang, C. A., & Esaki, L. (1978). Two-dimensional electronic structure in InAs-GaSb superlattices. *Solid State Communications*, 26, 589-592, 10.1016/0038-1098(78)90770-6.
- [4] Bastard, G. (1981). Superlattice band structure in the envelope-function approximation. *Phys. Rev. B*, 24, 5693-5697, 10.1103/PhysRevB.24.5693.
- [5] Tuchendler, J., Grynberg, M., Couder, Y., Thomé, H., & Le Toullec, R. (1973). Submillimeter Cyclotron Resonance and Related Phenomena in HgTe. *Phys. Rev. B*, 8, 3884-3894, PhysRevB.8.3884.
- [6] Bastard, G. (1982). Theoretical investigations of superlattice band structure in the envelope-function approximation. *Phys. Rev. B*, 25, 7584-7597, 10.1103/PhysRevB.25.7593.
- [7] Nafidi, Ab., El Kaaouachi, A., Sahsah, H., & Nafidi, Ah. (2002). Band structure and magneto-transport in HgTe/CdTe superlattice. Book of the International Conference on Theoretical Physics (HT 2002). 274-275, *Birkhäuser Verlag 2000*, 3-76432-433-3.
- [8] Braigue, M., Nafidi, A., Chaib, H., Devki, N., Talwar, Tirbiyine. A., Hemine, J., Idbaha, A., Boukassim, A., El Gouti, T., Massaqa, M., & Srinivasa, Vinod. M. (2011). Correlation Between Bands Structure and Magneto-Transport Properties in n-type HgTe/

- CdTe Superlattice with Relatively Thin CdTe Barrier. *AIP Conference Proceedings*, 1416,, New York: American Institute of Physics, 68-71.
- [9] Guldner, Y., Bastard, G., Vieren, J. P., Voos, M., Faurie, J. P., & Million, A. (1984). Magneto-optics in a II-VI superlattice: HgTe-CdTe. *Surface Science*, 142, 593-597, 10.1016/0039-6028(84)90367-4.
- [10] Kane, E. (1957). Band structure of indium antimonide. *Journal of Physics and Chemistry of Solids*, 1(4), 249-261.
- [11] Johnson, N. F., Hui, P. M., & Ehrenreich, H. (1988). Valence-Band-Offset Controversy in HgTe/CdTe Superlattices: A Possible Resolution. *Phys. Rev. Lett.*, 61(PhysRevLett. 61.1993), 1993-1995.
- [12] Weiler, M. H., Willardson, R. K., & Beer, A. C. (1981). Magneto-optical Properties of $\text{Hg}_{1-x}\text{Cd}_x\text{Te}$ Alloys,. In: *semiconductors and Semimetals*, (Academic, New York),, 119-191, 978-0-12752-116-9.
- [13] Kittel, C. (2001). *Introduction to solid state physics*, John Wiley and Sons, Inc, New York 333.
- [14] Seeger, K. (2002). *Semiconductor physics: an introduction* [8], Springer, chap.4,, 121, 978-3-54043-813-7.
- [15] Seeger, K. (2002). *Semiconductor physics: an introduction* [8], Springer, chap.6,, 159, 978-3-54043-813-7.
- [16] Hansen, G. L., Schmit, J. L., & Casselman, T. N. (1982). Energy gap versus alloy composition and temperature in $\text{Hg}_{1-x}\text{Cd}_x\text{Te}$. *J. Appl. Phys.*, 53, 7099-7101, 10.1063/1.330018.
- [17] Nafidi, A., et al. (2013). to be published.
- [18] Braigue, M., Nafidi, A., Benlaabidya, Y., Chaib, H., Daddabi, A., Morghi, R., Idbaha, A., Massa, M., El Gouti, T., Hemine, J., & Srinivasa, Vinod. M. (2011). Manifestation of the Transition Semiconductor-Semimetal and Intrinsic Interface State in Band Structure and Magneto-Transport Properties in Nanostructure Superlattice,. *J Supercond Nov Magn*, Springer,, 10.1007/s10948-011-1229-y.

Advances in Infrared Detector Array Technology

Nibir K. Dhar, Ravi Dat and Ashok K. Sood

Additional information is available at the end of the chapter

<http://dx.doi.org/10.5772/51665>

1. Introduction

This Chapter covers recent advances in Short Wavelength Infrared (SWIR), Medium Wavelength Infrared (MWIR) and Long Wavelength Infrared (LWIR) materials and device technologies for a variety of defense and commercial applications. Infrared technology is critical for military and security applications, as well as increasingly being used in many commercial products such as medical diagnostics, drivers' enhanced vision, machine vision and a multitude of other applications, including consumer products. The key enablers of such infrared products are the detector materials and designs used to fabricate focal plane arrays (FPAs).

Since the 1950s, there has been considerable progress towards the materials development and device design innovations. In particular, significant advances have been made during the past decade in the band-gap engineering of various compound semiconductors that has led to new and emerging detector architectures. Advances in optoelectronics related materials science, such as metamaterials and nanostructures, have opened doors for new approaches to apply device design methodologies, which are expected to offer enhanced performance and low cost products in a wide range of applications.

This chapter reviews advancements in the mainstream detector technologies and presents different device architectures and discussions. The chapter introduces the basics of infrared detection physics and various infrared wavelength band characteristics. The subject is divided into individual infrared atmospheric transmission windows to address related materials, detector design and device performance. Advances in pixel scaling, junction formation, materials growth, and processing technologies are discussed.

We discuss the SWIR band (1-3 microns) and address some of the recent advances in InGaAs, SiGe and HgCdTe based technologies and their applications. We also discuss MWIR band that covers 3-5 microns, and its applications. Some of the key work discussed includes InSb, HgCdTe, and III-V based Strained Layer Super Lattice (SLS) and barrier detector tech-

nologies (nBn). Each of these technologies has a place in the IR applications where a variety of detector configurations can be used.

We also present a discussion on the LWIR band that covers the wavelength range between 8 and 14 microns. The technologies that are addressed are bolometer (Microbolometer Arrays), HgCdTe arrays, and a variety of very ingenious band-gap engineered devices using III-V compound semiconductor materials.

2. Infrared Spectrum and Bands of Interest

The word “infrared” refers to a broad portion of the electromagnetic spectrum that spans a wavelength range from 1.0 μm to beyond 30 μm everything between visible light and microwave radiation. Much of the infrared spectrum is not useful for ground- or sea-based imaging because the radiation is blocked by the atmosphere. The remaining portions of the spectrum are often called “atmospheric transmission windows,” and define the infrared bands that are usable on Earth. The infrared spectrum is loosely segmented into near infrared (NIR, 0.8-1.1 μm), short wave infrared (SWIR, 0.9-2.5 μm), mid wave infrared (MWIR, 3-5 μm), long wave infrared (LWIR, 8-14 μm), very long wave infrared (VLWIR, 12- 25 μm) and far infrared (FIR, > 25 μm), as shown in Figure 1. The MWIR- LWIR wavebands are important for the imaging of objects that emit thermal radiation, while the NIR-SWIR bands are good for imaging scenes that reflect light, similar to visible light. Some of the materials technologies and device architectures used for detector fabrication in the various IR bands are discussed in references 1 - 4. Since NIR and SWIR are so near to the visible bands, their behavior is similar to the more familiar visible light. Energy in these bands must be reflected from the scene in order to produce good imagery, which means that there must be some external illumination source. Both NIR and SWIR imaging systems can take advantage of sunlight, moonlight, starlight, and an atmospheric phenomenon called “nightglow,” but typically require some type of artificial illumination at night. In lieu of photon starved scenes, arrays of infrared Light Emitting Diodes (LEDs) can provide a very cost effective solution for short-range illumination. However, achieving good performance at distances of over hundreds of meters requires more directed illumination, such as a focused beam from a laser or specialized spotlight, although special consideration of eye-safety issues is required.

NIR and SWIR imaging systems often employ sensors that are more exotic than those found in consumer-grade camcorders and digital cameras. Because NIR has a wavelength longer than visible light, and SWIR a wavelength that is longer still, energy in these bands is scattered less by particles suspended in the atmosphere. Consequently, SWIR, and to a lesser extent NIR, systems are tolerant of low levels of obscurants like fog and smoke compared to visible light.

An imaging system that operates in the MWIR and LWIR ranges can be completely passive, requiring no external illumination, because the thermal imager is able to sense the energy that is emitted directly from objects in the scene. The major factors that determine how bright an object appears to a thermal imager are: the object’s temperature and its emissivity. As an object gets hotter, it radiates more energy and appear brighter to a thermal imaging

system. Emissivity is a physical property of materials that describes how efficiently it radiates heat. Because cloth has a lower emissivity than skin, the former will appear darker in a thermal imager even when both are exactly at the same temperature.

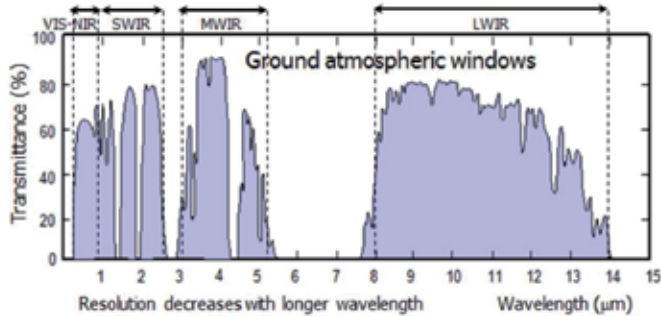


Figure 1. Definition of IR Spectral Band.

At the MWIR and LWIR wavelengths, infrared radiation behaves differently from visible light. For example, glass is transparent to wavelengths less than 3.0 μm , so glass optics can be used and windows can be seen through at these wavelengths. However, glass is opaque in the LWIR band and blocks most energy in the MWIR band. Consequently, the optics in LWIR and MWIR imaging systems cannot use inexpensive glass lenses, but are forced to use more expensive materials, such as germanium. Because glass windows are not transparent at the longer wavebands, they can appear to be brighter or darker according to their temperatures. Another difficulty with radiation in the MWIR and LWIR bands is that it is not transmitted through water. Imaging of a water (rain) coated scene with MWIR-LWIR wavelengths can wash out much of the scene's thermal contrast, resulting in a duller image.

The choice of wavelength band to exploit for IR imaging depends on the type of atmospheric conditions/obscurants between the target and the imager. Generally, atmospheric obscurants, such as haze or conventional smoke, cause much less scattering in the MWIR and LWIR bands than in the VIS-NIR or SWIR bands. This is because the haze or smoke particle size ($\sim 0.5 \mu\text{m}$) is much smaller than the IR wavelength (Rayleigh scattering). Obscurants such as fog and clouds can cause more scattering, since the particle size is comparable with the IR wavelength (Mie scattering). Infrared cameras sensitive to the longer wavelengths are more tolerant to smoke, dust and fog. In addition to obscurants, atmospheric turbulence can dictate the choice of IR wave band for a given application. The effects of optical turbulence, due to the fluctuations in the refractive index of the atmosphere, can add up over very long distances to impact range performance (blurring and image motion), allowing LWIR an edge over MWIR. As a rule of thumb, longer the wavelength better is the transmission through the earth's atmosphere.

According to Wien's Law, hotter objects emit more of their energy at shorter wavelengths. A blackbody source at 300 K has a peak exitance (power per unit area leaving a surface) at a wavelength of about 9.7 μm . For a source at 1000 K, the maximum exitance occurs at 2.9 μm . Therefore, detectors operating in the LWIR band are well suited to image room temperature

objects (people, buildings etc.), while MWIR band imagers are good for viewing objects at higher temperatures (hot engines and exhaust gasses). In general, LWIR and MWIR bands will produce thermal images if small temperature changes or varying emissivities exist within a scene. However, while the LWIR band imagery may exhibit a higher sensitivity for room temperature objects, the MWIR band imagery presents a better resolution.

3. Theoretical Considerations

IR detectors can be categorized as being either a quantum or thermal device. In a quantum detector, electromagnetic radiation absorbed in a semiconductor material generates electron-hole pairs (EHP), which are sensed by an electronic readout circuit (ROIC). In a thermal detector, on the other hand, the incident IR photons are absorbed by a thermally isolated detector element, resulting in an increase in the temperature of the element. The temperature is sensed by monitoring an electrical parameter such as resistivity or capacitance.

Because thermal detectors depend on the quantity of heat absorbed, their response is independent of wavelength, however, the sensitivity depends on the material design for sensing. There are two types of quantum detectors: a) photoconductive (PC) where the electrical conductivity of the semiconductor changes as a function of the photon intensity; b) photovoltaic (PV) where a voltage is generated across a PN junction as photons impinge the semiconductor. Quantum detectors convert photons directly into charge carriers and no intermediate process is involved, such as the heating in a thermal detector to cause a change of a measurable electrical property.

Due to the various mechanisms used by detectors to convert optical to electrical signals, several figures of merit (FOM) are used to characterize their performance [5-8]. The output of the detector consists of its response signal to the incident radiation and random noise fluctuations. One such FOM is the Responsivity (R) of the detector, defined as the ratio of the root mean squared (rms) value of the signal voltage (V_s) to the rms power (P in volts/watt) incident on the detector. The total power on an area (A_d) is associated with an irradiance E (in watts/ cm²). Therefore,

$$R = \frac{V_s}{P} = \frac{V_s}{EA_d} = [\text{volts} / \text{watts}] \quad (1)$$

The random fluctuations in a detector's output limit its sensitivity to a certain minimum detectable power. The power necessary to generate an output signal equal to the noise is known as the Noise Equivalent Power (NEP). NEP is determined by measuring the amount of radiative power from a blackbody that falls on the detector to produce an rms signal V_s , equal to that generated by the detector noise V_{N} , when it is shuttered from the blackbody. NEP must be specified for a particular source temperature (T), modulation frequency (f), system bandwidth (BW), and detector area (A_d).

$$NEP(T, f, BW) = \frac{P}{S/N} = \frac{EA_d}{S/N} = \frac{EA_d}{V_s/V_N} [\text{watts}] \quad (2)$$

The inverse of NEP is referred to as the Detectivity:

$$\text{Detectivity, } D = 1/NEP \quad (3)$$

To have a meaningful comparison between different detectors, their respective performance must be reduced to representative conditions, so that the detectivity is often normalized to a bandwidth of 1 Hz and a detector area of 1 cm². This figure of merit is called D-star (D*) and can be interpreted as the signal to noise ration (SNR) out of a detector when 1 watt of radiant power is incident on a 1 cm² detector area at a noise equivalent bandwidth of 1 Hz.

$$D^* = \frac{\sqrt{A_d BW}}{NEP} [\text{cm}\sqrt{\text{Hz}}/\text{watt}] \quad (4)$$

The performance of low-noise detectors may also be limited by radiative noise arriving at the detector from the background environment. When the background photon flux is much greater than the signal flux, the photodetector is said to be background-limited in performance or in the BLIP mode. The resulting detectivity of the photovoltaic detector is called D_{BLIP}^* and is expressed as:

$$D_{BLIP}^* = \frac{\lambda}{hc} \sqrt{\frac{\eta}{2\phi_B}} \quad (5)$$

where λ is the wavelength, η is the quantum efficiency, and ϕ_B is the incident photon flux in photons/cm²-s. Equation (5) is valid for photovoltaic detectors which are shot-noise limited. For photoconductive detectors that are generation-recombination (G-R) noise limited, the D_{BLIP}^* is lower by a factor of $\sqrt{2}$. The variances of the G-R noise are additive, causing an increase in the rms noise voltage by a factor of $\sqrt{2}$.

Background-limited performance of detectors can be improved by reducing the background photon flux, ϕ_B . There are two ways of implementing this: a) use a cooled and/or spectral filter to limit the spectral band, or b) use a cold shield to limit the angular FOV of the detector. The former approach eliminates most of the background radiation from spectral regions in which the detector does not need to respond. The best detectors can approach background limited detectivities by limiting the field of view with a cold shield. Detectivity curves across the infrared spectrum for various commercially available detectors are shown in Figure 2 [7]. Calculated detectivities for the background-limited performance for ideal photon and thermal detectors are also included in Figure 2 as dashed curves.

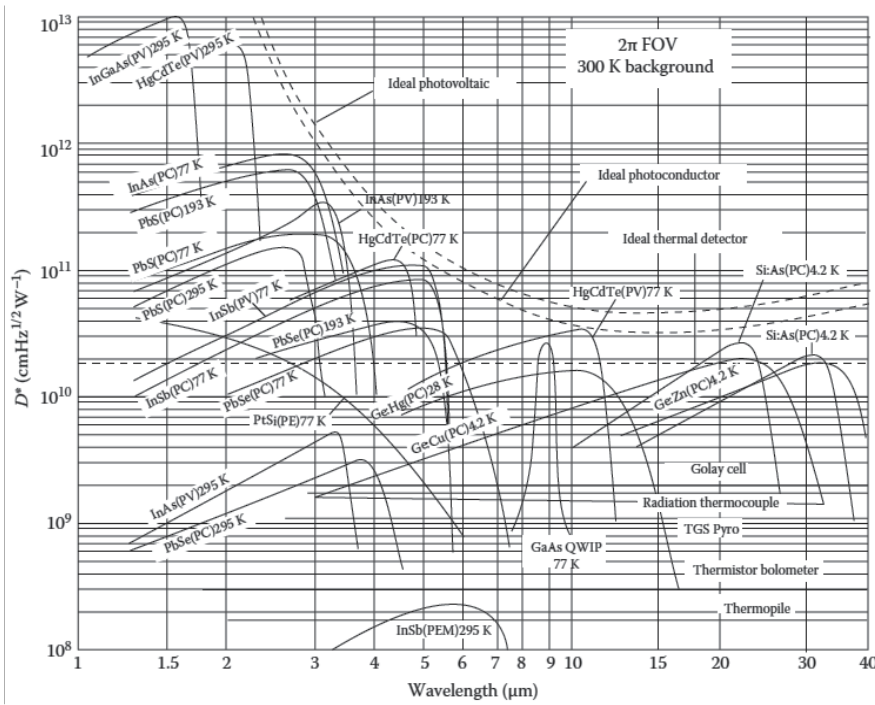


Figure 2. Detectivity curves for various commercially available photon and thermal IR detectors. Calculated detectivities are indicated by dashed lines [7].

Another frequently quoted figure of merit for a photodiode is its R_0A product, where R_0 is the dynamic resistance of the photodiode and is equal to the slope of the I-V curve at the zero bias voltage point. This FOM is independent of the junction area, except when the dimensions are comparable to the minority carrier diffusion length.

Thermal detectors require a temperature change to produce a signal and do not generally need cooling, in contrast to photo detectors which are cooled to minimize noise. Absorbed radiation causes a temperature change that alters a temperature sensitive property of the detector which can be measured externally. A few examples include: electrical resistance in a bolometer, thermal expansion of Goly cells, and polarization in pyroelectric materials. Since these detectors depend on temperature changes resulting from incident radiation, they must be thermally isolated from their surroundings and have low thermal capacities for fast response to the radiation. In the case of a bolometer, the FOM is its thermal time constant which is defined as:

$$\tau_{th} = \frac{C_{th}}{G_{th}} = C_{th} R_{th} \tag{6}$$

where C_{th} is the thermal capacity of the detector, R_{th} is the thermal resistance and G_{th} is the thermal coupling of the detector to its surroundings. The interaction of the bolometer with

the incident radiation needs to be optimized while, simultaneously, minimizing its thermal contacts to the surroundings. In practice, this requires a bolometer with small mass and fine connecting wires to the heat sink.

4. IR Material growth Techniques for HgCdTe

$\text{Hg}_{1-x}\text{Cd}_x\text{Te}$ (MCT) is the most widely used infrared (IR) detector material in military applications, compared to other IR detector materials, primarily because of two key features: it is a direct energy band gap semiconductor and its band gap can be engineered by varying the Cd composition to cover a broad range of wavelengths. The direct band gap of MCT allows for a high absorption of IR radiation, yielding high quantum efficiency in a relatively thin detector structure. As the Cd mole fraction, x , increases, the energy gap for MCT increases linearly from a semimetal (HgTe) to a wide band gap semiconductor (CdTe).

The ability to tune the band gap of MCT enables IR detectors to operate in the wavelength bands ranging from SWIR to VLWIR (0.7-30 microns). For low-cost high-performance detectors, the MCT material must be produced on large diameter wafers with low defect densities and reproducible stoichiometric properties. These requirements are satisfied by a host of crystal growth techniques ranging from high temperature, melt grown bulk crystals, to low temperature, multilayer epitaxial layers.

Depending on the detector architecture, the crystal growth strategy could utilize any of the following techniques: Bulk Crystal Growth, Liquid Phase Epitaxy (LPE), Metal-organic Chemical Vapor Deposition (MOCVD), and Molecular Beam Epitaxy (MBE). The sections below will highlight each of these growth techniques with references to publications that will provide additional coverage.

4.1. Bulk Crystal Growth

Bulk crystal growth of MCT continues to play an important role in producing IR detector materials for photoconductive arrays, despite the progress made with various epitaxial thin film deposition techniques. Bulk growth process is typically used for large area single detectors for applications such as spectrometry. However, for photovoltaic arrays there are challenges associated with crystal grain boundaries, which are electrically active and contribute to line defects. Also there are limitations in the ingot diameter, which makes bulk growth suitable for only quad or single detector arrays. Several methods have been developed for growing MCT bulk crystals: Solid State Recrystallization (SSR), Traveling Heater Method (THM), Bridgman, Czochralski, Slush Growth, and Zone Melting [9-14]. This section will cover SSR and THM techniques.

The general challenge with melt grown MCT is to maintain a relatively high Hg vapor pressure during growth; otherwise, it is difficult to control the stoichiometry of the grown crystal. Also, the large separation between the liquidus and solidus compositions (see Figure 3) across a constant thermal tie line can result in a steady variation in the composition of a moving growth interface.

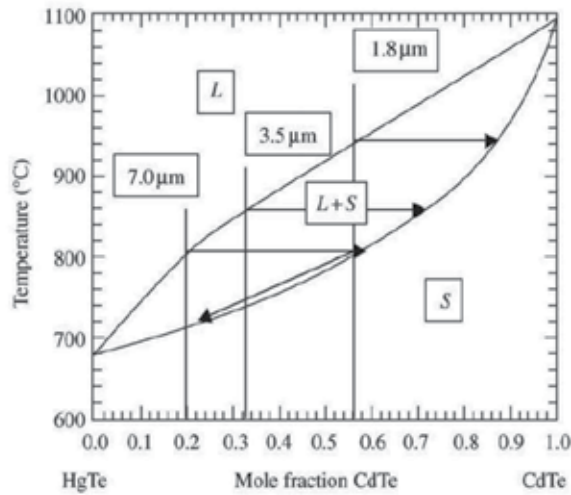


Figure 3. T - x phase diagram for the pseudo-binary CdTe-HgTe [14].

4.1.1. Solid State Recrystallization

The SSR technique is used to alleviate the compositional variation at the growth interface in ternary systems, such as MCT, where the solidus and liquidus lines are widely separated. In the basic technique, the three high purity elements of MCT are cleaned and loaded into a thick walled, small diameter quartz ampoule that is evacuated, sealed and placed into a furnace. The ampoule is heated to approximately 950 °C and the melt is mixed by rocking the furnace. The MCT ampoule is removed from the furnace and rapidly quenched to produce a uniform composition.

The rapid quenching produces a dendritic structure in the MCT that is reduced by an extended (several days) recrystallization step, at temperatures just below the melting point. Grain growth occurs during the re-crystallization step and remaining compositional inhomogeneities are removed. On the down side, the high melt temperatures and very high Hg vapor pressures used in SSR to produce MCT can cause the ampoule to explode. Also, very long annealing times are required and the resulting crystals are small. The typical diameter of the ingot is limited to about 2.0 cm in order to control impurity segregation in the crystal.

4.1.2. Traveling Heater Method

In the THM method, a solvent zone is created between a solid seed and the feed stock material. In the case of MCT, the crystal is grown by passing the solvent zone (e.g. Te rich) through a polycrystalline MCT rod having a composition that is to be replicated in grown crystal. The motion of the molten interface is produced by the slow movement of the heater along the charged crucible. Crystallization takes place at the advancing seed-solvent interface and dissolution of feed material occurs at the solvent-feed phase boundary. Through

convection and diffusion, the solid material is dissolved at the high temperature interface and deposited at the low temperature interface of the zone.

Crystal growth occurs in the 500-700 °C range, lower than the temperature used for Solid State Recrystallization growth method. The lower growth temperature used in THM reduces the incidence of antisite defects, resulting in crystals with more reproducible composition and higher resistivity. Also, the lower temperatures reduce contamination from the crucible walls and decrease the evaporation of the constituent species. One successful implementation of THM resulted in crystals up to 5 cm in diameter [15]. The perfect quality of crystals grown by this method is achieved at the cost of a low growth rate [11].

4.1.3. Liquid Phase Epitaxy (LPE)

LPE growth method offers, in comparison with bulk growth techniques, lower growth temperatures, shorter growth times, multilayered device structures, and better compositional homogeneity over large substrate areas. The versatility of LPE as a production tool for high performance device quality MCT epitaxial layers, with different Cd mole fractions and excellent compositional uniformity, is discussed in [16-20]. Today, detector arrays prepared from LPE based materials exhibit best performance, and majority of military IR applications use this technology.

LPE is a solution growth technique that involves the controlled precipitation of a solute dissolved in a solvent onto a single crystal substrate. For LPE growth of MCT, bulk grown CdZnTe single crystal substrates are suitable, since they are thermodynamically compatible and nearly lattice matched. The solvent can either be Hg [21] or Te-rich [22].

Both Te-solution growth (420–500 °C) and Hg-solution growth (360–500 °C) are used with equal success in a variety of configurations. The design of the Te-rich LPE system can be configured to allow the melt to contact the substrate by either sliding, tipping or dipping techniques. A sliding boat system uses a small melt volume and is adaptable for changing composition, thickness and doping. Tipping and dipping systems can be scaled up for large melts to provide thick, uniform layers. Both the tipping and dipping designs are being used for Te and Hg-rich solutions, while only the sliding technique is used for Te-rich solutions.

The major difference between the Hg and Te-rich solvents is that in the former case, the vapor pressure of Hg over the melt is much higher than in the latter case. The Hg partial pressure curves in Figure 4 indicate that at 500 °C and a Cd mole fraction of 0.1, the Hg partial pressure over Te-saturated MCT is 0.1 atm, while that of Hg-saturated MCT is 7 atm [23]. Te-rich solutions saturated with Hg vapor allow for small volume melts that do not appreciably deplete during growth in the temperature range 420-500 °C using the slider technique.

This is because the solubility of Cd in Te is high. On the other hand, the limited solubility of Cd in Hg requires the volume of Hg-rich melts to be much larger than Te melts, in order to minimize melt depletion during growth in the 360–500 °C temperature range. Unfortunately, the larger melt volume in Hg-rich LPE precludes the use of the slider boat approach and makes an open tube growth impossible [24]. For these reasons, it would not be surprising if many more manufacturers are pursuing LPE growth from Te-rich melts rather than from Hg-rich melts.

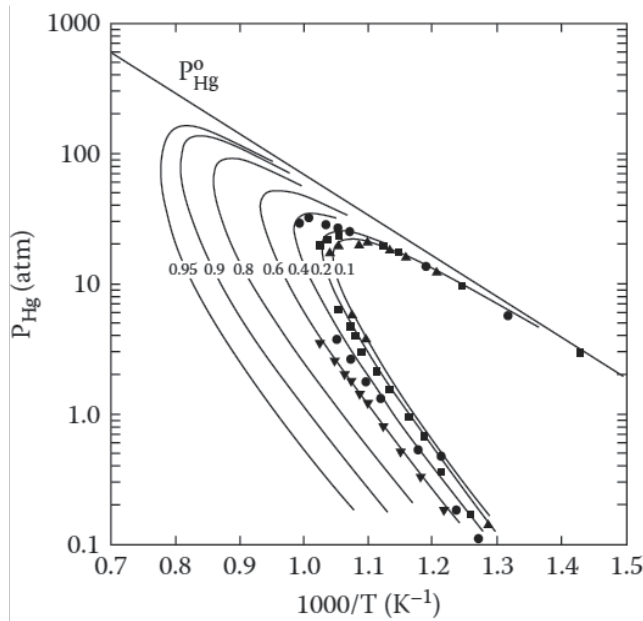


Figure 4. Partial pressure of Hg along the three-phase curves for various MCT solid solutions [23].

Despite the lower Hg vapor pressure in a Te-rich melt, the partial pressure of Hg must still be controlled in the growth system in order to obtain compositional uniformity, reproducibility, and stability. One way of controlling the Hg partial pressure under Te-rich conditions is to carry out the entire LPE growth process in a sealed ampoule. The disadvantages of this approach are low production levels because of the necessity of sealing the ampoule for each growth run and difficulty for in-situ preparation of multilayer growth that is necessary for advanced IR device structures.

In an open tube LPE-MCT, Te-rich system, the Hg partial pressure can be controlled by [25]: a) implementing an external Hg source to replenish the depleted Hg from the growth chamber, b) using chunks of HgTe near the melt as a solid source for Hg vapor, or c) using a high inert gas overpressure to minimize Hg loss.

As discussed above, the growth of MCT from Hg-rich melts is not as popular as growth from Te-rich solutions because of the low solubility of Cd and Te in Hg below 600 °C, and the high vapor pressure of Hg. On the other hand, LPE growth from a Hg-rich melt offers the following advantages: excellent surface morphology; high purity source material; good control over N- and P-type doping levels; very good compositional and thickness uniformity over large surface areas; and no need for post-growth anneals.

LPE layers grown from Te-rich melts are P-type due to the Hg vacancies induced during the growth process. These unintentionally doped layers can be converted to N-type by appropriate annealing schedules in Hg vapor. Layers grown from Hg-rich melts are usually N-type. LPE layers grown from Hg-rich solutions are intentionally doped with group VB

elements with high solubilities [20], but layers grown from Te-rich solutions are not [26]. Group VB dopants have low solubility and are not fully active electrically. Group IIIB elements, indium in particular, are easily incorporated from both solutions. Indium doping from Te-rich melts, however, has the advantage that the segregation coefficient is near unity.

From a device perspective, its performance is dependent on the electrical, optical and mechanical characteristics of the epitaxial layers. For IR FPA, the dislocation count controls the number of defective pixels. Typical etch pit (chemical etched decoration of dislocations) densities for LPE layers grown from a Te-rich melt onto a CdZnTe substrate are in the $3\text{-}7\text{E}4/\text{cm}^2$ range [27]. These defects are associated with threading dislocations that are normal to the epilayer surface. Compositional uniformity of $x=0.223 \pm 0.001$ has been demonstrated over areas ranging from 43-54 cm^2 . For a series of 200 growth runs, the run-to-run reproducibility in composition of $x=0.226 \pm 0.0033$ has been demonstrated [28].

4.1.4. Metal-Organic Chemical Vapor Deposition (MOCVD)

In general, MOCVD growth of MCT depends on transporting the elements Cd and Te (and dopants In, I and As) at room temperature as volatile organometallics. These species react with Hg vapor in the hot gas stream above the substrate or catalytically on the substrate surface at about 400 °C. The pyrolytic nature of the reaction requires that only the substrate be heated to ensure efficient deposition. In practice, the growth of MCT by MOCVD using dimethyl cadmium (DMCd) and diethyl telluride (DETe) is accomplished by two processes: a) CdTe synthesis from DMCd and DETe, and b) formation of HgTe from DETe and Hg at the heated substrate.

The challenge with this growth technique is to control the composition of the epitaxial layer and achieve uniformity over large surface areas. MOCVD-MCT composition is influenced by substrate temperature, DMCd and Hg partial pressures. Compositional control and layer uniformity are addressed using the inter-diffused multilayer process (IMP) technique in which very thin layers (0.1-0.2 μm) of HgTe and CdTe are deposited sequentially. These layers, with high diffusion coefficients, inter-diffuse during growth at about 400 °C to form a homogeneous ternary epilayer with a composition that is controlled by the thickness ratio of HgTe:CdTe layers [29].

The preferred precursor for Te is di-isopropyl telluride (DiPTe) that allows for a reduction in the MCT growth temperature from 400 °C to 350 °C. DiPTe in conjunction with DMCd can allow the deposition CdTe to occur at lower temperatures (300 °C). Doping for MOCVD-MCT layers is straightforward using Group III metals for P-type doping and Group VII halogens for N-type doping. The main morphological problem for MOCVD are macro defects called hillocks, which are caused by preferred (111) growth, nucleated from a particle or polishing defect. Hillocks can cause clusters of defects in focal plane arrays. Orientations 3-4 off (100) are used primarily to reduce both the size and density of hillocks.

The MOCVD technique is used to manufacture high-quality, large-area infrared focal plane arrays for many applications [30]. Consequently, there is a renewed interest in using MOCVD because of its ability to: achieve low surface defect densities, deposit MCT films on large area-

low cost substrates such as GaAs and control N- and P-type doping levels. In comparison to an MBE system, the overall maintenance and operational costs of an MOCVD system is lower.

4.1.5. Molecular Beam Epitaxy (MBE)

Thin film deposition by MBE enables the growth of large area epilayers with sophisticated multilayer structures having abrupt and complex compositions and doping profiles. Growth of MBE-MCT is carried out under an ultra-high vacuum environment with Knudsen-type effusion source cells charged with Hg, Te₂, and CdTe [31-32]. MBE-MCT deposition temperature plays a critical role in the introduction of extended defects. Typically, growth is carried out at 180 °C–190 °C on (211) CdZnTe substrates.

The low growth temperature and the ability to rapidly shutter the sources are key features that allow MBE to produce sharp interfaces for multilayered IR devices that operate in two or three different spectral bands. The ultra-high vacuum growth chamber allows for in-situ analytical tools to monitor and control the MCT growth process and evaluate the properties of the grown layers [33-34].

At the lower temperature range, a Hg-rich condition prevails at the substrate because the sticking coefficient of Hg increases as the temperature is reduced. The condition with excess Hg results in the formation micro-twins that are detrimental to the performance of the MCT IR focal plane array. Typical etch pit densities (EPD) of material grown under such Hg-rich conditions are high (10^6 – 10^7 cm⁻²). If the growth temperature is raised to about 190 °C, then a deficiency of Hg leads to the formation of voids in the MCT layer.

Hg is incorporated in the film only by reacting with free Te, thus the MCT composition is contingent on the Te to CdTe flux ratio. The structural perfection of the film depends strongly on the Hg to Te flux ratio and growth is usually restricted to a tight temperature range. By optimizing the Hg to Te flux ratio, the concentration of voids is about 100 cm⁻² which may be attributable to dust particles or substrate related imperfections. The EPD values for epilayers grown under these conditions are in the low 10^5 cm⁻² ranges.

Indium is the most widely used N-type extrinsic dopant in MCT epitaxial layers and is well activated. At low Indium doping levels, Hg vacancies can compensate some of the N-type impurities and affect dopant control. P-type dopants, such as Arsenic, are less conveniently incorporated into the epilayer. Significant efforts are being expended to improve the incorporation of As and Sb during the MBE process and to reduce the temperature required for activation. The metal saturation conditions cannot be reached at the temperatures required for high-quality MBE growth. The necessity to activate acceptor dopants at high temperatures diminishes the gains of low-temperature deposition. Nearly 100% activation has been achieved for a 2×10^{18} cm⁻³ As concentration, with as low as 300 °C activation anneal, followed by a 250 °C stoichiometric anneal [35].

Because of its various advantages, MBE-MCT technology is becoming more attractive than the other epitaxial technologies and is required for the fabrication of IR detectors with advanced architectures. The MBE-MCT technology has developed to the point where MBE lay-

ers grown on bulk CZT substrates exhibit characteristics comparable to those prepared by LPE. MBE technology is now routinely used for multicolor detector arrays.

The main challenge of MBE-MCT technology is to grow very high quality layers on low-cost, large-area substrates. The issues that complicate MBE growth on alternative large-area substrates are: lattice mismatch, nucleation phenomena, thermal mismatch, and contamination [36-37]. Sapphire, Si, and GaAs are some of the low-cost, large-area materials that have been successfully employed as substrates for MCT epitaxial growth [38-41]. However, appropriate buffer layers of CdTe or CZT are required on the alternative substrates before MCT films are deposited.

The best MBE-MCT layers grown on buffer/Si substrates achieved thus far exhibit defect densities of $2\text{-}5 \times 10^6 \text{ cm}^{-2}$. Novel thermal cycle annealing schedules have been used to further reduce the defect density. More effort is necessary to reduce this defect density by at least an order of magnitude to make MBE based materials for many military applications. The ability to grow MCT on large diameter Si wafers will enable low cost, large format infrared focal plane arrays.

5. SWIR Detector Technologies

The SWIR band (0.9-2.5 μm) bridges the spectral gap between the visible and thermal bands in the electromagnetic spectrum. In this spectral band, the primary phenomenology of interest is the reflectance signature of the target, manifested as either its variations in brightness or spectral reflectance, or both.

Infrared imaging in the SWIR band offers several advantages: can detect reflected light, offering more intuitive, visible-like images; better suited for imaging in adverse environments and weather conditions, including fog, dust, and smoke; can also see in low light conditions, and use eye safe 1550 nm illumination that is totally undetectable by regular night vision equipment; and can generate digital video outputs and thus offering more advantages than traditional image intensifier night vision equipment. Under low light conditions, the sensitivity of the focal plane array is ultimately determined by the $R_0 A$ product of the photodiode.

5.1. $\text{In}_x\text{Ga}_{1-x}\text{As}$ Detector Array Development

For SWIR imaging, InGaAs is one of the widely used detector materials due to its low dark current. The detector material can be prepared using any of the following techniques: Molecular beam epitaxy (MBE), metal-organic chemical vapor deposition (MOCVD), liquid phase epitaxy (LPE), hydride-transport vapor phase epitaxy (VPE), and atomic layer epitaxy (ALE). InGaAs layers are typically grown on lattice matched InP substrates using an alloy composition of $x = 0.53$.

The spectral response typically covers 0.9-1.7 μm at room temperature. By increasing the composition to $x=0.82$, InGaAs is able to extend its cutoff to 2.6 μm . However, the crystal

defects due to epitaxy and the decreased shunt resistance, due to a smaller band gap, degrade performance at the longer cutoff wavelengths.

The band gap [42] of the strained $\text{In}_x\text{Ga}_{1-x}\text{As}:\text{InP}$ structure can be tailored by varying the alloy composition during crystal growth according to the equation:

$$E_g \text{ (eV)} = \left(E_{g_{\text{GaAs}}} - \frac{\alpha_{\text{GaAs}} T^2}{T + \beta_{\text{GaAs}}} + \left(E_{g_{\text{InAs}}} - \frac{\alpha_{\text{InAs}} T^2}{T + \beta_{\text{InAs}}} - E_{g_{\text{GaAs}}} + \frac{\alpha_{\text{GaAs}} T^2}{T + \beta_{\text{GaAs}}} \right) x - 0.475x(1-x) \right) \quad (7)$$

Where E_g is the band gap in (eV), α and β are fitting parameters, and x is the In:As ratio. The cut-off wavelength can be calculated from the expression $\lambda_{\text{co}} = hc / E_{\text{gap}}$.

The response can be extended to include the visible wavelength range by removing the InP substrate. There has been an intensive effort to develop InGaAs arrays for Low Light Level (LLL) SWIR imaging [42-47]. An example is in astrophysical space based observatories that are very demanding on the detectors due to the very low IR flux levels. Such low flux levels represent the detection of few photons over long integration times and, therefore, require extremely low dark current photodiodes hybridized to a high performance ROIC stage. For such LLL applications there are challenges ahead to further lower noise, reduce pixel size, fabricate larger arrays, achieve higher operating temperatures, and reduce production cost.

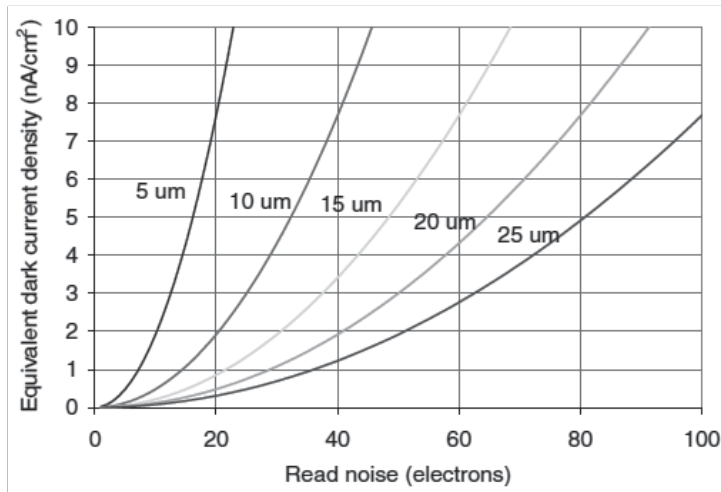


Figure 5. Dark current density versus read noise for different pixel pitches [46].

The spectral response of InGaAs diodes at room temperature is in the $0.9 - 1.67 \mu\text{m}$ wavelength range which matches the ambient night glow spectrum. Imaging under such low light conditions requires that the noise of the detector be extremely low. A significant portion of the noise is contributed by the dark current of the InGaAs detector and the readout

noise. Dark current consists of unwanted thermally generated carriers that can cause the detector to produce a random varying output signal.

It is associated with interfacial, diffusional, G-R, and tunneling currents. The temperature dependence of the dark current is primarily due to the intrinsic carrier concentration which depends exponentially on the temperature. The dark current of the detector can be reduced through appropriate fabrication processes and device design. The impact of dark current noise as a function of read noise is shown in Figure 5, where the curves for different pixel pitch map the dark current noise into an equivalent read noise.

For a given read noise, the required dark current density increases as the pixel pitch is decreased. The challenge is to maintain a low dark current density as the pixel pitch is reduced. Simultaneously, the challenge for the read out circuit is to reduce the read noise. If the limitation is due to the detector and its noise level overwhelms the source signal, the solution may be to use an external illuminator or cool the detector. The choice of either solution will depend on a tradeoff between size, weight, and power requirements (SWaP).

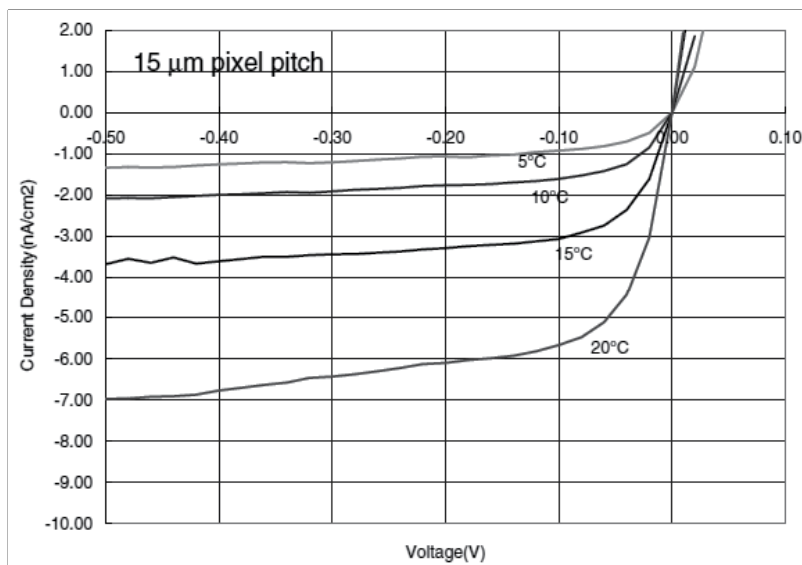


Figure 6. Dark current density at different temperatures using test structures on the wafer. Test arrays have 225 pixels (15 μm pitch) and the guard ring is not biased [46].

Applications involving situational awareness require FPAs to have more pixels (large format/high resolution) for increased surveillance coverage. For soldier portable and some airborne platforms, it is desirable to reduce the size of the pixel in order to satisfy the constraints of low SWaP and cost, without sacrificing performance. However, as the pixel pitch is scaled to smaller geometries, there is a tendency for the dark current density to increase. The reduced pixel diameter can cause the sidewall related dark current to become more pronounced and overwhelm the area related contribution, resulting in

an effective increase in the dark current density. The sidewall contribution can be avoided with appropriate surface passivation of the exposed PN junction.

As mentioned above, the dark current of the detector can be reduced through appropriate fabrication processes and device designs. By focusing on the growth conditions for the InGaAs absorption layer, heterointerfaces and the passivation layer, researchers have been able to demonstrate dark current densities below 1.5 nA/cm^2 at 7°C and a bias of 100 mV for $15 \mu\text{m}$ pitch InGaAs arrays as shown Figure 6.

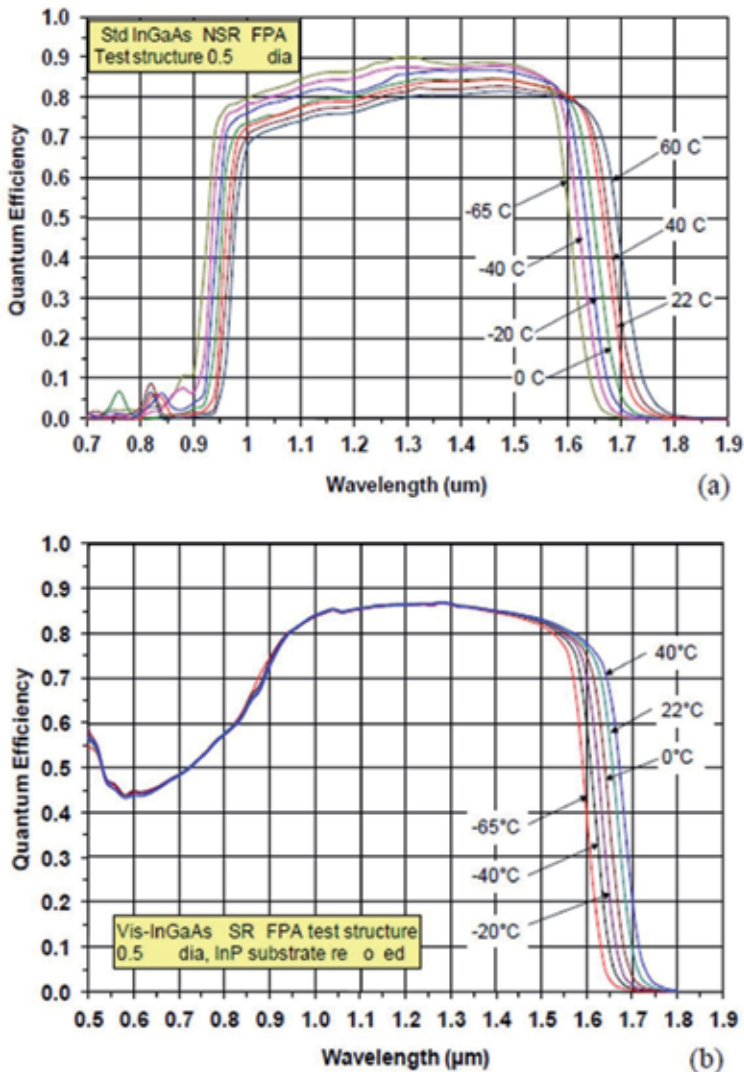


Figure 7. Spectral QE vs. wavelength at different temperatures measured for backside illuminated InGaAs photodiodes test array demonstrating Visible-Near IR response with a) InP substrate not removed and b) InP removed [47].

To achieve the constraints of low SWaP and cost, manufacturers are now developing InGaAs detectors on 4" diameter wafers. For example, 16 - 1280x1024 InGaAs arrays with 15 μm pixels have been demonstrated on 4" InP wafers. To extend the spectral response of these detector arrays down to the UV band, the InP substrates are removed [47]. The test results for a backside illuminated 0.5 mm InGaAs detector is shown in Figure 7 [47]. The Quantum Efficiency (QE) achieved across the 1.2-1.6 μm band is about 80 % over a temperature range of -65 °C to 40 °C. As a result of removing the InP substrate (see Figure 7 (b)), the QE is about 40 % over the entire visible band.

Continued effort is underway to demonstrate large format (>2Kx2K) and small pixel (<10 μm) InGaAs FPAs for a variety of room temperature, low light level (LLL) imaging applications, such as night vision. These applications demand extremely low detector dark current and reduced ROIC noise to maintain performance, since the photon collection area is reduced [47].

5.2. SWIR Hg_{1-x}Cd_xTe (MCT) Detector Arrays

Another approach to accomplish SWIR imaging under low light level (LLL) conditions is to use MCT detectors grown by either MBE or LPE techniques. For Hg_{1-x}Cd_xTe, the alloy composition can be fixed to provide an energy band gap equal to the longest wavelength to be measured in the SWIR band. The larger energy band gap enables higher operating temperatures; MCT arrays operating at near 150 K have achieved BLIP limits at background levels as low as 10¹¹ photons/sec/cm² [48]. There are continued efforts to increase the operating temperature of SWIR MCT detectors [49].

To operate in the SWIR band, the Cd mole fraction in In Hg_{1-x}Cd_xTe is tailored to the appropriate energy band gap [50] according to the expression:

$$E_g(eV) = -0.302 + 1.930x + 5.35 \times 10^{-4}T(1 - 2x) - 0.810x^2 + 0.832x^3 \quad (8)$$

The absorption coefficient of MCT is very large and in order to have high responsivity, the rule of thumb is that the thickness of the MCT absorber layer should be at least equal to the cutoff wavelength. For the MCT material system, the choice of P-on-N polarity is generally driven by dark current considerations. The presence of Hg vacancies in the P base layer of an N-on-P diode degrades the minority carrier lifetime, resulting in larger dark currents. Nevertheless, to meet very low dark current requirements, diodes can be cooled down to very low temperatures at the expense of SWaP.

Figure 8 presents results for ion implanted P-on-N (MBE with N_D= 1E¹⁶ cm⁻³, 4-μm thick) and N-on-P (LPE with N_A=3-5E¹⁶ cm⁻³, 7 μm thick) diodes fabricated on lattice matched CZT in order to ensure a low dislocation density (mid 10⁴/cm²). Diodes are based on planar technologies, with CdTe and ZnSe passivation layers [51]. Very low, state of the art dark currents are observed over a wide temperature range as shown in Figure 8.

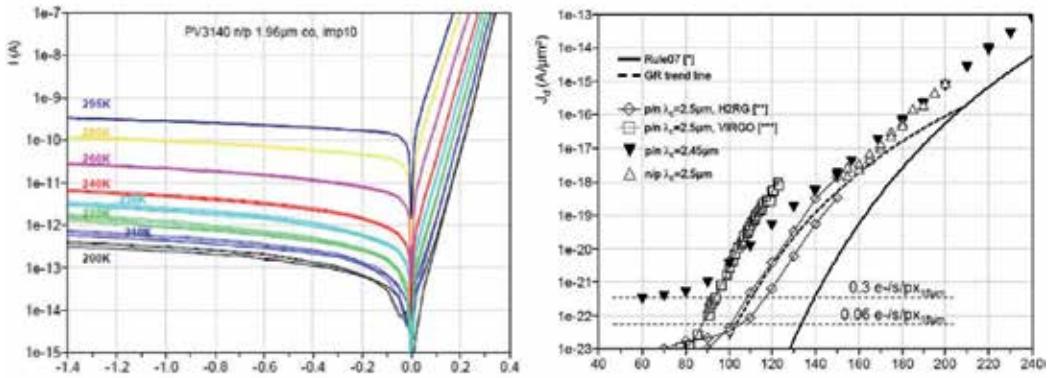


Figure 8. a) I-V curves measured on isolated 10 μm N-on-P implanted diodes; Cutoff=2.0 μm. b) Measured dark currents and comparison with literature data at 2.5 μm cut-off [51].

5.3. Si_{1-x}Ge_x(SiGe) Detector Arrays

Like the other two alloy semiconductors mentioned above, SiGe is another example of material that can be used for the fabrication of SWIR detectors. The key attractive feature of SiGe IR detectors is that they can be fabricated on large diameter Si substrates with size as large as 12-inch diameter using standard integrated circuit processing techniques. Furthermore, the SiGe detectors can be directly integrated onto low noise Si ROICs to yield low SWaP, low cost and highly uniform IR FPAs. The primary motivation for SiGe SWIR FPA development is the CMOS-like fabrication allowing for very low cost technology.

Some of the earlier attempts in developing SiGe IR detectors focused on their LWIR applications by using internal photoemission [52-53]. Renewed efforts are now developing these detectors for application in the NIR-SWIR band [54]. For the SiGe material to respond to the SWIR band, its cutoff wavelength is tuned by adjusting the SiGe alloy composition. Si and Ge have the same crystallographic structure and both materials can be alloyed with various Ge concentration. The lattice constant of Ge is 4.18% larger than that of Si, and for a Si_{1-x}Ge_x alloy ("a" for alloy) the lattice constant does not exactly follow Vegard's law. The relative change of the lattice constant is given by [55]:

$$a_{Si_{1-x}Ge_x} = 0.5431 + 0.01992x + 0.0002733x^2 \text{ (nm)} \tag{9}$$

For a Si_{1-x}Ge_x layer with x > 0 on a Si substrate means that the layer is under compressive stress. A perfect epitaxial growth of such a strained heteroepitaxial layer can be achieved as long as its thickness does not exceed a critical thickness for stability. Beyond the critical thickness, the strain is relaxed through the formation of misfit dislocations, which can cause an increase in the dark current. Several approaches have been proposed to reduce the dark current in SiGe detector arrays by several orders of magnitude. These include fabrication methodologies, de-

vice size and novel device architectures, such as Superlattice, Quantum dot and Buried junction designs [54]. Furthermore, some of these approaches have the potential of extending the wavelength of operation beyond 1.8-2.0 microns. The challenge is to take advantage of these innovative device designs and reduce the dark currents to 1-10 nA cm⁻².

A proposed diagnostic device structure to evaluate the impact of various fabrication methodologies to reduce leakage currents and produce higher detector performance in SiGe/Si is shown in Figure 9. The structure can help to assess the following: ability to grow high quality/low defect density Ge on Si; layer thickness necessary for minimal topological and defect density requirements; isolation of defect states at the Ge/oxide interface from the signal carrying layers; and optimum doping and thickness of the P-type Ge layer under the oxide to isolate interface states and lateral leakage current that could result between the highly doped N⁺ Ge region used for contacts and the lighter doped P-type Ge region.

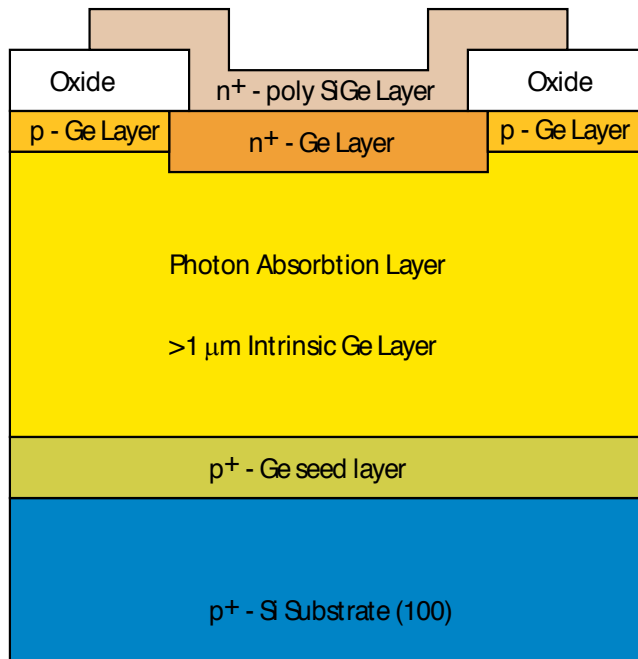


Figure 9. SiGe/Si diagnostic structure to evaluate impact of various fabrication methodologies.

Dark currents in SiGe detectors can be reduced by reducing the pixel size, since dark currents track with the volume of the pixel. Reductions in size are advantageous for resolution; however, for low light level conditions, such as nightglow, a large pixel size or at least a large collection area is required. The I-V characteristics of photodiodes with different areas fabricated on 2 μm thick intrinsic epitaxial Ge layers are shown in Figure 10(a). The curves indicate that the dark current is lowered as the device area is reduced. The responsivity as a function of wavelength for a 100 μm x 100 μm diode without an anti-reflection coating is given in Figure 10(b). The reverse leakage current at a reverse bias of 1 vol is 32 mA/cm².

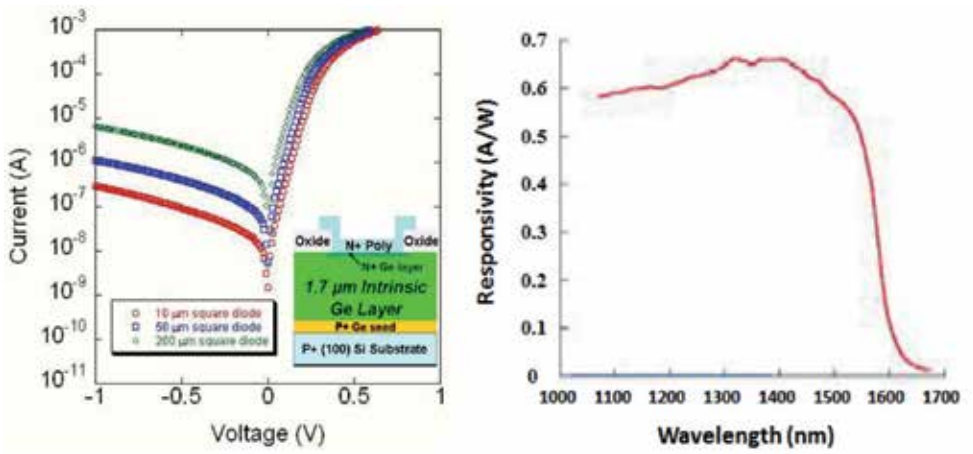


Figure 10. a) Measured room temperature I-V characteristics for large area diodes with 20, 50 and 200 micron unit cell. The inset shows the schematic device cross section. b) The spectral response data for SiGe detector [56].

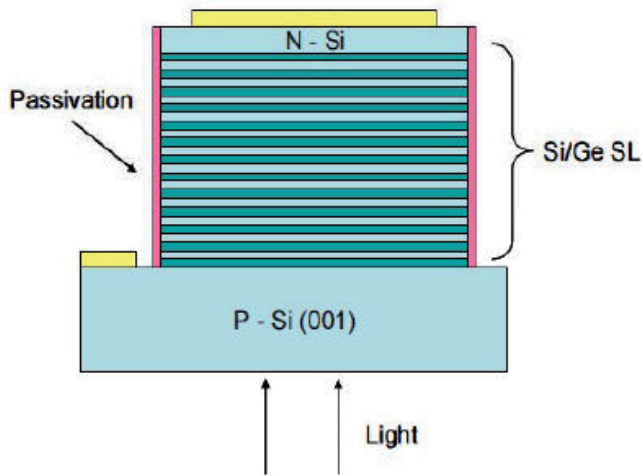


Figure 11. Schematic of detector array structure consisting of a SiGe /Si strained layer Superlattice grown on (001) silicon [54].

Figure 11 shows the Strained-Layer Superlattice (SLS) structure being evaluated for longer detector array response to 2 microns. It consists of SiGe quantum wells and Si barrier layers, grown on p-type (001) Si substrates. Super lattices having differing Si barrier and Ge well thicknesses to control the strain are grown to optimize wavelength response and dark current. The SiGe well thicknesses are kept below the critical layer thickness for dislocation formation. To complete the structure, the undoped superlattice is capped with a thin n+ Si cap layer to form the p-n junction. After growth the devices are patterned with a top contact,

mesas are etched to provide isolation and the substrate contact is formed. The etched mesa can also be passivated to minimize surface recombination as indicated in Figure 11. The device shown in Figure 11 uses substrate sideillumination, as is needed for use in FPA arrays, and short wavelength response can be improved by thinning the Si substrate.

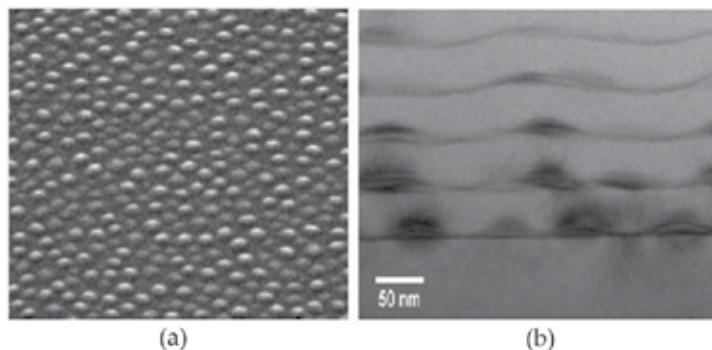


Figure 12. (a) SEM image (45° tilt) of a Ge QD layer deposited on Si. The QDs are ~60 nm in diameter with a density of 10^{20} /cm². (b) Cross-sectional TEM image of Ge/Si QDSL. Ge QDs appear with dark contrast compared to Si barriers [54].

The strained-layer superlattice and quantum dot superlattice (QDSL) in the SiGe material system have the potential of developing Vis-NIR detector arrays with longer cutoff wavelength and potentially lower dark current. The advantage of quantum dots is the potential to exploit the optical properties of Ge while avoiding dislocation formation. Ge QDs grown on Si in Stranski-Krastanov mode can be deposited well beyond the critical thickness without dislocation nucleation [56].

Figure 12 (a) shows the SEM image of an array of Ge nanodots grown by MOCVD. These dots are typically 50-75 nm in diameter with area coverage of ~20%. To increase optical absorption and sensitivity, MOCVD-based growth techniques are being developed for the deposition of Ge/Si quantum dot superlattices (QDSLs), where Ge QDs are alternated with thin (10-30 nm) Si barrier layers. A cross-sectional TEM image of QDSLs is shown in Figure 12(b).

6. MWIR/LWIR Detector Array Technologies and Applications (InSb, HgCdTe, HOT, SLS and Bolometers)

Most objects in earth's environment emit radiation in the MWIR/LWIR wavelength range, commonly referred to as the thermal band. For example, the human body, by virtue of being at a temperature of ~300K, emits radiation that peaks around 10 microns. Also, most chemical species have spectral signatures in this infrared regime due to fundamental absorption processes associated with vibrational states of the molecules. Thus, in many applications that require the observation and identification of chemical species using point detection or standoff detection, such as pollution monitoring, gas leak detection, gas sensing and spec-

troscopy, one needs to work in the MWIR/LWIR bands. Another distinct advantage is that the atmosphere has clear transmission windows in the MWIR and LWIR bands, making it very attractive for terrestrial applications.

6.1. InSb Detector Array

InSb detector arrays have found many applications in MWIR due to their spatial uniformity, low dark current and image quality. This technology has evolved over the years in response to the stringent requirements for applications in missile seekers and missile warning systems (MWS) [57-58]. For these applications, the IR imagers need to exhibit high dynamic range, fast frame rates, high resolution, very wide fields of view (FOV), and high sensitivity. The wide FOV optical design must consider the large incident angle of incoming photons, which if not included, can cause the appearance of ghost images and imaging of strong illumination sources outside the FOV. High spatial resolutions are achieved by using large arrays (640x512 and 1280x1024) with small pixels (unit cell size of 15 μm). The bandgap of this binary alloy is relatively constant and cannot be varied much as is the case with HgCdTe or SLS devices. Hence, to use InSb for high sensitivity multicolor applications requires the incorporation of filters to select bands of interest.

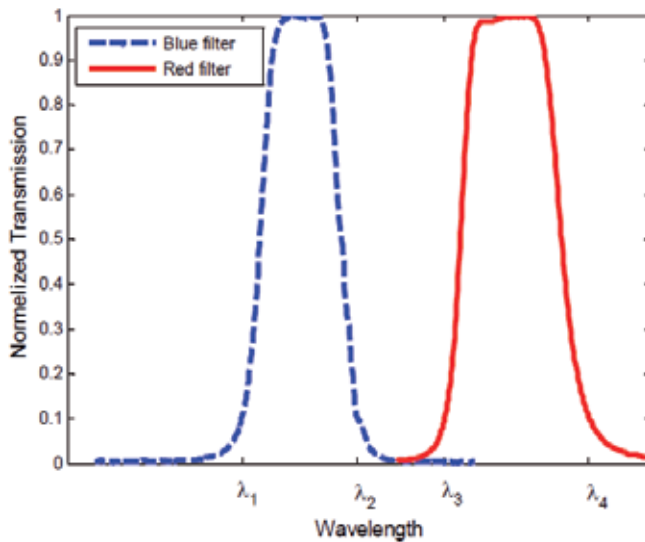


Figure 13. Normalized transmission of the cold filter in MWIR bands that are commonly referred to Blue (MWIR -1) and Red (MWIR-2) [58].

Many of the missile applications in the MWIR band require the use of two color InSb detectors, in order to discriminate the missile signature from the clutter background and reduce the false alarm rate. One band detects the target while the other band subtracts the background for noise suppression. The actual wavelength bands in 3-5 micron range vary from application to application [58].

Figure 13 presents the transmission of the integrated InSb sensor with cold filters for the two MWIR bands that are commonly referred to as the blue band (shorter wavelength) and the red band with the longer spectral response. The optical coatings on the detector arrays and the optics are designed for maximum transmission and to minimize the spectral crosstalk between the bands, typically less than 0.1%, as can be seen in Figure 13.

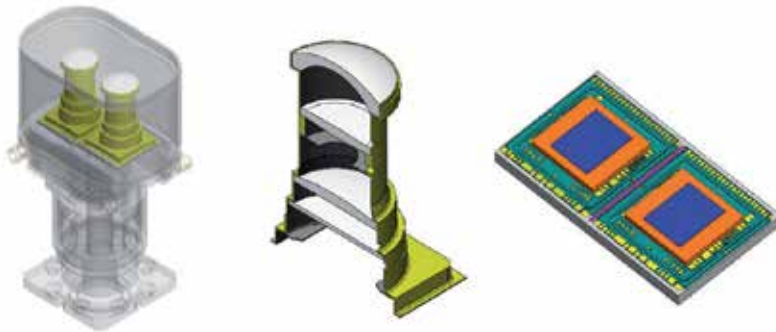


Figure 14. Dual-color Integrated Detector Cooler Assembly (IDCA) with two InSb FPA's and two cold radiation shields with integrated optics [58].

Figure 14 presents the schematics of various key building blocks for a Dual-color Integrated Detector Cooler Assembly (IDCA) with two InSb FPA's connected to their circuit card assemblies. Each of the InSb focal plane arrays has been optimized for the blue and red bands of interest in the broad MWIR region. As a dual band system, both FPA's can operate simultaneously at high frame rates.

6.2. Multicolor HgCdTe (MCT) Detectors Arrays for MWIR/LWIR Applications

MCT is the material of choice for a variety of high performance IRFPA systems for a variety of defense and commercial applications. Many of these applications use state-of-the-art HgCdTe growth using a bulk Cadmium ZincTelluride (CdZnTe) substrate. However, as the push for larger array sizes continues, it is recognized that an alternative substrate technology for large area needs to be developed for HgCdTe IRFPAs.

A significant effort has been under way in developing CdTe/Si or GaAs as a desired substrate. This substrate technology has been successful for short-wavelength (SWIR) and mid wavelength (MWIR) focal plane arrays; current HgCdTe/Si material quality is being further developed for long-wavelength (LWIR) arrays, due to the high density of dislocations present in the material [59]. To remedy the high dislocation counts, researchers are focusing on both composite substrate development and improvement, and on HgCdTe/Si post-growth processes [60]. The impact of ex-situ annealing on the quality of the epitaxial surface is shown in the Figure 15 for HgCdTe/Si substrates. Several groups have demonstrated HgCdTe/Si material with dislocation density measuring $1 \times 10^6 \text{ cm}^{-2}$. This is a five times reduction in the baseline material dislocation density that is currently used in the fabrication of devices.

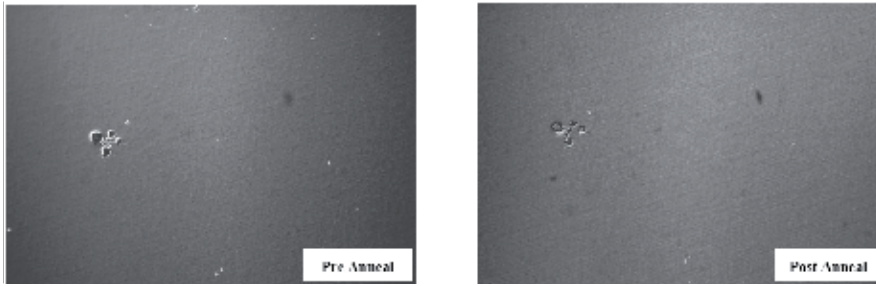


Figure 15. Optical microscopy images of the HgCdTe/Si before and after ex-situ cycle annealing. Note the landmark defect used to identify the same area of material for both pre and post anneal images [59].

| | Substrate Technology | | |
|----------------------------------|-------------------------|-----------------------|-----------|
| | Bulk CdZnTe | Si | Advantage |
| Maximum size | 7 x 7 cm ² | 6 inch diameter | Si |
| Maximum area | ~50 cm ² | ~180 cm ² | Si |
| Scalability | No | Yes | Si |
| Cost | \$220/cm ² | ~\$1/cm ² | Si |
| Thermal match to Si ROIC | No | Yes | Si |
| Robustness | Brittle | Hard | Si |
| Lattice match to MCT | Yes | No | CZT |
| Surface | Smooth | Smooth | None |
| Orientation available | (112) | (112) | None |
| Vendors | 1 (foreign) | Numerous (domestic) | Si |
| Substrate quality (dislocations) | < 10000 cm ² | < 100 cm ² | Si |
| Impurities | Low | Extremely low | Si |

Table 1. Advantages of Si-based composite substrate technology for HgCdTe material development [59].

Table 1 highlights the advantages for transitioning away from a bulk CdZnTe substrate technology for large area HgCdTe IR detectors and focal plane arrays. Past effort has focused on using a Si-based composite substrate technology, specifically CdTe/Si, for HgCdTe material development. As shown in Table 1, Si has better attributes with respect to bulk CdZnTe in every category except for lattice and thermal matching to HgCdTe. The lattice mismatch between Si and HgCdTe is 19.3% and has proven to be a significant challenge to overcome. To address this issue, a great effort within the HgCdTe community has been expended on developing MBE grown CdTe/Si as a composite substrate for subsequent HgCdTe growth. Much research and investigation has gone into understanding and improving the surface passivation, nucleation, buffer layer growth, and material characterization of CdTe/Si material itself. Currently, CdTe (112)/Si (112) is of extreme high quality with x-ray rocking curve full width at half maximum (FWHM) values measuring less than 60 arcsec for an 8 μm thick epilayer [59]. Significant efforts are also being expended in developing HgCdTe on GaAs substrates.

Both composite substrate development, whether it is using Si, GaAs or some other alternative substrate system, and HgCdTe material improvement are active areas of study within the Infrared community. In fact, it might be a combination of techniques currently being developed that ultimately lead to HgCdTe grown on scalable alternative substrates supplanting HgCdTe grown on bulk CdZnTe substrates for large area array applications [60].

Figure 16 shows a HgCdTe/Si FPA architecture hybridized via indium interconnects to the silicon Readout Integrated Circuit (ROIC). The FPA in Figure 16 consists of MBE grown HgCdTe single band detector arrays with in-situ doped, P-on-N architecture fabricated on a 6-inch silicon substrate.

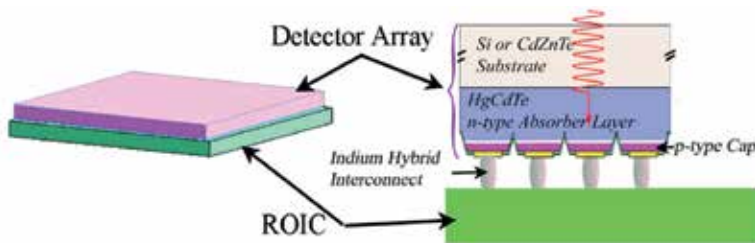


Figure 16. Architecture of an IRFPAs made with HgCdTe/Si hybridized to a Read Out Integrated Circuit (ROIC) [61].

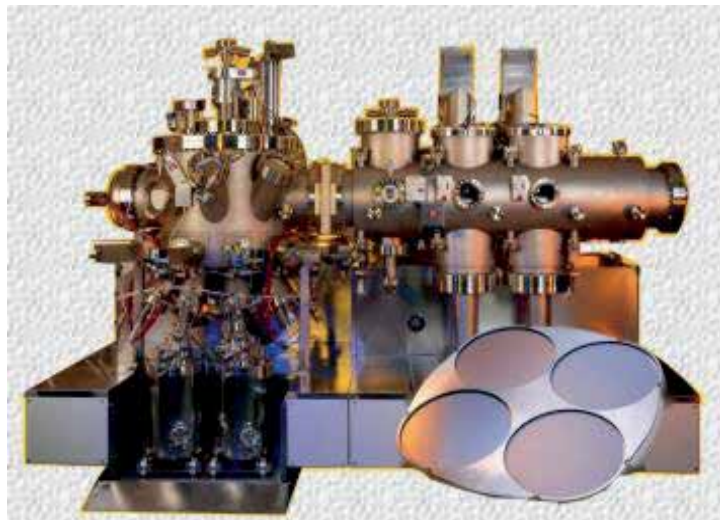


Figure 17. VG V100 Molecular Beam Epitaxial System

Using MBE system (see Figure 17), researchers produced epitaxial HgCdTe layers on (211) Si substrates with very low macro defect density and uniform Cd composition across the epitaxial wafers. These HgCdTe/Si composite wafers have shown growth defect densities less than 10 defects /cm², approximately 100 times better than can be achieved on CdZnTe substrates, due to the better crystalline quality of the starting substrate [61].

The HgCdTe/Si epitaxial substrates with a P-on-N configuration can be fabricated into mesa delineated detectors using the same etch, passivation, and metallization schemes as detectors processed on HgCdTe/CdZnTe substrates. Detector fabrication processes across the full area of 6-inch HgCdTe/Si wafers have routinely produced high performing detector pixels from edge to edge of the photolithographic limits across the wafer, offering 5 times the printable area as compared with 6×6 cm CdZnTe substrates. Large-format (2K×2K) MWIR FPAs fabricated using large area HgCdTe layers grown on 6-inch diameter (211) silicon substrates demonstrated NEDT operabilities better than 99.9% (see Figure 18). SWIR and MWIR detector performance characteristic on HgCdTe/Si substrates are comparable to those on the established HgCdTe/CdZnTe wafers. HgCdTe devices fabricated on both types of substrates have demonstrated very low dark current, high quantum efficiency and full spectral band fill factor characteristic of HgCdTe [61].

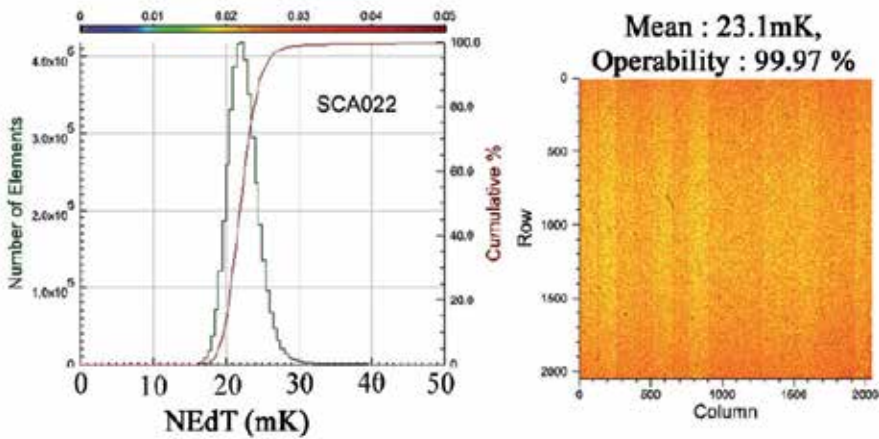


Figure 18. NEDT measured from 2K×2K HgCdTe/Si MWIR HgCdTe/Si FPA with 15 micron unit cell demonstrating better than 99.9% operability [61].

6.2.1. HgCdTe on Silicon Two-Color IRFPAs

As noted above, the motivation for HgCdTe growth on large-area Si substrates is to enable larger array formats and potentially reduced FPA cost compared to smaller, more expensive CdZnTe substrates. In addition to the successful demonstration of single color IRFPA on composite HgCdTe/Si substrates, researchers produced MWIR/LWIR dual band FPAs on large area Si substrates. The device structure is based on a triple-layer N-P-N heterojunction (TLHJ) architecture grown by molecular-beam epitaxy (MBE) on 100 mm (211) Si wafers with ZnTe and CdTe buffer layers [62]. The MWIR/LWIR dual band epitaxial wafers have low macro defect densities (<300 cm⁻²). Inductively coupled plasma etched detector arrays with 640×480 dual band pixels (20 μm) are mated to dual-band readout integrated circuits (ROICs) to produce FPAs (see Figure 19). The measured 80 K cutoff wavelengths are 5.5 μm for MWIR and 9.4 μm for LWIR, respectively. The FPAs exhibit high pixel operabilities in

each band, with noise equivalent differential temperature (NEDT) operabilities of 99.98% for the MWIR band and 99.6% for the LWIR band at 84 K [62].

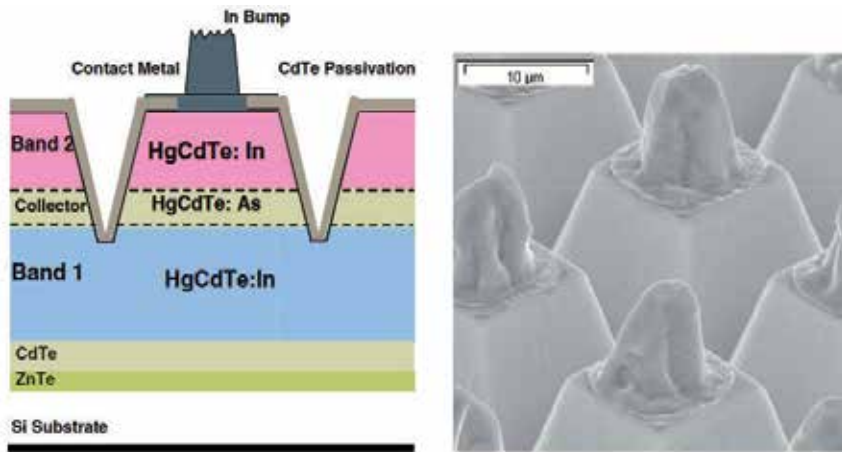


Figure 19. Cross-section of single-mesa dual-band detector architecture applied to HgCdTe on Si (Left). Shown on the Right is Scanning electron micrograph of 20-micron-unit-cell dual-band detectors array [62].

6.3. High Operating Temperature (HOT) Detectors

High performance MWIR and LWIR FPAs are normally cooled to cryogenic temperatures at about 80 K, in order to suppress the dark current noise from overwhelming the photo-generated signals. If the operating temperature of the FPA is increased without degrading image quality, then smaller coolers can be used and the SWaP and cost of the system could be reduced. Of course, a more significant advantage can result if the operating temperature is increased to > 200 K where a low cost thermoelectric cooler can be implemented. There is a growing effort to increase the operating temperature of MWIR and LWIR infrared detectors by: reducing leakage currents; reducing thermal generation rates in the active region and minimizing the active volume of the detector without reducing quantum efficiency. While a number of strategies can be used to achieve high operating temperature (HOT) detectors, a recent DARPA program (AWARE-Broadband) focused on reducing detector material volume via a photon trap/photonic crystal approach to reduce dark current without degrading quantum efficiency [63-64].

The principle of volume reduction is demonstrated in Figure 20 which illustrates the effect of reducing the fill factor on device performance for a baseline shrinking mesa and an idealized photon trap detector. The fill factor is defined as the volume of material remaining divided by the volume of the unit cell. The mesa reduction in volume initially reduces the NEDT as noise generating volume is removed, until the volume removed causes the signal to be reduced relative to the noise. Two types of IR photon trapping structures have been investigated: In AsSb pyramidal arrays and HgCdTe pillars and holes. Photon trap detectors on MBE HgCdTe/Si epitaxial wafers (see Figure 21) exhibit improved performance com-

pared to single mesas, with measured NEDT of 40 mK and 100 mK at temperatures of 180 K and 200 K, with good operability. Large format arrays of these detectors exhibit cut-offs from 4.3 μm to 5.1 μm at 200 K. For the In AsSb pyramidal arrays, the measured dark current at the bias for peaked QE is in the low 10^{-3} A/cm² range at 200 K and low 10^{-5} A/cm² range at 150 K [64]. The general nBn band diagram and the dark current density curves at various temperatures are shown in Figure 22a and b, respectively. The I-V curves shown in figure 22b are from anCBn design, where the C stands for compound.

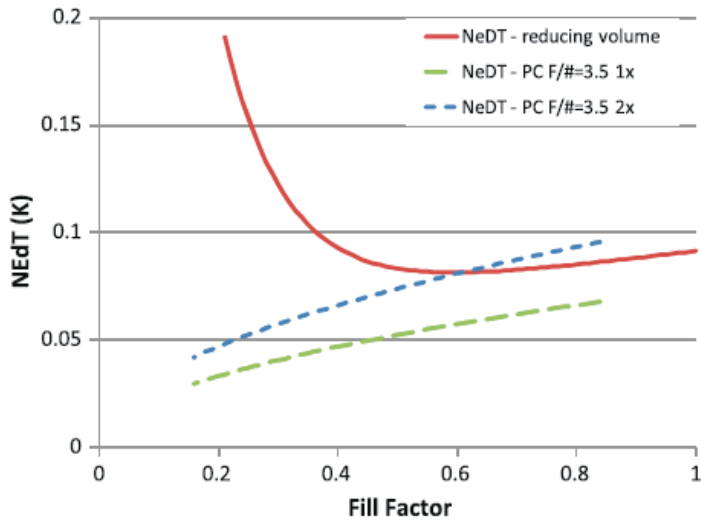


Figure 20. NEDT for a HgCdTe detector with a 5 μm cutoff at 200 K for baseline reducing mesa approach compared with a photonic crystal approach for 1x mean NEDT operability metric and 2x mean NEDT operability metric [63].

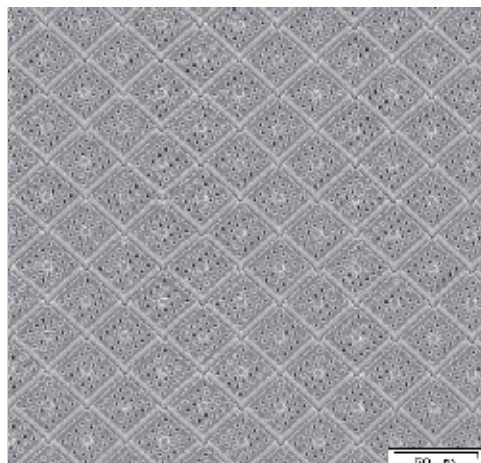


Figure 21. x 512 30 μm array consisting of unit cell design with photonic crystal holes on a 5 μm pitch in a MWIR HgCdTe [63].

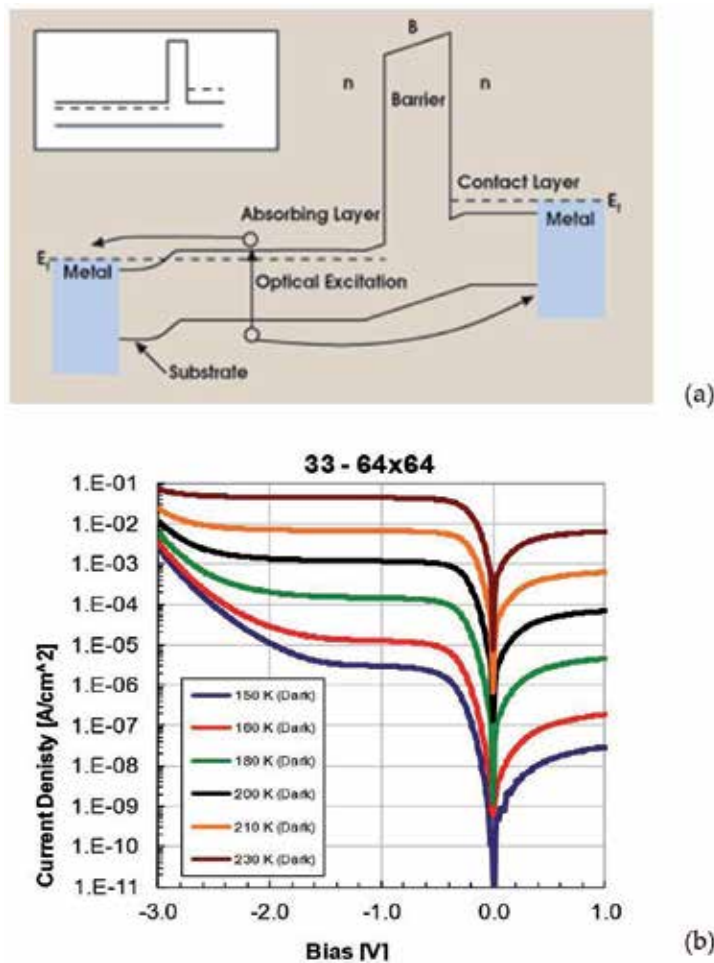


Figure 22. a) nBn band diagram illustrating the carrier flow [http://www.photonics.com/Article.aspx?AID=27744]. b) Dark current density curves as a function of temperature for an nCBn pyramidal InAs_{1-x}Sb_x detector with a cutoff of 5.05 μ m at 200 K [64].

The nBn [65] detector design consists of a n-type absorption layer, a conduction band offset barrier layer and a n-type contact layer. This design suppresses majority carrier currents (electrons in this case) while maintaining low electric fields. The ideal design would require a flat valence band as shown in the inset of figure 22(a). However, in practice and depending on the choice of materials used, a small valence band offset may or may not exist. The conduction band large potential barrier blocks the flow of electrons while the flat valence band allows easy flow of holes. As a result, the thermally generated majority carrier, which contributes to dark current, is suppressed. Because the nBn architectures suppress the thermal noise, it is very suitable to operate this device at higher temperatures. As mentioned above (also see figure 22(b)), operation as high as 150K with excellent performances have been demonstrated under the DARPA AWARE program.

6.4. Type II Strained Layer Superlattices (T2SL)

Proposed by Smith and Mailhot [66] in 1987, detectors based on InAs/GaSb strained layer superlattice (SLS) have attracted a lot of attention over the past few years as a possible alternative to the II-VI based IR sensors. The motivation for pursuing the III-V based SLS resulted from two major difficulties with LWIR MCT detectors: large tunneling currents and precise compositional control for accurate cutoff wavelengths. The InAs/GaSb SLS is engineered to achieve small bandgap materials with thin repeating layers for enhanced optical absorption and good electrical transport in the growth direction. The SLS structure typically consists of alternating layers with thicknesses varying from 4-20 nm.

These InAs/GaSb heterostructures are characterized by the broken-gap type-II alignment where the conduction band of the InAs layer is lower than the valence band of the GaSb layer as illustrated in Figure 23. The bandgap is the energy difference between the top of the heavy-hole mini-band (HH1) and the bottom of the electron miniband (C1), as indicated in Figure 23. The overlap of electron (hole) wave functions between adjacent InAs (GaSb) layers results in the formation of an electron (hole) minibands in the conduction (valence) band. For IR sensing, optical transitions between holes localized in GaSb layers and electrons confined in InAs layers are employed. As the layer thickness decreases, the wave-function overlap increases causing a more favorable optical absorption. As the thickness is increased beyond about 5 nm, the wavefunction overlap is reduced with a corresponding decrease in optical coupling. The effective bandgap of the InAs/InGaSb SLs can be tailored from 3 μm to 30 μm absorption by varying the thickness of the constituent layers, thus enabling detectors spanning the entire IR spectrum [67-68].

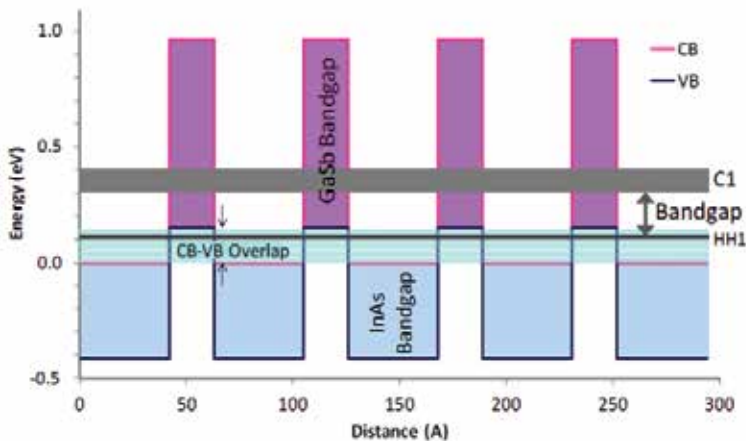


Figure 23. Schematic bandgap alignment of Type II InAs/GaSb superlattices [69].

The effective mass of the charge carriers in the superlattice is not dependent on the semiconductor bandgap, as in the case of bulk materials. The larger effective mass of the electrons and holes in SLs combined with the slower Auger recombination rate can lead to a reduc-

tion of tunneling currents and higher operating temperatures compared to HgCdTe. The large splitting between heavy-hole and light-hole valence sub-bands, due to strain in the SLs, contributes to the suppression of Auger recombination rate. The maturity of the III-V materials technology offers technological advantages to the SLS effort by providing a source of commercially available low defect density substrates and recipes for very uniform processes utilizing large area substrates. This makes detectors based on SLs an attractive technology for realization of high performance single element detectors and FPAs [67-68].

SLS detectors are fabricated with either a p-on-n or n-on-p photodiode design. In either case, the optically active area of the photodiode is defined by an etched mesa as shown in Figure 24 (a). During the mesa isolation process, the periodic nature of the idealized crystal structure ends abruptly at the mesa sidewall surface. Disturbance of the periodic potential function, due to a broken crystal lattice, leads to allowed electronic quantum states within the energy band gap of the SLS resulting in large surface leakage currents. The suppression of these currents is the most demanding challenge for present day SLS technology, especially for LWIR and VLWIR spectral regions, since the dimensions of the SLS pixels have to be scaled to about 20 μm . The limitation imposed by surface leakage currents can be avoided by depositing a stable surface passivation layer onto the mesa sidewall. Currently, there is a lack of a robust passivating material and approach. The proposed approaches include: deposition of polyimide layer, overgrowth of wide band gap material, deposition of passivation sulphur coating electrochemically and post etch treatment in chemical solutions. However, these methods can affect cut-off wavelength of the device or complicate the fabrication process of the detectors [67-68].

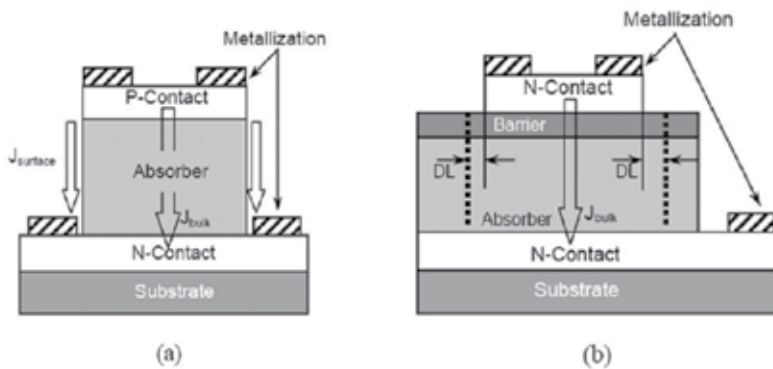


Figure 24. Schematic of (a) conventionally defined mesa (b) shallow etched isolation nBn device. In the latter case, the area is defined by the by diffusion length (DL) of the minority carriers (holes) [68].

A new heterostructure design to limit the surface leakage currents is depicted in Figure 24 (b) as the nBn architecture. Similar to the nBn discussion above, the SLS-nBn design allows for flexibility in employing band-engineered structures. The nBn detector consists of an n-type narrow band-gap contact that is separated from the absorber layers by a 50-100 nm thick, wide band-gap barrier layer. Unlike a conventional photodiode fabrication, the size of the nBn de-

vice is defined by the lateral diffusion length of minority carriers (holes), as illustrated in Figure 24 (b). A 100 K increase in the BLIP temperature has been demonstrated [68]. SLS-based detectors with nBn design and special processing schemes showed dark current reduction of two orders of magnitude (at 77 K) in comparison to conventional photodiode processing techniques. Quantum efficiency and shot-noise-limited specific detectivity are comparable to current SLS-based p-i-n diodes. While nBn detectors have been demonstrated, focal plane arrays based on InAs/GaSb SLS detectors with nBn designs are being developed [68-69].

6.5. Microbolometers

A microbolometer is a resistive element fabricated from a material that has a very small thermal capacity and a large temperature coefficient of resistance (TCR). The absorbed IR radiation is converted into heat which changes the resistance of the microbolometer such that measurable electrical signals can be detected. The spectral response of the bolometer is flat across the IR spectrum, since the sensing mechanism is independent of the photoexcited carriers jumping across an energy band-gap. A schematic representation of a bolometer pixel on top of a ROIC is shown in Figure 25 details of which can be found in reference 70. The pixel design shows a resonant cavity formed by an absorbing layer suspended above a reflecting metal layer. The cavity is used to amplify the absorptance of the incident IR radiation. The microbridge is supported by two beams and is thermally isolated from the ROIC to increase the sensitivity of the microbolometer.

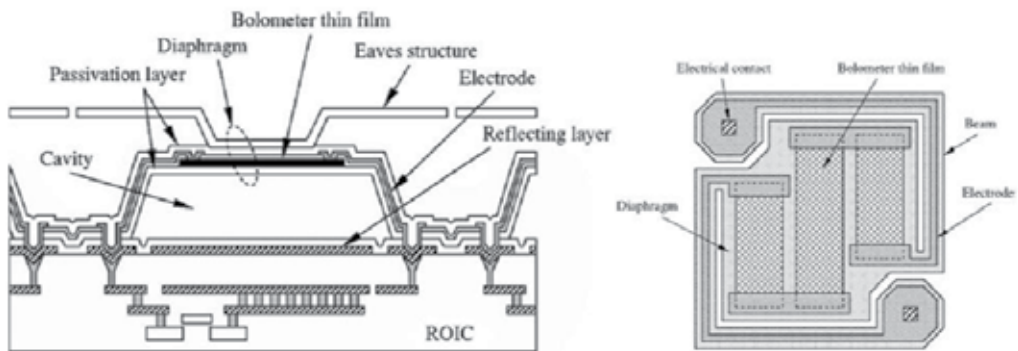


Figure 25. Schematic cross sectional and top views of Microbolometer IR Detector [70].

The microbolometer based on Si-MEMS device structure has been under development for over 20 years with support from DARPA and the Army. Most microbolometer structures utilize VO_x and amorphous silicon thin film technologies. Companies such as Raytheon, BAE Systems and DRS Technologies are developing and producing 17 micron pixels in 640×480 and larger arrays using VO_x [71-72]. L3 Communications and CEA-LETI are developing and producing 640×480 arrays with 17 micron unit cells using amorphous-Silicon technology [73-74]. Figure 26 presents examples of the microbolometer structures using VO_x and amorphous silicon technologies.

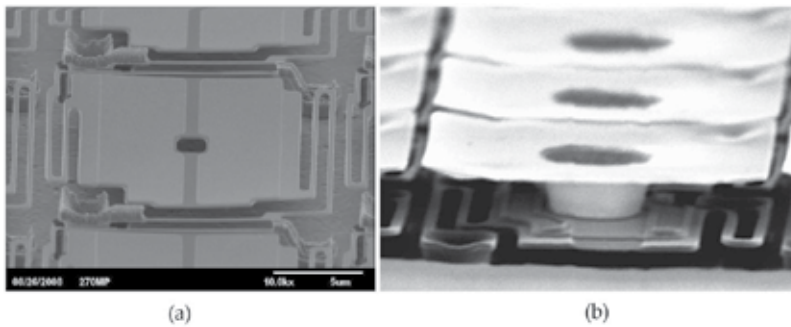


Figure 26. SEM images of a) amorphous Si and b) VO_x microbolometers IR Detector [72-73].

7. Future IR Technology Directions

Further advancement in imaging systems requires solutions for many fundamental and technological issues related to wide field of view (FOV), resolution, pixel pitch, optics, multicolor, form-factor, low SWaP, and low cost. This section highlights two projects currently fielded through the Microsystems Technology Office (MTO) of the Defense Advanced Project Agency (DARPA) to prepare for these advancements. The first is called AWARE (Advanced Wide Field of View Architectures for Image Reconstruction and Exploitation) and addresses several fundamental issues that will enable technologies for wide field-of-view, pixel scaling, broadband and multiband imaging [75-77]. The second project is LCTIM (Low Cost Thermal Imager-Manufacturing) which is addressing a cost effective solution for manufacturing microbolometers.

Traditional detector arrays are typically designed for a narrow band of wavelengths due to inadequate absorption and charge collection from photons with varying wavelengths. Broadband absorption is usually inadequate due to quantum efficiency (QE) roll-off. To design a detector with high QE, low NETD and high operating temperature across a very broad band of wavelengths, say visible to 5 μm range, traditional detector design would be less than optimum. A detector design that can accomplish these goals is based on a photonic pillar-type architecture. Photonic crystals are relatively well understood and have been demonstrated for applications like VCSELs, which are similar to photovoltaic detectors. Sub-wavelengthsize semiconductor pillar arrays within a single detector can be designed and structured as an ensemble of photon trapping units to significantly increase absorption and QE for a wide band of wavelengths. Each sub-element in each pixel can be a 3D photonic structure fabricated using either a top-down or bottom-up process scheme. The sub-element architecture can be of different shapes such as pyramidal, sinusoidal or rectangular [75].

Using unique pyramidal and pillar topologies etched into the photon absorbing layer, researchers have demonstrated 3D photon trapping, achieved significant reduction in dark current and established uniform QE (see Figure 27). This is the first demonstration of broad-

band performance in a single infrared detector using a pillared microstructure in a semiconducting material. The broadband technology has been demonstrated independently in II-VI and III-V based epitaxial materials. This achievement paves the way to replace multiple cameras with one [75]. It also gives the ability for hyper spectral sensing that will enable better target discrimination compared to a single narrow band camera. The high performance at 200 K compared to traditional 80 K operation allows for a smaller SWaP design, since high power and large cryogenic coolers can be replaced by low power miniature coolers. Such cameras would have significant impact on smaller platforms.

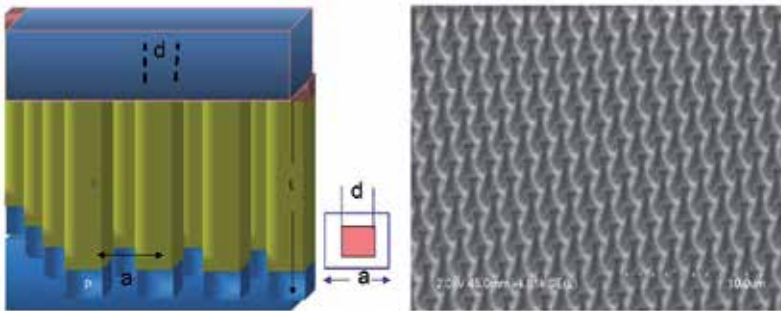


Figure 27. (Left) Illustration of pillared photonic detector architecture; (right) Micrograph of pyramidal PT structure fabricated in epitaxial InAsSb.

The pixel scaling effort is developing very high density LWIR and MWIR FPAs with pixel dimensions approaching the Nyquist- limit. Unlike visible sensors where the pixel size has been reduced to 1.4 μm , the scaling of infrared pixels is much more difficult. As the pixel size is reduced, “bump-bonding”, ROIC, signal integrating capacitor and signal to noise ratio become difficult. Achieving very small pixels however, will enable larger FPAs with small optics and cold shield, better resolution and yielding a huge reduction in SWaP. In one of the approaches, three layers (detector array, ROIC and MEMS capacitor array) are being developed separately, followed by integrating individual cells via indium bumps and through silicon vias (TSV).

To achieve high sensitivity (say $< 30 \text{ mK}$) LWIR FPAs with 5 μm pixels require large amounts of integrated charge to be accommodated in a very small unit cells. For a 5 μm planar unit cell, the charge capacity in standard ROIC technology is less than 1 million electrons, whereas 8 to 12 million electrons are required for good sensitivity – a reason why small pitch IR detectors are not available today. As an enabler for this small pitch LWIR detector, the challenge of charge storage in small pixels is being addressed by fabricating MEMS capacitors suited to a 3D ROIC design. The MEMS capacitor array can be fabricated in a separate 8" wafer. This technology yielded 20 million electrons in a 5 micron unit cell. This breakthrough will pave the way for small pitch FPAs to operate with very high sensitivity. Figure 28(b) shows a Transmission Electron Micrograph (TEM) picture of a portion of the MEMS capacitor array. Using the High Density Vertically Integrated Photodetector (HDVIP) technology, a fully functional 1280X720, 5 μm unit cell LWIR FPA has been dem-

onstrated [75]. The characterization shows excellent results with 99.8 % response operability within 50 % of the median.

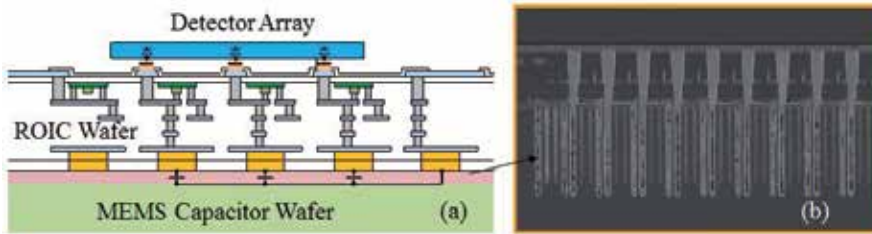


Figure 28. a) Schematic illustration of the 3D integrated AWARE Lambda-Scale LWIR FPA design; b) Micrograph of the MEMS capacitor array cross section [75].

Another DARPA program, LCTI-M addresses the development of an advanced low cost room temperature IR cameras based upon cell phone CMOS camera technology, where the imaging sensor, optics and electronics are fabricated at the wafer level. IR imaging capability, such as thermal cameras, provides significant advantages in terms of visibility and target detection in all weather conditions making it a vital tool for day/night operations. However, the cost of thermal cameras is one of the key factors limiting the availability of high performance IR imagers at consumer level. Further, current form-factors are unacceptable for new applications in smaller handheld devices (such as PDAs) and glasses similar to Google Glass. Availability of very low cost and small form-factor IR cameras will enable a variety of applications such as fire-fighting, security, medical and gaming industry.

Nanotechnology and science of emerging materials and material designs have stirred up a slew of research that has significant impact on sensors and many other electronic devices. Nanostructures offer very thin absorption layers due to many intricate designs such as plasmonics and metamaterials to concentrate photons and enhance electric field. The advantages of thinner absorber in a photodetector means shorter carrier transit time, thus high speed detectors and greater structural compatibility with ever-shrinking electronic devices. Many advances in nanomaterials for detectors have been made allowing for very low cost technology. A detailed review of nano-based detector research is given in reference [78].

DARPA has funded several new approaches for detector development using carbon nanotube, graphene, nanoparticles and other nanomaterials. These researches demonstrate high potential for future detector technologies that could be very beneficial for both, military and commercial sectors.

8. Summary

In this chapter, we have discussed growth, fabrication and characteristics of mainstream infrared materials and devices on a variety of substrates. We have discussed SWIR band of interest

that involves InGaAs, SiGe and HgCdTe based technologies and their applications. We also discussed the technologies and applications of MWIR, LWIR and multi-color devices for the 3-5 and 8-14 micron bands. Some of the key work discussed includes InSb, HgCdTe, and III-V based nBn and Strained Layer Super Lattice (SLS). Discussion of thermal bolometer devices provide introduction to future low cost LWIR technology. Each of these technologies has a place in the infrared band where a variety of detector configurations are being used. We also discussed the application of photonic type structures to IR detectors with broadband spectral response and high operating temperatures. It was shown that sub-wavelength size semiconductor pillar arrays can be designed and structured as an ensemble of photon trapping units to significantly increase absorption and QE over a wide band of wavelengths. It is anticipated that the current research and development presented in Section 7 will enable a host of new technologies for a variety of defense and commercial applications.

Although numerous research activities are ongoing in the area of nanoscience and technology, we briefly made comments on such technologies to make readers aware of various research activities.

Acknowledgements

The authors gratefully acknowledge the contributions of the many performers on the DARPA-AWARE program who have provided the results described in this manuscript and have been essential in advancing new infrared imaging capabilities.

Author details

Nibir K. Dhar^{1*}, Ravi Dat² and Ashok K. Sood³

*Address all correspondence to:

1 Defense Advanced Project Agency, Arlington

2 Booz Allen Hamilton, Arlington, USA

3 Magnolia Optical Technologies Inc., Woburn, USA

References

- [1] Pollehn, H., Choi, K. K., Svensson, S., & Dhar, N. (2007). IR Material Research at the Army Research Laboratory," Invited Keynote Paper. *Proceedings of SPIE*, 6542C.

- [2] Martin, T. J., Cohen, M. J., Dries, J. C., & Lange, M. J. (2004). InGaAs/InP Focal Plane Arrays for Visible Light Imaging. *Proceedings of SPIE*, 5406, 38-45.
- [3] Davis, M., Devitt, J., Greiner, M., Rawe, R., Timlin, A., & Wade, D. (2004). Advanced FPA Technology Development at CMC Electronics. *Proceedings of SPIE*, 5563, 62-73.
- [4] Becker, L. (2005). Current and Future trends in Infrared Focal Plane Array technology" Invited Paper. *Proceedings of SPIE*, 5881, 105.
- [5] Dereniak, E. L., & Boreman, G. D. (1996). *Infrared Detectors and Systems*, Wiley, New York, NY.
- [6] Kinch, M. A. (2007). *Fundamentals of Infrared Detector Materials*, SPIE Press, Bellingham, WA.
- [7] Rogalski, A. (2011). *Infrared detectors*, CRC Press, Boca Raton, FL.
- [8] Reine, M. B., Sood, A. K., & Tredwell, T. J. (1981). Photovoltaic Infrared Detectors. in *Semiconductors and Semimetals*, eds. R. K. Willardson and A. C. Beer, 18, 201-311, Academic Press, New York.
- [9] Micklethwaite, W. F. H. (1981). The Crystal Growth of Mercury Cadmium Telluride. *Semiconductors and Semimetals*, eds. R. K. Willardson and A. C. Beer, 18, 48-119, Academic Press, New York.
- [10] Tregilgas, J. H. (1994). Developments in Recrystallized Bulk HgCdTe. *Progress in Crystal Growth and Characterization of Materials*, 28, 57-83.
- [11] Triboulet, R. (1994). The Travelling Heater Method (THM) for Hg_{1-x}Cd_xTe and Related Materials. *Progress in Crystal Growth and Characterization of Materials*, 28, 85-114.
- [12] Capper, P. (2006). Bulk Crystal Growth- Methods and Materials. in *Springer Handbook of Electronic and Photonic Materials*, (Eds.) S. Kasap and P. Capper, Springer Science, New York.
- [13] Capper, P. (1989). Bridgman Growth of Cd_xHg_{1-x}Te: A Review. *Progress in Crystal Growth and Characterization of Materials*, 19, 259-93.
- [14] Capper, P., Maxey, C., Butler, C., Grist, M., & Price, J. (2004). Bulk growth of near-IR cadmium mercury telluride (CMT). *Journal of Materials Science: Materials in Electronics*, 15, 721-725.
- [15] Colombo, L., Chang, R. R., Chang, C. J., & Baird, B. A. (1988). Growth of Hg-Based Alloys by the Travelling Heater Method. *Journal of Vacuum Science and Technology A*, 6, 2795-99.
- [16] Lanir, M., & Riley, K. J. (1982). Performance of PV HgCdTe Arrays for 1-14- μ m Applications. *IEEE Transactions on Electronic Devices ED*, 29, 274-79.
- [17] Wang, C. C. (1991). Mercury Cadmium Telluride Junctions Grown by Liquid Phase Epitaxy. *Journal of Vacuum Science and Technology B*, 9, 1740-45.

- [18] Pultz, G. N., Norton, P. W., Krueger, E. E., & Reine, M. B. (1991). Growth and Characterization of p-on-n HgCdTe Liquid-Phase Epitaxy Heterojunction Material for 11-18 μm Applications. *Journal of Vacuum Science and Technology B*, 9, 1724-30.
- [19] Tung, T., Kalisher, M. H., Stevens, A. P., & Herning, P. E. (1987). Liquid-Phase Epitaxy of Hg_{1-x}Cd_xTe from Hg Solution: A Route to Infrared Detector Structures. *Materials Research Society Symposium Proceedings*, 90, 321-56.
- [20] Tung, T., De Armond, L. V., Herald, R. F., Herning, P. E., Kalisher, M. H., Olson, D. A., Risser, R. F., Stevens, A. P., & Tighe, S. J. (1992). State of the Art of Hg-melt LPE HgCdTe at Santa Barbara Research Center. *Proceedings of SPIE*, 1735, 109-31.
- [21] Herning, P. E. (1984). Experimental Determination of the Mercury-Rich Corner of the Hg-Cd-Te Phase Diagram. *Journal of Electronic Materials*, 13, 1-14.
- [22] Harman, T. C. (1980). Liquidus Isotherms, Solidus Lines and LPE Growth in the Te-Rich Corner of the Hg-Cd-Te System. *Journal of Electronic Materials*, 9, 945-61.
- [23] Tung, T., Su, C. H., Liao, P. K., & Brebrick, R. F. (1982). Measurement and Analysis of the Phase Diagram and Thermodynamic Properties in the Hg-Cd-Te System. *Journal of Vacuum Science and Technology*, 21, 117-24.
- [24] Bowers, J. E., Schmit, J. L., Speerschnieder, C. J., & Maciolek, R. B. (1980). Comparison of HgCdTe LPE Layer Growth from Te, Hg, and HgTe Rich Solutions. *IEEE Transactions on Electron Devices*, 27, 24-28.
- [25] Schmit, J. (1983). Growth, Properties and Applications of HgCdTe. *Journal of Crystal Growth*, 65, 249-261.
- [26] Chen, M. C., & Dodge, J. A. (1986). Electrical properties of antimony-doped p-type Hg/sub 0.78/Cd/sub 0.22/Te liquid-phase-epitaxy films. *Solid State Communications*, 59, 449-452.
- [27] Baker, I. M. (2002). HgCdTe 2D Arrays-Technology and Performance Limitis in. *Handbook of Infrared Detection Technologies*, eds. M. Henini and M. Razeghi, Elsevier Science, New York, NY.
- [28] Colombo, L., Westphal, G. H., Liao, P. K., Chen, M. C., & Schaake, H. F. (1992). Infrared focal plane array producibility and related materials. *Proceedings of SPIE*, 1683, 33.
- [29] Mitra, P., Case, F. C., & Reine, M. B. (1998). Progress in MOVPE of HgCdTe for Advanced Infrared Detectors. *J. Electron. Mater.*, 27(6), 510-520.
- [30] Hipwood, L. G., Baker, I. M., Jones, C. L., Maxey, C., Lau, H. W., Fitzmaurice, J., Wilson, M., & Knowles, P. (2008). LW IRFPAs made from HgCdTe grown by MOVPE for use in Multispectral Imaging. *Proceedings of SPIE*, 6940.
- [31] Wu, O. K. (1993). Status of HgCdTe MBE technology for IRFPA. *Proceedings of SPIE*, 202179.

- [32] , J., & Faurie, P. (1994). Molecular Beam Epitaxy of HgCdTe: Growth and Characterization. *Prog. Crystal Growth and Charact*, 29, 85-159.
- [33] Dat, R., Aqariden, F., Duncan, W. M., Chandra, D., & Shih, H. D. (1997). In Situ Spectroscopic Ellipsometry for Real Time Composition Control of HgCdTe Grown by Molecular Beam Epitaxy. *Mater. Res. Soc. Symp. Proc.*, 484, 613-18.
- [34] Irvine, S. I. C., & Bajaj, J. (1994). Recent progress with in situ monitoring of MCTGrowth. *Proceedings of SPIE*, 2274, 24-36.
- [35] Lee, T. S., Garland, J., Grein, C. H., Sumstine, M., Jandeska, A., Selamet, Y., & Sivanathan, S. (2000). Correlation of Arsenic Incorporation and Its Electrical Activation in MBE HgCdTe. *Journal of Electronic Materials*, 29, 869-72.
- [36] Tennant, W. E., Cockrum, C. A., Gilpin, J. B., Kinch, M. A., Reine, M. B., & Ruth, R. P. (1992). Key Issue in HgCdTe-Based Focal Plane Arrays: An Industry Perspective. *Journal of Vacuum Science and Technology B*, 10, 1359-69.
- [37] Triboulet, R., Tromson-Carli, A., Lorans, D., & Nguyen Duy, T. (1993). Substrate Issues for the Growth of Mercury Cadmium Telluride. *Journal of Electronic Materials*, 22, 827-34.
- [38] Gertner, E. R., Tennant, W. E., Blackwell, J. D., & Rode, J. P. (1985). HgCdTe on sapphire: A New Approach to Infrared Detector Arrays. *Journal of Crystal Growth*, 72, 462-67.
- [39] Edwall, D. D., Chen, J. S., Bajaj, J., & Gertner, E. R. (1990). MOCVD HgCdTe/GaAs for IR Detectors. *Semiconductor Science and Technology*, 5, 221-224.
- [40] Dhar, N. K., Wood, C. E. C., Gray, A., Wei, H. Y., Salamanca-Riba, L., & Dinan, J. H. (1996). Heteroepitaxy of CdTe on {211} Si using crystallized amorphous ZnTe templates. *J. Vac. Sci. Technol. B*, 14(3), 2366-70.
- [41] Peterson, J. M., Franklin, J. A., Readdy, M., Johnson, S. M., Smith, E., Radford, W. A., & Kasai, I. (2006). High-Quality Large-Area MBE HgCdTe/Si. *Journal of Electronic Materials*, 35, 1283-86.
- [42] van der Hoogeveen, R. J. A. R. W. M., Spruijt, H. J., & Goede, A. P. H. (1997). Low noise InGaAs infrared (1.0-2.4 microns) focal plane arrays for SCIAMACHY. *Proc. SPIE*, 2957, 54-65.
- [43] Acton, D., Jack, M., & Sessler, T. (2009). Large format short-wave infrared (SWIR) focal plane array (FPA) with extremely low noise and high dynamic range. *Proceedings of SPIE*, 7298, 72983E.
- [44] Onat, B. M., Huang, W., Masaun, N., Lange, M., Ettenberg, M. H., & Dries, C. (2007). Ultra low dark current InGaAs technology for focal plane arrays for low-light level visible-shortwave infrared imaging. *Proceedings of SPIE*, 6542, 65420L.
- [45] Boisvert, J., Isshiki, T., Sudharsanan, R., Yuan, P., & Mc Donald, P. (2008). Performance of very low dark current SWIR PIN arrays. *Proceedings of SPIE*, 6940, 69400L.

- [46] Mac, M., Dougal, J., Geske, J., Wang, , & Follman, D. (2011). Short-wavelength infrared imaging using low dark current InGaAs detector arrays and vertical-cavity surface-emitting laser illuminators. *Optical Engineering*, 50(6), 061011.
- [47] Yuan, H., Meixell, M., Zhang, J., Bey, P., Kimchi, J., & Kilmer, L. C. (2012). Low Dark Current Small Pixel Large Format InGaAs 2-D Photodetector array Development. *Proceedings of SPIE*, 8353, 8353309.
- [48] Kozlowski, L. J., Johnston, S. L., Mc Levice, W. V., Vanderwyck, A. H. B., Cooper, D. E., Cabelli, S. A., Blazejewski, E. R., Vural, K., & Tennant, W. E. (1992). x128 PACE-I HgCdTe hybrid FPAs for thermoelectrically cooled applications. *Proceedings of SPIE*, 1685, 193-204.
- [49] D'Souza, A. I., Robinson, E. W., Stapelbroek, M. G., Wong, W., Skokan, M., & Shih, D. H. (2009). Visible to SWIR Response of HgCdTe HDVIP Detectors. *Proceedings of SPIE*, 7298, 72981X-1.
- [50] Hansen, G. L., Schmit, J. L., & Casselman, T. N. (1982). Energy gap versus alloy composition and temperature in $\text{Hg}_{1-x}\text{Cd}_x\text{Te}$. *J. Appl. Phys.*, 53, 7099-710.
- [51] Gravrand, O., Mollard, L., Boulade, O., Moreau, V., Sanson, E., & Destefanis, G. (2011). Ultra low dark current CdHgTe FPAs in the SWIR range at CEA and Sofradir. *Proceedings of SPIE*, 8176, 81761H.
- [52] Tsauro, B.-Y., Chen, C. K., & Marino, S. A. (1991). Long-wavelength $\text{Ge}_x\text{Si}_{1-x}/\text{Si}$ heterojunction infrared detectors and focal plane array. *Proceedings of SPIE*, 1540, 580-595.
- [53] Wada, H., Nagashima, M., Hayashi, K., Nakanishi, J., Kimata, M., Kumada, N., & Ito, S. (1999). 512x512 element GeSi/Si heterojunction infrared focal plane array. *Proceedings of SPIE*, 3698, 584-595.
- [54] Sood, A. K., Richwine, R. A., Puri, Y. R., Di Lello, N., Hoyt, J. L., Akinwande, T. I., Horn, S., Balcerak, R. S., Bulman, G., & Venkatasubramanian, R. (2009). Development of Low Dark Current SiGe-Detector Arrays for Visible-Near IR Imaging Sensor. *Proceedings of SPIE*, 7298, 72983D.
- [55] Bublik, V. T., Gorelik, S. S., Zaitsev, A. A., & Polyakov, A. Y. (1974). Calculation on the Binding Energy of Ge-Si Solid Solution. *Phys. Status Solidi*, 65, K79-84.
- [56] Sood, A. K., Richwine, R. A., Puri, Y. R., Olubuyide, O. O., Di Lello, N., Hoyt, J. L., Akinwande, T., Balcerak, R. S., Horn, S., Bramhall, T. G., & Radack, D. J. (2008). Design considerations for SiGe-based NIR Imaging Sensor. *Proceedings of SPIE*, 6940, 69400M.
- [57] Markovitz, T., Pivnik, I., Calahorra, Z., Ilan, E., Hirsch, I., Zeierman, E., Eylon, M., Kahanov, E., Kogan, I., Fishler, N., Brumer, M., & Lukomsky, I. (2011). Digital 640x512 InSb detector for high frame rate, high sensitivity and low power applications. *Proceedings of SPIE*, 8012, 80122Y.

- [58] Hirsch, L., Shkedy, L., Chen, D., Fishler, N., Hagbi, Y., Koifman, A., Openhaim, Y., Vaserman, I., Singer, M., & Shtrichman, I. (2012). Hybrid Dual-Color MWIR Detector for Airborne Missile Warning Systems. *Proceedings of SPIE*, 8353, 83530H.
- [59] Brill, G., Chen, Y., Wijewarnasuriya, P., & Dhar, N. K. (2009). Infrared Focal Plane Array Technology Utilizing HgCdTe / Si: Successes, Roadblocks and material Improvements. *Proceedings of SPIE*, 7419, 74190L.
- [60] Chen, Y., Farrell, S., Brill, G., Wijewarnasuriya, P., & Dhar, N. K. (2008). Infrared Focal Plane Array Technology using HgCdTe/Si Material Growth. *Journal of Crystal Growth*, 310(24).
- [61] Bangs, J., Langell, M., Reddy, M., Melkonian, L., Johnson, S., Elizondo, L., Rybnicek, K., Norton, E., Jaworski, F., Asbrock, J., & Baur, S. (2011). Large Format High Operability SWIR and MWIR Focal Plane Array Performance and Capabilities. *Proceedings of SPIE*, 8012, 801234.
- [62] Patten, E. A., Goetz, P. M., Viela, F. A., Olsson, K., Lofgren, D. F., Vodicka, J. G., & Johnson, S. M. (2010). High-Performance MWIR/LWIR Dual-Band 640x480 HgCdTe/Si FPA's. *Journal of Electronic Materials*, 39(10).
- [63] Smith, K. D., Wehner, J. G. A., Graham, R. W., Randolph, J. E., Ramirez, A. M., Venzor, G. M., Olsson, K., Vilela, M. F., & Smith, E. P. G. (2012). High Operating temperature Mid-wavelength Infrared HgCdTe photon trapping focal plane arrays. *Proceedings of SPIE*, 8353, 83532R.
- [64] D'Souza, A. I., Robinson, E., Ionescu, A. C., Okerlund, D., de Lyon, T. J., Rajavel, R. D., Sharifi, H., Yap, D., Dhar, N., Wijewarnasuriya, P. S., & Grein, C. (2012). MWIR InAs_{1-x}Sb_xnBn Detectors Data and Analysis. *Proceedings of SPIE*, 8353, 835333.
- [65] Maimon, S., & Wicks, G. W. (2006). nBn detector, an infrared detector with reduced dark current and higher operating temperature. *APL* 89, 151109.
- [66] Smith, D. L., & Mailhot, C. (1987). Proposal for Strained type II superlattice infrared detectors. *Journal of Applied Physics*, 62(2545).
- [67] Rodriguez, J. B., Plis, E., Bishop, G., Sharma, Y. D., Kim, H., Dawson, L. R., & Krishna, S. (2007). nBn structure based on InAs/GaSb type-II strained layer superlattices. *Applied Physics Letters*, 91, 043514.
- [68] Krishna, S. (2009). Infrared focal plane arrays based on dots in a well and strained layer superlattices. *Proceedings of SPIE*, 7222, 72220P.
- [69] Ariyawansa, G., Duran, J. M., Grupen, M., Scheihing, J. E., Nelson, T. R., & Eismann, M. T. (2012). Multispectral Imaging with Type II Superlattice detectors. *Proceedings of SPIE*, 8353, 835530E.
- [70] Tohyama, S., Miyoshi, M., Kurashina, S., Ito, N., Sasaki, T., Ajisawa, A., Tanaka, Y., Kawahara, A., Iida, K., & Oda, N. (2006). New thermally isolated pixel structure for

- high-resolution (640×480) uncooled infrared focal plane arrays. *Optical Engineering*, 45, 014001.
- [71] Blackwell, R., Lacroix, D., & Bach, T. (2009). micron microbolometer FPA Technology at BAE Systems. *Proceedings of SPIE*, 7298, 72980P.
- [72] Li, C., Skidmore, G., Howard, C., Clarke, E., & Han, J. (2009). Advancement in 17 micron pixel pitch uncooled focal plane arrays. *Proceedings of SPIE*, 7298, 72980S.
- [73] Schimert, T., Hanson, C., & Brady, J. (2009). Advanced in small-pixel, large-format alpha-silicon bolometer arrays. *Proceedings of SPIE*, 7298, 72980T.
- [74] Trouilleau, C., Fieque, B., Noblet, S., & Giner, F. (2009). High Performance uncooled-amorphous silicon TEC less XGA IRFPA with 17 micron pixel. *Proceedings of SPIE*, 7298, 72980Q.
- [75] Dhar, N. K., & Dat, R. (2012). Advanced Imaging Research and Development at DARPA. *Proceedings of SPIE*, 8353, 835302.
- [76] D'Souza, A. I., Robinson, E., Ionescu, A. C., Okerlund, D., de Lyon, T. J., Rajavel, R. D., Sharifi, H., Yap, D., Dhar, N., Wijewarnasuriya, P. S., & Grein, C. (2012). MWIR InAs_{1-x}Sb_xnCBn Detectors Data and Analysis. *Proceedings of SPIE*, 8353, 835333.
- [77] Smith, K. D., Wehner, J. G. A., Graham, R. W., Randolph, J. E., Ramirez, A. M., Venzor, G. M., Olsson, K., Vilela, M. F., & Smith, E. P. G. (2012). High Operating temperature Mid-wavelength Infrared HgCdTe photon trapping focal plane arrays. *Proceedings of SPIE*, 8353, 8353 2R.
- [78] Logeeswaran, V. J., Jinyong, O., Nayak, A. P., Katzenmeyer, A. M., Gilchrist, K. H., Grego, S., Kobayashi, N. P., Wang, S. Y., Talin, A. A., Dhar, N. K., & Islam, M. S. (2011). A perspective on Nanowire Photodetectors: Current Status, Future Challenges, and Opportunities. *IEEE Journal of selected topics in quantum electronics*, 17(4), 1002-1023.

Theoretical Analysis of the Spectral Photocurrent Distribution of Semiconductors

Bruno Ullrich and Haowen Xi

Additional information is available at the end of the chapter

<http://dx.doi.org/10.5772/51412>

1. Introduction

Measurements of semiconductor photocurrent (PC) spectra have a long and rich history. During the 1960s and 1970s, the topic became one of the most studied phenomena in semiconductor research so that entire textbooks were dedicated to the subject [1-4]. In spite these considerable activities, only a few theoretical efforts were published in order to fit PC spectra. The first attempt is attributed to DeVore [5], who, with the purpose to find an explanation for the typically measured PC peak in the vicinity of the band gap, presumed enhanced carrier recombinations at the semiconductor surface with respect to the bulk. In other words, along the light propagating coordinate the carrier lifetime (and therefore the recombination rate) is changing. However, instead to transfer this idea directly into a mathematical model, DeVore used the non-measurable parameter carrier surface recombination velocity in order to achieve PC fits with a peak.

Much more recently, investigating the PC of thin-film Bi_2S_3 , Kebbab et al. and Pejova reported that the photoconductivity peak cannot be explained using the DeVore model [6-8], while, on the other hand, Pejova noticed that the PC formula published by Bouchenaki, Ullrich et al. (BU model hereafter) in 1991 [9] fits the measured spectra very well. The expression in Ref. [9] was intuitively derived and does not use surface recombination velocity but indeed different recombination rates at the surface and the bulk by introducing different carrier lifetimes along the propagation coordinate of the impinging light. Besides the above mentioned references, Ullrich's formula was successfully employed to fit PC spectra of thin-film CdS [9,10], GaAs [11], ZnS [12] and of the non-common semiconductor YBCO_6 [13].

Considering its correctness for a vast variety of semiconductors, we present here a precise derivation of the BU model and, using bulk CdS as representative semiconducting material, the work reveals the identical excellent agreement between PC experiments and theory for

both: Experimental absorption data and absorption coefficient calculations by combination of density of states and modified Urbach rule [14]. The work further stresses the correct link between the here promoted PC model and the actually measured surface to bulk lifetime ratio, and presents an extended and more detailed manuscript based on our recently published paper [15].

2. General Theory

2.1. Fundamental Equations

The sample geometry for the experiments and theoretical analysis is shown in Fig. 1. The impinging light intensity along the z -axis is I_0 [in J/(s cm²)], and $n(x, y, z, t)$, $p(x, y, z, t)$ are the nonequilibrium electron and hole densities [in 1/cm³], respectively, generated by the incoming photons. The continuity equations are expressed by their general form,

$$\frac{\partial n}{\partial t} = +\frac{1}{e} \nabla \cdot \vec{j}_n - \frac{n}{\tau_n} + \eta \frac{I_0}{\hbar \omega} \alpha \exp(-\alpha z) \quad (1)$$

$$\frac{\partial p}{\partial t} = -\frac{1}{e} \nabla \cdot \vec{j}_p - \frac{p}{\tau_p} + \eta \frac{I_0}{\hbar \omega} \alpha \exp(-\alpha z) \quad (2)$$

where the terms n/τ_n and p/τ_p represent the recombination rates for the electrons and holes, and τ_n and τ_p as their respective lifetimes. The term $I_0/(\hbar \omega) \alpha \exp(-\alpha z)$ is the decay of the generation rate [in 1/(s cm²)] along the penetration of light of the nonequilibrium carriers, where $\hbar \omega$ is the impinging light energy and α is the absorption coefficient [in 1/cm], η is the unit less conversion efficiency coefficient, and e the elementary charge. The vectors \vec{j}_n and \vec{j}_p are the electron and hole components of the current density and are given by,

$$\vec{j}_n = \vec{j}_{n,E} + \vec{j}_{n,D} = eN\mu_n\vec{E} + eD_e\nabla n \quad (3)$$

$$\vec{j}_p = \vec{j}_{p,E} + \vec{j}_{p,D} = eP\mu_p\vec{E} - eD_h\nabla p \quad (4)$$

where $\vec{j}_{n,D}$, $\vec{j}_{p,D}$ stands for the diffusion current driven by the density gradient and $\vec{j}_{n,E}$, $\vec{j}_{p,E}$ represents the conduction current driven by an external electric field \vec{E} . The terms $D_e\nabla n$ and $D_h\nabla p$ refers to the diffusion of the non-equilibrium carriers, whereas D_e and D_h is the diffusion constant of electrons and holes, respectively. The drift mobility of electrons and holes is μ_n and μ_p , and the total electron and hole densities are N and P , which are given by

$$N = N_0 + n \tag{5}$$

$$P = P_0 + p \tag{6}$$

where N_0 and P_0 are the electron and hole equilibrium uniform densities. Hence, the total current density is given by the sum of Esq. (3) and (4),

$$\vec{j} = \vec{j}_n + \vec{j}_p = e(N\mu_n + P\mu_p)\vec{E} + e(D_e\nabla n - D_h\nabla p) \tag{7}$$

We may decompose now Eq. (7) in the total current density \vec{j} in terms of dark current density \vec{j}_{dark} , i.e., current in absence of illumination, and the PC density \vec{j}_{ph} , which is the current generated by the impinging light on the semiconductor,

$$\vec{j} = \vec{j}_{dark} + \vec{j}_{ph} \tag{8}$$

where,

$$\vec{j}_{dark} = e(N_0\mu_n + P_0\mu_p)\vec{E} \tag{9}$$

and

$$\vec{j}_{ph} = e(n\mu_n + p\mu_p)\vec{E} + e(D_e\nabla n - D_h\nabla p) \tag{10}$$

We now assume (i) local neutrality condition, i.e., $n=p$, which implies equal lifetimes of electrons and holes, $\tau_n=\tau_p=\tau$. (ii) the equilibrium electron and hole density N_0 and P_0 are uniform and time independent, i.e., $\partial N_0/\partial t = \partial P_0/\partial t = \nabla N_0 = \nabla P_0 = 0$, and (iii) $\nabla \cdot \vec{E} = 0$ under local neutrality condition. With the substitution of the current density \vec{j}_n, \vec{j}_p into Eqs. (1) and (2), we obtain:

$$\frac{\partial n}{\partial t} = +D_e\nabla^2 n - \frac{n}{\tau} + \eta \frac{I_0}{\hbar\omega} \alpha \exp(-\alpha z) + \mu_n \vec{E} \cdot \nabla n \tag{11}$$

$$\frac{\partial p}{\partial t} = +D_h\nabla^2 p - \frac{p}{\tau} + \eta \frac{I_0}{\hbar\omega} \alpha \exp(-\alpha z) - \mu_p \vec{E} \cdot \nabla p \tag{12}$$

We multiply now Eq. (11) and Eq. (12) with the hole and electron conductivity, i.e., σ_p and σ_n , respectively, and, by adding both equations and simultaneously replacing p with n ($n=p$), we obtain the following relationship:

$$\frac{\partial n}{\partial t} = \frac{\sigma_p D_e + \sigma_n D_h}{\sigma_n + \sigma_p} \nabla^2 n - \frac{n}{\tau} + \eta \frac{I_0}{\hbar \omega} \alpha \exp(-\alpha z) + \frac{\mu_n \sigma_p - \mu_p \sigma_n}{\sigma_n + \sigma_p} \vec{E} \cdot \nabla n \quad (13)$$

Furthermore, we define the bipolar diffusion coefficient as,

$$D = \frac{\sigma_p D_e + \sigma_n D_h}{\sigma_n + \sigma_p} \quad (14)$$

and the bipolar drift mobility μ_E as,

$$\mu_E = \frac{\mu_n \sigma_p - \mu_p \sigma_n}{\sigma_n + \sigma_p} \quad (15)$$

Note that the bipolar drift mobility μ_E is different from the bipolar diffusion mobility μ_D , which is defined as

$$\mu_D = \frac{\mu_n \sigma_p + \mu_p \sigma_n}{\sigma_n + \sigma_p} \quad (16)$$

Thus, we have the continuity equation for n (and consequently for p, because $n=p$),

$$\frac{\partial n}{\partial t} = D \nabla^2 n - \frac{n}{\tau} + \frac{\eta I_0}{\hbar \omega} \alpha \exp(-\alpha z) + \mu_E \vec{E} \cdot \nabla n \quad (17)$$

and for the PC density:

$$\vec{j}_{ph} = e(\mu_n + \mu_p)n\vec{E} + e(D_e - D_h)\nabla n \quad (18)$$

The Eqs. (17) and (18) are the fundamental equations that allow us, in case the energy dispersion of α is known, to calculate the distribution of the carrier density, carrier current, and the PC spectra.

2.2. Photocurrent spectra for experimental setup condition

So far, we have made some general assumption regarding the process of nonequilibrium carriers. We shall now restrict ourselves to the detailed determination of PC spectra, considering the following general conditions:

- i. stationary state, i.e., $\partial n/\partial t=0$,
- ii. the light illuminates uniformly the entire semiconductor sample, whereas the direction of the impinging light is along the z-axis and the volume of the sample is given by $l_x \times l_y \times l_z$, where $l_z=d$ is the thickness of the sample,
- iii. the sample possesses a uniform nonequilibrium carrier density in the x-y plane, and diffusion takes place along the z-axis only, i.e., $n(x, y, z)=n(z)$, and
- iv. (iv) the external electric field \vec{E} applied to the sample is perpendicular to the incident light and along x-direction, i.e., $\vec{E}=E_x \hat{e}_x$. Hence, with the stationary continuity equation (Eq. 17), we get,

$$D \frac{d^2 n}{dz^2} - \frac{n}{\tau} + \eta \frac{I_0}{h\omega} \alpha \exp(-\alpha z) = 0 \quad (19)$$

In Eq. (19), we have dropped the term $\vec{E} \cdot \nabla n=0$ due to the fact that the two vectors are perpendicular to each other.

In the following step we introduce the boundary condition for solving Eq. (19). Since the PC is measured along the x-axis, i.e., the external electric field is perpendicularly to the direction of the impinging light as shown in Fig. 1, consequently, no closed current loop exists in the z-direction. In other words, no physical carrier diffusion current j_D will take place at the boundary $z=0$ and $z=d$. From Eq. (18), we arrive at the boundary conditions,

$$\left. \frac{dn}{dz} \right|_{z=0} = 0$$

and

$$\left. \frac{dn}{dz} \right|_{z=d} = 0 \quad (20)$$

By using Eq. (18), we can obtain the PC passing through the sample as $I_{ph} = \iint \vec{j}_{ph} \cdot d\vec{A}$. Here, the electrical current cross-section area vector $d\vec{A}$ is given by $d\vec{A}=dzdy\hat{e}_x$. Notice that the vector $d\vec{A}$ is perpendicular to the cross-section area vector $(D_e - D_h)\nabla n$. Therefore, the diffusion current term $\nabla n = (dn/dz)\hat{e}_z$ in Eq. (18) which is along z-direction does not contribute to the PC. Finally, we obtain the PC for the specific experimental setup as,

$$I_{\text{ph}} = \left(\frac{I_y}{I_x}\right)(\Delta U e \mu) \int_0^d n(z) dz \quad (21)$$

where $\mu = \mu_n + \mu_p$ is the mobility and $\Delta U = E_x L_x$ and the voltage drop across the sample. It is worthwhile noting that I_{ph} has the physical unit of Ampere (A). Equations (19-21), the energy dependence of the absorption coefficient [$\alpha(\hbar\omega)$], and the spatial lifetime distribution of carriers (τ) form the complete set needed for the fit of PC spectra measured with the configuration displayed in Fig. 1.

3. DeVore's approach vs. BU model

In this section, we present the comparison of the two existing theoretical PC models, which were initially introduced in Refs. [5] and [9]. The PC spectra are based on the common experimental setup shown in Fig.1, where the direction of the applied electric field is perpendicular to the direction of illumination.

3.1. The DeVore's photocurrent spectral theory

It has been the conventional way of engage DeVore's formula to fit PC spectra. However, as presented below, for the standard PC experiments displayed in Fig 1, DeVore's formula is actually not the correct one to use. We now briefly outline DeVore's early work [5], in which th calculation is based on the following equation,

$$\frac{1}{\tau\beta^2} \frac{d^2 n}{dz^2} - \frac{n}{\tau} + \eta \frac{I_0}{\hbar\omega} \alpha \exp(-\alpha z) = 0 \quad (22)$$

This formulation is based on four assumptions:

- i. the external electric field is perpendicular to the incident light direction, which corresponds the experimental configuration in Fig. 1 (additional discussions of this point will be presented in a forthcoming paper).
- ii. Assuming steady state, i.e., $\partial n/\partial t = 0$.
- iii. The recombination rate $1/\tau$ and diffusion length β^{-1} are a constant.
- iv. The recombination current at the surface is given by setting the following boundary conditions:

$$-\frac{1}{\tau\beta^2} \frac{\partial n}{\partial z} \Big|_{z=0} = -n \Big|_{z=0} S \quad \text{and} \quad -\frac{1}{\tau\beta^2} \frac{\partial n}{\partial z} \Big|_{z=d} = +n \Big|_{z=d} S \quad (23)$$

Where the constant S is called surface recombination velocity. By solving the standard second order differential equation $n(z)$ with the boundary conditions [Eq. (22)], and substitute $n(z)$ into the expression of I_{ph} [Eq. (21)], we arrive at DeVore's formula,

$$I_{ph} = I_{PC}^0 F \tag{24}$$

where the PC magnitude is given by,

$$I_{ph}^0 = \left(\frac{I_y}{I_x}\right)(\Delta U e \mu) \left(\tau \frac{I_0}{\hbar \omega}\right) \tag{25}$$

and the dimensionless spectrum factor F has the form,

$$F = \frac{1}{1 - \alpha^2 / \beta^2} \left[1 - \exp(-\alpha d) - \frac{\alpha S \tau (1 + \exp(-\alpha d) + \alpha^2 \beta^2 (1 - \exp(-\alpha d)))}{1 + S \tau \beta \coth(\beta d / 2)} \right] \tag{26}$$

where α is the energy dependent absorption coefficient. We argue that the boundary conditions [Eq. (22)] are not consistent with the experimental setup, i.e. the PC is driven by an applied electric field, which is perpendicular to the impinging light. Therefore, at the surface along the incident light there is an open circuit. The correct boundary condition is that there will be no particle current across the sample surface, i.e., $-\frac{1}{\tau \beta^2} \frac{\partial n}{\partial z} \Big|_{z=0} = -\frac{1}{\tau \beta^2} \frac{\partial n}{\partial z} \Big|_{z=d} = 0$. Under this boundary condition, the DeVore's PC becomes,

$$I_{ph} = I_{PC}^0 [1 - \exp(-\alpha d)] \tag{27}$$

i.e., the spectral factor F in Eq. (25) is reduced to the absorption,

$$F = 1 - \exp(-\alpha d) \tag{28}$$

Consequently, DeVore's formula is not able to explain the PC maximum in the vicinity of the band gap for the geometry shown in Fig. 1. The boundary conditions expressed by Eq. (22) are artificially acting as source of non-equilibrium carriers.

3.2. PC theory based on the spatial non-uniform recombination rate (BU model)

The ansatz of the original BU model in Ref. [9] led to an intuitive and straightforward theory that implemented DeVore's assumption directly. It simply assumed that the spatial distribu-

tion recombination rates along the light propagation - i.e., at the surface and in the bulk region - are different. At the surface, due to the increased density of recombination centers with respect to the bulk, the carrier lifetime is much shorter than in the bulk region. Specifically, it was assumed that the spatial lifetime decay $\tau(z)$ takes the simple form:

$$\tau(z) = \tau_b \left[1 - \left(1 - \frac{\tau_s}{\tau_b} \right) \exp(-z/L) \right] \quad (29)$$

Where τ_s is the lifetime of the nonequilibrium carriers at the surface, τ_b is the lifetime of the nonequilibrium carriers in the bulk, and L is the length scale beyond which the recombination rate is predominately ruled by τ_b . Thus we have a multi-time scale relaxation model. We rearrange Eq. (19), resulting in,

$$n = \frac{1}{\beta^2} \frac{d^2 n}{dz^2} + \tau \eta \frac{I_0}{\hbar \omega} \alpha \exp(-\alpha z) \quad (30)$$

Here, we have used the mean field approximation for the term $D\tau \approx D\langle\tau\rangle = 1/\beta^2$ and assumed that diffusion length β^{-1} is a constant. We now substitute Eq. (30) into the general PC expression Eq. (21), we find,

$$I_{ph} = \left(\frac{l_y}{l_x} \right) (\Delta U e \mu) \int_0^d \left(\frac{1}{\beta^2} \frac{d^2 n}{dz^2} + \tau(z) \eta \frac{I_0}{\hbar \omega} \alpha \exp(-\alpha z) \right) dz = I_{ph}^0 F \quad (31)$$

The first integral over the diffusion term is zero because of the zero flux boundary condition [Eq. (20)]. Thus, the dimensionless spectrum factor F takes the following form:

$$F = \int_0^d \frac{\tau(z)}{\tau_b} \alpha \exp(-\alpha z) dz = 1 - \exp(-\alpha d) - \left(1 - \frac{\tau_s}{\tau_b} \right) \frac{\alpha L}{1 + \alpha L} [1 - \exp(-\alpha d - d/L)] \quad (32)$$

where, the PC magnitude is given by,

$$I_{ph}^0 = \left(\frac{l_y}{l_x} \right) (\Delta U e \mu) \left(\frac{I_0}{\hbar \omega} \tau_b \right) \eta \quad (33)$$

Equations (31-33) basically correspond to the intuitively deduced PC dispersion Ref. [9]. We note that by expressing the PC in terms of the responsivity (R) in [Ampere/Watt], i.e., for constant impinging light power, the proportionality $R \propto F$ holds.

4. Experimental PC Results and Fits

The spectral PC dispersion was investigated by using the experimental arrangement in Fig. 1: The x, y plane of the CdS bulk material faces the incoming monochromatic light, while the z coordinate is parallel to the light propagation. The electric field of the light is perpendicularly oriented to the c -axis of the CdS sample, which was an industrially produced single crystal with $d=1$ mm. Two vacuum evaporated Al contacts with a gap of 0.5 mm between them were used for the electrical connection. The applied electric field driving the PC was 200 V/cm and the optical excitation was carried out with intensities typically in $\mu\text{W}/\text{cm}^2$ range. The PC was recorded at room temperature with lock-in technique by chopping the impinging light at 25 Hz. The measured spectrum was corrected by a calibrated Si photodiode in order to express the PC in terms of responsivity.

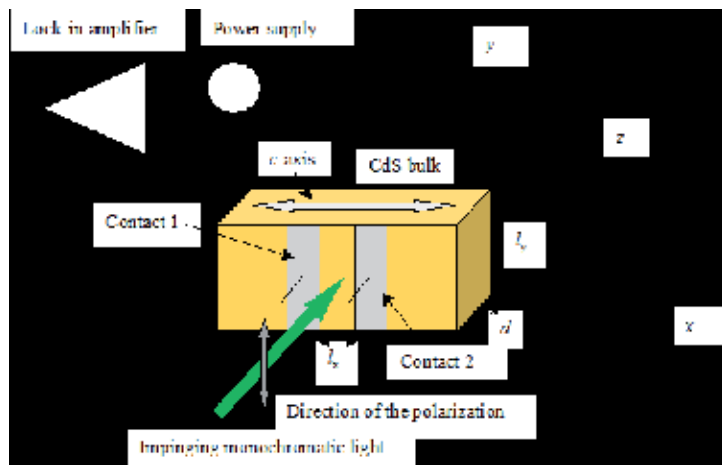


Figure 1. Experimental arrangement employed for the experiments. Note that $d=l_z$.

4.1. PC fit using Dutton's experimentally determined absorption coefficient

The comparison of the experiment (symbols) with the fit (dotted line) using Eq. (31-32) is shown in Fig. 2(a). The best fit between the experimental data and theoretical formula was achieved with $d=3.60 \times 10^{-3}$ cm, $L=8.65 \times 10^{-5}$ cm, and $\tau_s/\tau_b=0.068$, while the used $\alpha(\omega\hbar)$ values, which are shown in Fig. 2 (b), have been extracted from Dutton's paper [16]. The fit reveals that only an effective thickness of the sample, which does not necessarily correspond to the physical thickness, contribute to the formation of the PC signal. The corresponding conclusion was found by analyzing the photoluminescence of thin-film CdS [17].

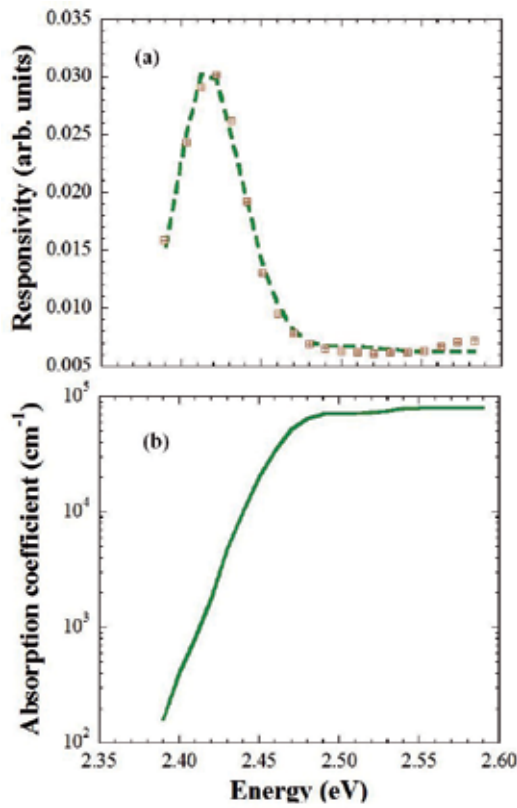


Figure 2. a) The symbols represent the photocurrent measurements while the broken line was fitted with the Eq. (32). (b) The absorption coefficient for perpendicularly oriented CdS was used for the fit. The data were deduced from Dut-ton’s paper (Ref. [16]).

Using Eq. (32) one can link the absorption coefficient to the location of the maximum of the PC spectra. We set $\frac{dF}{d\hbar\omega} = \frac{dF}{d\alpha} \frac{d\alpha}{d\hbar\omega} = 0$, and obtain,

$$d \exp(-\alpha d) - \left(1 - \frac{\tau_s}{\tau_b}\right) \left[\frac{L}{(1 + \alpha L)^2} (1 - \exp(-\alpha d - d/L)) + \frac{\alpha L}{(1 + \alpha L)} d \exp(-\alpha d - d/L) \right] = 0$$

Since the term $\exp(-\alpha d - d/L) \ll 1$, we simplify the above condition to,

$$d \exp(-\alpha d) - \left(1 - \frac{\tau_s}{\tau_b}\right) \frac{L}{(1 + \alpha L)^2} = 0 \tag{34}$$

resulting in $-\alpha d = \ln\left(1 - \frac{\tau_s}{\tau_b}\right) \frac{L}{d} - 2 \ln(1 + \alpha L) = 0$ and by using the approximation $\ln(1 + \alpha L) \approx \alpha L$ and $L/d \ll 1$, we finally find the α^* where the PC has the maximum value

$$\alpha^*d = -\ln\left(\left(1 - \frac{\tau_s}{\tau_b}\right)\frac{L}{d}\right)\left(\frac{1}{1 - 2L/d}\right) \cong -\ln\left(\left(1 - \frac{\tau_s}{\tau_b}\right)\frac{L}{d}\right) \quad (35)$$

This shows that the maximum location (α^*d) in PC spectra is mainly controlled by two parameters τ_s/τ_b , L/d . Now we substitute the parameters $d=3.60 \times 10^{-3}$ cm, $L=8.65 \times 10^{-5}$ cm, and $\tau_s/\tau_b=0.068$ into α^* expression, we obtain $\alpha^*=1108.54$ cm⁻¹. This corresponds to the energy E value between 2.41eV-2.42eV, and is exactly the energy region where the maximum PC occurred.

4.2. PC fit employing the theoretical absorption coefficient based on the modified Urbach rule

So far, we have used the experimental absorption edge data from Dutton directly, we may also fit the PC by modeling $\alpha(\hbar\omega)$ with the density of states and the modified Urbach tail, which are expressed by [14],

$$\begin{aligned} \alpha(\hbar\omega) &= A_0 \sqrt{\hbar\omega - E_g} \\ \text{if} \\ \hbar\omega &\geq E_{cr} \end{aligned} \quad (36)$$

and

$$\begin{aligned} \alpha(\hbar\omega) &= A_0 \sqrt{\frac{kT}{2\sigma}} \exp\left[\frac{\sigma}{kT}(\hbar\omega - E_{cr})\right] \\ \text{if} \\ \hbar\omega &\leq E_{cr} \end{aligned} \quad (37)$$

where E_g is band gap energy, A_0 is linked to the saturation value of $\alpha(\hbar\omega)$, kT is the thermal energy, and the crossover between Eqs. (36) and (37) takes place at $E_{cr}=E_g+kT/(2\sigma)$ [14], where σ defines the steepness of the Urbach tail [17]. Figure 3 shows the comparison of the measured PC [which is identical with the one in Fig. 2 (a)] with the fit using Esq. (32), (36), and (37), whereas the following fitting parameters were used: $kT=26$ meV, $A_0=3.26 \times 10^5$ cm⁻¹ (eV)^{-1/2}, $d=3.69 \times 10^{-3}$ cm, $L=9.14 \times 10^{-5}$ cm, $\sigma=2.15$, $E_g=2.445$ eV, and $\tau_s/\tau_b=0.100$. The fit parameters d and L are very close to the previous fit and we should stress that the σ value found ($=2.15$) is almost identical with the promoted CdS value ($=2.17$) of Dutton. Figure 4 shows the comparison of the calculated function $\alpha(\hbar\omega)$ with Dutton's measurement and the good agreement of both curves proves the suitability of the straightforward concept represented by Esq. (35) and (36).

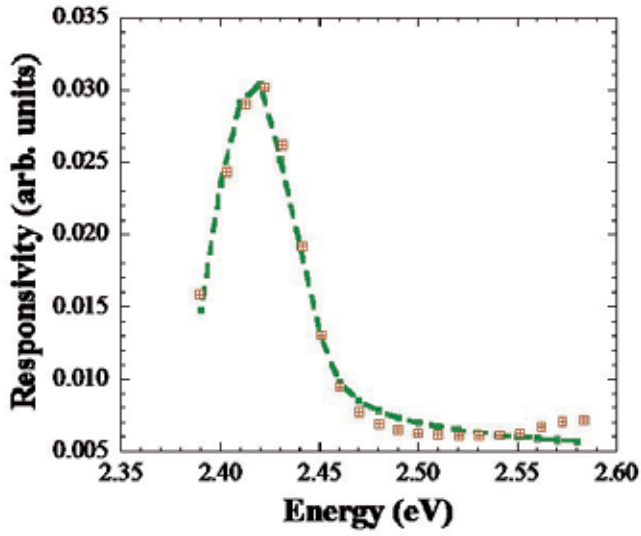


Figure 3. Fit (broken line) of the measured photocurrent spectrum in Fig. 1 (symbols) using Eqs. (36) and (37). The fit hardly differs from the one in Fig. 2 (a).

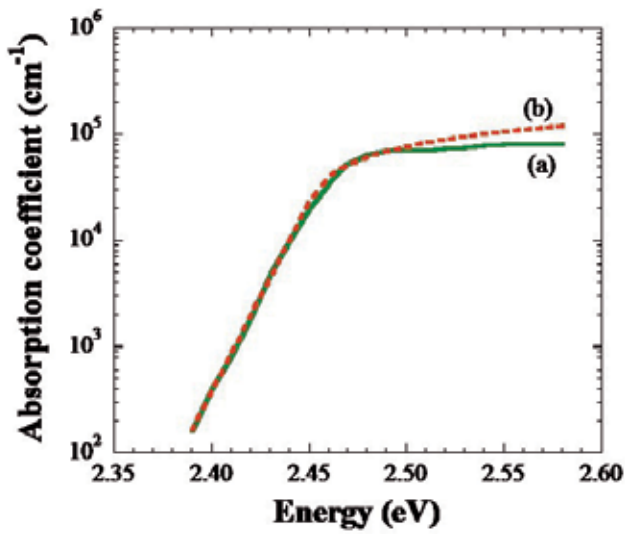


Figure 4. Comparison of the absorption coefficient (a) after Dutton and (b) modeled with Eqs. (36) and (37).

5. Measurement of the lifetime at the surface (τ_s) and in the bulk (τ_b)

By measuring the temporal decay of the PC illuminating the sample with highly ($\alpha(\hbar\omega)=10^5$ cm⁻¹) and less absorbed light ($\alpha(\hbar\omega)\ll 10^2$ cm⁻¹) it should be possible to measure τ_s and τ_b . We made the temporal PC decay visible with a 500 MHz scope by employing chopped (18 Hz) continuous wave (cw) laser beams at 488.0 nm (2.54 eV) and 632.8 nm (1.96 eV), by using an Ar-Kr and He-Ne laser, respectively. Both laser beams were unfocused resulting in the rather moderate intensity of about 0.6 W/cm² and, as for the PC measurements above, the driving electric field was again 200 V/cm.

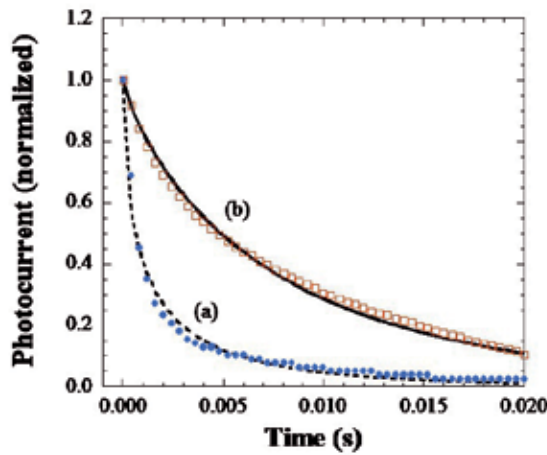


Figure 5. Photocurrent decay vs. time measured under the illumination of a laser emitting at (a) 488.0 nm and (b) 632.8 nm. The symbols represent the measurements, while solid and broken lines represent the fits done with Eq. (38).

Figure 5 shows the experimental results (symbols) and fits (solid and broken lines) of the decay. The fits were performed with the Kohlrausch function [19], which is an extension of the exponential function with one additional parameter γ that can range between 0 and 1,

$$I_{ph}(t) = I_{ph}^0 \exp[-(t / \tau_{s,b})^\gamma] \quad (38)$$

The following parameters resulted in the best fits for surface and bulk: $\tau_s=1.2$ ms and $\gamma=0.53$, and $\tau_b=7.6$ ms and $\gamma=0.82$, respectively, resulting in $\tau_s/\tau_b=0.16$. Despite the straightforwardness of the experiment, which did not consider electric charging effects, the number is only approximately a factor 2.4 and 1.6 off from the predicted value using the data of Dutton and the modeled absorption edge, respectively. It is worthwhile to note that the Kohlrausch decay can be expressed as linear superposition of simple exponential decays, i.e.,

$\exp[-(t/\tau_{s,b})^\gamma] = \int_0^\infty p(u, \gamma) \exp[-t/(u\tau_{s,b})] du$, where $p(u, \gamma)$ is the weight function for the decay

time $\tau = u\tau_{s,b}$. The mean relaxation time is $\langle \tau \rangle = \int_0^\infty \exp[-(t/\tau_{s,b})^\gamma] dt = \frac{\tau_{s,b}}{\gamma} \Gamma(\frac{1}{\gamma})$, where Γ is the gamma function. For a simple exponential decay, $\langle \tau \rangle = \tau_{s,b}$, and, therefore, the necessity of the Kohlrausch function to fit the temporal PC decay confirms the involvement of various time constants and is strong supportive evidence for the multi-time scale relaxation model introduced by Eq. (29).

6. Conclusion

We have derived a spectral PC formula based on general principles for the standard set-up used in experiments. By explicitly including the spatial variation of the recombination rate along the light propagation - i.e., at the surface and in the bulk region - we were able to demonstrate that PC spectra can be accurately described by the BU model. Equivalently good agreements between theory and experiment were found by using $\alpha(\hbar\omega)$ values either experimentally determined or straightforwardly modeled by the density of states and the modified Urbach rule. Furthermore, we have shown that the detailed theoretical model of the spatial variation of $\tau(z)$ is not critical for the generation of the PC near the band gap. However, the presented detailed theory correctly fit and explains the experimental observations. It reveals the firm physical key mechanism for understanding of the PC peak near the gap energy: The peak takes place due to the different recombination rates of the excited carries near the surface and bulk. We also showed that the τ_s/τ_b ratio found by temporally resolved PC measurements reasonably agrees with the results from the PC fits, accommodating the commonly used concept in optoelectronics, i.e., the use of carrier lifetimes.

Author details

Bruno Ullrich^{1,2,3*} and Haowen Xi⁴

*Address all correspondence to: bruno.ullrich@yahoo.com

1 Ullrich Photonics LLC, USA

2 Air Force Research Laboratory, Materials & Manufacturing Directorate, Wright Patterson, USA

3 Instituto de Ciencias Físicas, Universidad Nacional Autónoma de México, Cuernavaca, Morelos, México

4 Department of Physics and Astronomy, Bowling Green State University, USA

References

- [1] Bube, R. H. (1960). *Photoconductivity of Solids*. New York:, Wiley.
- [2] Ryvkin, S. M. (1964). *Photoelectric Effects in Semiconductors*. New York:, Consultants Bureau.
- [3] Rose, A. (1978). *Concepts in Photoconductivity and Allied Problems*. New York:, Krieger.
- [4] Mort, J., & Pai, D. M. (1976). *Photoconductivity and Related Phenomena*. Amsterdam, Elsevier.
- [5] DeVore, H. B. (1955). Spectral Distribution of Photoconductivity. *Phys. Rev.*, 102, 86-91.
- [6] Kebbab, Z., Benramdane, Medles. M., Bouzidi, A., & Tabet-Derraz, H. (2002). Optical and Photoelectrical Properties of Bi_2S_3 Thin Films btained by Spray Pyrolysis Technique. *Solar Energy Materials & Solar Cells*, 71, 449-457.
- [7] Pejova, B. (2007). Structural, Optical and Photoelectrical Properties of Low-dimensional Semiconductors deposited in Thin Film Form by Chemical and Sonochemical Methods, in *Progress in Solid State Chemistry Research*. Buckley RW, editor. Nova Science Publishers, New York , 55-115.
- [8] Pejova, B. (2008). Analysis of the Shape of Spectral Dependence of Absorption Coefficient and Stationary Photoconductivity Spectral Response in Nanocrystalline Bismuth (III) Sulfide Thin Films. *Mater. Res. Bull.*, 43, 2887-2903.
- [9] Bouchenaki, C., Ullrich, B., Zielinger, J. P., Cong, H. N., & Chartier, P. (1991). Preparation, Characterization, and Bistable Photoconduction Properties of Thin CdS layers. *J. Opt. Soc. Am. B*, 8(3), 691-700.
- [10] Bouchenaki, C., Ullrich, B., Zielinger, J. P., Cong, H. N., & Chartier, P. (1990). Photoconduction and Thermo-optical Hysteresis Measurements in Thin CdS Films. *J. Crystal Growth*, 101, 797-801.
- [11] Erlacher, A., Ambrico, M., Capozzi, V., Augelli, V., Jaeger, H., & Ullrich, B. (2004). X-ray, Absorption and Photocurrent Properties of Thin-Film GaAs on Glass formed by Pulsed-laser Deposition. *Semicond.Sci. Technol.*, 19, 1322-1324.
- [12] Yano, S, Schroeder, R, Sakai, H, & Ullrich, B. (2003). High-electric-field photocurrent in thin-film ZnS formed by pulsed-laser deposition. *Appl. Phys. Lett.*, 82, 2026.
- [13] Ullrich, B., Kulac, I., & Pint, H. (1992). Photocurrent in Thin $\text{YBa}_2\text{Cu}_3\text{O}_6$ Films on Sapphire. *Jpn. J. Appl. Phys.*, 31, L 856-L859.

- [14] Ullrich, B., & Bouchenaki, C. (1991). Bistable Optical Thin CdS Film Devices: All-optical and Optoelectronic Features. *Jap. J. Appl. Phys.*, 30, L 1285-L1288.
- [15] Ullrich, B., & Xi, H. (2010). Photocurrent Theory based on Coordinate Dependent Lifetime. *Optics Letters*, 35(23), 3910-3912.
- [16] Dutton, D. (1958). Fundamental Absorption Edge in Cadmium Sulfide. *Phys. Rev.*, 112(3), 785-792.
- [17] Ullrich, B., Yano, S., Schroeder, R., & Sakai, H. (2003). Analysis of single- and two-photon-excited green emission spectra of thin-film cadmium sulfide. *J. Appl. Phys.*, 93, 1914-1917.
- [18] Urbach, F. (1953). The Long-Wavelength Edge of Photographic Sensitivity and of the Electronic Absorption of Solids. *Phys. Rev.*, 92, 1324.
- [19] Queisser, H. J. (1985). Nonexponential Relaxation of Conductance near Semiconductor Interfaces. *Phys. Rev. Lett.*, 54, 234-236.

Recent Progress in the Understanding and Manipulation of Morphology in Polymer: Fullerene Photovoltaic Cells

Gabriel Bernardo and David G. Bucknall

Additional information is available at the end of the chapter

<http://dx.doi.org/10.5772/51115>

1. Introduction

The morphology of the active layer in OPV devices is widely recognized as being crucial for their photovoltaic performance [1-4]. The physics of the system dictates that excitons must dissociate efficiently at a donor-acceptor interface, and that sufficient pathways for charge transport to the electrodes are also required. Conjugated polymer crystals are considered to be the primary hole carrier and thus are essential for effective charge transport. With this in mind, the ideal morphology for an organic photovoltaic BHJ film was often considered until a few years ago to be a bicontinuous, interpenetrating network morphology composed of pure P3HT and pure PCBM phases, with both phases of order ~ 20 nm in size [5, 6] and numerous cartoon depictions have helped to propagate this view, as the one shown in Figure 1.

In this idealized model, the two pure phases of donor and acceptor within the bulk heterojunction are interdigitated in percolated highways with an average length scale of around 10-20 nm, equal to or less than the exciton diffusion length, to ensure exciton dissociation and high mobility charge carrier transport with reduced recombination. Furthermore, a pure donor phase at the hole collecting electrode and a pure acceptor phase at the electron collecting electrodes should exist in order to minimize the losses by recombination of opposite charges or acting as diffusion barriers for the opposite sign charge carriers at the respective electrodes. The presence of mixed phases in these BHJ were considered to be counterproductive to device performance, since isolated molecules could act as traps for separated charges and centers for charge recombination within the percolation pathways.

Many efforts have used this ideal model to design studies that examine the effect of the chemical structure of conjugated polymer, composition, and processing methods on the abil-

ity to achieve this ideal interpenetrating two-phase system [1]. Furthermore, when describing the device physics of such organic photovoltaic devices, theoretical models have been developed which mainly relied on the assumption that the components existed as two separated pure phases [7-10].

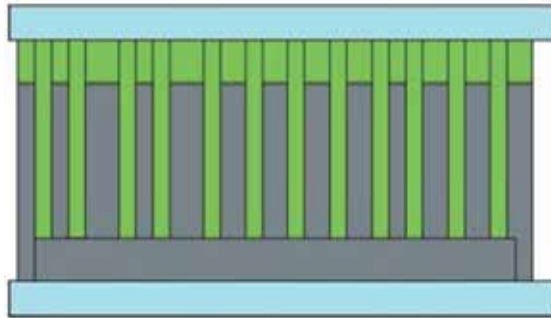


Figure 1. The ideal structure of a bulk heterojunction solar cell as represented by Sariciftci *et al* [5]. "Reprinted with permission from (Chemical Reviews 107 (2007) 1324). Copyright (2012) American Chemical Society."

Experimentally, although several different techniques have been used to study the morphology of these systems, part of the difficulties in the past in determining the precise composition of phases, interfacial structure, and morphology of bulk heterojunctions has been the limitations of contrast between the phases. For instance in standard electron-based techniques, crystalline P3HT and PCBM offer sufficient contrast between those two phases; however their amorphous counterparts are almost indistinguishable. Consequently conventional x-ray diffraction methods are unable to probe the amorphous regions in these conjugated polymer-fullerene mixtures. On the other hand, AFM techniques only allow the study of the morphology of surfaces and this might be very different from the morphology of the underlying bulk of the film. Differential scanning calorimetry (DSC) and dynamic mechanical analysis (DMA) have also been used but they can only provide indirect information about the morphology of these BHJ. For these reasons, more recently neutron and soft x-ray scattering techniques have started being used to provide heretofore unavailable information concerning the bulk morphology of these bulk heterojunctions. Additionally techniques utilizing specific atomic or group specific contrast such as secondary ion mass spectroscopy (SIMS) have added further information to the growing wealth of morphological information about BHJs. One clear advantage on the use of neutrons lies in the fact that for instance in the case of P3HT/PCBM systems, the scattering length density (SLD) difference between P3HT ($0.83 \times 10^{-6} \text{ \AA}^{-2}$) and PCBM ($4.3 \times 10^{-6} \text{ \AA}^{-2}$) is sufficiently high, and no additional deuteration of one component is necessary.

Over approximately the last five years a reinterpretation of the existing idealized model has lead to a new understanding on the thermodynamics and the morphology of these bulk heterojunction systems. This chapter reviews some of the relevant literature relating to this new

emerging understanding with concentration on the system of P3HT and PCBM, which has been the most widely studied OPV system to date.

2. The Thermodynamics and Phase Behavior of Conjugated Polymer-Fullerene Systems

Until a few years ago, the conventional wisdom was that the most widely studied OPV system of P3HT:PCBM was a simple two phase bulk heterojunction with well-defined interfaces between regions of approximately pure P3HT and pure PCBM. Then, from 2008 onwards several works in the literature began to show that this model was deficient in a number of ways since it did not account for the phase behavior of the mixtures or explain what the interface was between the phases or the two electrode interfaces. However, the results reported are often contradictory or conflicting as explained below.

One of the early studies to refute the concept of simple pure two phase behavior in BHJ systems was made by Muller *et al.* [11], who studied the phase behavior of PCBM with P3BT, P3HT and P3DDT using a combination of DSC, optical microscopy and X-ray diffraction (XRD) and related this to the solar cell efficiency for a series of devices with different blend compositions. These binary systems were shown to feature simple eutectic phase behavior (Figure 2(a)), with a eutectic composition of 35 wt% PCBM in the PCBM:P3HT system, and that the optimum composition for device performance is slightly hypoeutectic when expressed in terms of the polymer component.

Additional studies by Kim *et al.* [12], again using a combination of XRD and DSC, investigated the phase behavior of PCBM with P3HT, MDMO-PPV and MEH-PPV. They observed both P3HT melting point depression and glass transition temperature elevation in the P3HT:PCBM blends as a function of increasing PCBM wt%. However, as shown in Figure 2, the phase diagram they obtained differs from that of Muller *et al.* [11]. The determined solubility limits of PCBM in P3HT (Figure 2(b)), MDMO-PPV and MEH-PPV were 30, 40 and 50 wt% respectively. By measuring field effect conduction in transistors, a strong correlation was found between the phase behavior and the charge transport in the studied conjugated polymer/fullerene blends with hole-only transport being observed below the solubility limit and ambipolar transport at higher PCBM fractions.

A further measurement of the phase diagram of P3HT:PCBM blends was made by Zhao *et al.* [13] (Figure 2(c)) using conventional and modulated temperature DSC (DSC and MTDSC). Again the phase behavior differs from both Muller *et al.* and Kim *et al.* Zhao and co-workers observed a single glass transition temperature (T_g) for all compositions, which increases with increasing concentration of PCBM from 12.1°C for pure P3HT to 131.2°C for pure PCBM. It was found that the film morphology of the blends results from a dual crystallization behavior in which the crystallization of each component is hindered by the other component. The phase diagram also showed that the morphology of the blends with 45-50 wt% PCBM, whilst giving the highest device performance, is intrinsically unstable at the desired maximum operating temperature of 80°C, as the T_g is less than 40°C. More recently, the

same authors investigated the phase behavior of PCBM blends with different PPV polymers [14] using these same techniques together with rapid heat-cool calorimetry (RHC). They observed the occurrence of liquid-liquid phase separation in the molten state of MDMO-PPV:PCBM and high T_g -PPV:PCBM blends, as indicated by the coexistence of two T_g s for blends with a PCBM weight fraction of around 80 wt% which contrasted to the P3HT:PCBM blends where no phase separation was observed in the molten state [13].

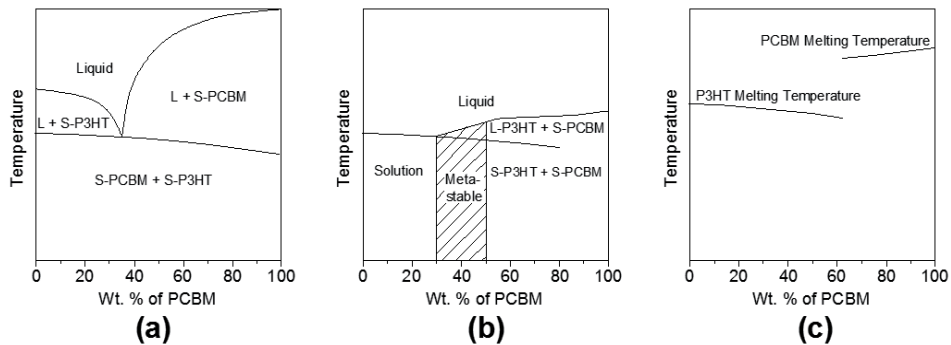


Figure 2. Phase diagrams of the system P3HT:PCBM as reported by Muller *et al.* [11] (a); Kim *et al.* [12] (b) and Zhao *et al.* [13] (c).

Hopkinson *et al.* [15] also measured the phase diagram of P3HT:PCBM blends using DMTA and GI-WAXS. Evidence for a transition to a phase separated state is observed at PCBM concentrations greater than 70 wt% and the T_g of the blends increases from $\sim 40^\circ\text{C}$ for pure P3HT to $\sim 70^\circ\text{C}$ for a PCBM loading of 65 wt% and then drops between 70 and 75 wt% indicating phase separation. Interestingly, this T_g variation differs considerably from the corresponding variation reported by Zhao *et al.* [13]. By varying degrees of crystallinity of P3HT, Woo *et al.* [16] were able to control phase segregation in P3HT/PCBM mixtures and have shown that under the same annealing conditions, highly regioregular (RR) P3HT induces a larger extent of phase segregation (i.e., larger domains of pure phases) in a blend film with PCBM than lowly regioregular P3HT. This makes sense, since without co-crystallization the fullerenes can only exist in the amorphous regions of the polymer.

The effects of polymer crystallinity on miscibility have also been studied for P3HT and MDMO-PPV blended with PCBM by Collins *et al.* [17]. The miscibility curves for the P3HT:PCBM system obtained from NEXAFS measurements are shown in Figure 3. All systems show an increasing miscibility of PCBM with temperature, suggesting an upper critical solution temperature (UCST) for the binary phase diagram. Both the middle and high-RR grades of P3HT exhibit very similar levels of PCBM miscibility starting at 3% and 4% concentration at 120°C , respectively, up to approximately 10% at 180°C . Contrasting this is the regiorandom grade of P3HT that display much larger miscibility levels of 16-22%. Their results also showed that, while no intercalation occurs in P3HT crystals, amorphous portions of P3HT and MDMO-PPV contain significant concentrations of PCBM after annealing, calling into question mod-

els based on pure phases and discrete interfaces. Furthermore, depth profiles of P3HT/PCBM bilayers have been measured using SIMS and the results obtained revealed that even short annealing causes significant inter-diffusion of both materials, showing that under no conditions do pure amorphous phases exist in BHJ or annealed bilayer devices.

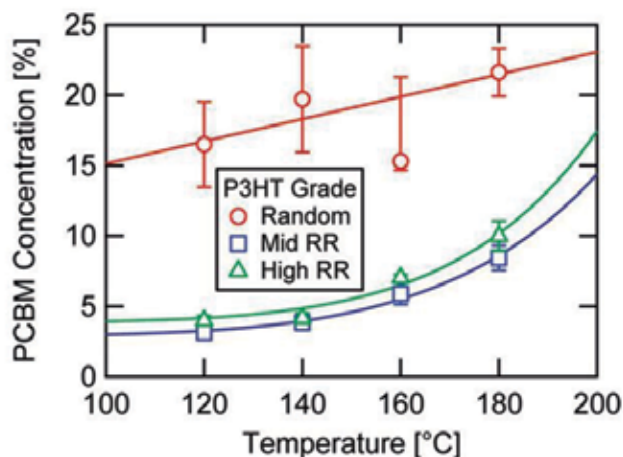


Figure 3. Miscibility phase diagram for P3HT mixed with PCBM according with Collins *et al.*[17]. “Reprinted with permission from (Journal of Physical Chemistry Letters 1 (2010) 3160). Copyright (2012) American Chemical Society.”

Small-angle neutron scattering (SANS) studies on 1:1 P3HT:PCBM blend thin films by Kiel *et al.* [18] examined the change in scattering and consequently the location of PCBM upon thermal annealing (at 140 °C for 20min). They found that after thermal annealing PCBM is soluble in the P3HT matrix up to a concentration of ~15-16 vol%. Although the data were not able to conclusively show that the dissolved PCBM was located in the amorphous P3HT, the authors suggested this as the probable location. They also observed that annealing has the effect of increasing the PCBM agglomeration and domain size and volume fraction suggesting a coarsening of the phase separated morphology.

Recently, Kozub *et al.* [19] have combined energy-filtered transmission electron microscopy (EFTEM) with grazing incidence small-angle X-ray scattering (GISAXS), to study the morphology evolution in P3HT/PCBM mixtures. They found that a significant amount of amorphous polymer exists as a homogeneous polythiophene-fullerene mixture. Elemental analysis of the amorphous regions demonstrated partial miscibility of P3HT and PCBM. They have also determined the χ parameter in P3HT-PCBM mixtures by measuring the melting point depression of P3HT in P3HT:PCBM mixtures. Through differential scanning calorimetry, they have obtained an estimate of the Flory-Huggins interaction parameter, χ , using Equation 1:

$$\frac{1}{T_m} + \frac{1}{T_m^0} = \frac{R}{\Delta H_f} \frac{v_m}{v_s} (\phi_s - \chi \phi_s^2) \quad (1)$$

where T_m is the melting point at a solvent (i.e. PCBM) volume fraction ϕ_s , T_m^0 is the melting point of pure polymer, R is the ideal gas constant, ΔH_f is the heat of fusion of polymer obtained from the melting endotherm, v_m is the monomer molar volume of polymer ($v_{m, P3HT} = 151 \text{ cm}^3/\text{mol}$) and v_s is the solvent molar volume ($v_{s, PCBM} = 607 \text{ cm}^3/\text{mol}$). Fitting Equation 1 to the melting point data shown in Figure 4(a) with χ as the only adjustable parameter yielded $\chi = 0.86 \pm 0.09$. Based on the assumption of Flory-Huggins free energy of mixing for polymer solutions, they obtained the spinodal, shown in Figure 4(b). The combination of the spinodal and χ allowed for the determination of the miscibility of amorphous P3HT:PCBM mixtures. They found that for P3HT concentrations greater than 0.42 by volume, the mixtures are miscible and this miscibility suppresses fullerene crystallization. They therefore concluded that the intricate mesoscopic structure of P3HT/PCBM mixtures present in 1:1 by mass mixtures ($\phi_{P3HT} = 0.58$), commonly reported in the literature and critical for device performance, is not a result of demixing of the amorphous phases, but instead, must be a consequence of polymer crystallization.

Small-angle x-ray scattering (SAXS) studies of the phase separation of P3HT-PCBM thick films showed that a bulk heterojunction system blend of 1:0.7 P3HT:PCBM is not just a simple two-phase system with well-defined interfaces [20]. As other workers have shown the phase behavior was shown to be a much more complicated system incorporating regions of crystalline P3HT and PCBM, and a mixed phase of amorphous P3HT and PCBM. The phase separation length scale was found to be $\sim 25 \text{ nm}$ both before and after thermal annealing. The thermal annealing was also shown to cause a reduction in the phase separation associated with diffusion of PCBM into the amorphous P3HT, as previously also reported by Kiel *et al.* [18].

The influence played by the electrode interfaces on BHJ phase behavior has been studied by Chen *et al.* [21] on the multicomponent P3HT:PCBM system. Small angle neutron scattering and electron microscopy showed that a nanoscopic, bicontinuous morphology develops within seconds of annealing at $150 \text{ }^\circ\text{C}$ and coarsens slightly with further annealing. P3HT and PCBM are shown to be highly miscible, to exhibit a rapid interdiffusion, and to display a preferential segregation of one component to the electrode interfaces.

Yin *et al.* [22] have also used SANS to study the bulk morphology of P3HT/PCBM samples prepared by drop casting a solution on a heated ($\sim 110^\circ\text{C}$) quartz disk window (to accelerate drying). Blends of PCBM and P3HT were studied and the effects of composition and thermal annealing at $150 \text{ }^\circ\text{C}$ on the resultant morphology and interfacial structure were examined. The SANS results indicate that P3HT and PCBM form homogeneous mixtures up to $\sim 20 \text{ vol } \% \text{ PCBM}$, which was assigned as the approximate miscibility limit. At all PCBM fractions between 10 and 50 vol%, the resultant matrix also contains pure (crystalline) P3HT. At higher PCBM loadings, PCBM phase separates to form larger domains. In the system with 50 vol% PCBM, i.e. the system which is more representative of the active layer in organic photovoltaics, neutron scattering shows that there exist at least three coexisting phases; pure P3HT and PCBM phases, and a mixture of amorphous PCBM and P3HT that serves as the surrounding matrix. A simple geometric calculation indicates that the PCBM molecules in the amorphous phase are sufficiently close to allow charge transport, i.e. 4.3 \AA at $\Phi =$

15% loading and 3.3 Å at $\Phi = 20\%$ fullerene loading. These distances are consistent with intermolecular charge transport models verifying therefore the ability of this morphology to create significant photocurrent when illuminated. The morphological model indicated by the SANS analysis is of “rivers and streams”, as the PCBM/P3HT amorphous matrix contains an abundance of donor/acceptor interfaces resulting in an efficient dissociation of excitons. These charges then “flow” in the streams of PCBM or P3HT within the amorphous phase to the larger pure PCBM (electrons) or P3HT (holes) phases, which act as “rivers” to transport the charges to the electrodes. This efficient charge mobility morphology exists due to the extended miscibility of PCBM in P3HT, which is required to create sufficient close packing in the amorphous phase to allow charge transport in the “streams”. Their proposed mechanism also explains the large difference in efficiency between P3HT/C₆₀ and P3HT/PCBM bulk heterojunctions, where the immiscibility of C₆₀ in P3HT presumably inhibits the formation of a morphology that allows effective charge transport to the “rivers”.

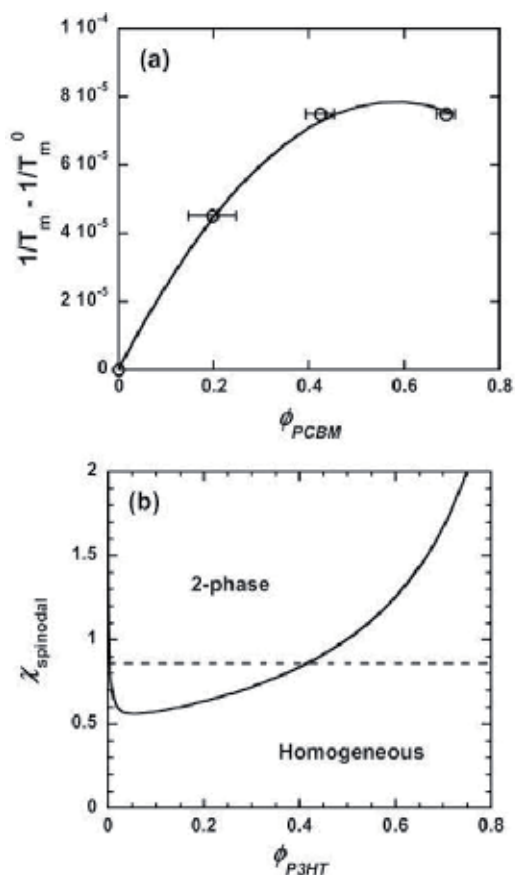


Figure 4. Estimate of the miscibility from measurements of the melting point depression, as described by Kozub *et al.* [19]. (a) Melting point depression of P3HT as a function of PCBM volume fraction, Φ_{PCBM} , obtained from DSC experiments. The solid line is from eq 1 with $\chi = 0.86$. Error bars represent the uncertainty in composition due to the limited

accuracy of the scale. (b) Spinodal as a function of P3HT volume fraction, Φ_{P3HT} , obtained by modeling P3HT:PCBM mixtures as polymer solutions with MWP3HT = 50 000 g/mol. The dotted line denotes $\chi = 0.86$, and in combination with the spinodal indicates that homogeneous P3HT:PCBM mixtures are unstable for $\Phi_{\text{P3HT}} < 0.42$. "Reprinted with permission from (Macromolecules 44 (2011) 5722). Copyright (2012) American Chemical Society."

Treat *et al.* [23] have used a bilayer of P3HT and PCBM, as a model system, to develop a more complete understanding of the miscibility and diffusion of PCBM within P3HT during thermal annealing. Fast interdiffusion of these two components was observed when annealed at 150 °C for 30 s confirming the results of Che *et al.* [21]. This interdiffusion resulted in a homogeneous blend with an estimated diffusion coefficient of $3 \times 10^{-10} \text{ cm}^2/\text{s}$. The fact that there is a clear drive towards a homogeneous mixture of P3HT and PCBM from a distinctly heterogeneous structure strongly suggests that PCBM (molecular or aggregated species) is dispersible in disordered P3HT under typical annealing conditions of BHJ OPV. The authors estimate that PCBM has a concentration greater than 40 wt% in P3HT, which is consistent with previously reported estimates for bulk samples. It was also shown that PCBM diffuses to the P3HT film without affecting the crystal size, structure, or orientation of P3HT, even at an equal P3HT:PCBM weight ratio. These results indicate that the fast diffusion occurs only through the disordered regions of P3HT and shows how favorable the mixing in this system is. This again opposes the previously held belief that phase-pure domains form in BHJs due to immiscibility of these two components. These results confirm that the BHJ film is comprised of a dispersion of aggregates of PCBM, molecularly dispersed PCBM in disordered P3HT, and crystallites of P3HT and suggests that the pure polymer domains widely thought to exist in BHJ films are, in fact, disordered solutions of crystalline and disordered polymer and amorphous fullerene.

A direct comparison between conventionally prepared P3HT/PCBM BHJs (C-BHJ) and an active layer created by solution processed, layer-by-layer, sequential deposition (layer evolved BHJ, LE-BHJ) has been studied by Moon *et al.* [24]. Following annealing at 100°C for 10 min. both OPVs based on P3HT/PCBM LE-BHJ and C-BHJ films show similar device efficiencies and transport properties. Within the limits of contrast, cross-sectional TEM images show that the intermixing of polymer and fullerene within the active layer of both OPVs (LE-BHJ and C-BHJ) is identical. Therefore, despite being dramatically different in preparation, these two methods produce nearly identical nano-morphologies. This spontaneous formation of equivalent morphologies through multiple routes implies that the resulting BHJ nanostructure is the lowest energy state of the system.

A systematic study to understand how the P3HT molecular weight influences the P3HT/PCBM phase behavior and the corresponding device performance has been undertaken by Nicolet *et al.* [25]. The phase diagrams for all P3HT:PCBM binary blends were obtained using DSC, displaying a eutectic phase diagram in all cases with a eutectic point found to decrease from 65 to 50 wt % for P3HT molecular weights increasing between 9.6 k and 60 k g/mol, respectively.

Molecular mixing in P3HT/PCBM thin films annealed at 140°C was also the focus of a grazing incidence small-angle neutron scattering (GISANS) study by Ruderer *et al.* [26], which utilized a detailed analysis based on the distorted wave Born approximation (DWBA). A

broad range of compositions from 9 to 67 wt % PCBM content were investigated. The structure size obtained associated with the distance between PCBM domains, is found to be broadly distributed around 80 nm for systems with a small PCBM content of 9 wt % (see Figure 5(a)). For the systems with higher PCBM content, the distance was revealed to be constant at about 20 nm, which is in the range of the predicted exciton diffusion length and therefore beneficial for charge generation. While most analyzing methods are only able to extract overall structural length scales, the use of advanced modeling reveals much more detailed information. To fit the scattering data of such a complex system, up to three phase types associated with different PCBM domains have to be incorporated in the model. Over all blend ratios, large PCBM domains (Figure 5(a), triangles) with a radius of 100–200 nm are observed with low frequency (less than 0.05%). Much more frequently observed (>90%) smaller PCBM domains (Figure 5(a), squares), dominate the morphology. Their radius ranges from 3 to 10 nm with the maximum object size at a PCBM content of 50 wt %, which is in the range of the blend ratio where typically the most efficient P3HT/PCBM solar cells are found. For the systems with 25 and 33 wt % PCBM content, an additional PCBM domain with a radius in the range of 16–18 nm was observed again with low probability (<8%). Such an additional PCBM domain size might indicate a non-equilibrium morphology. The volume fraction of the molecularly dispersed PCBM, Φ_{PCBM} , a function of the overall PCBM content (see Figure 5(b)) shows that for the 9 wt % PCBM content films, a very low amount of molecularly dispersed PCBM is found. However, P3HT/PCBM films with a higher overall PCBM content (between 5 and 15 vol %) show molecularly dispersed PCBM.

As discussed above, the thermodynamics and phase behavior of conjugated polymer/fullerene systems is very complex and except in specific examples (such as P3HT/PCBM) it is still poorly understood. Even in the highly studied example of P3HT/PCBM there are conflicting results about the phase behavior. For example while some consider that these systems have an eutectic type of phase behavior [11–13] (as is usually found in metal mixtures and salt mixtures), others [19] are more in favor of the classical Flory-Huggins phase behavior common in amorphous polymer systems [27]. There is also disagreement in the P3HT/PCBM miscibility limits (i.e. in the amount of molecularly dispersed PCBM in the P3HT phase) reported in the literature. For instance, while Kozub *et al* [19] reported a value of > 42% vol % P3HT, Yin *et al.* [22] reported a miscibility limit of 20 vol % of PCBM molecularly dispersed in P3HT, and Ruderer *et al.* [26] reported a molecularly dispersed PCBM content of up to 35% in the amorphous P3HT phase. Despite these conflicting arguments, all of these studies are consensual in that all of them show clearly that the ideal model of pure phase separated donor and acceptor domains, as shown in Figure 1, is unattainable using the standard processing techniques (spin-coating followed by annealing) and therefore in order to explain the efficiencies of the currently existing devices, a paradigm shift in the physics behind device operation may be required, as has been suggested by some authors [17, 22].

In most of the studies described above, the main focus has been the study of the thermodynamics of the bulk and therefore the experimental samples were thick enough to avoid any relevant effect from the substrate's surface energy. It is however known that in very thin polymer films (~100 nm) as used in OPVs, the thin film morphology and phase behavior is

also affected by the substrate's surface energy. This phenomenon has also been the object of intense research and it is known that the substrate's free energy can induce vertical phase segregation (normal to the substrate's surface). However, just like reports of bulk BHJ behavior there are also contradictory reports in the literature concerning the effect of the substrate's surface energy on the final film morphology.

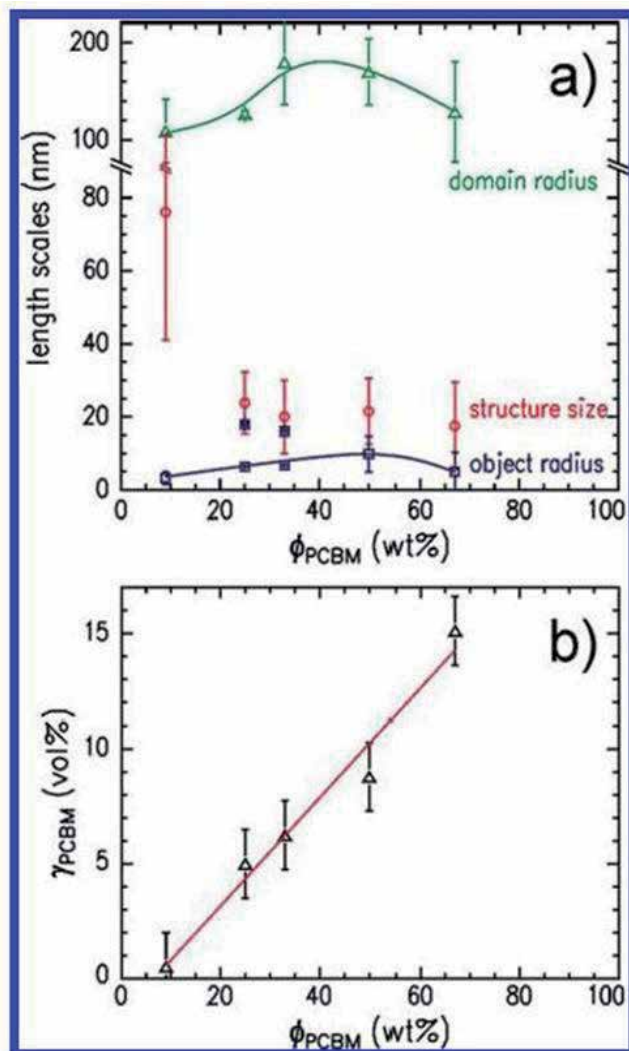


Figure 5. a) Distances (structure size) and small (object radius) and large PCBM domains (domain radius) used for the simulations of the GISANS data depending on the PCBM content [26]. The error bars represent the distribution of these lengths. (b) Fraction of the molecularly dissolved PCBM in the P3HT phase depending on the overall PCBM content. The solid lines are guides to the eyes. "Reprinted with permission from (Journal of Physical Chemistry Letters 3 (2012) 683). Copyright (2012) American Chemical Society."

The compositional depth profiles in thin films of APFO-3:PCBM blends spin-coated from chloroform solutions onto silicon has been studied by Björström *et al.* [28] using dynamic secondary ion mass spectrometry (D-SIMS). Vertical phase segregation was found to be caused by specific interactions between the substrates and the components of the APFO-3:PCBM mixtures. By changing the substrate from silicon to gold it was shown that the composition profile near the substrate interface varied. Later work by Campoy-Quiles *et al.* [29] also showed that changing the surface energy of a substrate can change the concentration profile of PCBM and, in the case of thermal annealing, cause PCBM to cluster together on an SiO₂ substrate.

Vertical segregation behavior in P3HT:PCBM (1:1) blend films were also studied by Kim *et al.* [30] using a glow discharge spectrometer equipped with a RF plasma (Ar ion) depth profiling system. They found that the relative distribution of P3HT and PCBM molecules changed considerably by thermal annealing, with increasing PCBM and P3HT enrichment close to the electron-collecting (Al) and to the hole-collecting (PEDOT:PSS/ITO) electrodes, respectively. Even in the absence of the Al electrode P3HT enrichment at the free (air) surfaces and abundance of fullerene derivatives at the organic/substrate interfaces was also observed by Xu *et al.* [31]. The vertical phase separation in this system was attributed to the surface energy difference of the components and hence their differential interaction with the substrates.

The importance of film thickness has been investigated by Verploegen *et al.* [32] who showed that very thin films (20 to 25 nm thick) of P3HT:PCBM 1:3 display dewetting when annealed at 160°C. Films of 75 nm thickness of the same composition when annealed did not dewet, but showed some signs of crystallization induced phase separation. Using neutron reflectivity (NR) Kiel *et al.* [33] showed that in a P3HT:PCBM BHJ, although the concentration profile is complicated through the film thickness, the PCBM concentrated at the substrate interface and also close to, but not at, the air interface where the aluminum counter-electrode was deposited. Upon annealing, however, the PCBM accumulates at the air interface creating an improved pathway for electrons to leave the device through the deposited metal electrode. PCBM migration upon thermal annealing is a clear indicator that it is in a kinetically trapped state upon spin coating and has some mobility within the device.

Further NR studies of morphology of the P3HT:PCBM thin films either freshly cast, or after solvent and thermally annealing have been made by Parnell *et al.* [34]. They found that the freshly cast films have a surface layer that is relatively depleted in PCBM, while being relatively rich in PCBM at the film–substrate interface. Solvent annealing was shown to have little effect on the PCBM distribution within the film, however thermal annealing increased the PCBM concentration at the surface to a level found in the bulk of the film. Neutron reflectivity measurements also suggest that the free surface of the films (i.e. without top metal electrode layer) undergo surface roughening when subject to solvent vapor and thermal annealing, a conclusion verified by scanning probe microscopy. It was presumed that the PCBM-depleted layers found in ‘as-cast’ P3HT/PCBM thin films are partly responsible for their relatively poor performance in OPV devices, and that thermal annealing OPV devices improves device efficiency not only by the creation of a percolated PCBM network, but also by improving electron extraction via increasing the PCBM concentration next to the device cathode.

The use of ToF-SIMS has been able to add to the morphological model derived by NR measurements by examining both the vertical as well as the lateral distribution of PCBM and P3HT in BHJ films [35]. In 150 nm thick films spun coated from a 1:1 weight ratio of P3HT:PCBM chlorobenzene solutions, ToF-SIMS imaging showed that the lateral phase separation (within the limit of the micron resolution of SIMS imaging) was similar before and after an annealing treatment at 140°C for 30 min. However, depth profiling clearly shows a vertical phase separation of P3HT:PCBM on the pristine blend (before annealing), with a higher concentration of PCBM close to the PEDOT:PSS interface. On the other hand, after annealing, the cross-sectional images of PCBM and P3HT are both uniform along the vertical axis showing that the annealing treatment suppresses the vertical phase segregation. Using low voltage, high resolution TEM, Beal *et al.* [36] revealed some details of the mechanism of PCBM domain migration associated with the vertical segregation within P3HT:PCBM solar cells by giving direct confirmation of P3HT and PCBM crystallization.

Xue *et al.* [37] have used the variation of the post-annealing cooling rate to create a series of “snapshots” of the reorganization processes that occur upon annealing. P3HT:PCBM blend devices exhibit a complex vertical stratification of both crystallinity and blend composition. Using a combination of UV-vis spectroscopy, XRD, NEXAFS, AFM, and contact angle measurements, they showed that annealing resulted in the formation of three distinct vertical layers. Diffusion of PCBM from the interfaces into the bulk of the film results in the formation of (a) a P3HT rich substrate interfacial (wetting) layer, (b) a homogeneous ‘bulk’ central layer, and (c) a P3HT-rich air interfacial (capping) layer. The orientation of the P3HT molecules was shown to vary from *c*-axis P3HT alignment in the wetting layer at the substrate interface to an *a*-axis aligned in the capping layer at the air interface and also in the bulk layer. The data showed that by slowing the post-annealing cooling rate devices with significantly enhanced efficiencies can be prepared. This improvement in device performance was correlated with the observed increased crystallinity and hence polymer alignment, and also phase segregation both at the interfaces and in the bulk film. In particular, they found that slow cooling resulted in an aligned interfacial active layer/substrate structure that is beneficial for charge transport.

Theoretical descriptions indicate a segregation preference for a typical photovoltaic device is where the donor (P3HT) is concentrated close to the substrate, and the acceptor (PCBM) next to the top surface, onto which the cathode (for example Al) is deposited. This distribution of components is expected to enhance the selectivity of the contacts towards one type of charge carrier and so reduce charge leakage. As discussed above, there are clearly contradictory results in the experimental literature concerning the exact nature of this vertical phase segregation. However, there is agreement that annealing leads to an increase of the PCBM concentration closer to the cathode [30, 33-35], and this has been pointed out as being one of the reasons for the improvement of device efficiencies that is usually observed upon annealing treatments. The timing of the annealing process, i.e. before or after the deposition of a metal electrode, is also known to influence the results. Post-production thermal annealing can improve the evolution of well-ordered nanoscale morphology because of a limitation of PCBM overgrowth, that is, due to the confinement effect.

3. Kinetic Considerations

As shown in Figure 2, Muller *et al.* [11] and Kim *et al.* [12] reported an eutectic composition (C_e) of Ce \approx 35 – 40 wt% PCBM and Zhao *et al.* [13] a value of $C_e \approx$ 60 wt% PCBM. However, whilst these authors were trying to extract the thermodynamic behavior of the blends, kinetic factors are clearly affecting the resulting observations. It is these types of discrepancies in observed phase behavior that highlights the difficulty in understanding the fundamental relationship between morphology and device performance. Although the morphology of the BHJ is ultimately determined by thermodynamic factors, the observed thin film morphology can be dominated by the kinetics of the film preparation methods and parameters used, including solvent evaporation/drying rates and by the kinetics of cooling after annealing. Herein lies some of the answer as to the reason for the contradictions in the observed phase behavior and morphology of these systems, since in putting together a device, the processing conditions between different groups often vary and also almost certainly do not allow the system to reach a global free energy minima and hence true a thermodynamic state. Changes to processing conditions are well known to make big variations in device performance, but there are also much subtler effects associated with the well-known irreproducibility in otherwise identical processing conditions, which are problematic for OPV development.

The effect of drying kinetics on the resultant P3HT:PCBM blend has a profound effect on the final device characteristics [38], where it was found that films dried slowly had better performance characteristics (higher external quantum efficiency, higher power conversion efficiency, higher fill factor, and lower series resistance) than the rapidly dried films. The charge carrier mobility of holes and electrons in P3HT:PCBM thick films was shown to have more balanced transport properties and non-dispersive dynamics for the slowly dried films, where as the rapidly dried film displayed dispersive dynamics and unbalanced transport. All these differences in performance were explained by the rate of solvent evaporation, as fast solvent loss quenches the phase separation process, and conversely the longer the blend is mobile and contains solvent the more the mixture will proceed to a more phase separated state. Campoy-Quiles *et al.* [29] have studied the morphology changes induced by slow drying and vapour annealing and showed that the PCBM concentration profile changes as the spin-coating speed (and hence the rate of drying) is reduced. Slow drying has a qualitatively similar effect to thermal annealing, whereby the composition gradient becomes more pronounced and the surface-segregated PCBM concentration increases.

The time-dependent morphology evolution of blend films of P3HT and PCBM, was investigated by Jo *et al.* [39], using two different annealing treatments with different morphology evolution time scales, i.e. a high-temperature thermal annealing (150 °C), and a room-temperature solvent annealing. Comparing the morphological changes of the blend films after the two annealing treatments, solvent annealing resulted in a more favorable BHJ morphology than thermal annealing. The poor BHJ morphology after thermal annealing under these experimental conditions was attributed to the relatively fast diffusion and aggregation of the PCBM molecules during P3HT crystallization, which interfered with the growth of the elongated fibrillar P3HT crystals and subsequent evolution of the well-ordered BHJ morpholo-

gy. These results are however, seemingly contradictory to those of Parnell *et al.* [34], suggesting that there are other factors that are contributing to the observed behaviors.

The reasons for the irreproducibility of the performance of P3HT:PCBM BHJ solar cells fabricated using nominally identical conditions has been investigated by de Villers *et al.* [40]. They showed that this irreproducibility is the result of the occurrence of vertical phase segregation of P3HT to the top surface, which is controlled by subtle factors in the kinetics of solvent evaporation during spin-coating. When this type of vertical phase separation occurs, electron extraction is hindered by the poor contact between the PCBM component of the BHJ and the cathode.

Wang *et al.* [41] have used in-situ ellipsometry and grazing incidence x-ray scattering (GIS) to study molecular self-organization in P3HT and PCBM blend films in real time, during the drying process as they are cast from solution. They have identified three stages in film drying: (I) rapid solvent-evaporation, (II) moderate solvent-evaporation and rapid crystallization, and (III) slow solvent-evaporation and slow crystallization. They showed that the onset of fast crystallization commences when the volume fraction of P3HT:PCBM in a wet film reaches a critical volume fraction of 50%. The observed crystallization growth-mechanism is consistent with a heterogeneous nucleation process in which defects or impurities act as nucleation sites.

The rate of evaporation is clearly affected by the boiling point and vapor pressure of the solvents used. The influence solvent boiling point on the morphology and photovoltaic performance of P3HT:PCBM:BHJ films produced via spin-coating, has been studied by Ruderer *et al.* [42]. The four solvents considered were chloroform (CF), toluene, chlorobenzene (CB) and xylene. Solar cells made using these solvents had different photovoltaic performances. Using a wide range of experimental techniques it was shown that solubility-driven cluster formation of PCBM occurred in these systems. In films made using solvents with poor solubility of PCBM many more clusters were formed. As-spun films showed no P3HT crystallinity, independent of the solvent used. After annealing, P3HT crystals formed with edge-on configuration relative to the substrate as the main orientation, with crystal lattice constants that were also independent of the solvent used. However the crystal sizes increased with increasing boiling point (i.e. decreasing evaporation rates) of the solvents used, which was attributed to the increased drying time during spin-coating and residual solvent in the BHJ films. For toluene-, CB-, and xylene-made films, lateral nanostructures were found. In the vertical direction P3HT enrichment layers were detected for toluene- and CB-made films and PCBM enrichment layers for the films made using toluene and xylene. Nevertheless films made using toluene, CB, and xylene showed similar photovoltaic performance. Conversely, films made using chloroform presented a layered structure with a disadvantageous material distribution, with the P3HT hole conductor at the top electrode and the PCBM electron conductor at the electron-blocking layer, consequently producing efficiencies that were significantly lower.

Schmidt-Hansberg *et al.* [43] have investigated the dynamics and thermodynamics of molecular ordering, in P3HT/PCBM mixtures, during film drying from 1,2-dichlorobenzene (DCB). The pathway through the phase diagrams of P3HT and PCBM solutions, as shown in

Figure 6, was compared with the structural changes during crystallization of the ternary P3HT:PCBM:solvent system observed in real time by grazing incidence x-ray diffraction (GIXD). It was shown that PCBM only crystallizes at the final stage of drying although its solubility limit is reached a very early stage of solvent evaporation.

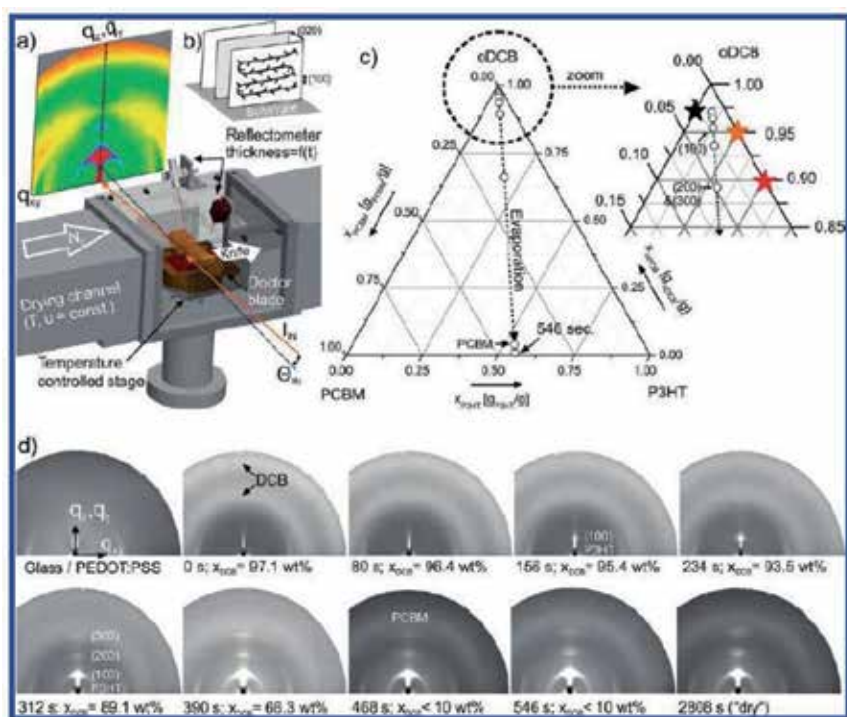


Figure 6. a) Schematic of the experimental setup for simultaneous real time GIXD and laser reflectometry of doctor-bladed thin films in a controlled drying environment. (b) Schematic of P3HT unit cell. (c) Ternary phase diagram of P3HT-PCBM-DCB; the star symbols denote phase transitions in the binary cases. From reference [43]. "Reprinted with permission from (ACS Nano 5 (2011) 8579). Copyright (2012) American Chemical Society."

Sobkowicz *et al.* [44] have measured the time- and temperature dependent aggregation of P3HT in *o*-dichlorobenzene solutions using rheometry and small-angle neutron scattering (SANS). They tried to set a starting point for understanding important aspects of morphology development in drying BHJ films. They found that the presence of PCBM dramatically slows the aggregation of P3HT in solution. Concentration and temperature dependencies were identified, with the latter being the more sensitive parameter. Analysis of the SANS data showed a strong affinity between P3HT and DCB with an interaction parameter that becomes more negative with increasing concentration, and elevated temperature dissolution suggesting UCST behavior in this polymer-solvent system. Modest cooling of P3HT solutions even in "good" solvents such as DCB resulted in rapid aggregation, although the aggregated solutions do not completely phase separate, but rather form physical gels consisting of anisotropic structures. An increase in solution modulus of several orders of

magnitude accompanies the aggregation and the pure polymer solution modulus becomes frequency-independent. Although the percent crystallinity in the aggregated solutions cannot be calculated directly from these results, it appears that the crystalline fraction is lower in the solutions with PCBM present. These results also lend insight into the film drying process and will ultimately lead to improved processing procedures in pursuit of an optimized morphology for bulk heterojunction devices.

The rate of cooling, after annealing, also has a dramatic influence on the final morphology of the film. A slower cooling rate leads to a greater extent of crystallization, when semi-crystalline polymers or crystalline nano-particles are involved. Despite this fact, only recently have some authors drawn attention to this important factor [37].

4. Conclusions

Recent detailed studies of the phase behavior of conjugated polymer:fullerene blends have begun to provide important information for understanding the property-processing relationships in organic solar cell blends. Until these studies conventional wisdom suggested that the P3HT:PCBM system was a simple two phase bulk heterojunction with well-defined interfaces between regions of pure P3HT and pure PCBM. The latest results clearly demonstrate that this assumption is not correct, but instead unequivocally show that BHJ materials are more complex systems incorporating regions of crystalline P3HT, PCBM, and intermixed regions of amorphous P3HT and PCBM. Upon annealing there is considerable interdiffusion of PCBM into the amorphous P3HT. It has also been shown that in the case of thin BHJ films (~100 nm) such as those used in OPVs, the substrate's surface energy can have a crucial role on the final morphology.

Furthermore, the kinetics as manifested in the processing routes and conditions can also play a dominant role in the observed structure/morphology. For all these reasons it is very difficult to predict the structure of the BHJ since apparently the same process used by different groups can end to with different results.

Whilst significant insight has been derived in understanding the behavior of a limited number of systems, with P3HT:PCBM the most widely studied system by far, there is still no predictive understanding in even this system. If technologically meaningful device efficiencies are to be achieved significant additional work must be undertaken to derive predictive capability for these complex BHJ systems. This will ultimately require a global effort of complementary experimental measurements combined with theoretical and computational modeling.

5. Nomenclature

AFM – Atomic Force Microscopy

BHJ – Bulk Hetero-Junction

DMTA – Dynamic Mechanical Thermal Analysis

GISANS - Grazing Incidence Small-Angle Neutron Scattering

GIXS – Grazing Incidence X-ray Scattering

GIWAXS/GIXD – Grazing Incidence Wide-Angle X-ray Scattering/x-ray diffraction

ITO – Indium Tin Oxide

MEH-PPV - poly [2-methoxy-5-(2-ethyl-hexyloxy)-1,4-phenylene-vinylene]

MDMO-PPV – poly(2-methoxy-5-(3',7'-dimethyloctyloxy)-1,4-phenylenevinylene)

NEXAFS – Near-Edge X-ray Absorption Fine Structure

NR – Neutron Reflectivity

OPV – Organic Photo-Voltaic

P3HT – poly(3-hexylthiophene)

PCBM – phenyl-C61-butyric acid methyl ester

PEDOT:PSS – Poly(3,4-EthyleneDiOxyThiophene):Poly(StyreneSulfonate)

SANS – Small Angle Neutron Scattering

SAXS – Small-Angle X-ray Scattering

SIMS – Secondary Ion Mass Spectrometry

TEM – Transmission Electron Microscopy

ToF-SIMS – Time-of-Flight Secondary Ion Mass Spectrometry

UCST – Upper Critical Solubility Temperature

UV-Vis – Ultra-Violet Visible

XRD – X-ray diffraction

WAXS – Wide-Angle X-ray Scattering

Acknowledgements

Gabriel Bernardo acknowledges financial support from the IPC's (Institute for Polymers and Composites) strategic project: "PEst-C/CTM/LA0025/2011" (Projecto Estratégico—LA 25—2011-2012—Strategic Project—LA 25—2011-2012).

Author details

Gabriel Bernardo^{1*} and David G. Bucknall²

*Address all correspondence to: gabriel.bernardo@dep.uminho.pt

1 Institute for Polymers and Composites/I3N, University of Minho, Campus de Azurém, Portugal

2 Materials Science and Engineering, Georgia Institute of Technology, USA

References

- [1] Hoppe, H., & N. S. (2006). Sariciftci, Morphology of polymer/fullerene bulk hetero-junction solar cells. *Journal of Materials Chemistry*, 16(1), 45-61.
- [2] Hoppe, H., et al. (2004). Nanoscale morphology of conjugated polymer/fullerene-based bulk-heterojunction solar cells. *Advanced Functional Materials*, 14(10), 1005-1011.
- [3] Chen, L. M., et al. (2009). Recent Progress in Polymer Solar Cells: Manipulation of Polymer: Fullerene Morphology and the Formation of Efficient Inverted Polymer Solar Cells. *Advanced Materials*, 1434-1449.
- [4] Brady, M. A., Su, G. M., & Chabynyc, M. L. (2011). Recent progress in the morphology of bulk heterojunction photovoltaics. *Soft Matter*, 7(23), 11065-11077.
- [5] Gunes, S., Neugebauer, H., & Sariciftci, N. S. (2007). Sariciftci, Conjugated polymer-based organic solar cells. *Chemical Reviews*, 107(4), 1324-1338.
- [6] Saunders, B. R., & Turner, M. L. (2008). Nanoparticle-polymer photovoltaic cells. *Advances in Colloid and Interface Science*, 138(1), 1-23.
- [7] Sylvester-Hvid, K. O., Rettrup, S., & Ratner, M. A. (2004). Two-dimensional model for polymer-based photovoltaic cells: Numerical simulations of morphology effects. *Journal of Physical Chemistry B*, 108(14), 4296-4307.
- [8] Sylvester-Hvid, K. O., & Ratner, M. A. (2005). Simplified charge separation energetics in a two-dimensional model for polymer-based photovoltaic cells. *Journal of Physical Chemistry B*, 109(1), 200-208.
- [9] Lei, B., et al. (2008). Quantifying the relation between the morphology and performance of polymer solar cells using Monte Carlo simulations. *Journal of Applied Physics*, 104(2), 024504.
- [10] Meng, L. Y., et al. (2010). Dynamic Monte Carlo Simulation for Highly Efficient Polymer Blend Photovoltaics. *Journal of Physical Chemistry B*, 114(1), 36-41.

- [11] Muller, C., et al. (2008). Binary organic photovoltaic blends: A simple rationale for optimum compositions. *Advanced Materials*, 20(18), 3510.
- [12] Kim, J. Y., & Frisbie, D. (2008). Correlation of Phase Behavior and Charge Transport in Conjugated Polymer/Fullerene Blends. *Journal of Physical Chemistry C*, 112(45), 17726-17736.
- [13] Zhao, J., et al. (2009). Phase Diagram of P3HT PCBM Blends and Its Implication for the Stability of Morphology. *Journal of Physical Chemistry B*, 113(6), 1587-1591.
- [14] Zhao, J., et al. (2011). Phase behavior of PCBM blends with different conjugated polymers. *Physical Chemistry Chemical Physics*, 13, 12285-12292.
- [15] Hopkinson, P. E., et al. (2011). A Phase Diagram of the P3HT PCBM Organic Photovoltaic System: Implications for Device Processing and Performance. *Macromolecules*, 44(8), 2908-2917.
- [16] Woo, C. H., et al. (2008). The Influence of Poly(3-hexylthiophene) Regioregularity on Fullerene-Composite Solar Cell Performance. *Journal of the American Chemical Society*, 130(48), 16324-16329.
- [17] Collins, B. A., et al. (2010). Molecular Miscibility of Polymer-Fullerene Blends. *Journal of Physical Chemistry Letters*, 1(21), 3160-3166.
- [18] Kiel, J. W., Eberle, A. P. R., & Mackay, M. E. (2010). Nanoparticle Agglomeration in Polymer-Based Solar Cells. *Physical Review Letters*, 105(16), 168701.
- [19] Kozub, D. R., et al. (2011). Polymer Crystallization of Partially Miscible Polythiophene/Fullerene Mixtures Controls Morphology. *Macromolecules*, 44(14), 5722-5726.
- [20] Parnell, A. J., et al. (2011). Nanoscale Phase Separation of P3HT PCBM Thick Films As Measured by Small-Angle X-ray Scattering. *Macromolecules*, 44(16), 6503-6508.
- [21] Chen, D., et al. (2011). P3HT PCBM Bulk Heterojunction Organic Photovoltaics: Correlating Efficiency and Morphology. *Nano Letters*, 11(2), 561-567.
- [22] Yin, W., & Dadmun, M. (2011). A New Model for the Morphology of P3HT PCBM Organic Photovoltaics from Small-Angle Neutron Scattering: Rivers and Streams. *ACS Nano*, 5(6), 4756-4768.
- [23] Treat, N. D., et al. (2011). Interdiffusion of PCBM and P3HT Reveals Miscibility in a Photovoltaically Active Blend. *Advanced Energy Materials*, 1(1), 82-89.
- [24] Moon, J. S., et al. (2011). Spontaneous Formation of Bulk Heterojunction Nanostructures: Multiple Routes to Equivalent Morphologies. *Nano Letters*, 11(3), 1036-1039.
- [25] Nicolet, C., et al. (2011). Optimization of the Bulk Heterojunction Composition for Enhanced Photovoltaic Properties: Correlation between the Molecular Weight of the Semiconducting Polymer and Device Performance. *Journal of Physical Chemistry B*, 115(44), 12717-12727.

- [26] Ruderer, M. A., et al. (2012). Phase Separation and Molecular Intermixing in Polymer-Fullerene Bulk Heterojunction Thin Films. *Journal of Physical Chemistry Letters*, 3(6), 683-688.
- [27] Eitouni, H. B., & Balsara, N. P. (2007). Thermodynamics of Polymer Blends. in J.E. Mark (Ed) *Physical Properties of Polymers* Springer , 339-356.
- [28] Bjorstrom, C. M., et al. (2007). Vertical phase separation in spin-coated films of a low bandgap polyfluorene/PCBM blend- Effects of specific substrate interaction. *Applied Surface Science*, 253(8), 3906-3912.
- [29] Campoy-Quiles, M., et al. (2008). Morphology evolution via self-organization and lateral and vertical diffusion in polymer: fullerene solar cell blends. *Nature Materials*, 7(2), 158-164.
- [30] Kim, Y., et al. (2009). Distorted Asymmetric Cubic Nanostructure of Soluble Fullerene Crystals in Efficient Polymer:Fullerene Solar Cells. *Acs Nano*, 3(9), 2557-2562.
- [31] Xu, Z., et al. (2009). Vertical Phase Separation in Poly(3-hexylthiophene): Fullerene Derivative Blends and its Advantage for Inverted Structure Solar Cells. *Advanced Functional Materials*, 19(8), 1227-1234.
- [32] Verploegen, E., et al. (2010). Effects of Thermal Annealing Upon the Morphology of Polymer-Fullerene Blends. *Advanced Functional Materials*, 20(20), 3519-3529.
- [33] Kiel, J. W., et al. (2010). Nanoparticle concentration profile in polymer-based solar cells. *Soft Matter*, 6(3), 641-646.
- [34] Parnell, , et al. (2010). Depletion of PCBM at the Cathode Interface in P3HT/PCBM Thin Films as Quantified via Neutron Reflectivity Measurements. *Advanced Materials*, 22(22), 2444.
- [35] Yu, B. Y., et al. (2010). Effect of Fabrication Parameters on Three-Dimensional Nanostructures of Bulk Heterojunctions Imaged by High-Resolution Scanning ToF-SIMS. *Acs Nano*, 4(2), 833-840.
- [36] Beal, R.M., et al. (2010). The Molecular Structure of Polymer-Fullerene Composite Solar Cells and Its Influence on Device Performance. *Macromolecules*, 43(5), 2343-2348.
- [37] Xue, B. F., et al. (2010). Vertical Stratification and Interfacial Structure in P3HT PCBM Organic Solar Cells. *Journal of Physical Chemistry C*, 114(37), 15797-15805.
- [38] Li, G., et al. (2005). High-efficiency solution processable polymer photovoltaic cells by self-organization of polymer blends. *Nature Materials*, 4(11), 864-868.
- [39] Jo, J., et al. (2009). Time-Dependent Morphology Evolution by Annealing Processes on Polymer:Fullerene Blend Solar Cells. *Advanced Functional Materials*, 19(6), 866-874.
- [40] de Villers, B. T., et al. (2009). Improving the Reproducibility of P3HT PCBM Solar Cells by Controlling the PCBM/Cathode Interface. *Journal of Physical Chemistry C*, 113(44), 18978-18982.

- [41] Wang, T., et al. (2010). The development of nanoscale morphology in polymer: fullerene photovoltaic blends during solvent casting. *Soft Matter*, 6(17), 4128-4134.
- [42] Ruderer, M. A., et al. (2011). Solvent-Induced Morphology in Polymer-Based Systems for Organic Photovoltaics. *Advanced Functional Materials*, 21(17), 3382-3391.
- [43] Schmidt-Hansberg, B., et al. (2011). Moving through the Phase Diagram: Morphology Formation in Solution Cast Polymer-Fullerene Blend Films for Organic Solar Cells. *Acs Nano*, 5(11), 8579-8590.
- [44] Sobkowicz, M. J., et al. (2012). Effect of Fullerenes on Crystallization-Induced Aggregation in Polymer Photovoltaics Casting Solutions. *Macromolecules*, 45(2), 1046-1055.

Dewetting Stability of ITO Surfaces in Organic Optoelectronic Devices

Ayse Turak

Additional information is available at the end of the chapter

<http://dx.doi.org/10.5772/52417>

1. Introduction

Heterojunctions are inherent in and essential to all molecular optoelectronic devices. In organic light emitting diodes (OLEDs), the interfacial region between the active organic layers and the inorganic contacts plays a primary role in device performance, through the control of effective carrier injection and long term device reliability. In organic solar cells (OPVs), heterojunctions play a defining role in all of the major processes: charge separation relies on effective organic/organic interfaces; charge transport is critically determined by the structure of the thin film, controlled by the organic/inorganic interfaces with substrates; and charge extraction can only occur at high quality inorganic/organic interfaces at the electrodes. Studies of various organic/inorganic interfaces have indicated that a wide range of interfacial types are possible in organic optoelectronic devices. To foster the next generation of devices, it is critical to understand the connections between heterojunction structure and morphology, and device performance. This connection is especially important with regard to the interfacial stability and lifetime in organic optoelectronic devices. Control of the complex interactions and the microstructure at the electrode-organic interfaces would allow the optimization of performance and lifetime.

In this chapter, we aim to review the current state of the art with regards to interfacial stability and control of the anode (indium tin oxide) electrode/active layer interfaces to understand the performance of organic optoelectronic devices. From examples of our own research and others relating to interfacial morphological changes, a comprehensive picture of the role of the interface in device stability can be formed. This chapter begins with a brief overview of degradation in organic devices, including definitions. Following that, the main focus of the chapter is on the morphological instability at the ITO surface as a main mechanisms of device degradation. Various approaches to overcoming device instability are given,

with special attention paid to the various interlayers that have been introduced into devices. This also includes examples where dewetting is used advantageously to produce novel device architectures and surprising solutions to device degradation.

2. Degradation

Unlike the field of inorganic electronics, organic electronics encompasses highly diverse technologies with devices that can be prepared with different architectures, using many different materials, processed by many different methods. Unlike their inorganic counterparts, all organic devices are to some extent unstable and their performance degrades over time [1]. After efficiency, lifetime is the second most important parameter for organic devices [2]. While inorganic semiconductors are for the most part intrinsically chemically stable, and insensitive to the ambient environment, for organic devices, the polymer or small molecule active layers themselves, the inorganic electrodes, and the interfaces between them are all potential locations for degradation. Degradation for organic devices is, therefore, highly complex and typically cannot be described by a single mechanism.

OLEDs [3] and OPVs [4-6] are known to degrade during both operation and storage (called shelf life or dark stability). From the moment the metal electrode is applied, the device is subject to degradation: in vacuum, in the dark and under operation [1]. The three physical mechanisms that degradation can take are the loss of conjugation and irreversible deterioration of the active organic layers; degradation of the interface conductive properties; and mechanical disintegration of device (dewetting, phase segregation, crystallization), all of which manifest themselves as a change in the electrical properties. The basic requirement of an emissive or absorptive technology with regards to lifetime is to provide adequate device performance over the intended time of use for the application. Stability for short term displays, such as cell phone monitors, requires different criteria than long term high performance solid state lighting. For solar cells, the requirements are different still with exposure to external environments that are not even a consideration for OLEDs, aggravated by the fact that many organic molecules undergo serious degradation in electrical properties upon exposure to light [7-11]. The desire for flexible substrates for both technologies brings yet another set of challenges. These requirements have stimulated much research in the thirty years since the first OLEDs and OPVs were produced at Kodak [12-13].

Though efforts are underway to establish standardized protocols for OLED and OPV characterization [14-16], official qualification procedures have not yet been established for lifetime testing. Stability testing protocols were proposed for OPVs by consensus among 21 international research groups in May 2011 to improve the reliability of reported values [17], and are still in the process of being adopted by other researchers. A comparison of reported lifetime values between different groups is difficult, as device lifetime is greatly affected by the driving voltage, number of duty cycles, length of rest cycles, initial luminance or power conversion efficiency, deposition conditions, and exposed environment. Though it is possible to estimate values for standardized test conditions using acceleration factors for both

OLEDs [18] and OPVs [19-20], in general it is more instructive to look at the relative improvement in the device lifetime, which is how it will be discussed in this chapter.

Known degradation mechanisms include diffusion of molecular oxygen and water into the device, crystallization or oxidation of organic layers, degradation of interfaces, inter-layer and electrode diffusion, electrode reaction with the organic materials, electrode oxidation, phase segregation or intermixing, dewetting from the substrate, delamination of any layer, and the formation of particles, bubbles, and cracks. There are four major decay mechanisms related to the bulk active layers: organic layer oxidation, crystallization, charge carrier/exciton damage, and photobleaching. There are also four decay mechanisms directly associated with degradation at the top contact: electrode oxidation, dark spot formation, electrode bubbling and delamination, and metal diffusion. As this chapter is focussed on the morphological stability on the anode surface, interested readers are directed to recent topical reviews specifically focussed on polymer photovoltaics [21-22], on OLEDs [23], and on interfaces [24], for a comprehensive look at degradation and degradation mechanisms. As many of the issues related to anodic degradation at interfaces are common for both OPV and OLEDs, and for polymer and small molecule active layers, all types will be discussed within this chapter.

3. Dewetting theory

It is the interplay between molecule-molecule self-interaction and substrate-molecule interactions that determines the stability on a given surface [25-26]. For thin films (<100nm) coated onto non-wetting substrates, van der Waals forces play the dominant role in determining film stability [27-28]. The Hamaker model [29] allows quantification of the instabilities that arise in thin films when VdW forces induce an attractive potential between two interfaces

$$E(h) = \frac{-A_H}{12\pi h^2} \quad (1)$$

where A_H is the effective Hamaker constant for the film and film-substrate interactions ($A_H = A_F - A_{FS}$) and h is the film thickness on an infinite substrate.

The thermodynamic instability is given by the "disjoining pressure" [26, 30], or the second derivative of the energy. For a single film, this is given by

$$\frac{d^2 E(h)}{dh^2} = \frac{-A_F + A_{FS}}{2\pi h^4} \quad (2)$$

As the disjoining pressure is inversely proportional to the film thickness to the fourth power, producing stable and defect free films is particularly difficult as the thickness decreases.

At the lowest limits, thermally or mechanically induced fluctuations (capillary waves) tend to cause film rupture [27, 31-32], a process known as spinodal dewetting. The surface undulations give rise to a pressure gradient which drives film instability if the effective Hamaker constant is negative (i.e. non-wetting) [31]. As the film thickness decreases, there is a trade-off between destabilizing vdW forces and stabilizing surface tension that leads to an amplification of capillary waves [33] and can therefore cause spontaneous rupture if the film is thin enough (typically <200nm, greatly enhanced at <10nm [32-33]). Additionally, the glass transition temperature (T_g) is lower for thin films due to confinement effects [34], further aggravating dewetting effects. Most OLED and OPV layers are less than 200nm thickness, making them highly susceptible to spinodal dewetting.

Aside from capillary wave destabilization, dewetting can be driven by nucleation and hole growth from defects (i.e. airborne particles) [27, 35], by the release of residual stress [36], by density variations [37] or by thermal expansion mismatch between substrate and organic film [27, 38], which can be highly anisotropic for organic molecules [39].

Dewetting effects are strongly related to the crystalline structure of organic thin films [40], and are thus quite different from the wetting – dewetting problems of an isotropic liquid. The situation is further complicated by the fact that many organic molecular crystals exhibit several distinct crystal structures, which are energetically very similar and may coexist [41-42]. For crystalline films, pseudo-epitaxy with the substrate can simultaneously drive both film stabilization and dewetting [42]. The predominance of physisorption, combined with the relatively large size of the molecule compared to the inorganic substrate allows organic films to accommodate much larger strains than those observed in inorganic epitaxy [42]. As having lateral organization in the thin film can stabilize against dewetting [40], the amorphous films often used in devices are even more susceptible to extreme morphological instabilities.

Regardless of the mechanism, dewetting begins with a nucleation event leading to the formation of a hollow which proceeds to grow by the transport of material away from the nucleation site to a retreating rim surrounding the hole. These holes eventually intersect, leading to the formation of ribbons of material along the contact line [27].

4. Anode/active layer contacts

The interface at the high work function electrode is especially influential in device stability as it often also forms the substrate upon which subsequent layers are deposited. The electrical, chemical, and morphological features of the electrode surface play a significant role for both OLEDs and OPVs as the quality of the interface and of the hole transporting (electron donating) (HTL) film deposited on it [38, 43] is often the limiting feature of the device, both for performance [38, 44-47] and stability [9, 38, 48-50].

For a high quality device, the HTL needs to fulfill a number of criteria including high hole mobility, good energy level matching with anodes and other active layers, good thermal

properties, high optical transparency to visible light, and a smooth, often amorphous morphology with good film forming properties [12, 51-59]. In small molecule OLEDs, excellent examples, and the first HTL materials [12], are triphenylamines such as TPD and NPB; in polymer OLEDs and OPVs, this function is often fulfilled by PEDOT:PSS (Poly(3,4-ethylene-dioxythiophene):poly(styrenesulfonate)) [60].

An indium tin oxide (ITO) thin film on a glass substrate could be considered an archetypical anode for both OLEDs and OPVs due to its high transparency over the visible region, high electrical conductivity, and high work function [61-64]. Although ITO use is almost ubiquitous as the transparent conducting electrode in organic optoelectronic devices, it has a number of drawbacks, including variations in the surface properties depending on preparation method [47, 62, 64-67], poor energetic compatibility with active organics [68-69], and instability with a wide variety of hole transporting materials that directly impacts on the device stability. ITO has a bixbyite crystal structure [70-71] and the surface of polycrystalline thin films are dominated by the oxygen terminated (111) plane with many dangling O bonds [72] (see figure 1). Due to this rich oxygen landscape, the electrode surface has a highly variable electronic structure [73] that can be modified by a wide variety of surface treatments, and is very susceptible to moisture [74] and light irradiation [63, 75]. As the difference between the active layer highest occupied molecular orbital (HOMO) and the electrode surface work function plays a limiting role in device performance [76], ITO surface modification is typically focussed on increasing work function, by passivation with surface-active species [77] or by over 50 kinds of chemical and physical treatments [76, 78-79].

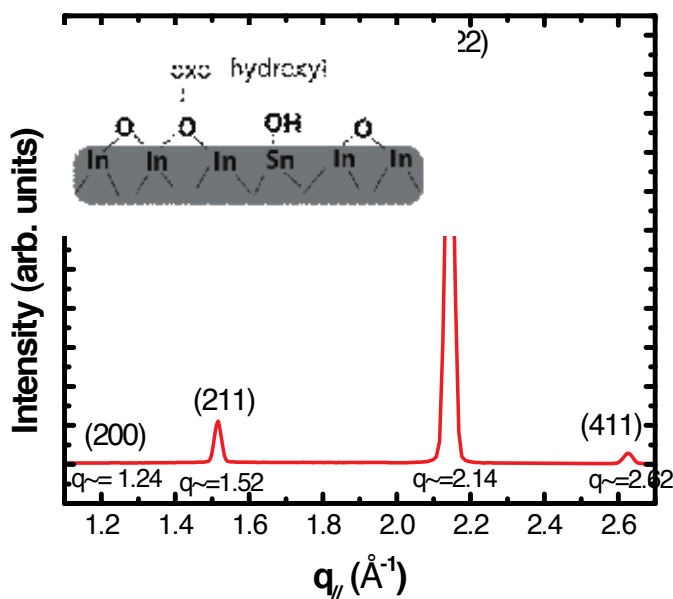


Figure 1. Grazing incidence x-ray diffraction of polycrystalline indium tin oxide surface with major planes identified showing the predominance of (111) planes, with a schematic of the ITO (111) surface with hydroxyl and oxo-terminations as an inset.

5. Morphological instabilities on ITO

In general, instability at the ITO/active layer interface can be related to morphological, chemical and electronic changes over the lifetime of the device. There are four major criteria which lead to an unstable interface: surface energy mismatch, low glass transition temperature (T_g) materials, surface reactivity with organics, and work function instability. The surface energy mismatch and low transition temperatures are the driving characteristics for the morphological instability discussed in this chapter.

As the ITO surface consists of many dangling O, surface treatments tend to saturate the surface with hydroxides, making it hydrophilic [80]. Advancing aqueous contact angles range from ~ 0 - 30° on treated surfaces [80-86]. By contrast, many electron donating organic materials are hydrophobic. Two widely used HTLs for small molecule OLEDs, TPD and NPB, have advancing contact angles of 80° , and 90° respectively [80]. This large mismatch in surface energy makes it difficult to grow continuous films necessary for devices. Thermally evaporated oligomers, such as NPB [87-88] and TPD [89] as well as many others, show a strong tendency to island (Volmer-Weber) growth (see figure 2a), with highly active surface diffusion to step edges and defects. Often, the initially formed islands can ripen laterally with continued deposition to form what appear to be continuous films [87], which are highly metastable. For molecules deposited from solution, the surface energy mismatch with ITO can also lead to inhomogeneous deposition, as seen in figure 2b for PEDOT:PSS.

Even when continuous films are able to form upon deposition, the relatively low T_g for many oligomer hole transporting materials (NPB 96°C , TPD 65°C [53]), can lead to dewetting under mild thermal treatments or even with storage over time at ambient temperatures [42, 90]. Diindenoperylene, a novel material of interest due to its well defined ordering [91], interesting growth behaviour [92-93], promising electron transport properties [94-95], favourable electronic structure [96], long exciton diffusion lengths [97], has recently been shown by us to have tuneable behaviour in solar cells based on its morphology [98]. As seen in figure 3, upon initial deposition, films of DIP form large flat islands on ITO with a high

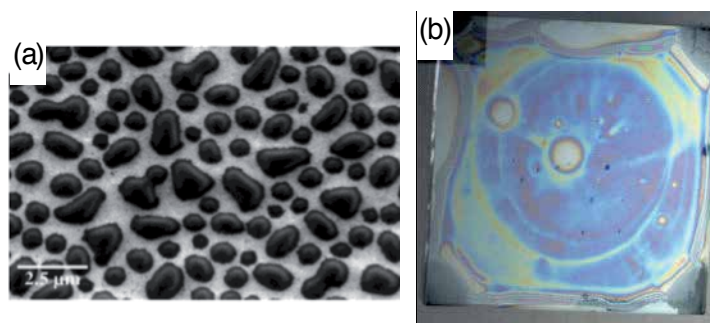


Figure 2. (a) SEM image of $(\text{EtCz})_2$ films deposited at $T_s = 90^\circ\text{C}$ on a bare-ITO substrate. Reprinted with permission from [68]. Copyright 2002 John Wiley and Sons (b) Incomplete coverage of ITO surface with PEDOT:PSS deposited from solution.

degree of order [98]; however, they are metastable at room temperature, showing very strong dewetting during storage at room temperature under vacuum for one month [99].

Though sometimes observed under high temperature treatments [3, 100], dewetting is not as significant a problem for polymer systems, due to the generally higher T_g of polymer materials [101]. However, device performance is heavily influenced by the morphology, especially in polymer-based bulk heterojunction solar cells [102]. The optimal morphologies require the spontaneous phase segregation of the donor and acceptor polymers during co-deposition. As such, the interpenetrating morphology required for high device performance, is also highly metastable, and driven by the substrate surface energy mismatch [103-105].

Beyond the limitations in the shelf life, metastability of the active layers can be a significant driving force for degradation during operation. The organic layers are subjected to thermal stress in a variety of ways at a number of points in the device lifetime. During fabrication, the metal cathode is vacuum deposited directly on the organic films, which can lead to localized heating of the organic film. During normal device operation, low mobility in the organic films can lead to high electric fields and local Joule heating [106-110]. Zhou et al. observed that the surface temperature for TPD based OLEDs can reach as high as 86°C, suggesting that the temperature inside the actual devices could be higher than 200°C [110]. Tessler et al. [111] saw temperature variation during operation as high as 60°C in the recombination zone. As semiconducting organic molecules tend to show poor natural heat dissipation [110, 112-113], such large temperature variations cannot be handled by the limited heat sink at the glass surface. Choi et al. [114] were able to find an inverse correlation between the OLED device lifetime and the internal device temperature, as measured by a scanning thermal microscope.

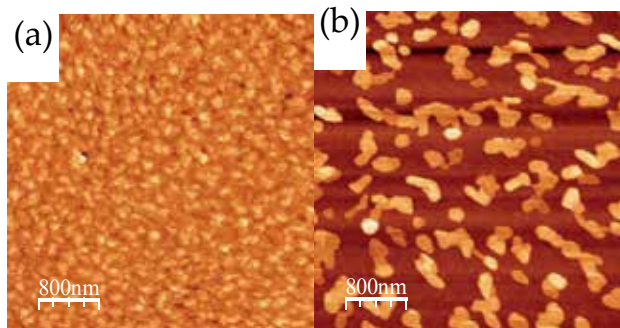


Figure 3. AFM micrograph of diindenoperylene (DIP) deposited on ITO surface at room temperature (a) immediately after deposition (b) after one month in a low vacuum, low humidity environment.

OPVs have the additional burden of illumination induced heating and cooling cycles, which can cause the internal temperatures to reach well beyond the T_g when coupled with Joule heating. Sullivan et al. [115] observed that UV induced heating (through UV absorption by the glass substrate) lead to a structural reorganization of pentacene, decoupling it from the ITO surface, causing kinks to form in the current density-voltage (J-V)

curves for PEN:C₆₀ solar cells. Paci et al. [116] observed that the metastable morphology of P3HT:PCBM solar cells was modified in a similar way under illumination as by deliberate thermal annealing.

Irreversible device failure has also been observed in operating OLEDs [38] and OPVs [117] heated above T_g of one of the molecular organic components. For many devices, the weakest link in the device lifetime is the low T_g of the HTL immediately adjacent to the ITO surface [117-121], as many electron accepting and transporting materials have relatively high T_g [53]. Fenter et al. proposed that device failure was a result of significant expansion of the least thermally stable material, TPD, leading to delamination from the ITO surface [38]. Do et al. for MEH-PPV [3] and Choi et al [114] for PFO, observed buckling behaviour, where the polymer layer completely detached from the ITO in a number of areas on the electrode surface. This inhomogeneous delamination results in significant disruption of the multilayer structure, which can cause non-uniform contact between the electrode and organic layers. TPD undergoes significant structural changes even well below its glass transition temperature: at ~60°C, changes have been observed in its thickness and density by XRR [38] and serious dewetting has been observed by AFM [122]. Tokito et al. [123] observed a direct correlation between the glass transition temperature of the HTL and device degradation as a function of temperature; however, this was disputed by Adachi et al. [51], who saw no correlation specifically with the T_g, relating the stability more to the interfacial barrier to injection (and hence to Joule heating [124]). It is conceivable that dewetting, which compromises the integrity of the hole transport layer, would lead to inefficient hole injection by non-uniform coverage, and a modification of the other layers deposited atop the dewetted layer [125].

Any local failures due to morphological inhomogeneities on the ITO surface (In spikes, thinner organic regions, etc) [90], where the high local electric field would already encourage Joule heating, would also tend to both accelerate and be accelerated by dewetting. As many materials are also subject to annealing heat treatments for improved performance, film metastability can have catastrophic consequences for the device in operation. Do et al. observed complete separation of the active MEH-PPV layer during operation in a number of areas on the electrode surface, resulting in dead areas that eventually covered the whole surface [3]. Even without dewetting induced failures, over-annealing or elevated temperature storage over long time can lead to significant phase-segregation beyond the exciton diffusion length for bulk heterojunction devices [126-128], which ultimately decreases the performance over time [101, 127, 129-130].

Both dewetting and work function instability at ITO surfaces are accelerated by humidity [86, 90] or light irradiation [115-116]. The same mechanism is at work in both cases – the modification of the hydroxyl termination on the ITO surface [47], which leads to a change in the surface energy. This also helps to explain the strong correlation observed between the interfacial barrier to hole injection and OLED device degradation [51, 131-133], as both are related to this hydroxyl terminated surface.

6. Preventing interfacial morphological instability

There has been much research into methods of counter-acting dewetting from the ITO surface, as the integrity of the active layers is of paramount importance in the device performance and stability. Incorporation of the unstable film into a device, with a multi-layer film stack, already significantly suppresses the dewetting of single films [40, 125, 134]. Deliberate use of a stable inorganic capping layer, such as Al_2O_3 [135] or an electrode metal such as Ag [136] or Au [137], within the device can also greatly improve the stability of the underlying organic phases. Utilizing a rough substrate can also encourage wetting and stability [32, 46, 138-140], but that can lead to undesirable morphologies in the original deposition [99]. In order to further improve the stability at the ITO surface, two general approaches have been adopted: increasing the T_g of the active layer itself, or introducing stabilizing interlayers.

6.1. Increasing the glass transition temperature

There has been much work over the last 30 years focused on finding new hole transporting/electron donating molecules that have high morphological stability, as recently reviewed by Shirota [56]. General strategies for designing morphologically stable molecules were developed by Shirota [55-56], Wirth [141] and Naito and Muira [53] -- the underlying philosophy was to decrease the degrees of freedom and increase the rigidity of the molecules, through replacement/augmentation of the core; linear or branch linkages; or long substituents leading to starburst type molecules. The first and most widely used replacement of the original triphenyldiamine used in the Tang OLED (TPD) [12], was a benzedine derivative, NPB. It had excellent hole transporting and film forming properties in addition to a slightly higher T_g (~96°C) [133, 142-143]. Though NPB was widely adopted in OLEDs, unfortunately it too had a propensity to crystallization and dewetting albeit at higher temperatures [118, 144]. The original family of triphenyldiamines were successful in most other aspects as a hole transporting layer leading to the development of various derivatives, including triphenyl amines [120, 123], biphenyl amines [142], binaphthene diamines [145], asymmetric triaryldiamines (TPD derivatives) [146], triphenylamine-based starburst molecules [147-149], and recently star-shaped oligotriarylamines [150]. Other approaches include using a fluorene core to increase the rigidity of biphenyl HTLs [121], carbazole derivatives [151], vinyl-type polynorborenes with ethyl ester linked triarylamines [152], thermocleavable densified polymers [153-154], defect reduced polymers [130, 155-156], among many others. Though new materials are synthesized regularly with significantly higher glass transition temperatures than the classically utilized molecules, the correct combination of high hole mobility, good energetic compatibility with electron-accepting materials, and good optical absorbance has proven elusive, and many of these materials currently do not see widespread use in devices.

6.2. Interfacial structure stabilizing interlayers

Due to the difficulties in finding complete replacements to traditional hole transport/electron donating layers, much research has gone into introducing thin adhesion-promoting buffer layers between the active material and the ITO anode. The ideal interlayer should ex-

hibit strong adhesion to both the anode and the HTL, via physical adhesion or chemical bonds. Other desirable criteria for an effective buffer should include (1) high hole transport mobility; (2) easy deposition onto anode surfaces via straight-forward methods such as spin-coating, vapor-deposition, or self-assembly; (3) good conformal matching to substrate; (4) substantial thickness control; and (5) well-defined microstructure free of pinhole defects.

In addition to promoting adhesion and stabilizing against dewetting, buffer layers often have a number of added benefits for the device, including enhancing initial device performance [81, 86, 133, 157-167], encouraging better charge balance [45, 168-169] (often by preventing hole injection [131]), preventing chemical reactions between the active layer and ITO [9, 162, 170-172], blocking In and Sn diffusion [170, 173-176], increasing mechanical strength [177], and smoothing the ITO surface (preventing electric field inhomogeneities that are potentially responsible for dark spot formation) [64, 161-162, 171, 175-176, 178-180].

There are two broad classes of interlayers that have been used to suppress dewetting specifically, or device degradation more broadly: modifications of HTLs (covalently bound or polymerized versions of traditional hole transport layers; HTL materials doped with or into a stabilizing material); and any organic, metal or oxide buffer that is not also used as the HTL.

6.2.1. Generic buffer layers

The most widely explored class is that of generic buffer layers. These run the gamut from vapor or solution deposited organic layers, self-assembled monolayers, dielectrics, conducting oxides, insulating oxides, to metals. Virtually every element in the periodic table has been incorporated into the device with the aim of increasing the device lifetime. A wide variety of interlayers have also been introduced with no interest in their stabilizing properties, though film stability often also results as a side effect. These interlayers include metal doped ITO [181-183]; oxides including Y_2O_3 [184], Tb_4O_7 [184], TiO_2 [184-185], ZnO [184], Nb_2O_3 [184], Ga_2O_3 [184], SnO_2 [184], CuO_x [186], Fe_2O_3 [187], SiO_2 [188], VO_x [189-190], RuO_x [189], AZO [189], Al_2O_3 [191], NiO [192]; ultrathin metal layers such as Ni [184], Au [184], Sn [184], Pb [184]; $F_{16}CuPc$ [193]; conducting polymers [194]; and a wide variety of self-assembled monolayers [44-45, 195]. While this is not an exhaustive list, it demonstrates that a wide variety of buffer layers have been attempted by researchers. The focus for the rest of this section will be on interlayers that are specifically shown to influence the device lifetime or stability of the organic layers deposited on the surface. The reported improvements in device lifetime for a variety of interlayers are summarized in table 1.

One of the first and still most widely used buffer layer for small molecule OLEDs is copper phthalocyanine (CuPc). Though an interesting semiconducting material in its own right [196-199] with current widespread use in solar cells as an electron donating material [200], it was first introduced as a stabilizing buffer layer for NPB [133]. It has been extensively employed as an anode HTL buffer layer, mostly due to its reported ability to enhance OLED performance [44, 132-133, 164, 201-202], energetic level matching [203-205], high thermal stability [204, 206], and low cost as a result of its use as a blue dye [207]. Other phthalocyanines have also been employed as buffer layers below the active layers [207]; the recent use of

ZnPc [63], for example, improved the stability of ZnPc:C₆₀ bulk heterojunction solar cells by ~3.5x (see table 1).

The use of CuPc prevents the ambient dewetting observed for NPB directly deposited on ITO [88], providing a metastable equilibrium structure for devices at room temperature. CuPc was also seen to increase the crystallization temperature of NPB significantly, to above 160°C [118, 144, 208]. This stabilization effect allows for longer lifetimes: Aziz et al. [169] observed more than a 5x increase in the luminance t_{50} using CuPc as a buffer (see table 1). Though the impact varies, many researchers have seen significant improvements in stability using CuPc under ambient conditions. However, poor device performance has been observed if the devices are used at even mildly elevated temperature [209-212]. It has been established that moderate heating as low as 60°C leads to CuPc crystallization [80, 88] (see figure 4), intermixing with NPB [118, 144, 213] and TPD [213], and dewetting. Ultimately, CuPc-buffered ITO does not prevent HTL crystallization and decohesion upon heating to temperatures near/above the HTL T_g. Additionally, CuPc is highly reactive with the ITO surface [118, 214], and its use leads to significant increases in the driving voltage for OLEDs [215]. To overcome some of these difficulties, researchers have used another buffer layer under the CuPc layer, such as Pr₂O₃ [158] or LiF [161], with some success.

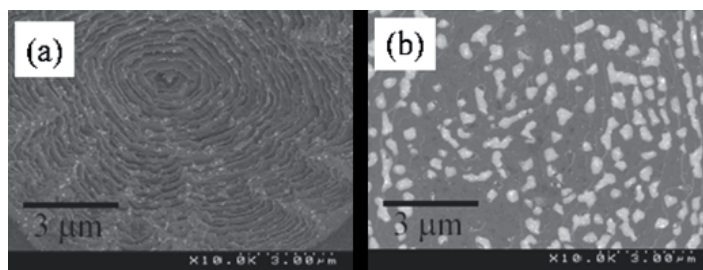


Figure 4. SEM micrographs for crystalline areas of: (a) CuPc type sample, and (b) NPB type sample. Reprinted with permission from [88]. Copyright 2007 American Institute of Physics.

The second commonly used interlayer material is PEDOT:PSS [234]. Due to its high hole mobility [217, 234], PEDOT:PSS is often actually classified as a conductor and referred to as a polymeric anode [50], rather than a buffer layer. Considered as an essential component of most polymer based devices, both PLEDs and OPVs, it is used in almost all polymer solar cells for its significant impact on the device performance rather than to improve stability. It was, however, initially introduced into PLEDs as a stabilizing layer [60, 166, 235] and many researchers saw substantial improvements in device lifetimes with its use [9, 60, 166, 235-237] (e.g. ~7x improvement in luminance t_{50} [217] table 1). The introduction of PEDOT:PSS into PLEDs allowed the device lifetime to go from a few days to hundreds [60, 166] or even thousands [235] of hours, effectively making early organic devices into a viable technology. Figure 5 shows DIP deposited on PEDOT after storage in vacuum for one month [99]. Unlike on bare ITO, where severe dewetting was observed (figure 3), the film is completely stabilized with a PEDOT buffer layer. X-ray

diffraction measurements (figure 5c) confirms that the crystal structure is also preserved during storage [238]. Although, PEDOT:PSS is widely used, much like CuPc, there are a number of drawbacks, most significantly its extremely high reactivity with ITO [59, 170, 239-241]. In some cases, this is a benefit, as the high solubility of In in PEDOT:PSS allows it to be used as a barrier against In migration into PPV [174, 242], or PCBM [242] improving the device stability. Again much like CuPc, one approach to overcoming these limitations is to introduce an underlying buffer layer, such as diamond-like carbon [170] or alkylsiloxane SAMs [173] to prevent In diffusion. PEDOT:PSS is also prone to oxidation [239], both from moisture in the ambient environment [243] and from the ITO surface, which decreases the device performance and stability [75, 230, 239, 244-245]. Unencapsulated P3HT:PCBM solar cell devices with PEDOT:PSS show rapid decay of the short circuit current, with t_{80} essentially equal with or without ITO [246]. Recently, the group of Karl Leo in Dresden introduced an ethylene glycol soaking treatment that improves solar cell lifetime by a factor of 1.3, by removing the insulating and hygroscopic PSS components in the layer [233]. As these PSS components can also react with other polymer layers [247], eliminating excess PSS leads to greatly increased lifetimes.

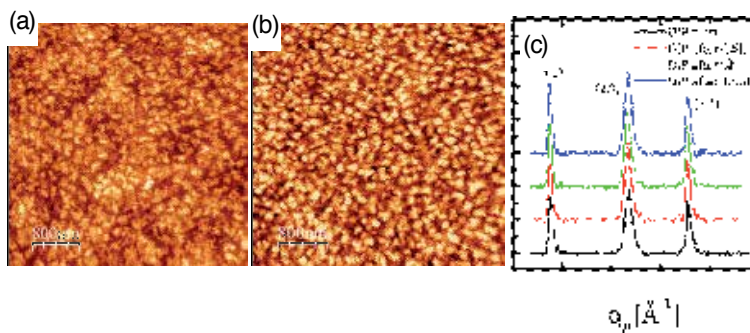


Figure 5. DIP on PEDOT:PSS (a) AFM micrographs of the bilayer structure as deposited (b) AFM micrograph of the same surface after one month in a low vacuum, low humidity environment. (c) grazing incidence x-ray diffraction scan of characteristic DIP crystal planes with accelerated aging at 90°C with 60% humidity (13.5hr equivalent of 1 month ambient exposure).

As a third approach, plasma or ozone treatment of the ITO surface is widely used to modify the work function and surface energy prior to deposition of the active layers. Though not technically an interlayer, the modifications are limited to a small region immediately adjacent to the active layer, resulting in effects similar to that of a buffer layer. The treatment of the ITO surface with plasma or UV ozone has a profound effect on the surface energy and hence the stability of the active layers deposited on the surface. The aqueous contact angle increases with plasma treatment [62, 85], correlated to the coverage of the surface with hydroxyl terminated O [85, 248]. As this saturation also controls the surface work function, and wetting behavior has been recently shown to correlate to the surface work function [248-249], the hydroxylated surface should encourage improved adhesion of the active layers and lead to better performance. Wu et al [78] saw almost two orders of magnitude im-

improvements in t_{50} with plasma treatments. Not all plasma treatments lead to the same response, however. The study by Huang et al [67] showed that the wettability of NPB is increased by H_2 , CF_4 and O_2 plasmas, but decreases with Ar plasma. They suggested that decontamination of the surface without hydroxylation leads to a dipole field on the surface that is stronger than the grain boundary and defect effects, promoting NPB nucleation. On the other hand, CF_4 and O_2 strongly encourage layer-by-layer growth, smoothing [219] and passivating the surface against defects that can lead to inhomogeneous electric fields. As an interesting aside, the results for UV-ozone treatment of the ITO surface by Fukushi et al [220] contradict the above. They saw ~5-6x improvement in t_{50} with a treatment that decreased the aqueous contact angle to 4° . They speculate that stronger adhesion of the HTL was possible, which contradicts thermodynamic wetting theory as the surface energy mismatch would be incredibly large. This underscores the likelihood that, as with many aspects of organic semiconductors, more than one mechanism is responsible for lifetime improvements in devices.

Silane based SAMs, such as tetraaryldiamine (TAA) [80, 213, 250], epoxysilane functionalized triphenylamine (TPA-silane) [81], dodecyltrichlorosilane (DDTS) [82], phenyltriethoxysilane (PTES) [82], 3-aminopropyl-methyl-diethoxysilane (APMDS) [82], alkylsiloxane [173], and alkyltrichlorosilanes (OTCS and FOTCS) [83] use a Si-O bond to anchor on the ITO surface, providing a robust interface with substantially higher surface energy. Chong et al [82] observed that the sticking and dewetting of NPB on various SAMs shows an inverse correlation with the measured aqueous contact angle, but Choi et al saw substantially longer lifetimes ($\times 11$ increase in t_{50} with 105° contact angle on FOTCS [83]). The improved adhesion of the active layer was attributed to interfacial reconstruction and interpenetration with the SAM [251]. Our recent study of quaternary ammonium molecules on SAM buffered surfaces showed a significant release of interfacial strain when the buffer was present [252]. As strain release is another mechanism that drives dewetting [36], better pseudo-epitaxial conformation with the surface for buffered films could be a mechanism for the observed improvement in performance.

A wide variety of other organic molecular interlayers have been used, with varying success in improving the lifetime, as summarized in table 1. These include oligomers such as 4,4',4''-(3-methylphenyl-phenylamino)triphenylamine (MTDATA) [147, 178, 253], parylene [162, 175, 254], cross-linked perylene diimide (PDMI) [255], N,N-bis(4-trifluoromethoxybenzyl)-1,4,5,8-naphthalene-tetracarboxylic diimide (NTCDI-OCF₃) [159], Alq₃, or fullerene (C₆₀). Most of these interlayers are thought to improve the active layer film formation on the surface, by smoothing [147, 162, 180, 255]. The high T_g of MTDATA [253] and NTCDI-OCF₃ [159] are also thought to contribute to preventing crystallization of the HTL overlayer. Polymer approaches include polyaniline (PAni) [172], fluoropolymer (FC-227) [179], plasma polymerized fluorocarbons [74, 160], tetrahedral amorphous carbon [171], polyimide [176] or radical ion salt doped amine polymer [221], which are thought to prevent oxidation [74, 160, 172] or block hole injection [221], in addition to stabilizing the surface against dewetting

Metals such as Pt and Mg have also been used as interlayers, and though both show improvements, the mechanisms are almost completely opposed. High work function Pt enhan-

ces TPD wetting on ITO surfaces [46], while low work function materials such as Mg, Ca and Al give many orders of magnitude improvement in the luminance stability, correlated to the work function of the metal, by preventing the injection of holes into the Alq layer in OLEDs (intrinsic degradation) [169].

Most recently, MoO_x has been successfully employed to improve lifetimes in both OLEDs [157, 218] and OPVs [75, 230-232], especially as a replacement for PEDOT:PSS, and though the mechanism is still controversial, the energy barrier at the active layer/ITO interface is thought to play a significant role. Other oxides, such as SiO_xN_y [86] or ZnO [256], which can act as oxygen and moisture getters, have been successfully used to stabilize the ITO surface against contamination.

6.2.2. Modified HTLs

There are three modifications that have been made to the hole transporting/electron donating layer adjacent to the ITO surface to improve its wetting properties: doping, polymerization, and functionalization to allow for covalent bonding to the surface. Though many of the layers discussed in this section have also been tried as the HTL for a given device structure, they have found more success for high device performance coupled with stability when they are used as an ultra-thin buffer layer beneath the unmodified version of the molecule acting as the HTL.

Doping

The first approach to stabilization is through doping, either with nanoparticles or with other molecules. Doping with other molecules, often referred to as alloying or more recently as a bulk heterojunction, has been very successful in suppressing crystallization and dewetting in hole transporting molecules [131, 159, 169, 206, 225-227, 257-258]. Mori et al. used metal-free Pc to disrupt the crystallization of CuPc, showing ~2x improvement in lifetimes for operation above 85°C [206]. Chu et al. [159] and Lee et al. [227] used higher stability molecules NTCDI (diimide) and PFI (perfluorinatedionomer) to stabilize NPB and PEDOT:PSS, respectively. The incorporation of PCBM into various polymers, including P3HT [100, 259], PPV, MDMO:PPV [260], also stabilizes the morphology against heat treatment, and improves long-term stability [100, 259-260]. Addition of a diblock co-polymer of P3HT-C₆₀ to a P3HT:PCBM composite has led to even greater stabilization against phase desegregation [261-262]. In some cases, the hole transport molecule was doped into a more stable matrix, such as TPD into high T_g polymers [263] or MgF₂ [120], which significantly suppressed the crystallization. Rubrene:TPD [257], MADN:NPB [226], F4TCNQ:NPB [131, 169], DSA_Ph:NPB [225]) combinations have all been employed with various levels of doping, leading in most cases to ~2x improvement in the 80% luminance lifetime in small molecule OLEDs (see table 2). One very successful method of improving device stability has been doping of the Alq₃ layer in small molecule OLEDs with other molecules including TPD [258], NPB [210], NPD [218], quadricone [209], styrlamine [225], DMQA [264], rubrene [257, 265], DNP [266], Bphen [267], perylene [265-266], among many others [265]. This approach, however, is focused on combating the intrinsic degradation of Alq₃ by holes [168]. This mechanism, hole blocking, was also suggested as an additional mechanism for a few of the

doped hole transport layers (MADN:NPB [226], F4TCNQ:NPB [131, 169], DSA_Ph:NPB [225], Ir(piq)₃:NPD [268]). As the focus of this section is on the stabilization at the ITO surface, the summary in table 1 has been limited to doping in the HTL.

Doping with nanoparticles (LiF [88], C₆₀ [32, 88, 269-271], NaCl [215], Au [33]) has also been very successful in stabilizing hole transport layers, though there is sometimes a trade-off between stability and performance for such systems [88]. As particulates in the layer can act as nucleation centres for crystallization [272-273], care must be taken when selecting doping parameters. The concentration and layer thickness must be chosen such that the electrical performance is not adversely affected by the presence of the doped layer. Interparticle or surface forces strongly influence suspension behaviour of nanoparticles; therefore, not every nanofiller works with every organic. We observed that LiF greatly enhances the stability of NPB at 120°C, while having no impact on the crystallization of CuPc [88]. There is a long history of nanoparticle inclusions for stabilization in non-conducting polymers [32, 274-275]. Luo et al. [275] suggests that a combination of factors are responsible for the stabilization effects, such as the mobility of nanofillers, their size, interaction with the organic, and additional pinning effects at contact lines. Fillers work best if they are immobile; therefore, diffusion to and pinning at the substrate interface is one suggested mechanism for stabilization [32, 274]. Chu et al. [222] did in fact see similar improvement in stability with a C₆₀ layer deposited at the interface below NPB as Yuan et al. [270] saw with doping C₆₀ into NPB; Barnes et al. [32], however, saw greatly enhanced dewetting with C₆₀ at the Si surface for polystyrene thin films. Additionally, there are a number of cases where diffusion to the substrate is unlikely, as no phase separation was observed [88, 120, 215] even though stability was improved. Mukherjee et al. [33] recently observed a concentration dependence on the stabilization, where dewetting droplets form a core-shell structure, rather than leaving behind nanoparticles as the polymer layer retreats as would be expected for substrate segregation. In such cases, strong electrostatic or charge-transfer interactions between the particle and the organic layer leading to a cross-linked network are the most likely route to highly stable films [88, 274]. Other possible mechanisms for stabilization include changing the T_g with high volume-surface area ratio (effectively modifying the film rheology), preventing heterogeneous nucleation, and relief of residual stress in the film through de-segregation [33].

Functionalized HTL

Another approach to stabilization, spearheaded by Tobin Marks' at Northwestern University [45, 80, 163-164, 213, 250, 276-278], focuses on functionalizing traditional hole transport materials with siloxane groups. This allows the molecules to covalently bond to the ITO surface through the formation of Si-O bonds (see figure 6) in a manner similar to the SAMs discussed in section 5.2.1. Covalent bonds ensure strong adhesion and directly eliminate the surface energy mismatch [84, 163]. As the interlayer is the same molecule as the HTL, deposition continues in a self-epitaxial fashion, yielding uniform films as large as 25 μm² without cracks or pinholes [163]. Aqueous contact angles of 90° compared to 110° for the active layer ensures good wetting and physical cohesion in MDMO-PPV:PCBM bulk heterojunction solar cells [277-278] with dewetting prevention above 60°C. Typical examples include TPD-Si₂ [80, 163, 213, 276-277], NPB-Si₂ [80, 163, 279], PABT-Si₂ [278], penta(organo)fullerenes [84] (which use

phosphonic acid linkages [72] rather than silane), and fluorinated triphenyldiamine (FTPD) [280]. An additional step of thermal curing leads to a cross-linked siloxane network, resulting in thin layer with HTL characteristics covalently anchored on surface [163, 280].

Polymerized HTL

The final widely used method of increasing the stability of the active layer on the ITO surface requires a crosslinked polymer or highly crystallized version of a traditional HTL as an interlayer [55, 143, 146, 280-283]. This approach has been most commonly applied to TPD [55, 146, 280-282], where significant stabilization was observed above 80°C with polymerization. Bellman et al also observed that the voltage increase with time for small molecule OLEDs was slower compared to those without the crosslinked interlayer [280], suggesting increased stability. In-situ polymerization/crystallization, by heat treatment or high temperature deposition (NPB [143, 284]) or by UV irradiation (TPD [282]), lead to significant increases in the shelf life (>2 months for NPB), and operational stability at high temperatures. This approach has also been applied to polymers, where the most common approach is to use a heat-treatment [228-229, 285](already widely used in solar cells to improve efficiency [102]), with as much as two orders of magnitude improvement in lifetime [229]. Some success has also be observed for doping and irradiation induced polymerization, mainly with PEDOT:PSS [286].

| Interlayer | t_{50}/t_{80} | HTL | |
|-------------------------------------|-------------------|--------------------------------|-----------|
| OLEDs | | | |
| CuPc | 1.8x | NPB | [215] |
| CuPc | 5.3x | NPB | [169] |
| PEDOT:PSS | 6.7x | TDAPB | [217] |
| MoO ₃ | 5.9x (t_{90}) | α -NPD | [218] |
| MoO _x | 2.8x | NPB | [157]* |
| MoO _x | 3x | NPB | [157]* |
| sc-MTDATA | 4.7x | NPB | [178]** |
| MTDATA | 1.75x | TPD | [147] |
| O ₂ plasma | 20x | PVK:Alq ₃ :Nile red | [78] |
| O ₂ plasma | 2x | PEDOT | [219] |
| UV ozone | 4.7x | α -NPD | [220] |
| Mg | ~60x (t_{90}) | NPB:F ₄ TCNQ | [169] |
| CF ₃ /CF _x | 2x | NPB | [74, 160] |
| OTCS | 4x | MEHPPV | [83] |
| TMTPD+SbF ₆ :PC-TPB-DEGL | 2700x | NPB | [221] |
| FOTCS | 11x | MEH:PPV | [83] |
| C ₆₀ | 8x | NPB | [222] |

| | | | |
|--------------------------------|-------------------------|-----------------------------|----------|
| NTCDI-OCF ₃ | 1.2x | NPB | [159] |
| Pr ₂ O ₃ | ~7x | CuPc/TPD | [158] |
| Alq ₃ | 4.2x (t ₈₀) | NPB | [223] |
| ta-C | orders of mag | PEDOT | [171] |
| Pani | ~10x (t ₃₀) | MEH:PPV | [172] |
| NaCl:NPB | 2.3x | NPB | [215] |
| metal free Pc:CuPc | 3.4x | TPTE | [206]* |
| BHJ NPB:Alq | 5.4x | NPB | [224]* |
| gradient HJ NPB:Alq | 3.15x | NPB | [224]* |
| DSA_Ph:NPB | 1.3x | NPB | [225] |
| F4TCNQ (5%-20%):NPB | 40x | NPB | [169] |
| F4TCNQ (30%):NPB | 14x | NPB | [169] |
| F4TCNQ (2%):NPB | 2.5x | NPB | [169] |
| MADN:NPB | 2.7x | NPB | [226] |
| PFI (3%):PEDOT:PSS | 9.4x | PFO | [227]*** |
| PFI (6%):PEDOT:PSS | 8x | PFO | [227]*** |
| heat treatment 35°C | 3.5x | MEH-PPV LB | [228] |
| heat treatment 65°C | 5.5x | MEH-PPV LB | [228] |
| heat treatment 110°C | 9.4x | polyfluorene | [229]*** |
| heat treatment 150°C | 167.5x | polyfluorene | [229]*** |
| OPVs | | | |
| ZnPc | ~3.5x | ZnPc:C ₆₀ | [63] |
| MoO ₃ | ~ 4x | H2TPP | [75] |
| MoO ₃ | ~24x | α-NPD | [75] |
| MoO ₃ | ~27x | P3HT:PCBM | [230]*** |
| MoO _x | ~80x | PCDTBT:PC ₇₀ BM | [231]*** |
| sMoO _x | 39x | P3HT:PCBM | [232]*** |
| PEDOT | 8.7x (t ₇₀) | FFTCNQ/ZnPc:C ₆₀ | [233] |

* modified using data from [215] ** modified using data from [147] *** modified using data from [217]

¹The most common description of lifetime for OLEDs is the illumination half-life (t₅₀) – the time it takes for the luminance to decrease to half of its initial value [216]. In OPVs, a similar standard has been used with t₅₀ defined as the time for the power conversion efficiency (PCE) to decrease to half of its initial value [21]. More recently, it has become more common to report the t₈₀, the time when the device has decayed to 80% of its initial performance [17]. In this chapter, t₅₀ and t₈₀ will be the commonly adopted lifetime values for OLEDs and OPVs respectively, unless otherwise stated.

Table 1. Relative improvement in t₅₀ (for OLEDs) & t₈₀ (for OPVs) compared to bare ITO for various interlayers used at the ITO surface¹

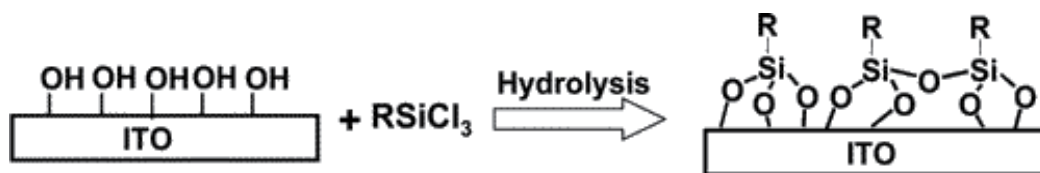


Figure 6. Scheme for ITO surface modified by covalently bound HTL materials. Reprinted with permission from [163]. Copyright 2005 American Chemical Society.

7. Using dewetting as an advantage

Though dewetting of the active layer is generally undesirable and implicated as a main mechanism in device failure, some groups have harnessed the effect to produce novel device architectures. As many of the films are metastable, they have a natural tendency to dewet into a stable equilibrium form, which can then be used as the starting point for device fabrication. Developing methods of tuning film morphology and rate of dewetting through total coverage, surface templating and temperature control are of significant interest in forming controlled organic nanostructures. Recently, we [98] used the strong island growth and dewetting tendency of DIP on ITO to produce columnar structures necessary for an interdigitated ideal bulk heterojunction solar cell, with four orders of magnitude improvement in the device efficiency. Ryu et al. [287] used the energy difference between PEDOT and PFO to form nanoscale dewetted islands of PEDOT at the internal interface in tandem polymer OLEDs. Wang et al. [288] produced sub-micrometer channel OFETs (field effect transistors) using SAM patterned SiO_2 to force PEDOT:PSS dewetting. With the PEDOT:PSS acting as the source and drain electrodes, a submicrometer channel of F8T2 polymer was formed. Benor et al. [289] was able to produce resist patterns of PMMA or PEDOT using selective wetting on hydrophobic and hydrophilic SAM patterns. Deposition on these patterned substrates lead to the formation of mesoscale patterns for radio frequency ID tags or thin film transistor electrodes. Chen et al. [104] used a similar patterning motif with SAMs that were selectively wet by the two components to encourage phase separation of P3HT:PCBM into an interdigitated columnar structure. Most recently, Harirchian-Saei et al. [290] used the phase separation of PS and PMMA on OTS striped patterns to deliver a periodic array of CdS nanoparticles. By dissolution of the nanoparticle into only one component; then taking advantage of the selective wetting, a templated nanoparticle array was produced.

8. Summary

This chapter represents a comprehensive summary of the state of the art with regards to interfacial wetting stability in organic light emitting diodes and organic photovoltaics. Though the challenges are slightly different, both types of optoelectronic devices are heavily influenced by the stability of the interfaces with the bottom side contact. As organic optoelectron-

ic technologies mature, the metastability of interfaces becomes more and more significant in the quest for greater performance.

Acknowledgements

The author would like to acknowledge collaborators at the Max-Planck-Institute for Metals Research, specifically Prof. Dr. H. Dosch and students supervised by the author (F. Maye, J. Heidkamp) who have contributed some experimental results to this chapter.

Author details

Ayşe Turak

Department of Engineering Physics, McMaster University, Hamilton, Canada

References

- [1] Krebs F C and Norrman K Analysis of the failure mechanism for a stable organic photovoltaic during 10000 h of testing *Prog Photovoltaics* 2007;15(8) 697-712.
- [2] Brabec C J, Hauch J A, Schilinsky P and Waldauf C Production Aspects of Organic Photovoltaics and Commercialization of Devices *MRS Bulletin* 2005;30(Jan) 50-2.
- [3] Do L-m, Kim K, Zyung T and Kim J-j In situ investigation of degradation in polymer-electroluminescent devices using time-resolved confocal laser scanning microscope *Appl Phys Lett* 1997;70(25) 3470-2.
- [4] Reese M O, Morfa A J, White M S, Kopidakis N, Shaheen S E, Rumbles G and Ginley D S Pathways for the degradation of organic photovoltaic P3HT: PCBM based devices *Sol Energ Mat Sol C* 2008;92(7) 746-52.
- [5] Paci B, Generosi A, Albertini V R, Perfetti P, Bettignies R D and Sentein C Time-resolved morphological study of organic thin film solar cells based on calcium / aluminium cathode material *Chem Phys Lett* 2008;461(1-3) 77-81.
- [6] Jeranko T, Tributsch H, Sariciftci N S and Hummelen J C Patterns of efficiency and degradation of composite polymer solar cells *Sol Energ Mat Sol C* 2004;83(2-3) 247-62.
- [7] Kuwabara T, Nakayama T, Uozumi K, Yamaguchi T and Takahashi K Highly durable inverted-type organic solar cell using amorphous titanium oxide as electron collection electrode inserted between ITO and organic layer *Sol Energ Mat Sol C* 2008;92(11) 1476-82.

- [8] Cumpston B H, Parker I D and Jensen K F In situ characterization of the oxidative degradation of a polymeric light emitting device *J Appl Phys* 2001;81(8) 3716-20.
- [9] Scott J C, Kaufman J H, Brock P J, DiPietro R, Salem J and Goitia J A Degradation and failure of MEH-PPV light-emitting diodes *J Appl Phys* 1996;79(5) 2745-51.
- [10] Morgado J, Friend R H and Cacialli F Environmental aging of poly(p-phenylenevinylene) based light-emitting diodes *Synthetic Met* 2000;114(2) 189-96.
- [11] Dam N, Scurlock R D, Wang B J, Ma L C, Sundahl M and Ogilby P R Singlet oxygen as a reactive intermediate in the photodegradation of phenylenevinylene oligomers *Chem Mater* 1999;11(5) 1302-5.
- [12] Tang C W and Vanslyke S A Organic Electroluminescent Diodes *Appl Phys Lett* 1987;51(12) 913-5.
- [13] Tang C W 2-Layer Organic Photovoltaic Cell *Appl Phys Lett* 1986;48(2) 183-5.
- [14] Opera project <http://opera-project.eu/index.php?id=18&lang=EN>; International Summit on Organic Photovoltaic Stability (ISOS) <http://isos.wikispaces.com/>; OLED100 project <http://OLED100.eu>
- [15] Kroon J M, Wienk M M and Hummelen J C Accurate efficiency determination and stability studies of conjugated polymeryfullerene solar cells *Thin Solid Films* 2002;403-404(1 Feb) 223-8.
- [16] Shrotriya V, Li G, Yao Y, Moriarty T, Emery K and Yang Y Accurate measurement and characterization of organic solar cells *Adv Funct Mater* 2006;16(15) 2016-23.
- [17] Reese M O, Gevorgyan S A, Jorgensen M, Bundgaard E, Kurtz S R, Ginley D S, Olson D C, Lloyd M T, Moryllo P, Katz E A, Elschner A, Haillant O, Currier T R, Shrotriya V, Hermenau M, Riede M, Kirov K R, Trimmel G, Rath T, Inganas O, Zhang F L, Andersson M, Tvingstedt K, Lira-Cantu M, Laird D, McGuinness C, Gowrisanker S, Pannone M, Xiao M, Hauch J, Steim R, DeLongchamp D M, Rosch R, Hoppe H, Espinosa N, Urbina A, Yaman-Uzunoglu G, Bonekamp J B, van Breemen A J J M, Girotto C, Voroshazi E and Krebs F C Consensus stability testing protocols for organic photovoltaic materials and devices *Sol Energ Mat Sol C* 2011;95(5) 1253-67.
- [18] Fery C, Racine B, Vaufrey D, Doyeux H and Cina S Physical mechanism responsible for the stretched exponential decay behavior of aging organic light-emitting diodes *Appl Phys Lett* 2005;87(21) 213502.
- [19] De Bettignies R, Leroy J, Firon M and Sentein C Accelerated lifetime measurements of P3HT: PCBM solar cells *Synthetic Met* 2006;156(7-8) 510-3.
- [20] Schuller S, Schilinsky P, Hauch J and Brabec C J Determination of the degradation constant of bulk heterojunction solar cells by accelerated lifetime measurements *Appl Phys a-Mater* 2004;79(1) 37-40.
- [21] Jorgensen M, Norrman K and Krebs F C Stability/degradation of polymer solar cells *Sol Energ Mat Sol C* 2008;92(7) 686-714.

- [22] Jørgensen M, Norrman K, Gevorgyan S A, Tromholt T, Andreasen B and Krebs F C Stability of Polymer Solar Cells *Adv Mater* 2012;24(5) 580-612.
- [23] So F and Kondakov D Degradation Mechanisms in Small-Molecule and Polymer Organic Light-Emitting Diodes *Adv Mater* 2010;22(34) 3762-77.
- [24] A. Turak, Interfacial degradation in organic optoelectronics, *RSC Adv.*, DOI:10.1039/C2RA22770C.
- [25] Zinkeallmang M, Feldman L C and Grabow M H Clustering on Surfaces *Surf Sci Rep* 1992;16(8) 377-463.
- [26] Israelachvili J N *Intermolecular and surface forces*. Burlington, MA: Academic Press; 2011.
- [27] Strange T G, Evans D F and Hendrickson W A Nucleation and Growth of Defects Leading to Dewetting of Thin Polymer Films *Langmuir* 1997;13(16) 4459-65.
- [28] Kheshgi H S and Scriven L E Dewetting - Nucleation and Growth of Dry Regions *Chem Eng Sci* 1991;46(2) 519-26.
- [29] Hamaker H C The London – van der Waals attraction between spherical particles *Physica* 1937; 4(10) 1058-72.
- [30] Chattopadhyay S and Meredith J C Combinatorial screening of organic electronic materials: thin film stability *Measurement Science and Technology* 2005;16(1) 128-36.
- [31] Xie R, Karim A, Douglas J F, Han C C and Weiss R A Spinodal Dewetting of Thin Polymer Films *Phys Rev Lett* 1998;81(6) 1251-4.
- [32] Barnes K A, Karim A, Douglas J F, Nakatani A I, Gruell H and Amis E J Suppression of Dewetting in Nanoparticle-Filled Polymer Films *Macromolecules* 2000;33(11) 4177-85.
- [33] Mukherjee R, Das S, Das A, Sharma S K, Raychaudhuri A K and Sharma A Stability and Dewetting of Metal Nanoparticle Filled Thin Polymer Films: Dynamics *ACS Nano* 2010;4(7) 3709-24.
- [34] Reiter G Mobility of Polymers in Films Thinner Than Their Unperturbed Size *Europhys Lett* 1993;23(8) 579-84.
- [35] Jacobs K, Herminghaus S and Mecke K R Thin liquid polymer films rupture via defects *Langmuir* 1998;14(4) 965-9.
- [36] Reiter G, Hamieh M, Damman P, Sclavons S, Gabriele S, Vilmin T and Raphael E Residual stresses in thin polymer films cause rupture and dominate early stages of dewetting *Nat Mater* 2005;4(10) 754-8.
- [37] Sharma A, Mittal J and Verma R Instability and dewetting of thin films induced by density variations *Langmuir* 2002;18(26) 10213-20.

- [38] Fenter P, Schreiber F, Bulovic V and Forrest S R Thermally induced failure mechanisms of organic light emitting device structures probed by X-ray specular reflectivity *Chem Phys Lett* 1997;277(5-6) 521-6.
- [39] Vansmaalen S, Deboer J L, Haas C and Kommandeur J Anisotropic Thermal-Expansion in Crystals with Stacks of Planar Molecules, Such as Tetracyanoquinodimethanide (Tcnq) Salts *Phys Rev B* 1985;31(6) 3496-503.
- [40] Vix A B E, Mu P, Stocker W, Stamm M and Rabe J P Crossover between Dewetting and Stabilization of Ultrathin Liquid Crystalline Polymer Films *Langmuir* 2000;16(26) 10456-62.
- [41] Krause B, Durr A C, Schreiber F, Dosch H and Seeck O H Thermal stability and partial dewetting of crystalline organic thin films: 3,4,9,10-perylenetetracarboxylic dianhydride on Ag(111) *J Chem Phys* 2003;119(6) 3429-35.
- [42] Burke S A, Topple J M and Guttter P Molecular dewetting on insulators *Journal of Physics: Condensed Matter* 2009;21(42) 423101.
- [43] Adachi C, Tsutsui T and Saito S Blue Light-Emitting Organic Electroluminescent Devices *Appl Phys Lett* 1990;56(9) 799-801.
- [44] Appleyard S F J, Day S R, Pickford R D and Willis M R Organic electroluminescent devices: enhanced carrier injection using SAM derivatized ITO electrodes *J Mater Chem* 2000;10(1) 169-73.
- [45] Malinsky J E, Jabbour G E, Shaheen S E, Anderson J D, Richter A G, Marks T J, Armstrong N R, Kippelen B, Dutta P and Peyghambarian N Self-assembly processes for organic LED electrode passivation and charge injection balance *Adv Mater* 1999;11(3) 227-31.
- [46] Shen Y L, Jacobs D B, Malliaras G G, Koley G, Spencer M G and Ioannidis A Modification of indium tin oxide for improved hole injection in organic light emitting diodes *Adv Mater* 2001;13(16) 1234-8.
- [47] Nuesch F, Forsythe E W, Le Q T, Gao Y and Rothberg L J Importance of indium tin oxide surface acidity/basicity for charge injection into organic materials based light emitting diodes *J Appl Phys* 2000;87(11) 7973-80.
- [48] Ke L, Chua S J, Zhang K R and Chen P Bubble formation due to electrical stress in organic light emitting devices *Appl Phys Lett* 2002;80(2) 171-3.
- [49] Liu G, Kerr J B and Johnson S Dark spot formation relative to ITO surface roughness for polyfluorene devices *Synthetic Met* 2004;144(1) 1-6.
- [50] Scott J C, Carter S A, Karg S and Angelopoulos M Polymeric anodes for organic light-emitting diodes *Synthetic Met* 1997;85(1-3) 1197-200.
- [51] Adachi C, Nagai K and Tamoto N Molecular Design of Hole Transport Materials for Obtaining High Durability in Organic Electroluminescent Diodes *Appl Phys Lett* 1995;66(20) 2679-81.

- [52] Gong X, Moses D, Heeger A J, Liu S and Jen A K Y High-performance polymer light-emitting diodes fabricated with a polymer hole injection *Appl Phys Lett* 2003;83(1) 183-5.
- [53] Naito K and Miura A Molecular Design for Nonpolymeric Organic-Dye Glasses with Thermal-Stability - Relations between Thermodynamic Parameters and Amorphous Properties *J Phys Chem* 1993;97(23) 6240-8.
- [54] D'Iorio M Molecular materials for microelectronics *Can J Phys* 2000;78(3) 231-41.
- [55] Shirota Y Organic materials for electronic and optoelectronic devices *J Mater Chem* 2000;10(1) 1-25.
- [56] Shirota Y and Kageyama H Charge carrier transporting molecular materials and their applications in devices *Chem Rev* 2007;107(4) 953-1010.
- [57] Hung L S and Chen C H Recent progress of molecular organic electroluminescent materials and devices *Mat Sci Eng R* 2002;39(5-6) 143-222.
- [58] Rothberg L J and Lovinger A J Status of and prospects for organic electroluminescence *J Mater Res* 1996;11(12) 3174-87.
- [59] Hains A W, Liang Z Q, Woodhouse M A and Gregg B A Molecular Semiconductors in Organic Photovoltaic Cells *Chem Rev* 2010;110(11) 6689-735.
- [60] Cao Y, Yu G, Zhang C, Menon R and Heeger A J Polymer light-emitting diodes with polyethylene dioxythiophene-polystyrene sulfonate as the transparent anode *Synthetic Met* 1997;87(2) 171-4.
- [61] Ishii H, Sugiyama K, Ito E and Seki K Energy level alignment and interfacial electronic structures at organic metal and organic organic interfaces *Adv Mater* 1999;11(8) 605-25.
- [62] Kim H, Pique A, Horwitz J S, Mattoussi H, Murata H, Kafafi Z H and Chrisey D B Indium tin oxide thin films for organic light-emitting devices *Appl Phys Lett* 1999;74(23) 3444-6.
- [63] Schafer S, Petersen A, Wagner T A, Kniprath R, Lingenfelter D, Zen A, Kirchartz T, Zimmermann B, Wurfel U, Feng X J and Mayer T Influence of the indium tin oxide/organic interface on open-circuit voltage, recombination, and cell degradation in organic small-molecule solar cells *Phys Rev B* 2011;83(16) 165311.
- [64] Tak Y H, Kim K B, Park H G, Lee K H and Lee J R Criteria for ITO (indium-tin-oxide) an organic light thin film as the bottom electrode of emitting diode *Thin Solid Films* 2002;411(1) 12-6.
- [65] Kim J S, Granstrom M, Friend R H, Johansson N, Salaneck W R, Daik R, Feast W J and Cacialli F Indium-tin oxide treatments for single- and double-layer polymeric light-emitting diodes: The relation between the anode physical, chemical, and morphological properties and the device performance *J Appl Phys* 1998;84(12) 6859-70.

- [66] Djurisic A B, Lau T N, Kwong C Y, Guo W L, Bai Y K, Li E H and Chan W K Surface treatments of indium-tin-oxide substrates: comprehensive investigation of mechanical, chemical, thermal, and plasma treatments Proc SPIE 2002;4464 273-80.
- [67] Huang Z H, Zeng X T, Sun X Y, Kang E T, Fuh J Y H and Lu L Influence of plasma treatment of ITO surface on the growth and properties of hole transport layer and the device performance of OLEDs Org Electron 2008;9(1) 51-62.
- [68] Goncalves-Conto S, Carrard M, Si-Ahmed L and Zuppiroli L Interface morphology in organic light-emitting diodes Adv Mater 1999;11(2) 112-5.
- [69] Shen Y L, Klein M W, Jacobs D B, Scott J C and Malliaras G G Mobility-dependent charge injection into an organic semiconductor Phys Rev Lett 2001;86(17) 3867-70.
- [70] Gonzalez G B, Cohen J B, Hwang J H, Mason T O, Hodges J P and Jorgensen J D Neutron diffraction study on the defect structure of indium-tin-oxide J Appl Phys 2001;89(5) 2550-5.
- [71] Kim H, Gilmore C M, Pique A, Horwitz J S, Mattoussi H, Murata H, Kafafi Z H and Chrisey D B Electrical, optical, and structural properties of indium-tin-oxide thin films for organic light-emitting devices J Appl Phys 1999;86(11) 6451-61.
- [72] Paramonov P B and Paniagua S A Theoretical Characterization of the Indium Tin Oxide Surface and of Its Binding Sites for Adsorption of Phosphonic Acid Monolayers Chem Mater 2008;20(16) 5131-3.
- [73] Armstrong N R, Veneman P A, Ratcliff E, Placencia D and Brumbach M Oxide Contacts in Organic Photovoltaics: Characterization and Control of Near-Surface Composition in Indium-Tin Oxide (ITO) Electrodes Accounts Chem Res 2009;42(11) 1748-57.
- [74] Tang J X, Li Y Q, Zheng L R and Hung L S Anode/organic interface modification by plasma polymerized fluorocarbon films J Appl Phys 2004;95(8) 4397-403.
- [75] Kanai Y, Matsushima T and Murata H Improvement of stability for organic solar cells by using molybdenum trioxide buffer layer Thin Solid Films 2009;518(2) 537-40.
- [76] Milliron D J, Hill I G, Shen C, Kahn A and Schwartz J Surface oxidation activates indium tin oxide for hole injection J Appl Phys 2000;87(1) 572-6.
- [77] Sharma A, Kippelen B, Hotchkiss P J and Marder S R Stabilization of the work function of indium tin oxide using organic surface modifiers in organic light-emitting diodes Appl Phys Lett 2008;93(16)
- [78] Wu C C, Wu C I, Sturm J C and Kahn A Surface modification of indium tin oxide by plasma treatment: An effective method to improve the efficiency, brightness, and reliability of organic light emitting devices Appl Phys Lett 1997;70(11) 1348-50.
- [79] Koch N, Kahn A, Ghijsen J, Pireaux J J, Schwartz J, Johnson R L and Elschner A Conjugated organic molecules on metal versus polymer electrodes: Demonstration of a key energy level alignment mechanism Appl Phys Lett 2003;82(1) 70-2.

- [80] Cui J, Huang Q L, Veinot J C G, Yan H, Wang Q W, Hutchison G R, Richter A G, Evmenenko G, Dutta P and Marks T J Anode interfacial engineering approaches to enhancing anode/hole transport layer interfacial stability and charge injection efficiency in organic light-emitting diodes *Langmuir* 2002;18(25) 9958-70.
- [81] Lee J, Jung B-j, Lee J-i, Chu Y, Do L-m and Shim H-k Modification of an ITO anode with a hole-transporting SAM for improved OLED device characteristics *J Mater Chem* 2002;12 3494-8.
- [82] Chong L-w, Lee Y-l and Wen T-c Surface modification of indium tin oxide anodes by self-assembly monolayers: Effects on interfacial morphology and charge injection in organic light-emitting diodes *Thin Solid Films* 2007;515(5) 2833-41.
- [83] Choi B, Rhee J and Lee H H Tailoring of self-assembled monolayer for polymer light-emitting diodes *Appl Phys Lett* 2001;79(13) 2109-11.
- [84] Lacher S, Matsuo Y and Nakamura E Molecular and Supramolecular Control of the Work Function of an Inorganic Electrode with Self-Assembled Monolayer of Umbrella-Shaped Fullerene Derivatives *J Am Chem Soc* 2011;133(42) 16997-7004.
- [85] You Z Z Combined AFM, XPS, and contact angle studies on treated indium-tin-oxide films for organic light-emitting devices *Mater Lett* 2007;61(18) 3809-14.
- [86] Poon C O, Wong F L, Tong S W, Zhang R Q, Lee C S and Lee S T Improved performance and stability of organic light-emitting devices with silicon oxy-nitride buffer layer *Appl Phys Lett* 2003;83(5) 1038-40.
- [87] Le Q T, Forsythe E W, Nuesch F, Rothberg L J, Yan L and Gao Y Interface formation between NPB and processed indium tin oxide *Thin Solid Films* 2000;363(1-2) 42-6.
- [88] Grozea D, Turak A, Yuan Y, Han S, Lu Z H and Kim W Y Enhanced thermal stability in organic light-emitting diodes through nanocomposite buffer layers at the anode/organic interface *J Appl Phys* 2007;101(3) 033522.
- [89] Ribic P R and Bratina G Initial stages of growth of organic semiconductors on vicinal (0 0 0 1) sapphire surfaces *Surface Science* 2008;602(7) 1368-75.
- [90] Ettetdgui E, Davis G T, Hu B and Karasz F E Degradation of polymer-based light-emitting diodes during operation *Synthetic Met* 1997;90(1) 73-6.
- [91] Durr A C, Schreiber F, Munch M, Karl N, Krause B, Kruppa V and Dosch H High structural order in thin films of the organic semiconductor diindenoperylene *Appl Phys Lett* 2002;81(12) 2276-8.
- [92] Durr A C, Schreiber F, Ritley K A, Kruppa V, Krug J, Dosch H and Struth B Rapid roughening in thin film growth of an organic semiconductor (diindenoperylene) *Phys Rev Lett* 2003;90(1) 016104.
- [93] Zhang X N, Barrera E, de Oteyza D G and Dosch H Transition from layer-by-layer to rapid roughening in the growth of DIP on SiO₂ *Surface Science* 2007;601(12) 2420-5.

- [94] Ramaniah L M and Boero M Structural, electronic, and optical properties of the diindenoperylene molecule from first-principles density-functional theory *Phys Rev A* 2006;74(4) 042505.
- [95] Karl N Charge carrier transport in organic semiconductors *Synthetic Met* 2003;133-134(13 March) 649-57.
- [96] Huang Y L, Chen W, Huang H, Qi D C, Chen S, Gao X Y, Pflaum J and Wee A T S Ultrathin Films of Diindenoperylene on Graphite and SiO₂ *J Phys Chem C* 2009;113(21) 9251-5.
- [97] Kurrle D and Pflaum J Exciton diffusion length in the organic semiconductor diindenoperylene *Appl Phys Lett* 2008;92(13) 133306.
- [98] Turak A, Nguyen M, Maye F, Heidkamp J, Lienerth P, Wrachtrup J and Dosch H Nanoscale Engineering of Exciton Dissociating Interfaces in Organic Photovoltaics *J Nano Res* 2011;14 125-36.
- [99] Heidkamp J. DIP growth on substrates relevant for organic solar cells. Diploma thesis. University of Stuttgart;2009.
- [100] Zhu Z, Hadjikyriacou S, Waller D and Gaudiana R Stabilization of film morphology in polymer-fullerene heterojunction solar cells *J Macromol Sci Pure* 2004;A41(12) 1467-87.
- [101] Bertho S, Haeldermans I, Swinnen A, Moons W, Martens T, Lutsen L, Vanderzande D, Manca J, Senes A and Bonfiglio A Influence of thermal ageing on the stability of polymer bulk heterojunction solar cells *Sol Energ Mat Sol C* 2007;91(5) 385-9.
- [102] Turak A, Hanisch J, Barrena E, Welzel U, Widmaier F, Ahlswede E and Dosch H Systematic analysis of processing parameters on the ordering and performance of working poly(3-hexyl-thiophene):[6,6]-phenyl C(61)-butyric acid methyl ester solar cells *J Renew Sustain Ener* 2010;2(5) 053103.
- [103] Bulliard X, Ihn S G, Yun S, Kim Y, Choi D, Choi J Y, Kim M, Sim M, Park J H, Choi W and Cho K Enhanced Performance in Polymer Solar Cells by Surface Energy Control *Adv Funct Mater* 2010;20(24) 4381-7.
- [104] Chen F C, Lin Y K and Ko C J Submicron-scale manipulation of phase separation in organic solar cells *Appl Phys Lett* 2008;92(2) 023307.
- [105] Bjorstrom C M, Nilsson S, Bernasik A, Budkowski A, Andersson M, Magnusson K O and Moons E Vertical phase separation in spin-coated films of a low bandgap polyfluorene/PCBM blend - Effects of specific substrate interaction *Appl Surf Sci* 2007;253(8) 3906-12.
- [106] Gardonio S, Gregoratti L, Melpignano P, Aballe L, Biondo V, Zamboni R, Murgia M, Caria S and Kiskinova A Degradation of organic light-emitting diodes under different environment at high drive conditions *Org Electron* 2007;8(1) 37-43.

- [107] Luo Y, Aziz H, Popovic Z D and Xu G Correlation between electroluminescence efficiency and stability in organic light-emitting devices under pulsed driving conditions *J Appl Phys* 2006;99(5) 054508.
- [108] Gärditz C and Winnacker A Impact of Joule heating on the brightness homogeneity of organic light *Appl Phys Lett* 2007;90(10) 103506.
- [109] Chao C I, Chuang K R and Chen S A Failure phenomena and mechanisms of polymeric light-emitting diodes: Indium-tin-oxide-damage *Appl Phys Lett* 1996;69(19) 2894-6.
- [110] Zhou X, He J, Liao L S, Lu M, Ding X M, Hou X Y, Zhang X M, He X Q and Lee S T Real-time observation of temperature rise and thermal breakdown processes in organic LEDs using an IR imaging and analysis system *Adv Mater* 2000;12(4) 265-9.
- [111] Tessler N, Harrison N T, Thomas D S and Friend R H Current heating in polymer light emitting diodes *Appl Phys Lett* 1998;73(6) 732-4.
- [112] Nakanotani H, Sasabe H and Adachi C Singlet-singlet and singlet-heat annihilations in fluorescence-based organic light-emitting diodes under steady-state high current density *Appl Phys Lett* 2005;86(21) 213506.
- [113] Zhan Y Q, Xiong Z H, Shi H Z, Zhang S T, Xu Z, Zhong G Y, He J, Zhao J M, Wang Z J, Obbard E, Ding H J, Wang X J, Ding X M, Huang W and Hou X Y Sodium stearate , an effective amphiphilic molecule buffer material between organic and metal layers in organic light-emitting devices *Appl Phys Lett* 2003;83(8) 1656-8.
- [114] Choi S H, Lee T I, Baik H K, Roh H H, Kwon O and Suh D H The effect of electrode heat sink in organic-electronic devices *Appl Phys Lett* 2008;93(18) 183301.
- [115] Sullivan P and Jones T S Pentacene / fullerene (C 60) heterojunction solar cells: Device performance and degradation mechanisms *Org Electron* 2008;9(5) 656-60.
- [116] Paci B, Generosi A, Albertini V R, Generosi R, Perfetti P, de Bettignies R and Sentin C Time-resolved morphological study of bulk heterojunction films for efficient organic solar devices *J Phys Chem C* 2008;112(26) 9931-6.
- [117] Franke R, Maennig B, Petrich A and Pfeiffer M Long-term stability of tandem solar cells containing small organic molecules *Sol Energ Mat Sol C* 2008;92(7) 732-5.
- [118] Xu M S, Xu J B and An J Visualization of thermally activated morphology evolution of N,N'-di(naphthalene-1-yl)-N,N'-diphthalbenzidine films on ITO/copper phthalocyanine underlying layer *Appl Phys a-Mater* 2005;81(6) 1151-6.
- [119] Han E M, Do L M, Yamamoto N and Fujihira M Study of Interfacial Degradation of the Vapor-Deposited Bilayer of Alq3/Tpd for Organic Electroluminescent (El) Devices by Photoluminescence *Chem Lett* 1995;24(1) 57-8.
- [120] Tokito S and Taga Y Organic Electroluminescent Devices Fabricated Using a Diamine Doped MgF₂ Thin-Film as a Hole-Transporting Layer *Appl Phys Lett* 1995;66(6) 673-5.

- [121] Loy B D E, Koene B E and Thompson M E Thermally Stable Hole-Transporting Materials Based upon a Fluorene Core *Adv Funct Mater* 2002;12(4) 245-9.
- [122] Orita K, Morimura T, Horiuchi T and Matsushige K In situ energy-dispersive X-ray reflectivity measurements of structural changes in thin films for organic electroluminescent devices *Synthetic Met* 1997;91(1-3) 155-8.
- [123] Tokito S, Tanaka H, Noda K, Okada A and Taga Y Thermal stability in oligomeric triphenylamine / tris (8-quinolinolato) aluminum electroluminescent devices *Appl Phys Lett* 1997;70(15) 1929-31.
- [124] Brown T M, Kim J S, Friend R H, Cacialli F, Daik R and Feast W J Built-in field electroabsorption spectroscopy of polymer light-emitting diodes incorporating a doped poly(3,4-ethylene dioxythiophene) hole injection layer *Appl Phys Lett* 1999;75(12) 1679-81.
- [125] Xu M S and Xu J B Real-time visualization of thermally activated degradation of the ITO/CuPC/NPB/Alq(3) stack used in one of the organic light-emitting diodes *J Phys D Appl Phys* 2004;37(12) 1603-8.
- [126] Hoppe H, Niggemann M, Winder C, Kraut J, Hiesgen R, Hinsch A, Meissner D and Sariciftci N S Nanoscale morphology of conjugated polymer/fullerene-based bulk-heterojunction solar cells *Adv Funct Mater* 2004;14(10) 1005-11.
- [127] Yang X N, van Duren J K J, Janssen R A J, Michels M A J and Loos J Morphology and thermal stability of the active layer in poly(p-phenylenevinylene)/methanofullerene plastic photovoltaic devices *Macromolecules* 2004;37(6) 2151-8.
- [128] Motaung D E, Malgas G F and Arendse C J Insights into the stability and thermal degradation of P3HT:C-60 blended films for solar cell applications *J Mater Sci* 2011;46(14) 4942-52.
- [129] Conings B, Bertho S, Vandewal K, Senes A, Haen J D, Conings B, Bertho S, Vandewal K, Senes A, Haen J D, Manca J and Janssen R A J Modeling the temperature induced degradation kinetics of the short circuit current in organic bulk heterojunction solar cells *Appl Phys Lett* 2010;96(16) 163301.
- [130] Bertho S, Janssen G, Cleij T J, Conings B, Moons W, Gadisa A, Haen J D, Goovaerts E, Lutsen L, Manca J and Vanderzande D Effect of temperature on the morphological and photovoltaic stability of bulk heterojunction polymer: fullerene solar cells *Sol Energ Mat Sol C* 2008;92(7) 753-60.
- [131] Luo Y C, Aziz H, Xu G and Popovic Z D Improving the stability of organic light-emitting devices by using a hole-injection-tunable-anode-buffer-layer *J Appl Phys* 2007;101(5) 054512.
- [132] Forsythe E W, Abkowitz M A and Gao Y L Tuning the carrier injection efficiency for organic light-emitting diodes *J Phys Chem B* 2000;104(16) 3948-52.

- [133] van Slyke S A, Chen C H and Tang C W Organic electroluminescent devices with improved stability *Appl Phys Lett* 1996;69(15) 2160-2.
- [134] Lee Y-j, Lee H, Byun Y, Song S, Kim J-e, Eom D, Cha W, Park S-s, Kim J and Kim H Study of thermal degradation of organic light emitting device structures by X-ray scattering *Thin Solid Films* 2007;515(14) 5674-7.
- [135] Sellner B S, Gerlach A, Schreiber F, Kelsch M, Kasper N, Dosch H, Meyer S, Pflaum J, Fischer M and Gompf B Strongly Enhanced Thermal Stability of Crystalline Organic Thin Films Induced by Aluminum Oxide Capping Layers *Adv Mater* 2004;16(19) 1750-3.
- [136] Peumans P, Uchida S and Forrest S R Efficient bulk heterojunction photovoltaic cells using small- molecular-weight organic thin films *Nature* 2003;425(September) 158-62.
- [137] Durr A C, Koch N, Kelsch M, Ruhm A, Ghijsen J, Johnson R L, Pireaux J J, Schwartz J, Schreiber F, Dosch H and Kahn A Interplay between morphology, structure, and electronic properties at diindenoperylene-gold interfaces *Phys Rev B* 2003;68(11) 115428.
- [138] Zhang F, Baralia G, Boborodea A, Bailly C, Nysten B and Jonas A M Partial Dewetting of Polyethylene Thin Films on Rough Silicon Dioxide Surfaces *Langmuir* 2005;21(16) 7427-32.
- [139] Karapanagiotis I, Evans D F and Gerberich W W Dewetting dynamics of thin polystyrene films from sputtered silicon and gold surfaces *Colloid Surface A* 2002;207(1-3) 59-67.
- [140] Netz R R and Andelman D Roughness-induced wetting *Physical Review E* 1997;55(1) 687-700.
- [141] Wirth H O Organische Gläser mit hohen Glasumwandlungstemperaturen auf Basis niedermolekularer Verbindungen *Die Angewandte Makromolekulare Chemie* 1991;185(1) 329-34.
- [142] O'Brien D F, Burrows P E, Forrest S R, Koene B E, Loy D E and Thompson M E Hole Transporting Materials with High Glass Transition Temperatures for Use in Organic Light-Emitting Devices *Adv Mater* 1998;10(14) 1108-12.
- [143] Gao Z Q, Lai W Y, Wong T C, Lee C S and Bello I Organic electroluminescent devices by high-temperature processing and crystalline hole transporting layer *Appl Phys Lett* 1999;74(22) 3269-71.
- [144] Xu M S, Xu J B, Chen H Z and Wang M Nanoscale investigation of moisture-induced degradation mechanisms of tris (8-hydroxyquinoline) aluminium-based organic light-emitting *Journal of Physics D: Applied Physics* 2004;37(18) 2618-22.
- [145] Sato Y, Ogata T, Ichinosawa S, Fugono M and Kanai H Interface and material considerations of OLEDs *Proc SPIE* 1999;3797 198-208.

- [146] Koene B E, Loy D E and Thompson M E Asymmetric Triaryldiamines as Thermally Stable Hole Transporting Layers for Organic Light-Emitting Devices *Chem Mater* 1998;10(8) 2235-50.
- [147] Shirota Y, Kuwabara Y, Inada H, Wakimoto T, Nakada H, Yonemoto Y, Kawami S and Imai K Multilayered organic electroluminescent device using a novel starburst 4,4',4''-tris(3-methylphenylphenylamino)triphenylamine as a hole transport material *Appl Phys Lett* 1994;65(7) 807-9.
- [148] Tong Q-x, Lai S-l, Chan M-y, Lai K-h, Tang J-x, Kwong H-L, Lee C-S and Lee S-T High Tg Triphenylamine-Based Starburst Hole-Transporting Material for Organic Light-Emitting Devices *Chem Mater* 2007;19(24) 5851-5.
- [149] Murata H, Merritt C D, Inada H, Shirota Y and Kafafi Z H Molecular organic light-emitting diodes with temperature-independent quantum efficiency and improved thermal durability *Appl Phys Lett* 1999;75(21) 3252-4.
- [150] Jiang Z, Ye T, Yang C, Yang D and Zhu M Star-Shaped Oligotriarylamines with Planarized Triphenylamine Core: Solution processable high Tg hole injecting and hole transporting Materials for Organic Light-Emitting Devices *Chem Mater* 2011;23(3) 771-7.
- [151] Li J, Liu D, Li Y, Lee C-s, Kwong H-l and Lee S A High Tg Carbazole-Based Hole-Transporting Material for Organic Light-Emitting Devices *Chem Mater* 2005;17(5) 1208-12.
- [152] Park M H, Yun C, Huh J O, Do Y, Yoo S and Lee M H Synthesis and hole-transporting properties of vinyl-type polynorbornenes with ethyl ester linked triarylamine side groups *Synthetic Met* 2010;160(17-18) 2000-7.
- [153] Krebs F C and Spanggaard H Significant improvement of polymer solar cell stability *Chem Mater* 2005;17(21) 5235-7.
- [154] Petersen M H, Gevorgyan S A and Krebs F C Thermocleavable Low Band Gap Polymers and Solar Cells Therefrom with Remarkable Stability toward Oxygen Macromolecules 2008;41(23) 8986-94.
- [155] Becker H, Spreitzer H, Kreuder W, Kluge E, Schenk H, Parker I and Cao Y Soluble PPVs with enhanced performance - A mechanistic approach *Adv Mater* 2000;12(1) 42-8.
- [156] Liang Z, Reese M O and Gregg B A Chemically Treating Poly (3-hexylthiophene) Defects to Improve Bulk Heterojunction Photovoltaics *ACS Appl Mater Inter* 2011;3(6) 2042-50.
- [157] Jiang X-y, Zhang Z-l, Cao J, Khan M A, Ul-Haq K and Zhu W-Q White OLED with high stability and low driving voltage based on a novel buffer layer MoO_x *Journal of Physics D: Applied Physics* 2007;40(18) 5553-7.

- [158] Qiu C, Chen H, Xie Z, Wong M and Kwok H S Praseodymium oxide coated anode for organic light-emitting diode Appl Phys Lett 2002;80(19) 3485-7.
- [159] Chu T-y, Kwong C Y and Song O-k Enhanced performance of organic light-emitting diodes with an air- stable n-type hole-injection layer n-type hole-injection layer Appl Phys Lett 2008;92(23) 233307.
- [160] Hung L S, Zheng L R and Mason M G Anode modification in organic light-emitting diodes by low-frequency plasma polymerization of CHF₃ Appl Phys Lett 2001;78(5) 673-5.
- [161] Lee S N, Hsu S F, Hwang S W and Chen C H Effects of substrate treatment on the electroluminescence performance of flexible OLEDs Curr Appl Phys 2004;4(6) 651-4.
- [162] Ke L, Kumar R S, Zhang K R, Chua S J and Wee A T S Effect of parylene layer on the performance of OLED Microelectron J 2004;35(4) 325-8.
- [163] Huang Q, Evmenenko G A, Dutta P, Lee P, Armstrong N R and Marks T J Covalently Bound Hole-Injecting Nanostructures . Systematics of Molecular Architecture , Thickness , Saturation , and Electron-Blocking Characteristics on Organic Light-Emitting Diode Luminance , Turn-on Voltage , and Quantum Efficiency the focus of an ex J Am Chem Soc 2005;10(3) 10227-42.
- [164] Cui J, Huang Q, Veinot J C G, Yan H, Wang Q, Hutchison G R, Richter A G, Evmenenko G, Dutta P and Marks T J Anode Interfacial Engineering Approaches to Enhancing Anode / Hole Transport Layer Interfacial Stability and Charge Injection Efficiency in Organic Light-Emitting Diodes Langmuir 2002;18(5) 9958-70.
- [165] Berntsen A, Croonen Y, Liedtke C, Schoo H, Visser R J, Vleggaar J and Weijer P V D Stability of polymer LEDs Optical Materials 1998;9(January) 125-33.
- [166] Carter S A, Angelopoulos M, Karg S, Brock P J and Scott J C Polymeric anodes for improved polymer light-emitting diode performance Appl Phys Lett 1997;70(16) 2067-9.
- [167] Aernouts T, Geens W, Poortmans J, Heremans P, Borghs S and Mertens R Extraction of bulk and contact components of the series resistance in organic bulk donor-acceptor-heterojunctions Thin Solid Films 2002;403(1 Feb) 297-301.
- [168] Siboni H Z, Luo Y and Aziz H Luminescence degradation in phosphorescent organic light-emitting devices by hole space charges J Appl Phys 2011;109(4) 044501.
- [169] Aziz H, Luo Y, Xu G and Popovic Z D Improving the stability of organic light-emitting devices by using a thin Mg Appl Phys Lett 2006;89(10) 103515.
- [170] Choi S H, Jeong S M, Koo W H, Jo S J, Baik H K, Lee S J, Song K M and Han D W Diamond-like carbon as a buffer layer in polymeric electroluminescent device Thin Solid Films 2005;483(1-2) 351-7.

- [171] Chen B J, Sun X W and Tay B K Improvement of efficiency and stability of polymer light-emitting devices by modifying indium tin oxide anode surface with ultrathin tetrahedral amorphous carbon film *Appl Phys Lett* 2005;86(6) 063506.
- [172] Karg S, Scott J C, Salem J R and Angelopoulos M Increased brightness and lifetime of polymer light-emitting diodes with polyaniline anodes *Synthetic Met* 1996;80(2) 111-7.
- [173] Wong K W, Yip H L, Luo Y, Wong K Y, Lau W M, Low K H, Chow H F, Gao Z Q, Yeung W L and Chang C C Blocking reactions between indium-tin oxide and poly(3,4-ethylene dioxythiophene): poly(styrene sulphonate) with a self-assembly monolayer *Appl Phys Lett* 2002;80(15) 2788-90.
- [174] de Jong M P, van IJendoorn L J and de Voigt M J A Stability of the interface between indium-tin-oxide and poly(3,4-ethylenedioxythiophene)/poly(styrenesulfonate) in polymer light-emitting diodes *Appl Phys Lett* 2000;77(14) 2255-7.
- [175] Chua S J, Ke L, Kumar R S and Zhang K Stabilization of electrode migration in polymer electroluminescent devices *Appl Phys Lett* 2002;81(6) 1119-21.
- [176] Cho S J, Kwon T and Yoo D S Blocking of metallic impurities in polymer EL device by PI interlayer *Synthetic Met* 2003;137(1-3) 1043-4.
- [177] Gandhi D D, Lane M, Zhou Y, Singh A P, Nayak S, Tisch U, Eizenberg M and Ramnath G Annealing-induced interfacial toughening using a molecular nanolayer *Nature* 2007;447(7142) 299-302.
- [178] Zhang X W, Wu Z X, Wang D D, Wang D W and Hou X Improving the stability of organic light-emitting devices using a solution-processed hole-injecting layer *Appl Surf Sci* 2009;255(18) 7970-3.
- [179] Yang N C, Lee J, Song M-w, Ahn N, Lee S and Chin B D Ultra-thin fluoropolymer buffer layer as an anode stabilizer of organic light emitting devices *Journal of Physics D: Applied Physics* 2007;40(15) 4466-70.
- [180] Kao C C, Lin P, Lee C C, Wang Y K, Ho J C and Shen Y Y High-performance bottom-contact devices based on an air-stable n-type organic semiconductor N,N-bis(4-trifluoromethoxybenzyl)-1,4,5,8-naphthalene-tetracarboxylic di-imide *Appl Phys Lett* 2007;90(21) 212101.
- [181] Chen T H, Liou Y, Wu T J and Chen J Y Enhancement of organic light-emitting device performances with Hf-doped indium tin oxide anodes *Appl Phys Lett* 2004;85(11) 2092-4.
- [182] Chen T H, Liou Y, Wu T J and Chen J Y Vanadium-doped indium tin oxide as hole-injection layer in organic light-emitting devices *Appl Phys Lett* 2005;87(24) 243510.
- [183] Chen T H, Wu T J, Chen J Y and Liou Y Effects of metal-doped indium-tin-oxide buffer layers in organic light-emitting devices *J Appl Phys* 2006;99(11) 114515.

- [184] Qiu C F, Xie Z L, Chen H Y, Wong M and Kwok H S Comparative study of metal or oxide capped indium-tin oxide anodes for organic light-emitting diodes *J Appl Phys* 2003;93(6) 3253-8.
- [185] Hou L T, Liu P Y, Li Y W and Wu C H Enhanced performance in organic light-emitting diodes by sputtering TiO₂ ultra-thin film as the hole buffer layer *Thin Solid Films* 2009;517(17) 4926-9.
- [186] Hu W P and Matsumura M Organic single-layer electroluminescent devices fabricated on CuOx-coated indium tin oxide substrate *Appl Phys Lett* 2002;81(5) 806-7.
- [187] Zhang D-d, Feng J, Liu Y-f, Zhong Y-q, Bai Y, Jin Y and Xie G-h Enhanced hole injection in organic light-emitting devices by using Fe₃O₄ as an anodic buffer layer *Appl Phys Lett* 2009;94(22) 223306.
- [188] Deng Z B, Ding X M, Lee S T and Gambling W A Enhanced brightness and efficiency in organic electroluminescent devices using SiO₂ buffer layers *Appl Phys Lett* 1999;74(15) 2227-9.
- [189] Tokito S, Noda K and Taga Y Metal oxides as a hole-injecting layer for an organic electroluminescent device *J Phys D Appl Phys* 1996;29(11) 2750-3.
- [190] Shrotriya V, Li G, Yao Y, Chu C W and Yang Y Transition metal oxides as the buffer layer for polymer photovoltaic cells *Appl Phys Lett* 2006;88(7) 073508.
- [191] Kurosaka Y, Tada N, Ohmori Y and Yoshino K Improvement of Metal-Organic Interface by Insertion of Mono-layer Size Insulating Layer in Organic EL Device *Synthetic Met* 1999;102(1-3) 1101-2.
- [192] Chan I M, Hsu T Y and Hong F C Enhanced hole injections in organic light-emitting devices by depositing nickel oxide on indium tin oxide anode *Appl Phys Lett* 2002;81(10) 1899-901.
- [193] Di C A, Yu G, Liu Y Q, Xu X J, Song Y B and Zhu D B Effective modification of indium tin oxide for improved hole injection in organic light-emitting devices *Appl Phys Lett* 2006;89(3)
- [194] Gross M, Muller D C, Scherf U, Nothofer H-G, Neher D, Brauchle C and Meerholz K Improving the performance of doped pi-conjugated polymers for use in organic light-emitting diodes *Nature* 2000;405(June) 661-5.
- [195] Ganzorig C, Kwak K J, Yagi K and Fujihira M Fine tuning work function of indium tin oxide by surface molecular design: Enhanced hole injection in organic electroluminescent devices *Appl Phys Lett* 2001;79(2) 272-4.
- [196] Papageorgiou N, Salomon E, Angot T, Layet J M, Giovanelli L and Le Lay G Physics of ultra-thin phthalocyanine films on semiconductors *Prog Surf Sci* 2004;77(5-8) 139-70.
- [197] Claessens C G, Hahn U and Torres T Phthalocyanines: From outstanding electronic properties to emerging applications *Chem Rec* 2008;8(2) 75-97.

- [198] de Oteyza D G, El-Sayed A, Garcia-Lastra J M, Goiri E, Krauss T N, Turak A, Barrena E, Dosch H, Zegenhagen J, Rubio A, Wakayama Y and Ortega J E Copper-phthalocyanine based metal-organic interfaces: The effect of fluorination, the substrate, and its symmetry *J Chem Phys* 2010;133(21)
- [199] Scientific W 2012 *Journal of Porphyrins and Phthalocyanines (JPP)*.
- [200] Walter M G, Rudine A B and Wamser C C Porphyrins and phthalocyanines in solar photovoltaic cells *J Porphyr Phthalocya* 2010;14(9) 759-92.
- [201] Yu W L, Pei J, Cao Y and Huang W Hole-injection enhancement by copper phthalocyanine (CuPc) in blue polymer light-emitting diodes *J Appl Phys* 2001;89(4) 2343-50.
- [202] Kim S C, Lee G B, Choi M W, Roh Y, Whang C N, Jeong K, Lee J G and Kim S Controlling hole injection in organic electroluminescent device by sputter-grown Cu-phthalocyanine thin films *Appl Phys Lett* 2001;78(10) 1445-7.
- [203] Lee S T, Wang Y M, Hou X Y and Tang C W Interfacial electronic structures in an organic light-emitting diode *Appl Phys Lett* 1999;74(5) 670-2.
- [204] Fenenko L and Adachi C Influence of heat treatment on indium – tin-oxide anodes and copper phthalocyanine hole injection layers in organic light-emitting diodes *Thin Solid Films* 2007;515(11) 4812-8.
- [205] Tadayyon S M, Grandin H M, Griffiths K, Norton P R, Aziz H and Popovic Z D CuPc buffer layer role in OLED performance: a study of the interfacial band energies *Org Electron* 2004;5(4) 157-66.
- [206] Mori T, Mitsuoka T, Ishii M, Fujikawa H and Taga Y Improving the thermal stability of organic light-emitting diodes by using a modified phthalocyanine layer *Appl Phys Lett* 2002;80(21) 3895-7.
- [207] Lobbert G 2000 Phthalocyanines. In: *Ullmann's Encyclopedia of Industrial Chemistry*, ed F Ullmann: Wiley-VCH Verlag)
- [208] Lee Y J, Park S-s, Kim J and Kim H Interface morphologies and interlayer diffusions in organic light emitting device by x-ray scattering *Appl Phys Lett* 2009;94(22) 223305.
- [209] Aziz H, Popovic Z D and Hu N-x Organic light emitting devices with enhanced operational stability at elevated temperatures *Appl Phys Lett* 2002;81(2) 370-2.
- [210] Choong V-e, Shen J, Curless J, Shi S and Yang J Efficient and durable organic alloys for electroluminescent displays *Journal of Physics D: Applied Physics* 2000;33(7) 760-3.
- [211] Sheats J R, Antoniadis H, Hueschen M, Leonard W, Miller J, Moon R, Roitman D and Stocking A Organic electroluminescent devices *Science* 1996;273(5277) 884-8.

- [212] dos Anjos P N M, Aziz H, Hu N X and Popovic Z D Temperature dependence of electroluminescence degradation in organic light emitting devices without and with a copper phthalocyanine buffer layer *Org Electron* 2002;3(1) 9-13.
- [213] Cui J, Huang Q L, Veinot J G C, Yan H and Marks T J Interfacial microstructure function in organic light-emitting diodes: Assembled tetraaryldiamine and copper phthalocyanine interlayers *Adv Mater* 2002;14(8) 565-9.
- [214] Peisert H, Knupfer M, Schwieger T and Fink J Strong chemical interaction between indium tin oxide and phthalocyanines *Appl Phys Lett* 2002;80(16) 2916-8.
- [215] Kim J, Kim M, Kim J W, Yi Y and Kang H Organic light emitting diodes using NaCl: N,N-bis(naphthalene-1-yl)-N,N-bis(phenyl) benzidine composite as a hole injection buffer layer *J Appl Phys* 2010;108(10) 103703.
- [216] Aziz H and Popovic Z D Degradation Phenomena in Small-Molecule Organic Light-Emitting Devices *Chem Mater* 2004;16(23) 4522-32.
- [217] Elschner A, Bruder F, Heuer H, Jonas F, Karbach A, Kirchmeyer S, Thrum S and Wehrmann R PEDT:PSS for efficient hole-injection in hybrid organic light-emitting diodes *Synthetic Met* 2000;111-112(1 June) 139-43.
- [218] Matsushima T and Murata H Enhancing power conversion efficiencies and operational stability of organic light-emitting diodes by increasing carrier injection efficiencies at anode / organic and organic / organic heterojunction interfaces Enhancing power conversion efficiencies and *J Appl Phys* 2008;104(3) 034507.
- [219] Cacialli F, Kim J S, Brown T M, Morgado J, Granstrom M, Friend R H, Gigli G, Cingolani R, Favaretto L, Barbarella G, Daik R and Feast W J Surface and bulk phenomena in conjugated polymers devices *Synthetic Met* 2000;109(1-3) 7-11.
- [220] Fukushi Y, Kominami H, Nakanishi Y and Hatanaka Y Effect of ITO surface state to the aging characteristics of thin film OLED *Appl Surf Sci* 2005;244(1-4) 537-40.
- [221] Mathai M K, Papadimitrakopoulos F and Hsieh B R Alq₃-based organic light emitting diodes to improve the device lifetime by an oxidized transport layer *J Appl Phys* 2004;95(12) 8240-6.
- [222] Chu T-y, Lee Y-h and Song O-k Effects of interfacial stability between electron transporting layer and cathode on the degradation process of organic light-emitting diodes *Appl Phys Lett* 2007;91(22) 223509.
- [223] Liew Y-f, Zhu F, Chua S-j and Tang J-x Tris-(8-hydroxyquinoline)aluminum-modified indium tin oxide for enhancing the efficiency and reliability of organic light-emitting devices *Appl Phys Lett* 2004;85(19) 4511-3.
- [224] Chwang A B, Kwong R C and Brown J J Graded mixed-layer organic light-emitting devices *Appl Phys Lett* 2002;80(5) 725-7.

- [225] Lee M-t, Liao C-h and Tsai C-h Improved stability of organic electroluminescent devices by doping styrylamines in hole or electron transporting layer *Appl Phys Lett* 2005;86(10) 103501.
- [226] Tsai C-h, Liao C-h, Lee M-t and Chen C H Highly stable organic light-emitting devices with a uniformly mixed hole transport layer *Appl Phys Lett* 2005;87(24) 243505.
- [227] Lee T-w, Kwon O, Kim M-g, Park S H, Chung J, Kim S Y, Chung Y, Park J-Y, Han E, Huh D H, Park J-J and Pu L Hole-injecting conducting-polymer compositions for highly efficient and stable organic light-emitting diodes *Appl Phys Lett* 2005;87(23) 231106.
- [228] Jung G Y, Yates A, Samuel I D W and Petty M C Lifetime studies of light-emitting diode structures incorporating polymeric Langmuir – Blodgett films *Materials Science and Engineering C* 2001;14(1-2) 1-10.
- [229] Kim J, Lee J, Han C W, Lee N Y and Chung I J Effect of thermal annealing on the lifetime of polymer light-emitting diodes *Appl Phys Lett* 2003;82(24) 4238-40.
- [230] Voroshazi E, Verreet B, Buri A, Muller R, Di Nuzzo D and Heremans P Influence of cathode oxidation via the hole extraction layer in polymer:fullerene solar cells *Org Electron* 2011;12(5) 736-44.
- [231] Sun Y M, Takacs C J, Cowan S R, Seo J H, Gong X, Roy A and Heeger A J Efficient, Air-Stable Bulk Heterojunction Polymer Solar Cells Using MoOx as the Anode Interfacial Layer *Adv Mater* 2011;23(19) 2226-30.
- [232] Zilberberg K, Gharbi H, Behrendt A, Trost S and Riedl T Low-Temperature, Solution-Processed MoOx for Efficient and Stable Organic Solar Cells *ACS Appl Mater Inter* 2012;4(3) 1164-8.
- [233] Kim Y H, Sachse C, Hermenau M, Fehse K, Riede M, Muller-Meskamp L and Leo K Improved efficiency and lifetime in small molecule organic solar cells with optimized conductive polymer electrodes *Appl Phys Lett* 2011;99(11) 113305.
- [234] Kirchmeyer S and Reuter K Scientific importance, properties and growing applications of poly(3,4-ethylenedioxythiophene) *J Mater Chem* 2005;15(21) 2077-88.
- [235] Carter J C, Grizzi I, Heeks S K, Lacey D J, Latham S G, May P G, Los O R D, Pichler K, Towns C R and Wittmann H F Operating stability of light-emitting polymer diodes based on poly(p-phenylene vinylene) *Appl Phys Lett* 1997;71(1) 34-6.
- [236] Jonda C, Mayer A B R, Stolz U, Elschner A and Karbach A Surface roughness effects and their influence on the degradation of organic light emitting devices *J Mater Sci* 2000;35(22) 5645-51.
- [237] Stephan O, Tran-van F and Chevrot C New organic materials for light emitting devices based on dihexylfluorene-co-ethylenedioxythiophene copolymers exhibiting improved hole-injecting properties *Synthetic Met* 2002;131(1-3) 31-40.

- [238] Maye F. Morphological and structural study of ultrathin lithium fluoride films on organic molecule surfaces. Doctorate thesis. University of Stuttgart; 2011.
- [239] Kawano K, Pacios R, Poplavskyy D, Nelson J, Bradley D D C and Durrant J R Degradation of organic solar cells due to air exposure *Sol Energ Mat Sol C* 2006;90(20) 3520-30.
- [240] Sharma A, Andersson G and Lewis D A Role of humidity on indium and tin migration in organic photovoltaic devices *Phys Chem Chem Phys* 2011;13(10) 4381-7.
- [241] Nguyen T P, Le Rendu P, Long P D and De Vos S A Chemical and thermal treatment of PEDOT: PSS thin films for use in organic light emitting diodes *Surf Coat Tech* 2004;180-181(1 March) 646-9.
- [242] Bulle-Lieuwma C W T, van Gennip W J H, van Duren J K J, Jonkheijm P, Janssen R A J and Niemantsverdriet J W Characterization of polymer solar cells by TOF-SIMS depth profiling *Appl Surf Sci* 2003;203-204(15 Jan) 547-50.
- [243] Huang J, Miller P F, Wilson J S, Mello A J D, Mello J C D and Bradley D D C Investigation of the Effects of Doping and Post-Deposition Treatments on the Conductivity, Morphology, and Work Function of Poly(3,4-ethylenedioxythiophene)/Poly(styrene sulfonate) Films *Adv Funct Mater* 2005;15(2) 290-6.
- [244] Norrman K, Madsen M V, Gevorgyan S A and Krebs F C Degradation Patterns in Water and Oxygen of an Inverted Polymer Solar Cell *J Am Chem Soc* 2010;132(47) 16883-92.
- [245] Moujoud A, Oh S H, Hye J J, Jae H and Kim H J C61-butyric acid methyl ester bulk heterojunction solar cell by using UV light irradiation *Solar Energy Materials and Solar Cells* 2011;95(4) 1037-41.
- [246] Arora S, Rajouria S K, Kumar P and Bhatnagar P K Role of donor – acceptor domain formation and interface states in initial degradation of P3HT: PCBM-based solar cells *Phys. Scr.* 2011;83(3) 035804.
- [247] Norrman K, Larsen N B and Krebs F C Lifetimes of organic photovoltaics: Combining chemical and physical characterisation techniques to study degradation mechanisms *Sol Energ Mat Sol C* 2006;90(17) 2793-814.
- [248] Archambeau S, Seguy I, Jolinet P, Farenc J, Destruel P, Nguyen T P, Bock H and Grellet E Stabilization of discotic liquid organic thin films by ITO surface treatment *Appl Surf Sci* 2006;253(4) 2078-86.
- [249] Chen C Y, Wu K Y, Chao Y C, Zan H W, Meng H F and Tao Y T Concomitant tuning of metal work function and wetting property with mixed self-assembled monolayers *Org Electron* 2011;12(1) 148-53.
- [250] Cui J, Huang Q, Wang Q and Marks T J Enhancing Anode / Hole-Transport Layer Interfacial Light-Emitting Diodes *Langmuir* 2001;17(7) 2051-4.

- [251] Kacker N, Kumar S K and Allara D L Wetting-induced reconstruction in molecular surfaces *Langmuir* 1997;13(24) 6366-9.
- [252] Hayakawa R, Turak A, Zhang X, Hiroshiba N, Dosch H, Chikyow T and Wakayama Y Strain-effect for controlled growth mode and well-ordered structure of quaterrylene thin films *J Chem Phys* 2010;133(3) 034706.
- [253] Han E-m, Do L-m, Fujihira M, Inada H and Shirota Y Scanning force microscopy of organic thin-film amorphous hole transport materials *J Appl Phys* 1996;80(6) 3297-9.
- [254] Ke L, Senthil R, Zhang K, Jin S and Wee A T S Organic light emitting devices performance improvement by inserting thin parylene layer *Synthetic Met* 2004;140(2-3) 295-9.
- [255] Hains A W, Chen H-y, Reilly T H and Gregg B A Cross-Linked Perylene Diimide-Based n-Type Interfacial Layer for Inverted Organic Photovoltaic Devices *ACS Appl Mater Inter* 2011;3(11) 4381-7.
- [256] Madsen M V, Krebs F C, Madsen M V, Norrman K and Krebs F C Oxygen- and water-induced degradation of an inverted polymer solar cell: the barrier effect *Journal of Photonics for Energy* 2011;1(1) 011104.
- [257] Vestweber H and Riels W Highly efficient and stable organic light-emitting *Synthetic Met* 1997;91(97) 181-5.
- [258] Han E M, Do L M, Yamamoto N and Fujihira M Crystallization of organic thin films for electroluminescent devices *Thin Solid Films* 1996;273(1-2) 202-8.
- [259] Camaioni N, Ridolfi G, Casalbore-Miceli G, Possamai G, Garlaschelli L and Maggini M A stabilization effect of [60]fullerene in donor-acceptor organic solar cells *Sol Energ Mat Sol C* 2003;76(1) 107-13.
- [260] Neugebauer H, Brabec C, Hummelen J C and Sariciftci N S Stability and photodegradation mechanisms of conjugated polymer/fullerene plastic solar cells *Sol Energ Mat Sol C* 2000;61(1) 35-42.
- [261] Lee J U, Jung J W, Emrick T, Russell T P and Jo W H Synthesis of C(60)-end capped P3HT and its application for high performance of P3HT/PCBM bulk heterojunction solar cells *J Mater Chem* 2010;20(16) 3287-94.
- [262] Lee J U, Jung J W, Emrick T, Russell T P and Jo W H Morphology control of a polythiophene-fullerene bulk heterojunction for enhancement of the high-temperature stability of solar cell performance by a new donor-acceptor diblock copolymer *Nanotechnology* 2010;21(10) 105201.
- [263] Santerre F, Bedja I, Dodelet J P, Sun Y, Lu J, Hay A S and D'Iorio M Hole transport molecules in high T-g polymers: Their effect on the performance of organic light-emitting diodes *Chem Mater* 2001;13(5) 1739-45.
- [264] Shi J M and Tang C W Doped organic electroluminescent devices with improved stability *Appl Phys Lett* 1997;70(13) 1665-7.

- [265] Jarikov V V Improving operating lifetime of organic light-emitting diodes with polycyclic aromatic hydrocarbons as aggregating light-emitting-layer additives *J Appl Phys* 2006;100(1) 014901.
- [266] Jarikov V V, Young R H, Vargas J R, Brown C T, Klubek K P and Liao L-s Operating longevity of organic light-emitting diodes with perylene derivatives as aggregating light-emitting-layer additives: Expansion of the emission zone *J Appl Phys* 2006;100(9) 094907.
- [267] Fong H H, Choy W C H, Hui K N and Liang Y J Organic light-emitting diodes based on a cohost electron transporting composite *Appl Phys Lett* 2006;88(11) 113510.
- [268] Meerheim R, Walzer K, Pfeiffer M and Leo K Ultrastable and efficient red organic light emitting diodes with doped transport layers *Appl Phys Lett* 2006;89(6) 061111.
- [269] Yuan Y, Grozea D and Lu Z H Fullerene-doped hole transport molecular films for organic light-emitting diodes *Appl Phys Lett* 2005;86(14) 143509.
- [270] Yuan Y Y, Han S, Grozea D and Lu Z H Fullerene-organic nanocomposite: A flexible material platform for organic light-emitting diodes *Appl Phys Lett* 2006;88(9) 093503.
- [271] Holmes M A, Mackay M E and Giunta R K Nanoparticles for dewetting suppression of thin polymer films used in chemical sensors *Journal of Nanoparticle Research* 2007;9(5) 753-63.
- [272] Ling G P and He J H The influence of nano-Al₂O₃ additive on the adhesion between enamel and steel substrate *Mat Sci Eng a-Struct* 2004;379(1-2) 432-6.
- [273] Hsu S H, Chou C W and Tseng S M Enhanced thermal and mechanical properties in polyurethane/Au nanocomposites *Macromol Mater Eng* 2004;289(12) 1096-101.
- [274] Sharma S, Rafailovich M H, Peiffer D and Sokolov J Control of Dewetting Dynamics by Adding Nanoparticle Fillers *Nano letters* 2001;1(10) 511-4.
- [275] Luo H and Gersappe D Dewetting Dynamics of Nanofilled Polymer Thin Films *Macromolecules* 2004;37(15) 5792-9.
- [276] Hains A W, Liu J, Martinson A B F, Irwin M D and Marks T J Anode Interfacial Tuning via Electron-Blocking / Hole- Transport Layers and Indium Tin Oxide Surface Treatment in Bulk-Heterojunction Organic Photovoltaic Cells *Adv Funct Mater* 2010;20(4) 595-606.
- [277] Hains A W and Marks T J High-efficiency hole extraction / electron-blocking layer to replace heterojunction polymer solar cells *Appl Phys Lett* 2008;92(2) 023504.
- [278] Hains A W, Ramanan C, Irwin M D, Liu J, Wasielewski M R and Marks T J Designed Bithiophene-Based Interfacial Layer for High-Efficiency Bulk-Heterojunction Organic Photovoltaic Cells. Importance of Interfacial Energy Level Matching *ACS Appl Mater Inter* 2010;2(1) 175-85.

- [279] Cahen D and Hodes G Molecules and electronic materials *Adv Mater* 2002;14(11) 789-98.
- [280] Bellmann E, Jabbour G E and Grubbs R H Hole Transport Polymers with Improved Interfacial Contact to the Anode Material *Chem Mater* 2000;12(8) 1349-53.
- [281] Mori T, Miyake S and Mizutani T Effects of Plasma Modification on Hole Transport Layer in Organic Electroluminescent Diode *Jpn J Appl Phys* 2 1995;34(7A) L845-L8.
- [282] Han E M, Yun J J, Oh G C, Park S M, Park N K, Yoon Y S and Fujihira M Enhanced stability of organic thin films for electroluminescence by photoirradiation *Optical Materials* 2002;21(1-3) 243-8.
- [283] Sun Y, Chien S-c, Yip H-l, Zhang Y, Chen K-s, Zeigler D F, Chen F-c, Lin B and Jen A K Chemically Doped and Cross-linked Hole-Transporting Materials as an Efficient Anode Buffer Layer for Polymer Solar Cells *Chem Mater* 2011;23(22) 5006-15.
- [284] Chan M Y, Lai S L, Wong F L, Lengyel O, Lee C S and Lee S T Efficiency enhancement and retarded dark-spots growth of organic light-emitting devices by high-temperature processing *Chem Phys Lett* 2003;371(5-6) 700-6.
- [285] Chin B D, Duan L, Kim M-h, Lee S T and Chung H K Effects of cathode thickness and thermal treatment on the design of balanced blue light-emitting polymer device *Appl Phys Lett* 2004;85(19) 4496-8.
- [286] Fenwick O, Oliver K and Cacialli F Cross-linking of a poly(3,4-ethylene dioxythiophene):(polystyrene sulfonic acid) hole injection layer with a bis-azide salt and the effect of atmospheric processing conditions on device properties *Appl Phys Lett* 2012;100(5) 053309.
- [287] Ryu S Y, Kim J T, Noh J H, Hwang B H, Kim C S, Jo S J, Hwang H S, Kang S J, Baik H K, Lee C H, Song S Y and Lee S J Polymeric tandem organic light-emitting diodes using a self-organized interfacial layer *Appl Phys Lett* 2008;92(10) 103301.
- [288] Wang J Z, Zheng Z H, Li H W, Huck W T S and Siringhaus H Polymer field effect transistors fabricated by dewetting *Synthetic Met* 2004;146(3) 287-90.
- [289] Benor A, Hoppe A, Wagner V and Knipp D Microcontact printing and selective surface dewetting for large area electronic applications *Thin Solid Films* 2007;515(19) 7679-82.
- [290] Harirchian-Saei S, Wang M C P, Gates B D and Moffitt M G Directed Polystyrene/Poly(methyl methacrylate) Phase Separation and Nanoparticle Ordering on Transparent Chemically Patterned Substrates *Langmuir* 2012;28(29) 10838-48.

Organo-Soluble Semi-Alicyclic Polyimides Derived from Substituted-Tetralin Dianhydrides and Aromatic Diamines: Synthesis, Characterization and Potential Applications as Alignment Layer for TFT-LCDs

Jin-gang Liu, Yuan-zheng Guo, Hai-xia Yang and Shi-yong Yang

Additional information is available at the end of the chapter

<http://dx.doi.org/10.5772/51182>

1. Introduction

In advanced thin film transistor liquid crystal display devices (TFT-LCDs), alignment layers (ALs) are playing an ever-increasing important role for achieving a high-quality optoelectronic display [1]. The main function of AL materials is to align the rod-like liquid crystal (LC) molecules at a constant angle (so-called pretilt angle) to the local surface. Thus, when the electrical field is applied, the LC molecules can respond rapidly so as to result in a display effect. The characteristics of AL materials, including their abilities to achieve a proper pretilt angle for LC molecules, to achieve a high voltage holding ratio (VHR) and a low residual direct circuit voltage (RDC) value for the LCD devices, high thermal stability, high mechanical strength to resist rubbing process and their planarization ability are often taken into deliberate consideration in developing new generations of TFT-LCDs [2].

Currently, polyimides (PIs) are one of the most important AL materials for TFT-LCDs due to their intrinsic high thermal resistance, good mechanical properties and unique LC alignment ability [3]. However, conventional wholly aromatic PIs suffer from their poor solubility in common solvents. Thus, in practice, they can only be used in the form of soluble precursors, poly(amic acid)s (PAAs). For example, in conventional twisted nematic LCD (TN-LCD) and super-twisted nematic LCD (STN-LCD) fabrications, wholly aromatic PAA solution is first spin-coated onto an indium tin oxide (ITO) substrate, and then the solution is imidized at elevated temperatures up to 300 °C to form the imidized PI alignment layer. However, the

high curing temperature of PAAs often causes serious damage for the temperature-sensitive components in TFT-LCDs, such as the color filters which would be destroyed when the temperatures are higher than 230 °C [4]. Hence, PI alignment layers with low curing temperatures (<220 °C) have been developed in the past decades [5-7].

Besides the curing temperature consideration, the high VHR and low RDC values of the devices are also highly desired for advanced TFT-LCD fabrication in order to achieve a high-resolution display (high contrast, low image sticking, etc) [8]. VHR and RDC values of the TFT-LCD devices are influenced by many factors, including the characteristics of LC materials, the features of the PI alignment layers and the display modes of the devices. Among the factors, the effects of the chemical structures of the PI alignment layers are often critical. For instance, it has been well established that the highly conjugated molecular skeletons in wholly-aromatic PIs often lead to low VHR and high RDC values for the devices [9]. Thus, PI alignment layers with low conjugated structures have been paid increasing attentions.

Considering the above-mentioned structure-property relationship for PI alignment layers used for advanced TFT-LCDs, alicyclic or semi-alicyclic PIs have been confirmed to be the best candidates as AL materials up to now. Especially, semi-alicyclic PIs derived from alicyclic dianhydrides and aromatic diamines possess the best combined properties, including good thermal stability, good solubility in organic solvents, acceptable mechanical properties, good optical transparency, high VHR and low RDC values. Thus, semi-alicyclic PIs have been widely investigated as AL materials for advanced TFT-LCDs [10-12]. Figure 1 illustrates the developing trajectory of PI alignment layers with different kinds of display modes.

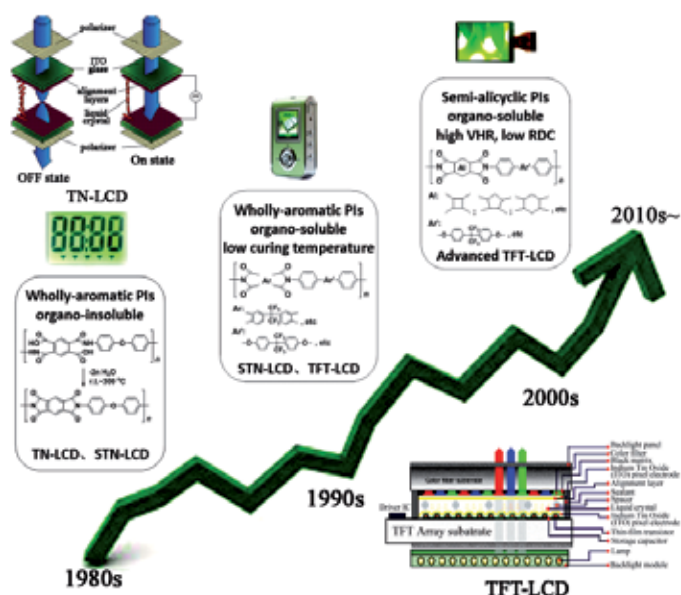


Figure 1. Developing trends of PI alignment layers for LCDs.

In this chapter, a series of novel semi-alicyclic PI alignment layers were designed and synthesized. The designed novel PI materials are expected to show good solubility in organic solvents (thus low curing temperatures) and exhibit high VHR and low RDC values for TFT-LCDs. For this purpose, a class of substituted-tetralin alicyclic dianhydrides was synthesized first via a low-cost route using maleic anhydride and substituted styrene compounds as the starting materials (Scheme 1). Then, a series of semi-alicyclic PIs were synthesized from the newly-developed dianhydrides and commercially available aromatic diamines. The effects of the structures of the semi-alicyclic PIs on their thermal stability and optical properties were investigated. At last, a series of test LCD cells with fringe field switching (FFS) mode were fabricated using the novel PIs as the alignment layers. The electrical characteristics (pretilt angle, VHR and RDC) of the cells were preliminarily studied.

2. Experiments

2.1. Materials

Styrene, *p*-methylstyrene, *p*-*tert*-butylstyrene and *p*-fluorostyrene were purchased from Tokyo Chemical Industry Co., Ltd., Japan (TCI) and used as received. It is unnecessary to remove the inhibitors in the chemicals. Maleic anhydride was obtained from Beijing Yili Fine Chemicals, China and used as received. 4,4'-Methylenedianiline (MDA, TCI, Japan) was recrystallized from ethanol and dried in vacuum at 80 °C overnight prior to use. 2,4-Diamino-(*n*-hexadecanoxy)benzene (16PDA) was synthesized in our laboratory and purified by continuous recrystallization from ethanol. Commercially available *N*-methyl-2-pyrrolidone (NMP), *N,N*-dimethylacetamide (DMAc), cyclopentanone (CPA), γ -butyrolactone (GBL) and ethylene glycol monobutyl ether (butyl cellosolve, BC) were purified by distillation prior to use. The other commercially available reagents were used without further purification.

2.2. Measurements

Inherent viscosity was measured using an Ubbelohde viscometer with a 0.5 g/dL NMP solution at 25 °C. Absolute viscosity was measured using a Brookfield DV-II+ Pro viscometer at 25 °C. Fourier transform infrared (FT IR) spectra were obtained with a Tensor 27 Fourier transform spectrometer. Ultraviolet-visible (UV-vis) spectra were recorded on a Hitachi U-3210 spectrophotometer at room temperature. The cutoff wavelength was defined as the point where the transmittance drops below 1% in the spectrum. Prior to test, PI samples were dried at 100 °C for 1 h to remove the absorbed moisture. Yellow index (YI) and haze values of the PI films were measured using an X-rite color i7 spectrophotometer with PI film samples at a thickness of 30-40 μm in accordance with the procedure described in ASTM D1925 "Test method for yellowness index of plastics" and in ASTM D1003 "Standard test method for haze and luminous transmittance of transparent plastics", respectively. The color parameters were calculated according to a CIE Lab equation. L^* is the lightness, where 100 means white and 0 implies black. A positive a^* means a red color, and a negative one indicates a green color. A positive b^* means a yellow color, and a negative one indicates a blue

color. Nuclear magnetic resonances (^1H NMR and ^{13}C NMR) were performed on a AV 400 spectrometer operating at 400 MHz in $\text{DMSO-}d_6$ or CDCl_3 . Differential scanning calorimetry (DSC) and thermogravimetric analysis (TGA) were recorded on a TA-Q series thermal analysis system at a heating rate of $10\text{ }^\circ\text{C}/\text{min}$ and $20\text{ }^\circ\text{C}/\text{min}$ in nitrogen or air, respectively. Gel permeation chromatography (GPC) measurements were performed using a Waters 1515 HPLC pump equipped with a Waters 2414 refractive index detector. Two Waters Styragel HR 4 columns kept at $35^\circ\text{C}\pm 0.1^\circ\text{C}$ were used with HPLC grade NMP as the mobile phase at a flow rate of $1.0\text{ mL}/\text{min}$. Number average weight (M_n), weight average molecular weight (M_w) and polydispersity (M_w/M_n) were then determined with polystyrene as a standard.

Solubility was determined as follows: 1.5 g of the PI resin was mixed with 8.5 g of the tested solvent at room temperature (15 wt% solid content), which was then mechanically stirred in nitrogen for 24 h. The solubility was determined visually as three grades: completely soluble (++), partially soluble (+), and insoluble (-). The complete solubility is defined as a homogeneous and clean solution is obtained, in which no phase separation, precipitation or gel formation is detected.

The electrical characteristics, including VHR, RDC and pretilt angle values of the LC test cells were measured on a Toyo Model 6254 measurement system. VHR measurements were performed at LC test cells with a gap of 5-6 μm . The peak value of the square wave voltage and pulse duration was +5V and 60 μs , respectively. RDC measurements were performed using the "flick free" method. The test cells were first addressed with +5V direct circuit (DC) offset voltage for 3600 s. After the time, the +5V DC offset was switched off. The resulting flicker was monitored and the DC offset voltage was increased until the flickering was no longer visible. The compensating voltage was the residual DC voltage (RDC). Pretilt angles measurements were performed using the crystal rotation method with LC cells with a gap of 50 μm fabricated by anti-parallel rubbing process. The values of all measurements of VHR, RDC and pretilt angles are averages of at least 10 independent LC cells.

2.3. Monomer synthesis

3,4-Dicarboxy-1,2,3,4-tetrahydro-6-methyl-1-naphthalene succinic dianhydride (MTDA). Into a 500-mL three-necked flask equipped with a mechanical stirrer, a gas inlet and a condenser, 43.75 g (0.446 mol) of maleic anhydride, 80.60 g (0.682 mol) of *p*-methylstyrene, and 0.1138 g (0.5 mmol) of 2,5-di-*tert*-butyl hydroquinone were added. Nitrogen was introduced to remove the air in the system. Then, nitric oxide (NO) gas was introduced from a gas inlet placing under the surface of the reaction solution. The reaction mixture were heated to 120°C and maintained for 5 h under an atmosphere of nitric oxide. The produced red-brown nitrogen oxide gas was trapped by passing through an aqueous solution of 20 wt% sodium hydroxide. An orange precipitate formed during the reaction. After the reaction, the mixture was cooled to room temperature and 60 ml of acetonitrile was then added. The reaction mixture was heated to reflux for another 0.5 h. Then, 60 ml of toluene was added and the reaction mixture was cooled to temperature. The produced white needle crystals were collected by filtration and the solid was washed with toluene and petroleum ether in succession. After

being dried in vacuum at 80 °C for 24h, the pure MTDA was obtained as white crystals. Yield: 51.44 g (73.4%).

Melting point: 229 °C (DSC peak temperature). FT IR (KBr, cm^{-1}): 2941, 1855, 1778, 1506, 1412, 1223, 1076, and 916. ^1H NMR (DMSO- d_6 , ppm): 7.35 (s, 1H), 7.15-7.13 (m, 1H), 7.10-7.09 (m, 1H), 4.56-4.54 (d, 1H), 4.12-4.10 (m, 1H), 3.83-3.81 (m, 1H), 3.18-3.13 (m, 1H), 3.09 (m, 1H), 2.82-2.78 (m, 1H), 2.32 (s, 3H), 1.97-1.95 (m, 1H), and 1.86-1.85 (m, 1H). ^{13}C NMR (DMSO- d_6 , ppm): 175.8, 175.3, 173.8, 172.4, 138.1, 135.0, 131.8, 130.5, 129.9, 127.7, 45.1, 44.2, 36.4, 32.3, 26.4, and 22.0. MS (EI, m/e, percentage of relative intensity): 142 (M^+ -172, 100). Elemental analysis: calculated for $\text{C}_{17}\text{H}_{14}\text{O}_6$: C, 64.97%, H, 4.49%; Found: C, 64.32%, H, 4.44%.

3,4-Dicarboxy-1,2,3,4-tetrahydro-1-naphthalene succinic dianhydride (TDA). The dianhydride was synthesized from styrene and maleic anhydride through a similar route to MTDA. The product was obtained as white crystals. Yield: 50.35 g (75.2%).

Melting point: 199 °C (DSC peak temperature). FT IR (KBr, cm^{-1}): 2966, 1861, 1780, 1493, 1405, 1229, 1058, and 928. ^1H NMR (DMSO- d_6 , ppm): 7.69-7.67 (d, 1H), 7.38-7.27 (m, 2H), 7.20-7.19 (d, 1H), 4.67-4.64 (d, 1H), 3.73-3.58 (m, 2H), 3.40-3.33 (m, 1H), 2.85-2.80 (m, 2H), and 2.12-2.07 (m, 2H). ^{13}C NMR (DMSO- d_6 , ppm): 173.8, 173.5, 172.1, 170.8, 136.4, 129.5, 128.4, 128.1, 127.5, 127.4, 42.8, 42.1, 37.3, 36.7, 32.8, and 26.2. MS (EI): 128 (M^+ -172, 100). Elemental analysis: calculated for $\text{C}_{16}\text{H}_{12}\text{O}_6$: C, 64.00%, H, 4.03%; Found: C, 64.10%, H, 4.03%.

3,4-Dicarboxy-1,2,3,4-tetrahydro-6-tert-butyl-1-naphthalene succinic dianhydride (TTDA). The dianhydride was synthesized from *p*-*tert*-butylstyrene and maleic anhydride through a similar route to MTDA. The product was obtained as white crystals. Yield: 58.49 g (73.6%).

Melting point: 218 °C (DSC peak temperature). FT IR (KBr, cm^{-1}): 2962, 1859, 1789, 1504, 1410, 1222, 1055, and 925. ^1H NMR (DMSO- d_6 , ppm): 7.70 (s, 1H), 7.34-7.32 (d, 2H), 7.13-7.11 (d, 1H), 4.65-4.62 (d, 1H), 3.74-3.67 (m, 1H), 3.62-3.58 (m, 1H), 3.31-3.30 (m, 1H), 2.93-2.76 (m, 2H), 2.44-2.39 (m, 1H), 2.13-2.07 (m, 1H) and 1.29 (s, 9H). ^{13}C NMR (DMSO- d_6 , ppm): 174.4, 174.0, 172.7, 171.3, 150.2, 134.0, 128.4, 128.1, 126.6, 125.0, 43.3, 42.8, 38.0, 36.8, 34.7, 33.3, 31.5, and 26.8. MS (EI): 239 (M^+ -118, 100). Elemental analysis: calculated for $\text{C}_{20}\text{H}_{20}\text{O}_6$: C, 67.41%, H, 5.66%; Found: C, 67.23%, H, 5.70%.

3,4-Dicarboxy-1,2,3,4-tetrahydro-6-fluoro-1-naphthalene succinic dianhydride (FTDA). The dianhydride was synthesized from *p*-fluorostyrene and maleic anhydride through a similar route to MTDA. The product was obtained as white crystals. Yield: 55.60 g (77.3%).

Melting point: 201 °C (DSC peak temperature). FT IR (KBr, cm^{-1}): 2912, 1864, 1782, 1664, 1441, 1376, 1304, 1262, 1211, 1151, 1080, 1027, 967, 914, 870, 819, 754, 633, 594, 558 and 498. ^1H NMR (DMSO- d_6 , ppm): 7.51-7.49 (d, 1H), 7.29-7.27 (m, 2H), 7.17-7.14 (m, 1H), 4.69-4.68 (d, 1H), 3.75-3.71 (m, 1H), 3.60-3.57 (m, 1H), 3.44-3.43 (m, 1H), 2.85-2.83 (m, 2H), 2.57-2.53 (m, 1H) and 2.10-2.06 (m, 1H). ^{13}C NMR (DMSO- d_6 , ppm): 173.9, 172.3, 171.2, 162.3, 160.7, 133.1, 131.3, 130.6, 116.2, 114.9, 43.3, 42.4, 37.3, 36.7, 33.2 and 26.5. MS (EI): 146 (M^+ -172, 100). Elemental analysis: calculated for $\text{C}_{16}\text{H}_{11}\text{FO}_6$: C, 60.38%, H, 3.48%; Found: C, 59.90%, H, 3.53%.

2.4. Polyimide synthesis

The general procedure for the synthesis of PIs can be illustrated by the preparation of PI-8 (Table 1). Into a 250 mL three-necked, round-bottomed flask equipped with a mechanical stirrer, a Dean-Stark trap and a nitrogen inlet, MDA (17.8434 g, 0.09 mol) and 16PDA (3.457 g, 0.01 mol) was dissolved in *m*-cresol (100 g) to give a clear diamine solution. Then, FTDA (31.825 g, 0.1 mol) was added in one batch and an additional volume of *m*-cresol (112 g) was added to wash the residual dianhydride, and at the same time to adjust the solid content of the reaction system to be 20 wt%. After stirring in nitrogen for 1 h, a mixture of toluene (230 ml) and isoquinoline (catalytic amount) was then added. The reaction mixture was heated to 180 °C and maintained for 6 h. During the reaction, the toluene-water azeotrope was distilled out of the system and collected in the Dean-Stark trap. After cooling to room temperature, the viscous solution was slowly poured into an excess of ethanol to yield a silky resin. The resin was collected and dried at 80 °C in vacuo for 24 h. Yield: 47.54 g (96%).

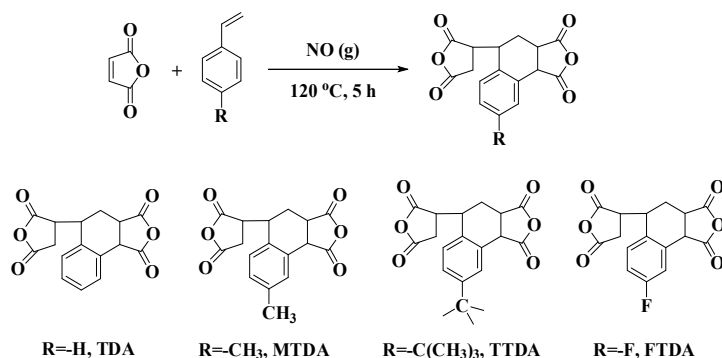
PI-8 resin (15 g) was dissolved in NMP (85 g) at room temperature to afford a 15 wt% solution. The solution was filtered through a 0.45 μm Teflon syringe filter to remove any undissolved impurities. Then, the solution was spin-coated on a clean silicon wafer or quartz substrate. The thickness of the PI film was controlled by regulating the spinning rate. PI-8 films with thicknesses ranged from 10–100 μm were obtained by thermally baking the solution in a flowing nitrogen according to the following heating procedure: 80 °C/2 h, 150 °C/1 h, 200 °C/1 h, and 220 °C/1 h. The other PI resin and films were prepared according to a similar procedure as mentioned above.

3. Results and discussion

3.1. Monomer synthesis

Scheme 1 illustrates the synthetic procedure for the substituted-tetralin alicyclic dianhydrides. Four dianhydrides, including TDA ($R=H$), MTDA ($R=CH_3$), TTDA ($R=C(CH_3)_3$) and FTDA ($R=F$) were synthesized by the Diels-Alder reactions of *R*-substituted-styrene compounds and maleic anhydride followed by the rearrangement reactions of the intermediates. The yields are all higher than 70%. The styrene compounds were used as both of the reactant and the solvent. In the literature, TDA has been synthesized from styrene and maleic anhydride with a molar ratio of 2.1:1 [13]. Toluene and a flowing air (15 liters per hour) were used as the solvent and catalyst, respectively. The obtained TDA dianhydride needed to be purified by recrystallization from a toluene/acetone mixture to remove the oxidized by-products. In our experiments, the reductive nitric oxide (NO) gas was used instead of the oxidative air. The obtained dianhydrides have good purity and can be used directly for polymerization. Also, they can be further purified by dissolution in a good solvent of acetonitrile and then precipitated slowly by adding a poor solvent of toluene although the yields might be slightly sacrificed. Due to the low cost of the starting materials and the high synthesizing yields for the new dianhydrides, this route is a promising procedure reducing the high cost of the present alicyclic PI alignment layers (usually hundreds of dollars per li-

ter). In addition, this reaction is easily to expand to a large scale. A scale of kilograms per batch has been successfully achieved in our lab.



Scheme 1 Synthesis of new alicyclic dianhydrides via a low-cost route

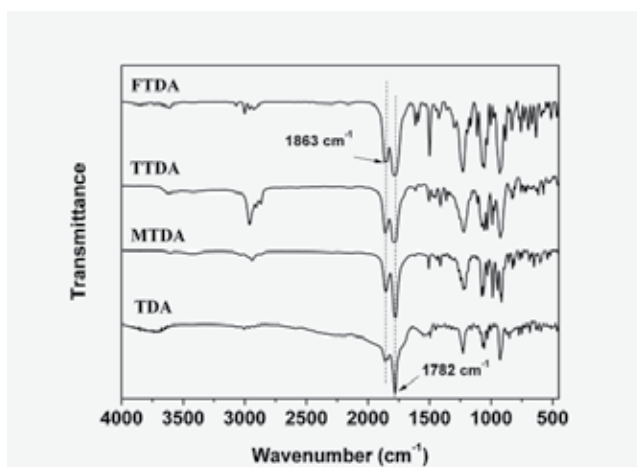
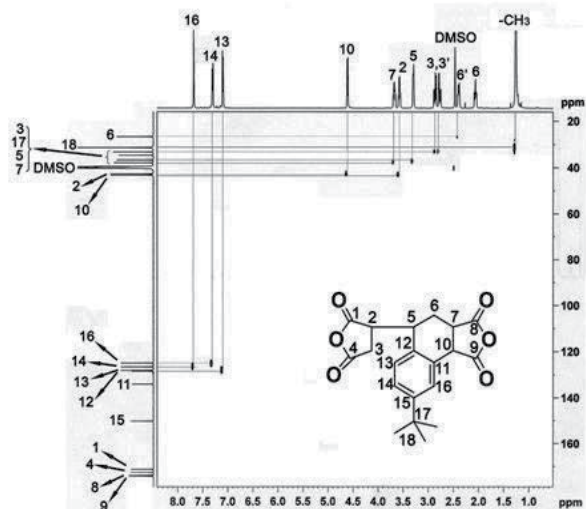


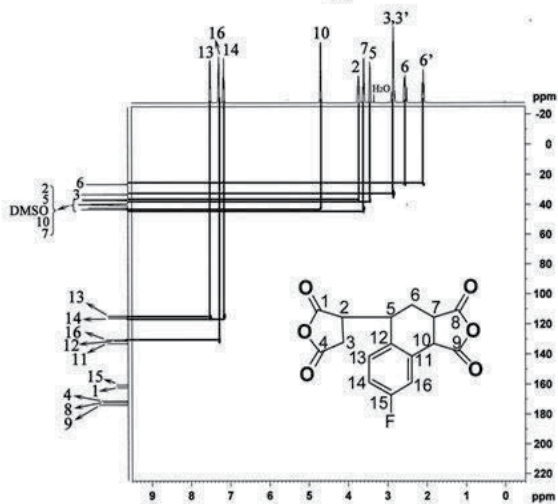
Figure 2. FT IR spectra of tetralin dianhydrides

Figure 2 shows the FT IR spectra of the dianhydrides, in which the characteristic bands of carbonyl groups in the anhydride moiety were clearly observed at around 1863 and 1782 cm^{-1} for all of the compounds. In addition, the characteristic absorption of methyl group appeared at 2941 cm^{-1} for MTDA and TTDA. The ^{13}C NMR and the two-dimensional ^1H - ^{13}C heteronuclear single-quantum coherence (HSQC) spectra of TTDA and FTDA are illustrated in Figure 3, together with the assignments of the observed resonances. As depicted in Figure 3, 18 carbon signals are clearly revealed for TTDA and 15 signals for FTDA. The absorptions of the protons cohered well with those of the corresponding carbon signals. This result is consistent with their proposed structures. Interestingly, the two pairs of protons in methylene groups ($\text{H}_{3,3'}$ and $\text{H}_{6,6'}$) for both of the dianhydrides exhibited individual absorptions in

their ^1H NMR spectra due to the slightly different chemical environments of the protons in the dianhydrides. The protons in the aromatic ring (H_{13} , H_{14} and H_{16}) appeared at the lowest field in the spectra. In addition, elemental analysis results also revealed the successful preparation of the target dianhydrides.



(a)

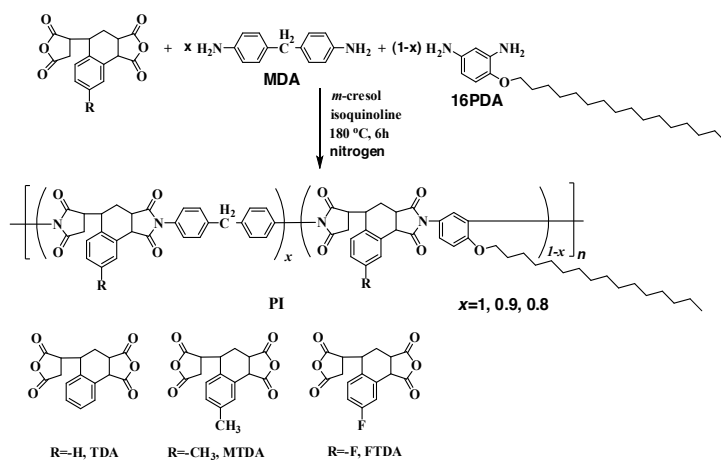


(b)

Figure 3. ^1H - ^{13}C HSQC spectra of dianhydrides (a) TTDA; (b) FTDA.

3.2. Polyimide synthesis

As shown in Scheme 2, three series, totally 9 species of PIs were designed and synthesized from TDA (PI-1~PI-3), MTDA (PI-4~PI-6), FTDA (PI-7~PI-9) and aromatic diamines (MDA and 16PDA) by a one-step, high temperature polycondensation procedure in *m*-cresol solution at a temperature of 180 °C. Introduction of C₁₆ long alkyl chain in the PI systems is mainly to induce the alignment of LC molecules [14-16]. The reaction proceeded smoothly during the polymerization, indicating good solubility of the reactants and the yielded PIs in the solvents.



Scheme 2. Synthesis of semi-alicyclic PIs

Table 1 presents the chemical formulations, inherent viscosities and molecular weights of the obtained PIs. The utilization of high temperature polycondensation procedure in the present work is mainly based on the fact that the two anhydride moiety in the substituted-tetralin dianhydrides might exhibit different reactivities due to the asymmetrical molecular structures of the monomers. High polymerization temperatures might eliminate the reactivity differentia of the anhydride units so as to obtain the PI resins with higher molecular weights. White or pale-yellow fibrous PI resins were obtained quantitatively, which had inherent viscosities of 0.81~1.03 dL/g for TDA-PIs (PI-1~3), 0.76~1.04 dL/g for MTDA-PIs (PI-4~6) and 0.69~0.97 dL/g for FTDA-PIs (PI-7~9), respectively (Table 1). These values indicate that the current PIs possess moderate to high molecular weights, which can be further confirmed by the GPC measurements. As tabulated in Table 1, the average numerical (M_n) and weight (M_w) molecular weights of the PI resins were higher than 17762 g/mol and 35356 g/mol, respectively. In addition, the PI resins exhibited a polydispersity index (M_w/M_n) lower than 2.43. This indicates that the substituted-tetralin alicyclic dianhydrides exhibited good reactivity in polymerization with aromatic diamines. Flexible and tough PI films were obtained by casting their solutions in NMP followed by baking at elevated temperatures from 80-220°C. All the films exhibited creasable nature and good tensile properties. For instance, PI-8 showed a tensile strength of 76 MPa, an elongation at break of 6.2%, and a ten-

sile modulus of 2.2 GPa. Figure 4 presents the free-standing (left) and creased appearance of PI-8 film at a thickness of 25 μm .

| PI | Dianhydride | Diamine (mol %) | | $[\eta]_{\text{inh}}^*$ (dL/g) | Molecular weight (g/mol) | | |
|------|-------------|-----------------|-------|-----------------------------------|--------------------------|--------|-----------|
| | | MDA | 16PDA | | M_n | M_w | M_w/M_n |
| PI-1 | TDA | 100 | 0 | 1.03 | 31,326 | 73,798 | 2.36 |
| PI-2 | | 90 | 10 | 0.90 | 22,319 | 53,387 | 2.39 |
| PI-3 | | 80 | 20 | 0.81 | 17,762 | 36,715 | 2.07 |
| PI-4 | MTDA | 100 | 0 | 1.04 | 30,321 | 68,823 | 2.27 |
| PI-5 | | 90 | 10 | 0.94 | 25,319 | 61,528 | 2.43 |
| PI-6 | | 80 | 20 | 0.76 | 18,463 | 35,729 | 1.94 |
| PI-7 | FTDA | 100 | 0 | 0.97 | 33,192 | 80,281 | 2.42 |
| PI-8 | | 90 | 10 | 0.88 | 27,834 | 57,339 | 2.06 |
| PI-9 | | 80 | 20 | 0.69 | 20,121 | 35,356 | 1.76 |

* $[\eta]_{\text{inh}}$: inherent viscosity measured with a PI resin at a concentration of 0.5 g/dL in NMP at 25 °C.

Table 1. Inherent viscosities and molecular weights of the PIs

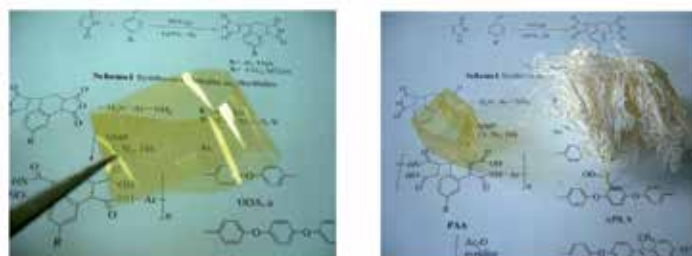


Figure 4. Appearance of PI-8 film (left) and resin (right)

Figure 5 illustrates the typical FT IR spectra of the PIs. It can be obviously observed that the characteristic absorptions of imide moiety at 1778 and 1711 cm^{-1} , due to the asymmetric and symmetric carbonyl stretching vibrations of the imide groups, and the absorptions at 1383 cm^{-1} assigned to the C-N stretching vibration of the imide structure are observed in all of the PIs. Typical ^1H NMR spectra of PI-7 and PI-8 are shown in Figure 6. For both of the PIs, the spectra are clearly divided into two parts. One part is the aliphatic, alicyclic and methylene protons in the upfield region; the other part is the aromatic protons in dianhydride moiety (H_9 , H_{10} and H_{11}) and diamine moiety (H_{12} and H_{13}) in the lowfield region. Similarly, the two pairs of protons in methylene groups ($\text{H}_{2,3}$ and $\text{H}_{5,6}$) exhibited individual absorptions in the spectra due to the different chemical environments of the protons in the polymers. For PI-8,

the absorptions of C₁₆ long alkyl chain protons are obviously observed at 0.83 ppm, 1.21 ppm, 1.89 ppm and 3.42 ppm, respectively, although some of the absorptions are overlapped by the absorptions of tetralin protons. In addition, the resonances observed at around 6.80 ppm (H₁₅, H₁₆ and H₁₇) assigned to the absorptions of aromatic ring protons in 16PDA moiety proved the successful preparation of the target polymer.

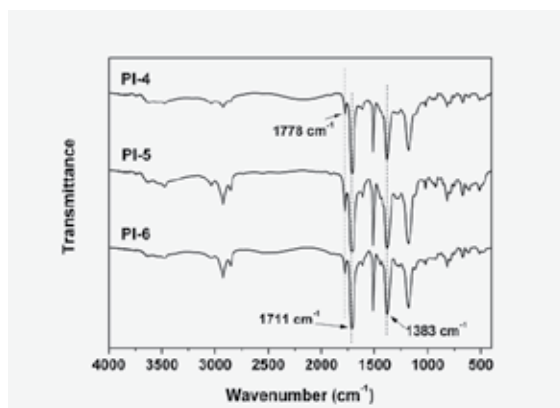


Figure 5. FT IR spectra of MTDA-PIs (PI-4–PI-6)

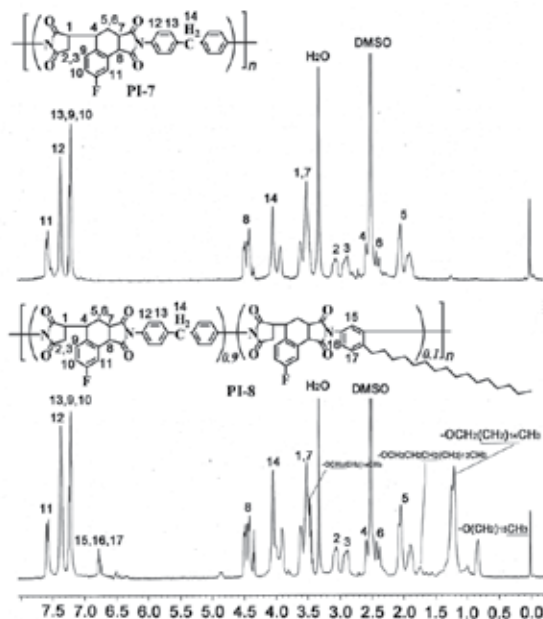


Figure 6. NMR spectra of PI-7 and PI-8

3.3. Solubility

The solubility of PIs is summarized in Table 2. All the PIs were easily soluble in polar aprotic solvents (NMP and DMAc), *m*-cresol, and γ -butyrolactone (GBL) at a concentration of 15 wt%. Among the PIs, those derived from MTDA (PI-4~PI-6) showed the best solubility due to the synergic effects of bulky tetralin moiety and pendant methyl substituent in the dihydride unit, and flexible alkyl side chains in the diamine unit. PI-5 and PI-6 were even wholly soluble in dichloromethane at room temperature. In the same condition, the PIs derived from TDA or FTDA were only partially or not soluble in dichloromethane. The enhancement of the solubility of MTDA-PIs can be attributed to the more loose packing of the molecular chains induced by the substituents mentioned above.

| PI | Solvent | | | | | | |
|------|---------|------|--------------|----|------------------|-----|---------------------------------|
| | NMP | DMAc | γ -BL | BC | <i>m</i> -cresol | THF | CH ₂ Cl ₂ |
| PI-1 | ++ | ++ | ++ | — | ++ | — | — |
| PI-2 | ++ | ++ | ++ | — | ++ | — | + |
| PI-3 | ++ | ++ | ++ | — | ++ | — | + |
| PI-4 | ++ | ++ | ++ | — | ++ | — | + |
| PI-5 | ++ | ++ | ++ | — | ++ | — | ++ |
| PI-6 | ++ | ++ | ++ | — | ++ | — | ++ |
| PI-7 | ++ | ++ | ++ | — | ++ | — | — |
| PI-8 | ++ | ++ | ++ | — | ++ | — | + |
| PI-9 | ++ | ++ | ++ | — | ++ | + | + |

* ++: Wholly soluble at room temperature; +: Partially soluble; —: Insoluble; NMP: *N*-methyl-2-pyrrolidinone; DMAc: *N,N*-dimethylacetamide; GBL: γ -butyrolactone; BC: ethylene glycol monobutyl ether.

Table 2. Solubility of the PIs*

The effects of solid contents (S_c) on the viscosities (η) of the PIs were further investigated. This investigation is very important for applications of the PIs as alignment layers for TFT-LCDs because a proper S_c - η relationship for PI would be beneficial for its orientation to LC molecules. Figure 7 illustrates the correlations between the absolute viscosities and solid contents of PI-2, PI-5 and PI-8 solution in NMP. Although these three PIs were all soluble in NMP, the η values of the solutions were quite different. For instance, at the same solid content of 35 wt%, PI-2 had a η value of 26750 mPa.s, which was much lower than those of PI-5 (64440 mPa.s) and PI-8 (116000 mPa.s). Thus, in practical application, PI-2 is more suitable to be utilized to develop a soluble PI solution with a high solid content and at the same time a relatively low viscosity. However, for the applications as alignment layers for TFT-LCDs, in which the solid content of the PIs are usually lower than 15 wt%, all of the PIs developed in

this work might be suitable because they all exhibit a relatively low absolute viscosities at a solid content of 15 wt% (PI-2: 150 mPa.s; PI-5: 200 mPa.s; PI-8: 160 mPa.s).

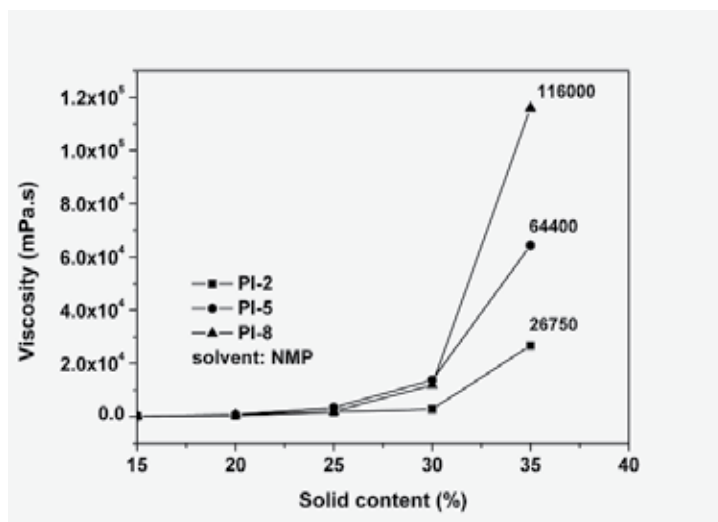


Figure 7. Viscosities as a function of solid contents for PI-2, PI-5 and PI-8 in NMP.

3.4. Thermal properties

The effects of asymmetrical *R*-substituted tetralin structure in the dianhydride units and the C_{16} long alkyl side chains in the diamine moieties on the thermal stabilities of the PIs were investigated by TGA and DSC measurements. Table 3 summarizes the thermal characterization of the polymers. Figure 8 depicts the thermogravimetry plots of PI films over a temperature range of 50 to 750 °C in nitrogen and PI-2 in nitrogen and in air. It can be seen from Figure 8a that the current PIs possess good thermal stability with no significant weight loss up to approximately 400 °C. After 400 °C, the PIs lose their original weight rapidly, leaving a residual weight ratio in the range 1.8–32.7% at 600 °C. The 10% weight loss temperatures ($T_{10\%}$) of the PIs are all higher than 410 °C in nitrogen. This implies that the incorporation of aliphatic or alicyclic moiety in the PIs did not apparently sacrifice their thermal stability. Among the series, FTDA-PIs (PI-7~PI-9) exhibited the best thermal stability, which might be due to the higher bond energy of C-F compared to those of C-H (TDA) and C-C (MTDA). As can be seen from Figure 8a that the PIs exhibited single-stage thermal decomposition behaviors in nitrogen. However, they showed a two-stage thermal decomposition in air, as can be depicted in Figure 8b. For example, PI-2 showed a first thermal decomposition at about 400 °C in air. When the temperature increased, a second thermal decomposition occurred at 580 °C. The first thermal decomposition might be due to the oxidative cleavage of the C_{16} long alkyl side chains at elevated temperature and the second one was attributed to the decomposition of the residual molecular skeleton of PI-2. Although the thermal stability of the cur-

rent PIs is lower than that of common aromatic PIs (usually with a $T_{10\%}$ values >500 °C), it is high enough for their applications in TFT-LCD fabrications.

| PI | T_g (°C) | $T_{5\%}$ (°C) | $T_{10\%}$ (°C) | R_{w600} (%) |
|------|------------|----------------|-----------------|----------------|
| PI-1 | 235 | 399 | 422 | 5.3 |
| PI-2 | 257 | 420 | 436 | 1.8 |
| PI-3 | 233 | 407 | 425 | 6.7 |
| PI-4 | 244 | 412 | 434 | 13.3 |
| PI-5 | 261 | 428 | 447 | 8.5 |
| PI-6 | 252 | 396 | 414 | 16.0 |
| PI-7 | 248 | 408 | 427 | 22.6 |
| PI-8 | 270 | 428 | 441 | 24.2 |
| PI-9 | 225 | 390 | 411 | 32.7 |

* T_g : glass transition temperature; $T_{5\%}$, $T_{10\%}$: temperatures at 5% and 10% weight loss, respectively; R_{w600} : residual weight ratio at 600 °C in nitrogen.

Table 3. Thermal properties of PI films

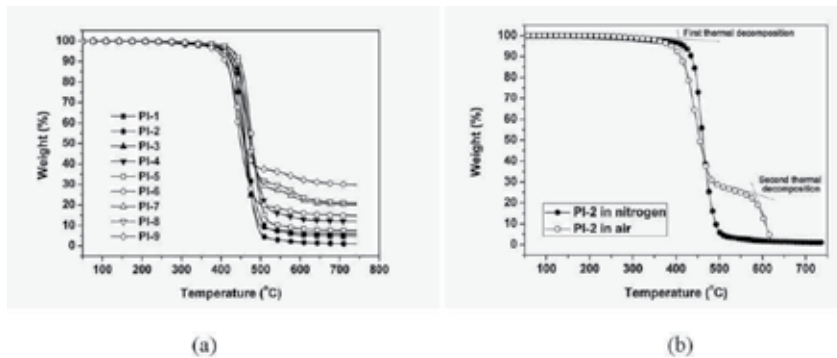


Figure 8. TGA curves of PI films. (a) PI films in nitrogen; (b) PI-2 in nitrogen and in air

Glass transition temperatures (T_g) values were obtained from the second heating scans of PI samples at a heating rate of 10 °C /min in nitrogen. The data were summarized in Table 3 and the typical DSC curves of FTDA-PIs are shown in Figure 9. All the PIs exhibit good thermal stabilities with the T_g values in the range of 233~270°C, depending on the rigidity of the polymers. It is observed that for the same dianhydride, PI containing 10% molar ratio of 16PDA exhibited the highest T_g values. For example, PI-2, PI-5 and PI-8 showed T_g values of 257 °C, 261 °C and 270 °C, respectively, which were all the highest one among their series. This indicates that introduction of 16PDA at a low proportion, such as 10%, can increase the

T_g s of the PIs due to the rigid nature of *meta*-phenylenediamine skeleton in the diamine; however, overloading of the diamine would conversely decrease the T_g s of the PIs due to the flexible long alkyl chains and ether linkage in the diamine.

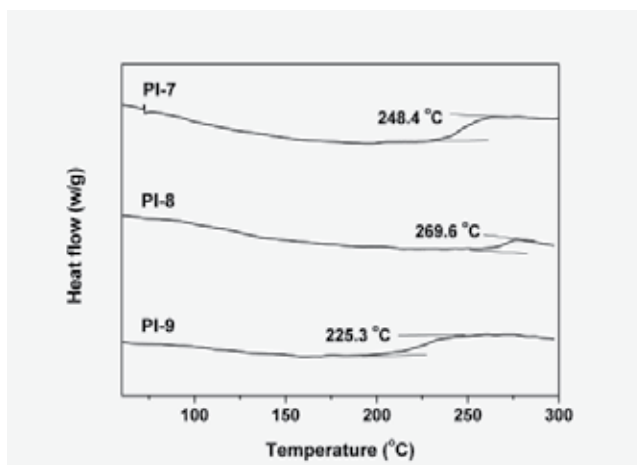


Figure 9. DSC curves of the FTDA-PI films (10 °C/min, in nitrogen)

| PI | λ (nm) | T_{450} (%) | a^* | b^* | L^* | Haze | YI |
|------|----------------|---------------|-------|-------|-------|------|-------|
| PI-1 | 319 | 66.7 | -2.80 | 17.46 | 92.06 | 2.50 | 29.32 |
| PI-2 | 302 | 82.7 | -1.74 | 7.84 | 94.31 | 5.85 | 13.39 |
| PI-3 | 331 | 52.3 | —** | — | — | — | — |
| PI-4 | 304 | 79.4 | -2.76 | 12.02 | 93.76 | 1.86 | 19.90 |
| PI-5 | 298 | 82.0 | -2.05 | 10.10 | 94.11 | 2.03 | 17.07 |
| PI-6 | 306 | 78.5 | -3.63 | 21.98 | 92.42 | 1.69 | 35.76 |
| PI-7 | 299 | 82.2 | — | — | — | — | — |
| PI-8 | 297 | 84.3 | -1.30 | 7.71 | 94.56 | 0.78 | 13.26 |
| PI-9 | 303 | 81.4 | — | — | — | — | — |

* λ : cutoff wavelength; T_{450} : transmittance at 450 nm; a^* , b^* , L^* : see 2.2 measurement; ** ND: not detected.

Table 4. Optical transparency and yellow indices of PI films*

3.5. Optical properties

It has been well established in the literature that the optical transparency of aromatic PI films can be efficiently improved by decreasing the formation of intra- and intermolecular charge transfer complexes (CTC) in the PI chains [17, 18]. When elaborately designed, color-

less PI films can even be obtained [19-21]. Among various methodologies decreasing the CTC formations, introduction of alicyclic moiety either in the dianhydride or in the diamine moiety has been proven to be one of the most effective procedures.

In the present work, the tetralin-containing PI films were obtained as pale-yellow free-standing films. The optical properties of the films are summarized in Table 4 and the UV-Vis spectra of the MTDA-PI films are illustrated in Figure 10. The PI films showed good optical transparency in the ultraviolet-visible light region with cutoff wavelengths lower than 300 nm. Some of the PI films, such as those derived from FTDA showed transmittances around 80% at 450 nm wavelength at a thickness of 10 μm . The good optical transparency of the PI films, on one hand, is attributed to the asymmetrical and bulky alicyclic tetralin structure in the dianhydride unit through steric hindrance. On the other hand, the high electronegativity of fluoro substituents in the dianhydride moiety is also beneficial for improving the optical transparency of the PI films by reducing the CTC formation.

The yellow index (YI) measurement results are shown in Table 4 and Figure 11. YI is usually adopted as a criterion evaluating the color of a polymer film. This value describes the color change of a film sample from clear or white toward yellow. Lower YI value usually indicates a weak coloration for a polymer film [22]. As shown in Table 5, PI-8 exhibited the lowest YI and Haze values compared with its analogs. This result correlated well with the results measured by UV-Vis measurements.

In summary, this low-color feature for the current PI films is desirable for their application as alignment layers for TFT-LCDs.

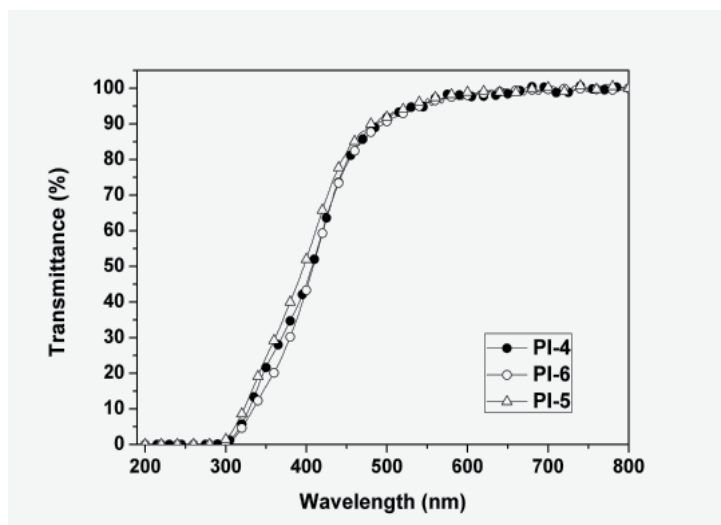


Figure 10. UV-Vis spectra of PI films derived from MTDA (PI-4~PI-6)

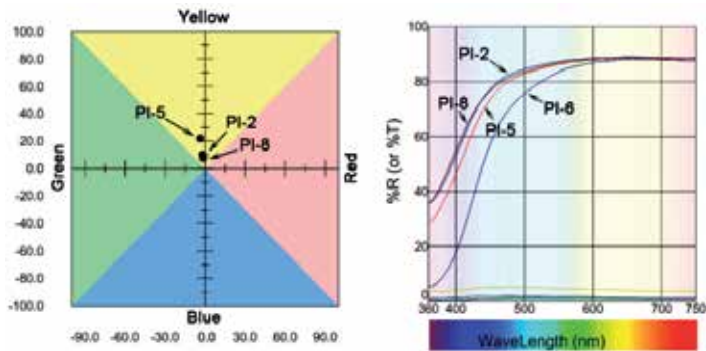


Figure 11. Yellow indices of PI films

3.6. Application in TFT-LCD fabrication

In order to investigate the practical application of the newly-developed alicyclic PIs as alignment layers for TFT-LCDs, a series of fringe field switching (FFS) mode [23, 24] liquid crystal cells (FFS-LCDs) were fabricated. PI-8 was chosen as the alignment layer due to its good combined properties. Figure 12 illustrates the LC cells fabrication procedure from monomer synthesis to devices.

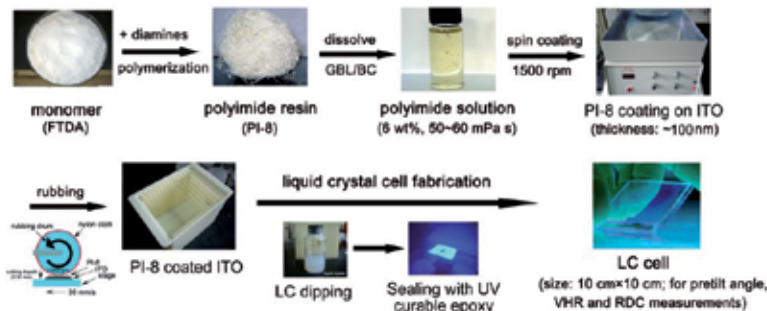


Figure 12. LC cells fabrication procedure from monomer synthesis to devices

First, PI-8 resin was dissolved in a mixture solvent of NMP/GBL/BC (55/30/15, volume ratio) at a solid content of 6.0 wt%. BC (butyl cellosolve) was used in the mixed solvents as a planarization agent so as to obtain a uniform PI coating. The obtained PI-8 solution was purified by filtering through a 0.25 μm Teflon filter and had a viscosity of 55 mPa s. The purified PI-8 solution was spin-coated on an ITO glass substrate (10 cm \times 10 cm) at a rotating speed of 3000 rpm. Then the ITO glasses with PI-8 coating were placed on a hot plate at 80 $^{\circ}\text{C}$ for 30 min, followed by curing in a nitrogen oven at 230 $^{\circ}\text{C}$ for 1h. The thicknesses of PI-8 film was measured with a profilometer (Dektak XT, Bruker) and found to be 553.7 \AA , as shown in Figure 13.

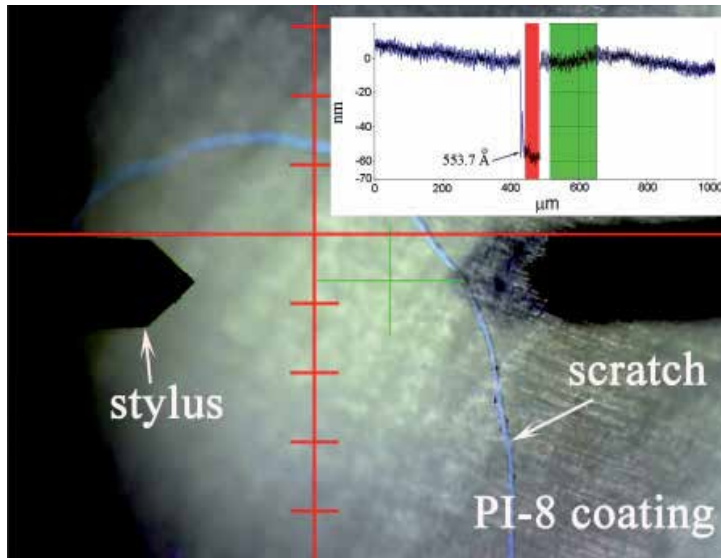


Figure 13. Thickness of PI-8 alignment layer

The cured PI-8 film was then rubbed with a nylon cloth-packed rubbing roller using the following parameters: radius of rubbing roller: 50 mm; rotation speed: 1000 rpm; pile impression: 0.32 mm and stage speed: 30 mm/s. Then, the FFS-LCD cells were assembled by two individual rubbed ITO glasses and the rubbing direction of the two glasses was anti-parallel to each other. For the pretilt angle measurements, the cell thickness was controlled to be about 50 μm by spraying spacers or glass fibers (50 μm) on PI-8 film surface; whereas for VHR and RDC measurements, the thickness was about 6 μm . The fabricated LC cells were sealed with a UV-curable epoxy sealant with two small filling holes left. LC molecules were then filled into the filling holes between the ITO plates via capillary action. The rod like LC molecules are thought to be oriented along the long alkyl chains pre-aligned by the rubbing treatments [25], as illustrated in Figure 14.

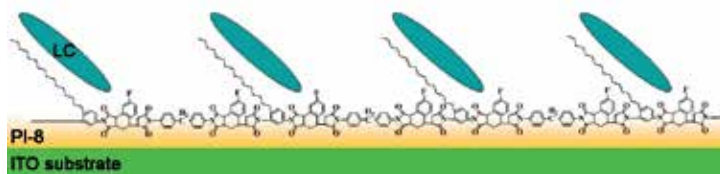


Figure 14. Schematic diagram of LC alignment on PI surfaces

Table 5 tabulates the electrical properties of the fabricated LC cells. The LC cells exhibited an average pretilt angle of 2.7° , which could meet the demands of the FFS-LCD applications. Meanwhile, a VHR of 98.2% and a RDC of 230 mV were also obtained. This result indicated that PI-8 alignment layer could endow the LC cells with a high VHR level; however, a few

charge accumulations occurred in the LC cells. The RDC value of 230 mV is a bit higher than the desired value (<100 mV) for FFS-LCD applications. It has been well established that a high residual DC voltage value might result in an image sticking for the LCD devices [26]. Thus, the formulation and structural characteristics of PI-8 should be modified to reduce the RDC values as low as possible. As we know, as compared to the pre-imidized PI alignment agents, their precursors, poly(amic acid)s usually exhibited much lower RDC levels [27]. Thus, it might be a compromised procedure to combine the imidized PI-8 and its PAA solution so as to achieve a balance of high VHR and low RDC levels for the TFT-LCDs. The detailed investigations are being performed in our laboratory.

| LC cells mode | Cell gap (μm) | Pretilt angle ($^{\circ}$)* | VHR (% , 30 $^{\circ}\text{C}$) | RDC (mV, 30 $^{\circ}\text{C}$) |
|---------------|----------------------------|-------------------------------|----------------------------------|----------------------------------|
| FFS | 5.6 | 2.7 | 98.2 | 230 |

* Measured with LC cells with 50 μm spacers.

Table 5. Electrical characterization of FFS-LCD cells

4. Conclusions

As one of our continuous endeavors developing low-cost and high performance PI alignment layers for TFT-LCDs, a systematic experiment was performed from monomer design and synthesis, PI preparation and characterization to final devices fabrication. First, several novel semi-alicyclic dianhydrides containing substituted-tetralin moiety were synthesized via a low-cost route with good yields. Then, a series of PIs were prepared from the dianhydrides and aromatic diamines. The asymmetrical alicyclic structures in the dianhydride units destroyed the regularity of the PI molecule chains; thus enhances their solubility in common solvents. Meanwhile, this irregular packing of the PI chains is beneficial for the penetration of UV and visible light. Thus, a good optical transparency is achieved in the present PIs. Incorporation of the bulky alicyclic tetralin moiety in the dianhydride units did not deteriorate their thermal stability. More importantly, the current PIs showed good orientating ability to LC molecules. The LC cells with PI-8 as the alignment layer exhibited good optoelectrical properties.

Thus, the present semi-alicyclic PIs are considered to be promising alignment layers for TFT-LCDs. Research on the applications of the PIs in large area TFT-LCD monitors are in progress now.

Acknowledgements

Financial support from the National Natural Science Foundation of China (51173188 and 50403025) is gratefully acknowledged.

Author details

Jin-gang Liu*, Yuan-zheng Guo, Hai-xia Yang and Shi-yong Yang

*Address all correspondence to: liujg@iccas.ac.cn

Laboratory of Advanced Polymer Materials, Institute of Chemistry, Chinese Academy of Sciences, Beijing 100190, People's Republic of China

References

- [1] Van Aerle, N.A.J.M., & Tol, A. J. W. (1994). Molecular orientation in rubbed polyimide alignment layers used for liquid-crystal displays. *Macromolecules*, 27(22), 6520-6526.
- [2] Nishikawa, M. (2000). Design of polyimides for liquid crystal alignment films. *Polym Adv Technol.*, 11, 404-412.
- [3] Seo, D.S., Araya, K., Yoshida, N., Nishikawa, M., Yabe, Y., & Kobayashi, S. Effect of the polymer tilt angle for generation of pretilt angle in nematic liquid crystal on rubbed polyimide surfaces. *Jpn. J. Appl. Phys.* (1995). LL506., 503.
- [4] Nishikawa, M., Yokoyama, Y., Bessho, N., Seo, D. S., & Iimura Kobayashi, S. (1994). Synthesis of a novel organic-solvent-soluble polyimide and its application to alignment film for liquid crystal displays. *Jpn. J. Appl. Phys.*, L810-L812.
- [5] Nishikawa, M., Suganuma, T., Tsuda, Y., Bessho, N., Iimura, Y., & Kobayashi, S. (1994). Properties of voltage holding ratios of liquid crystal cells using organic-solvent-soluble polyimide alignment films. *Jpn. J. Appl. Phys.*, L1113-L1116.
- [6] Nishikawa, M., Sano, K., Miyamoto, T., Yokoyama, Y., Bessho, N., Seo, D. S., Iimura, Y., & Kobayashi, S. (1994). Pretilt Angles of Liquid Crystal on Organic-Solvent-Soluble Polyimide Alignment Films. *Jpn. J. Appl. Phys.*, 33, 4152-4153.
- [7] Seo, D. S., Nishikawa, M., & Kobayashi, S. (1997). Generation of high pretilt angles of nematic liquid crystal (5CB) on rubbed organic solvent soluble polyimide surfaces with helical backbone structure and trifluoromethyl moieties. *Liquid Crystals*, 22, 515-517.
- [8] Zhang, B. L., Li, K. K., Chigrinov, V. G., Kwok, H. S., & Huang, H. C. (2005). Application of photoalignment technology to liquid-crystal-on-silicon microdisplays. *Jpn. J. Appl. Phys.*, 44, 3983-3991.
- [9] Lai, M. C., Chu, W. C., Chang, C. W., & Tsai, M. R. (2011). Liquid crystal alignment solution. 7914863, 2011-5-29.

- [10] Liu, J. G., He, M. H., Zhou, H. W., Qian, Z. G., Wang, F. S., & Yang, S. Y. (2002). Organosoluble and transparent polyimides derived from alicyclic dianhydride and aromatic diamines. *J Polym Sci, Part A: Polym Chem.*, 40, 110-119.
- [11] Zhang, W., Xu, H. J., Yin, J., Guo, X. X., Ye, Y. F., Fang, J. H., Sui, Y., Zhu, Z. K., & Wang, Z. G. (2001). Preparation and properties of organosoluble, colorless, and high-pretilt-angle polyimides based on an alicyclic dianhydride and long-main-chain alkyl-group-containing diamines. *J Appl Polym Sci.*, 81, 2814-2820.
- [12] Nishikawa, M. (2011). Development of novel polyimide alignment films for liquid crystal display televisions. *J. Photopolym Sci Technol.*, 24, 317-320.
- [13] Fairfield, G. M. S., & Norwalk, J. C. P. Preparation of dianhydrides from maleic anhydride and a vinyl benzene. 3769304, 1973.
- [14] Lee, Y. J., Kim, Y. W., Ha, J. D., Oh, J. M., & Yi, M. H. (2007). Synthesis and characterization of novel polyimides with 1-octadecyl side chains for liquid crystal alignment layers. *Polym Adv Technol.*, 18, 226-234.
- [15] Tsuda, Y. (2009). Soluble polyimides based on aromatic diamines bearing long-chain alkyl groups. Mittal K L. (ed.) *Polyimide and other high-temperature polymers: synthesis, characterization and applications*, Koninklijke Brill, Leiden, 5, 17-42.
- [16] Wang, D. H., Shen, Z. H., Guo, M. M., Cheng, S. Z. D., & Harris, F. W. (2007). Synthesis and properties of polyimides containing multiple alkyl side chains. *Macromolecules*.
- [17] Hasegawa, M., & Horie, K. (2001). Photophysics, photochemistry, and optical properties of polyimides. *Prog Polym Sci.*, 26, 259-335.
- [18] Ando, S., Matsuura, T., & Sasaki, S. (1997). Coloration of aromatic polyimides and electronic properties of their source materials. *Polym J.*, 29, 69-76.
- [19] Liaw, D. J., Wang, K. L., Huang, Y. C., Lee, K. R., Lai, J. Y., & Ha, C. S. (2012). Advanced polyimide materials: syntheses, physical properties and applications. *Prog Polym Sci.*, 37, 907-974.
- [20] Matsumoto, T., & Kurosaki, T. (1996). Soluble and colorless polyimides with polyalicyclic structures. *React Fun Polym.*, 30, 55-59.
- [21] Choi, I. H., & Chang, J. H. Colorless polyimide nanocomposite films containing hexafluoroisopropylidene group. *Polym Adv Technol.* (2011). , 22, 682-689.
- [22] Jang, W. B., Shin, D. Y., Choi, S. H., Park, S. G., & Han, H. S. (2007). Effects of internal linkage groups of fluorinated diamine on the optical and dielectric properties of polyimide thin films. *Polymer*, 48, 2130-2143.
- [23] Lee, S. H., Hong, A. H., Kim, J. M., & Lee, J. Y. (2001). An overview of product issues in wide-viewing TFT-LCDs. *J SID.*, 155-160.

- [24] Lyu, J. J., Sohn, J. W., Kim, H. Y., & Lee, S. H. (2007). Recent trends on patterned vertical alignment (PVA) and fringe-field switching (FFS) liquid crystal displays for liquid crystal television applications. *J Display Technol.*, 3, 404-412.
- [25] Huang, J. Y., Li, J. S., Juang, Y. S., & Chen, S. H. (1995). Rubbing-induced molecular alignment on an orienting layer of polyimide with and without alkyl side chains. *Jpn. J. Appl. Phys.*, 34, 3163-3169.
- [26] Masanobu, M., Tetsuya, M., & Tatsuo, U. (2011). Interaction between Impurity Ions and Alignment Polymer Layers Affecting the Image Sticking Effect on Liquid Crystal Displays. *Kobunshi Ronbunshu in Japanese*.
- [27] Seen, S. M., Kim, M. S., & Lee, S. H. (2010). Image sticking resistant liquid crystal display driven by fringe electric field for mobile applications. *Jpn J Appl Phys*.

Aromatic Derivatives Based Materials for Optoelectronic Applications

Florin Stanculescu and Anca Stanculescu

Additional information is available at the end of the chapter

<http://dx.doi.org/10.5772/51675>

1. Introduction

In the last decades a high interest has been paid to the field of organic materials for electronic and optoelectronic devices as potential candidates for replacing the more expensive, energy consumer and polluting technologies involved by inorganic semiconductor devices.

One of the most important advantages of the organic materials is the possibility to modify and optimize their molecular structure using the advantages of the design at the molecular level and the versatility of the synthetic chemistry with the purpose to tune their properties and make them adequate for a well defined optic, electronic or optoelectronic application.

Organic light emitting diodes (OLED) are interesting for applications in the full-colour flat panel displays and new generation of lighting source as an alternative to incandescent bulbs and compact fluorescent lamps. The OLEDs based technology has a large area of applications from small mobile phone displays to TV and monitors because they show two important advantages compared to the competitive liquid crystals based technology: high brightness and wide viewing angle.

Since the discovery of luminescence in anthracene [1], the crucial moment in the development of the OLEDs technology was the realisation of the first organic bilayer structure able to emit light at low applied voltages [2]. After that, different organic multilayer structures have been tested to improve carrier injection, carrier transport and radiative recombination with the purpose to increase the OLED efficiency and lifetime [3-5]. The performances of the devices can be enhanced either by the selection of an adequate architecture, such as multi-layer structure or by doping, by controlled impurification of the organics.

The research was focalised on different topics such as: effect of doping of the organic semiconductor to increase the “transparency” of the energetic barrier to the injection of electron from the contact [6], influence of the trapped and interfacial charges generated in multilayer organic heterostructures on the properties of the device [7], charge tunnelling in multilayer stack and at the interface between organic and anode [8], influence of the thickness and doping of the emission layer on the properties of OLEDs [9], injection of the charge carriers from the electrodes and their migration in correlation with different types of cathodes [10-13], transport phenomena in organics [14; 15], stacked geometry for efficient double-sided emitting OLED [16], graded mixed layer as active layer to replace heterojunction in OLEDs [17]. The awarding in 2000 of the Nobel prize for researches in the field of conducting polymers has stimulated the development of OLEDs based on polymeric materials, application emphasised years before [18], opening the way of reducing the applied voltages (< 10 V) and increasing the brightness and lifetime.

The development of the technologies in the field of the structures for optoelectronic applications based on organic compounds is dependent of the development of fundamental and applied knowledge of all the optical and electrical processes involved, because many particularities of the organic solid state are not yet well known and understand. This is a real challenge because the number of the organic luminescent compounds is much larger than the number of inorganic compounds and it is continuously increasing. To increase the quantum efficiency, lifetime and thermal stability of these devices requires the separate optimisation of the generation, injection and transport of the charge carriers and their controlled recombination in different layers. The electrical properties of the OLED are controlled by the mobility of the charge carriers and the heights of the barriers [19], whereas the optical properties by the refractive index mismatches at the glass/air and organic/ITO interfaces that generate the trapping of a large fraction of the light by the mechanism of total internal reflection into glass and ITO [20].

Therefore the organic materials must be designed and selected in such a way to show special properties to satisfy these requirements. Organic luminescent materials can be divided considering their molecular structure and the macro scale organization. From the first point of view there are low-molecular compounds characterised by the possibility of high purification, easy vacuum deposition, high quantum yield fluorescence and large variety and high-molecular compounds (oligomers and polymers) characterised by mechanical strength, flexibility and luminescence over various spectral regions from near UV to near IR but, by small quantum yield of fluorescence. From the second point of view, macro scale organization, there are bulk crystalline organic and organic thin films and heterostructures to be used in devices' fabrication.

A special attention will be paid in this chapter to investigate the properties of bulk and thin films organic compounds showing both good optical, including luminescent, and transport properties for potential optoelectronic applications.

2. Bulk aromatic derivatives for optoelectronic applications

Organic luminescent solids are attracting increasing interest in various field of application from optoelectronics to photonics. The interest in studying organic crystals is justified by the perspective to use these materials as a crystalline host matrix both for organic and inorganic guests (dopants) for developing new classes of materials combining the advantageous properties of both components host and guest. The organic matrix can assure an efficient fluorescence mechanism, can assure simple methods for processing and can contribute to electrical transport. On the other hand, the dopants could increase the charge carrier mobility and improve the emission properties and thermal stability of the organic.

Organic molecules containing electrons occupying nonlocalised molecular orbitals and strongly conjugated systems such as aromatic compounds, dyes, show important luminescence in solid state. This radiative emission involves transitions inside very well shielded systems of π -electrons. By light absorption, an electron is transferred to an antibonding π orbital on the lowest singlet excited state with a lifetime of 10^{-6} - 10^{-9} s, from which it decays by fluorescence emission.

The perspective to tailor the specific physical properties of a molecular solid by guest particles (dopant) embedded in the crystalline organic matrix is very attractive, but not so accessible because some complications can appear both from the crystalline structure and/or dopant sites.

Special research has been devoted to the growth of organic crystals doped with rare earth metallic ions to prepare materials for luminescent and laser applications and benzil doped with Cd^{2+} . The properties of the host/guest systems based on organic crystals depend on the crystalline perfection and chemical defects.

Growth of large and structural good organic crystals at good ratio cost/properties is very important for theoretical understanding of the phenomena taking place in organic solid state and development of new organic-organic, organic-inorganic materials for a target application. The main limitations in large-scale using of aromatic derivatives as crystalline matrix are correlated with the requirements for crystals growth, which involves identification of particularised solutions to overpass the low melting point, supercooling and low thermal conductivity of organic compounds.

Substituted aromatic molecules are a class of organic materials containing weakly coupled, strongly polarisable delocalised π electrons. Concerning the bulk organic crystals, our interest was focalised on aromatic derivatives that contain one and two aromatic rings and substituent groups which disturb the symmetry of the π -electrons cloud, such as meta-dinitrobenzene (m-DNB)/ $\text{C}_6\text{H}_4\text{N}_2\text{O}_4$ and benzil/ $\text{C}_6\text{H}_5\text{-CO-CO-C}_6\text{H}_5$, characterised by large transparency domain and good fluorescence emission.

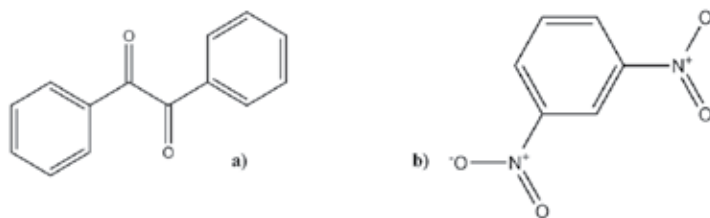


Figure 1. Benzil (a) and m-DNB (b) molecular structure [21].

Benzil with the molecular structure presented in Figure 1a is an uniaxial crystal that belongs to the space-group D_3^4 or D_3^6 and it is known as “organic quartz” being isomorphic with α quartz. By similarity of the microstructures developed in quartz through the diffusion of metal atoms could be of great interest to study benzil as matrix for composite materials and the effect of dopant atoms on the matrix properties.

Meta-dinitrobenzene with the molecular structure presented in Figure 1b is a negative biaxial crystal that belongs to the point group symmetry $mm2$ and space group $Pbn2_1$.

We have developed some investigations on the effect of dopant on the emission properties (shape of the spectra, position of the peaks) of the solid-state aromatic compounds by comparison with the emission properties of the pure organic matrix. We have also evidenced the differences between the influence of the inorganic dopant (iodine, sodium, silver) and/or organic dopant (m-DNB, naphthalene) on the luminescence of bulk m-DNB and benzil samples.

2.1. Aromatic derivatives crystal growth

The source materials used in crystal growth must be of high purity and the purification of organic compounds is a very long process. m-DNB was purified by three methods: chemical purification, vacuum distillation and two steps directional freezing in a horizontal configuration: length of the melted zone=2-3 cm, average travelling speed=2.5 cm/h [22; 23].

Some factors have contributed in the selection of Bridgman-Stockbarger method in vertical configuration to grow m-DNB crystals: low melting point, low vapour pressure and no decomposition at the melting temperature. The supercooling tendency of the organic compound was counteracted in a special design system with two zones (a hot zone: 110-115 °C generated in a furnace that assures the melting of the charge and a cold zone: 50 °C generated by a thermostat) characterised by a steeper thermal gradient at the growth interface created by an oil bath. It is very important to correctly positioning the growth interface compared to the interface air/oil. To allow the dissipation of the high melting heat in the organic material characterised by low thermal conductivity, the ampoule containing the crucible sealed under vacuum is moved slowly in the thermal field. The Teflon dismantle or undismantle crucible containing the organic compound powder has a special bottom configuration (a capillary tube with a diameter of 1 mm) to generate the nucleation and to favour the selection of the growth direction. Details about the experimental configuration are given in Figure 2.

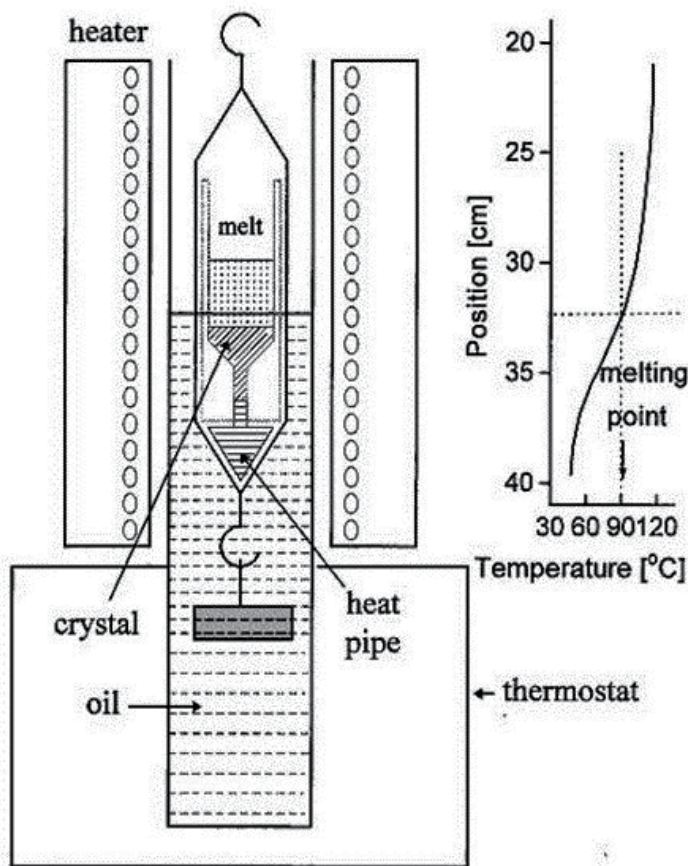


Figure 2. Experimental set-up for the growth of m-DNB crystals and the corresponding thermal profile [23].

The two parameters, thermal gradient at the melt-crystal interface of 4.5-5 °C/cm; 8.5-9 °C/cm and average moving speed of the ampoule in the furnace of 1-1.5 mm/h; 1 mm/h are very important for the crystal growth process because are determining the shape of the solid-liquid interface and position of the growth interface with effect on the properties of the crystals.

A similar configuration, presented in Figure 3 has been used for the growth of the benzil crystals. Some differences result from the fact that benzil is characterised by a weaker adhesion to the quartz wall than m-DNB (the use of a Teflon crucible being not necessary in this case) and from the necessity to assure the control of the nucleation and solidification processes in a configuration without crucible by the use of a conical shape of the ampoule tip with a narrower zone [24].

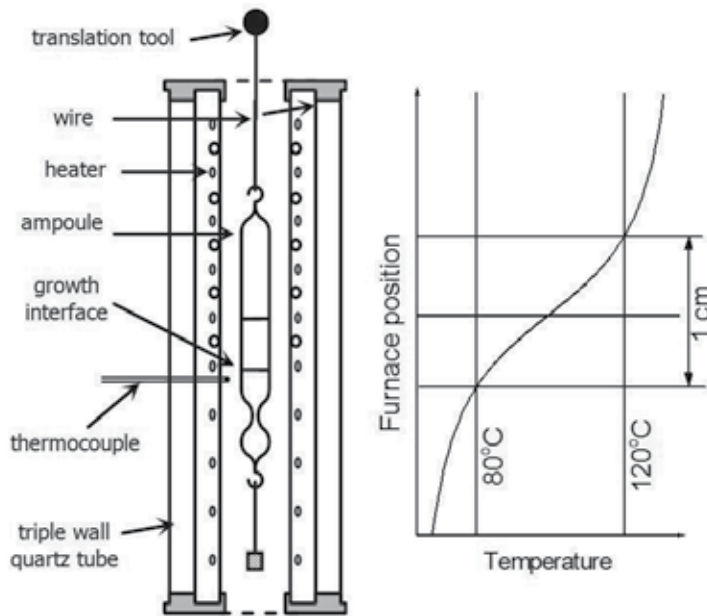


Figure 3. Experimental set-up for the growth of benzil crystals and the corresponding thermal profile [24].

A very important parameter in the process of crystals growth is the temperature, which has two counteracting actions:

1. low thermal gradients at the growth interface are necessary to prevent the generation of mechanical defects, favoured by the accumulation of tensions inside the crystal, like cracks;
2. steep gradients are necessary at the same growth interface to counteract the supercooling effect and the tendency to a faceted growth morphology [24; 25].

In general, the organic compounds are characterised by a low thermal conductivity in solid phase and high values of the solidification enthalpies that must be liberated during the crystallization process. In the system matrix/solvent can be developed many flow cells leading to non-uniform distribution of the dopant in the matrix. Constitutional supercooling characterises the doped organic melt because the freezing front rejects the particles of dopant, which can accumulate in front of the moving solid-liquid interface, the equilibrium freezing temperature of the adjacent liquid is above the actual temperature and the gradient of the equilibrium temperature is:

$$\Delta T_e = \Delta C \cdot m \quad (1)$$

where ΔC =concentration gradient at interface; m =slope of the liquidus curve. $\Delta C m > 0$ by convention, and for molecules rejected at the interface, that decrease the melting temperature, $m < 0$ [26].

The problem of the growth interface stability is very important because the growth interface has effect on the quality of the obtained crystals. Our benzil/dopant system was analysed using the Mullin-Sekerka criterion [26-29], that fixes the limits of the stable growth and the conditions necessary to initiate instabilities in the growth system, and is defined by the following relation:

$$\frac{(V \cdot \rho_m \cdot \Delta_f H - (k_m - k_s) \cdot \Delta T)}{(k_m + k_s) \cdot (\Delta T + \Delta C \cdot m)} \geq 1 \quad (2)$$

where V =ampoule moving speed; ρ_m =melted benzil density; k_m =melted benzil thermal conductivity; k_s =thermal conductivity of benzil crystal; $\Delta_f H$ =solidification enthalpy; ΔT =thermal gradient; ΔC =concentration gradient at the growth interface; m =slope of the liquidus curve. For the growth of pure benzil crystals the stability condition became:

$$\Delta C \cdot m \leq 10.0727 \cdot V - 0.4382 \cdot \Delta T \quad (3)$$

with $\Delta T < 0$ ($T_{\text{final}} < T_{\text{initial}}$ in the solidification process).

In benzil/dopant system for the given experimental conditions, the stable and unstable growth zones were delimited by the curves $\Delta C \cdot m = f(|\Delta T|)$ when V =constant or by the curves $\Delta C \cdot m = f(V)$ for $|\Delta T|$ =constant. In the first case, as can be seen in Figure 4, at high concentration gradients (ΔC) the system moves through the unstable growth zone situated above the curve given by equation (3). For a given thermal gradient at the growth interface small variations in the interface moving speed have no significant influence on the area of the stable growth zone. The main consequences refer to an increase in the morphological instabilities and in crystal's homogeneity. In the second case presented in Figure 5, the area of the stable growth zone increases with the increase of the thermal gradient for a given moving speed of the growth interface, the system remaining in the stable growth zone even for high concentration gradients at the interface.

For benzil crystals $k_m > k_s$ and as consequence the interface is more stable because the term $(k_m - k_s) \cdot \Delta T / (k_m + k_s)$ in equation (2) assures a large range of values situated in the stable growth zone.

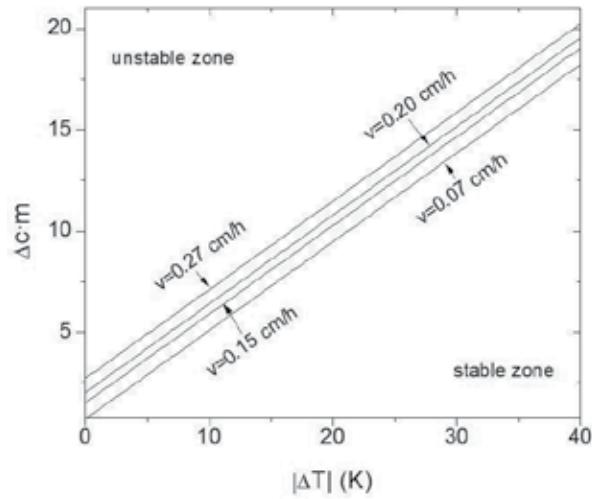


Figure 4. Stable (bellow the curves) and unstable (above the curves) growth zones for the system benzil/dopant in Bridgman-Stockbarger configuration delimited by the curves: $\Delta C \cdot m = f(|\Delta T|)$, $V = \text{constant}$ [24].

These considerations are very important in choosing the parameters for a stable growth generating homogeneous crystals. All the studied systems based on pure and doped benzil and m-DNB matrices are similar from the point of view of the solidus-liquidus interface stability criterion because the ratios $|\Delta T| / V$ are comparable [26; 24].

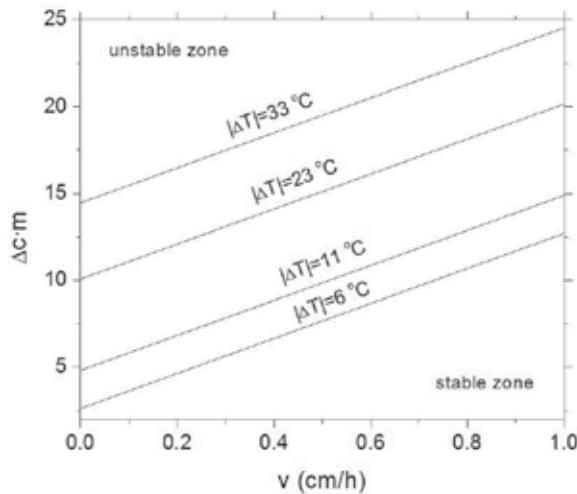


Figure 5. Stable (bellow the curves) and unstable (above the curves) growth zones for the system benzil/dopant in Bridgman-Stockbarger configuration delimited by the curves: $\Delta C \cdot m = f(V)$, $|\Delta T| = \text{constant}$ [24].

The same parameters, thermal field and the interface moving speed are important in the engulfment or rejection of the dopant particles in the crystallisation front. Compositional variations and growth micrononhomogeneities (named striations) appear because of the layer situated in front of the interface, which is enriched in foreign particles by rejection. The factor which influences the incorporation of the dopant atoms/molecules in the matrix are: the shape, volume and intermolecular bonds of the dopants' molecules. A free space around 2.9 Å has been evaluated considering the molecular structure and the geometry for both benzil and m-DNB [24]. The diameter of the dopant atoms favours the incorporation in interstitial positions and the incorporation is facilitated by the local deformation of the organic lattice characterised by weak Van der Waals forces [25; 24].

Sodium atoms could be incorporated interstitially with difficulty because the atomic diameter is greater than the diameter of the free space in benzil solid state, while silver and iodine with a diameter smaller than the free space could be easily interstitially incorporated. In the case of metals characterised by a high first ionisation enthalpy is sustained the generation of clusters, which can create difficulties in atoms incorporation (like iodine or silver).

For sodium atoms the situation is a little bit more complicated because of the high reactivity of sodium [25]. The interaction between the organic molecules and the alkali and alkali-earth metal atoms is determined by a chemical reaction leading to an organometallic complex or a charge transfer generating anion-cation pairs. The first situation is characterised by a very low probability because the hydrogen in benzil has not a very strong acid character to be directly substituted by alkali metal atoms and the crystal growth in closed sealed systems under vacuum reduces the possibility of sodium oxides formation. The charge transfer in sodium doped benzil crystals is caused by a nonbonding Van der Waals force present in all the organics and a dative bonding force corresponding to the situation in which two Na donor atoms could give each the outer 3s electron to two oxygen atoms from the carbonyl acceptor group in benzil. Because the ionisation energy for most alkali metal atoms is low (around 4-6 eV) the electron transfer from Na-guest to benzil-host is allowed without the formation of a covalent bound [25].

In the case of an organic dopant the situation is completely different and depends on the matrix. Because the organic molecules are big and can accommodate in the host lattice only substitutionally and not interstitially and must respect the condition for solubility in solid phase and the criterion for the geometrical similarity between the molecule of the dopant and matrix [30; 31]. If there are geometrical differences, the substitution is less probable and the microinclusions of dopant can generate distortion of the lattice and cracks.

The geometrical similarity is measured by the overlapping factor represented by the ratio between the unoverlapped and overlapped volume of the matrix and dopant [32]. This introduces a limitation of the doping level which can be allowed by each host/guest system. The volume of m-DNB, benzil and naphthalene molecules have been estimated supposing a spherical shape of the molecule and taking into account the length of the chemical bounds. Because the calculated unoccupied volume is much greater than the occupied volume, the possibility for m-DNB to replace benzil molecule and be included substitution-

ally in the lattice is very small. The m-DNB molecules, which are not completely dissolved in benzil, segregate and generate microinclusions that favour the light scattering. The smaller geometrical differences between benzil and naphthalene generate weaker segregation effect.

2.2. Optical properties of bulk aromatic derivatives

The segregation effect of the dopant was investigated experimentally by UV-VIS measurements. The transmission of benzil doped with m-DNB sample is lower than the transmission of benzil doped with naphthalene sample (for the same thickness ~ 2 mm) as can be seen in Figure 6, suggesting a stronger segregation of m-DNB than naphthalene in benzil matrix. The segregation of iodine in benzil matrix with effect on the homogeneity, reflected in UV-VIS spectra, is stronger in the presence of another dopant (naphthalene or m-DNB) and less significant in the absence of any other organic dopant as presented in Figure 7.

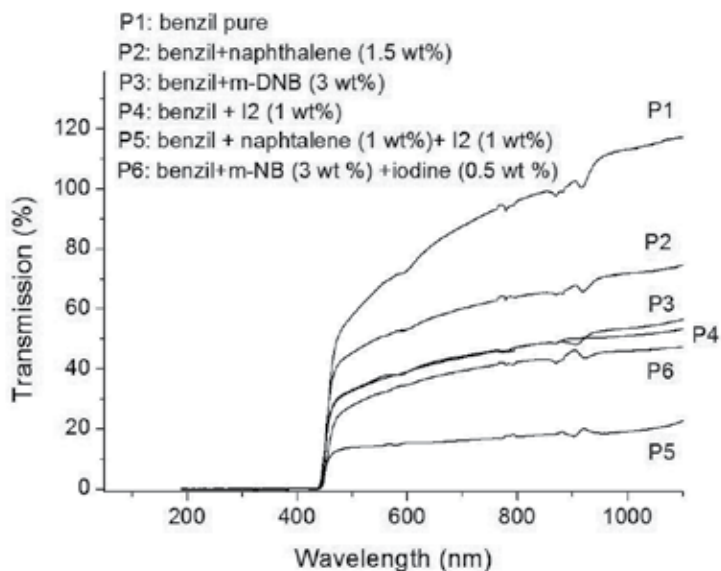


Figure 6. The effect of dopant on the UV-VIS transmission spectra of benzil matrix [24].

UV-VIS absorption spectra of pure benzil and benzil doped with Ag or Na, presented in Figure 8, Figure 9 and Figure 10, have specific shapes characterised by a narrow peaks structure at wavelength < 450 nm.

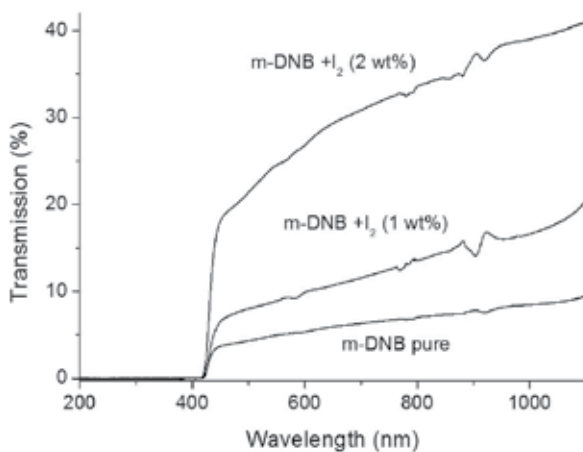


Figure 7. The effect of dopant on the UV-VIS transmission spectra of m-DNB matrix [24].

The UV-VIS spectrum of pure benzil, presented in Figure 8, preserves the pattern by doping with Ag, which is not interacting with benzil molecules. As result, the fundamental absorption edge is not affected and preserves the narrow peaks structure. The peak situated around 380 nm is correlated with some particularities of the benzil molecular configuration and is attributed to the absorption on the dicarbonyl groups [33; 21].

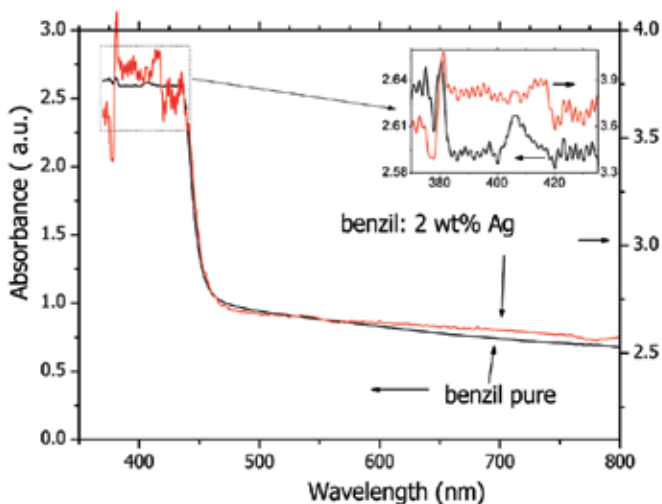


Figure 8. Comparison between the absorption spectra in bulk samples of pure benzil and benzil doped with Ag [25].

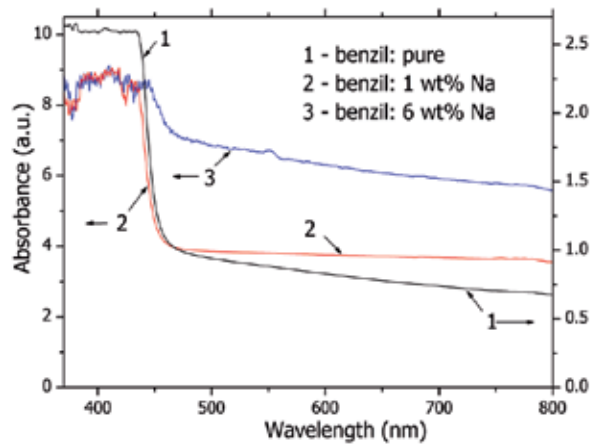


Figure 9. Comparison between the absorption spectra in bulk samples of pure benzil and benzil doped with Na [25].

At the contrary, doping with Na has introduced important changes in the shape of the fundamental absorption edge in benzil, as can be observed in Figure 9, a large structured band replacing the narrow peaks. This can be explained by the light scattering on the nonhomogeneities of the doped benzil or by changes in the forces acting between the host and guest [25].

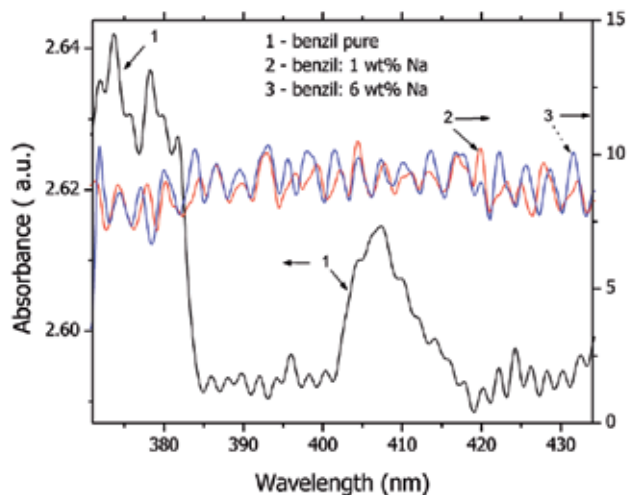


Figure 10. Absorption spectra of bulk pure and Na doped benzil matrix. Detail between 375 nm and 435 nm [25].

From the transmission data near the fundamental absorption edge processed using a linear-power model characterised by a formula obtained by superimposing a linear function and a power function [25]:

$$\alpha = a + b(E_g - c)^d + mE \quad (4)$$

or

$$\alpha = a + b(c - \lambda_g)^d + m\lambda \quad (5)$$

where: α =absorption coefficient; c =band gap energy, E_g , or edge of the fundamental absorption, λ_g , respectively, d =coefficient that depends on the light absorption mechanism and $(a + mE)$ or $(a + m\lambda)$ respectively, define all the other parasitical processes, including scattering of light on the nonhomogeneities of the sample and affecting the band to band absorption mechanism.

The light absorption process is characterised by the optical band gap, which in benzil has been evaluated at $E_g=2.65$ eV, emphasising the wide band gap semiconductor character of crystalline benzil. The narrowing of the optical band gap by introducing energetic levels in the band gap in pure crystal can be a consequence of physical defects or controlled doping that can generate chemical or structural defects.

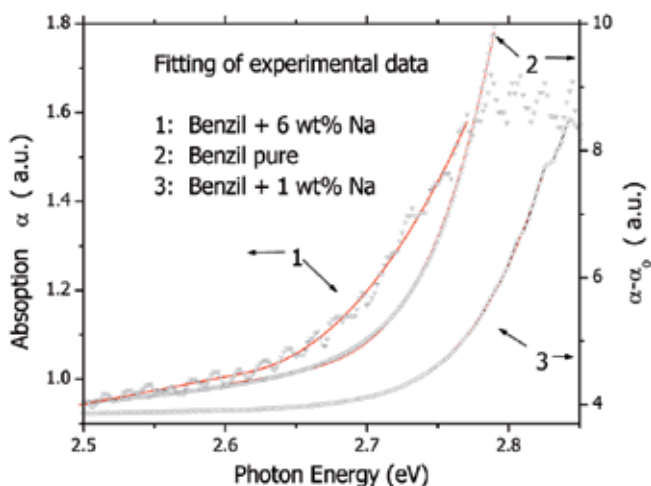


Figure 11. Fitting of the experimental data for bulk samples of pure and Na doped benzil [25].

As can be seen in Figure 11, the narrowing in the optical band gap is correlated with the presence of physical defects because the large radius metal atoms disturb the organic lattice and the effect of the dopant is hidden by the structural imperfections [25]. The impurities migrate and concentrate at these defects, such as grain boundaries, twins, dislocations.

For benzil doped with Ag presented in Figure 12, the situation is different and the optical absorption involves energetic levels from the band gap associated with the generation of cluster, as a consequence of the high first ionisation energy and weak reactivity of Ag.

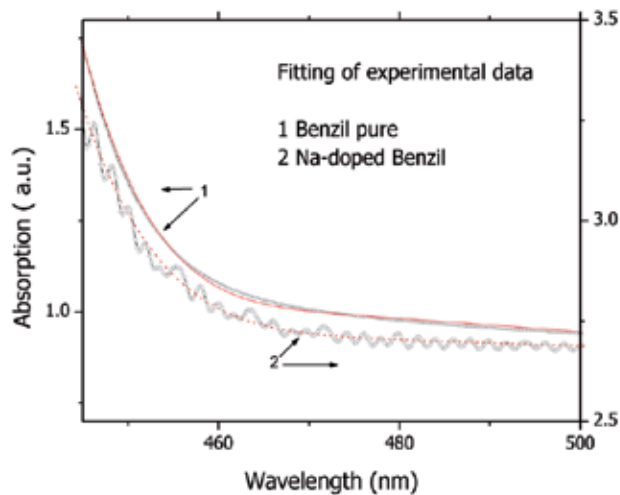


Figure 12. Fitting of the experimental data for bulk samples of pure and Ag doped benzil [25].

At excitation with $\lambda=335$ nm, the bulk sample of m-DNB shows a high, broad emission peak presented in Figure 13 [34], which correlated is with the radiative decays from the first excited energetic level, peak situated at 2.85 eV with a shoulder at 2.95 eV generated probably by the radiative decay from another vibrational level of the same excited energetic level.

A modification of the spectrum could be evidenced when m-DNB is doped with iodine, the position of the emission slightly moving through shorter wavelengths, the difference between the peak and shoulder being attenuated by the increase of the iodine concentration from 1 wt % to 2 wt %. The blue shift of the emission peak can be associated with the migration and trapping of the exciton on the defect zones characterised by slightly higher energy compared to m-DNB without defects. Despite the strong interaction between the molecules, the energy of the level associated to the defect still remains under the energy of the exciton level.

The peak situated at 2.8 eV evidenced both in pure and doped m-DNB can be obtained by a radiative decay from the lowest excited triplet state to the ground state. This forbidden transition became possible by the relaxation of the selection rule in m-DNB under the effect of

the vibrational interactions. The triplet state can be reached by a radiationless “intersystem crossing” process from the excited singlet state.

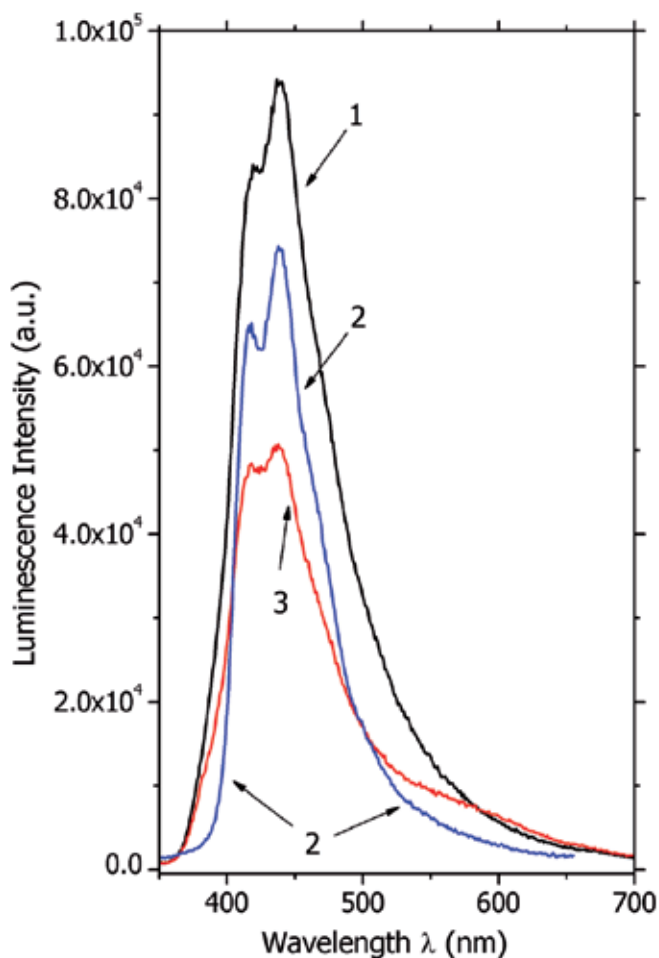


Figure 13. Luminescence spectra of m-DNB crystals: (1) pure m-DNB; (2) m-DNB doped with 1 wt % iodine; (3) m-DNB doped with 2 wt % iodine [34].

The m-DNB molecules contain oxygen atoms with lone electrons pairs which can be promoted to an unoccupied π orbital and give rise to a (n, π^*) singlet excited state and a triplet excited state, with an energy lower than the energy of usual (π, π^*) state. The (n, n^*) state in m-DNB is the lowest excited singlet state that favours the radiationless processes as “intersystem crossing” or “internal conversion” to a lower excited energetic level. The (n, π^*) transition in m-DNB is confirmed by the small value of the “singlet-triplet” splitting evaluated from the correlation of absorption and emission data [34].

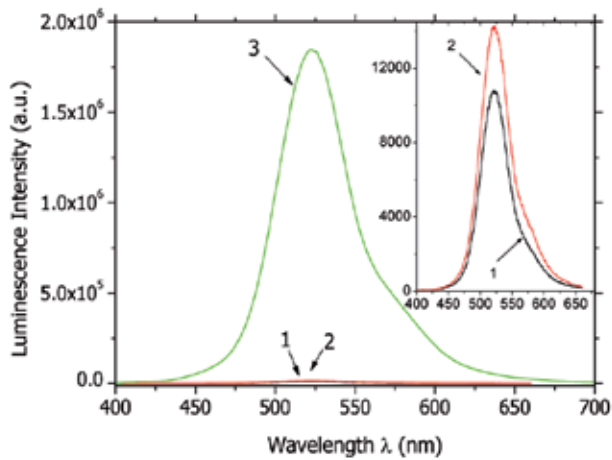


Figure 14. Luminescence spectra of benzil crystals: (1) pure benzil; (2) benzil doped with 1 wt % iodine; (3) benzil doped with 2 wt % iodine [34].

The luminescence spectra of pure benzil presented in Figure 14, shows an emission peak situated at 2.37 eV generated by the lone electron pairs of oxygen atoms in carbonyl groups emitting only from planar configuration, on which are localized the emission transition involving (n, π^*) states.

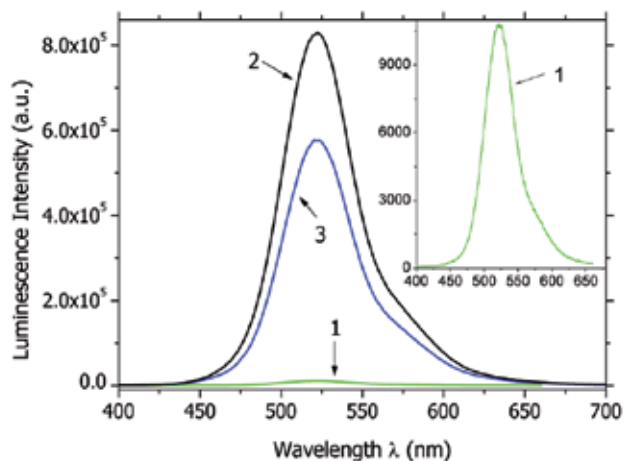


Figure 15. Luminescence spectra of benzil crystals: (1) pure benzil; (2) benzil doped with Ag (2.4 wt %); (3) benzil doped with Na (1 wt %) [34].

The doping with other metallic impurities such as silver (2.4 wt%) or Na (1 wt %) has not modified the sharp peak situated at 2.37 eV, which is present in pure benzil, as it is emphasized in Figure 15, and this peak could not be correlated with an exciton trapping mechanism [34]. The peak at 2.37 eV could be generated by the radiative decay from the excited triplet state (T_1) to the ground state (S_0), which is a transition forbidden for separated molecules becoming allowed through the vibrational interactions when the molecules are coupled in the solid state, in a crystalline lattice [23; 35; 36].

In Figure 16 is presented the spectrum of benzil doped with m-DNB. The benzene derivative, m-DNB, is active itself and has a direct action on the benzil matrix. The peak assigned to m-DNB is situated at 2.97 eV in the high-energy range of the emission spectrum. The preferential excitation of m-DNB molecule can be explained by the lower position of the excited singlet state (2.9 eV) in m-DNB compared to benzil (3.25 eV). At the contrary, naphthalene has not any significant influence on the emission spectrum of benzil presented in Figure 17, because the first singlet excited state in naphthalene is situated at ~ 3.84 eV and the triplet state at ~ 2.64 eV higher than the corresponding energetic levels in benzil (3.25 eV and 2.3 eV respectively). Therefore the peak observed in the emission spectrum of naphthalene doped benzil is obtained by the radiative deexcitation of benzil matrix.

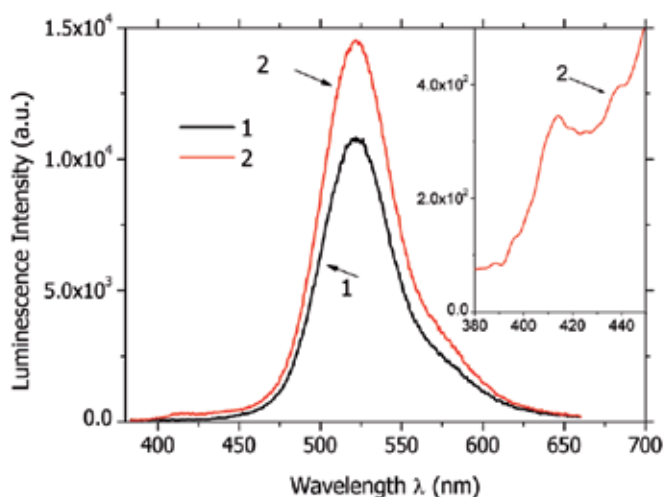


Figure 16. Luminescence spectra of benzil crystals: (1) pure benzil; (2) m-DNB doped benzil (3 wt %) [34].

As can be seen from Figure 17, the simultaneous doping with naphthalene and iodine has no significant effect on shape of the emission spectrum of benzil.

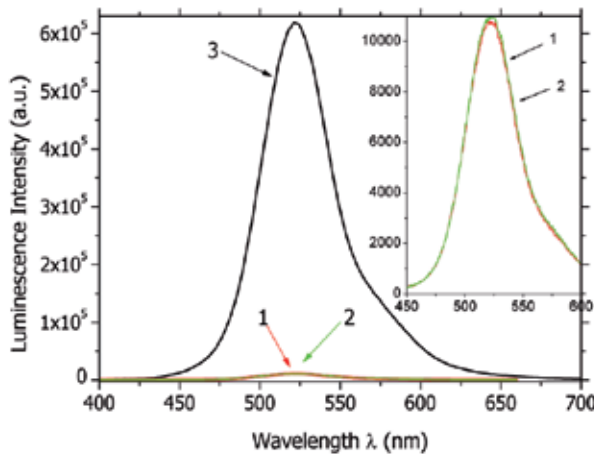


Figure 17. Luminescence spectra of benzil crystals: (1) pure benzil; (2) benzil doped with naphthalene (1.5 wt %); (3) benzil doped with naphthalene (1 wt %) and iodine (1 wt %) [34].

3. Aromatic derivatives thin films for optoelectronic applications

The major problems for large-scale application of crystalline matrices from these aromatic derivatives materials are associated with the difficulties to grow (low melting point, supercooling, and low thermal conductivity), process (weak mechanical properties determined by weak bonding forces between molecules) and doping organic crystals to assure an homogeneous distribution of the guest atoms.

Crystalline organic films are preferred in a variety of applications because of the complexity of the processes involved and long time necessary to grow bulk organic crystals. The use of thin films is more promising because represents an optimum between the cost of manufacturing and properties of interest for special and oriented applications.

Investigation of the properties of organic thin films is a very important aim because these films are components of the organic heterostructures as fundamental elements of any organic devices. It is also necessary to investigate the properties of heterostructures because the junction between two different semiconductors (organic/organic; organic/inorganic) or between a metal and a semiconductor (metal/organic) is the key building block of any modern electronic, photovoltaic and optoelectronic devices. Heterojunction technology has known a continuous development from the first heterojunction transistor, realized by Bardeen in 1948 at Bell Laboratory [37], to p-n junction transistor, realized by Shockley in 1949 [38], and to nowadays devices based on multilayer heterostructures.

The organic compounds which have been investigated as components of organic compound based heterostructures are:

- a. 3,4,9,10-perylenetetracarboxylic dianhydride (PTCDA);
- b. Zinc phthalocyanine (ZnPc);
- c. tris(8-hydroxyquinoline) aluminium (Alq3) and
- d. 5, 10, 15,20-yetra(4-pyridyl)21H, 23H-porphyrine (TPyP).

PTCDA is known as having p type conduction while Alq3 and TPyP are characterized by n type conduction. Their molecular structure is given in Figure 18.

ZnPc is an electron donor forming highly ordered layer, with a broad transmission window in visible region of the spectrum [39].

In PTCDA, an electron acceptor, the interaction between the π -electrons systems is favored by the planar molecule and the perpendicular stacks of molecular planes [40], which determine a quasi-one-dimensional molecular crystal structure [41].

Alq3 shows different stereoisomers (median, facial) determined by the mutual orientation of the ligands of hydroxyquinoline, which show different symmetries and as consequence different properties [42; 43].

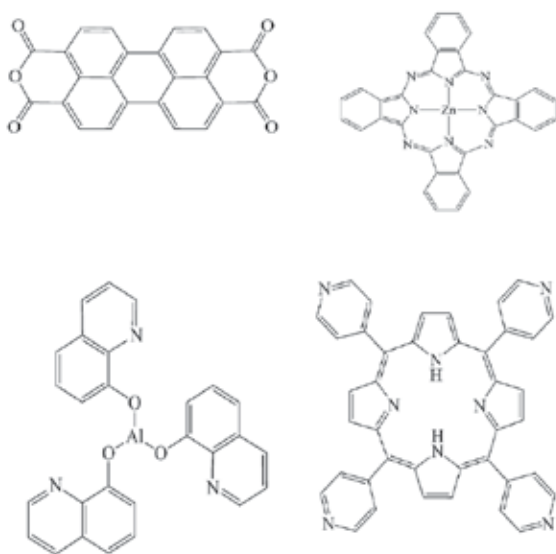


Figure 18. PTCDA (a), ZnPc (b), Alq3 (c) and TPyP (d) molecular structure.

TPyP is a non-metallic porphyrin with an increased electron affinity obtained by the substitution of phenyl group by pyridyl group determining the n type conduction. The basic structure of porphyrin consists in four pyrrolic entities linked by four unsaturated methene bridges with a skeleton showing an extended π -electrons system assuring a large spectral range for light absorption [44].

3.1. Preparation of the aromatic derivatives thin films

3.1.1. Aromatic derivatives thin films preparation by directional solidification process

It is not very easy to obtain organic thin films because of the same difficulties which affect the preparation of organic crystals and the quality of the organic layer is strongly influenced by the method, which have been selected to grow the film. For example there is a high concentration of structural defects in the benzil thin films which have been grown by a rapid directional solidification process, characterised by a non rigorous control of the thermal regime compared to the crystal growth process and these defects have caused the red shift of the emission peak. It is very difficult to grow, by vacuum evaporation, thin films of organic compounds characterized by a melting point $T_m < 100$ °C (including benzil and m-DNB) because the heating of the substrate during the evaporation process can favor a strong desorption of the organic molecules from the substrate. By the directional solidification process could be prepared organic thin films between two substrates, like quartz or glass substrates, during a rapid thermal solidification characterized by a temperature gradient for solidification, $\Delta T > 50$ °C, necessary to counteract the supercooling phenomenon [45]. Crystalline fragments from organic ingots of pure and doped m-DNB ($T_m = 89.9$ °C) or benzil ($T_m = 95$ °C), grown by Bridgman-Stockbarger method presented in paragraph 2.1, have been melted between the substrates by the hot plate technique and after that rapidly frozen by the cold plate technique obtaining films with a columnar structure with large dendrites branches in the plane of the film determined by the low thermal conductivity and anisotropy of these organic compounds. The thickness of the films has been evaluated (using the density in solid state) from geometrical considerations presuming that the total volume of the substance didn't change during the melting-solidification cycles.

3.1.2. Aromatic derivatives thin films and heterostructures preparation by vacuum evaporation

Thin films of PTCDA, Alq3 and TPyP have been prepared by vacuum evaporation and deposition on different substrates (glass/ITO, quartz, Si), which have been cleaned in acetone (glass/ITO, quartz) and with acetone, hydrofluoric acid and distillate water (Si).

Stable, homogeneous organic films, with good adhesion to the substrates have been prepared, by the evaporation of the organic powder contained in the quartz crucible heated by a self-sustaining kanthal winding, in an Alcatel system with turbo molecular pump [40; 46]. During the deposition with a duration between 10-15 min, the temperature was measured by a thermocouple situated at the bottom of the crucible and varied between 220-240 °C for PTCDA [40], 150-160 °C for Alq3 [40] and 175-185 °C for TPyP [46].

3.1.3. Aromatic derivatives thin films an heterostructures preparation by MAPLE

A special type of Pulsed laser Deposition (PLD) technique, Matrix Assisted Pulsed Laser Evaporation (MAPLE), has been used for the deposition of small molecule organic films (PTCDA, ZnPc, Alq3). This technique involves the ablation of a target formed by the frozen solution of the organic compound in a high molecular weight and strong laser wavelength

absorbing solvent, like dimethylsulphoxide (DMSO) or chloroform. Deposition was realized with a KrF* laser, Coherent ComplexPro 205 characterised by $\lambda=248$ nm, $\tau_{FWHM}\sim 25$ ns, repetition rate=10 Hz [47]. The incident laser energy absorbed by the solvent molecules is converted into thermal energy determining the heating and simultaneous evaporation of the two components. The solvent molecules are pumped away by the vacuum pump that maintains a pressure of 10^{-2} - 10^{-1} mbar in the deposition chamber, while the less volatile molecules of the organic compound deposit on the substrate maintained at room temperature. The low value fluence varied between 160 mJ/cm² and 430 mJ/cm² to avoid the deterioration of the organic molecule and the number of pulses between 10000 and 120000, with effect on the films' thickness (40 nm-150 nm), which has been evaluated by ellipsometry.

3.2. Optical properties of aromatic derivatives thin films

The absorption spectrum of m-DNB, presented in Figure 20, which is similar to a classical semiconductor, could be correlated with the strong interactions between the polar molecules and with the partial superposition of the π -electrons clouds from neighbour molecules generating narrower valence and conduction bands. This spectrum is different from that of benzil presented in Figure 19, which is characterized by a two edges of the fundamental absorption, with a subband light absorption peak situated at 380 nm, attributed to absorption by dicarbonyl groups, strongly interacting in the solid state and producing the split of the energetic level (n, π^*).

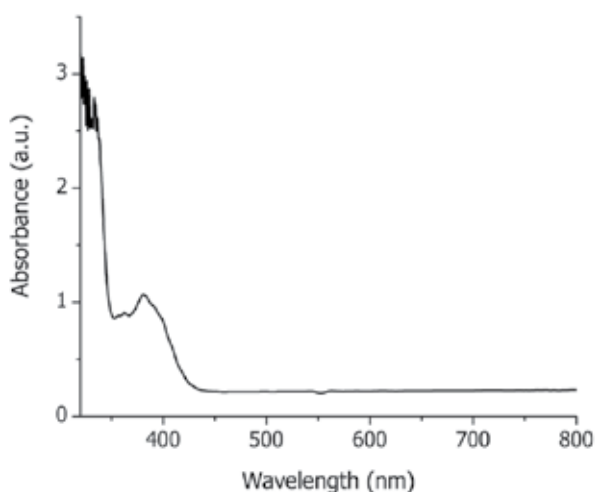


Figure 19. Absorption spectra of benzil film grown between two quartz plates [45].

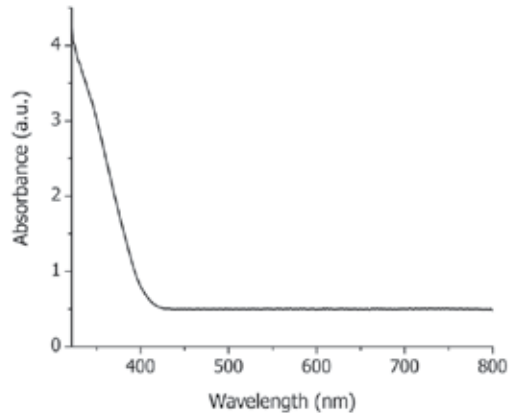


Figure 20. Absorption spectra of m-DNB film grown between two quartz plates [45].

From Figure 21 it can be emphasized that the shape of the fundamental absorption edge is not affected by the presence of impurities. No important changes have been evidenced at the absorption edge characterized by a lower energetic threshold. But the absorption at the edge characterized by the higher energetic threshold is attenuated in benzil doped with m-DNB or sodium compare to pure benzil because of the light scattering process on the nonhomogeneities of the films. This effect is stronger in benzil doped with Na because it is not completely dissolved, segregates and generates microinclusions as a distinct phase.

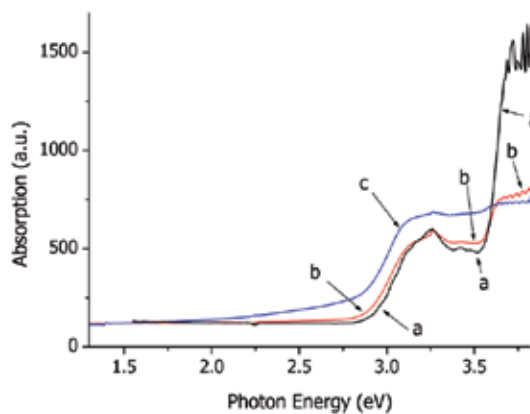


Figure 21. Comparative absorption spectra of: pure benzil (a); benzil doped with m-DNB (3 wt %) (b); benzil doped with Na (6 wt %) (c): grown between two quartz plates [45].

The effect of the impurities on the shape and position of the absorption peak in benzil situated at 3.25 eV and assigned to dicarbonyl group absorption is not important and no other absorption peaks have been evidenced in the longer wavelength range to sustain the trapping of the excitation energy by these impurities. Therefore we can conclude that the energetic levels of these impurities are not significantly lower than the lowest energetic level which characterizes the crystalline assembly [21].

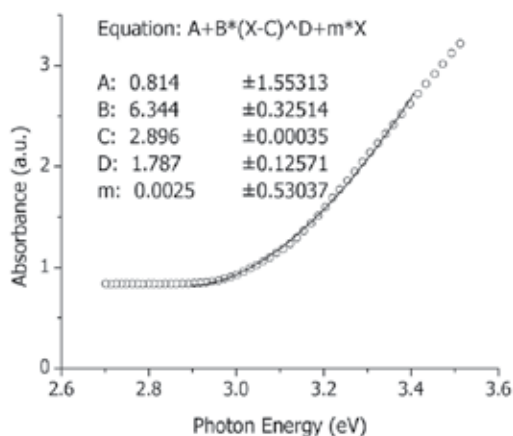


Figure 22. Fitting of the experimental data for pure m-DNB film [45].

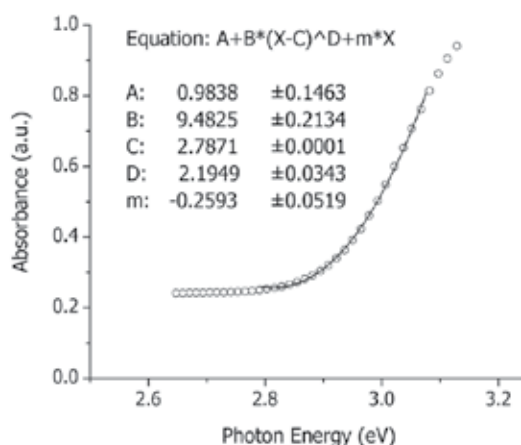


Figure 23. Fitting of the experimental data for pure benzil film in the range 2.6 eV-3.1 eV [45].

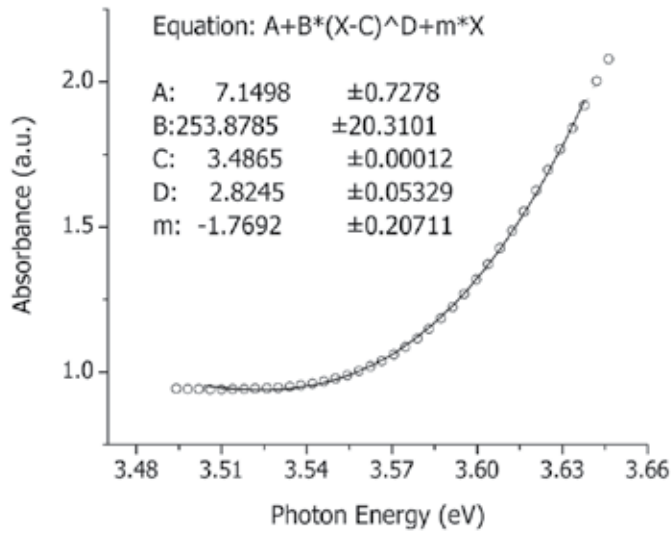


Figure 24. Fitting of the experimental data for pure benzil film in the range 3.49 eV-3.65 eV [45].

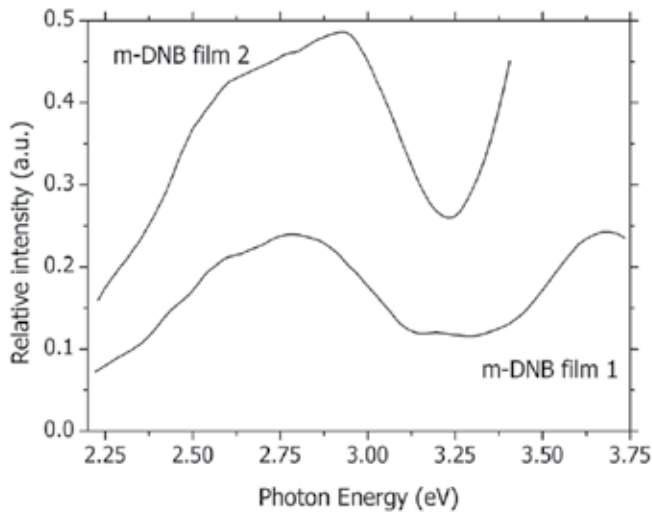


Figure 25. Emission spectra of pure m-DNB films of different thickness for $\lambda_{excitation}=300$ nm [21].

The band gap energy has been evaluated from the experimental data fitting, near the fundamental absorption edge, shown in Figure 22 for m-DNB and, Figure 23 and Figure 24 for

benzil, using the formula (4) and we have obtained $E_g=2.90$ eV for m-DNB and $E_{g1}=2.79$ eV and $E_{g2}=3.54$ eV for the two absorption edges in benzil.

Supplementary information about the optical properties of these aromatic derivatives in solid state have been obtained from the luminescence measurements. At excitation with $\lambda=300$ nm, the emission spectra of pure m-DNB present a peak situated at 2.92 eV with a shoulder at 2.63 eV, as it is shown in Figure 25. The apparent red shift of the emission peak situated at 2.92 eV to 2.78 eV in thicker film is due to a self-absorption process of the emitted radiation and not to a recombination on the energetic levels associated with physical defects or impurities.

Luminescence spectra of benzil films presented in Figure 26 show a peak at 2.30 eV attributed also to the radiative decay from the excited triplet state (T_1) to the ground state (S_0), transition possible because of the vibrational interactions as was mentioned for bulk samples in paragraph 2.2.

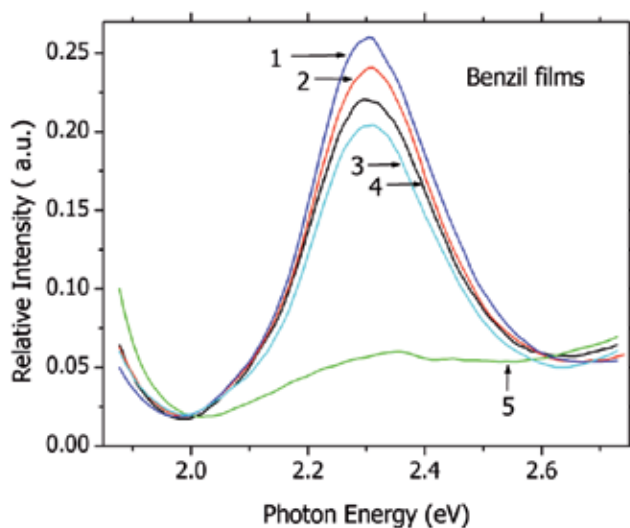


Figure 26. Emission spectra of pure and doped benzil films: (1) benzil doped with Na (1 wt %); (2) benzil doped with m-DNB (3 wt %); (3) benzil doped with Ag (2.4 wt %); (4) benzil pure; (5) benzil doped with Na (6 wt %) [21].

The excited molecules of benzil are more sensitive to a radiationless process and the conversion from the first singlet excited state to the lowest triplet excited state becomes possible by „intersystem crossing”, transition between states with different multiplicity, very efficient in systems containing carbonyl groups, like benzil. This radiationless process is followed by a radiative decay through phosphorescence from (T_1) to (S_0). The intersystem crossing appears in benzil as a transition between (n, π^*) states of singlet and triplet levels rather than between (π, π^*) states. Both absorption and emission transitions involve states localized on carbonyl groups, which emit only from planar configuration.

The behaviour of benzil molecule depends on the flexible conformation [48] because the torsion angle around the central bond C-C can change and the geometry of the molecule can change after excitation with light. In the ground state the benzil molecule has a skew configuration and can twist around the carbonyl-carbonyl bond with little interaction between the two benzyl halves of the molecule. This interaction becomes strong in excited molecule, which rearranges in a new configuration with a trans-planar dicarbonyl system characterized by a redistribution of the energy followed by the process of „intersystem crossing“. By phosphorescent emission the system passes from a trans-planar configuration to the ground state with also a trans-planar configuration considering the Frank-Condon principle [49]. In the next step the molecule relax from the emissive trans-planar configuration to a skew configuration and the differences in the emission spectra of benzil can be determined by changes in the molecular conformation of the ground state [50]. For most of the dopants we have not remarked any modification in the shape and position of the emission peak that sustains no modification in the molecular conformation of the (n, π^*) state with effect on the angle between the carbonyl groups. The only changes, a slightly blue shift and significant attenuation in intensity, have been remarked in Figure 26 for benzil highly doped with Na (6 wt %). A possible charge transfer from Na atoms to oxygen atoms in carbonyl groups can generate conformational changes, and the shift could be explained by the decrease in the dihedral angle between the two carbonyl groups [21]. The only impurity active in emission is sodium at high concentration because of the conformational changes in the emitting triplet state, while m-DNB, Ag, Na are not active in absorption.

In Figure 27 and Figure 28, we have emphasized the band structure of the absorption spectra in PTCDA and Alq3 with peaks situated at 358 nm, 374 nm, 475 nm, 552 nm and 232 nm, 261 nm, 380 nm respectively. This confirms the presence of median isomer in Alq3 film. The position of the two important peaks situated at 2.25 eV and 2.61 eV remain unchanged in the absorption spectrum of PTCDA deposited on glass covered by ITO while the absorption spectrum of the heterostructure with double organic layer, glass/ITO/PTCDA/Alq3, preserves the pattern of the absorption spectrum of PTCDA between 400 nm and 600 nm, which is very important in the stage of the charge carrier's generation.

In Figure 29 have been evidenced the presence of π - π^* absorption bands characteristic for free-base ethio type porphyrin. These bands are associated with π - π^* transition between bonding and anti-bonding molecular orbitals. Other bands which have been also evidenced are: an intense Soret band (B) with a peak centred at 430 nm and 4 Q bands situated at 520 nm, 555 nm, 590 nm and 645 nm.

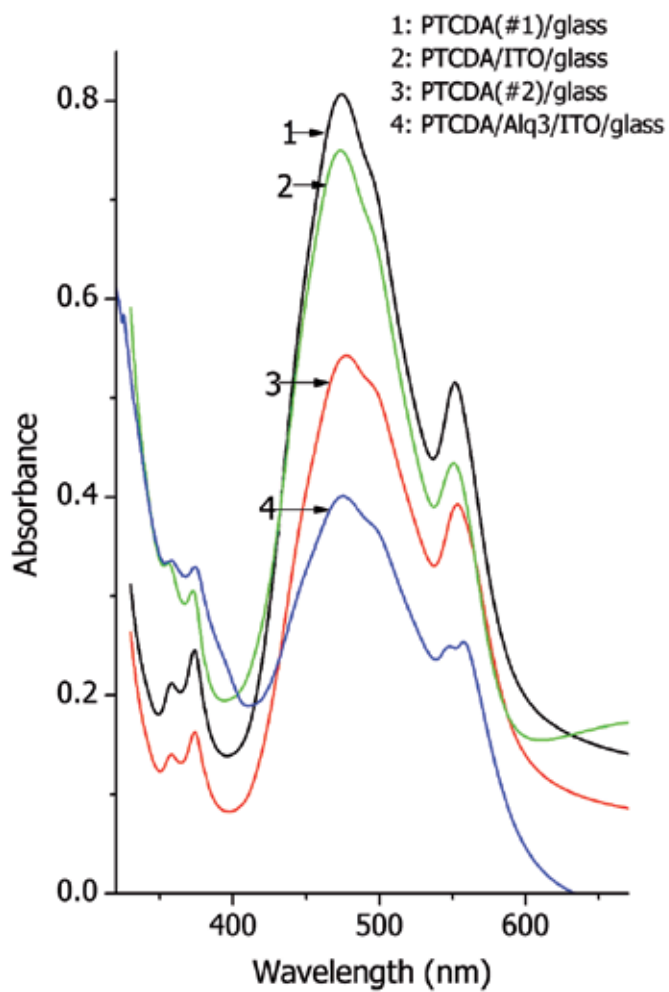


Figure 27. Absorption spectra of PTCDA thin films deposited by vacuum evaporation [40].

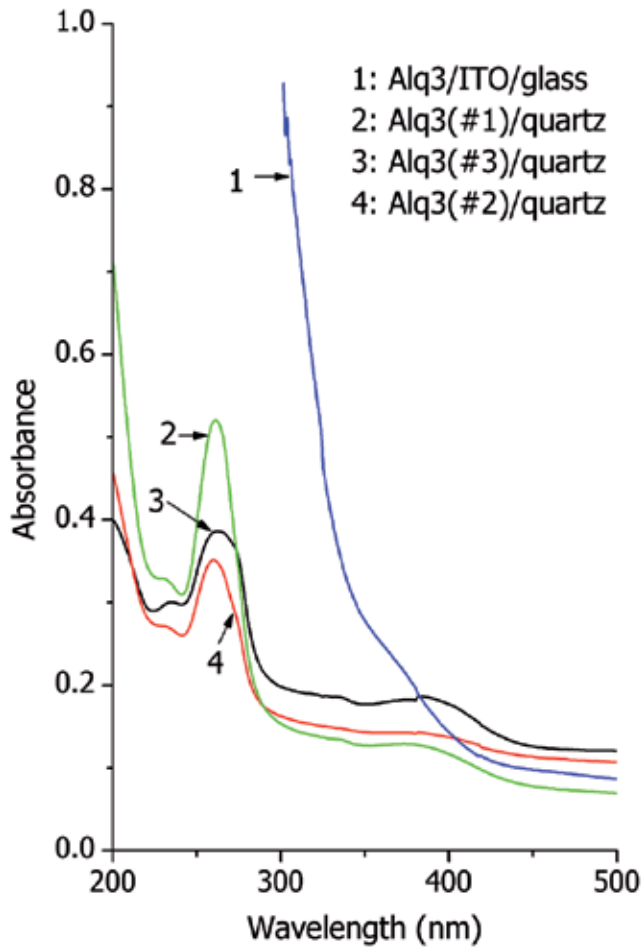


Figure 28. Absorption spectra of Alq3 thin films deposited by vacuum evaporation [40].

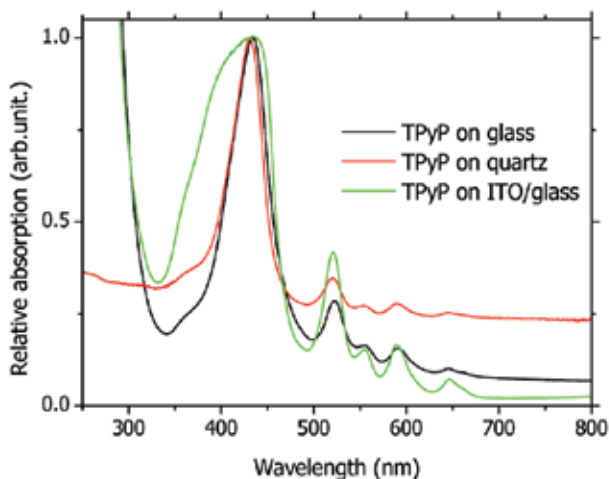


Figure 29. Absorption spectra of TPyP thin films deposited by vacuum evaporation [46].

The shape of the absorption spectra of TPyP thin films deposited on different substrates is preserved at $\lambda > 430$ nm. The slight red shift of the Soret band can be determined by the order induced by the interaction between the molecules in solid state influenced by the interaction with the substrate [51]. A possible bonding mechanism can be based on the pyridyl-surface interaction mediating the deformation of the molecule after adsorption on the substrate's surface. Subsequent packing of the molecules can be determined by the non-covalent interactions mediated by the terminal pyridyl groups and these interactions seem to prevail over the site-specific adsorption [52]. During these intermolecular interactions the porphyrin core can be deformed and the symmetry of the TPyP molecule modified because the conformation of this molecule is defined by several degree of freedom (dihedral angle in correlation with the rotation of the pyridyl group about C-C bond, inclination angle of the same bond and distortion angle determined by the steric repulsion between hydrogen atoms of the pyridyl group and the pyrrole moieties [53]).

The spectra in Figure 30 have revealed a wide absorption band situated between 400 nm and 600 nm in PTCDA with a maximum at 480 nm and a shoulder at 550 nm, this shape being determined by the interactions of the π -electrons system of the neighbour planar molecules very closed packed in solid state [21; 54]. The excited states can be the result of the superposition of the intramolecular Frenkel excitons and intermolecular charge transfer excitons existing near the excitation threshold [55]. The UV-VIS spectra of Alq3 confirm that the low temperature isomer (median) correlated with the presence of the weak absorption band situated at 380 nm, dominates in the films deposited at room temperature [56]. For ZnPc we have evidenced two absorption peaks situated at 690 nm, a strong band corresponding to Q band and a weak band situated at 330 nm corresponding to B band [57].

Modifications in the deposition parameters (target concentration, fluence and number of pulses) are reflected in the thickness of the layer and not in the shape of the transmission.

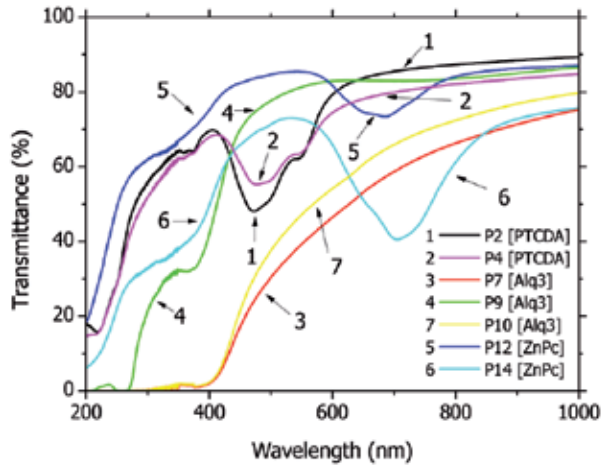


Figure 30. UV-VIS spectra of organic thin films deposited by MAPLE: PTCDA on quartz (1 and 2); PTCDA on ITO (7); Alq3 on quartz (3 and 4); ZnPc on quartz (5 and 6) [54].

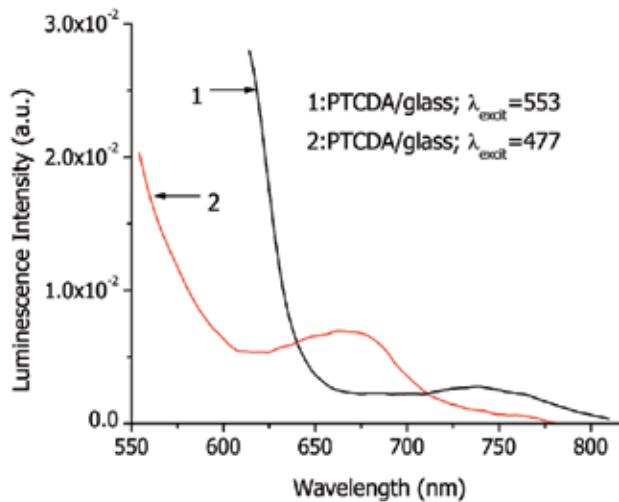


Figure 31. Emission spectra of PTCDA film deposited by vacuum evaporation on glass for two excitation wavelengths [40].

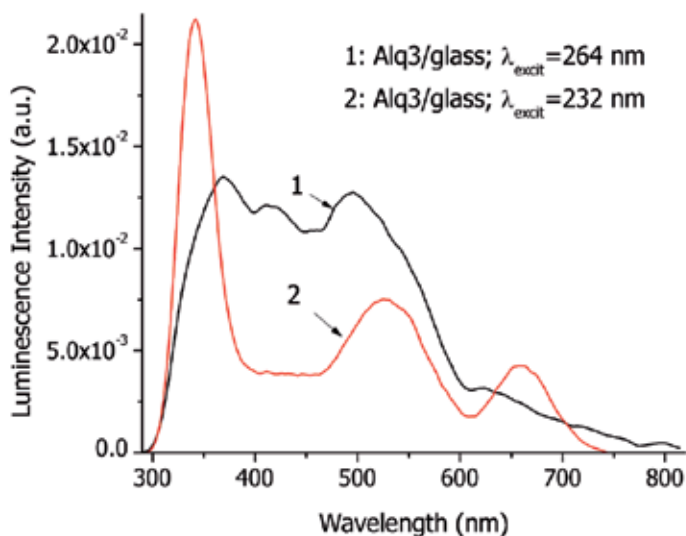


Figure 32. Emission spectra of Alq3 film deposited by vacuum evaporation on glass for two excitation wavelength [40].

The fluorescence emission spectrum of PTCDA film presented in Figure 31 shows a broad structureless band shifted significantly to the red compared to the PTCDA fluorescence spectrum in solution as a consequence of a strong interaction between the organic molecules in the solid state favoured by the close spacing and important overlap of the molecular planes. The emission takes place in PTCDA from the lowest excited singlet state (S_1) by the relaxation of the electron transferred by the light absorption on an antibonding π orbital [40]. The preservation of the emission peak situated at $\lambda=680$ nm for two different excitation wavelengths sustains the compositional homogeneity of the film. The luminescence in Alq3, presented in Figure 32, is generated by excitations localized on individual molecule with optical properties independent of molecular environment [58]. The presence of two isomers with different spatial configurations is sustained by the generation of different emission peaks for different excitation wavelengths. The significant Stokes shift in the both spectra of PTCDA ($\Delta E=0.40$ eV) and Alq3 ($\Delta E=0.9$ eV) between the peaks of the lowest level absorption and highest fluorescence emission level, and large Frank-Condon shift (0.40-2.3 eV) measured peak to peak between the absorption and emission spectra, can be correlated with effects determined by the solid state structure and with important conformational differences between the ground state and the excited state [40].

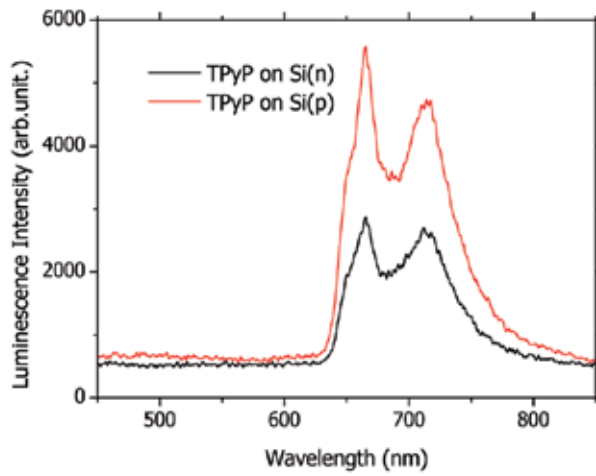


Figure 33. Photoluminescence spectra of TPyP films deposited by vacuum evaporation on different types of Si substrates [46].

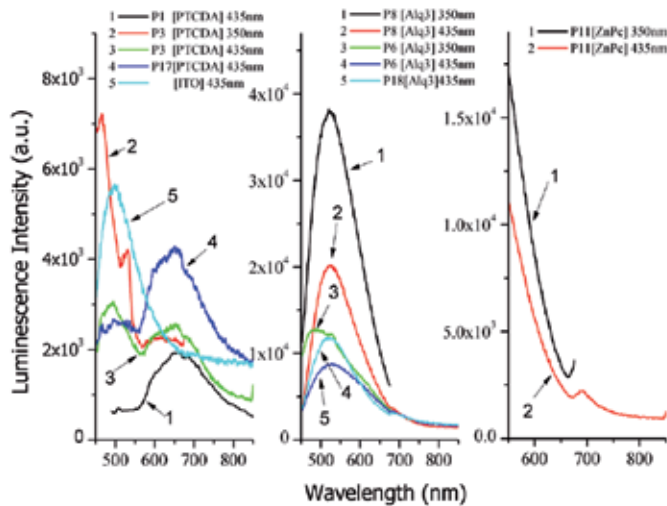


Figure 34. Photoluminescence spectra of organic thin films deposited by MAPLE for two excitation wavelengths: (a) PTCDA on Si (1 and 2), PTCDA on ITO/ZnPc (4); (b) Alq3 on Si (1 and 3), Alq3 on ITO/ZnPc (5); (c) ZnPc on Si (1) [54].

The photoluminescence spectra of TPyP films deposited on Si by vacuum evaporation have revealed in Figure 33 two emission bands situated at 660 nm and 700 nm associated to Q bands and corresponding to free-base ethio type porphyrin [46].

The photoluminescence investigations have evidenced the preservation of the chemical structure of the compounds (PTCDA, Alq₃, ZnPc) during the deposition by MAPLE, because we have identified the characteristic emission peaks corresponding to each compound, as can be seen in Figure 34. The emission peak situated at 500 nm, in PTCDA deposited on Si, is associated with monomer-like species and that situated at 650 nm can be associated with two excimeric states [54]. The emission peak in Alq₃ film deposited on Si is situated at 520 nm being associated with the excitation of median isomer dominant at the deposition temperature. The emission peak in ZnPc film deposited on Si is situated between 650 nm and 750 nm and can be associated with the deexcitation from the first excited singlet state with an energy of 1.8 eV [54]. In the heterostructures with double organic layer the weak emission of ZnPc is masked by the stronger emission of PTCDA and Alq₃.

3.3. Electrical properties of aromatic derivatives thin films

A material could become interesting for optoelectronic application if it is adequate from the point of view of both optical and electrical properties (such as good contact inject and transport the charge carriers). A good injection of the charge carrier was evidenced at the ITO/m-DNB contact compared to ITO/benzil contact as can be shown in Figure 35. This can be explain by the difference in the energetic contact barrier, which is higher between ITO and benzil than ITO and m-DNB, as a consequence of the position of the highest occupied molecular orbital (HOMO) and lowest unoccupied molecular orbital (LUMO) in these aromatic derivative compounds.

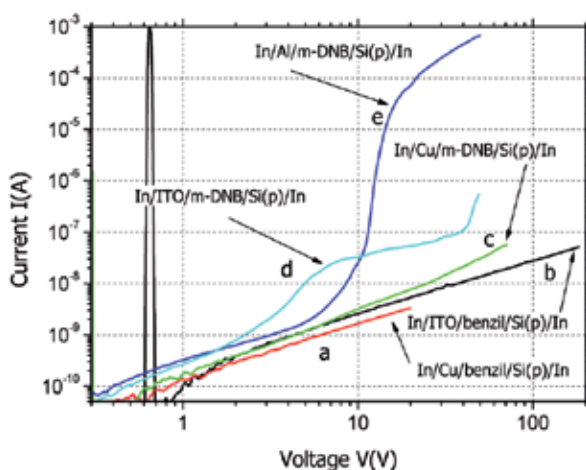


Figure 35. I-V characteristics of the benzil and m-DNB based heterostructures with Si(p) anode and different cathode (Cu, ITO, Al): (a) Cu for benzil; (b) ITO for benzil; (c) Cu for m-DNB; (d) ITO for m-DNB, (e) Al for m-DNB [61]. For contacting we have used very high purity In.

For the sample based on m-DNB two different regions were identified on the I-V characteristic: the ohmic behaviour region at low voltages and a region with a behaviour associated to the space charge limited effect at voltages > 5 V. Both in Figure 35 and Figure 36 can be seen that at voltages > 5 V the effect of the space charge limitation of the current becomes important in the heterostructure ITO/m-DNB/Si(p). The steep increase in the current at voltage ~ 10 V for Al/m-DNB/Si(p) and ITO/m-DNB/Si(p) can be associated with an avalanche generation mechanism involving energetic states situated in the band gap, in the interface region, state generated by the easy diffusion of Al in organic layer favoured by the first ionization potential of Al (5.98 eV).

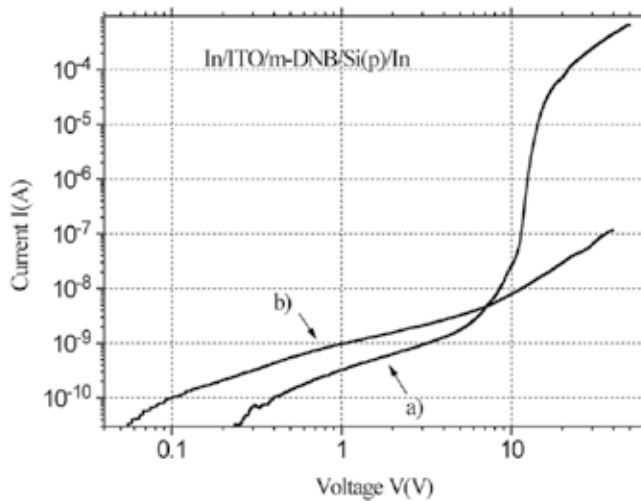


Figure 36. I-V characteristics for ITO/m-DNB/Si(p) heterostructures for different type ITO contacts. For contacting we have used very high purity In [61].

The different ITO/m-DNB/Si heterostructures have shown significantly different shapes of the I-V characteristics as a consequence of the crystalline quality of the organic layer, in correlation with the preparation method (rapid thermal directional solidification).

A blocking diode behaviour, both at direct and reverse bias, has been emphasized in Figure 37 at low applied voltages in ITO/TPyP/Si heterostructures, independent of the type of conduction of the Si electrode. For these heterostructures no photoelectric effect has been evidenced. These I-V characteristics are quasi-linear at low voltages and at higher voltages the limitation of the current determined by the space charge and/or by trap-charge became very important as can be seen in Figure 37.

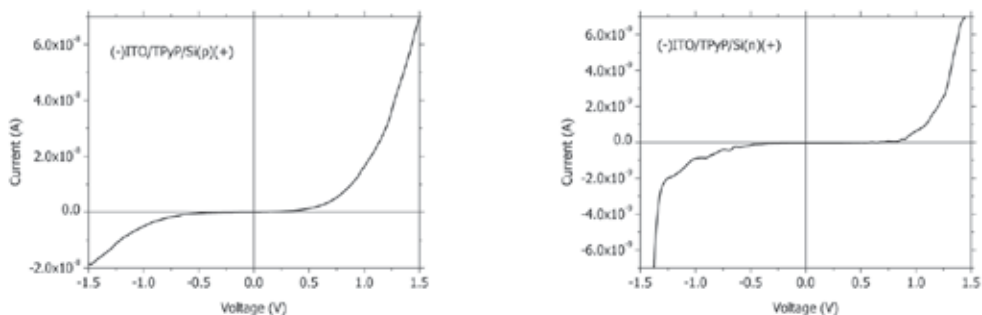


Figure 37. I-V characteristics for ITO/TPyP/Si heterostructures [46].

The heterostructure Au/TPyP/Si, at an illumination through the metallic electrode and direct polarization, shows a rectifier behaviour presented in Figure 38, determined by the energetic barrier at the contact Au/TPyP, which can be lowered applying a voltage > 0.30 eV. The linear behaviour at low applied voltages became a power dependence with $n>2$ at voltages >0.1 V and corresponds to trap charge limited current. At reverse bias, the same heterostructure shows a blocking behaviour independent of the applied voltage, because the energetic barrier is too high and can't be surpass by the charge carriers [46].

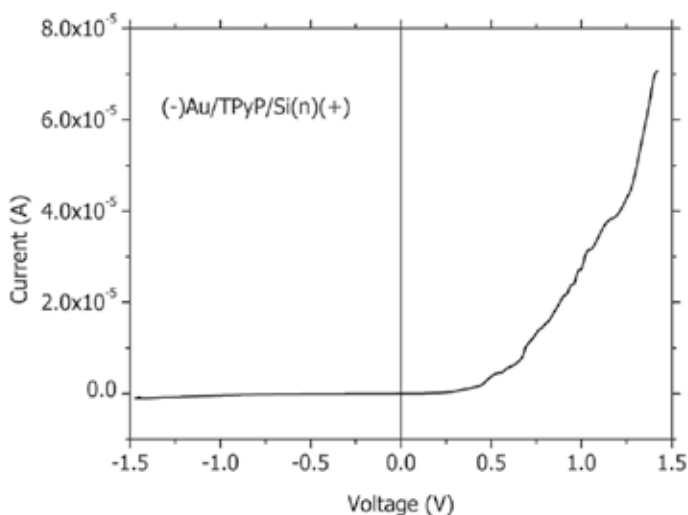


Figure 38. I-V characteristic of the Au/TPyP/Si heterostructure [46].

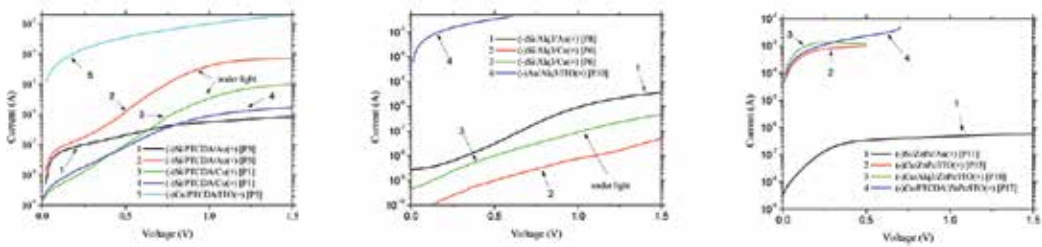


Figure 39. I-V characteristics of Si or ITO/organic layer(s)/Au or Cu heterostructures prepared by MAPLE: based on PTCDA (a) curves 2 and 3 under illumination; based on Alq3 (b) curve 3 under illumination; based on ZnPc (c) all in dark [54].

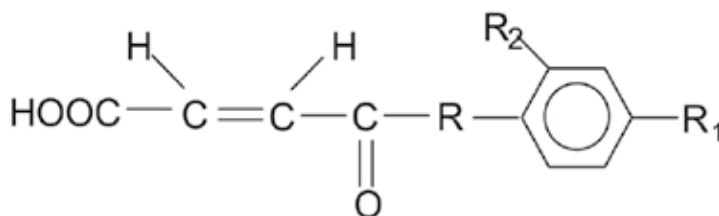
In Figure 39 a, b, c are presented the I-V characteristics in dark and under illumination, the highest current ($\sim 10^{-4}$ - 10^{-3} A) being obtained in dark with the structure prepared with PTCDA, Alq3 or ZnPc on ITO substrate, at low applied voltage of 0.5 V [54]. This current is with three orders higher than the current for the same structure realized on Si. This behaviour is correlated, in the first case, with the height of the energetic barriers at the interfaces that favour the injection of holes from ITO positively biased in organic. The I-V characteristics obtained under continuous illumination at an applied voltage of 1 V, indicate a higher current in the heterostructures realized with PTCDA and, Si and Cu electrodes, explained by the higher energetic barrier for electron injection at the contact Alq3/Cu ($\Delta E=1.5$ eV) compared to PTCDA/Cu ($\Delta E=0.7$ eV). The current is one order higher than the dark current confirming the photo generation process [54]. In the heterostructures with double organic layer and, ITO and Cu electrodes, we have obtained a current of 2×10^{-3} A at 0.5 V, explained by the energetic barrier in ITO/ZnPc/Alq3/Cu heterostructure and by the presence of the interface dipoles reducing the energetic barrier and improving the conduction in ITO/ZnPc/PTCDA/Cu heterostructure.

4. Organic/organic composite films based on aromatic derivative inclusions for optoelectronic applications

Lately, a special attention has been paid to composite materials based on different organic polymeric matrix and organic inclusions to obtain materials combining the properties of the both components [25; 34; 45; 62; 63]. This field of research has developed from fundamental investigations to the synthesis of new monomers to be introduced in polymeric matrix. The most important advantage of the polymeric matrix is the possibility to deposit thin films using inexpensive methods, such as the deposition from solution by spin-coating. The limiting parameter is the quality of the layer and can be controlled by the control of the experimental conditions. A special attention is focused to the identification and development of π -conjugated systems with functional groups that assure an improvement in the emission properties and charge carrier mobility necessary for optoelectronic applications.

We have emphasised the effect of the polycarbonate of bisphenol A matrix on the properties of the synthesised amidic monomers with $-\text{CN}$ and $-\text{NO}_2$ substituent groups with the purpose to manipulate the local molecular environment of the monomer for changing the physical properties of the films (transmission, luminescence, electrical transport) in correlation with the quality of the spin-coated layers.

The polycarbonate of bisphenol A, utilized as matrix, is characterised by a large domain of transparency, high transmission in visible, high refraction index, solubility in common solvents. As inclusions, to be embedded in the matrix, we have selected monomers characterised by a maleamic acid structure with different functional groups:



where $\text{R}=\text{NH}$, $\text{R}_1=-\text{CN}$ for (MM3); $\text{R}=\text{NH}$, $\text{R}_1=-\text{NO}_2$; $\text{R}_2=-\text{NO}_2$ for (MM5) [64].

After testing the process of layer formation in correlation with the surface energy by contact angle measurements using two different solvents, we have selected dimethylformamide (DMF) for the preparation of the “mother solution” that contain the both components, matrix and inclusion. We have varied the weight ratio between the components 1/3;1/2; 1/1, using the pre-wetting of the surface and different duration and rotation speeds for the spreading stage ($t_1=3\text{s}$; 6s; 9s; 12s; $v_1=0.5$ krpm; 0.7 krpm; 0.9 krpm; 1.13 krpm) and homogenisation stages ($t_2= 10\text{s}$; 20s; $v_2=1.6$ krpm; 1.9 krpm; 2.2 krpm; 2.7 krpm; 3 krpm), with the purpose to identify the most adequate conditions for the deposition of layers [64].

UV-Vis transmission spectra presented in Figure 40 have evidenced differences in the behaviour of the composite material prepared with (MM3) and (MM5), determined by differences in the chemical structure of these components. The shape of the transmission curve is determined by the substituent to the aromatic nucleus and depends on the lone electron pairs of the oxygen atoms in the carbonyl and nitrous groups involving (n, π^*) state, which are splitted because of the interaction in the solid state between the polycarbonate matrix and (MM5) monomer. No significant difference has been emphasised, in the UV-VIS spectra, between the monomer deposited by vacuum evaporation and the same monomer embedded in a polymeric matrix and deposited by spin-coating. Although (MM3) shows also lone electron pairs the interaction between the cyan groups and the carbonyl groups is not so intense in the solid state to favour the splitting of the (n, π^*) energetic level.

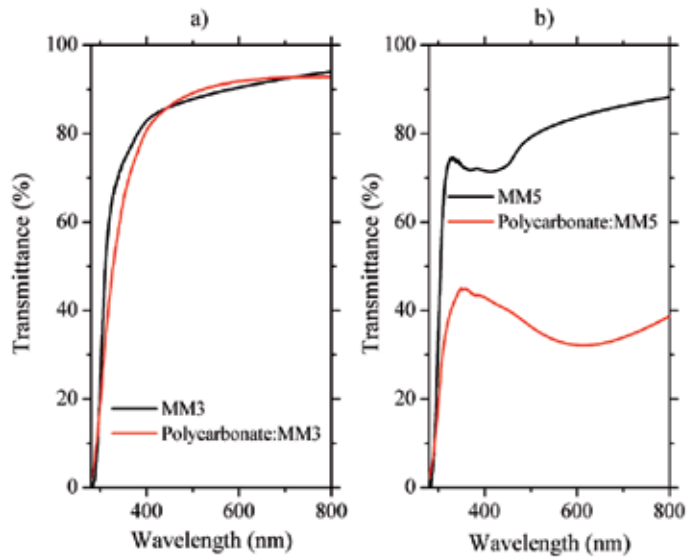


Figure 40. Comparative UV-VIS spectra of MM3 and MM5 monomers deposited by vacuum evaporation and polycarbonate /MM3 and polycarbonate /MM5 deposited by spin coating, on glass substrate [64].

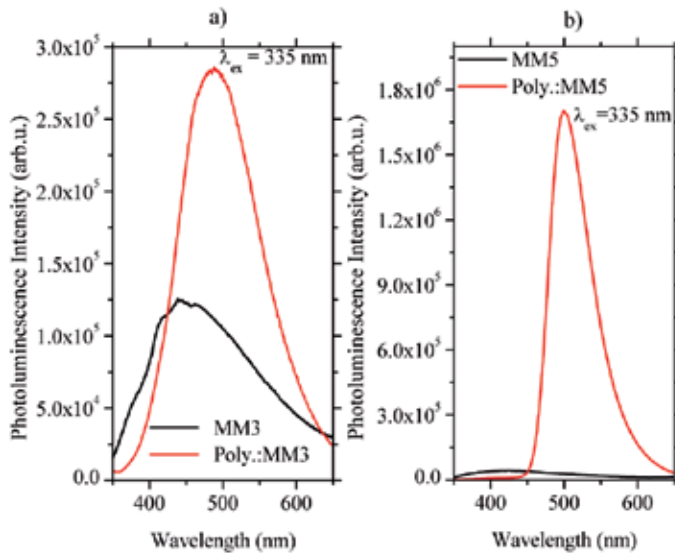


Figure 41. Photoluminescence spectra of monomers (MM3) and (MM5) deposited by vacuum evaporation and polycarbonate/MM3 and polycarbonate/MM5 deposited by spin coating on glass substrates [64].

The emission of the polymer/monomer composite material is determined by the interaction between the chromophoric groups in monomer with the polymeric matrix. This interaction can generate the shift, broadening or strengthening of the emission peak [64].

The Figure 41 shows that the polymeric matrix significantly affects the emission spectra of the monomers characterised by a peak situated at 430 nm in (MM5) and 450 nm in (MM3). These shapes of the spectra can be correlated with the emission properties of the substituted benzene nucleus [65] and with the involvement of the (n, π^*) states lower than the usual singlet excited states. The strongest emission was obtained for monomer (MM5) in polycarbonate of bisphenol A matrix probably due to the strong absorption of the excitation radiation ($\lambda=335$ nm) assuring a higher efficiency of the emission process.

In composite material based on (MM5) the emission spectra show a maximum around 510 nm and in composite material based on (MM3) a slightly weaker and broader maximum around 480 nm. Figure 41 has not evidenced a strong broadening effect of the matrix on the emission spectrum of monomers. The emission of polycarbonate:MM5 is not blue shifted and therefore we suppose that the monomer is not highly stressed in the polycarbonate matrix.

In Figure 42 are presented some results on the investigation of the effect of the polymeric matrix on the electrical transport properties of Si/monomer/Si and Si/polycarbonate:monomer/Si heterostructures.

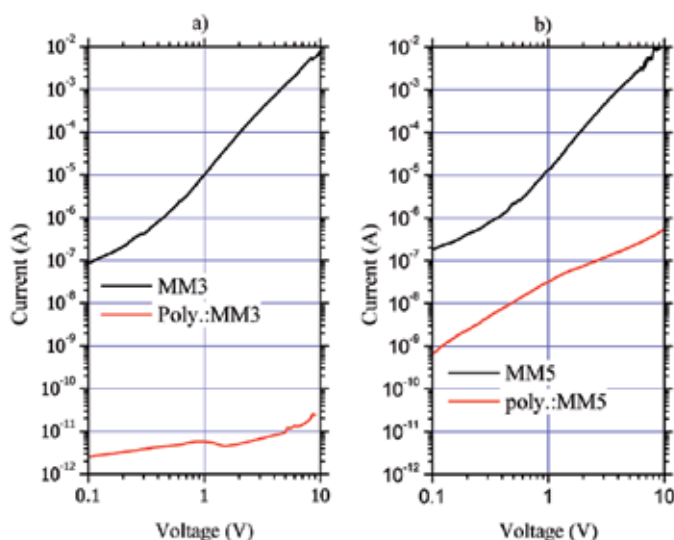


Figure 42. I-V characteristics of Si/MM3/Si and Si/polycarbonate:MM3/Si heterostructures (a) and Si/MM5/Si and Si/polycarbonate/MM5/Si heterostructures (b) [64].

We have analysed the electrical properties of the heterostructure Si/monomer/Si and Si/polycarbonate:monomer/Si at room temperature, testing the reproducibility of the measure-

ments and considering only the typical behaviour. The heterostructures realized with composite materials show a current with 3 orders lower than the heterostructures realized only with monomers. The charge carrier transport is mainly affected by the insulating character of the polymeric matrix. The highest current (3×10^{-8} A) has been obtained in heterostructure Si/polycarbonate:MM5/Si for an applied voltage of 1 V and for voltages between 0.1 V and 1 V the characteristic is weakly superlinear [61]. For the heterostructures realized only with monomers the I-V characteristics are linear at low voltages and become strongly superlinear for voltages >0.2 V.

The films obtained from the polycarbonate containing the monomer with two nitrous substituents (MM5) to the aromatic nucleus have shown good transparency, and photoluminescence in the green region and promising electrical properties at voltages >0.6 V ($I=10^{-8}$ A) with a close to linear characteristic at voltages between 1 V and 10 V [64].

Also this organic/organic composite material seems to be promising for optoelectronic applications, the spin coated composite layers are characterised by a specific morphology and a high degree of disorder which affect the optical and electrical properties and make difficult their control.

5. Conclusions

In this chapter we summarize some of the most important results of our work in the field of new materials for applications in the field of optoelectronics. Our interest was focused on organic molecules containing electrons, occupying non-localised molecular orbitals in strongly conjugated systems, such as aromatic derivatives compounds (benzil, m-DNB, PTCDA, ZnPc, Alq3, TPyP) for which we have evidenced large transparency domain and good fluorescence emission.

We have realised a comparative investigation on the properties of the same aromatic derivative compound as bulk and thin film material showing both good optical, including luminescent, properties. The interest in studying bulk organic crystals is justified by the perspective to use these materials as a crystalline host matrix both for organic and inorganic guests/inclusions. The organic matrix assures an efficient fluorescence mechanism and from the guest component it is expected an improvement in stability, emission properties of the matrix and electrical mobility. A special attention was paid to the preparation methods both for bulk crystals (emphasising the correlation between the growth interface stability and quality of the organic crystal) and thin films (emphasising the effect of the thin film deposition method -directional solidification, vacuum evaporation, MAPLE- on the properties of the organic film and heterostructures).

Thin films from the above mentioned aromatic derivatives are preferred as organic matrix for host/guest systems because of the major problems associated with bulk crystalline matrices determined by the difficulties of their growing, processing and doping to assure homogeneous distribution of the guest atoms.

Important results have been brought in the field of molecular organic matrix based on aromatic derivatives (benzil, m-DNB)/inorganic (iodine, silver, sodium) or/and organic (m-DNB, naphthalene, bulk) composite systems and in the field of composite films prepared from polymeric matrix and active monomeric inclusions based on π -conjugated systems containing functional groups with special properties, to improve the properties of film forming, emission properties of the matrix and the charge carrier mobility in the matrix, with the purpose to obtain materials for potential optoelectronic applications.

We have emphasised the effect of the polycarbonate of bisphenol A matrix on the properties of the synthesised amidic monomers with $-\text{CN}$ and $-\text{NO}_2$ substituent groups with the purpose to modify the local molecular environment of the monomer and change the optical and electrical properties of the films.

Author details

Florin Stanculescu^{1*} and Anca Stanculescu²

*Address all correspondence to: fstanculescu@fpce1.fizica.unibuc.ro

1 University of Bucharest, Bucharest-Magurele,, Romania

2 National Institute of Materials Physics, Bucharest-Magurele,, Romania

References

- [1] Helfrich, W., & Schneider, W. G. (1965). Recombination radiation in anthracene crystals. *Phys Rev. Lett.*, 14(7), 229-231.
- [2] Tang, C. W., & Van Slyke, S. A. (1987). Organic electroluminescent diodes. *Appl. Phys. Lett.*, 51(12), 913-915.
- [3] Van Slyke, S. A., Chen, C. H., & Tang, C. W. (1996). Organic electroluminescent devices with improved stability. *Appl. Phys. Lett.*, 69(15), 2162-2160.
- [4] Kijima, Y., Asai, N., & Tamura, S. I. (1999). A blue organic light emitting diode. *Jpn. J. Appl. Phys. Part 1*, 38(9A), 5274-5277.
- [5] Hung, L. S., Tang, C. W., & Mason, M. G. (1997). Enhanced electron injection in organic electroluminescence devices using an Al/LiF electrode. *Appl. Phys. Lett.*, 70(2), 152-154.
- [6] Parthasarathy, G., Shen, C., Kahn, A., & Forrest, S. R. (2001). Lithium doping of semi-conducting organic charge transport materials. *J. Appl. Phys.*, 89(9), 4986-4992.

- [7] Brütting, W., Riel, H., Beierlein, T., & Riess, W. (2001). Influence of trapped and interfacial charges in organic multilayer light-emitting devices. *J. Appl. Phys.*, 89(3), 1704-1712.
- [8] Xue, J., & Forrest, S. R. (2004). Carrier transport in multilayer organic photodetectors: I. Effects of layer structure on dark current and photoresponse. *J. Appl. Phys.*, 95(4), 1859-1868.
- [9] Huang, J., Blochwitz-Nimoth, J., Pfeiffer, J. M., & Leo, K. (2003). Influence of the thickness and doping of the emission layer on the performance of organic light-emitting diodes with PiN structure. *J. Appl. Phys.*, 93(2), 838-844.
- [10] Parthasarathy, G, Burrows, P. E, Khalfin, V, Kozlov, V. G, & Forrest, S. R. (1998). A metal-free cathode for organic semiconductor devices. *Appl. Phys. Lett.*, 72(17), 2138-2140.
- [11] Gu, G., Parthasarathy, G., & Forrest, S. R. (1999). A metal-free, full-color stacked organic light-emitting device. *Appl. Phys. Lett.*, 74(2), 305-307.
- [12] Ichikawa, M., Amagai, J., Horiba, Y., & Koyama, T. (2003). Dynamic turn-on behavior of organic light-emitting devices with different work function cathode metals under fast pulse excitation. *J. Appl. Phys.*, 94(12), 7796-7800.
- [13] Guo, T. F., Yang, F. S., Tsai, Z. J., & Feng, G. W. (2006). High-brightness top-emissive polymer light-emitting diodes utilizing organic oxide/Al/Ag composite cathode. *Appl. Phys. Lett.* 051103-1-051103-3, 89(5)
- [14] Barth, S., Müller, P., Riel, H., Seidler, P. F., Rieß, Vestweber, H., & Bäessler, H. (2001). Electron mobility in tris(8-hydroxy-quinoline)aluminium thin films determined via transient electroluminescence from single- and multilayer organic light-emitting diodes. *J. Appl. Phys.*, 89(7), 3711-3719.
- [15] Kalinowski, J, Picciolo, L. C, Murata, H, & Kafafi, Z. H. 2001. Effect of emitter disorder on the recombination zone and the quantum yield of organic electroluminescent diodes. *J. Appl. Phys.*, 89(3), 1866-1874.
- [16] Sun, J. X., Zhu, X. L., Meng, Z. G., Yu, X. M., Wong, M., & Kwok, H. S. (2006). An efficient stacked OLED with double-sided light emission SID International Symposium. *Digest of Technical Papers SID Symposium Digest*, 37, 1193-1196.
- [17] Shao, Y., & Yang, Y. (2005). Organic solid solutions: formation and applications in organic light-emitting diodes. *Adv. Funct. Mater.*, 15(12), 1781-1786.
- [18] Burroughes, J. H., Bradley, D. C., Brown, A. R., Marks, R. N., Mackay, K., Friend, R. H., Burn, P. L., & Holmes, A. B. (1990). Light-emitting diodes based on conjugated polymers. *Nature*, 347(6293), 539-541.
- [19] Tse, S. C., Tsung, K. K., & So, S. K. (2007). Single-layer organic light-emitting diodes using naphthyl diamine. *Appl. Phys. Lett.*, 90(21), 213502.

- [20] Lu, M. H., & Sturm, J. C. (2002). Optimization of external coupling and light emission in organic light-emitting devices: modeling and experiment. *J. Appl. Phys.* , 91(2), 595-604.
- [21] Stanculescu, A., Antohe, S., Alexandru, H. V., Tugulea, L., Stanculescu, F., & Socol, M. (2004). Effect of dopant on the intrinsic properties of some multifunctional aromatic compounds films for target applications. *Synthetic Metals*, 147(1-3), 215-220.
- [22] Stanculescu, A., & Popina, Al. (1996). M -Dinitrobenzene optical nonlinear organic crystals growth for optoelectronics. *SPIE Proc*, 2700.
- [23] Stanculescu, A., Stanculescu, F., & Alexandru, H. (1999). Melt growth and characterization of pure and doped meta-dinitrobenzene crystals. *J. Cryst. Growth*, 198/199(1-4), 572-577.
- [24] Stanculescu, A. (2007). Investigation of the growth process of organic/inorganic doped aromatic derivatives crystals. *J. Optoelectron. Adv. Mater.* , 9(5), 1329-1336.
- [25] Stanculescu, A., Tugulea, L., Alexandru, H. V., Stanculescu, F., & Socol, M. (2005). Molecular organic crystalline matrix for hybrid organic-inorganic (nano) composite materials. *J. Cryst. Growth*, 275(1-2), e1779-e1786.
- [26] Sekerka, R. F. (1968). Morphological Stability. *J. Cryst. Growth*, 3(4), 71-81.
- [27] Mullins, W. W., & Sekerka, R. F. (1963). Morphological Stability of a Particle Growing by Diffusion or Heat Flow. *J. Appl. Phys.* , 34(2), 323-329.
- [28] Mullins, W. W., & Sekerka, R. F. (1964). Stability of a Planar Interface During Solidification of a Dilute Binary Alloy. *J. Appl. Phys.* , 35(2), 444-451.
- [29] Flemings, M. C. (1974). Solidification processing. *Mc.Graw-Hill, Inc.*
- [30] Kitaigorodski, A. I. (1966). *J. Chem. Phys. Phys. Chem Biol.*, 63, 9-16.
- [31] Kitaigorodski, A. I. (1973). Molecular crystals and molecules. *Academic Press, New York*.
- [32] Halfpenny, P. J., Ristic, R. I., Shepherd, E. E. A., & Sherwood, J. N. (1993). The crystal growth behaviour of the organic non-linear optical material 2-(α -methylbenzylamino)-5nitropyridine (MBANP). *J. Cryst. Growth*, 128(1-4), 970-975.
- [33] Leonard, N. J., & Blout, E. R. (1950). The Ultraviolet Absorption Spectra of Hindered Benzils. *J. Am. Chem. Soc.* , 72(484), 487.
- [34] Stanculescu, A., Mihut, L., Stanculescu, F., & Alexandru, H. (2008). Investigation of emission properties of doped aromatic derivative organic semiconductor crystals. *J. Cryst. Growth*, 310(7-9), 1765-1771.
- [35] Windsor, M. W. (1965). Luminescence and energy transfer in: D. Fox, M. M. Labes, A. Weissberger (eds.). *Physics and chemistry of the organic solid state, vol. II, Interscience, New York*, 343.

- [36] Rothe, C., Guentner, R., Scherf, U., & Monkman, A. P. (2001). Trap influenced properties of the delayed luminescence in thin solid films of the conjugated polymer poly(9,9- di(ethylhexyl)fluorene). *J. Chem. Phys.* , 115(20), 9557-9562.
- [37] Bardeen, J., & Brattain, W. H. (1948). The transistor, a semi-conductor triode. *Phys. Rev.* , 74(2), 230-231.
- [38] Schockley, W. (1949). The theory of p-n junctions in semiconductors and p-n junction transistors. *Bell System Technical Journal*, 28(3), 435-489.
- [39] Gaffo, L., Cordeiro, M. R., Freitas, A. R., Moreira, W. C., Gitotto, E. M., & Zucolotto, V. (2010). The effects of temperature on the molecular orientation of zinc phthalocyanine films. *J. Mater. Sci.* , 45(5), 1366-1370.
- [40] Stanculescu, A., Stanculescu, F., Tugulea, L., & Socol, M. (2006). Optical properties of 3,4,9,10-perylenetetracarboxylic dianhydride and 8-hydroxyquinoline aluminium salt films prepared by vacuum deposition. *Mat. Sci. Forum*, 514-516, Part 2, 956-960.
- [41] Wu, C. I., Hirose, Y., Sirringhaus, H., & Kahn, A. (1997). Electron-hole interaction energy in the organic molecular semiconductor PTCDA. *Chem. Phys. Lett.* , 272(1-2), 43-47.
- [42] Zügang, L., & Nazare, H. (2000). White organic light-emitting diodes from both hole and electron transport layers. *Synthetic Metals*, 111-112, 47-51.
- [43] Curioni, A., & Andreoni, W. (2001). Computer simulations for organic light-emitting diodes. *IBM J of Research and Development*, 45(1), 101-114.
- [44] Auwärter, W., Weber-Bargioni, A., Riemann, A., Schiffrin, A., Gröning, O., Fasel, R., & Barth, J. V. (2006). Self-assembly and conformation of Tetra-pyridil-porphyrin molecules on Ag(111). *J. Chem. Phys.*, 124(19), 194708-1-194708-6.
- [45] Stanculescu, F., Stanculescu, A., & Socol, M. (2006). Light absorption in meta-dinitrobenzene and benzyl crystalline films. *J. Optoelectron. Adv. Mater.* , 8(3), 1053-1056.
- [46] Socol, M., Rasoga, O., Stanculescu, F., Girtan, M., & Stanculescu, A. (2010). Effect of the morphology on the optical and electrical properties of TPyP thin films deposited by vacuum evaporation. *Optoelectronics and Advanced Materials-Rapid Communications*, 4(12), 2032-2038.
- [47] Socol, G., Mihailescu, I. N., Albu, A. M., Antohe, S., Stanculescu, F., Stanculescu, A., Mihut, L., Preda, N., Socol, M., & Rasoga, O. (2009). MAPLE prepared polymer thin films for non-linear optic applications. *Appl. Surf. Sci.* , 255(10), 5611-5614.
- [48] Evans, T. R., & Leermakers, P. A. (1967). Emission spectra and excited-state geometry of α -diketones. *J. Am. Chem. Soc.* , 89(17), 4380-4382.
- [49] Kohler, B. E., & Loda, R. T. (1981). Spectroscopy of the benzil-bibenzyl mixed crystal system: High resolution optical studies. *J. Chem. Phys.* , 74(1), 18-24.

- [50] Coppens, P., Ma, B. Q., Gerlits, O., Zhang, Y., & Kulshrestha, P. (2002). Crystal engineering, solid state spectroscopy and time-resolved diffraction. *Cryst. Eng. Commun.*, 4(54), 302-309.
- [51] George, H., & Guo, Q. (2008). Self-assembled two-dimensional supramolecular architectures of zinc porphyrin molecules on mica. *J. Phys.: Conference series*, 100(5), 052077.
- [52] Auwärter, W., Klappenberger, F., Weber-Bargioni, A., Schiffrin, A., Strunskus, T., Wöll, C., Pennec, Y., Riemann, A., & Barth, J. V. (2007). Conformational adaptation and selective adatom capturing of tetrapyrrolyl-porphyrin molecules on a copper (111) surface. *J. Am. Chem. Soc.*, 129(36), 11279-11285.
- [53] Klappenberger, F., Weber-Bargioni, A., Auwärter, W., Marschall, M., Schiffrin, A., & Barth, J. V. (2008). Temperature dependence of conformation, chemical state and metal-direct assembly of tetrapyrrolyl-porphyrin on Cu (111). *J. Chem. Phys.*, 129(21), 214702-214702.
- [54] Stanculescu, A., Socol, M., Socol, G., Mihailescu, I. N., Girtan, M., & Stanculescu, F. (2011). Maple prepared organic heterostructures for photovoltaic applications. *Appl. Phys. A*, 104(3), 921-928.
- [55] Sadrai, M., Hadel, L., Sauer, R. R., Husain, S., Krogh-Jespersen, K., Westbrook, J. D., & Bird, G. R. (1992). Lasing action in a family of perylene derivatives: singlet absorption and emission spectra, triplet absorption and oxygen quenching constants and molecular mechanics and semiempirical molecular orbital calculations. *J. Phys. Chem.*, 96(20), 7988-7996.
- [56] Jian, Z. A., Luo, Y. Z., Chung, J. M., Tang, S. J., Kuo, M. C., Shen, J. L., Chiu, K. C., Yang, C. S., Chou, W. C., Dai, C. F., & Yeh, J. M. (2007). Effect of isomeric transformation on characteristics of Alq₃ amorphous layers prepared by vacuum deposition at various substrate temperature. *J. Appl. Phys.* 123708-1-123707-6, 101(12)
- [57] Senthilarasu, S., Sathyamoorthy, R., Latitha, S., Subbarayan, A., & Natarajan, K. (2004). Thermally evaporated ZnPc thin films-band gap dependence on thickness. *Sol. Energy Mater. Sol. Cells*, 82(1-2), 179-186.
- [58] Burrows, P. E., Shen, Z., McCarty, D. M., Forrest, S. R., Cronin, J. A., & Thompson, M. E. (1996). Relationship between electroluminescence and current transport in organic heterojunction light-emitting devices. *J. Appl. Phys.*, 79(10), 7991-8006.
- [59] Ferguson, A. J., & Jones, T. S. (2006). Photophysics of PTCDA and me-PTCDI thin films: effects of growth temperature. *J. Phys. Chem. B*, 110(13), 6891-6898.
- [60] Haas, M., Shi-Xia, L., Kahnt, A., Leiggner, C., Guldi, D. M., Hauser, A., & Decurtins, S. (2007). Photoinduced energy transfer processes within dyads of metallophthalocyanines compactly fused to a Ruthenium (II) polypyridine chromophore. *J. Org. Chem.*, 72(20), 7533-7543.

- [61] Stanculescu, A., & Stanculescu, F. (2007). Investigation of the properties of indium tin oxide-organic contacts for optoelectronic applications. *Thin Solid Films*, 515(24), 8733-8737.
- [62] Lee, K. J, Oh, J. H, Kim, Y, & Jang, J. (2006). Fabrication of photoluminescent-dye embedded poly(methyl methacrylate) nanofibers and their fluorescence resonance energy transfer properties. *Adv. Mater*, 18(17), 2216-2219.
- [63] Koratkar, N. A., Suhr, J., Johsi, A., Kane, R., Schadler, L., Ajayan, P. M., & Bertolucci, S. (2005). Characterizing energy dissipation in single-walled carbon nanotube polycarbonate composite. *Appl. Phys. Lett*, 87(6), 06312-1-06312-3.
- [64] Stanculescu, F., Stanculescu, A., Girtan, M., Socol, M., & Rasoga, O. (2012). Effect of the morphology on the optical and electrical properties of polycarbonate film doped with aniline derivatives monomers. *Synthetic Metals*, 161(23-24), 2589-2597.
- [65] Dulcic, A., & Sauteret, C. (1978). The Regularities Observed in the Second Order Hyperpolarizabilities of Variously Disubstituted Benzenes. *J. Chem. Phys.* , 69(8), 3453-3457.

Optoelectronic Oscillators Phase Noise and Stability Measurements

Patrice Salzenstein

Additional information is available at the end of the chapter

<http://dx.doi.org/10.5772/3463>

1. Introduction

A classical method to characterize the spectral density of phase noise of microwave oscillators is to compare the device under test (DUT) to another one, we call it the reference, with the same frequency if noise is expected to be better for the reference. In most of case it is possible to then characterize oscillators or synthesizers. But it is only possible if we can assign the same frequency to the DUT and the reference signal. However for some applications, we see that the DUT delivers a frequency hard to predict during the fabrication. We here focus on characterizing a special class of oscillators, called optoelectronic oscillators (OEO) [1]. An OEO is generally an oscillator based on an optical delay line and delivering a microwave signal [2]. Purity of microwave signal is achieved thanks to a delay line inserted into the loop. For example, a 4 km delay corresponds to a 20 μ s-long storage of the optical energy in the line. The continuous optical energy coming from a laser is converted to the microwave signal. This kind of oscillators were investigated [3]. By the way, such OEO based on delay line are still sensitive to the temperature due to the use of optical fiber. Recently, progress were made to set compact OEO thanks to optical mini-resonators or spheres [4 - 7]. Replacing the optical delay line with an ultra-high Q whispering gallery-mode optical resonator allows for a more compact setup and an easier temperature stabilization. In order to introduce into the loop the fabricated resonator in MgF_2 [8], CaF_2 or fused silica, it has to be coupled to the optical light coming from a fiber. Best way to couple is certainly to use a cut optical fiber through a prism. But a good reproducible way in a laboratory is to use a tapered fiber glued on a holder. Then appears a problem for determining the phase noise of such compact OEO, because the frequency is rarely predictable. It is impossible to choose the frequency of the modulation (for instance exactly 10 GHz) and that's why it is necessary to develop new instruments and systems to determine phase noise for any delivered signal

in X-band (8.2-12.4 GHz) for instance. Here we come to our goal. The aim of this chapter is to provide a tool for a better knowledge of the phase noise characterization of OEO's using an optoelectronic phase noise system. We logically start by giving the main principle of how work such a system. We see that the main idea is to use delay lines to perform phase noise measurements. We also considerably increase the performances of such a system by cross correlation measurement, thanks to the two quasi-identical arms developed instrument. Then we present a realized system and the evaluation of its uncertainty based on international standard for determination of uncertainties when characterizing an OEO in X-band.

2. Principle of the phase noise measurement system

A quasi-perfect RF-microwave sinusoidal signal can be written as :

$$v(t) = V_0 [1 + \alpha(t)] \cos(2\pi\nu_0 t + \varphi(t)) \quad (1)$$

where V_0 is the amplitude, ν_0 is the frequency, $\alpha(t)$ is the fractional amplitude fluctuation, and $\varphi(t)$ is the phase fluctuation. Equation (1) defines $\alpha(t)$ and $\varphi(t)$ in low noise conditions: $|\alpha(t)| \ll 1$ and $|\varphi(t)| \ll 1$. Short-term instabilities of signal are usually characterized in terms of the single sideband noise spectral density PSD $S(f)$. Phase noise $\mathcal{L}(f)$ is typically expressed in units of dBc/Hz, representing the noise power relative to the carrier contained in a 1 Hz bandwidth centered at a certain offsets from the carrier. So, S is typically expressed in units of decibels below the carrier per hertz (dBc/Hz) and is defined as the ratio between the one-side-band noise power in 1 Hz bandwidth and the carrier power:

$$\mathcal{L}(f) = \frac{1}{2} \cdot S\varphi(f) \quad (2)$$

This definition given in equation (2) includes the effect of both amplitude and phase fluctuations. Phase noise is the frequency domain representation of rapid, short-term, random fluctuations in the phase of a waveform, caused by time domain instabilities. However we must know the amplitude and phase noise separately because they act differently in the circuit. For example, the effect of amplitude noise can be reduced by amplitude limiting mechanism and mainly suppressed by using a saturated amplifier. Phase noise of microwave oscillators can usually be characterized by heterodyne measurement. Whereas, for such a system, we need a reference oscillator operating exactly at the frequency of the DUT with lower phase noise. Phase noise can be measured using a spectrum analyzer if the phase noise of the device under test (DUT) is large with respect to the spectrum analyzer's local oscillator. Care should be taken that observed values are due to the measured signal and not the Shape Factor of the spectrum analyzer's filters. Spectrum analyzer based measurement can show the phase-noise power over many decades of frequency. The slope with offset frequency in various offset frequency regions can provide clues as to the source of the noise, e.g. low frequency flicker noise decreasing at 30 dB per decade.

Reference is no more required for homodyne measurement with a delay line discriminator. At microwave frequencies, electrical delay is not suitable because of its high losses. However photonic delay line offers high delay and low attenuation equal to 0.2 dB/km at the wavelength $\lambda=1.55 \mu\text{m}$. Optoelectronic phase noise measurement system is schematically represented on Figure 1.

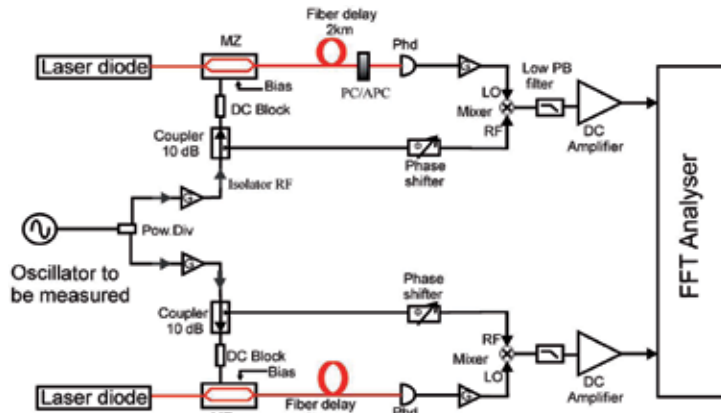


Figure 1. Phase noise bench.

It consists on two equal and fully independent channels. The phase noise of the oscillator is determined by comparing phase of the transmitted signal to a delayed replica through optical delay using a mixer. It converts the phase fluctuations into voltage fluctuations. An electro-optic modulator allows modulation of the optical carrier at microwave frequency. The length of the short branch where microwave signal is propagating is negligible compared to the optical delay line. Mixers are used as phase detectors with both saturate inputs in order to reduce the amplitude noise contribution. The low pass filters are used to eliminate high frequency contribution of the mixer output signal. DC amplifiers are low flicker noise.

The oscillator frequency fluctuation is converted to phase frequency fluctuation through the delay line. If the mixer voltage gain coefficient is K_φ (volts/radian), then mixer output rms voltage can be expressed as :

$$V_{out}^2(f) = K_\varphi^2 |H_\varphi(jf)|^2 S_\varphi(f) \tag{3}$$

Where $|H_\varphi(jf)|^2 = 4.\sin^2(\pi f\tau)$ is the transfer function of optical delay line, and f is the offset frequency from the microwave carrier. Equation (3) shows that the sensitivity of the bench depends directly on K_φ^2 and $|H_\varphi(jf)|$. The first is related to the mixer and the second essentially depends on the delay τ . In practice, we need an FFT analyzer to measure the spectral density of noise amplitude $V_{out}^2(f)/B$, where B is the bandwidth used to calculate $V_{out}(f)/B$. The phase noise of the DUT is finally defined by Eq. (4) and taking into account the gain of DC amplifier G_{DC} as :

$$\mathcal{L}(f) = [V_{out}^2(f)] \cdot / \cdot [2K_{\phi}^2 \cdot |H_{\phi}(jf)|^2 G_{DC}^2 \cdot B] \quad (4)$$

Such instruments has been recently introduced [3,9,10]. In section 3, we present concretely a realized optoelectronic phase noise measurement system.

3. Description of the realized system

In this section we concretely present a realization. We apply the principle detailed in the previous section to settle a phase noise optoelectronic system. For the demonstration, we characterize a frequency synthesizer as a DUT. It presents advantage to check different frequencies in X-band. System is shown on Figure 2.

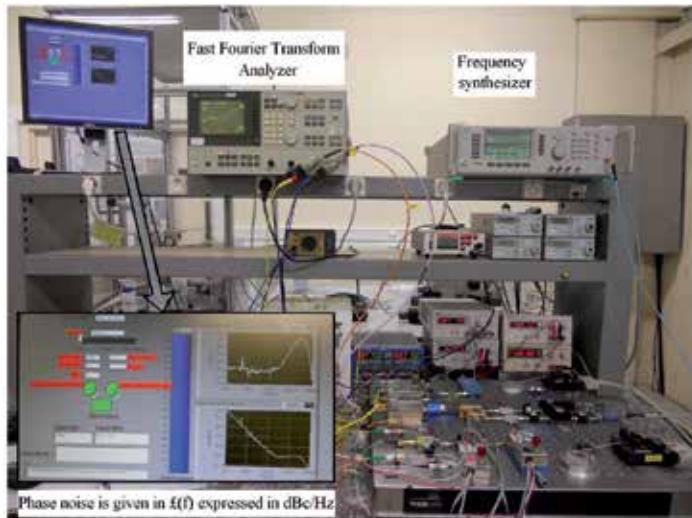


Figure 2. Picture of the phase noise measurement system.

The system is composed from different parts. We see on Figure 2, that we use a frequency synthesizer to check if the system works properly in X-band. On the picture we see the results of the phase noise characterization (inserted on the left of the picture) for a +3 dBm, 10 GHz signal. On the top of the picture we see the double channels Fast Fourier Transform analyzer used for this purpose (*Hewlett-Packard* HP3561A). $\mathcal{L}(f)$ expressed in dBc/Hz is deduced from the data provided by the FFT analyzer are given in V^2/Hz .

Figure 3 shows the picture of the *Hewlett-Packard* HP3561A FFT analyzer. Note that the data are expressed in V^2/Hz . It is necessary to use a program to get the expected quantity $\mathcal{L}(f)$ in dBc/Hz. It is developed in the next section of this chapter.



Figure 3. Picture of the double channels *Hewlett-Packard* HP3561A FFT analyzer.

4. Validation of the performances

The measured phase noise includes the DUT noise and the instrument background. The cross correlation method allows to decrease the cross spectrum terms of uncommon phase noise as $\sqrt{1/m}$, where m is the average number. Thereby uncorrelated noise is removed and sensitivity of measure is improved. To validate the measure of our phase noise bench, we need to compare data sheet of the commercial frequency synthesizer Anritsu/Wiltron 69000B [11] with the phase noise we measure using our system.

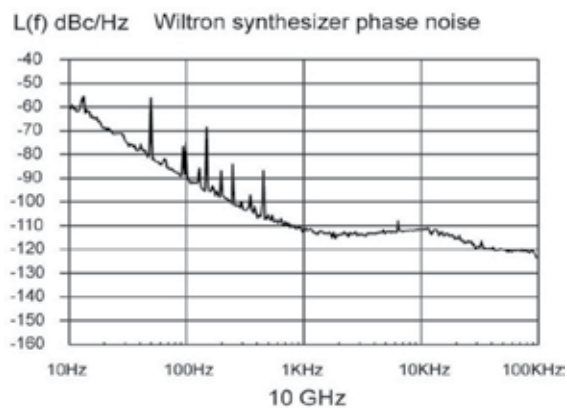


Figure 4. Phase noise (dBc/Hz) of the synthesizer measured at 10 GHz with $K_{\phi}=425$ mV/rad and $G_{DC}=40$ dB versus Fourier Frequency between 10 Hz and 100 kHz.

Figure 4 shows the result of this measure. We can see that our bandwidth is limited to 100 kHz ($\tau = 10 \mu\text{s}$) and the measured phase noise corresponds to the data sheet.

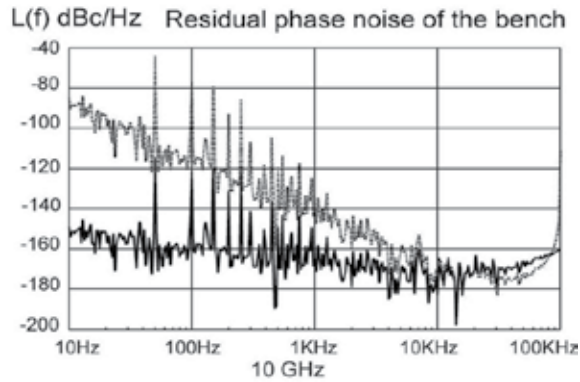


Figure 5. Phase noise floor (dBc/Hz) of the bench measured at 10 GHz with Anritsu synthesizer (500 averages) versus Fourier Frequency between 10 Hz and 100 kHz.

Figure 5 represents the background phase noise of the bench after performing 500 averaged with cross-correlation method, when removing the 2 km optical delay line. In this case, phase noise of the 10 GHz synthesizer is rejected. The solid curve shows noise floor (without optical transfer function) respectively better than -150 and -170 dBc/Hz at 10^1 and 10^4 Hz from the 10 GHz carrier. Dotted curve is the noise floor when optical fiber is introduced.

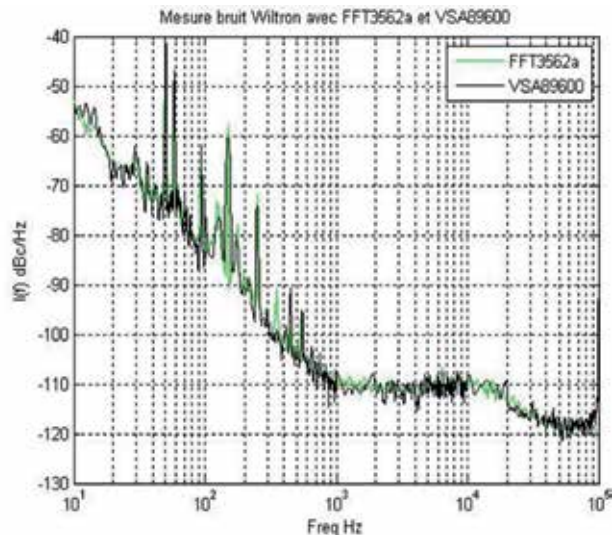


Figure 6. Spectral density of phase noise floor $L(f)$ expressed in dBc/Hz versus Fourier frequencies (in Hz) between 10 Hz and 100 kHz for a commercial synthesizer measured with our bench with $K_{\phi} = 425 \text{ mV/rad}$ and $GDC = 40 \text{ dB}$ for two different FFT analyzing system : *Hewlett-Packard 3562A* and *Agilent 89600*.

One can note that the use of a shorter delay line in a optoelectronic phase noise measurement system working in X-band, allow a characterization of the phase noise far from the carrier. Fourier frequency analysis can be extended from 10^5 to 2×10^6 Hz by introducing a 100 m delay line in addition of a 2 km optical fiber [12]. As the Fast Fourier Transform (FFT) analyzer (*Hewlett-Packard 3562A*) used for characterizing the noise up to 100 kHz from the carrier is not operating for higher frequencies, it is necessary to use another FFT such as an *Agilent 89600* for instance.

On Figure 6, we check that the two different FFT systems provide the same results for Fourier frequencies between 10 Hz and 100 kHz.

Note that our results are as expected with the data sheet of a 10 GHz phase noise spectrum for an *Wiltron 69000B* series. Our bandwidth is limited to 100 kHz ($\tau = 10 \mu\text{s}$) and the measured phase noise corresponds to the data sheet. Figure 6 then gives the noise floor of the instrument versus Fourier frequencies. The noise floor is respectively better than -90 and -170 dBc/Hz at 10^3 and 5×10^6 Hz from the carrier.

The introduction of a 100 m short fiber in addition to the 2 km fiber allows to characterize phase noise of oscillators with an optoelectronic phase noise measurement system.

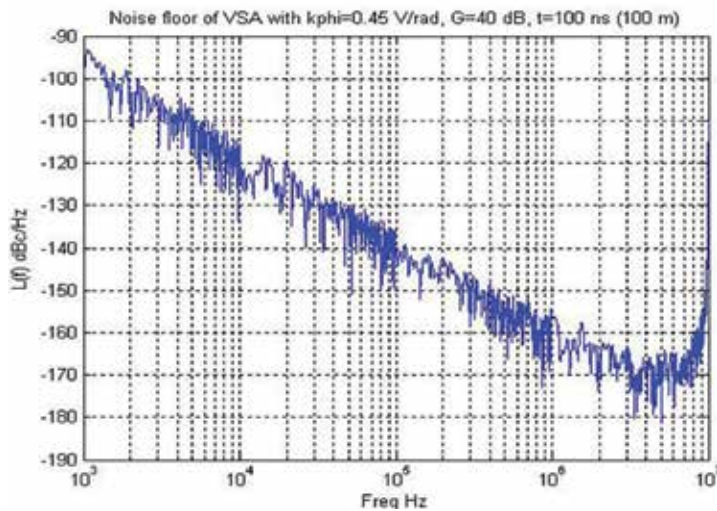


Figure 7. Spectral density of phase noise floor $L(f)$ expressed in dBc/Hz versus Fourier frequencies (in Hz) for the developed system when using the 100 meters delay lines.

100 m fiber corresponds to a 500 ns delay. So the 10^5 Hz limit due to the 2 km fiber can be extended from 10^5 to 2×10^6 Hz from the carrier. This system works for any microwave signal in X-band (8.2 – 12.4 GHz) especially for those delivered by optoelectronic oscillators. We see on Figure 7 that the noise floor of the system is in the range of -165 dBc/Hz at $5 \cdot 10^6$ Hz from the X-band microwave signal.

5. Evaluation of the uncertainty of such a measurement system

This evaluation is based on a previous work [13]. For the evaluation of the uncertainty, we use the main guideline delivered by the institution in charge of international metrology rules, *Bureau International des Poids et Mesures* (BIPM) in the guide "Evaluation of measurement data — Guide to the expression of uncertainty in measurement" [14]. According to this guideline, the uncertainty in the result of a measurement generally consists of several components which may be grouped into two categories according to the way in which their numerical value is estimated. The first category is called "type A". It is evaluated by statistical methods such as reproducibility, repeatability, special consideration about Fast Fourier Transform analysis, and the experimental standard deviation. The components in category A are characterized by the estimated variances. Second family of uncertainties contributions is for those which are evaluated by other mean. They are called "type B" and due to various components and temperature control. Experience with or general knowledge of the behavior and properties of relevant materials and instruments, manufacturer's specifications, data provided in calibration and other certificates (noted BR), uncertainties assigned to reference data taken from handbooks. The components in category B should be characterized by quantities which may be considered as approximations to the corresponding variances, the existence of which is assumed.

5.1. "Type A". Statistical contributions

Uncertainty on $\mathcal{L}(f)$ strongly depends on propagation of uncertainties through the transfer function as deduced from equation (3). We see here that "type A" is the main contribution. For statistical contributions aspects, the global uncertainty is strongly related to repeatability of the measurements. Repeatability (noted A1) is the variation in measurements obtained by one person on the same item and under the same conditions. Repeatability conditions include: the same measurement procedure, the same observer, the same measuring instrument, used under the same conditions, repetition over a short period of time, the same location. We switch on all the components of the instrument and perform a measurement keeping the data of the curve. Then we need to switch them off and switch them on again to obtain another curve. We must repeat this action several times until we have ten curves. Elementary term of uncertainty for repeatability is experimentally found to be equal to 0.68 dB.

Other elementary terms of statistical contributions still have lower contributions.

Reproducibility, noted A2, is the variability of the measurement system caused by differences in operator behavior. Mathematically, it is the variability of the average values obtained by several operators while measuring the same item. The variability of the individual operators are the same, but because each operator has a different bias, the total variability of the measurement system is higher when three operators are used than when one operator is used. When the instrument is connected, there is no change of each component or device inside. That makes this term negligible because, for example, the amplifier is never replaced by another one. We remark that, if one or more of the components would be replaced, it will be necessary to evaluate the influence of the new component on the results of measure-

ments. Main aspect is that operators are the same. In our case, operator don't change. It means a first approximation we can take 0 dB for this uncertainty.

Uncertainty term due to the number of samples is noted A3. It depend on how many points are chosen for each decades. For this term, we check how works the Fast Fourier Transform (FFT) analyzer, it leads to an elementary term of uncertainty less than 0.1 dB.

Finally, statistical contribution can be considered as:

$$A = \sqrt{\sum A_i^2} \quad (5)$$

According to equation (5), it can then be considered that the whole statistical contribution is better than 0.69 dB.

5.2. "Type B". Other means

Our system is not yet formally traceable to any standard, according to how the phase noise is determined. Phase noise measurement generally don't need to be referenced to a standard as the method is intrinsic. So the data provided in calibration and other certificates, noted BR, are not applicable. It results that we can take 0 dB as a good approximation of BR.

Influence of the gain of the DC amplifier, noted BL1, is determined to be less than 0.04 dB.

Temperature effects, noted BL2, are less than 0.1 dB as optical fiber regulation system of temperature in turned on.

Resolution of instruments, noted BL3, is determined by the value read on each voltmeter when we need to search minimum and maximum for the modulator but also for wattmeter. Resolution is then no worse than 0.1 dB.

During the measurement, what influence could bring the DUT, generally an oscillator to be characterized? We call BL4 the influence of the variation of the DUT. It stays negligible while the variation stay limited. It results that we can keep 0 dB as a reasonable value for BL4 if the DUT is not too unstable.

Uncertainty on the determination of the coefficient K_φ (noted BL5) dependent for the slope expressed in Volt/rad is found to be lower than 0.08dB.

For the contribution of the use of automatic/manual range, noted BL6, we can deduce from experimental curves that this influence is no more than 0.02 dB. In our case, all these terms were found lower than repeatability.

The influence of the chosen input power value of the DUT, noted BL7, is negligible as the input power in normal range i. e. between -4 dBm and +6 dBm, has a very limited influence. We experimentally observe an influence. It stay better than 0.02 dB.

Other elementary terms still have lower contributions. BL is the arithmetic sum of each elementary contribution. It is determine to be 0.38 dB.

5.3. Estimation of the global uncertainty of this system

According to the Guide to the expression of uncertainty in measurement, uncertainty at 1 sigma interval of confidence is calculated as follows:

$$u_c = \sqrt{(A^2 + BR^2 + BL^2)} \quad (6)$$

We deduce from equation (6) that uncertainty at 1 sigma, noted u_c , is better than 0.79 dB.

Table 1 summarizes how is deduced the global uncertainty for the spectral density of phase noise at 1 sigma.

| Uncertainty | Designation | Value (in dB) |
|-------------|--|---------------|
| A1 | Repeatability | 0.68 |
| A2 | Reproducibility | 0 |
| A3 | Uncertainty term due to the number of sample | 0.1 |
| A | $(\sum A_i^2)^{1/2}$ | 0.69 |
| BR | Not applicable | 0 |
| BL1 | Gain of the DC amplifier | 0.04 |
| BL2 | Influence of the temperature | 0.1 |
| BL3 | Influence of the resolution of the instrument | 0.1 |
| BL4 | Influence of the power of the DUT | 0 |
| BL5 | Uncertainty on the determination of K_ϕ | 0.08 |
| BL6 | Contribution of automatic/manual range | 0.02 |
| BL7 | Influence of the variation of the input power | 0.02 |
| BL | $\sum BL_i$ | 0.38 |
| u_c | Global uncertainty at 1 sigma: $(A^2+BR^2+BL^2)^{1/2}$ | 0.79 |

Table 1. Budget of uncertainties.

Its leads to a global uncertainty of $U = 2xu_c = 1.58$ dB at 2 sigma.

For convenience and to have an operational uncertainty in case of degradation or drift of any elementary term of uncertainty, it is wise to degrade the global uncertainty. That's why we choose to keep $U = 2$ dB at 2 sigma for a common use of the optoelectronic system for phase noise determination. According to this evaluation of the uncertainty at 1 sigma, it leads to 1.58 at two sigma. It concretely means that it is possible to determine the phase noise of a single oscillator in X-band with a global uncertainty set to be better than ± 2 dB.

6. Conclusion

The author wish that the phase noise optoelectronic system presented in this chapter is useful for those who want to understand how the phase noise can be experimentally determined. We detailed performances and consideration about estimation of the uncertainty to show the main advantage of such developed instrument for metrology or telecommunication applications and characterizations of compact OEO's operating in X-band. With high performance better than -170 dBc/Hz at 10 kHz from the 10 GHz carrier, it is interesting to underline that it is possible to determine the phase noise of a single oscillator in X-band with a global uncertainty set to be better than ± 2 dB. This system is to be extended at lower and higher microwave operating frequencies.

Acknowledgements

Author would like to thank his colleagues from FEMTO-ST, Besançon, Ms. Nathalie Cholley, Engineer, Dr. Abdelhamid Hmima and Dr. Yanne K. Chembo, CNRS senior researcher, for fruitful discussions. Author also acknowledges the French National Research Agency (ANR) grant "ANR 2010 BLAN 0312 02".

Author details

Patrice Salzenstein*

Address all correspondence to: patrice.salzenstein@femto-st.fr

Centre National de la Recherche Scientifique (CNRS), Unité Mixte de Recherche (UMR), Franche Comté Electronique Mécanique Thermique Optique Sciences et Technologies (FEMTO-ST), France

References

- [1] Salzenstein, P. (2011). Optoelectronic Oscillators. In: Sergiyenko O. (ed.) Optoelectronic Devices and Properties. Rijeka: InTech;. . Available from <http://www.intechopen.com/books/optoelectronic-devices-and-properties/optoelectronic-oscillators> (accessed 5 June 2012)., 401-410.
- [2] Yao, X. S., & Maleki, L. (1994). High frequency optical subcarrier generator. *Electronics Letters*, 30(18), 1525-1526.
- [3] Volyanskiy, K., Cussey, J., Tavernier, H., Salzenstein, P., Sauvage, G., Larger, L., & Rubiola, E. (2008). Applications of the optical fiber to the generation and to the meas-

- urement of low-phase-noise microwave signals. *Journal of the Optical Society of America B*, 25(12), 2140-2150.
- [4] Ilchenko, V. S., Yao, X. S., & Maleki, L. (1999). High-Q microsphere cavity for laser stabilization and optoelectronic microwave oscillator. *Proceedings of SPIE*, 3611-190.
- [5] Volyanskiy, K., Salzenstein, P., Tavernier, H., Pogurmirskiy, M., Chembo, Y. K., & Larger, L. (2010). Compact Optoelectronic Microwave Oscillators using Ultra-High Q Whispering Gallery Mode Disk-Resonators and Phase Modulation. *Optics Express* ., 18(21), 22358-22363.
- [6] Schliesser, A., & Kippenberg, T. J. (2010). Cavity Optomechanics with Whispering-Gallery Mode Optical Micro-Resonators. *Acta Avances in Atomic Molecular and Optical Physica*, 58-207.
- [7] Salzenstein, P., Tavernier, H., Volyanskiy, K., Kim, N. N. T., Larger, L., & Rubiola, E. (2009). Optical Mini-disk resonator integrated into a compact optoelectronic oscillator. *Acta Physica Polonica A*, 116(4), 661-663.
- [8] Tavernier, H., Salzenstein, P., Volyanskiy, K., Chembo, Y. K., & Larger, L. (2010). Magnesium Fluoride Whispering Gallery Mode Disk-Resonators for Microwave Photonics Applications. *IEEE Photonics Technology Letters*, 22(22), 1629-1631.
- [9] Salzenstein, P., Cussey, J., Jouvenceau, X., Tavernier, H., Larger, L., Rubiola, E., & Sauvage, G. (2008). Realization of a Phase Noise Measurement Bench Using Cross Correlation and Double Optical Delay Line. *Acta Physica Polonica A*, 112(5), 1107-1111.
- [10] Salzenstein, P., Cholley, N., Zarubin, M., Pavlyuchenko, E., Hmima, A., Chembo, Y. K., & Larger, L. (2011). Optoelectronic phase noise system designed for microwaves photonics sources measurements in metrology application. *Proceedings of SPIE* ., 8071-807111.
- [11] Anritsu (2000). Typical datasheet Anritsu 69B serie available on page at the following link: http://cem.inrets.fr/private/materiel-labo/images/m_011_doc_gene_65ghz.pdf (accessed 5 June 2012)., 8.
- [12] Salzenstein, P., Hmima, A., Zarubin, M., Pavlyuchenko, E., & Cholley, N. (2012). Optoelectronic phase noise measurement system with wideband analysis. *Proceedings of SPIE*, 8439, 84391M.
- [13] Salzenstein, P., Pavlyuchenko, E., Hmima, A., Cholley, N., Zarubin, M., Galliou, S., Chembo, Y. K., & Larger, L. (2012). Estimation of the uncertainty for a phase noise optoelectronic metrology system. *Physica Scripta* [T149], 014025, <http://dx.doi.org/10.1088/00318949/2012/T149/014025>.
- [14] GUM: (2008). Guide to the Expression of Uncertainty in Measurement, fundamental reference document. , JCGM 100: (GUM 1995 minor corrections) <http://www.bipm.org/en/publications/guides/gum.html> (accessed 5 June 2012).

Design and Modeling of Optoelectronic Photocurrent Reconfigurable (OPR) Multifunctional Logic Devices (MFLD) as the Universal Circuitry Basis for Advanced Parallel High-Performance Processing

Vladimir G. Krasilenko, Aleksandr I. Nikolsky and Alexander A. Lazarev

Additional information is available at the end of the chapter

<http://dx.doi.org/10.5772/54540>

1. Introduction

One of the problems in high speed computing is the limited capabilities of communication links in digital high performance electronic systems. Too slow and too few interconnects between VLSI circuits cause a bottleneck in the communication between processor and memory or, especially in multiprocessor systems, among the processors. Moreover, the problem is getting worse since the increasing integration density of devices like transistors leads to a higher requirement in the number of necessary channels for the off-chip communication. Hence, we are currently in a situation, which is characterized by too few off-chip links and too slow long on-chip lines, what is described as the interconnect crisis in VLSI technology [1]. More than ten years the use of optical interconnects is discussed as an alternative to solve the mentioned problems on interconnect in VLSI technology [2]. A lot of prototypes and demonstrator systems were built to prove the use of optics or optoelectronics for off-chip and on-chip interconnects [3]. The possibilities of current VLSI technology would allow integrating a massively-parallel array processor consisting of a few hundred thousand simple processor elements (PEs) on a chip. Unfortunately it would be a huge problem to arrange several of such PE arrays one after the other in order to realize a highly-parallel superscalar and super-pipelined architecture as well as an efficient coupling to a memory chip. The reason for these difficulties is the not sufficient number of external interconnects to move high data volumes from and to the circuits. In optoelectronic VLSI one tries to solve limitation problem by realizing external interconnects not at the edge of a chip but with ar-

rays of optical detectors and light emitters which send and receive data directly out from the chip area. Honeywell has developed such devices with VCSEL diodes (vertical surface emitting laser diodes) and metal – semiconductor – metal photo-detectors in research project [4].

This allows the realization of stacked 3-D chip architecture in principle. The main problems are not the manufacturing and operating of single devices but the combination of different passive optical elements with active optoelectronic and electronic circuits in one system. This requires sophisticated mounting and alignment techniques which allow low mechanical tolerances and the handling of thermal problems. At present the situation for smart detector circuits is much easier. They can be regarded as a subset of OE-VLSI circuits because they consist only of arrays of photo-detectors with corresponding evaluation circuit for analogue to digital converting. Optical detectors based on PN or PIN photodiodes can be monolithically integrated with digital electronics in silicon what simplifies the design enormously compared with OE-VLSI circuits that in addition contain sender devices realized in GaAs technologies. Furthermore smart detector circuits can be manufactured in nearly every semiconductor fabric. Smart detectors or smart optical sensors show a great application field and market potential. Therefore our approach favors a smart pixel like architecture combining parallel signal detection with parallel signal processing in one circuit. Each pixel has its own PE what guarantees the fastest processing.

The strategic direction of solution of various scientific problems, including the problem of creation of artificial intelligence (AI) systems, human brain simulators, robotics systems, monitoring and control systems, decision-making systems, as well as systems based on artificial neural networks, etc., becomes fast-acting and parallel processing of large 2-D arrays of data (up to 1024×1024 and higher) using non-conventional computational systems, corresponding matrix logics (multi-valued, signed-digit, fuzzy logics, continuous, neural-fuzzy and others) and corresponding mathematical apparatus [5-11]. For numerous perspective realizations of optical learning neural networks (NN) with two dimensional structure [5], of recurrent optical NN [6], of the continuous logic equivalency models (CLEM) NN [7-10], the elements of matrix logic are required, and not only of two-valued property, threshold, hybrid but also continuous, neural-fuzzy logics and adequate structure of vector-matrix computational procedures with basic operations of above-mentioned logics. Optic and optoelectronic technologies, methods and principles as well as corresponding element base provide attractive alternative for 2D data processing. These technologies and methods successfully decide problems of parallelism, input-output and interconnections. Advanced non-traditional parallel computing structures and systems, including neural networks, require both parallel processing and parallel information input/output. At the same time there are many new approaches that are based on new logics (neural-fuzzy, multi-valued, continuous etc.). The using of the standard sequential algorithms based on a few operations makes the approaches long-running. But only a few of them [12] can be used for processing of 2D data and perform wide range of needed arithmetic and logic operations). Generalization of scalar two-valued logic on matrix case has led to intensive development of binary images algebra (BIA) [13] and 2D Boolean elements for optic and optoelectronic processors [12-17].

Taking into consideration the above-described approach, consisting in universality, let us recollect some known facts regarding the number of functions. The number of Boolean functions of n variables in algebra of two-valued logic (TVL), which is also Boolean algebra, equals 2^{2^n} . In this TVL there are $N_2=2^n$ atoms, which are minterms. Functions of n variables k -valued logic ($k>2$) are reflections $A^n \rightarrow A$, where $A=\{0, 1, \dots, k-1\}$, and the number of functions equals $N_k=k^{k^n}$. Algebra, formed by set ${}^A C_u=[0, 1]$ or ${}^A C_b=[-1, 1]$ is called continuous logic (CL) algebra, and the number of CL functions, as reflections $C_u^n \rightarrow C_u$ depending on the CL algebra can be infinite or finite (the set of reflections is always infinite). CL functions are called only those functions of the set N_{\wedge} which are realized by formulas. The number N_{\wedge} of CL functions in the most developed CL algebra – quasi-Boolean Cleenee algebra ($\Delta=(C_u, \wedge, \vee, -)$), in which any function on any set of arguments takes the value of one of the arguments or its negation, is finite. In this case the number $N_{\wedge}(n)$ of functions of n arguments increases with increase of n very rapidly [4]: $N_{\wedge}(0)=2$; $N_{\wedge}(1)=6$; $N_{\wedge}(2)=84$; $N_{\wedge}(3)=43918$.

We would like to draw the attention to the fact, that both natural neurons and their more complex physical and mathematical models suggest discrete-analog and purely analog means for information processing with different level of accuracy, with the possibility of rearrangement of chosen coding system. This, in its turn, requires corresponding image neuron circuit engineering with programmable logic operations, with transition from analog to discrete processing, to storing etc.

Thus, the search of means aimed at construction of elements, especially universal (at least quasi-universal or multifunctional) with programmable tuning, able to perform not only operations of two-valued logic, but other matrix (multi-valued, continuous, neural-fuzzy, etc.) logic operations is very actual problem [15]. One of promising directions of research in this sphere is the application of time-pulse-coded architectures (TPCA) that were considered in works [18-20]. These architectures were generalized in [11], taking into account basic possible approaches as well as system and mathematical requirements. The time-pulse representation of matrix continuous-logic variables by two-level optic signals not only permits to increase functional possibilities (up to universality), stability to noise, stability and decrease requirements regarding alignment and optical system, but also simplify control circuits and adjustment circuits to required function, operation, and keep untouched the whole methodological basis of such universal elements construction, irrespective of valuedness of a logic and type of a logic.

But there is another approach based on the use of universal logic elements with the structure of multiple-input multiple-output (MIMO) and time-pulse coding. We call such elements - the elements of picture type (PT). At increase of number of input operands and valuedness of logic (up to continuous) the number of executable functions also increases by the exponential law. This property allows simplifying operation algorithms of such universal optoelectronic logical elements and hence to raise information processing speed. Most general conceptual approaches to construction of universal picture neural elements and their mathematical rationales were presented in paper [11]. But those were only system and structural

solutions that is why they require further development and perfection. Mathematical and other theoretical fundamentals of design of matrix multi-functional logical devices with fast acting programmable tuning were considered in paper[19], where expediency of functional basis unification, that is promising for optoelectronic parallel-pipeline systems (OEPS) with command-flow 2D-page (picture) organization [20], necessity in arrays of optic or optoelectronic triggers (memory elements) of picture type for storage of information and controlling adjusting operands as well as perspective principles of presentation and coding of multi-valued matrix data (spatial, time-pulse and spectral) were shown. Besides, the analysis of various algebra logics [11, 19, 21-24] for functional systems of switching functions, in spite of their diversity allows us to suggest a very useful idea, in our opinion, that lies in following.

It is possible to create more sophisticated problem-oriented processors, in which the specific time-pulse operands encoding and only elements of two-valued logic are used, which will realize functions of different logics, continuous etc. Taking into account the universality, parallel information processing of the universal elements and the use of only two-valued logic elements for implementation of all other operations the approach is a very promising.

That is why the aim of the given work is to consider the results of design and investigation of optoelectronic smart time-pulse coded photocurrent reconfigurable MFLD as basic components for 2D-array logic devices for advanced neural networks and optical computers.

2. Design and simulation of two variants of the OPR MFLD base cell

2.1. Picture continuous logic elements (PCLE)

Figure 1 shows the structural diagram of picture neural element (PNE) for computation of all basic matrix-continuous-logic (MCL) operations in matrix quasiBoolean algebra $C=((A,B),\wedge, \vee, -)$ [11] for which in any set of MCL arguments matrix continuous logic function (MCLF) F takes the value of a subregion of one of the arguments or its supplement. The PE of matrix two-valued logic (MTVL), performing MTVL operations over matrix temporal functions $O_{ij}^i(t)$ (in point of fact two-valued 2D-operands) realize MCLF over continuous logic variables (CLV) O_{ij}^i . The time-pulse coding of a grayscale picture is shown in Figure 1. As it is seen in Figure 2 at each point of picture output of PNE, MCL can be performed over continuous logic variables (CLV) $O_{ij}^1 \dots O_{ij}^{n=2}$, presented by $t_{ij}^1 \dots t_{ij}^n$ durations of time pulse signals, during each interval T one of the following operations of CL: $\min(a,b)$, $\max(a,b)$, $\text{mod}(a-b)$, $\text{complementary } \bar{a}=1-a$, equivalence, etc [10, 11, 23]. The duration of MTVL formed at the output and as a result of PNE, signal $f_{ij}^{NE}(t) = f_{ij}^{NE}(O_{ij}^1(t), O_{ij}^2(t))$, is CL function of input binary temporal variables durations. Thus, as it is seen from Figure 3, almost all basic operations of continuous logic, neural-fuzzy logic, that are shown in work [21], can be realized with the help of the time-pulse coding of variables X_1, \dots, X_n and universal (or multifunctional) picture element (UPE) of two-valued logic (TVL). But for that pulse width modulator (PWM) of PT is needed. It is not needed to

form contrast-conversion (complementary operand) image for analog picture optic inputs if PWMs PT have complementary outputs.

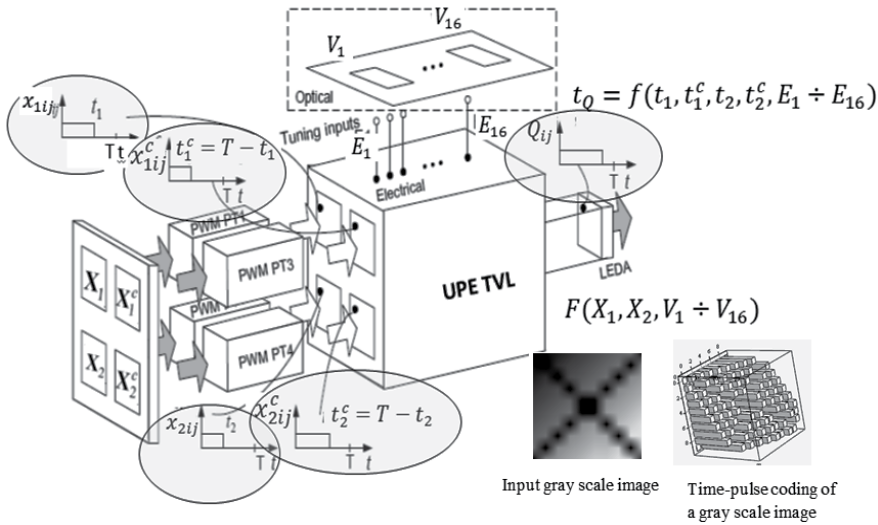


Figure 1. The PNE of matrix-continuous-logic (MCL) with programmable tuning

Thus, becomes obvious that for time – pulse coding realization of PNE of matrix-continuous-logic (MCL) with programmable tuning is necessary UPE of TVL or picture MFLD, by means of which continuously – logic operations over time – pulse signals can be realized. In Figure 1 selection of picture logic functions is carried out by electric adjusting signals and all array cells will realize the same function at the same time. For many appendices it is expedient to choose a logic function at each point of the matrix processor, and therefore there is a desire to make management and tuning also in the form of optical matrix operands. It essentially expands functionality of such processors and MFLD on which basis they are realized.

In work [25] MFLD of two-valued logic (TVL) on current mirrors, photodiodes and LEDs with schemes of their drivers are described and simulated. They are relatively difficult as contain four current mirrors (CM), four schemes XOR, four elements AND and one logic element OR. In the same work different optoelectronic circuitry were offered on base of 2-4 CM and one photo diode, realizing the Boolean operations AND, NOT, OR, NOR, et al with potential and current outputs. They are based on threshold elements, comparators of currents (photocurrents) on current mirrors and circuitry of limited subtraction (CLS). Such base elements also were used for realization of other elements of continuous logic, including operations equivalence (nonequivalence) and etc. [21, 26, 27]. Therefore developing further this approach we use for design of the OPR MFLD.

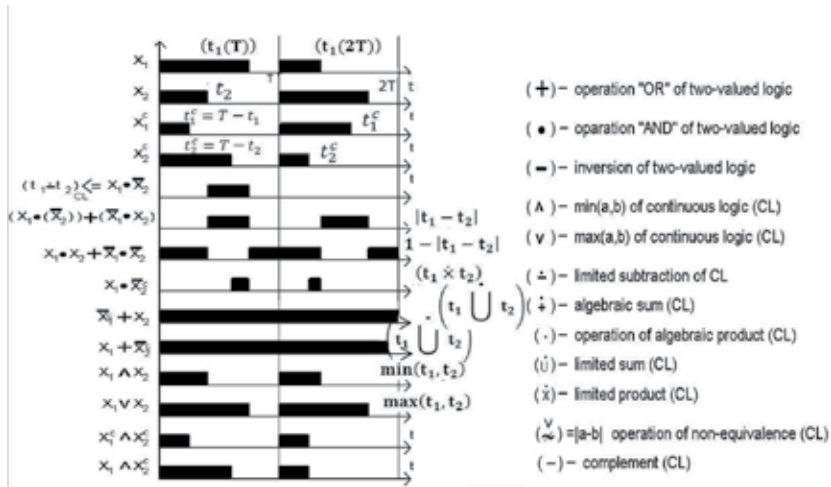


Figure 2. Time diagrams of CL operation fulfillment by means of time-pulse CL variables

2.2. Designing of the base cell for the first version of OPR MFLD-1

The function circuit of the OPR MFLD-1 (the first version) is shown in figure. 3, and the circuit diagram of the OPR MFLD-1 on 1.5 μ m CMOS transistors is shown in figure. 4. It contains 4 optical inputs (the aperture of photodiodes PD) four cells $(PD-CM)_1 \div (PD-CM)_4$ executing a role of threshold elements (a threshold $-i_0$) and realizing operation of the limited subtraction(LS): $i_{CM_i} = i_{pd} - i_0$; current mirror CM5 (or instead of its CM'5 with the optical adjusted threshold) for the reproduction of thresholds $i_0 = 2I_0$; current mirrors CM6-M and CM7-M (M denotes the multiplication currents) for formation together with drivers signals (currents) for four LEDs (2 direct outputs) and LED' (2 additional inverse outputs).

The cell for the first version of OPR MFLD-1 has a different sub-options, which correspond to different patterns of formation of the thresholds i_0 , namely: 1) sub-option with the formation of all four thresholds using individual current sources, 2) sub-option - with the help of a current mirror - multiplier CM5 and a single current source $2I_0$, 3) sub-option - using the current mirror-multiplier CM'5 with a photodiode for input of the threshold current $i_0 = 2I_0$.

In Figures 5a, 5b it is shown constructive (a matrix fragment – one OPR MFLD-1) the scheme of base nodes and the most simple optical imaging system for connections. The scheme contains 4 photo diodes, 5+8+5=18 transistors (without transistors of drivers) and the scheme is enough simple. By changing optical (or electrical) signals of tuning vector $y_1 \div y_4$ at input 4 photodiodes signals from light emitter diodes LED and \overline{LED} of the OPR MFLD-1 scheme are moved.

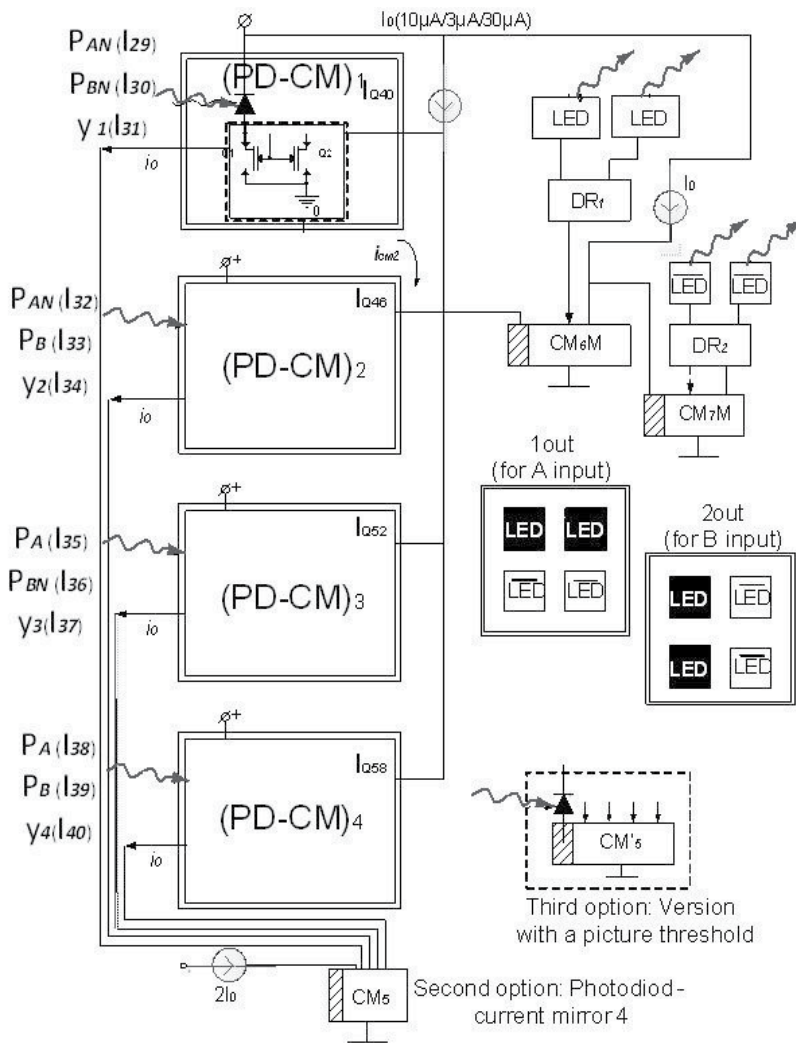


Figure 3. The function circuit of the OPR MFLD-1

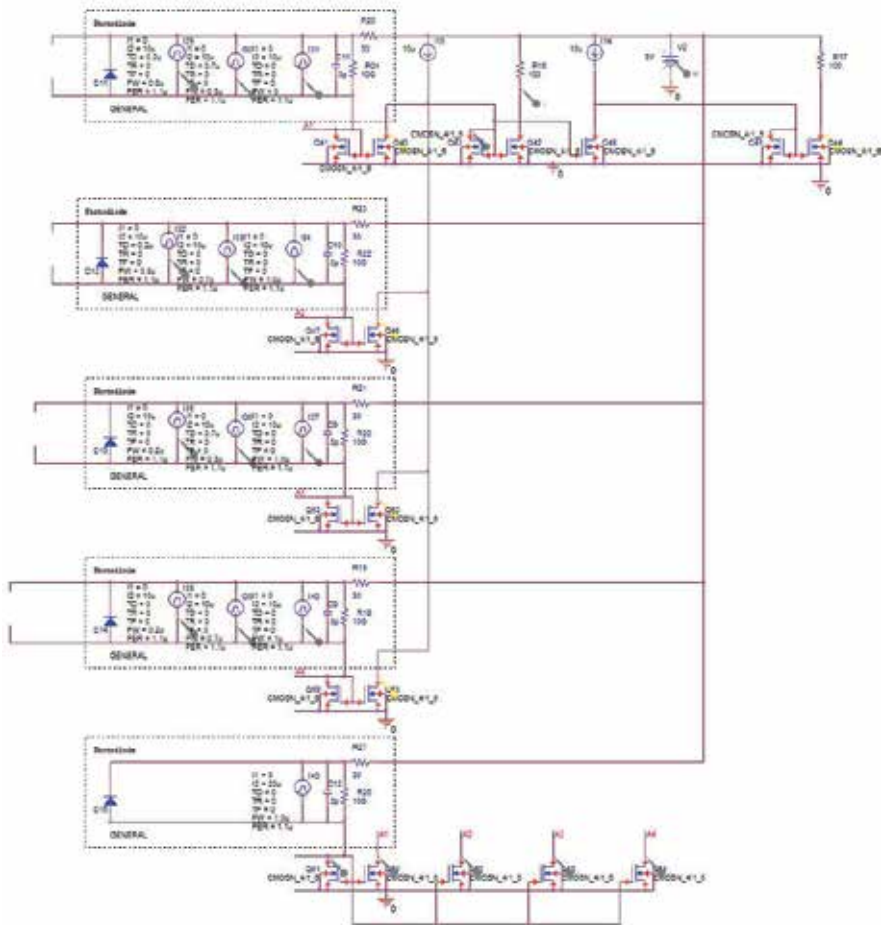


Figure 4. The circuit diagram of the OPR MFLD-1 on 1.5µm CMOS transistors for modeling with OrCAD 16.3 PSpice

Signals from the first input A and from the second input B (a variant of output II) together with tuning vector $y_1 \div y_4$ will be transformed to a total photocurrent. Base elements of limited subtraction (LS) based on (PD-CM), separate out corresponding logic minterms by subtraction of threshold currents i_{θ} from currents of PDs. We researched various updating of such base circuits. For the task of thresholds it is possible to use the various optical and electric approaches, besides operating generators of currents and various schemes of drivers are possible. A basic accent we nevertheless do on input part of conversion and processing, because forming of matrix of emitters is simpler task, if not to take into account the technological aspects of their integration on a chip.

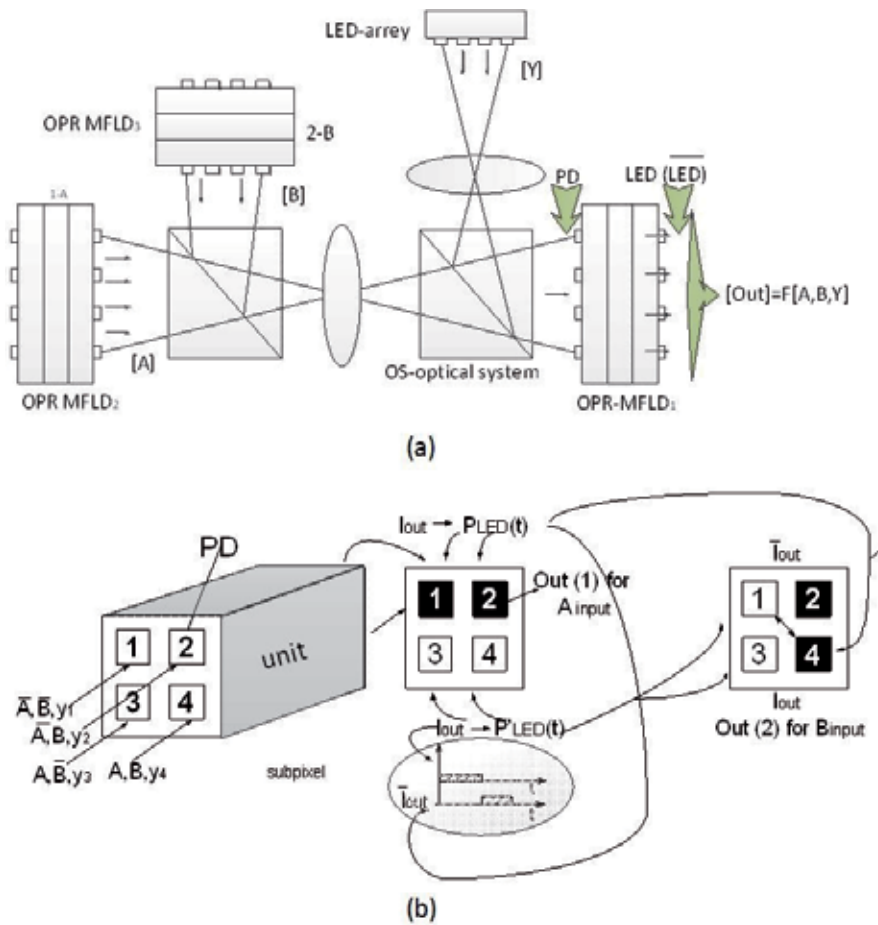


Figure 5. a) Optical plane-to-plane imaging system (b) The constructive scheme of a base cell (fragment) for the OPR MFLD-1

2.3. Simulation of the base cell for the first version of OPR MFLD-1

Results of modeling by means of package OrCAD 16.3 of the offered OPR MFLD-1 are shown in Figure 6 for different tuning signals $y_1 y_4$ which set necessary functions, for different supply voltage and different amplitudes of currents I_0 ($3\mu A$, $10\mu A$ and $30\mu A$) accordingly. In Figure 6a, the first diagram above shows the pulses of currents I_{30} , I_{29} , which correspond to the inputs of \bar{B} , \bar{A} , and current I_{D} (Q_{40}) at the output node $(PD-CM)_1$. On the same Figure, the second, third and fourth diagrams show, respectively, the input and output pulse currents of nodes $(PD-CM)_2 \div (PD-CM)_4$. Current pulse I_{35} duration (see the third diagram in Figure 6a), which is at the input A, equals $2\mu s$. Current pulse I_{39} duration (see the fourth diagram in Figure 6a) equals $7\mu s$ at the input B. The output pulse current I_{D} (Q_{44}) of the circuit is shown in the bottom diagram in Figure 6a and its duration equals $8\mu s$ ($8=10-2$). This confirms the correctness work of the circuit.

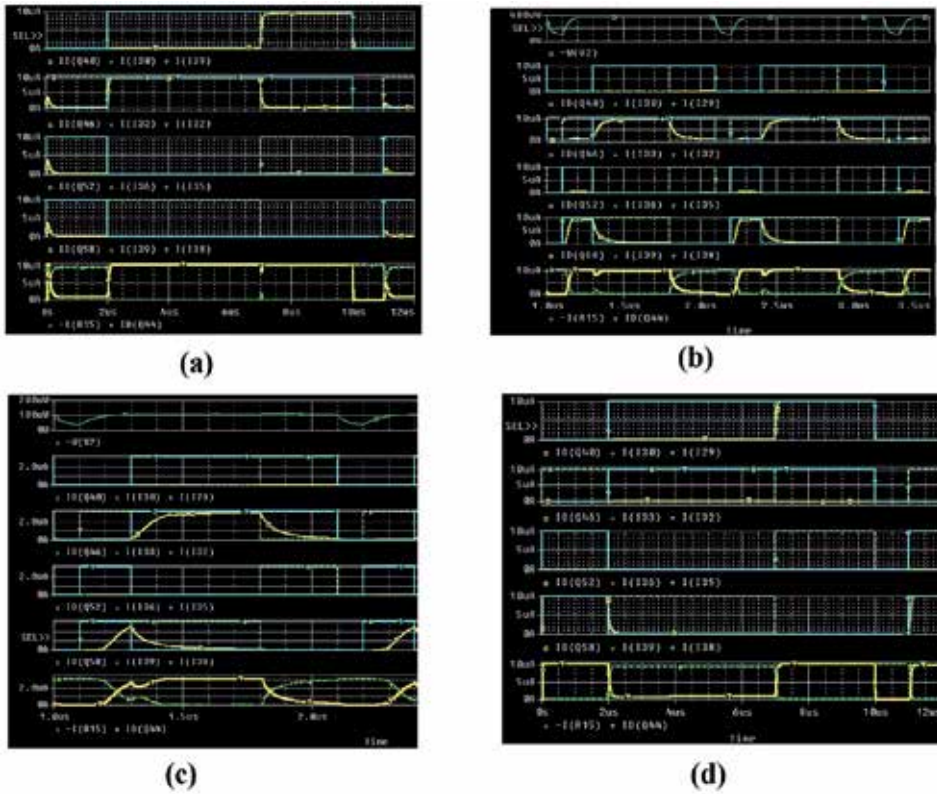


Figure 6. a) Simulation results of cell of OPR MFLD-1 for functions of NAND two-valued logic(TVL) and NMIN continuous logic (CL) at a supply voltage 5 V; (b) Simulation results of cell of OPR MFLD-1 for functions of OR TVL and MAX CL logic (3 V, $t(A)=t(I35)=200\text{nS}$, $t(B)=t(I39)=700\text{nS}$, $t=100\text{nS}$, $T=1,1\mu\text{s}$); (c) Simulation results of cell of OPR MFLD-1 for functions XOR TVL and NEQ CL (3V, 0.1mW, $3\mu\text{A}$, $t(A)=t(I35)=200\text{nS}$, $t(B)=t(I39)=700\text{nS}$, $T=1.1\mu\text{s}$); (d) Simulation results of cell of OPR MFLD-1 for functions NXOR TVL and EQ CL (3V, $10\mu\text{A}$, photo-configurable, $t(A)=t(I35)=2\mu\text{S}$, $t(B)=t(I39)=7\mu\text{S}$, $t_{\text{out}} = t(I(DQ44))=2+3=5\mu\text{S}$)

The diagrams in Figures 6b, 6c, 6d, similar to Figure 6a shows the corresponding input and output currents of the circuit. The difference lies in the different modes for different input pulse durations and the presence of additional power consumption graphics. In Figure 7a dependence of power consumption of OPR MFLD-1 from I_0 and supply voltage is shown, and in Figure 7b dependence of t_{preset} and t_{fronts} from $I_0=I_{\text{max}}$ is shown. From them it is visible, that the power consumption of OPR MFLD-1 P_{drain} (without drivers and output part) is about 0.1-2.5mW. If to take into account that the currents of LEDs must (taking into account the coefficient of transformation and sensitiveness of photo-detectors PD) to be at least in 5÷10 times more, the P_{drain} will increase in 2÷4 times. But, for example, at $I_0=10\mu\text{A}$, the power consumption will be $P_{\text{drain}} \leq 4\div 5\text{mW}$. At currents $1\div 3\mu\text{A}$ it decreases to 1mW. Delay time is no more than 50÷100 ns, and the period T of time pulse processed signals go into in a micro-second range $1\div 16\mu\text{s}$. If to use not 1.5 μm technologies CMOS transistors, but more ad-

vanced, that is possibility to receive processing time T at level $1 \div 10$ ns, i.e. to raise productivity of one channel OPR MFLD-1 to 10^8 - 10^9 CL-logic operations/sec.

We tested experimentally the circuit for all functions that it can implement. The experiments confirm the implementation of all theoretically possible functions in a wide range of voltages, currents and operating periods of treatment. But given the size limitations of article, here we do not present all results and charts.

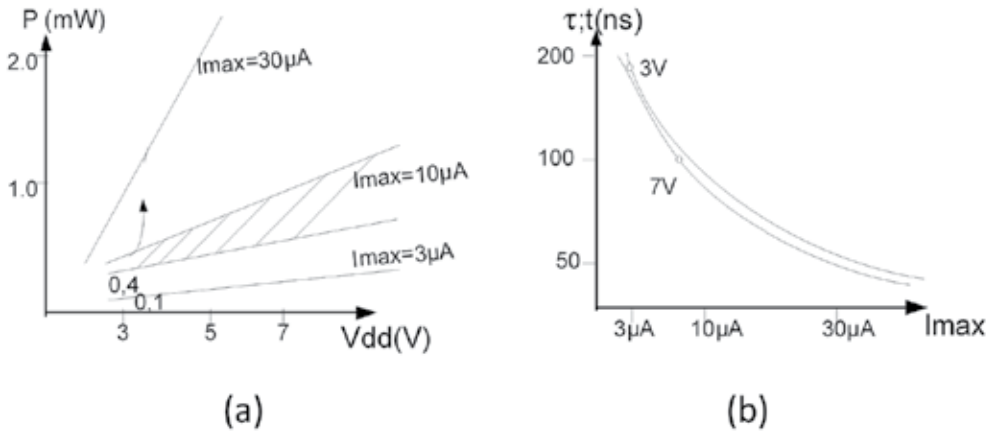


Figure 7. a) Dependence of the power consumption from supply voltage and input current range; (b) dependence of time delay and fronts from supply voltage and input current values

If cells of the MFLD-1 with $P_{drain} = 1 \div 5$ mW are integrated into array of 32×32 elements or more, the general productivity of such array OPR MFLD-1 will reach 10^{12} CL-logic operations/sec. A modified variant of OPR MFLD-1 in which signals y_1, y_4 are realized on current generators with possibility of their programming is also offered. Besides, if the array of cells MFLD-1 realizes the same function it is possible to choose signals with sample corresponding nodes (PD-CM)_i. The problem of simplification of the optical system is decided in this case. Because it is necessary to give signals not from three optical apertures, but only from two apertures on the OPR MFLD-1 chip.

2.4. Modeling of array of the OPR MFLD-1 with MathCAD

Modeling results of the OPR MFLD-1 with MathCAD which confirm normal functioning of OPR MFLD-1 for all 16 possible functions of binary logic and corresponding functions of continuous logic are shown in figure 8-11. Two inputs 2D operands X_A and X_B (Figure 8) with dimensional of 32×32 pixels are transformed to X_{AR} and X_{BR} by multiplication of one pixel to 2×2 pixels. Matrixes X_{AR} , X_{BR} have dimensional of 64×64 pixels.

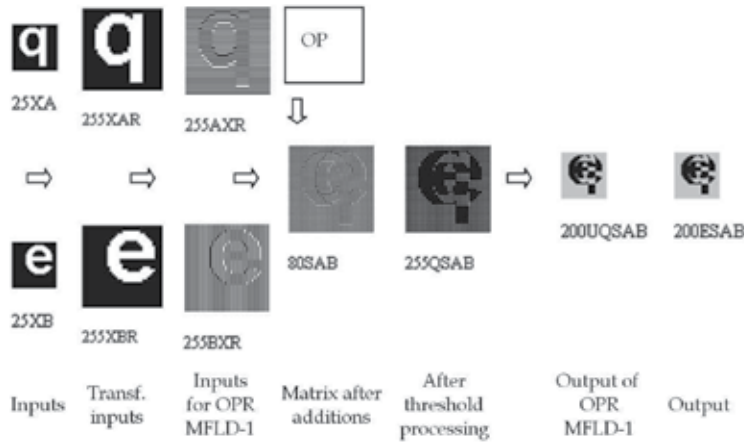


Figure 8. Simulation results of forming and processing processes using OPR MFLD-1

Four matrixes $M1÷M4$ are formed with formulas shown in Figure 9. These matrixes are used for selection of one subpixel of four pixels of XAR and XBR. Matrixes AXR and BXR are formed after XAR and XBR by elementwise non-equivalence (\oplus) operation on matrixes MA and MB. Tuning 2D operand OP is formed by matrixes $M1÷M4$ and scalar tuning signals $oy1÷oy4$ or by signals $y1÷y4$.

$$\begin{aligned}
 M1_{i,j} &:= \text{mod}[(i + 1), 2] \cdot \text{mod}[(j + 1), 2] & MA := M1 + M2 & OP := \sum_{i=1}^4 oy_i \cdot M_i, \\
 M2_{i,j} &:= \text{mod}[(i + 1), 2] \cdot \text{mod}[(j + 0), 2] & MB := M1 + M3 & \text{where } M_i \in M1 \div M4 \\
 M3_{i,j} &:= \text{mod}[(i + 0), 2] \cdot \text{mod}[(j + 1), 2] & AXR := (XAR \oplus MA) & BXR := (XBR \oplus MB) \\
 M4_{i,j} &:= \text{mod}[(i + 0), 2] \cdot \text{mod}[(j + 0), 2] & SAB := AXR + BXR + OP
 \end{aligned}$$

Figure 9. Transformations formulas for matrixes, tuning operand OP formation and additions

Matrix SAB is formed as sum of AXR, BXR and OP. Threshold processing is done over elements of SAB matrix and matrix QSAB is formed:

$$QSAB_{i,j} = \Phi \left[1 - \Phi \left(3 - SAB_{i,j} \right) \left(3 - SAB_{i,j} \right) \right] \left[1 - \Phi \left(3 - SAB_{i,j} \right) \left(3 - SAB_{i,j} \right) \right] \tag{1}$$

The threshold value $tr=3$. Four subpixels are united to one pixel with formula

$$UQSAB_{k,l} = QSAB_{2k,2l} + QSAB_{2k,2l+1} + QSAB_{2k+1,2l} + QSAB_{2k+1,2l+1} \tag{2}$$

and output matrix UQSAB dimension is 32×32 . Another final threshold processing ($t_0=1$) is done with formula

$$ESAB_{k,l} = \Phi \left[1 - \Phi \left(1 - UQSAB_{k,l} \right) \left(1 - UQSAB_{k,l} \right) \right] \left[1 - \Phi \left(UQSAB_{k,l} \right) \left(1 - UQSAB_{k,l} \right) \right] \quad (3)$$

and output matrix ESAB is formed.

For more detailed consideration fragments AP, BP, OPP, OSP, OQP, QSP with dimensional of 2x2 subpixels or 4x4 pixels from matrixes AXR, BXR, OP, SAB, UQSAB, ESAB are shown in Figure 10. The fragments are shown as matrixes and images. For conventional presentation of the images in MathCAD the matrixes are multiplied by 80. Output of equivalence operation is QSP with dimensional of 2x2, but for OPR MFLD correct operation matrixes QSAP and QABP with dimensional of 4x4 are used.

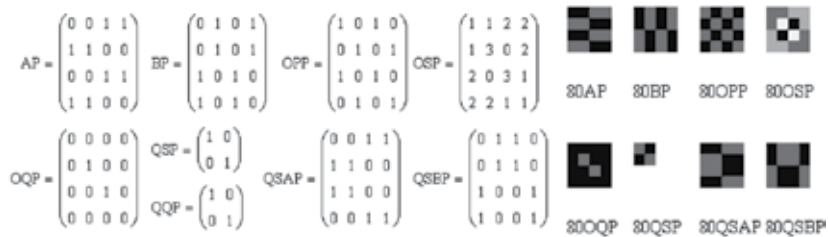


Figure 10. Simulation results of four base cells (2x2 subpixel) of matrix OPR MFLD-1 (function NXOR - EQ)

Examples of other functions realizations with the OPR MFLD-1 as fragments of images are shown in Figures 11

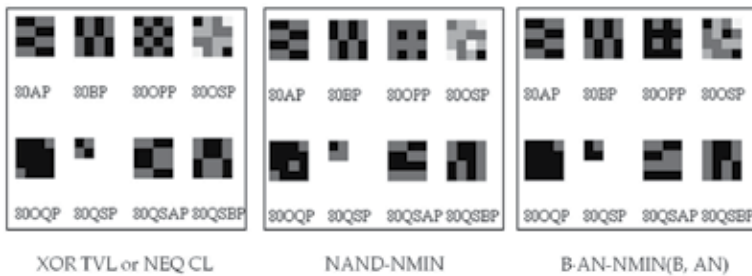


Figure 11. Simulation results for other functions realizations with the OPR MFLD-1

2.5. Investigation of the base cell for the second version of OPR MFLD-2

2.5.1. Simulation of OPR MFLD-2 with OrCAD 16.3

The second circuit variant is shown in Figure 12. It differs from the previously discussed first variant that the input optical signals from each of the i,j -th base cell of two picture operands are fed to a photo-detector. One of the picture input using the appropriate shadow mask weakens the signals of one of the operands is a factor of 2. Therefore, the first unit of

the circuit consists of current comparators, which convert the output voltages into a digital form that is uniquely appropriate input situation.

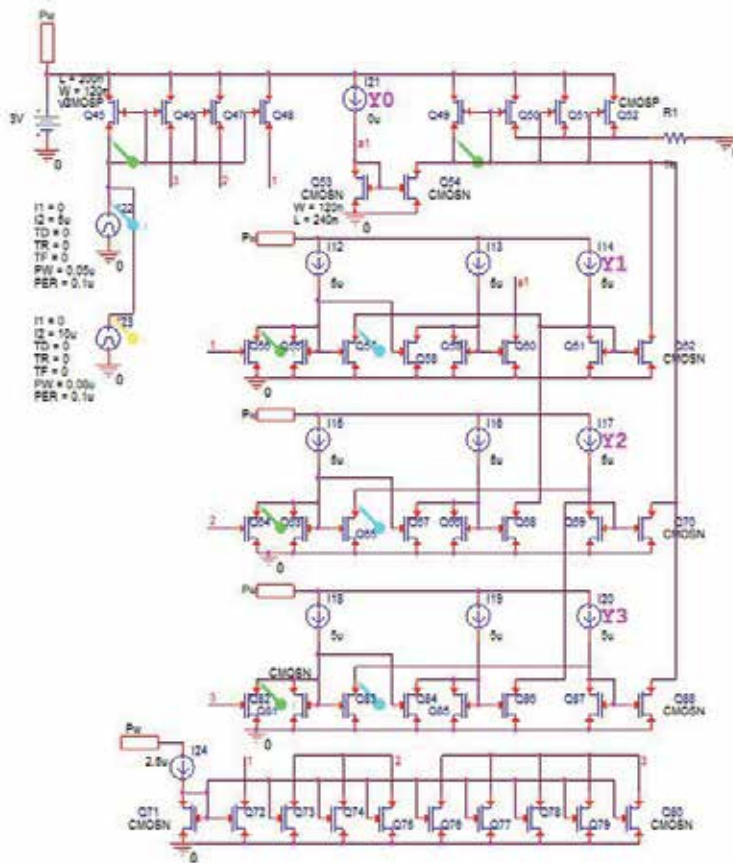


Figure 12. Circuit diagram of the base cell for the OPR MFLD-2 (the second version)

With the help of nodes in the current voltage conversion and control signals Y0-Y3 at the output node is formed by the resulting signal as a current, which corresponds to the selected desired logic function. The set of possible logical set of vector signals Y0-Y3 has 16 possible combinations. Selecting one of them allows you to implement any 16 of possible two-valued logic of binary operations. If the input signals are continuous in the time-pulse coded form, selecting the desired operation as a two-valued logic, such as AND, the operation MIN is implemented from time-pulse encoded signals. For the first model experiments in the scheme of an input photo-sensor used two of the current source to set the time of the input time-pulse signals (TPS). Instead of photo detectors are used to control the function of the sources of Y0 ÷ Y3 current. The reference currents are shown as current sources for simplicity. The current sources can be implemented on the same transistors or may be given by means of optical signals with fixed intensity. For the formation of the amplified output cur-

rent which is required for light emitters, or for driver circuit, you can use the multiplier current at the current mirror.

The simulation results of this scheme on 65nm CMOS transistors with OrCAD 16.3 PSpice, at different voltages and power levels of input signals are shown in fig. 13 -20.

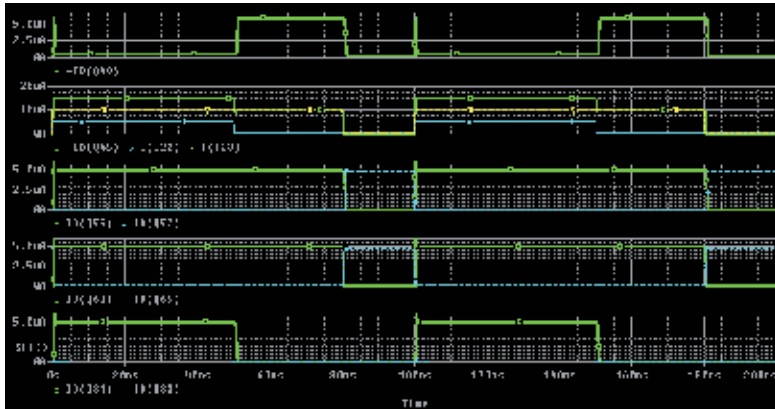


Figure 13. The results of modeling of the base cell for second version of OPR MFLD-2 for implementation of function nonequivalence of continuous logic (CL) based on XOR TVL

Experiments have shown that the power consumption of a cell does not exceed $200\div 300\mu W$, delay times and pulse fronts are less than 1 nanosecond, and the basic cell is realized on 44 (or 36) transistors and 11 current sources on $11\div 15$ transistors. The duration time of pulse-coded signal is in the range of processing cycles, and the pulse period is 100 nanoseconds. This shows that it is possible to increase the frame processing rate to 10 MHz but at the expense of accuracy and complexity of matching photodetectors with current mirrors. Simulation results with OrCAD16.3 of the same basic cell circuit of the OPR MFLD-2 in the mode of implementation of the functions of the nonequivalence CL or XOR TVL are shown in Fig. 13. Diagrams that explain the work of OPR MFLD-2 in the implementation of functions of the nonequivalence CL or XOR TVL: $I_d = 5\mu A$, 3V supply voltage, signal durations $t_{pulse}^a = 50ns$, $t_{pulse}^b = 80ns$. In the first diagram above - the output current signal, the second - two input signals and their weighted sum, the down three: the third, fourth and fifth - currents at the output of the threshold units (green solid) and their complements (blue dashed). It uses vector tuning signals $Y = \{Y_0, Y_1, Y_2, Y_3\} = \{0, 1, 1, 0\}$, and the current level is $5\mu A$. At the output the correct signal is formed ≈ 30 ns duration. The change of the vector set to $\{0, 1, 0, 0\}$ allows for the output function $I_{22} * NI_{23}$ (where NI_{23} – the complement of the signal I_{23}), as shown in Figure 14. For credibility, that the function is implemented correctly, we did a change in the duration of signals, such that the first signal $t_{pulse}(I_{22}) = 80ns$ and $t_{pulse}(I_{23}) = 50ns$ (the signals changed their duration). The results showed that there was a signal at the output, which has a duration ≈ 30 ns.

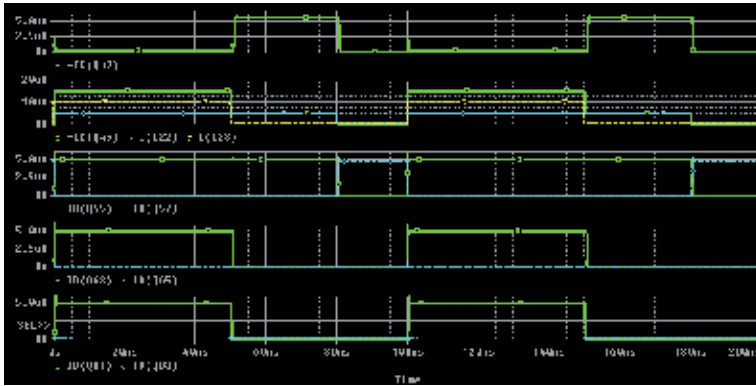


Figure 14. The diagrams of signals in the circuit with a vector set {0, 1, 0, 0} for the implementation of the function $AND(a, \bar{b})$, where $a=122, b=123$

If change of the vector set to {0, 0, 1, 0} than there is a signal at the output which differs only in the short false pulses. Change of durations of the input signals at the same vector set provides the desired signal at the output (see Figure 15). This confirms the correct operation of the scheme.

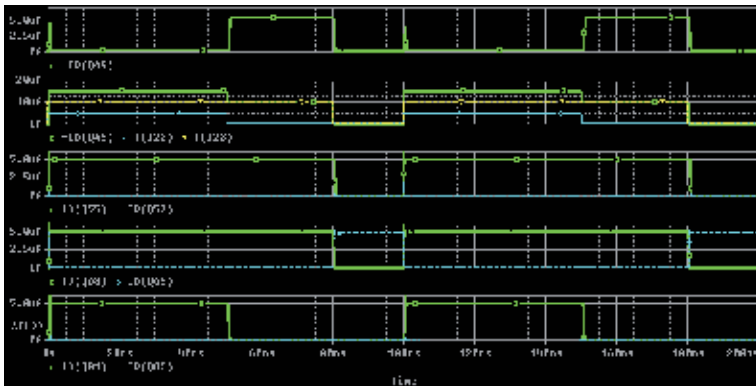


Figure 15. The diagrams of signals in the implementation of the function $AND(\bar{a}, b)$ defined by the vector set {0, 0, 1, 0}, where $a=122, b=123, t_p(122) = 50ns, t_p(123) = 80ns$.

In Figure 16 (left) the implementation of the equivalence CL (based on NXOR TVL) is shown. The output signal (the first graph above) has the total duration of 70ns. The operation NOR TVL and on its basis the operation $\overline{\max}(a, b)$ CL, or the same operation $\min(\bar{a}, \bar{b})$ CL is shown in Figure 16 (right). Duration of the output signal is 20ns. Signal diagrams for mode of formation of \min CL-function (based on AND) are shown in Figure 17. Left on the diagrams shows the control signals of the vector $Y = \{Y_0, Y_1, Y_2, Y_3\} = \{0, 0, 0, 1\}$, and the right - signals: output, input and intermediate. As can be seen from the simulations, device successfully implements the desired function when changing the supply voltage from 1,5V

to 3.3V and in accordance with the results: power consumption $P_{drain} \leq 150 \mu W$ by 1.5V, current pulses amplitudes are $5 \mu A$ and $10 \mu A$; power consumption $P_{drain} \leq 350 \mu W$ by 3.3V, current pulse amplitudes $5 \mu A$ and $10 \mu A$.

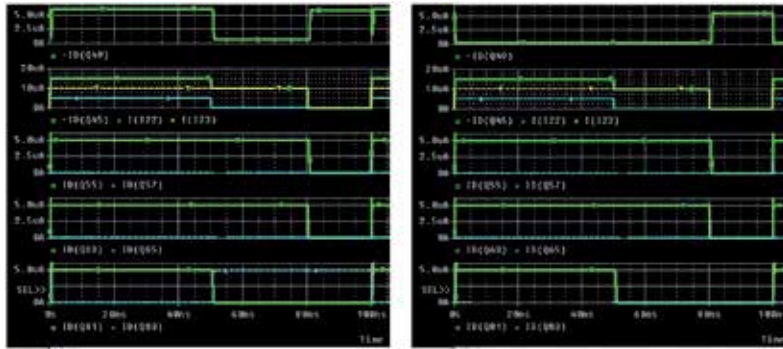


Figure 16. Simulation results of the base cell for second version of OPR MFLD-2 for implementation of function: left - equivalence operation CL (NXOR TVL), right - operation $\bar{m}ax(a, b)$ CL (NOR TVL)

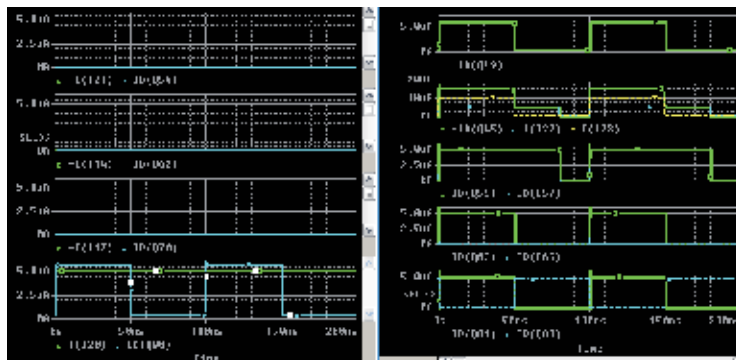


Figure 17. Signal diagrams for mode of AND (min CL) operation implementation

Circuit diagram (Figure 18) of the OPR MFLD-2 with photodiodes is used for simulations with OrCAD16.3 PSpice. The model of the photodiode is the same as in Figure 4. The simulation results are shown in Figure 19. Displaying 4 periods, at each different tuning vector set is applied and different functions is performed: the first period - vector $\{1,0,0,1\}$ (equivalence), the second period - vector $\{1,0, 1,0\}$ (inversion of the first variable), the third period - vector $\{0,1,1,0\}$ (non-equivalence), the fourth period - vector $\{0,1,0,0\}$ (AND (\bar{a}, b)).

The signals of these vectors are displayed on the lower four graphs yellow lines. The blue lines show the output currents generated configuration signals and the corresponding nodes. The sum of output currents of these nodes represents the output signal. It was featured on the second chart above the green line and the input photocurrent from the two argu-

ments shows a blue line. At the top graph shows the power consumption of the base cell. The main problem in these cells is a significant deterioration in fronts (an increase of up to 200 ns). Moreover, no change in the operating voltage from 3V to 5V, no change in amplitude of photocurrents (in the experiments, $I_o = 5\mu A, 10\mu A, 15\mu A$, but at $20\mu A$ did not work!), including at different levels of reference current generators, practice does not significantly affect the duration of the fronts. It is therefore necessary to look for other circuit solutions, for example, use the cascode circuit of current mirrors, more complex, but high-speed, current or voltage comparators. But at the same time significantly increase the hardware cost of a basic cell, and it does not allow for a high level of integration on a chip. So here we are showing the circuit with extended processing period up to $10\mu s$, which with $I_o = 5\mu A$ circuit will provide the required characteristics. Power consumption does not exceed $300\text{--}350\mu W$ at a supply voltage of 2.4V and the 3.0V on photodiodes. Results of experiments are shown in Figure 20. By dynamic reconfiguration of optical signals (vector Y) the desired function of the basic cell is provided and duration of the reconfiguration process is equal to the period $T = 10\text{--}100\mu s$. In addition, if use other technologies, the vectors set can be represented using electrical signals.

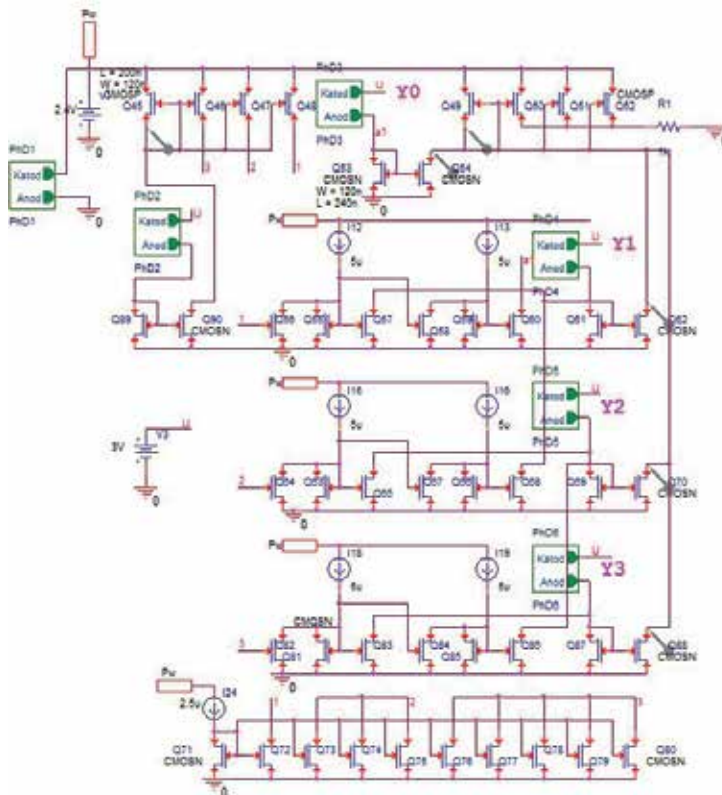


Figure 18. The base cell for OPR MFLD-2 with one input and four control photodiodes



Figure 19. Diagrams of signals at modeling cell with an optical configuration for the desired function and the input photodiode

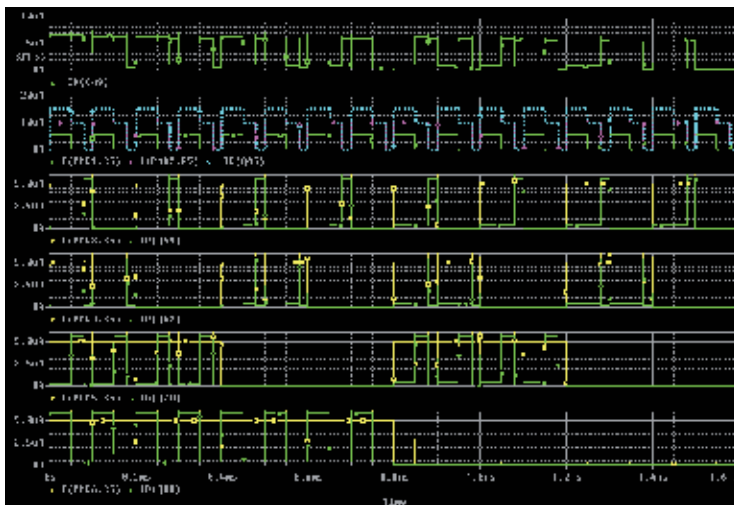


Figure 20. Diagrams showing the ability to dynamically reconfigurable the cells on the implementation of all 16 possible functions of TVL with period of 100µs (total duration 16 periods). The first graph shows the output signal and the second - the input signals. At the bottom four graphs in yellow show signals at photodiodes, and green - generated current logical components

2.5.2. Simulation of the OPR MFLD-2 with MathCAD


Simulation results of the offered OPR MFLD-2 with MathCAD and its usage for image processing and fuzzy logic operations are shown in fig. 21-24.

Formulas for simulation processing with MathCAD are shown in Figure 21. At first, input two 2D operands **A1** and **B1** and its weighted sum **SIAB** are formed. The coefficient and threshold $t_0=10$ because the current in the OPR MFLD-2 circuit is $10\mu\text{A}$. Contrast complementary images are matrixes **AN1** and **BN1**. After threshold processing by current comparators the direct matrixes **T1SIAB**, **T2SIAB**, **T3SIAB** and matrixes **TN1SIAB**, **TN2SIAB**, **TN3SIAB** of complementary images are formed. Four picture tuning operand **NY0**÷**NY3** are formed with tuning vector signals $ny0$ ÷ $ny3$. Four logical members **SY0**÷**SY3** are formed using simultaneous threshold and state decoding operations. The sum of those members is the output matrix function **NF**. All operands dimension is 64×64 elements. All images of above mentioned matrixes and some output functions are shown in Figure 22.

```

D1 := READBMP("D:\TatoD\tato2\tato\ff1.bmp")
D2 := READBMP("D:\TatoD\tato2\tato\ff2.bmp")

```



$$\begin{aligned}
 A1 &:= \text{submatrix}\left[\left[\frac{D1-10}{255}, 0, 63, 0, 63\right], AN1_{i,j} := 10 - A1_{i,j}\right. \\
 B1 &:= \text{submatrix}\left[\left[\frac{D2-10}{255}, 0, 63, 0, 63\right], BN1_{i,j} := 10 - B1_{i,j}\right. \\
 &\quad \left. R_{i,j} := 1 \quad RN_{i,j} := 0\right. \\
 &\quad \left. i := 0..63 \quad j := 0..63\right. \\
 &\quad \left. tr := 30 \quad to := 10\right.
 \end{aligned}$$

$$\begin{aligned}
 XD_{i,j} &:= 10 \cdot \Phi(65 - i - j) \\
 YD_{i,j} &:= 10 \cdot \Phi[(63 - j \cdot 2) + i - 60] \\
 SIAB &:= A1 + 2 \cdot B1 \\
 T1SIAB_{i,j} &:= 10 \cdot \Phi(SIAB_{i,j} - 10) & ny0 := 0 \quad ny1 := 1 \quad ny2 := 1 \quad ny3 := 1 \\
 T2SIAB_{i,j} &:= 10 \cdot \Phi(SIAB_{i,j} - 20) & NY0_{i,j} := 10 \cdot ny0 \quad NY1_{i,j} := 10 \cdot ny1 \\
 T3SIAB_{i,j} &:= 10 \cdot \Phi(SIAB_{i,j} - 30) & NY2_{i,j} := 10 \cdot ny2 \quad NY3_{i,j} := 10 \cdot ny3 \\
 TN1SIAB_{i,j} &:= 10 - T1SIAB_{i,j} \\
 TN2SIAB_{i,j} &:= 10 - T2SIAB_{i,j} \\
 TN3SIAB_{i,j} &:= 10 - T3SIAB_{i,j} \\
 SY0_{i,j} &:= \Phi(NY0_{i,j} - TN1SIAB_{i,j}) \cdot (NY0_{i,j} - TN1SIAB_{i,j}) \\
 SY1_{i,j} &:= \Phi(NY1_{i,j} - TN2SIAB_{i,j}) \cdot (NY1_{i,j} - TN2SIAB_{i,j}) \\
 SY2_{i,j} &:= \Phi(NY2_{i,j} - TN3SIAB_{i,j}) \cdot (NY2_{i,j} - TN3SIAB_{i,j}) \\
 SY3_{i,j} &:= \Phi(NY3_{i,j} - TN3SIAB_{i,j}) \cdot (NY3_{i,j} - TN3SIAB_{i,j}) \\
 NF_{i,j} &:= SY0_{i,j} + SY1_{i,j} + SY2_{i,j} + SY3_{i,j}
 \end{aligned}$$

Figure 21. Formulas for simulation of OPR MFLD-2 with MathCAD

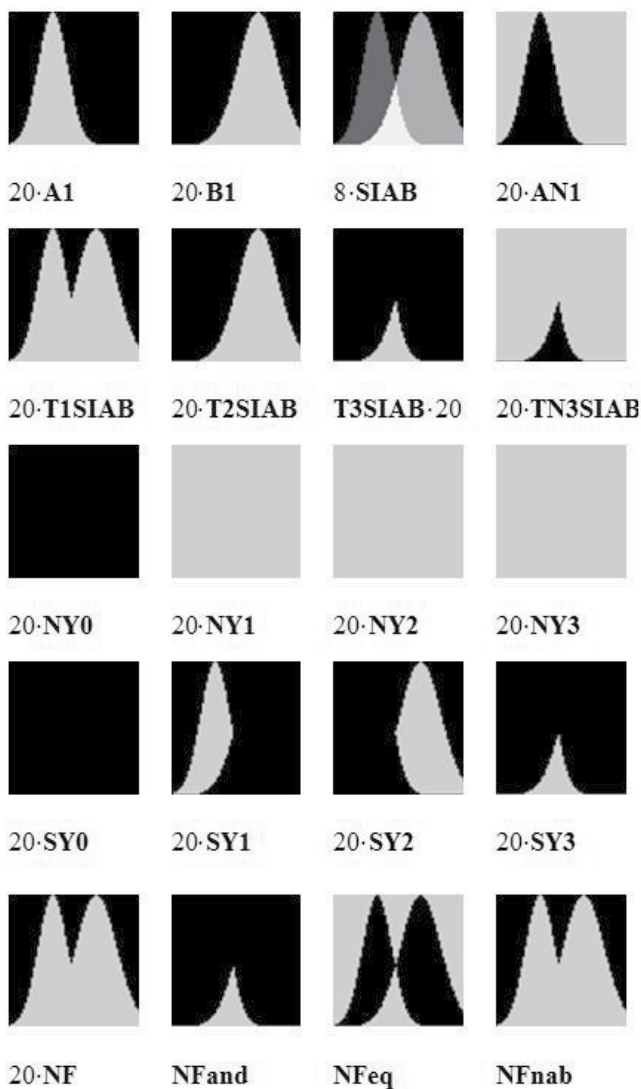


Figure 22. The simulation results of the OPR MFLD-2 with MathCAD for single-cycle high-speed computation of continuous logic operations and / or fuzzy logic for membership functions. In the bottom row the functions realization MAX/OR, MIN/AND, EQ/NXOR, $(\bar{A} \cdot B)$ over the two graphs presented in the form of membership functions of operands **A1** and **B1**

Simulation results for different functions (AND, EQ, NEQ, OR) implementation in four different sub-regions is shown in Figure 23. **XD** and **YD** are the input matrixes. Tuning matrixes **VY0÷VY3** have different values in sub-regions. Output matrix **VF** is concatenation of sub-region functions.

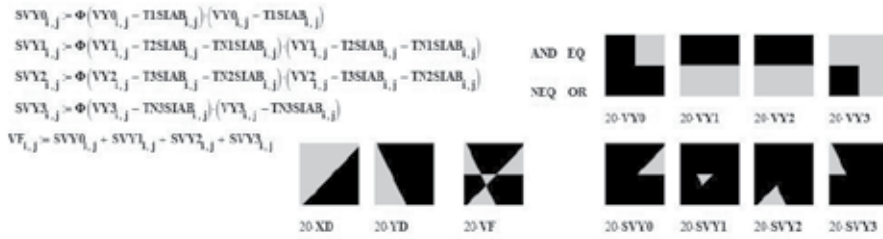


Figure 23. The simulation results for sub-region function AND, EQ, NEQ, OR implementation

Let’s demonstrate the possibilities for image processing with such devices. An example of contour extraction (NF) when processing the first input operand image A1 and its shifted copy AES1 as the second operand is shown in figure 24. In figure 24: NY0, NY1, NY2, NY3 – tuning matrixes for that operation; NF – the output image.



Figure 24. Simulation results of the OPR MFLD-2 with MathCAD for contour extraction

3. Conclusions

We have developed two version of OPR MFLD which realizes the universal binary logic on optical signals. They have subpixel configuration of 2x2 elements, consist of a small amount of photodiodes (4) and transistors (18), have low power consumption <1-5mW, high productivity and realize the basic set of operations of continuous logic with time pulse representation of processed signals. Modeling of such cells with OrCad is made. It is confirmed that all set of possible functions will be realized with such MFLD by a simple photo tuning. Such cells for OPR MFLD are integrated into array of 32x32 allow reaching productivity 10^{12} CL-logic operations/sec.

Author details

Vladimir G. Krasilenko^{1*}, Aleksandr I. Nikolsky^{2*} and Alexander A. Lazarev²

*Address all correspondence to: krasilenko@mail.ru, fortuna888@i.ua

1 Vinnitsa Social Economy Institute of Open International University of Human Development "Ukraine", Ukraine

2 Vinnitsa National Technical University, Ukraine

References

- [1] Semiconductor Industry Association. (2001). The international Technology Roadmap for Semiconductors San Jose, USA.
- [2] Fey, D. (2001). Architecture and technologies for an optoelectronic VLSI. *Optik*, 112(7), 274-282.
- [3] Li, G, Huang, D, Yucetukk, E, Marchand, P, Esener, J, Ozguz, S, & Liu, Y. (2002). There- Dimensional Optoelectronic Stacked Processor by use of Free-Spase Optical Interconnection and Three-Dimensional VLSI Chip Stacks. *Applied optics.*, 41.
- [4] Honeywell Technology Center. <http://htchoneywell.com/photonics>.
- [5] Masahiko, M, & Toyohiko, Y. (1997). Optical learning neural networks with two dimensional structures. *Proc. SPIE.*, 3402, 226-232.
- [6] Berger, C, Collings, N, & Gehriger, D. (1997). Recurrent Optical Neural Network for the Study of Pattern Dynamics. *Proc. SPIE.*, 3402, 233-244.

- [7] Krasilenko, V. G, Nikolsky, A. I, Zaitsev, A. V, & Voloshin, V. M. (2001). Optical pattern recognition algorithms on neural-logic equivalent models and demonstration of their prospects and possible implementations. *Proc. SPIE*, 4387, 247-260.
- [8] Krasilenko, V. G, Saletsky, F. M, Yatskovsky, V. I, & Konate, K. (1997). Continuous logic equivalent models of Hamming neural network architectures with adaptive correlated weighting. *Proc. SPIE*, 3402, 398-408.
- [9] Krasilenko, V. G, Nikolsky, A. I, Lazarev, A. A, & Sholohov, V. I. (2004). A concept of biologically motivated time-pulse information processing for design and construction of multifunctional devices of neural logic. *Proc. SPIE*, 5421, 183-195.
- [10] Krasilenko, V. G. (1988). Optoelectronic structures in information-measuring systems for image processing. Dissertation for the degree of candidat of tech. science. Vinnitsa., 188.
- [11] Krasilenko, V. G, Kolesnitsky, O. K, & Boguhvalsky, A. K. (1995). Creation Opportunities of Optoelectronic Continuous Logic Neural Elements, which are Universal Circuitry Macrobasis of Optical Neural Networks. *Proc. SPIE*, 2647, 208-217.
- [12] Huang, H, Itoh, M, & Yatagai, T. (1999). Optical scalable parallel modified signed-digit algorithms for large-scale array addition and multiplication using digit-decomposition-plane representation. *Opt. Eng.*, 38, 432-440.
- [13] Huang, K. S, Yenkin, B. K, & Sawchuk, A. A. (1989). Image algebra representation of parallel optical binary arithmetic. *Applied Optics*, 28, N6, 1263-1278.
- [14] Awwal, A. A, & Iftekharuddin, K. M. (1999). Computer arithmetic for optical computing. *Special Section Opt. Eng.*, 38.
- [15] Krasilenko, V. G, Yatskovsky, V. I, & Dubchak, V. N. (2001). Organization and design of computing structures of matrix-quaternion sign-digit arithmetic. *Measuring and Computer Technique in Technological Processes*, 1, 146-150.
- [16] Guilfoyle, P. S, & Mccallum, D. S. (1996). High-speed low-energy digital optical processors. *Opt. Eng.*, 35(2), 436-442.
- [17] Krasilenko, V. G, & Dubchak, V. N. (1988). Structure of optoelectronic processors of parallel type for image processing. *New electronic installations and devices*, 63-65.
- [18] Krasilenko, V. G, Kolesnitsky, O. K, & Dubchak, V. N. (1991). Creation principles and circuitry construction question of multichannel arrangements and systems for parallel image analysis and processing. *Proc. 1-st All-Union Meeting on Pattern recognition and image analysis*, Minsk, 3, 83-87.
- [19] Krasilenko, V. G, & Magas, A. T. (1999). Fundamentals of design of multi-functional devices of matrix multi-valued logic with fast programmed adjusting. *Measuring and computer technique in technological processes*, 4, 113-121.

- [20] Krasilenko, V. G, Dubchak, V. N, & Boyko, R. (1990). Development and application of optoelectronic 2D-array bi-stable structures. *Information Bulletin of Belarus Academy of Sciences*, 6, 69-72.
- [21] Krasilenko, V. G, Nikolsky, A. I, Yatskovsky, V. I, Ogorodnik, K. V, & Lischenko, S. (2002). The family of new operations "equivalency" of neuro-fuzzy logic, their optoelectronic realization and applications. *Proc. SPIE*, 4732, 106 -120 .
- [22] Shimbirev, P. N. (1990). Hybrid continuous-logic arrangements. Moscow: Energoizdat., 176.
- [23] Levin, V. I. (1990). Continuous logic, its generalization and application. *Automatica and telemekhanika*, 8, 3-22.
- [24] Samofalov, K. G, Korneychuk, V. N, Romankevich, A. I, & Tarasenko, V. P. (1974). Digital multi-valued logic devices. Kiev: Higher school, 168.
- [25] Krasilenko, V. G, Nikolsky, A. I, Lazarev, A. A, & Pavlov, S. N. (2005). Design and applications of a family of optoelectronic photocurrent logical elements on the basis of current mirror and comparators. *Proc. SPIE*, 5948, 426-435.
- [26] Krasilenko, V. G, Nikolsky, A. I, & Lazarev, A. A. (2009). Perfection of circuits for realization of the generalized equivalence (nonequivalence) operations neurobiologic. *Announcer of the Khmelnytsk national university*, 2, 174-178.
- [27] Krasilenko, V. G, Nikolsky, A. I, Lazarev, A. A, & Lobodzinska, R. F. (2007). Multi-threshold comparators with synchronous control of thresholds. *Proc. of «Dynamika naykowych badan- 2007»*, 8, Technical science: Przemysl. Nauka i studia:, 55-58.

All-Optical Autonomous First-in–First-out Buffer Managed with Carrier Sensing of Output Packets

Hiroki Kishikawa, Hirotaka Umegae,
Yoshitomo Shiramizu, Jiro Oda, Nobuo Goto and
Shin-ichiro Yanagiya

Additional information is available at the end of the chapter

<http://dx.doi.org/10.5772/51083>

1. Introduction

Along with rapid progress of optical fiber links in the physical layer of networks, optical processing in the control layer such as data links and internet layers is expected to realize photonic networks. Various kinds of architectures of optical routers and switches have been exploited. Optical buffering is one of the indispensable key technologies for avoiding packet collision in these network nodes.

Various optical buffering systems have been reported [1,2]. Most of them consist of optical fiber delay lines (FDLs). Although optical slow light can be a potential candidate to adjust short delay timing [3,4,5], FDLs are regarded to be most useful elements for packet buffering. Basically, two kinds of architectures of buffers with FDLs have been considered. One is a feedforward architecture, consisting of parallel FDLs that have different lengths corresponding to desired delay times. A combination of input and output buffered switch [6] and multistage FDL buffer [7] were reported as feedforward architectures. The other is an architecture consisting of feedback-looped FDLs. It potentially provides infinite delay time if waveform distortion caused by loss, noise, dispersion etc., is managed to be compensated. However, the FDLs can provide only a restricted function of a finite delay time as buffers because the optical packet cannot be read out during the propagation in the FDLs.

In most of the proposed architectures, electrical processing for scheduling and management has been employed [8-12]. Although flexible control including quality of service (QoS) can be realized using such a control method, simple autonomous control is preferable for simple and low-power consumption buffering.

We have proposed an autonomous first-in-first-out (FIFO) buffer management system using all-optical sensing of packets [13]. Each of FDLs in the reported system stores a single packet. In this chapter, we describe architecture and operation of the buffering system. The buffering performances such as packet loss rate (PLR) and delay time are evaluated by numerical simulation.

2. Proposed Buffering System

2.1. Architecture of the Buffering System

The proposed buffering system consists of N parallel buffering modules and a combiner as shown in Fig.1. Each module can manage the buffering in autonomous fashion by exchanging the information signals that include utilization of output port as indicated by dashed lines. Packets forwarded by the buffering modules are transmitted to output port through an $N \times 1$ combiner.

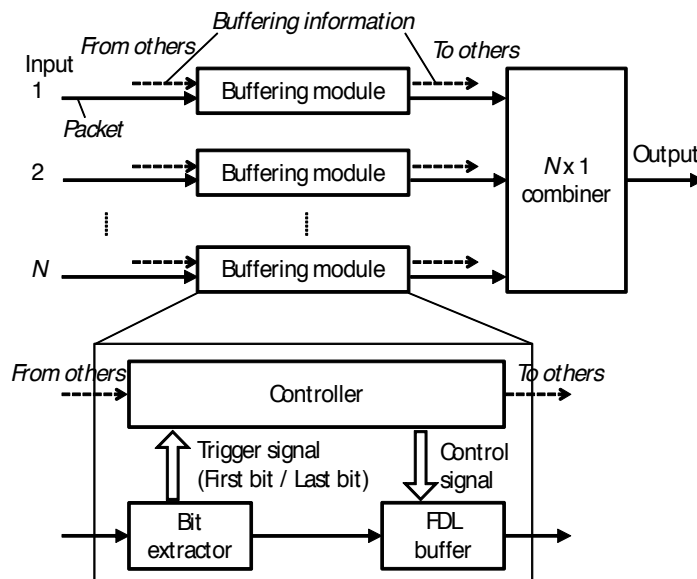


Figure 1. Schematic diagram of proposed buffering system.

The structure of a buffering module is also shown in inset of Fig. 1. It consists of a bit extractor, a controller, and an FDL buffer. The bit extractor creates trigger signal by detecting the first bit and the last bit of incoming packets. The first and last bits can be composed of specific coded bit patterns. Optical code-correlation processing can find the start and the end of the packet as the first and the last bits, respectively. The controller generates control signal autonomously by using the trigger signal. The FDL buffer stores and forwards packets by using the control signal.

2.2. Configuration of the Controller

Figure 2 shows the schematic diagram of the controller composed of four components. Controller A creates timing clock C_1 to be used to open the buffer for storing packets. Controller B creates 'store' signal which indicates the actually storing FDL in the buffer. Controller C creates another timing clock C_2 to be used to forward the already stored packets. Controller D creates 'forward' signal and the buffering information to other modules which indicates whether the buffer is now forwarding packets or not.

Figure 3 shows the configuration of controller A. Timing clock C_1 corresponds to the extracted first bit of incoming packets. The extracted last bit is not used in this case. However, it is reserved for future enhancement of the buffering system.

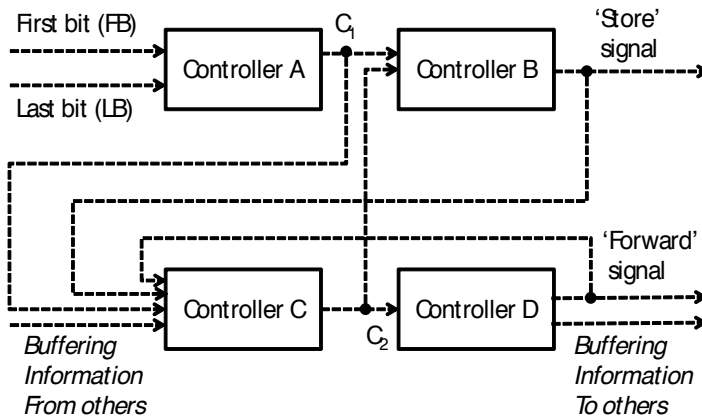


Figure 2. Schematic diagram of the controller.

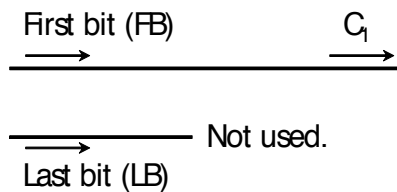


Figure 3. Configuration of controller A.

Figure 4 shows the configuration of controller B. It autonomously generates 'store' signals by processing C_1 and C_2 . The number of 'store' signals is $M+1$ where M corresponds to the number of FDLs in the buffer. In order to indicate actual storing position, none or only one of the 'store' signals becomes on-state. When C_1 comes, position of on-state moves up from #1 to $\#(M+1)$, namely, initially all off-state turns to #1-on, then moves to #2-on, #3-on, and so

on. On the contrary, when C_2 comes, position of on-state moves down from $\#(M+1)$ to $\#1$. There are some delay lines with delay time of $T_{FIFO}-T_1$ and T_1 , where T_{FIFO} and T_1 are delay of single FDL in the buffer and 1-bit, respectively. Note that these components are expressed by some sort of logic circuits. Although it depends on the function and the performance such as operating speed, power consumption, and footprint, both electrical and optical logic circuits might be candidates to be employed.

Figure 5 shows the configuration of controller C. It autonomously generates C_2 by processing C_1 , 'store' signal, buffering information signals from other modules, and 'forward' signal mentioned below. The operation of controller C is similar to the FDL buffer for packets. Therefore, we describe the detailed operation in the latter section about FDL buffer.

Figure 6 shows the configuration of controller D. It autonomously generates 'forward' signal by processing C_2 . The 'forward' signal keeps on-state for a period of T_{FIFO} by using the flip-flop triggered by C_2 .

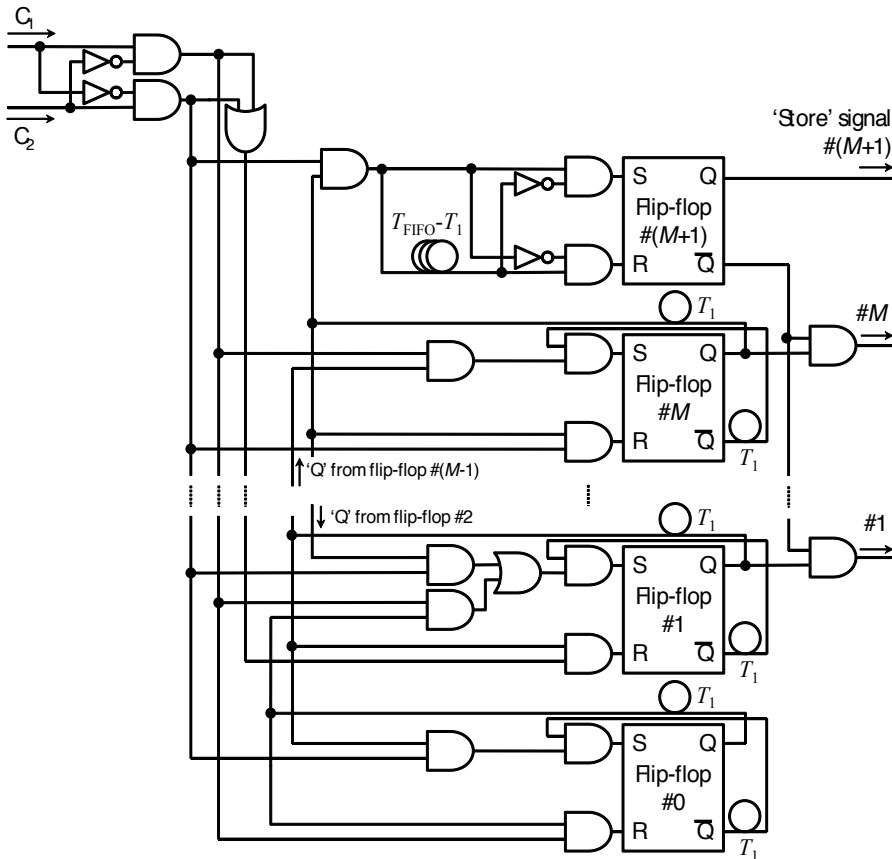


Figure 4. Configuration of controller B.

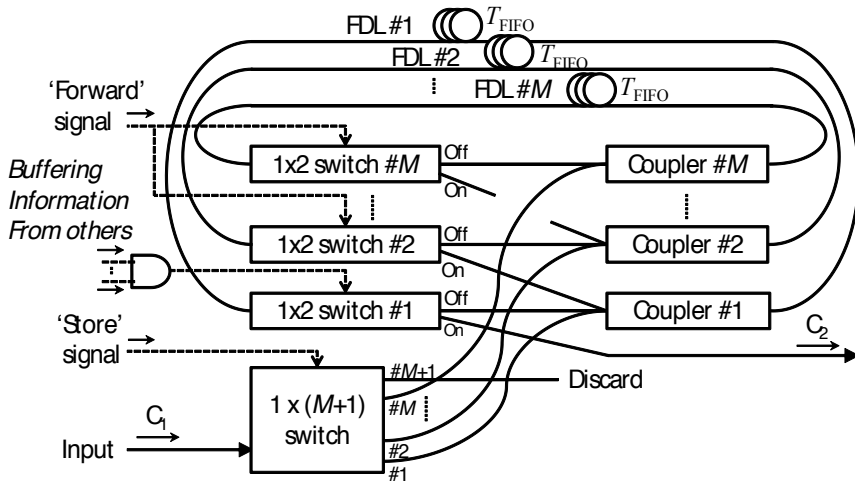


Figure 5. Configuration of controller C.

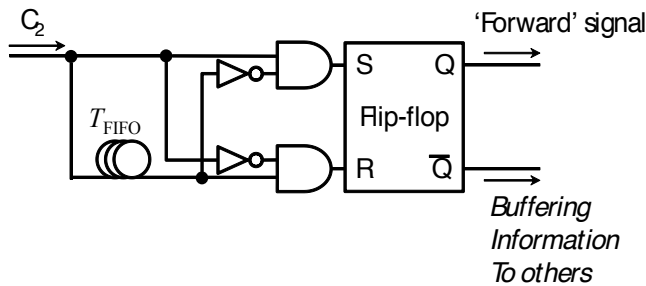


Figure 6. Configuration of Controller D.

2.3. Configuration of the FDL Buffer

The FIFO buffer consists of M parallel FDLs that have delay time of T_{FIFO} , a $1 \times (M+1)$ input switch, $M1 \times 2$ output switches and couplers as shown in Fig. 7. The buffer stores and forwards packets by using 'store' and 'forward' signals, respectively. The stored position is determined by the state of 'store' signal. Namely, when k -th signal is on-state ($k=1, \dots, M$), incoming packets are switched to k -th FDL by the input switch. In case that $(M+1)$ -th signal is on-state, then incoming packets will be discarded because all of the FDLs have already been occupied with other packets. The stored packets are forwarded to output by controlling the output switches. When the 'forward' signal is incident, all of the output switches move the stored packets to next neighbor FDLs. Note that T_{FIFO} is designed to be greater than or equal to the maximum packet length.

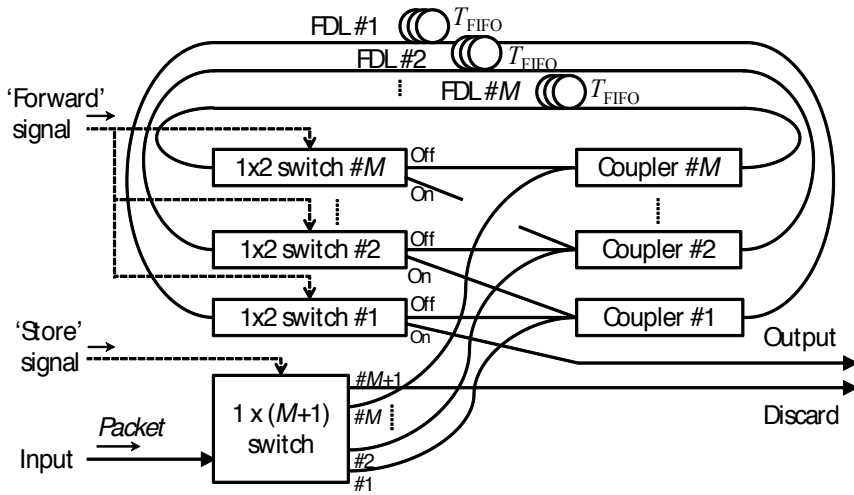


Figure 7. Configuration of the FDL buffer.

2.4. Operation Overview of Buffering

An example of timing chart for buffering process of a module is shown in Fig. 8.

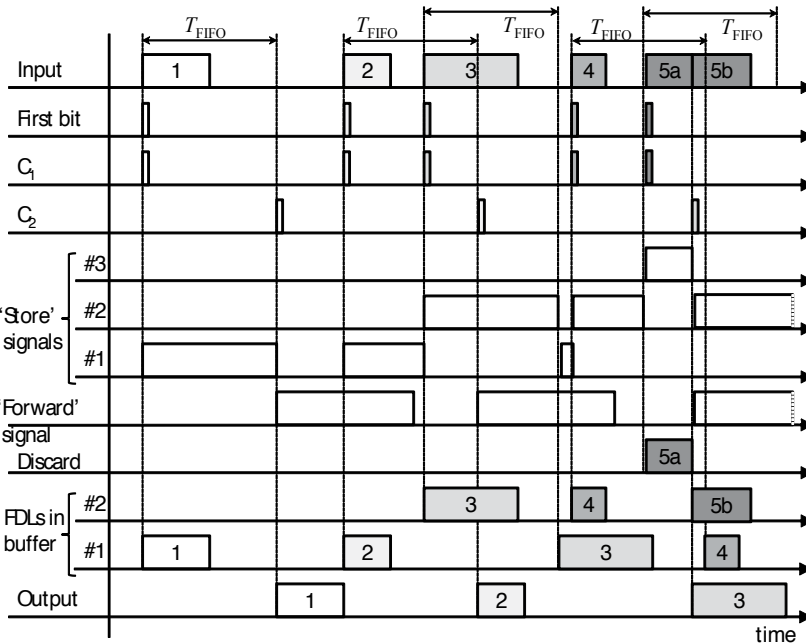


Figure 8. Timing chart example of a module of the buffer.

We assume that there are initially no packets stored in the FDLs, and then five packets are arriving sequentially with random timing and variable lengths. The number of FDLs M is assumed to be $M=2$.

When packet no.1 is incident, 'store' signal #1 turns on triggered by the first bit and C_1 . The state of the 'store' signal is kept for a period of T_{FIFO} . When T_{FIFO} is expired, 'forward' signal turns on triggered by the C_2 . Then, stored packets no.1 is forwarded to output. If another module has already been open for forwarding, the 'forward' signal of this module does not turn on in order to avoid collision between this module and the forwarding module. When packet no.3 is incident before the expiration period T_{FIFO} of packet no.2, it is stored into another FDL because each FDL is designed for storing only a single packet.

Although similar operation can be seen for following packets, packet no.5 is slightly different. The front part of it is discarded because all FDLs have already been occupied by other packets. When packet no.3 is forwarded, FDL #2 is open for storing. At the moment, the rear part of packet no.5 is stored into there. Note that the packet no.5 is therefore treated as a broken packet when it gets out from the buffer.

3. Computer Simulation

Two kinds of characteristics such as packet loss rate (PLR) and average delay time are investigated by computer simulation. We assume in the simulation that packets arrive randomly and have variable lengths from $L_{\text{min}}=10$ to $L_{\text{max}}=150$ bytes. We define load at input port by the ratio of the packet existence length to a unit length. For simplicity, operation speed of the composed devices, such as switching speed of some spatial switches and flip-flops, rise time of logic gates, are assumed to be much faster than bit-rate of arriving packets. Therefore, bit-rate is not specified in our simulation.

3.1. Packet Loss Rate

The PLR is verified with changing the number of FDLs M , length of each FDL L , number of input N , and the load. Because of a finite number of FDLs in the buffer system, overflow may occur when the load exceeds the capacity of the buffer, resulting in rejection of the overflowed packets. Even if the load is less than the capacity, collision of packets may occur when packets forwarded by some modules are simultaneously coming into the following combiner as shown in Fig.1. Therefore in the simulation, the overflow and the collision are both treated as loss of packet.

Figure 9 shows the PLR as a function of the load at module #1 with the number of FDLs M as a parameter. The number of modules is $N=2$. The load of the module #2 is set to 0.5. The length of each FDL is $L=L_{\text{max}}$. It is found that the PLR increases with load at module #1. Moreover, the PLR decreases when M increases.

Figure 10 shows the PLR as a function of the load at module #1 with the length of FDLs L as a parameter. The number of modules is $N=2$. The load of the module #2 is set to 0.5. The

number of FDLs is $M=10$. It is found that the PLR increases both with load at module #1 and L . This is because incoming packets are separately stored in different FDLs, resulting in many FDLs are occupied with unused space remained. When L becomes long, the duration of occupation becomes long, and then it takes longer time to get out from the buffer. Therefore, it may cause the increase of packet loss because of the occupied FDLs.

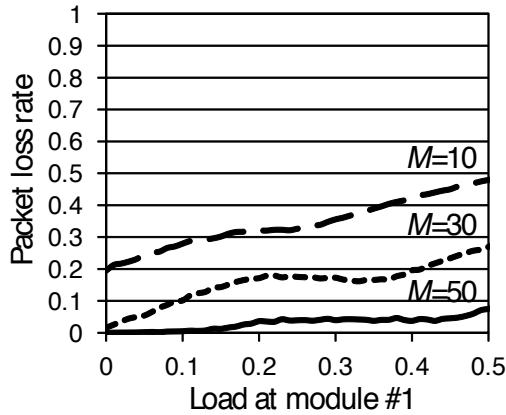


Figure 9. PLR with parameter M .

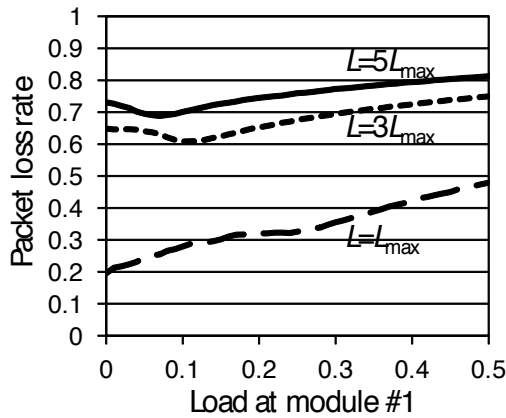


Figure 10. PLR with parameter L .

Figure 11 shows the PLR as a function of the load at module #1 with the load at module #2 as a parameter. The number of modules is $N=2$. The number of FDLs is $M=30$. The length of each FDL is $L=L_{max}$. It is found that the PLR increases with load at module #1 and #2.

Figure 12 shows the PLR as a function of the load at module #1 with the number of module N as a parameter. The number of FDLs is $M=30$. The length of each FDL is $L=L_{max}$.

Loads of modules other than #1 are all set to 0.3. It is found that the PLR increases with load at module #1 and N .

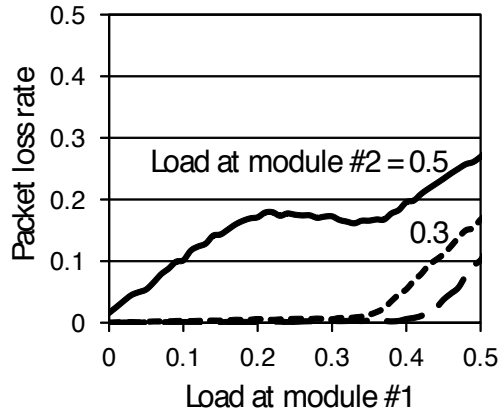


Figure 11. PLR with parameter load at module #2.

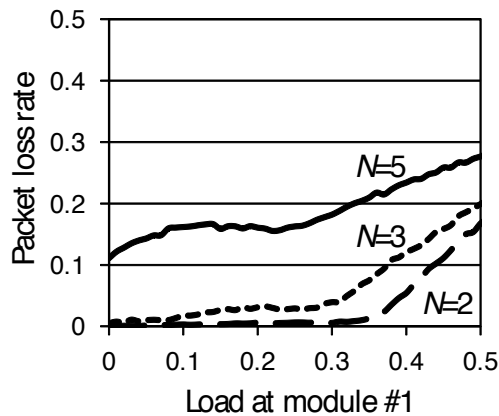
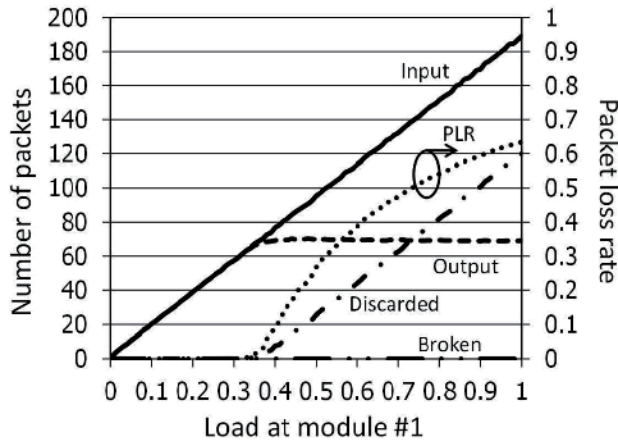


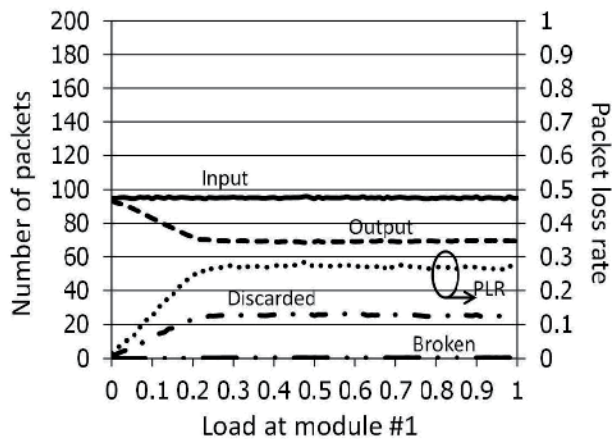
Figure 12. PLR with parameter N .

Figure 13 shows the breakdown of such numbers as input, output, discarded and broken packet in (a) module #1 and (b) module #2. Parameters are set to as follows; the number of modules is $N=2$, the number of FDLs is $M=30$, the length of each FDL is $L=L_{max}$, the load of module #1 is changed, and that of module #2 is 0.5 fixed. It is found from Fig. 13(a) that the number of output packets saturates up to 70 when the load at module #1 exceeds 0.3. This is because it starts overflow at that point, namely the number of discarded packets increases in proportion to the input. As a result, the PLR also increases. In case of module #2 shown in Fig. 13(b) that the fixed number of input initially exceeds its overflow limit, and so the num-

ber of discarded packets increases up to a certain value. Then, the number of output decreases to the same level as that of module #1. Therefore, this 2×1 buffer puts the identical output priority to the two modules.



(a) Module #1



(b) Module #2

Figure 13. Breakdown of such numbers as input, output, discarded, and broken packet in each module.

3.2. Average Delay

Packets stored and forwarded through the buffer have been experienced a certain amount of delay determined mainly by the load and parameters M and L . We examine the average delay time by computer simulation.

Figure 14 shows the average delay as a function of the load at module #1 with the number of FDLs M as a parameter. The number of modules is $N=2$. The load of the module #2 is set to

0.5. The length of each FDL is $L=L_{\max}$. It is found that the average delay increases with load at module #1 and M .

Figure 15 shows the average delay as a function of the load at module #1 with the length of each FDL L as a parameter. The number of modules is $N=2$. The load of the module #2 is set to 0.5. The number of FDLs is $M=10$. It is found that the average delay increases with load at module #1 and L .

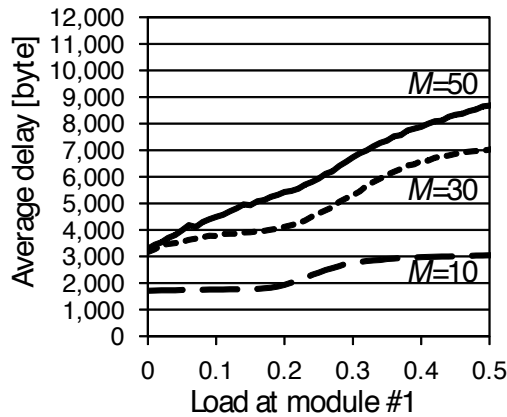


Figure 14. Average delay with parameter M .

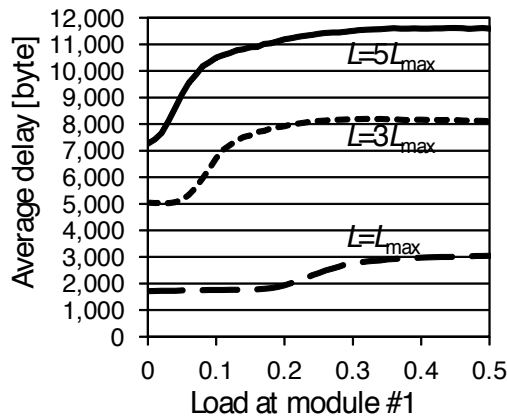
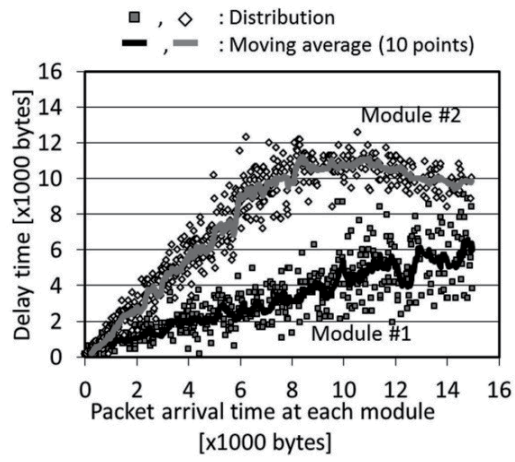
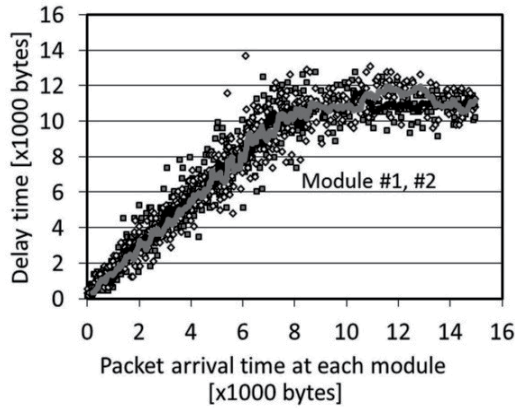


Figure 15. Average delay with parameter L .

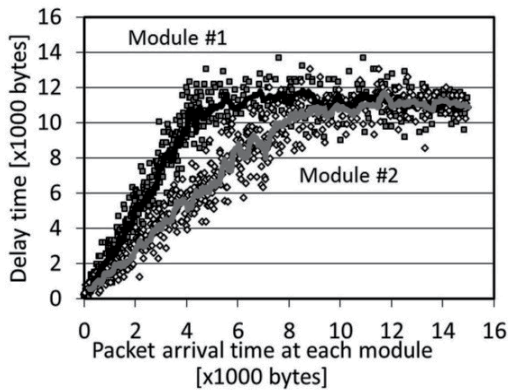
Figure 16 shows distribution and moving average indicated by dots and solid curves, respectively, of delay time as a function of packet arrival time to each module with loads as parameters. The load of the module #1 is changed between 0.3, 0.5, and 0.7. The load of the module #2 is set to 0.5. The number of modules is $N=2$. The number of FDLs is $M=30$.



(a) Load at module #1=0.3, and load at module #2=0.5



(b) Load at module #1=0.5, and load at module #2=0.5



(c) Load at module #1=0.7, and load at module #2=0.5

Figure 16. Distribution of delay time at each module.

The length of each FDL is $L=L_{\max}$. It is found that the delay time shows linear increase with packet arrival time because of the growth of buffer occupation. Moreover, the delay time shows saturation where the buffer occupation comes up to a maximum capacity. In addition, the heavily-loaded module, which corresponds to module #2 at Fig. 16(a) whereas module #1 at (c), shows faster increase and saturation than another module.

4. Conclusion

We have proposed an autonomous first-in-first-out buffer with capability of storing a single packet in each of FDLs. Characteristics of PLR and average delay have been investigated by numerical simulation. As a result, the PLR and the average delay have a trade-off relation at such parameters as number of FDL M and length of each FDL L . Therefore they should be determined by system demand. Smaller M and larger L can be options for implementing the system from viewpoints of footprint, power consumption, and avoid complicated control. Our future works include detailed investigation of buffering performance considering response time in switching and other constituent devices, and experimental verification.

Author details

Hiroki Kishikawa¹, Hiroataka Umegae¹, Yoshitomo Shiramizu², Jiro Oda², Nobuo Goto^{1*} and Shin-ichiro Yanagiya¹

*Address all correspondence to: goto@opt.tokushima-u.ac.jp

1 Department of Optical Science and Technology, The University of Tokushima, Japan

2 Department of Information and Computer Sciences, Toyohashi University of Technology, Japan

References

- [1] Burmeister, E. F., Blumenthal, D. J., & Bowers, J. E. (2008, Mar). A comparison of optical buffering technology. *Optical Switching and Networking*, 5(1), 10-18.
- [2] Hunter, D. K., Chia, M. C., & Andonovic, I. (1998, Dec). Buffering in optical packet switches. *J. Lightwave Technol.*, 16(12), 2081-2094.
- [3] Tucker, R. S., Ku, P., C., & Chang-Hasnain, C. J. (2005, Dec). Slow-light optical buffers: Capabilities and fundamental limitations. *J. Lightwave Technol.*, 23(12), 4046-4066.
- [4] Baba, T. (2008, Aug). Slow light in photonic crystals. *Nature Photonics* [8], 465-473.

- [5] Fontaine, N. K., Yang, J., Pan, Z., Chu, S., Chen, W., Little, B. E., & Yoo, S. J. B. (2008, Dec). Continuously tunable optical buffering at 40Gb/s for optical packet switching networks. *J. Lightwave Technol.* [23], 3776-3783.
- [6] Yang, H., & Yoo, S. J. B. (2005, June). Combined input and output all-optical variable buffered switch architecture for future optical routers. *IEEE Photonics Technol. Lett.*, 17(6), 1292-1294.
- [7] Ogashiwa, N., Harai, H., Wada, N., Kubota, F., & Shinoda, Y. (2005, Jan). Multistage fiber delay line buffer in photonic packet switch for asynchronously arriving variable-length packets. *IEICE Trans. Commun.*, E88-B(1), 258-265.
- [8] Harai, H., & Murata, M. (2006, Aug). Optical fiber-delay-line buffer management in optical-buffered photonic packet switch to support service differentiation. *IEEE J. on Sel. Areas in Commun.*, 24(8), 108-116.
- [9] Wang, Z., Chi, C., & Yu, S. (2006, Aug). Time-slot assignment using optical buffer with a large variable delay range based on AVC crosspoint switch. *J. Lightwave Technol.*, 24(8), 2994-3001.
- [10] Liew, S. Y., Hu, G., & Chao, H. J. (2005, Apr). Scheduling algorithms for shared fiber-delay-line optical packet switches- part I: The single-stage case. *J. Lightwave Technol.*, 23(4), 1586-1600.
- [11] Shinada, S., Furukawa, H., & Wada, N. (2011, Dec). Huge capacity optical packet switching and buffering. *Optics Express*, 19(26), B406-B414.
- [12] Kurumida, J., & Yoo, S. J. Ben. (2012, Mar/Apr). Nonlinear optical signal processing in optical packet switching systems. *IEEE J. Selected Topics in Quantum. Electron.*, 18(2), 978-987.
- [13] Shiramizu, Y., Oda, J., & Goto, N. (2008, Aug). All-optical autonomous first-in-first-out buffer managed with carrier sensing of output packet. *Optical Engineering*, 47(8), 085006-1-8.

A Method and Electronic Device to Detect the Optoelectronic Scanning Signal Energy Centre

Moisés Rivas, Wendy Flores, Javier Rivera,
Oleg Sergiyenko, Daniel Hernández-Balbuena and
Alejandro Sánchez-Bueno

Additional information is available at the end of the chapter

<http://dx.doi.org/10.5772/51993>

1. Introduction

In optoelectronic scanning, it has been found that in order to find the position of a light source, the signal obtained looks like a Gaussian signal shape. This is mainly observed when the light source searched by the optoelectronic scanning is punctual, due to the fact that when the punctual light source expands its radius a cone-like or an even more complex shape is formed depending on the properties of the medium through which the light is travelling. To reduce errors in position measurements, the best solution is taking the measurement in the energy centre of the signal generated by the scanner, see [1].

The Energy Centre of the signal concept considers the points listed below, see [2], in order to search which one of them represents the most precise measurement results:

- The Signal Energy Centre could be found in the peak of the signal.
- The Signal Energy Centre could be found in the centroid of the area under the curve Gaussian-like shape signal.
- The Signal Energy Centre could be found in the Power Spectrum Centroid.

The Energy Centre of the signal could be found by means of the optoelectronic scanner sensor output processing, through a computer programming algorithm, taking into account the points mentioned above, in a high level technical computing software for engineering and science like MATLAB. However, our contribution is a method and an electronic hardware to produce an output signal related to the Energy Centre in the optoelectronic scanning sensor, for applications in position measurements.

This method is based on the assumption that the signal generated by optical scanners for position measurements is a Gaussian-like shape signal. However, during experimentation it has been seen that the optoelectronic scanning sensor output is a Gaussian-like shape signal with some noise and deformation. This is due to some internal and external error sources like the motor eccentricity at low speed scanning, noise and deformation that could interfere with the wavelength of the light sources. Other phenomena could also affect such as of reflection, diffraction, absorption and refraction, producing a trouble that can be minimized by taking measurement in the energy centre of the signal.

The main interest of this chapter is to describe and explain a method to find the energy centre of the signal generated by optical scanners based on a dynamic triangulation, see [3], to reduce errors in position measurements.

2. Optoelectronic scanners for position measurements

Nowadays optoelectronic scanners are widely used for multiple applications; most of the position or geometry measuring scanners use the triangulation principle or a variant of this measurement method. There are two kinds of scanners for position measuring tasks: scanners with static sensors and scanners with rotating mirrors. Optical triangulation sensors with CCD or PSD are typically used to measure manufactured goods, such as tire treads, coins, printed circuit boards and ships, principally for monitoring the target distance of small, fragile parts or soft surfaces likely to be deformed if touched by a contact probe.

2.1. Scanners with position triangulation sensors using CCD or PSD

A triangulation scanner sensor can be formed by three subsystems: emitter, receiver, and electronic processor as shown in figure 1. A spot light is projected onto the work target; a portion of the light reflected by the target is collected through the lens by the detector which can be a CCD, CMOS or PSD array. The angle(α) is calculated, depending on the position of the beam on the detectors CCD or PSD array, hence the distance from the sensor to the target is computed by the electronic processor. As stated by Kennedy William P. in [4], the size of the spot is determined by the optical design, and influences the overall system design by setting a target feature size detection limit. For instance, if the spot diameter is 30 μm , it will be difficult to resolve a lateral feature $<30 \mu\text{m}$.

Many devices are commonly utilized in different types of optical triangulation position scanners and have been built or considered in the past for measuring the position of light spot more efficiently. One method of position detection uses a video camera to electronically capture an image of an object. Image processing techniques are then used to determine the location of the object. For situations requiring the location of a light source on a plane, a position sensitive detector (PSD) offers the potential for better resolution at a lower system cost[5]. However, there are other kinds of scanners used commonly in large distances measurement or in structural health monitoring tasks, these scanners will be explained in the next section.

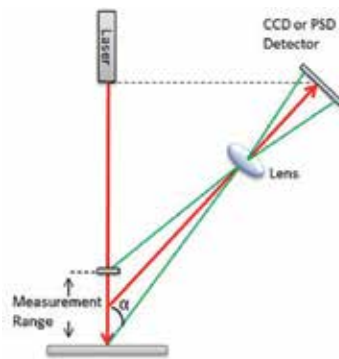


Figure 1. Principle of Triangulation.

2.2. Scanners with rotating mirrors and remote sensing

In the previous section, we described the operational principle of scanners for monitoring the distance of small objects, now we will describe the operational principle of scanners with rotating mirrors for large distances measurement or in structural health monitoring tasks.

There are two main classification of optical scanning: remote sensing and input/output scanning. Remote sensing detects objects from a distance, as by a space-borne observation platform. For example an infrared imaging of terrain. Sensing is usually passive and the radiation incoherent and often multispectral. Input / output scanning, on the other hand, is local. A familiar example is the document reading (input) or writing (output). The intensive use of the laser makes the scanning active and the radiation coherent. The scanned point is focused via finite-conjugate optics from a local fixed source, see [6].

In remote sensing there is a variety of scanning methods for capturing the data needed for image formation. These methods may be classified into framing, push broom, and mechanical. In the first one, there is no need for physical scan motion since it uses electronic scanning and implies that the sensor has a two-dimensional array of detectors. At present the most used sensor is the CCD and such array requires an optical system with 2-D wide-angle capability. In push broom methods a linear array of detectors are moved along the area to be imaged, e. g. airborne and satellite scanners. A mechanical method includes one and two dimensional scanning techniques incorporating one or multiple detectors and the image formation by one dimensional mechanical scanning requires the platform with the sensor or the object to be moved in order to create the second dimension of the image.

In these days there is a technique that is being used in many research fields named Hyperspectral imaging (also known as imaging spectroscopy). It is used in remotely sensed satellite imaging and aerial reconnaissance like the NASA's premier instruments for Earth exploration, the Jet Propulsion Laboratory's Airborne Visible-Infrared Imaging Spectrometer (AVIRIS) system. With this technique the instruments are capable of collecting high-dimensional image data, using hundreds of contiguous spectral channels, over the same area

on the surface of the Earth, as shown in figure 2. where the image measures the reflected radiation in the wavelength region from 0.4 to 2.5 μm using 224 spectral channels, at nominal spectral resolution of 10 nm. The wealth of spectral information provided by the latest generation hyperspectral sensors has opened ground breaking perspectives in many applications, including environmental modelling and assessment; target detection for military and defence/security deployment; urban planning and management studies, risk/hazard prevention and response including wild-land fire tracking; biological threat detection, monitoring of oil spills and other types of chemical contamination [7].

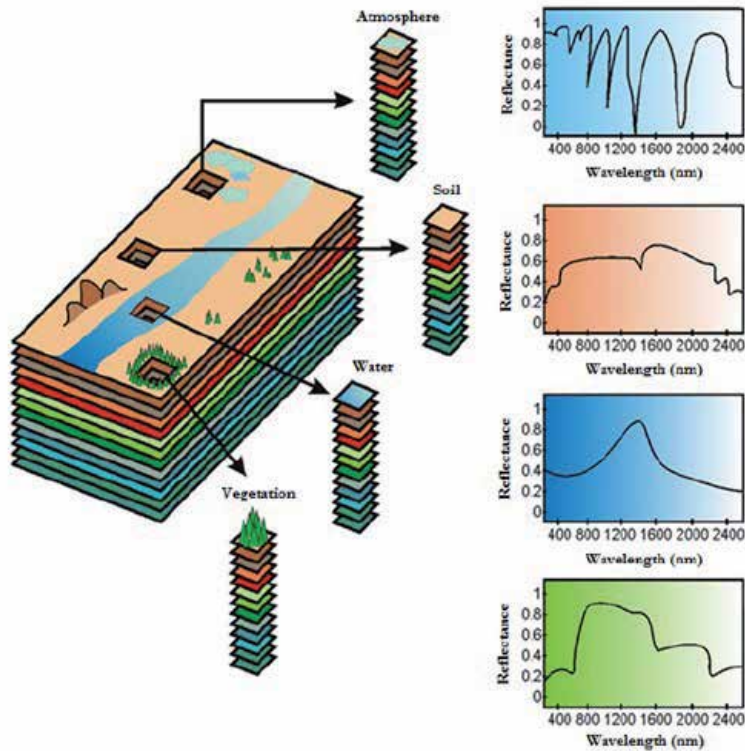


Figure 2. The concept of hyperspectral imaging illustrated using NASA's AVIRIS sensor [7].

While remote sensing requires capturing passive radiation for image formation, active input/output scanning needs to illuminate an object or medium with a "flying spot," derived typically from a laser source. In Table 1, we listed some examples divided into two principal functions: input (when the scattered radiation from the scanning spot is detected) and output (when the radiation is used for recording or displaying). Therefore, we can say that in input scanning the radiation is modulated by the target to form a signal and in the output scanning it is modulated by a signal.

| Input / Output Scanning | |
|-------------------------------|----------------------------|
| Input | Output |
| Image scanning / digitising | Image recording / printing |
| Bar-code reading | Colour image reproduction |
| Optical inspection | Medical image outputs |
| Optical character recognition | Data marking and engraving |
| Optical data readout | Micro image recording |
| Graphic arts camera | Reconnaissance recording |
| Scanning confocal microscopy | Optical data storage |
| Colour separation | Phototypesetting |
| Robot vision | Graphic arts platemaking |
| Laser radar | Earth resources imaging |
| Mensuration (Measurement) | Data / Image display |

Table 1. Examples of Input / Output Scanning.

2.2.1. Polygonal scanners

These scanners have a polygonal mirror rotating at constant speed by way of an electric motor and the radiation received by the lens is reflected on a detector. The primary advantages of polygonal scanners are speed, the availability of wide scan angles, and velocity stability. They are usually rotated continuously in one direction at a fixed speed to provide repetitive unidirectional scans which are superimposed in the scan field, or plane, as the case may be. When the number of facets reduces to one, it is identified as a monogon scanner, figure 3 illustrates an hexagonal rotating mirror scanner.

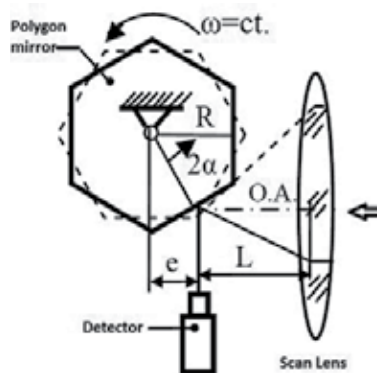


Figure 3. Polygon scanner.

2.2.2. Pyramidal and prismatic facets

In these types of scanners, the incoming radiation is focused on a regular pyramidal polygon with a number of plane mirrors facets at an angle, rather than parallel, to the rotational axis. This configuration permits smaller scan angles with fewer facets than those with polygonal mirrors. Principal arrangements of facets are termed prismatic or pyramidal. The pyramidal arrangement allows the lens to be oriented close to the polygon, while the prismatic configuration requires space for a clear passage of the input beam.

2.2.3. Holographic scanners

Almost all holographic scanners comprise a substrate which is rotated about an axis, and utilize many of the characterising concepts of polygons. An array of holographic elements disposed about the substrate serves as facets, to transfer a fixed incident beam to one which scans. As with polygons, the number of facets is determined by the optical scan angle and duty cycle, and the elemental resolution is determined by the incident beam width and the scan angle. In radially symmetric systems, scan functions can be identical to those of the pyramidal polygon. Meanwhile there are many similarities to polygons, there are significant advantages and limitations.

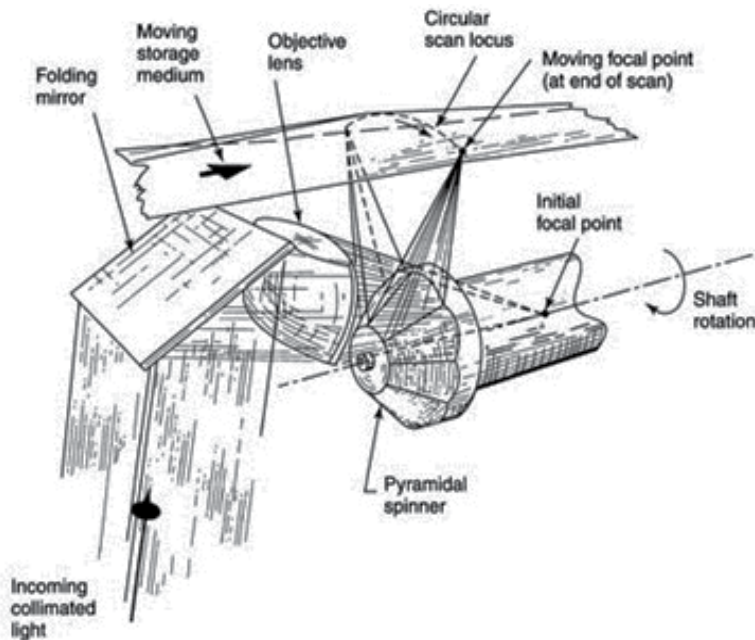


Figure 4. Polygonal scanner (From <http://beta.globalspec.com/reference/34369/160210/chapter-4-3-5-4-scanner-devices-and-techniques-postobjective-configurations>).

2.2.4. Galvanometer and resonant scanners

To avoid the scan non uniformities which can arise from facet variations of polygons or holographic deflectors, one might avoid multifacets. Reducing the number to one, the polygon becomes a monogon. This adapts well to the internal drum scanner, which achieves a high duty cycle, executing a very large angular scan within a cylindrical image surface. Flat-field scanning, however, as projected through a flat-field lens, allows limited optical scan angle, resulting in a limited duty cycle from a rotating monogon. If the mirror is vibrated rather than rotated completely, the wasted scan interval may be reduced. Such components must, however, satisfy system speed, resolution, and linearity. Vibrational scanners include the familiar galvanometer and resonant devices and the least commonly encountered piezoelectrically driven mirror transducer as shown in figure 5.

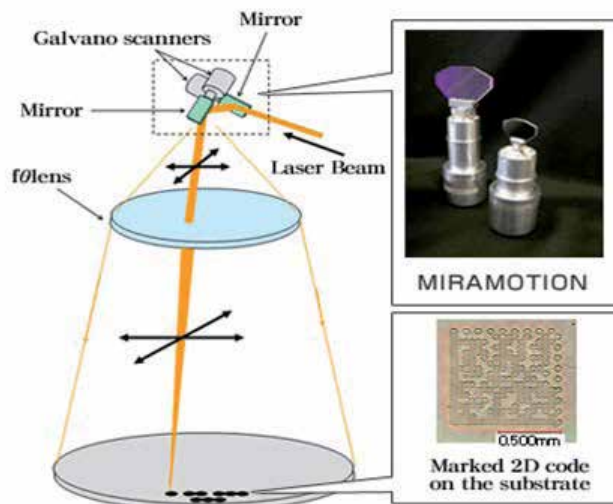


Figure 5. Galvanometer scanner (From <http://www.yedata.com>).

2.2.5. 45° cylindrical mirror scanner

Optical scanning systems can use coherent light emitting sources, such as laser or incoherent light sources like the lights of a vehicle. In the use of laser as light emitting source, the measurements are independent of environment lighting, so it is possible to explore during day and night, however, there are some disadvantages such as the initial cost, the hazard due to its high energy output, and that they cannot penetrate dense fog, rain, and warm air currents that rise to the structures, interfering the laser beam, besides, it is difficult to properly align the emitter and receiver. A passive optical scanning system for SHM can use conventional light emitting sources placed in a structure to determine if its position changes due to deteriorating. Figure 6 illustrates a general schematic diagram with the main elements of the optical scanning aperture used to generate the signals to test the proposed method.

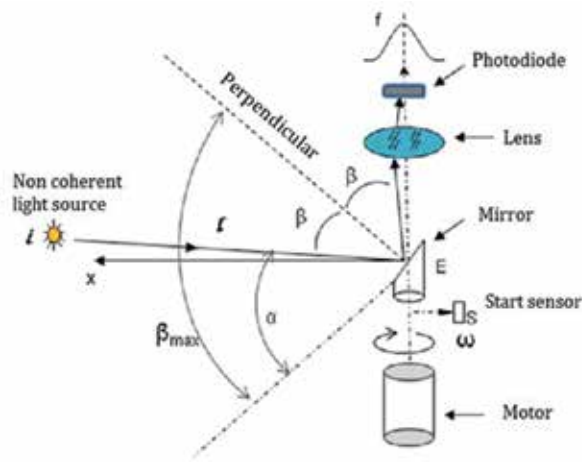


Figure 6. Cylindrical Mirror Scanner.

The optical system is integrated by the light emitter source set at a distance from the receiver; the receiver is compound by the mirror E, which spins with an angular velocity ω . The beam emitted arrives with an incident angle β with respect to the perpendicular mirror, and is reflected with the same angle β , according to the reflecting principle (C L. Wyatt, 1991) to pass through a lens that concentrates the beam to be captured by the photodiode, which generates a signal “f” with a shape similar to the Gaussian function. When the mirror starts to spin, the sensor “s” is synchronized with the origin generating a pulse that indicates the starting of measurement that finishes when the photodiode releases the stop signal. This signal is released when the Gaussian signal energetic centre has been detected.

Figure 7 shows that light intensity increments in the centre of the signal generated by the scanner. The sensor “s” generates a starting signal when $t\alpha = 0$, then the stop signal is activated when the Gaussian function geometric centre has been detected.

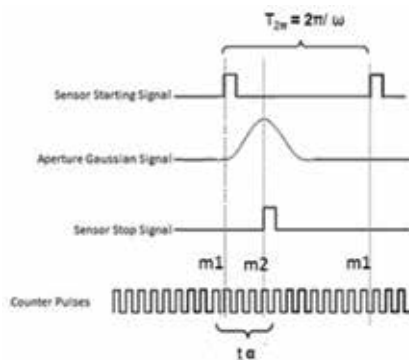


Figure 7. Signal generated by a 45° cylindrical mirror scanner.

The distance $T2\pi$ is equal to the time between $m1$ and $m1$, that are expressed by the code $N2\pi$ as defined in equation 1.

$$N_{2\pi} = T2\pi \cdot f_0 \quad (1)$$

On the other hand, the time t_α is equal to the distance between $m1$ and $m2$, could be expressed by the code defined in equation 2.

$$N\alpha = t_\alpha \cdot f_0 \quad (2)$$

Where f_0 is a standard frequency reference. With this consideration the time variable could be eliminated from equation 2 obtaining equation 3, see [8].

$$\alpha = 2\pi \cdot N_\alpha / N_{2\pi} \quad (3)$$

3. Scanner sensors

All detectors (sensors) act as transducer that receive photons and produce an electrical response that can be amplified and converted into a form of relevant parameters to handle the input data for results interpretation. Among relevant parameters we can find spectral response, spectral bandwidth, linearity, dynamic range, quantum efficiency, noise, imaging properties and time response. Photon detectors respond directly to individual photons. Absorbed photons release one or more bound charge carriers in the detector that modulates the electric current in the material and moves it directly to an output amplifier. Photon detectors can be used in a spectral band width from X-ray and ultraviolet to visible and infrared spectral regions. We can classify them as analogue waveform output and image detectors, however, another type of classification is also possible but we will only describe this type of sensors in this section.

Analogue waveform output detectors

Analogue waveform output detectors are used as an optical receiver to convert light into electricity. This principle applies to photo detectors, phototransistors and other detectors as photovoltaic cells, and photo resistance, but the most widely used today in position measuring process are the photodiode and the phototransistors.

3.1.1. Photodiode

The photodiode could convert light in either current or voltage, depending upon the mode of operation. A photodiode is based on a junction of oppositely doped regions (pn junction) in a sample of a semiconductor. This creates a region depleted of charge carriers that results

in high impedance. The high impedance allows the construction of detectors using silicon and germanium to operate with high sensitivity at room temperatures.

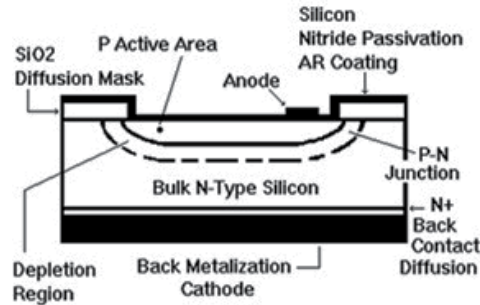


Figure 8. Cross section of a typical silicon photodiode.

A cross section of a typical silicon photodiode is shown in the figure. 8. N type silicon is the starting material. A thin "p" layer is formed on the front surface of the device by thermal diffusion or ion implantation of the appropriate doping material (usually boron). The interface between the "p" layer and the "n" silicon is known as a pn junction. Small metal contacts are applied to the front surface of the device and the entire back is coated with a contact metal. The back contact is the cathode; the front contact is the anode. The active area is coated with silicon nitride, silicon monoxide or silicon dioxide for protection and to serve as an anti-reflection coating. The thickness of this coating is optimized for particular irradiation wavelengths.

In semiconductors whose bandgaps permit intrinsic operation in the 1-15 μm , a junction is often necessary to achieve good performance at any temperature. Because these detectors operate through intrinsic rather than extrinsic absorption, they can achieve high quantum efficiency in small volumes. However, high performance photodiodes are not available at wavelengths longer than about 1.5 μm because of the lack of high-quality intrinsic semiconductors with extremely small bandgaps. Standard techniques of semiconductor device fabrication allow photodiodes to be constructed in arrays with many thousands, even millions, of pixels. Photodiodes are usually the detectors of choice for 1-6 μm and are often useful not only at longer infrared wavelengths but also in the visible and near ultraviolet.

The photodiode operates by using an illumination window, which allows the use of light as an external input. Since light is used as an input, the diode is operated under reverse bias conditions. Under the reverse bias condition the current through the junction is zero when no light is present, this allows the diode to be used as a switch or relay when sufficient light is present.

Photodiodes are mainly made from gallium arsenide instead of silicon because silicon creates crystal lattice vibrations called phonons when photons are absorbed in order to create electron-hole pairs. Gallium arsenide can produce electron-hole pairs without the slowly

moving phonons; this allows faster switching between on and off states and Ga As also is more sensitive to the light intensity. Once charge carriers are produced in the diode material, the carriers reach the junction by diffusion.

Photodiodes are similar to regular semiconductor diodes except that they may be either exposed to detect vacuum UV or X-ray or packaged with a windows or optical fibre connection to allow light to reach the sensitive part of the device. Many diodes designed to use specifically as a photodiode use a PIN junction rather than a p-n junction, to increase the speed of response [9].

Spectral response: The wavelength of the radiation to be detected is an important parameter. As shown in figure 9, silicon becomes transparent to radiation of a wavelength longer than 1100 nm.

Linearity: Current output of the photodiode is very linear with radiant power throughout a wide range. Nonlinearity remains below approximately 0.02% up to 100mA photodiode current. The photodiode can produce output currents of 1mA or greater with high radiant power, but nonlinearity increases to a certain percent in this region. This excellent linearity at high radiant power assumes that the full photodiode area is uniformly illuminated. If the light source is focused on a small area of the photodiode, nonlinearity will occur at lower radiant power.

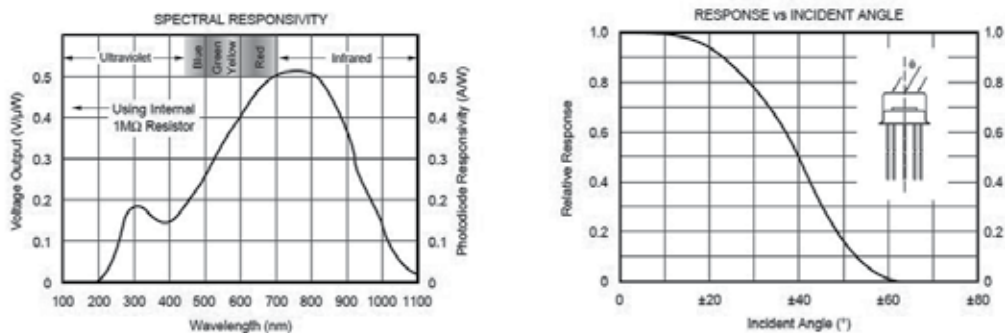


Figure 9. Spectral responsivity and response vs. incident angle of a photodiode.

Dynamic Range: Dynamic response varies with feedback resistor, using 1M resistor, the dynamic response of the photodiode can be modelled as a simple R/C circuit with a –3dB cut off frequency of 4kHz. This yields a rise time of approximately 90µs (10% to 90%). See figure 10.

Noise: The noise performance of a photo detector is sometimes characterized by Noise Effective Power (NEP). This is the radiant power which would produce an output signal equal to the noise level. NEP has the units of radiant power (watts). The typical performance curve “Noise Effective Power vs. Measurement Bandwidth” shows how NEP varies with RF and measurement bandwidth.

Imagining Properties: The output is measured in voltage thru time, imaging like a Gaussian-like signal shape [10].

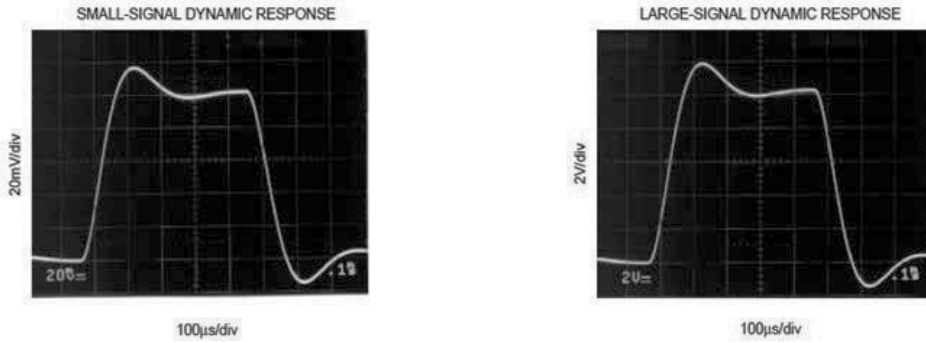


Figure 10. Small and large signal dynamic response of a photodiode.

3.1.2. Phototransistors

The Phototransistor is similar to the photodiode except for an n-type region added to the photodiode configuration. The phototransistor includes a photodiode with an internal gain. A phototransistor can be represented as a bipolar transistor that is enclosed in a transparent case so that photons can reach the base-collector junction. The electrons that are generated by photons in the base-collector junction are injected into the base, and the photodiode current is then amplified by the transistor’s current gain β (or hfe). Unlike photodiode phototransistor cannot detect light any better, it means that they are unable to detect low levels of light. The drawback of a phototransistor is the slower response time in comparison to a photodiode. If the emitter is left unconnected, the phototransistor becomes a photodiode [11].

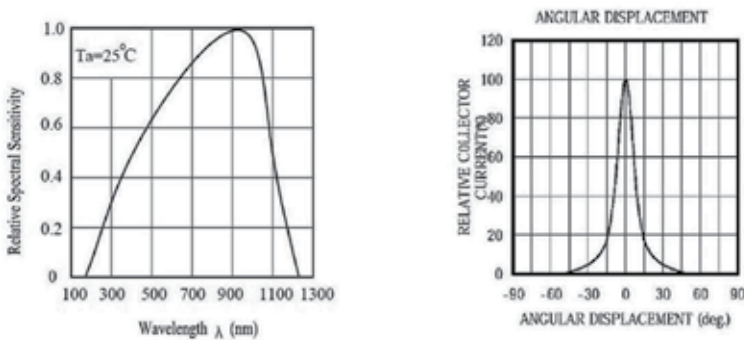


Figure 11. Relative spectral sensitivity and collector current vs. angular displacement of a phototransistor.

3.2. Image sensors

Nowadays image sensors are recognized as the most advanced technology to record electronic images.

These sensors are based on the photoelectric effect in silicon. When a photon of an appropriate wavelength (in general between 200 and 1000 nm) hits silicon, it generates an electron-hole pair. If an electric field is present, the electron and the hole are separated and charge can accumulate, proportional to the number of incident photons, and therefore the scene imaged onto the detector will be reproduced if a proper X-Y structure is present. Each basic element, defining the granularity of the sensor, is called a pixel (picture element) [12].

3.2.1. CCD sensor (charge coupled device)

This sensor is used in scanners to capture digital Images. Typically, it is an array to perform the scanning row by row, scanning one horizontal row pixel at a time, moving the scan line down with a carriage motor. The scanners that use this CCD sensor cell use an optical lens, often like a fine camera lens, and a system of mirrors to focus the image onto the CCD sensor cells.

The CCD sensor cell is an analogue device, when light strikes the chip, it is held as a small electrical charge in each photo sensor. The charges are converted to voltage, one pixel at a time, as they are read from the chip. An additional circuitry is also required to convert analogue to digital signal to produce an image as shown in figure 12.

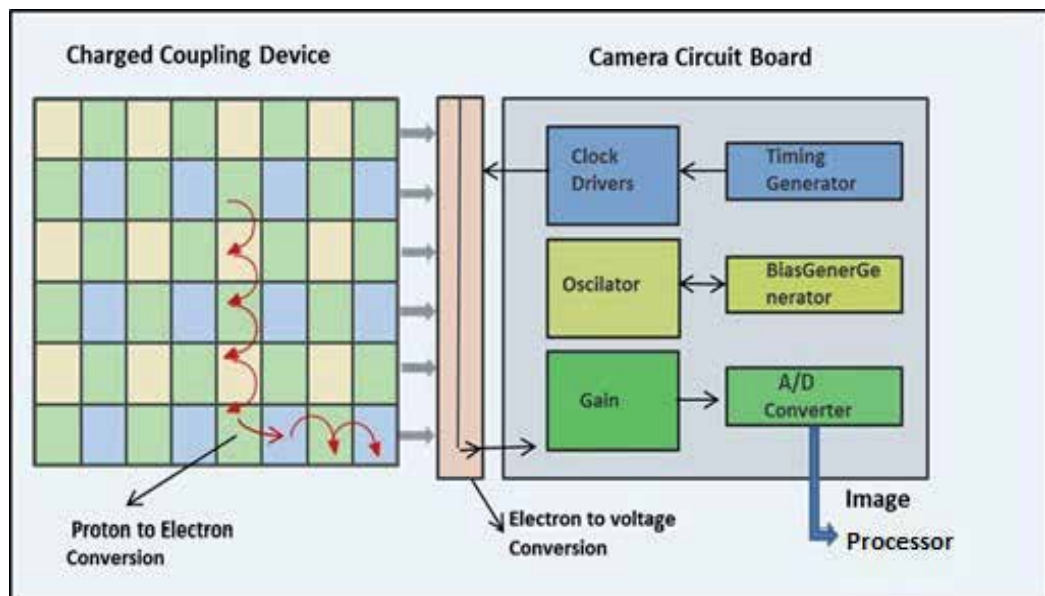


Figure 12. CCD operating principle.

The basic concept of CCDs is a simple series connection of Metal-Oxide-Semiconductor capacitors (MOS capacitors). The individual capacitors are physically located very close to each other. The CCD is a type of charge storage and transport device: charge carriers are stored on the MOS capacitors and transported. To operate the CCDs, digital pulses are applied to the top plates of the MOS structures. The charge packets can be transported from one capacitor to its neighbour capacitor. If the chain of MOS capacitors is closed with an output node and an appropriate output amplifier, the charges forming part of a moving charge packet can be translated into a voltage and measured at the outside of the device. The way the charges are loaded into the CCDs is application dependent.

The advantages of CCDs are size, weight, cost, power consumption, stability and image quality (low noise, good dynamic range, and colour uniformity). A disadvantage is that it is susceptible to vertical smear from bright light sources when the sensor is overloaded [13].

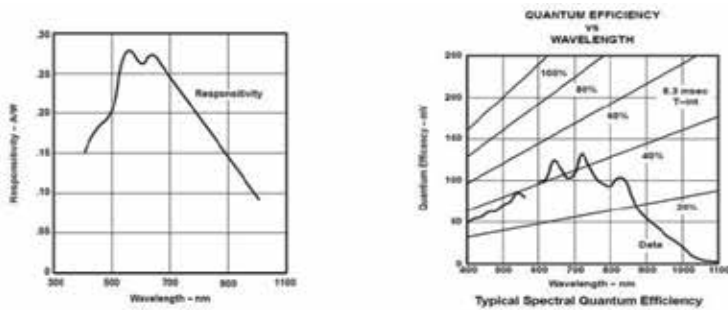


Figure 13. Responsivity and quantum efficiency vs. wavelength of a CCD.

As light enters the active photo sites in the image area, electron hole pairs are generated and the electrons are collected in the potential wells of the pixels. The wells have a finite charge storage capacity determined by the pixel design [14].

3.2.2. CMOS sensor (*complementary metal oxide semiconductor*)

This is an active pixel sensor or image sensor fabricated with an integrated circuit that has an array of pixel sensors, each pixel containing both a CMOS component and an active amplifier. Extra circuitry next to each photo sensor converts the light energy to a voltage and additional circuitry is also required to convert analogue to digital signal. In CMOS sensor the incoming photons go through colour filters, then through glass layers supporting the metal interconnect layers, and then into silicon, where they are absorbed, exciting electrons that then travel to photodiode structures to be stored as signal. These are commonly used in cell phone cameras and web cameras. They can potentially be implemented with fewer components, use less power, and/or provide faster readout than CCDs, scaling to high resolution formats. CMOS sensors are cheaper to manufacture than CCD sensors. However, a disadvantage is that they are susceptible to undesired effects that come as a result of rolling shutter [15].

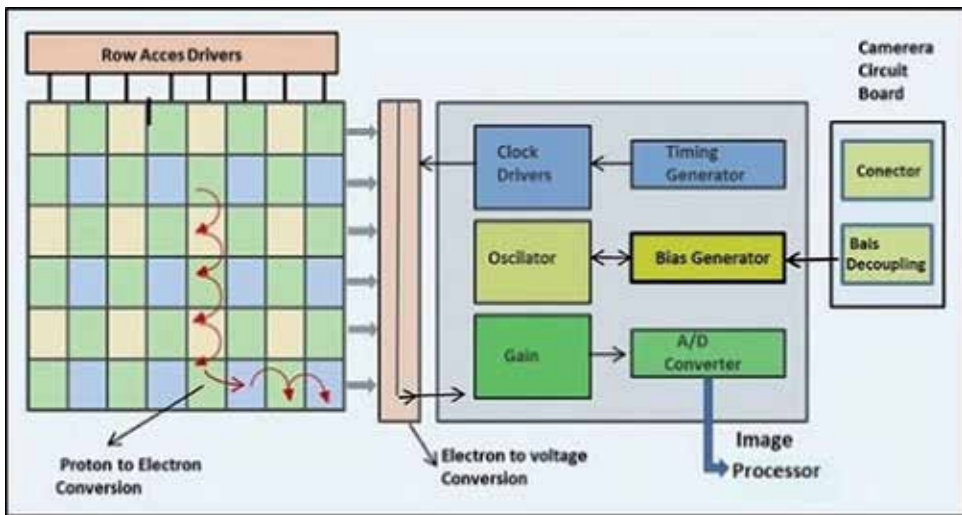


Figure 14. CMOS sensor.

Typically the sensitivity of the sensor is evaluated based on the quantum efficiency, QE, or the chance that one photon generates one electron in the sensor at a given wavelength. This is a good indicator. This gives the minimum amount of light you can see. In general, CMOS sensors have a higher QE in the sensitivity due to their design structure, and this can be further optimized by producing the sensor using a thicker epitaxial layer (shown as CMOS 1-b in Figure 15 below). Hence, at 800nm, the CMOS sensor with the thicker epitaxial layer has the best QE.

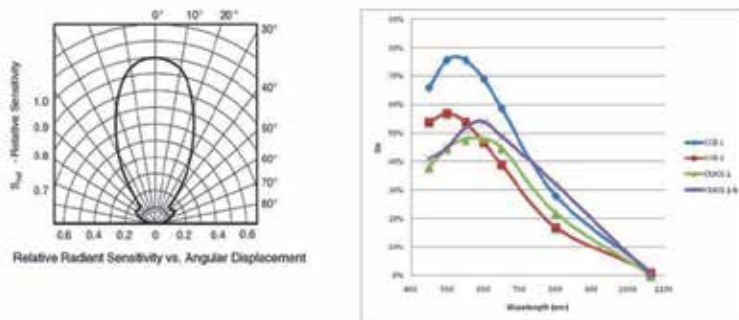


Figure 15. Relative radiant sensitivity vs. angular displacement and CCD vs. CMOS sensitivity.

3.2.3. Position sensing detector

Other device widely used as triangulation position sensor is the PSD (Position Sensing Detector), which converts an incident light spot into continuous position data (figure 16) and is

more accurate and faster than CCD because the PSD is a continuous sensor, while CCD is a matrix of dots switched on and off and its resolution depends on how many dots are located on the sensor. Typically a linear CCD has 1024 or 2048 dots.

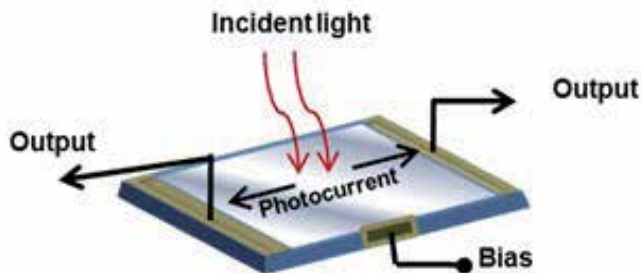


Figure 16. PSD Operating principle.

PSD has an infinite resolution because it is a continuous sensor, therefore the digital resolution of a PSD depends not on the PSD itself. Alignment sensors using CCDs have to be programmed to do multiple measurements at every step to improve accuracy and to lower noise because linear CCDs have a low resolution. To have the same accuracy of a PSD, CCD should perform no less than 32 measurements and hence calculate the average measurement. However, CCD is generally preferred to PSD because PSD needs an expensive circuit design including Analogue-to-Digital conversion [17].

4. Typical optoelectronic scanners signals

Different shapes of signals are generated during an optical scanning process, depending on the kind of light source and the sensor of the scanner. Some precision semiconductor optical sensors like CCD or PSD produce output currents related to the “centre of mass” of light incident on the surface of the device See [18]. All light registered by the CCD or PSD originates an ideal signal shape as shown in figure 17(Image credit: Measurecentral.com).

A typical position measuring process includes an emitter source of light, as a laser diode or an incoherent light lamp and the position sensitive detector like CCD or PSD as a receiving device, which collects a portion of the back-reflected light from the target. The position of the spot on the PSD is related to the target position and the distance from the source, see[19].However, the real photon distribution on the sensor depends on the characteristic dimensions related to the diffraction pattern of the light in the space. Common examples of signals generated by the light registered on a CCD camera appear in a study about super-resolution by spectrally selective imaging, shown in figure 18 (Image credit: A.M. van Oijen and J.Köhler).

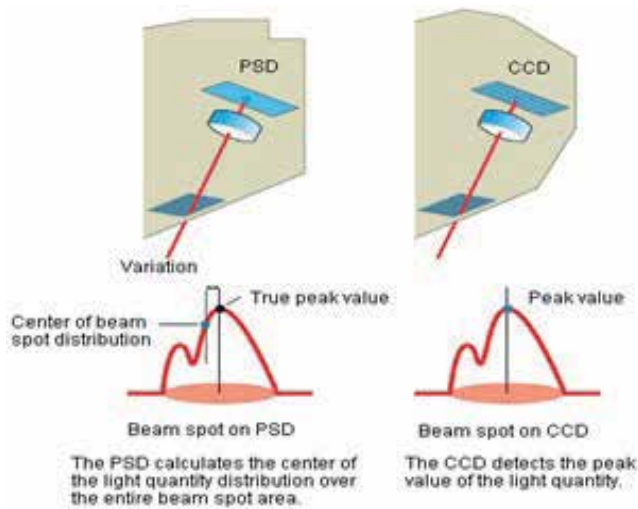


Figure 17. Ideal photon distribution on CCD and PSD sensors.

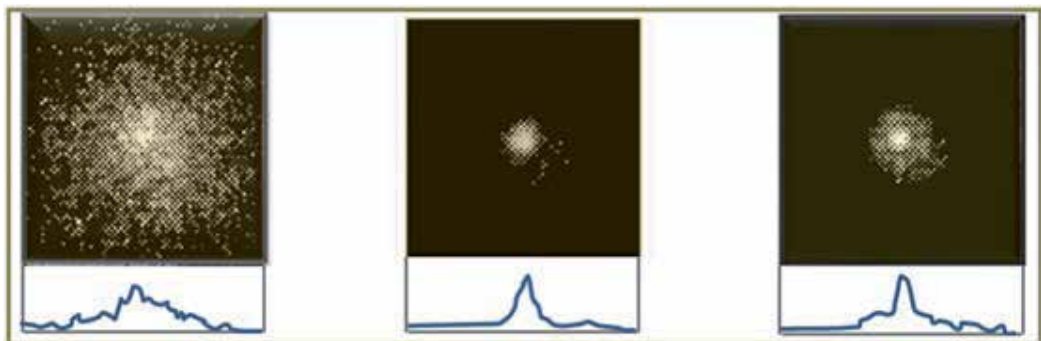


Figure 18. Real photon distributions as a function of the detector for different diffraction patterns.

Based on A.M. van Oijen and J.Köhler study, we can observe that the spatial distribution function of light has an Airy-function-like shape, see [20]. It is well known that CCD, CMOS and SPD use the light quantity distribution of the entire beam spot entering the light receiving element to determine the beam spot centre or centroid and identifies this as the target position. However, they are not the only sensors that generate a similar Gaussian-like shape, there are still a lot of sensors to be further investigated. For example, a simple photodiode can also originate a similar Gaussian-like shape, when it is used as a sensor on a scanner with a rotating mirror, [21]. Figure 19 below illustrates a hypothetical spot model, and attempts to explain how the signal is created by the photodiode on a scanner with a rotating mirror.

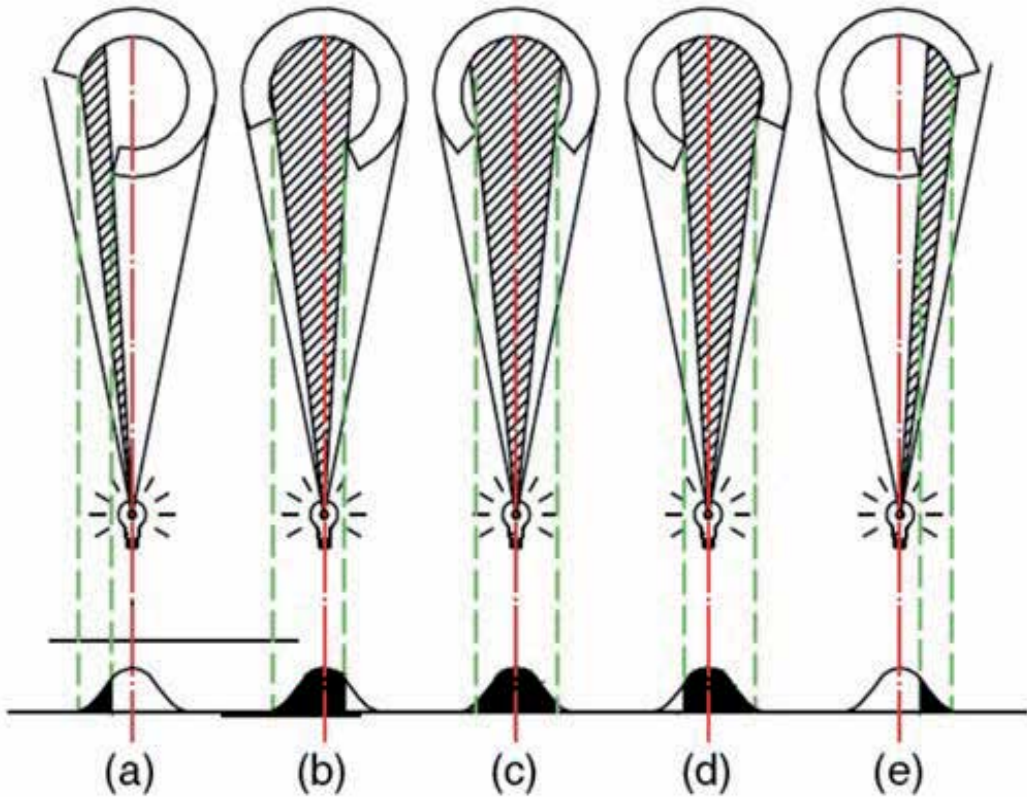


Figure 19. Principle of electrical signal formation during rotational scanning.

In this case, the signal created, as a similar Gaussian-like shape, goes up (Fig. 19, a) and falls down (Fig. 19, e), and a fluctuating activity takes place around its maximum area in figs. 19 (b-d). As we mentioned before, in a real practice the signal becomes noisy, see [22]. The experiment recently developed by Rivas M. and Flores W., with the scanner shown in Figure 6, for angular position measuring and using an incoherent light source and a simple photodiode, validated the model shown in Figure 20. During experimentation, it has been observed that the optoelectronic scanning sensor (photodiode) output is a Gaussian-like shape signal with some noise and deformation. This is due to some internal and external error sources like the motor eccentricity at low speed scanning, noise and deformation that could interfere with the wavelength of the light sources. Other phenomena could also affect, though, such as reflection, diffraction, absorption and refraction, producing a as seen in Figure 20.

As we can see, the photodiode signal originates a similar function to a CCD, consequently, it is possible to enhance the accuracy measurements in optical scanners with a rotating mirror, using a method for improving centroid accuracy by taking measurement in the energy cen-

tre of the signal. In the following section, we propose a new method and its respective circuit to find the centre of the signal by an optical scanner.

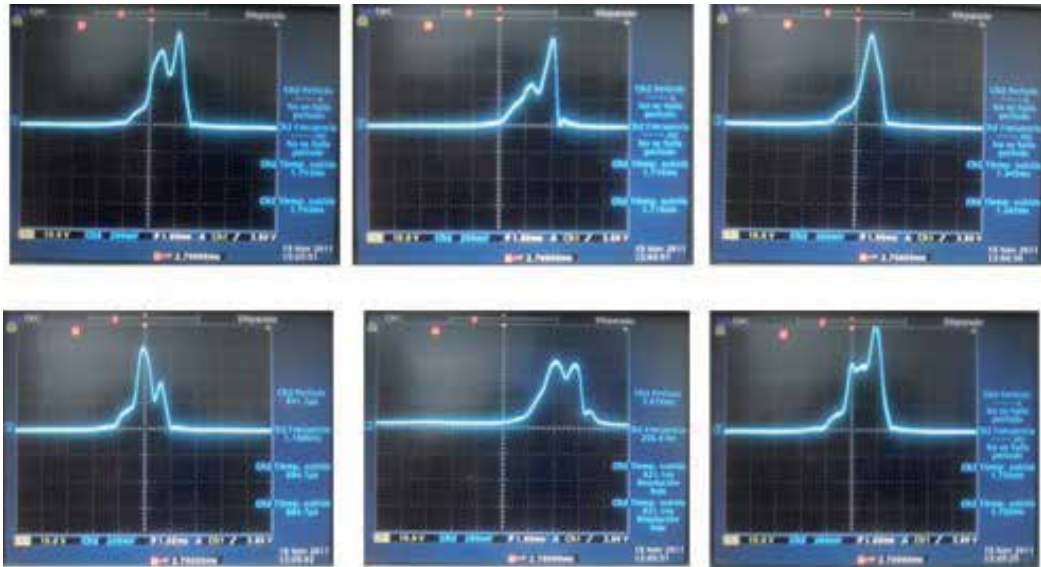


Figure 20. Scanning sensor Gaussian like shape, measurements at different angular positions of the light source.

5. Signal processing methods to locate signal energy centre

In the previous sections, we described different sensors and scanners that produce output currents related to the "the centre of mass" of the light incident in the surface of the device. In this section we will compare some techniques to find the energy centre of the signal and eventually discuss their advantages.

5.1. Time-series simple statistics algorithms for peak detection

Peak Signal Algorithms are simple statistic algorithms for non-normally distributed data series [23] to find the peak signal through threshold criteria statically calculated [23]. The algorithms which identify peaks in a given normally distributed time-series were selected to be applied in a power distribution data, whose peaks indicate high demands, and the highest corresponds to the energy centre. Each different algorithm is based on specific formalization of the notion of a peak according to the characteristics of the optical signal. These algorithms are classified as simple since the signal does not require to be pre-processed to smooth it, neither to be fit to a known function. However, the used algorithm detects all peaks whether strong or not, and to reduce the effects of noise it is required that the signal-to-noise ratio (SNR) should be over a certain threshold [23]:

$$h = \frac{\max + \text{abs_avg}}{2} + K * \text{abs_dev} \tag{4}$$

$$S_1(k, i, x_i, T) = \frac{\max\{x_i - x_{i-1}, x_i - x_{i-2}, \dots, x_i - x_{i-k}\} + \max\{x_i - x_{i+1}, x_i - x_{i+2}, \dots, x_i - x_{i+k}\}}{2} \tag{5}$$

$$S_2(k, i, x_i, T) = \frac{\frac{x_i - x_{i-1} + x_i - x_{i-2} + \dots + x_i - x_{i-k}}{k} + \frac{x_i - x_{i+1} + x_i - x_{i+2} + \dots + x_i - x_{i+k}}{k}}{2} \tag{6}$$

$$S_3(k, i, x_i, T) = \frac{\left(x_i - \frac{x_i - x_{i-1} + x_i - x_{i-2} + \dots + x_i - x_{i-k}}{k}\right) + \left(x_i - \frac{x_i - x_{i+1} + x_i - x_{i+2} + \dots + x_i - x_{i+k}}{k}\right)}{2} \tag{7}$$

$$S_4(k, i, x_i, T) = H_w(N(k, i, T)) - H_w(N'(k, i, T)) \tag{8}$$

This method consists in define the variables: $T = x_1, x_2, \dots, x_N$ be a given univariate uniformly sampled time-series containing N values $(1, 2, \dots, N)$. x_i be a given it h point in T . $k > 0$ is a given integer. $N+(k,i,T) = \langle x_{i+1}, x_{i+2}, \dots, x_{i+k} \rangle$ the sequence of k right temporal neighbours of x_i . $N-(k,i,T) = \langle x_{i-1}, x_{i-2}, \dots, x_{i-k} \rangle$ the sequence of k left temporal neighbours of x_i . $N(k,i,T) = N+(k,i,T) \bullet N-(k,i,T)$ denote the sequence of $2k$ points around the it h point (without the it h point itself) in T (\bullet denotes concatenation). $N'(k,i,T) = N+(k,i,T) \bullet \{x_i\} \bullet N-(k,i,T)$. And S be a given peak function, (which is a non-negative real number). $S(i, x_i, T)$ with it h element x_i of the given time-series T .

A given point x_i in T is a peak if $S(i, x_i, T) > \theta$, where θ is a user-specified (or suitably calculated) threshold value.

5.2. Calculation of the centroid of the light distribution

This method has been widely used in digital imaging for the location of different image features with subpixel accuracy. By definition, the centroid of a continuous 1-D light intensity distribution is given by:

$$x = \frac{\int_{-\infty}^{\infty} x f(x) dx}{\int_{-\infty}^{\infty} f(x) dx} \tag{9}$$

where $f(x)$ is the irradiance distribution at the position x on the image, see [24].

In our case the signal geometric centroid is a function of the voltage signal shape generated by the scanner (a plane figure of two dimensional shape X) and is the intersection of all straight lines that divide X into two parts of equal moment about the line [25].

For the geometric centroid computation the “integral plane figures method” will be used to provide two coordinates: \dot{X} which we will assign to the time axis, thus $\dot{X}=T$ and \dot{Y} that we will assign to the voltage axis, thus $\dot{Y}=V$, where we will only take the t coordinate to correlate the geometric centroid with the position on time (sample number) where the energy

centre is located. The signal generated by the optical aperture should be represented by a function:

$$y = f(t) = v(t) \quad (10)$$

In Figure 21 the area under the curve delimited by the function $y=v(t)$ and the lines Aa and Bb define the function integral limits of the plane figure. Selecting the differential area

$$dA = v(t) dt \quad (11)$$

The integral limits are on t (a, b). As the differential dt is a rectangle, the geometric centroid is in the half base and half height. As dt tends to zero and the half of it is a very small value, we could consider that half of dt is dt , therefore the next equations are used to calculate the geometric centroid [5]:

$$T = tV = v / 2 \quad (12)$$

First Integral, to calculate the complete area under the signal curve.

$$A = \int dA = \int v(t) dt \quad (13)$$

Second Integral, to find the T coordinate that corresponds to the energetic signal centre.

$$TA = \int TdA = \int tv(t) dt \quad (14)$$

Solving for T

$$T = \frac{\int TdA}{A} = \frac{\int tv dt}{A} \quad (15)$$

Third Integral, to find the V coordinate to know which voltage value was present in the energetic signal centre coordinate, if required for future experimentation.

$$VA = \int VdA = \int (v / 2)v dt = 1 / 2 \int v^2 dt \quad (16)$$

Where

$$V = \frac{\int V da}{A} = \frac{\int (v/2) v dt}{A} = \frac{1}{2A} \int v^2 dt \quad (17)$$

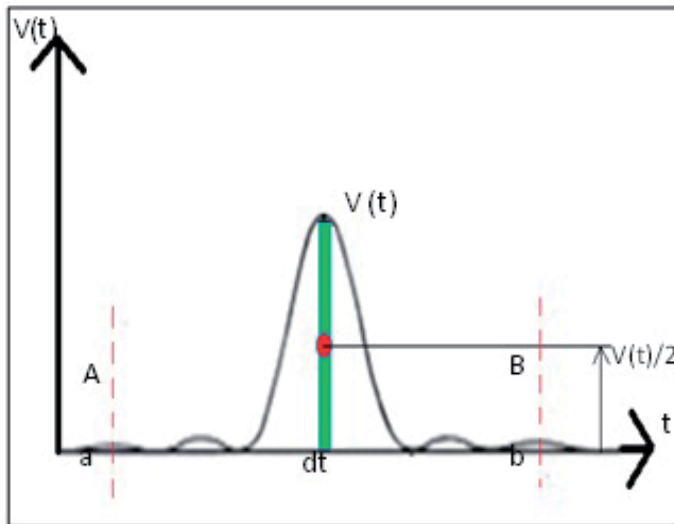


Figure 21. Optical Signal represented as a plane figure.

5.3. Power (energy) spectrum centroid

The Power Spectrum Centroid is a parameter from the spectrum characterization mainly used until now for musical computing due to the spectral centroid corresponding to a timbral feature that describes the brightness of a sound. In this application we will correlate the Power Spectrum Centroid with the Energy Centre of the Signal due to the fact that the Power Spectrum Centroid can be thought as the centre of gravity for the frequency components in a spectrum. The power spectrum is a positive real function of a frequency variable associated with the function of time, which has dimensions of power per hertz (Hz) or energy per hertz, that means the power carried by the wave (signal) per unit frequency.

Power Spectrum Method:

The first step to go from time-series domain to frequency-series domain is to apply the Fourier series, which provides an alternate way of representing data. Instead of representing the signal amplitude as a function of time, Fourier Series represent the signal by how much information (power) is contained at different frequencies and also allow to isolate certain frequency ranges that could be from noise sources, if necessary. Whenever we have a vector of data (finite series) with Matlab we can apply the FFT (Fast Fourier Transform) to convert from time to frequency domain, computing the Discrete Fourier transform (DFT), which is the Fourier application for discrete data and whose non-zero values are finite series.

The second step is to compute the power spectrum, that is to compute the square of the absolute value of the FFT, which result is considered as the power of the signal at each frequency.

$$P(f) = \left| \frac{1}{\sqrt{2\pi}} \sum_{n=-\infty}^{\infty} f_n e^{-i\omega n} \right|^2 = \frac{F(\omega)F^*(\omega)}{2\pi} \quad (18)$$

Where $F(\omega)$ is the discrete-time Fourier Transform of f_n .

The third step consists of applying the Power Spectrum Centroid:

$$SC_{Hz} = \frac{\sum_{k=1}^{N-1} k \cdot X^d[k]}{\sum_{k=1}^{N-1} X^d[k]} \quad (19)$$

6. Method and electronic device to locate signal energy centre

The principal focus of this chapter is a method to find the energy centre of the signal generated by optical scanners and to reduce errors in position measurements. The method is based on the assumption that the signal generated by optical scanners for position measurement is a Gaussian-like shape signal, and this signal is processed by means of an electronic circuit.

6.1. Electronic method operating theory

A signal $V(t)$ is obtained from the optical scanning aperture, as shown in Figure 22.



Figure 22. a) Chanel 1 Original signal from aperture b) Original signal representation.

The signal $V(t)$ is amplified through an operational amplifier until saturation to obtain a square signal, this signal can be expressed as:

$$V_s(t) = V_s \max \quad (20)$$

which is a constant for $a \leq t \leq b$ as shown in Figure 23.

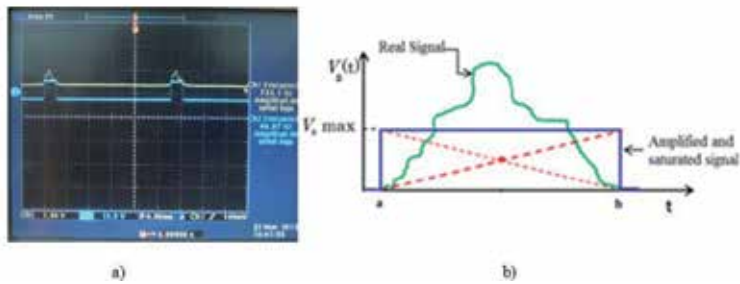


Figure 23. a) Channel 1 Original Signal from aperture. Channel 2 Square Signal. b) Square signal representation.

The signal $V_s(t)$ is integrated with respect to dt in order to get the ramp $V_r(t)$ as shown below in Figure 24.

$$V_r(t) = \int V_s(t) dt \tag{21}$$

then energetic signal centre is located in $V_{rmax}/2 = V_{smax} / 2$ as shown in Figure 24.

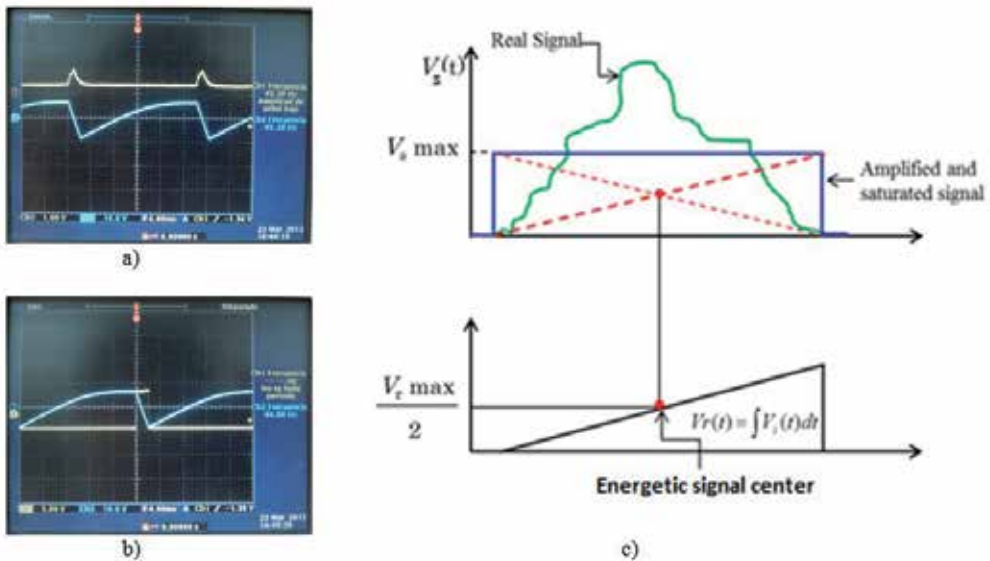


Figure 24. a) Channel 1 original signal from aperture, Channel 2 ramp signal. b) Channel 1 ramp signal, Channel 2 Pulse indicating the energetic signal centre overlapped on ramp signal c) Energetic signal centre search process representation.

All this process is carried out by a circuit similar to the one shown in figure 25.

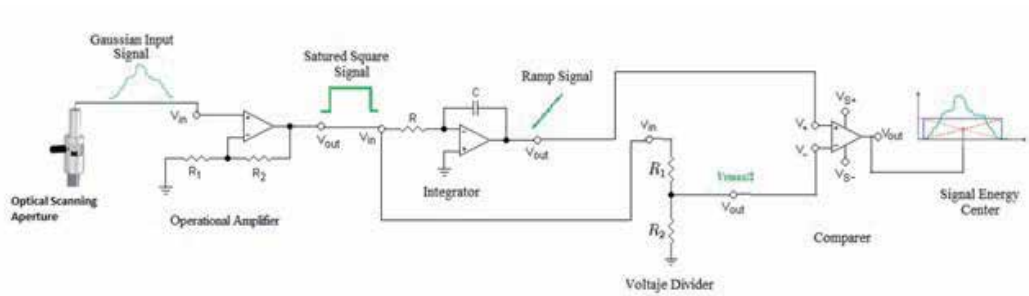


Figure 25. Electronic control circuit representation.

The advantage of this method is that the mathematical processing is performed by using electronic components in real time to get the data vector of the saturated signal which can be handled in Matlab [8].

6.2. Electronic control circuit method experimentation

The first stage of the experimentation started with regular signals simulated by a function generator, the signals utilized were: a rectified sin signal, a rectified square signal, rectified triangle signal and an Airy function, as illustrated in figure 26.

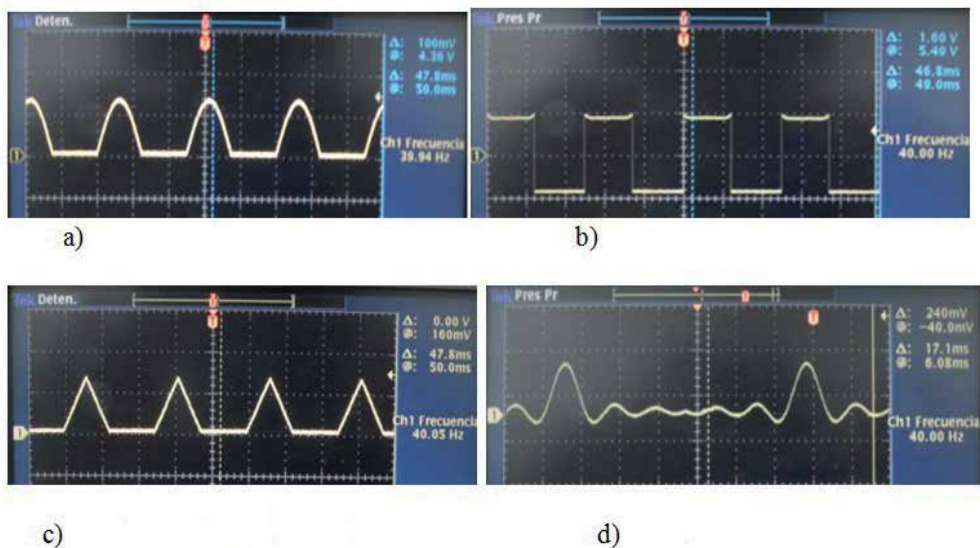


Figure 26. Regular signals simulated by a function generator: a) Rectified Sin signal. b) Square signal. c) Rectified triangle signal d) Airy function signal.

The second stage consisted of processing each signal by means of the electronic circuit to get the energetic centre, as shown in figure 27.

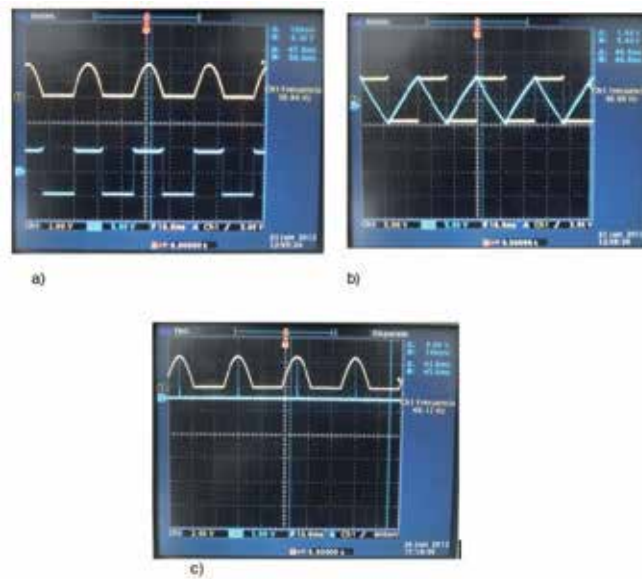


Figure 27. Detailed example. a) Channel 1: original signal from function generator; Channel 2: square signal obtained from saturation. b) Channel 1: saturated signal Channel 2: ramp signal obtained from integration. c) Channel 1: original signal from generator; Channel 2: impulse signal overlapped on original signal from generator to indicate the energetic signal centre.

The circuit was tested with different signals obtaining satisfactory results. In figure 28, the results are illustrated with a triangle signal and an airy function signal.

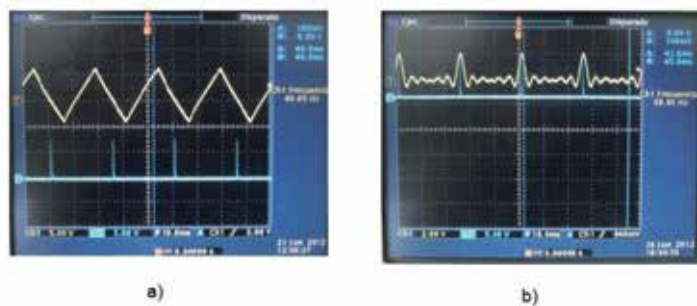


Figure 28. Impulse signal indicating the energetic signal centre overlapped on: a) triangle signal. b) Airy function signal.

Finally, to characterize and increase the accuracy and resolution of signal measurements four methods were selected and compared to obtain the most applicable settings in order to find the energetic centre of the signal. The given results are shown in [2].

7. Conclusion

A pertinent method to detect the energetic centre of signal generated by optical scanning with a rotating mirror and a simple photodiode was presented. The results of a series of experiments and simulations were used to analyse the performance of the method and the circuit considering regular signals. Consequently, further work is required to reduce problems encountered in processing real signals. Besides, The method can also be used to detect geometrical centre of the light distribution on CCD and PSD, future experiments with this kind of sensors should be considered. The results suggest that the circuit proposed can support different patterns of light distributions. To conclude, it is strongly recommended that this circuit and the photodiode be manufactured in the same integrated circuit.

Author details

Moisés Rivas, Wendy Flores, Javier Rivera, Oleg Sergiyenko,
Daniel Hernández-Balbuena and Alejandro Sánchez-Bueno

Engineering Institute of Autonomous University of Baja California (UABC), Mexico

References

- [1] Rivas, L., Moisés, Sergiyenko., Oleg, Tyrsa., Vera, Hernández., & Wilmar, . Optoelectronic method for structural health monitoring. *International Journal of Structural Health Monitoring* (2010). , 9(1), 105-120.
- [2] Flores, F., Wendy, Rivas. L., Moisés, Sergiyenko., Oleg, Y., Rivera, C., & Javier, . Comparison of Signal Peak Detection Algorithms in the Search of the Signal Energy Center for measuring with optical scanning. In: Falcon S. Bertha, Trejo O. René, Gómez E. Raúl: *IEEE ROC&C2011:XXII autumn international conference on communications, computer, electronics, automation, robotics and industrial exposition:ROC&C2011*, 27 Nov-1 Dec. (2011). Acapulco Gro., México.
- [3] Rodríguez Q. Julio C., Sergiyenko Oleg, Tyrsa Vera., Básaca P Luis C., Rivas L. Moisés, Hernández B. Daniel, 3D Body& Medical Scanners`Technologies: Methodology and Spatial Discriminations, in: Srgiyenko Oleg (ed.) *Optoelectronic Devices and Proprieties*. In-Tech: 2011.p307-322.
- [4] Kennedy, William. P. The Basics of triangulation sensors, Cyber Optics Corp. <http://archives.sensorsmag.com/articles/0598/tri0598/main.shtml>, accessed June 18 (2012).
- [5] Vahelal, Ahmedabad. Seminar report 3 of Cryptography: Sensors on 3D Digitization, Hasmukh Goswami College of Engineering, Gujarat, India:. (2010).

- [6] M. Bass, Handbook of Optics, Vol. II- Devices, Measurements and Properties, New York: McGRAW-HILL , INC, 1995.
- [7] J. P. *. a. C. B. Javier Plaza, Multi-Channel Morphological Profiles for Classification of Hyperspectral Images Using Support Vector Machines, Sensors:2009.p197
- [8] Rivas M., Sergiyenko O., Aguirre M, Devia L, Tyrsa V, Rendón I, Spatial data acquisition by laser scanning for robot or SHM task: IEEE-IES: International. Symposium on Industrial Electronics:(ISIE-2008), Cambridge, United Kingdom, 2008, p.1458-1463
- [9] Rieke, George. Detection of Light: From the Ultraviolet to the Sub millimeter.Optical detectors.(2002). Publisher: Cambridge University Press. West Nyack, NY, USA. eUSBN: 978113948351. pISBN:9780521816366.
- [10] Burr-Brown, Corporation. P. D., S-12, , 199, B., & , O. P. (1994). OPT301. Integrated photodiode and amplifier datasheet.
- [11] Everlight, Electronics., Co, , Ltd, D. P., & T-03305 , . (2005). PT334-6C. Technical data sheet 5mm phototransistor T-1 3/4.
- [12] Jung, R. Image sensors technology for beam instrumentation, CERN, CH1211 Geneva 23, Switzerland
- [13] Albert, J. P., & Theuwissen, Solid. Solid-State Imaging with Charge-Coupled Devices. (1995). Kluwer Academic Publishers.
- [14] Texas, Instruments. S. O. C., S0, , & , D. (2003). TC281.X1010-Pixel CCD image sensor datasheet., 1036.
- [15] Sebastiano Battiato. Arcangelo Ranieri Bruna. Giuseppe Messina.Image Processing for Embedded Devices. (2010). Bentham Science Publisher. Sharjah, UAE.
- [16] ADIMEC. CCD vs. CMOS Image Sensors in Defense Cameras. 2011.<http://info.adimec.com/blogposts/bid/58840/CCD-vs-CMOS-Image-Sensors-in-Defense-Cameras>
- [17] Boni Fabio, What is the difference between PSD and CCD sensor technology?, FA-SEP.http://www.fasep.it/english/support/tech_talks/tt013_psd%20and%20ccd.aspx accessed 20 Jun (2012).
- [18] Williams, R. D., Schaferg, P., Davis, G. K., & Ross, R. A. Accuracy of position detection using a position sensitive detector, "IEEE transactions on instrumentation and measurement. (1998). , 1998(47), 4-914.
- [19] Massari, N., Gottardi, M., Gonzo, L., & Simoni, A. High Speed Digital CMOS 2D Optical Position Sensitive Detector in:Castello C., Baschirotto A. (eds.) ESSCIRC 2002.Proceedings of 28th European Solid-State Circuits Conference of IEEE Solid-State Circuits Society: ESSCIRC 2002,September (2002). Firenze, Italy., 24-26.

- [20] van Oijen A.M., J. Köhler, Schmidt J., Müller M., Brakenhoff G.J. 3-Dimensional super-resolution by spectrally selective imaging *Chemical Physics Letters*, 1998; 292(1998)183-187
- [21] Rivas L. Moisés, Sergiyenko Oleg, and Tyrsa Vera. *Machine Vision: Approaches and Limitations*. In: Xiong Zhihui. (ed.) *Computer Vision*. InTech; 2008.p396-428.
- [22] Sergiyenko Oleg ,Tyrsa Vira, Basaca P. Luis., Rodríguez Q. Julio C., Hernandez W., Nieto H.Juan I. , Rivas L M. Electromechanical 3D optoelectronic scanners: resolution constraints and possible ways of its improvement. In: Seriyenko (ed.) *Optoelectronic Devices and Properties*. InTech: 2011p549-582.
- [23] Girish Keshav Palshikar, *Simple Algorithms for Peak Detection in Time-Series*, Tata Research Development and Design Centre (TRDDC), 54B Hadapsar Industrial Estate.Pune 411013,India.
- [24] Stanton, R., Alexander, J. W., Dennison, E. W., Glavich, T. A., & Hovland, L. F. Optical tracing using charge-coupled devices. (1987). *Opt. Eng.* , 26(9), 930-938.
- [25] Larry Herrera, Magister in Educational Planning, Oriente University of Bolívar, <http://www.udobasico.net/mecanica/CLASES%20centroide%204.html> (accessed 10 Jun 2012).

Opto-Electronic Packaging

Ulrich H. P. Fischer

Additional information is available at the end of the chapter

<http://dx.doi.org/10.5772/51626>

1. Introduction

Future optical communication systems will use the high bandwidth of optical fiber in the optical frequency domain. Fast transmitter and receiver modules are basic elements of these systems, which are able now to transmit terabits/s of information via the fiber. Experiments with opto-electronic integrated circuits (OEICs) in laboratory test beds and field tests require a special packaging that respects system requirements such as high environmental stability and low optical insertion loss. Several concepts for fiber-chip coupling schemes had been proposed in the past. One of these is laser micro welding shown by [1], [2], [3], [4], [5], [6], [7]. This scheme is referring to the standard for high volume industrial manufacture. The investment costs for this laser welding equipment are considerably high. There are numerous proven techniques for aligning OEICs effectively. For laboratory use and rapid prototyping a flexible design is needed which is able to adapt different OEICs with changing dimensions to an existing module type.

In this chapter you will get general information what does opto-electronic packaging mean. Here fiber-chip coupling with basic coupling concepts will be illustrated. The different types of active adjusting and passive techniques are explained. Optical connectors play a very important role to interconnect different transmission systems. In passage 7 an overview of existing fiber connectors is shown. Afterwards, different optical module types for active and passive opto-electronic devices are described in details. Finally, the long-term stability of the modules must be tested and all reliability requirements for international test procedures are specified.

In its simplest arrangement, the packaging of OEICs involves the alignment and attachment of the light guiding areas of the OEIC and the optical fiber. At the beginning of this section, the basics of optical coupling theory with an introduction to optical mode fields and their matching by lenses is presented. Afterwards, a description of active and passive waveguide to waveguide coupling techniques will follow. Finally, optical connectors and the outline of

different kinds of state of the art optical modules will be depicted followed by a short overview of long-term stability tests.

At this point I would like to define the opto-electronic packaging which was given by [8]:

„Opto-electronic packaging means working on the connection of opto-electronic integrated circuits to optical and electrical transmission lines and bias supply combined in a environmental stable housing.“

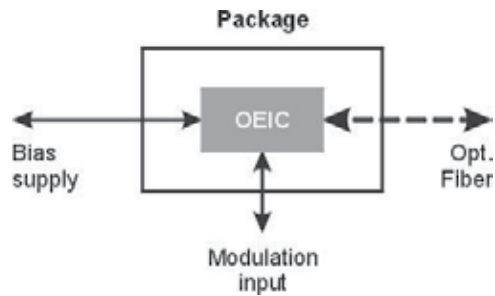


Figure 1. Basic package design for opto-electronic modules.

In the following several different technologies are listed which are essential to develop a new package:

1. RF-technique
2. Classical ray tracing optics & wave optics
3. Mechanical construction / CAD-design
4. Wire bond technique
5. Heat dissipating management / cooling
6. Communications engineering
7. Solid state physics
8. Micro systems design
9. Thick film circuits
10. Gluing, welding, soldering

2. Fiber-chip coupling

The behavior of the optical beam can normally be described by classical ray optical functions for lenses with focus length and focus point. If the dimensions of the optical beam come close to $1.5\mu\text{m}$, which is the wavelength used in optical networks, the behavior of the beam must be described by wave optical functions.

$$p(r) = p(0) \times \exp \left\{ -2 \left[\frac{r}{w_0} \right]^2 \right\} \quad (1)$$

$2w_0$ = Mode field diameter(MFD)

$$w(z) = \sqrt{w_0^2 + \left(\frac{z\lambda}{2n\pi w_0^2} \right)^2} \quad (2)$$

Here, the optical field within a wave-guide can be described nearly perfectly by a Gaussian intensity distribution, called $p(r)$, which can be expressed with equation (1). If the wave travels within the waveguide, the mode field diameter is constant due to the combining function of the waveguide itself. At the end of the waveguide, the optical field is not guided and the field expands with increasing distance to the output facet. The expansion of the field can be calculated by equation (2). The point at which the intensity has fallen down to $1/e^2$ or 13.5% of the maximum intensity in radial direction, which is shown in figure 2, defines the mode field diameter.

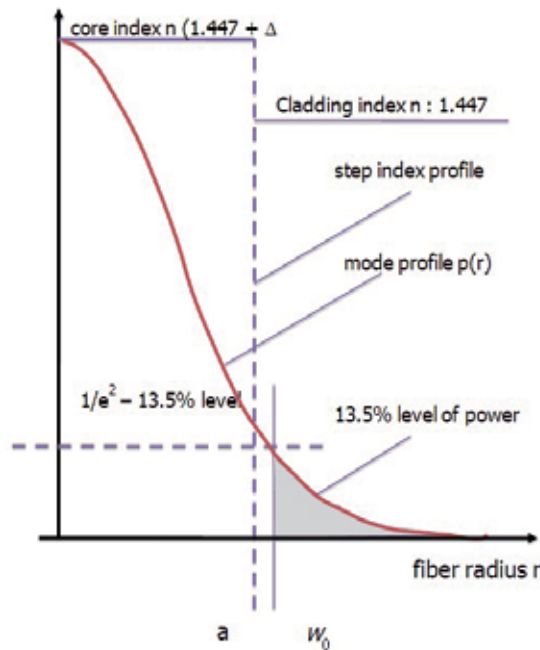


Figure 2. Intensity distribution of the optical mode field.

After leaving the waveguide, the optical mode field radius, which is half of the spot-size, expands with increasing distance to the facet. For distances of less than $200 \mu\text{m}$ the field dis-

tribution is called "near-field" and for larger distances "far-field". The angle where the intensity is fallen to $1/e^2$ or 13.5% of the maximum intensity is called "far-field angle" which corresponds to the near-field radius. These parameters are normally shown in the data sheets of laser diodes or LEDs.

For an efficient transfer of optical energy from the SMF and a laser diode wave guide, the mode profiles should "overlap" as much as possible which is described by [9] and is depicted in equation (3). The coupling efficiency η between two Gaussian beams can be expressed by means of the mode fields of laser diode w_{LD} and fiber w_{SMF} and also as a function of lateral, angular and longitudinal misalignment between the two wave guides:

$$\eta = \kappa \cdot \exp \left[-\kappa \left\{ \frac{x_0^2}{2} (1/w_{LD}^2 + 1/w_{SMF}^2) + \pi^2 \theta^2 [w_{LD}^2(z) + w_{SMF}^2] / 2\lambda^2 - x_0 \theta z / w_{AWG}^2 \right\} \right] \quad (3)$$

Where

$$\kappa = 4w_{LD}^2 w_{SMF}^2 / \left[(w_{LD}^2 + w_{SMF}^2)^2 + \lambda^2 z^2 / \pi^2 n_{gap}^2 \right] \quad (4)$$

With

λ - wavelength

n_{gap} – refractive index of medium between the waveguide and fiber

x_0 – lateral misalignment

θ - angular misalignment

Z – longitudinal misalignment

To measure the loss in decibel, the efficiency η must be multiplied 10 times by the logarithm₁₀ which is designated here as L:

$$L(\eta) = 10 \log(\eta) \quad [\text{dB}] \quad (5)$$

3. Basic coupling concepts

A comparison of the optical mode fields of the optical standard monomode fiber called SMF with a typical laser diode is shown in figure 3, where also the mode field diameter of a standard single mode fiber is depicted, respectively The properties of the SMF are standardized through the International Telecommunication Union [10].

The far field angle of the fiber is defined to a small value of 11.5°. A typical laser diode shows different values for lateral and vertical axis of 20° to 30° and 30° to 40°, respectively.

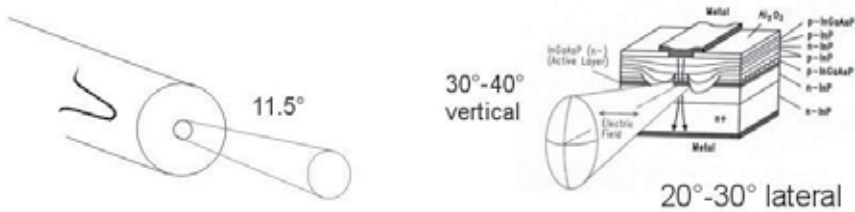


Figure 3. Far field of an optical fiber in comparison to the field of a laser diode.

If one compares the field parameters of fiber and laser diode a great mismatch can be found. Consequently, the optical coupling efficiency between these two devices is very low. The coupling loss between the two fields without additional mechanical misalignments can be calculated in decibel with Saruwatari’s formula from equ. (3), which can be simplified into the formula (7):

$$Loss(R) \approx -10 \log(R) [dB] \tag{6}$$

$$R = \frac{4}{\left\{ \frac{w_1}{w_2} + \frac{w_2}{w_1} \right\}^2} \tag{7}$$

With this formula the mode field mismatches between the single mode components and the corresponding mismatch loss can be calculated to equ. (6), all lateral and angular misalignments of the fiber axis relative to the incident beam of the laser waveguide are set to zero.

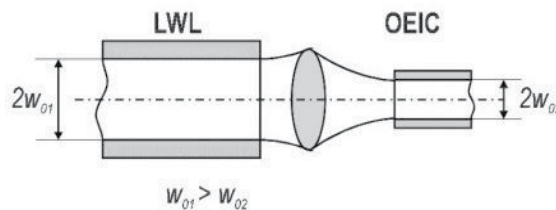


Figure 4. Mode field adaptation by an optical lens or lens system.

Different mode fields can be adapted by so called “mode field transformers”. These devices are, for example, lenses or lens systems, which are shown in figure 4. With these devices, a

nearly perfect coupling between the two wave-guides is possible. Due to limitations in costs, several lens configurations have been proposed for the optical coupling of laser diodes to single mode fibers. As shown in figure 5, simple ball lenses can be used to adapt the two mode fields. Coupling efficiencies of up to 30% are possible. A better approach is the use of graded index lenses or Selfoc-lenses. For a focusing lens, so-called half-pitch devices are used. Whereas quarter-pitch lenses are used to form parallel beams. These can reach efficiencies of 70%. Another approach is to form a lens at the end of the fiber, which is called fiber taper. With this device, efficiencies up to 90% have been achieved.

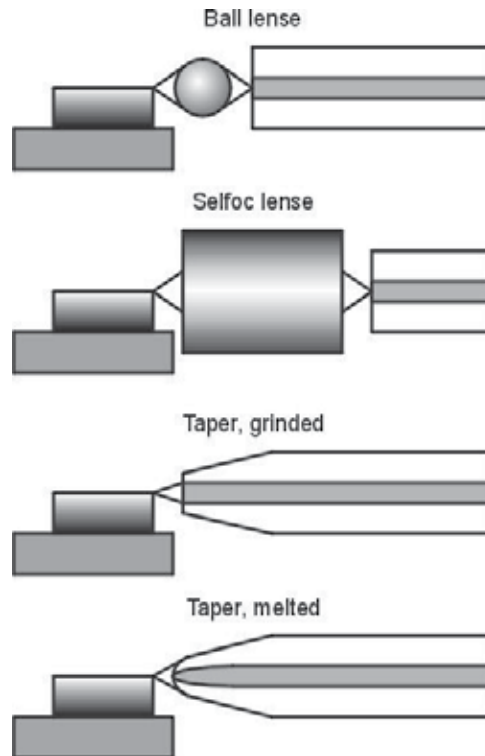


Figure 5. Mode field adaptation by several micro-optic solutions.

4. Adaptation of mode fields

As depicted in chapter 3, comparison of the optical fields of a butt ended standard single-mode fiber (SMF) and of edge emitting laser diodes shows a great mismatch. This mismatch is the reason for the very low coupling efficiency of approx. 15% for a butt ended fiber

This low efficiency can be overcome by a better adaptation of the two optical mode fields with lenses. A coupling efficiency of more than 90% has been shown. Disadvantages occur at the

handling of the parts because there are several parts including one or two lenses, the fiber and the chip, which must be handled for optical alignment. The consequence is a rather cost-ly of opto-electronic packaging.

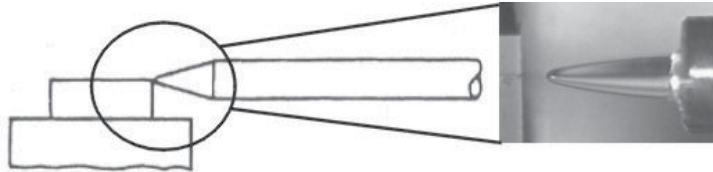


Figure 6. left side: Sketch of a melted fiber taper in front of an OEIC, right side: photograph.

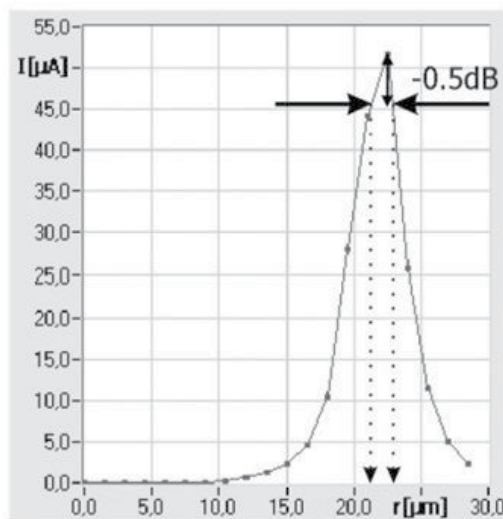


Figure 7. X and Y-axis: 2μm tolerance for 0.5 dB additional coupling loss.

As an example for integrated lens design, lenses can be made at the end of the fiber by melting the glass fiber and pulling it. This kind of fiber end is called fiber taper and works like a lens with typical diameters from 20 μm to 50 μm. In figure 6 you can see at the left side the chip facet and its wave guide and at the right side the melted fiber taper in front of the wave-guide. The fiber is additionally fixed into a metal cannula. With these tapered fibers a coupling efficiency of more than 50% can be realized. Unfortunately, a high precision fixation of better than 0.5 μm is necessary to mount the tapered fiber in front of the OEIC without additional losses. Therefore, the mechanical resolution of the coupling mechanism must be better than this value. The fixing procedure after coupling should not introduce additional displacements and must be stable enough to fix the coupling mechanism, which is important for a good long-term stability. The short working distance of 10 μm between fiber taper and laser which can be seen in the photograph is

also dangerous for the life of the laser diode if it comes into contact with the with the fiber end. But there is only one low-priced device on the market, which makes this device very comfortable for use in small and very reasonably priced modules.

The tolerances for lateral and longitudinal fixing of the fiber taper in front of the opto-electronic circuit or OEIC are shown in figure 7 and figure 8. Both graphs show the distance in micrometers at the x-axis and a relative intensity of the coupling efficiency between the tapered fiber and the OEIC. You can see in figure 7 that within 2 micrometers the intensity will not be lower than 0.5 dB of the maximum intensity. For the longitudinal direction the tolerance is much greater: in this case $8\mu\text{m}$, which can be seen in figure 8.

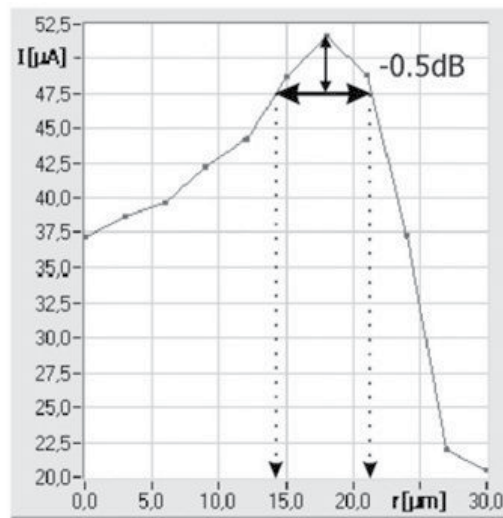


Figure 8. Z-axis with higher tolerance of $8\mu\text{m}$.

Please remember: it is easier by a factor of four to perform the optical coupling in longitudinal direction in comparison to the lateral direction.

5. Active adjusting techniques

In optical packaging laboratories, fiber-chip coupling is performed within sub-micrometer precision in order to get a high coupling efficiency between the optical devices. Precision optical experiments depend upon reliable position stability. Vibration sources in and around the work are depicted in figure 9. Floors carry vertical vibrations in the range of 10 Hz to 30 Hz caused by people, traffic, seismic activity, and construction work. Tall buildings sway up to a meter in the wind, at frequencies from 1 Hz to 10 Hz. Machinery generates vibrations up to 200 Hz. Optical benches and their associated vibration isolating support systems provide a rigid and virtually vibration-free working surface that holds the components of an ex-

periment in a fixed relative position. The legs support the tabletop: Air suspension mechanisms reduce practically all vibrations by two orders of magnitude.

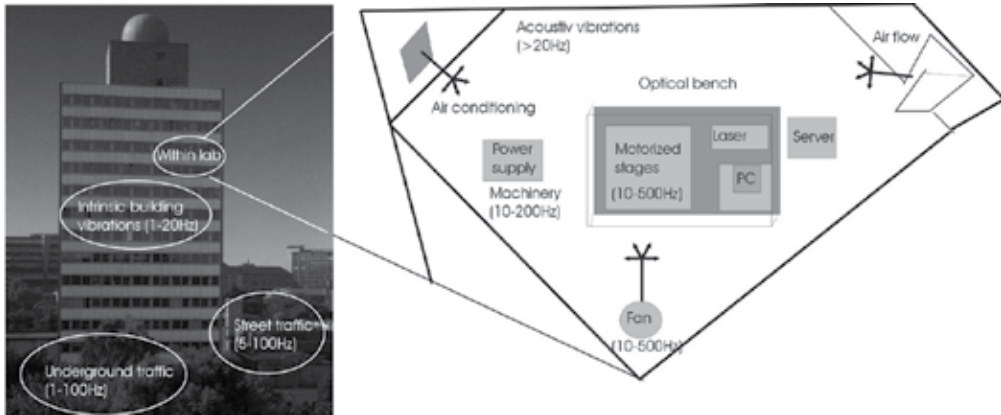


Figure 9. Influence of vibrations for micro positioning.

In order to align a fiber optically to another component, one has to move either the fiber, the component or both. Three linear and three angular motions are necessary to describe fully the motion and position of a solid body in space. The figure below identifies the six degrees of freedom using the common Cartesian frame of reference. When each of these degrees of freedom is singularly constrained by a hardware device, the device is labelled kinematic.

The device used to move a component in the linear x , y , or z direction is a translation stage. The device used to move a component in the angular θ_x , θ_y , or θ_z direction is a rotation stage.

Actuators are used to move the component on a translation stage to its desired position. There are three basic types of actuators used with precision stages: manual drives, stepper motor drives, and piezoelectric transducers. Manual drives and stepper-motor drives can move components over long distances, constrained only by the size of the manual drive or, in the case of stepper motors, the length of the lead screw. Piezoelectric transducers can move components over very short distances with nanometre precision. The range and resolution of the various drives and stage technologies is shown in figure 10 below.

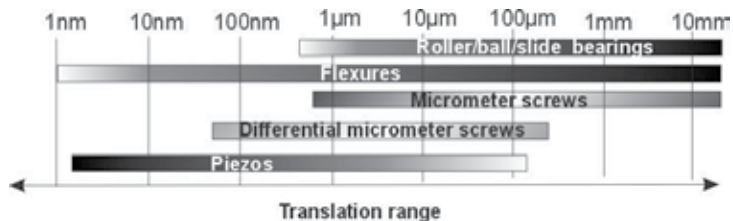


Figure 10. Translation ranges of available micro mechanical stages and screw systems.

For fiber-chip-alignment mostly all six degrees of freedom must be moved. Several commercial six axes motion systems have been developed with translational resolution of better than $0.02\mu\text{m}$ and angular resolution of better than one arc second. As an example, a mechanical/piezoelectric driven system with six degrees of freedom is shown in figure 11. Software tools are also included for automated coupling for one fiber and fiber arrays. Most of the software applications are available as a Labview virtual Instrument (VI).

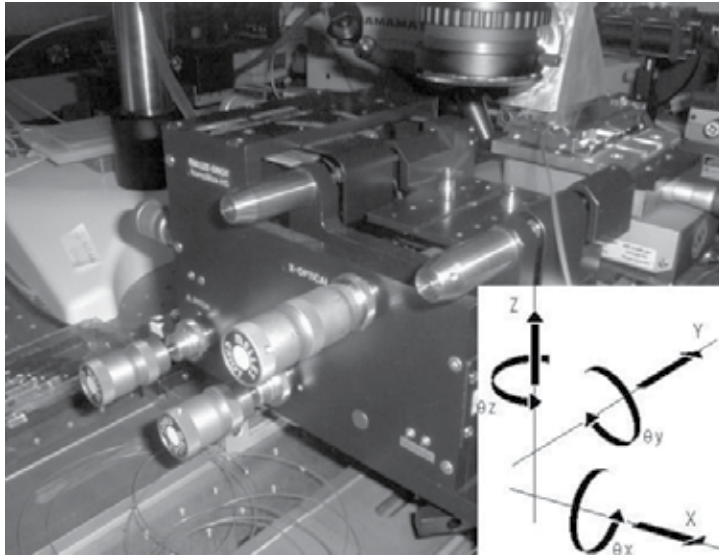


Figure 11. Six axes Nano-positioning system.

6. Passive adjusting techniques

6.1. Flip-chip-technique

The flip-chip (FC) bond technology was developed in 1964 by IBM for high dense packages for hybrid modules. At that time it was called C4-technology or Controlled Collapse Chip Connection [11]. Its main goal was to replace the uneconomical wire bonds. The FC-technique allows the highest density of connections on the chip scale. For this reason this technique is a possible candidate for high volume production in the micro electronic industry. [1, 12] and [13] have shown that the FC-technique could meet the precision needed for optical fiber-chip coupling ($\pm 3\mu\text{m}$). Figure 12 shows the working principle of the optical FC-connection. The OEIC is connected bottom up to the substrate. Bonding is performed by a thermal reflow process which is depicted in figure 13. The surface forces of the melted solder trek the OEIC into a preferred position, that differs very little from connection to connection. This is called “self-alignment”. [14], [15] and [16] had developed a fluxless FC-bonding technique which allows a self-alignment of better than $1\mu\text{m}$. Additionally, the short bond-dis-

tances promise very good RF-features up to 100GHz bandwidth. Today this progress allows the introduction of batch processing for the optical and electrical part of the optoelectronic packaging of OEICs. This benefit opens the market for high volume production of devices for optical communications systems that allows cost effective production of low budget products for the consumer market.

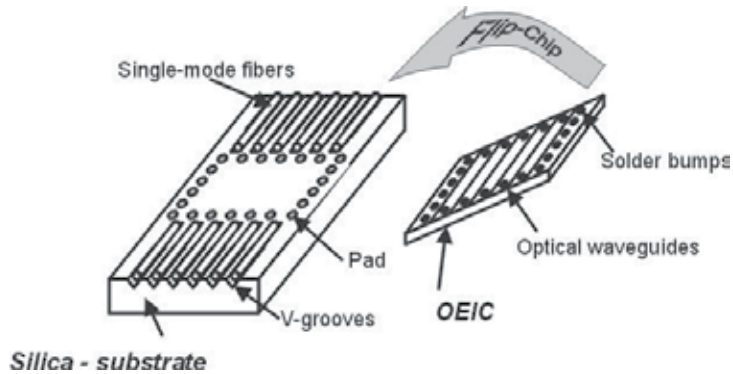


Figure 12. Flip-chip set-up.

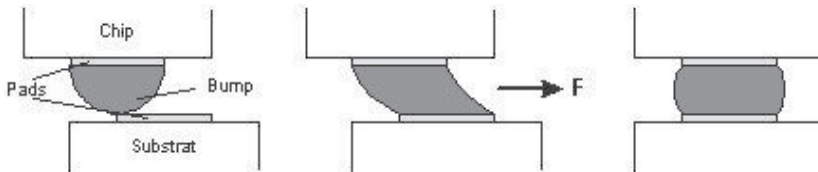


Figure 13. Flip-chip self-alignment.

6.2. Optical board technology

The progress in mechanical precision of the FC-bonds makes it possible to align one or multiple optical fibers direct to OEICs. Firstly, the OEIC will be FC-bonded as shown in figure 14. In the next step the fibers are inserted into V-grooves, fabricated by an anisotropic wet etching of the silica substrate. After insertion, the fiber must be fixed mostly by UV-hardened glue. Here more than 100 fibers can be arranged passively in one single fabrication step to the OEIC. An example of the connection of four lasers to an array of single mode fibers is shown in photograph 15.

In the next development step additional electrical amplifiers, multiplexers, modulators etc. can also be located on the substrate. This kind of hybrid integration is called optical motherboard or photonic lightwave circuit (PLC) depicted in figure 16. This type of integration is the most promising technique today for reaching an adequate price level of optical communications products for the consumer market.

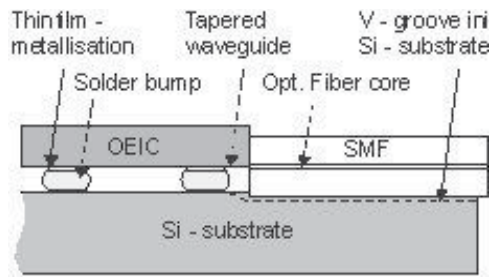


Figure 14. Fiber-chip connection with flip-chip.

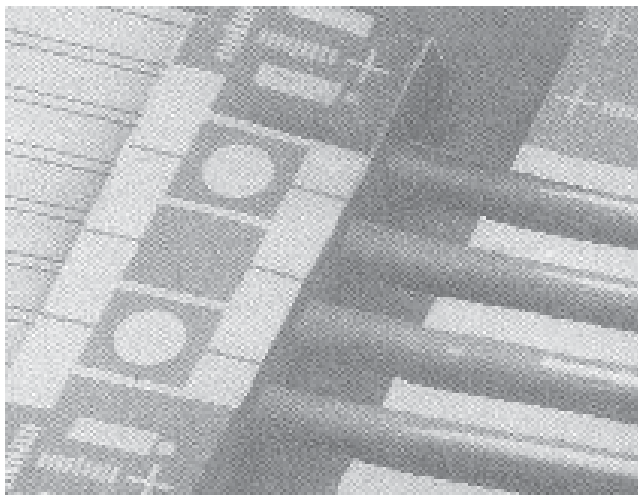


Figure 15. Photograph of flip-chip bonded laser array(Heinrich-Hertz-Institute, Berlin).

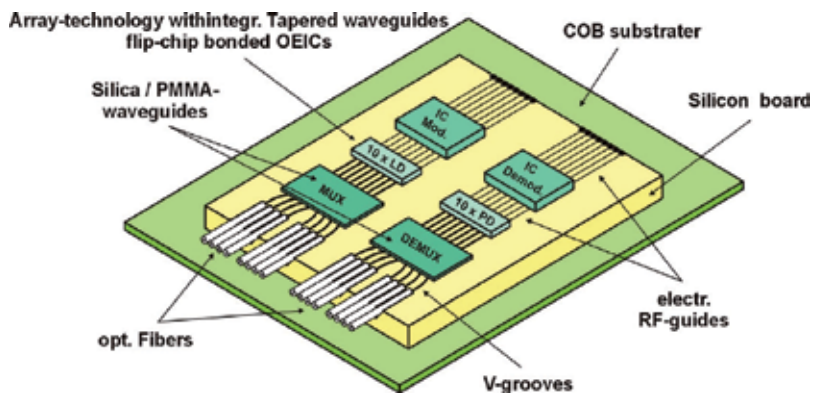


Figure 16. Concept for a complete optical motherboard [1], [17].

7. Optical connectors

7.1. Single fiber connectors

This chapter will give a summary of the optical connectors used today. There are several different types of connectors used for single mode and for multimode operation. Additionally, there are straight polished types and slant polished ones, which are used in high speed optical communication systems because of their high reflection loss characteristics. Further on, connectors are used in various applications including:

11. Polarization maintaining fibers
12. Matching gel/coating
13. Physical contact
14. Air gap
15. Automated light shutter function
16. Duplex connectors

| Name | losses | Straight cut | Slant cut | Single (SM) Multi (MM) mode | Polarization maintaining | Durability (insertions) | Price |
|---------------|--------|--------------|-----------|--------------------------------|--------------------------|-------------------------|-------|
| Mini BNC | 0.21dB | -20dB | | MM | | "/500 | low |
| ST | 0.28dB | -20dB | | SM,MM | | "/500 | med |
| FC/PC | 0.35dB | -30dB | | SM,MM | | "/500 | low |
| FC/APC | 0.4dB | | -55dB | SM | | "/500 | med |
| SMA | 0.38dB | -20dB | | MM | | "/500 | low |
| Radiall VFO | 0.4dB | -30dB | | SM | yes | "/250 | high |
| | 0.7dB | | -55dB | SM | | "/250 | high |
| Radiall EC | 0.2dB | | -50dB | MM | | "/250 | med |
| | 0.5dB | | -60dB | SM | yes | "/250 | med |
| Diamond E2000 | 0.18dB | -30dB | | SM | | "/1000 | low |
| | 0.18dB | | -55dB | SM | yes | "/1000 | low |
| SC | 0.5dB | -30dB | | SM | | "/1000 | low |
| | 0.5dB | | -60dB | SM | yes | "/1000 | low |
| HRL-10 | 0.3dB | | -60dB | SM | | "/1000 | High |
| LC-Duplex | 0.2dB | -30dB | | SM/MM | | "/10.000 | low |

Table 1. Optical connectors summary.

All loss failure mechanisms that can be acknowledged at the fiber to fiber coupling are also detectable at connector-connector coupling. All possible losses are depicted in figure 17. Only highly precise mechanical feed and exact surface polishing can avoid high loss at the connection. Intrinsic losses can be avoided by using matching fibers, while extrinsic losses can be overcome by strong mechanical feed. Today feeder elements with better than 2 μm lateral deviation are commercially available. Polishing and cleaning the connector surface can avoid absorption and the scattering of the optical power. With the help of anti reflection coatings or angled surfaces, reflections can be (7°-8° degrees) overcome. All connectors are very similar in their mechanical structure. The fiber is fed through a ferrule made of ceramics, which centers the fiber. Then the ferrule is filled with UV-curing glue. After hardening, the end of the fiber is cut and polished. The outer diameter of the normally used ferrule is 2.5mm or 1.25mm. In figure 18 a cross section of a connector is depicted.

In the following, typical connectors used today are listed in table 1.

The most popular connector today is the FC/PC one direct followed by the Diamond E2000 and the very small SC connector. FC/PC-connectors (see figure 19) are mostly used in optical equipment but have the disadvantage to be easily soiled with dust and dirt. The E2000 is used by several Telecoms because of the integrated dust cover and beam shutter.

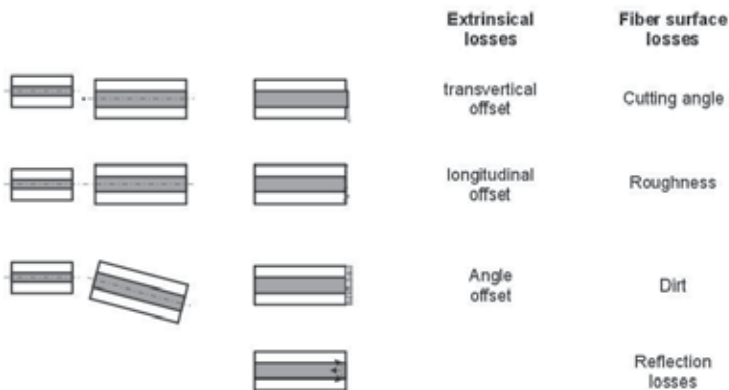


Figure 17. Loss mechanisms at connector end surface.

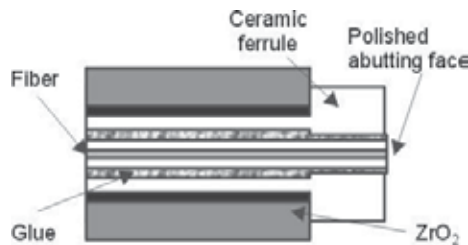


Figure 18. Cross section of an optical connector.



Figure 19. Optical FC/PC connector.

7.2. Multi-fiber connectors

These types of connectors are often used for the connections of mainframes or servers and at Fiber Distributed Data Interface (FDDI) links. Here the data were transmitted via several optical data links between the server stations with up to 10 Gbit/s per link. Also multi-sensor systems are using these kinds of connectors. Commercial available types are listed in table 2. The most commonly used connector is the MT one which is depicted in figure 20.



Figure 20. Multi-fiber MT-connector.

| Name | Losses | Straight polished | Single (SM) Multi (MM) mode | durability (insertions) | User | Price |
|-----------|-------------|-------------------|-----------------------------|-------------------------|-------------------|-------|
| ESCON | 0.5dB | -20dB | MM | "/500 | LAN,Comp. Network | low |
| FDDI M | 0.5dB 0,5dB | -20dB -20dB | MMSM | "/500"/500 | WDM | med |
| MTConnect | 0.3dB 0,5dB | -25dB -25dB | MMSM | "/200"/200 | WDM | high |

Table 2. Optical multi-fiber connectors.

8. Modules

This chapter will summarize several types of modules, which are used in commercial standard opto-electronic packages. These can be divided into four basic categories:

1. Transmitter (laser) -modules w/o cooling
2. Receiver (photodiode) -modules
3. Transceiver modules (Transmitter/Receiver)
4. Passive devices (sensor) -modules

Each category will be demonstrated by an example, but first some words about the required coupling method.

8.1. Fiber-chip coupling in modules

The performance of an optical coupling and the affordable operating expense are strongly dependent on the coupling device and the fiber used. The performance is directly correlated to the coupling efficiency. All commercial implementations are a trade off between cost and efficiency. To reach a very good efficiency you have to invest much manpower, which must be reflected in the price of the product. On the mass market only very low cost modules are available. That's the reason why here only modules with very low coupling efficiency can be found. The coupling of devices to multi mode fibers is less expensive than to single mode fibers, which are also priced lower than fiber-taper couplers. These are on the other hand are cheaper than lens-couplers, because of the time effort required to adjust additional coupling devices.

8.2. Multimode fiber coupling

The multimode fiber has an diameter of $50\mu\text{m}$ and a numerical aperture of 0.25 (15° aperture). Usually this type of coupling is used in photodiode modules where the fiber is directly connected to the photo-absorbing surface of the diode, which is depicted in figure 21.

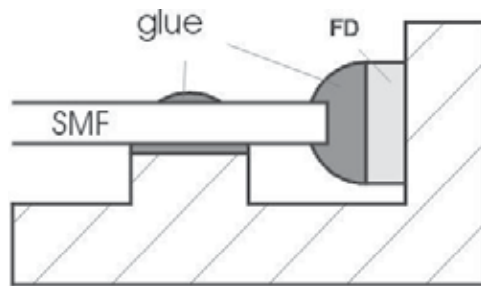


Figure 21. Direct attach of an optical fiber to a photo diode.

8.3. Singlemode-fiber coupling

In section 3 it has been demonstrated that a single mode butt fiber coupling to a Laser diode can have only 10 % efficiency. But with a lens system, which adapts the different optical mode fields, 50 % to 90 % coupling efficiency can be achieved (see figure 22). Table 4 gives a view of the mechanical aspects for coupling efficiencies with several coupling designs.

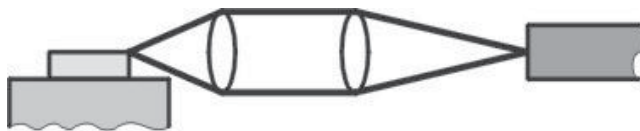


Figure 22. Fiber-chip coupling by a two-lens system.

| Coupling technique (Laser-fiber) | Alignment precision (μm) for 1 dB add. loss at lateral/longitudinal displacement | Coupling loss (dB) |
|----------------------------------|---|--------------------|
| Butt fiber (50 μm) | 15/50 | 7-10 |
| Butt fiber (9 μm) | 2/20 | 7-10 |
| System with one lens | 0,5/5 | 3 |
| Double lens system | 0,5/5 | 1-3 |
| Fiber taper | 0,3/3 | 3-5 |

Table 3. Alignment precision for one dB additional coupling loss.

8.4. Transmitter and receiver modules

Transmitter modules for low cost applications are normally designed for simple butt fiber to chip coupling without temperature control of the emitting OEIC. Today more lensed coupling arrangements fixed by laser welding are often introduced. In figure 23, a coaxial coupled receiver module for high data rates of 40Gbit/s is depicted. This set-up is also used in low-priced transmitter modules for single mode operation.

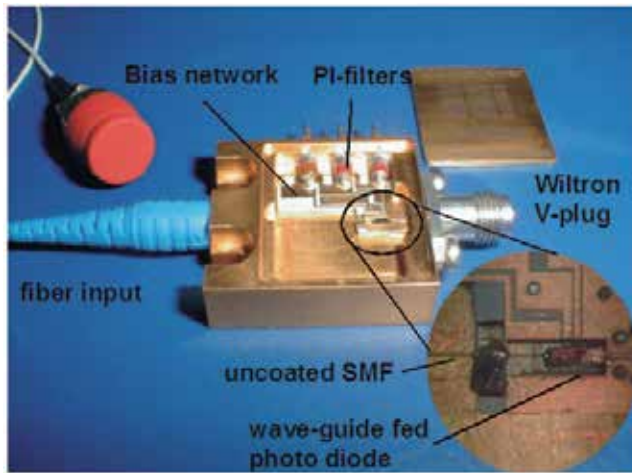


Figure 23. Receiver module.

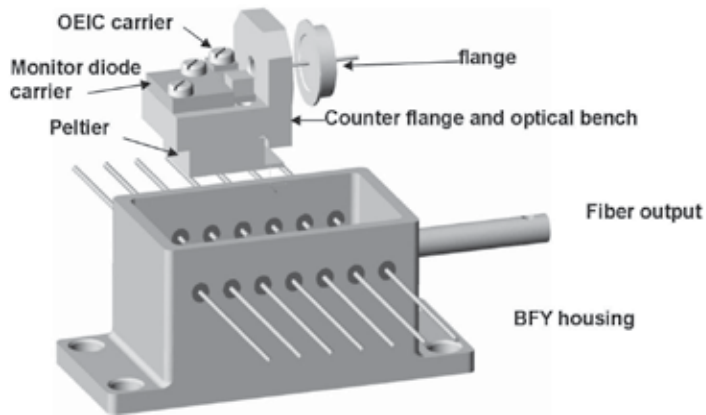


Figure 24. Temperature controlled laser module with fiber-taper coupling.

For high bit rate optical communications systems, cooled laser devices are needed. These modules are much more complicated in their mechanical set-up which is shown in figure 24. Here a tapered fiber was adjusted in front of the OEIC which is temperature stabilized by a Peltier cooler and a temperature sensor (thermistor) shown by [18].

8.5. Transceiver modules

These kind of modules are used in optical transmission systems where both terminals of the communications line can talk at the same time, which is called bi-directional communication. Transmitter and receiver functions must be integrated in these modules, which are shown in figure 25.

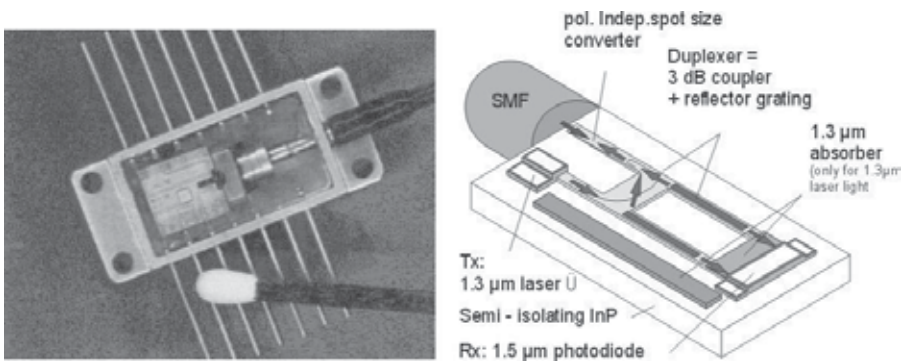


Figure 25. Monolithically integrated transceiver module.

8.6. Sensor and passive devices modules

These kind of modules are normally very easy to fabricate. Bragg sensors are used in a very wide spectrum of applications such as temperature sensors and strain gauge. The grating is centered into a metal or plastic tube and fixed with special glue.

Other passive devices use multiple fiber ports which can be combined in an array. Typical array devices are arrayed waveguide gratings (AWG) for multi wavelength optical transmission systems. These OEICs must be connected to up to 64 IO-ports at both chip sides as presented by [2], which can be seen in figure 27.

Typical housings are shown in figure 26.

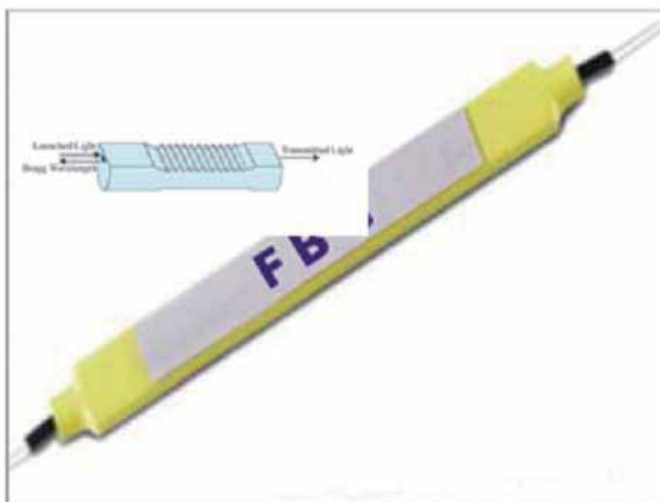


Figure 26. Fiber Bragg grating module.

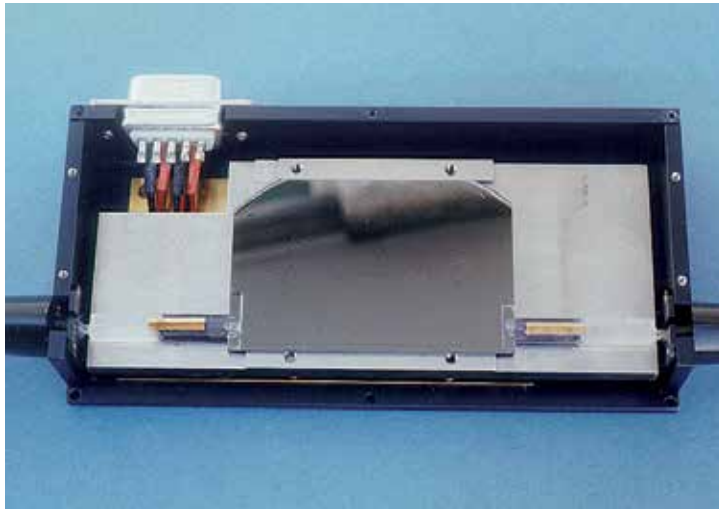


Figure 27. Arrayed waveguide grating module [19].

9. Reliability requirements

For application in optical networks, modules must be stable with respect to temperature changes and mechanical stresses. At present, there are several definite environmental and mechanical criteria for optical devices such as sensor and transmitter modules, which are investigated with reference to the [20] requirements. In the tests, insertion losses were measured online for each sample.

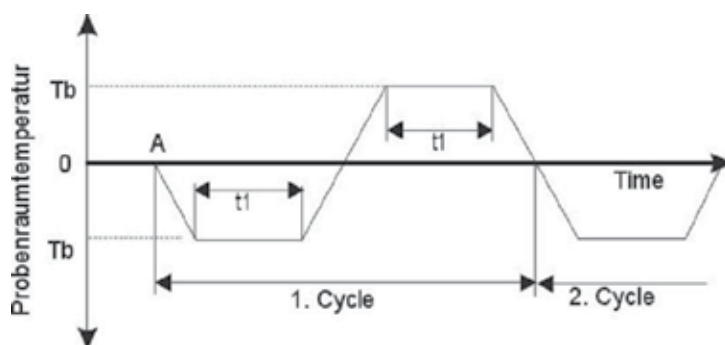


Figure 28. Temperature cycle test structure.

Temperature stress can be invoked into the modules by cycling the environmental temperature between a high temperature called T_A and a low temperature T_B that is depicted in

figure 28. Additionally, relative air humidity can be increased up to 80 % or 95. The following institutions have developed the commonly used testing standards:

5. DIN (Deutsche Industrie Norm, German Industrial Standard Organization) 40046
6. MIL-STD (Military Standard/USA) 810/202
7. IEC (International Engineering Committee) 60068-X
8. Telcordia 6R-78, -326, -357, -468

| Stress parameters | Tests |
|-----------------------------|--|
| Climate | Cold, dry heat, dust and sand Low pressure Wheat heat at constant temperature Dry heat at cycling temperatures Solar radiation |
| Mechanical | Dropping, acceleration, vibrations |
| Chemical and biological | Corrosive atmosphere, growths of mold |
| Packaging and manufacturing | Welding, ultrasonic cleaning, mechanical strength of connector pins |
| div. | Sealing |

Table 4. Environmental test parameters.

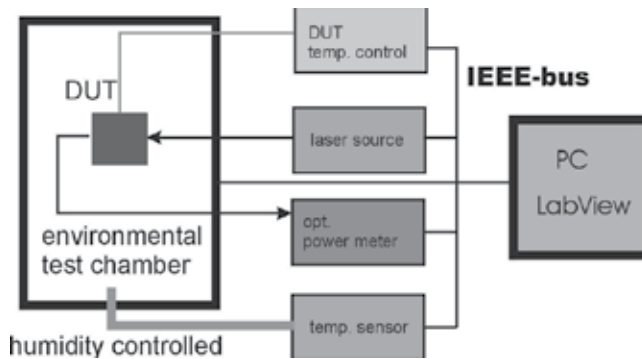


Figure 29. Environmental test set-up.

A typical set-up used for temperature testing is depicted in figure 29. Further, the device under test (DUT) is placed into a humidity controlled environmental test chamber. The temperature behavior of the opto-electronic module is mostly characterized by measuring the variation of optical output power. A plot of a typical temperature test between +15°C and +40°C is shown in figure 30. The temperature behavior of a laser module shows a maximum output variation of ± 0.15 dB with temperature which is a real good result. Three cycles with-

in 4 hours of measuring time were performed with temperature controlling of the OEIC shown in figure 30.

After thermal cycling, the test for mechanical shock and vibration stress was completed. Mechanical shock tests must be performed in all three Cartesian directions. The measured accelerations amounted to more than 200 g within 3 ms. The vibration tests were performed by a so called "shaker machine". The excitation of the module was measured with an acceleration sensor and a digital oscilloscope. The acceleration was controlled to be stronger than 16 g within a broad spectral bandwidth of 50-5000 Hz. Several tests figures can be run with the so called "shaker machine":

5. Sinusoidal acceleration 1-1.000g
6. Noisy acceleration 1-10.000 Hz
7. Resonance test and -strain
8. Shock excitation 10 – 10.000g

To reach a certified test label for opto-electronic modules according to the Telcordia specifications, eleven modules must undergo the environmental and mechanical stress test. None of the tested specimens is allowed to show a failure. The strong requirements for the test procedures are only achieved by substantial preliminary testing of the modules.

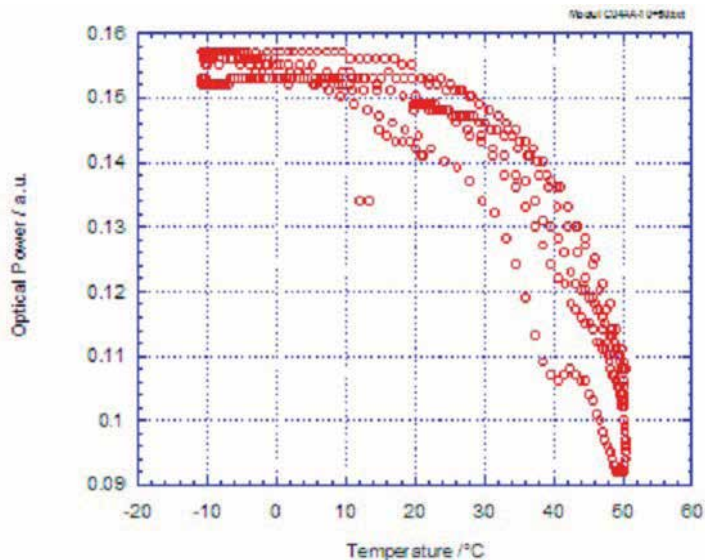


Figure 30. Temperature test of the laser module between -15°C and 50°C.

Sources of supply for environmental standard tests-

VDE-Verlag <http://www.vde-verlag.de>

DIN <http://www.din.de>

IEC-standards-shop <http://www.iec-normen.de>

Telcordia <http://www.telecom-info.telcordia.com>

10. Conclusion

We designed and fabricated a series of modules for one-sided and double-sided fiber-chip coupling for single mode and multimode fibers with simultaneous coupling of both chip sides by a new-patented set-up. Additional, we created passive and active modules with temperature control and multi fiber connections up to 16 fibers via fiber arrays. The modules have been tested in a reliability stress program between -40° C and +80°C and by a vibration shaker. Electrical modulation signals up to 50 GHz can be fed via RF connectors to the OEIC. The packages show good long-term stability and are well suited for rapid prototyping in laboratory environment and high volume production.

Author details

Ulrich H. P. Fischer*

Address all correspondence to: ufischerhirschert@hs-harz.de

Harz University of Applied Sciences Friedrichstraße, Wernigerode

References

- [1] Fischer, U. (2002). *Optoelectronic Packaging*, Berlin, VDE Verlag.
- [2] Wild, T., & Stremitzer, S. (2007). *Digitale Wundanalyse mit W.H.A.T. (Wound Healing Analyzing Tool)*.
- [3] <http://www.mostnet.de>, Available, <http://www.mostnet.de/home/index.html>.
- [4] Homepage Aufbau- und Verbindungstechnik im HHI. Available, <http://www.hhi.de/avt>.
- [5] Siegmund, S., Fischer-Hirschert, U. H. P., & Bauer, A. (2012). Technikgestützte Pflege-Assistenzsysteme und rehabilitativ-soziale Integration unter dem starken demografischen Wandel in Sachsen-Anhalt. Berlin. in 5. *Deutscher AAL-Kongress*.
- [6] Reinboth, C., Fischer-Hirschert, U. H. P., & Witzak, U. (2012). Berlin. Technische Assistenzsysteme zur Unterstützung von Pflege und selbst-bestimmtem Leben im Alter- das ZIM-NEMO-Netzwerk TECLA, in 5. *Deutscher AAL-Kongress*.

- [7] Siegmund, S., Hirschert, A., Apfelbaum, A., & Fischer-Hirschert, U. H. P. (2012). Innovationslabor Technikakzeptanz. Görlitz. in *13. Nachwuchs-Wissenschaftlerkonferenz mitteldeutscher Fachhochschulen*, 449-452.
- [8] Fischer, U. H. P. (2002). *Optoelectronic Packaging*.
- [9] Saruwatari, M., & Nawata, K. (1979). Semiconductor laser to single-mode fiber coupler. *Applied Optics*, 18, 1847-1856.
- [10] ITU-G.652,. (1997). Characteristics of a single-mode optical fibre and cable. ed.
- [11] http://www.fzk.de/imt/liga/d_index.html.
- [12] <http://www.izm.fhg.de/avt/kloeser.htm>.
- [13] Makiuchi, M., Norimatsu, M., Sakurai, T., Kondo, K., & Yano, M. (1993). Flip-Chip Planar Ga InAs/InP p-i-n Photodiode Array for Parallel Optical Transmission. *IEEE Photonics Technology Letters*, 5, 518-520.
- [14] Kuhmann, J. F. (1996). Untersuchungen zu einer flußmittelfreien und selbstjustierenden Flip-Bondtechnologie für photonische Komponenten. TU, Berlin.
- [15] Kuhmann, J. F., & Pedersen, E. H. (1998). Fluxless FC-soldering in O₂ purged ambient. Seattle, WA. in *48TH IEEE Electronic Components & Technology Conference*, 256-258.
- [16] Kuhmann, J. F., & Pech, D. (1996). In situ observation of the self-alignment during FC-bonding under vacuum with and without H₂. *IEEE Photonics Technology Letters*, 8, 1665-1667.
- [17] Fischer, U. H. P. (2006). *Optische Modenfeldadaption in photonischen Modulen der optischen Aufbau- und Verbindungstechnik*, Göttingen, Cuvillier-Verlag.
- [18] <http://www.imm-mainz.de>, Available, <http://www.imm-mainz.de/>.
- [19] Ehlers, H., Biletzke, M., Kuhlow, B., Przyrembel, G., & Fischer, U. H. P. (2000). Optoelectronic Packaging of Arrayed-Waveguide Grating Modules and Their Environmental Stability Tests. *Optical Fiber Technology*, 6, 344-356.
- [20] Meyer, S., & Schulze, E. (2009). *Smart Home für ältere Menschen. Handbuch für die Praxis*, Fraunhofer Irb verlag.

III-V Multi-Junction Solar Cells

Gui jiang Lin, Jingfeng Bi, Minghui Song,
Jianqing Liu, Weiping Xiong and Meichun Huang

Additional information is available at the end of the chapter

<http://dx.doi.org/10.5772/50965>

1. Introduction

Photovoltaic is accepted as a promising technology that directly takes advantage of our planet's ultimate source of power, the sun. When exposed to light, solar cells are capable of producing electricity without any harmful effect to the environment or devices. Therefore, they can generate power for many years (at least 20 years) while requiring only minimal maintenance and operational costs. Currently the wide-spread use of photovoltaic over other energy sources is impeded by the relatively high cost and low efficiency of solar cells [1].

III-V multi-junction solar cells, as a new technology, offer extremely high efficiencies compared with traditional solar cells made of a single layer of semiconductor material [2]. The strong demand for higher efficiency photovoltaic has recently attracted considerable interest in multi-junction solar cells based on III-V semiconductors [3]. Depending on a particular technology, multi-junction solar cells are capable of generating approximately twice as much power under the same conditions as traditional solar cells made of silicon. Unfortunately, multi-junction solar cells are very expensive, so they are mainly used in high performance applications such as satellites at present. However, in our opinion, with the concentrator technology, the tandem cell will play a role in the future energy market. The state-of-the-art high efficiency III-V solar cells utilize a triple junction structure which consists of the Ge bottom sub-cell (0.67 eV) formed on the Ge substrate homogeneously, the $\text{Ga}_{0.99}\text{In}_{0.01}\text{As}$ middle sub-cell (1.36 eV), and the lattice matched (LM) $\text{Ga}_{0.5}\text{In}_{0.5}\text{P}$ top sub-cell (1.86 eV) [4,5]. It has reached conversion efficiencies up to 40% at concentrations of hundreds of suns under the AM1.5D low aerosol optical depth (AOD) spectrum [4]. The GaInP/GaInAs/Ge triple-junction cells have also been demonstrated with efficiencies up to 30% under one-sun AM0 spectrum for space applications. Multi-junction solar cells based on III-V materials have achieved the highest efficiencies of any present photovoltaic devices. Addi-

tionally, these devices are the only solar cells currently available with efficiencies above 30%. The high efficiency is due to the reduction of thermalization and transmission losses in solar cells when the number of p-n junctions is increased.

Future terrestrial cells will likely feature four or more junctions with a performance potential capable of reaching over 45% efficiency at concentration of hundreds of suns. The 4-, 5-, or 6-junction solar cells with concentrator trade lower current densities for higher voltage and divide the solar spectrum more efficiently. The lower current densities in these cells can significantly reduce the resistive power loss (I^2R) at high concentrations of suns when compared with the 3-junction cell [6].

High-efficiency GaInP/GaAs/InGaAs triple-junction solar cells grown inversely with a metamorphic bottom junction could be achieved by replacing the bottom Ge sub-cell with 1 eV energy gap material. $\text{In}_{0.3}\text{Ga}_{0.7}\text{As}$ is the promised candidate, if without the lattices mis-match (LMM, around 2%) with the other two sub-cells. Therefore, the LM top and middle sub-cells were grown first, and the graded buffers were employed between middle and bottom cells to overcome the mismatch and to prevent the threading dislocations. The substrate was removed for the reusing. This inverted metamorphic, monolithic triple junction solar cells could be obtained with at least 2% higher efficiency than the traditional one theoretically [7].

A metamorphic $\text{Ga}_{0.35}\text{In}_{0.65}\text{P}/\text{Ga}_{0.83}\text{In}_{0.17}\text{As}/\text{Ge}$ triple-junction solar cell is studied to provide current-matching of all three sub-cells and thus give a device structure with virtually ideal energy gap combination. It is demonstrated that the key for the realization of this device is the improvement of material quality of the lattice-mismatched layers as well as the development of a highly relaxed $\text{Ga}_{1-y}\text{In}_y\text{As}$ buffer structure between the Ge substrate and the middle cell. This allows the metamorphic growth with low dislocation densities below 10^6 cm^{-2} . The performance of the device has been demonstrated by a conversion efficiency of 41.1% at 454 suns AM1.5D [8].

In this chapter, the theoretical and experimental investigation of the most sophisticated, industrialized and commercialized GaInP/GaInAs/Ge triple junction solar cell was extensively described. Accelerated aging tests of the high concentration multi-junction solar cells and discussions on outdoor power plant performances were also presented.

2. Theoretical study on optimization of high efficiency multi-junction solar cells

In designing GaInP/GaInAs/Ge triple-junction cells, the principles for maximising cell efficiency are: (1) increasing the amount of light collected by each cell that is turned into carriers, (2) increasing the collection of light-generated carriers by each p-n junction, (3) minimising the forward bias dark current, and (4) photocurrents matching among sub-cells.

In practice, basic designs for these solar cells involve various doping concentrations and layer thicknesses for the window, emitter, base, and back surface field (BSF) regions in each sub-cell. In order to optimize the designs, a rigorous model including optical and electrical

modules was developed to analyse the bulk parameters effect on the external quantum efficiency, photocurrent and photovoltage of the GaInP/GaInAs/Ge multi-junction solar cells.

2.1. Theoretical approach

We present here a brief description of the equations used in our model. Thorough treatments of photovoltaic devices can be found elsewhere [9]. A schematic of a typical lattice-matched GaInP/GaInAs/Ge solar cell is shown in Figure1. It consists of an n/p GaInP junction on top of an n/p GaInAs junction which lies on an n/p Ge junction. The triple junction cells are series connected by two p⁺⁺/n⁺⁺ tunnel junctions.

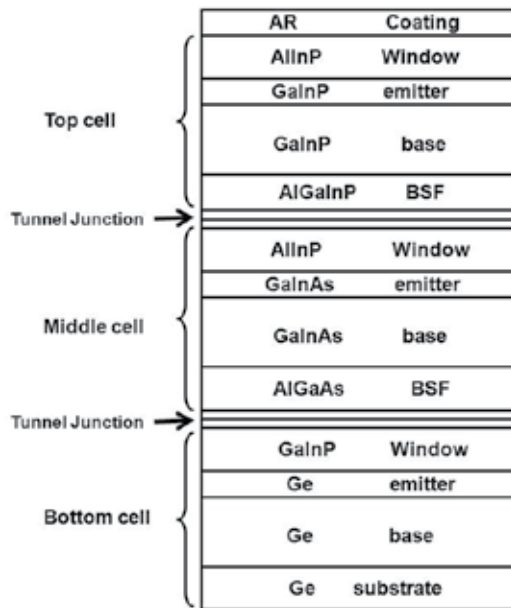


Figure 1. Solar cell structure used for simulation.

The solar spectrum, striking the front of the cell, includes ultraviolet, visible, and infrared lights. The absorption coefficient for short-wavelength light is quite large, and most of the blue light is absorbed very close to the front of the cell for generating photo carriers. Light with energy slightly larger than the energy gap is weakly absorbed throughout the cell. Light with energy less than the energy gap passes through the front cell and is absorbed in the next one. The photo carriers generated by the short-wavelength light diffuse inside the cell until they are either collected at the p-n junction or recombined with a majority carrier in bulk or at interface. The efficiency of the solar cell increase when all the photo carriers are collected at the junction instead of recombining elsewhere. Thus, recombination is at the front and back of the cell effects on the efficiency of the cell.

At the first level approximation, multi-junction cells behave like homo-junction cells in series, so their open circuit voltage is the summation of the voltages of the sub-cells, while their

short circuit current is that of the sub-cell with the smallest current. Hence, the performance of a multi-junction cell can be obtained from the performance of each sub-cell, evaluated independently. The load current density J is represented by the superposition of two diode currents and the photo-generated current,

$$J = J_{ph} - J_{01}(e^{qV/kT} - 1) - J_{02}(e^{qV/2kT} - 1) \quad (1)$$

Where J_{ph} is the photocurrent density, J_{01} the ideal dark saturation current component and J_{02} the space charge non-ideal dark saturation current component.

The photocurrent density and dark current density are given by the sum of the photocurrents and the sum of the dark current density, respectively, generated in the emitter, the base and the depleted region of the cell. [9] We have

$$J_{ph} = J_{emitter} + J_{base} + J_{depleted} \quad (2)$$

$$J_{emitter} = \frac{qF(1-R)\alpha L_p}{(\alpha L_p)^2 - 1} \left\{ \begin{array}{l} \frac{S_p L_p}{D_p} + \alpha L_p e^{-\alpha(d_e - W_n)} \\ \left(\frac{S_p L_p}{D_p} \cosh[(d_e - W_n)/L_p] + \sinh[(d_e - W_n)/L_p] \right) \\ \frac{S_p L_p}{D_p} \sinh[(d_e - W_n)/L_p] + \cosh[(d_e - W_n)/L_p] \end{array} \right\} - \alpha L_p e^{-\alpha(d_e - W_n)} \quad (3)$$

$$J_{base} = \frac{qF(1-R)\alpha L_n}{(\alpha L_n)^2 - 1} e^{-\alpha(d_b - W_n + W)} \left\{ \begin{array}{l} \frac{S_n L_n}{D_n} (\cosh[(d_e - W_n)/L_n] - e^{-\alpha(d_b - W_p)}) \\ + \sinh[(d_b - W_p)/L_n] + \alpha L_n e^{-\alpha(d_b - W_p)} \\ \frac{S_n L_n}{D_n} \sinh[(d_b - W_p)/L_n] + \cosh[(d_b - W_p)/L_n] \end{array} \right\} \quad (4)$$

$$J_{depleted} = qF(1-R)e^{-\alpha(d_e - W_n)}(1 - e^{-\alpha W}) \quad (5)$$

$$J_{01} = J_{01,emitter} + J_{01,base} \quad (6)$$

$$J_{01,emitter} = q \frac{n_i^2}{N_D} \frac{D_p}{L_p} \left\{ \frac{S_p L_p / D_p \cosh[(d_e - W_n) / L_p] + \sinh[(d_e - W_n) / L_p]}{S_p L_p / D_p \sinh[(d_e - W_n) / L_p] + \cosh[(d_e - W_n) / L_p]} \right\} \quad (7)$$

$$J_{01,base} = q \frac{n_i^2}{N_A} \frac{D_n}{L_n} \left\{ \frac{S_n L_n / D_n \cosh[(d_b - W_p) / L_n] + \sinh[(d_b - W_p) / L_n]}{S_n L_n / D_n \sinh[(d_b - W_p) / L_n] + \cosh[(d_b - W_p) / L_n]} \right\} \quad (8)$$

$$J_{02} = \frac{W n_i}{2(V_d - V)\tau} \quad (9)$$

Where q is electron charge, F the incident photon flux, α is an optical absorption coefficient and R is the reflectance of the anti-reflective coating. n_i is the intrinsic carrier concentration, N_A and N_D are the concentrations of acceptors and donors. d_e is the emitter thickness, d_b the base thickness, L_p the hole diffusion length in the emitter, L_n the electron diffusion length in the base, S_p the hole surface recombination velocity in the emitter, S_n the electron surface recombination velocity in the base, D_p the hole diffusion coefficient in the emitter, D_n the electron diffusion coefficient in the base, and τ is the non-radiative carrier lifetime. T_F is the transmission of incident photon flux into the sub-cell under consideration.

The build-in voltage V_d of the junction, the thickness of the depleted layer in the emitter W_n , the thickness of the depleted layer in the base W_p , and the total depleted zone thickness W , are given by [10],

$$V_d = kT \log\left(\frac{N_D N_A}{n_i^2}\right) \quad (10)$$

$$W = \sqrt{2\epsilon \frac{N_D + N_A}{N_D N_A} (V_d - V - 2kT)} \quad (11)$$

$$W_n = W / (1 + N_D / N_A) \quad (12)$$

$$W_p = W - W_n \quad (13)$$

Where k is the Boltzmann constant, ϵ the dielectric constant and T the temperature ($T = 25^\circ\text{C}$ was used in this paper). It is important to note that F and α depend on the wavelength, whereas D_p , D_n , L_p , L_n and τ depend on the doping concentration [11].

The optical model proposed in this paper is based on the transfer matrix formalism. It allows calculating the incident optical spectrum on each sub-cell from the solar spectrum. Each layer of the multi-junction is described by a transfer matrix M which is defined by

$$M = \begin{pmatrix} M_{0,0} & M_{0,1} \\ M_{1,0} & M_{1,1} \end{pmatrix} = \begin{pmatrix} \cos\left(d \frac{2\pi(n-i\lambda\alpha/4\pi)}{\lambda}\right) i \frac{\sin\left(d \frac{2\pi(n-i\lambda\alpha/4\pi)}{\lambda}\right)}{(n-i\lambda\alpha/4\pi)} \\ (n-i\lambda\alpha/4\pi) \sin\left(d \frac{2\pi(n-i\lambda\alpha/4\pi)}{\lambda}\right) \cos\left(d \frac{2\pi(n-i\lambda\alpha/4\pi)}{\lambda}\right) \end{pmatrix} \quad (14)$$

Where n and d are the refraction index and the thickness of the layer, respectively. The transmission coefficient T_M [12] of the layer is then given by

$$T_M = \frac{4n_0^2}{(n_0 M_{0,0} + n_0 n_s M_{0,1} + M_{1,0} + n_s M_{1,1})^2} \quad (15)$$

Where n_0 is the superstrate refraction index and n_s is the substrate refraction index of the sub-cell. The $M_{i,j}$ coefficients refer to the matrix transfer elements. Thus, it is possible to determine the incident spectrum on each sub-cell. The incident photon flux in GaInP, GaInAs and Ge sub-cells are given by

$$F_{GaInP} = T_{ARC} F_{solar} \quad (16)$$

$$F_{GaInAs} = T_{ARC} T_{GaInP} F_{solar} \quad (17)$$

$$F_{Ge} = T_{GaInAs} T_{GaInP} T_{ARC} F_{solar} \quad (18)$$

where F_{solar} is the incident photon flux, T_{ARC} , T_{GaInP} and T_{GaInAs} are the transmission coefficient of the anti-reflective coating, the GaInP sub-cell and the GaInAs sub-cell, respectively. This model includes optical and electrical modules. Thus, it allows the calculation of the quantity of photons arriving at each junction from the solar spectrum. Then, the electrical model calculates, via interface recombination velocity, the photocurrents in the space charge region, the emitter and the base for each junction.

2.2. Solar cell structures and parameters

To calculate the power production of the GaInP/GaInAs/Ge triple-junction cells for space applications, the incident photon flux F_{solar} was taken from a newly proposed reference air mass zero (AM0) spectra (ASTM E-490). The integration of ASTM E490 AM0 solar spectral irradiance has been made to conform to the value of the solar constant accepted by the space community, which is 1366.1 W/m². The transmission coefficient of the anti-reflective coating T_{ARC} was set to be a constant of 98%, while the transmission coefficients of the GaInP sub-cell and the GaInAs sub-cell are calculated according to Eqs.14 and 15, which have wavelength dependence.

| Parameter | Ge | GaInAs | GaInP |
|----------------------------|----------------------|----------------------|----------------------|
| D_n (cm ² /s) | 22.86 | 140.02 | 29.39 |
| D_p (cm ² /s) | 10.71 | 4.02 | 1.03 |
| L_n (cm) | 5.3×10^{-3} | 9.7×10^{-4} | 6.3×10^{-4} |
| L_p (cm) | 8.8×10^{-4} | 7.3×10^{-5} | 3.7×10^{-5} |
| τ (s) | 8.9×10^{-7} | 8.9×10^{-9} | 4.2×10^{-9} |

Table 1. Material parameters used for calculation in this paper.

As shown in Figure 1, typical two-terminal triple-junction cells for space application with a Ge bottom cell, a GaInAs middle cell and a GaInP top cell with energy gaps of 0.661, 1.405 and 1.85 eV, respectively. The Ge cell is built on the p-type initial substrate; therefore, the Ge base is about 150 micrometers thick, with doping concentration of about 6×10^{17} cm⁻³; the Ge emitter is about 0.3 micrometers thick, with an n-type doping concentration of about 1×10^{19} cm⁻³. The emitters for the other two cells are 0.1 micrometers thick with doping concentration of about 1×10^{18} cm⁻³. Since the AM0 spectrum contains relatively more high-energy photons with energy greater than the GaInP top cell's energy gap, triple-junction cell with a very thick top cell will generally be photocurrent limited by the middle (GaInAs) cell. Therefore, the middle cell thickness was set to be thick enough (3.6 micrometers in this paper) with the doping concentration of about 2×10^{17} cm⁻³, and the optimal top cell thickness was suggested to be about 0.52 micrometers with doping concentration of about 1×10^{17} cm⁻³.

The absorption coefficient of the GaInP can be fitted by

$$\alpha_{GaInP} = 5.5\sqrt{(E - E_g)} + 1.5\sqrt{(E - E_g - 1)} \quad (19)$$

The absorption coefficient of the GaInAs (with In content of about 0.01) can be fitted by

$$\alpha_{GaInAs} = 3.3\sqrt{(E - E_g)} \quad (20)$$

The direct gap absorption spectra of the bulk Ge was used for calculation

$$\alpha_{Ge} = 1.9\sqrt{(E - E_g^{\Gamma})} / E \quad (21)$$

Where E is the photon energy and E_g the fundamental energy gap, both in eV, and α in 1/micrometers.

The diffusion length, the diffusion coefficient and the nonradiative carrier lifetime are calculated as a function of the doping concentration. The material parameters used for calculation are summarized in table 1.

2.3. The effect of the interface recombination on the performance of GaInP/GaInAs/Ge tandem solar cell

To have an analytical analysis, recombination velocity at only one interface among six interfaces is assumed to have a non-zero value, which is 1×10^6 cm/s. Figure 2-4 shows the total external quantum efficiencies η and the integrated photocurrent density J_{ph} of the three sub-cells, calculated from Eqs. 2-5 with the constant parameters in table 1 and with varying values of S_p and S_n . The external quantum efficiency η , defined as the probability of collecting a photo carrier for each photon, is a function of wavelength, λ , because of the λ -dependence of the absorption coefficient, α . The photocurrent density J_{ph} is obtained from the integral of the product of the η with the spectrum of interest. For large absorption coefficients, a high S_p causes dramatic decrease in the blue response as shown in Figure 2 (a), Figure 3 (a) and Figure 4 (a).

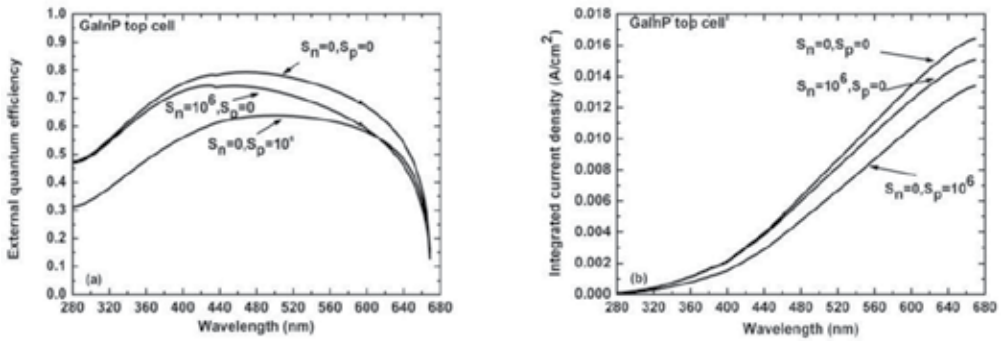


Figure 2. a) External quantum efficiency, and (b) integrated photocurrent density of the top GaInP cell for various interface recombination velocities.

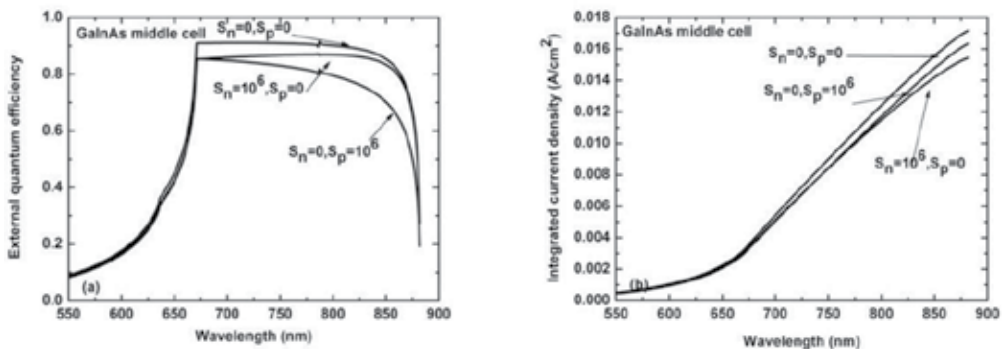


Figure 3. a) External quantum efficiency, and (b) integrated photocurrent density of the middle GaInAs cell for various interface recombination velocities.

However, a high S_p also causes a reduction in the red response. In contrast, high S_n causes a reduction only in the red response (Figure 2 (a), Figure 3(a)), with almost no measurable effect in the blue response for a thick cell as shown in Figure 4 (a).

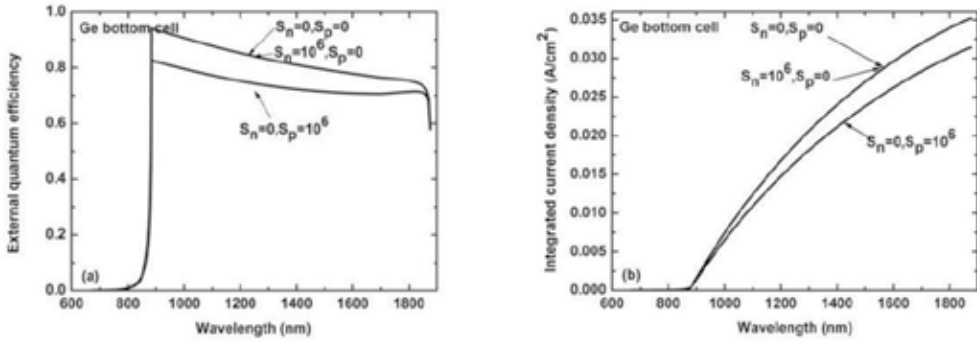


Figure 4. a) External quantum efficiency, and (b) integrated photocurrent density of the middle GaInAs cell for various interface recombination velocities.

Once the photocurrents of the three sub-cells are calculated, the short circuit current of the tandem cell is set to be the smallest of these three photocurrents. The open-circuit voltage is set to be the voltage at which the magnitude of the dark currents equals the photocurrents. The corresponding I-V characteristics of the tandem cell are plotted in Figure 5. Among all the interfaces, recombination at the top cell emitter surface is most detrimental due to the considerable drop of the cell short circuit current and to a less extent to the associated reduction in the cell voltage. While recombination effect at back interface of the bottom cell can be almost negligible because the base layer of the cell is thick enough.

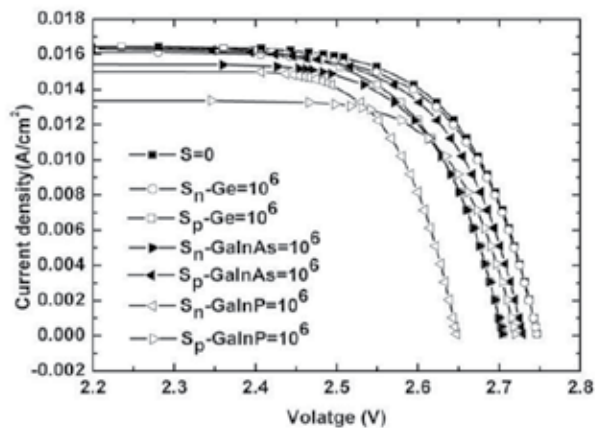


Figure 5. I-V characteristics of the GaInP/ GaInAs/ Ge tandem cell under AM0 with a recombination velocity at the indicated interface and zero elsewhere.

2.4. Optimization of high efficiency GaInP/GaInAs/Ge multi-junction solar cells

Lattice-matched GaInP/GaInAs/Ge triple-junction cells under investigation include a Ge bottom cell, a GaInAs middle cell and a GaInP top cell with energy gaps of 0.661, 1.405 and 1.85 eV, respectively. The Ge cell is built on the p-type initial substrate; the Ge base is 150 micrometers thick with doping concentration of $6 \times 10^{17} \text{ cm}^{-3}$, and the Ge emitter is 300 nm thick with an n-type doping concentration of $1 \times 10^{19} \text{ cm}^{-3}$. The middle cell's base is set to be thick enough (3.6 micrometers in this paper) with doping concentration of $2 \times 10^{17} \text{ cm}^{-3}$, and its emitter is 100 nm thick with doping concentration of $1 \times 10^{18} \text{ cm}^{-3}$. The incident photon flux is taken from a newly proposed reference air mass zero (AM0) spectra (ASTM E-490). The anti-reflective coating used in simulation includes a 30 nm AlInP top window layer; ARC composed of 52 nm ZnS and 90 nm MgF2.

It is at first assumed that recombination velocity for a top cell back surface is $1.3 \times 10^5 \text{ cm/s}$, a middle cell back surface 105 cm/s and a top cell emitter surface $5.15 \times 10^4 \text{ cm/s}$, while recombination velocities at the other three interfaces are zero. Then, the optimal top cell thickness and dopant profiles were obtained to meet high efficiency.

| top cell base thickness d-base (nm) | open-circuit voltage Voc (V) | short-circuit current Jsc (A/cm ²) | fill factor | tandem cell efficiency |
|-------------------------------------|------------------------------|--|-------------|------------------------|
| d-base=400 nm | 2.6660 | 0.01720 | 90.56% | 30.40% |
| d-base=450 nm | 2.6664 | 0.01768 | 89.82% | 30.99% |
| d-base=500 nm | 2.6667 | 0.01812 | 88.40% | 31.27% |
| d-base=550 nm | 2.6669 | 0.01777 | 89.82% | 31.05% |

Table 2. Figure-of-merits of the tandem cell for various top cell base thickness.

| top cell base doping concentration (1/cm ³) | open-circuit voltage Voc (V) | short-circuit current Jsc (A/cm ²) | fill factor | tandem cell efficiency |
|---|------------------------------|--|-------------|------------------------|
| NA-base = 1×10^{16} | 2.6095 | 0.01816 | 88.62% | 30.74% |
| NA-base = 5×10^{16} | 2.6503 | 0.01814 | 89.15% | 31.32% |
| NA-base = 1×10^{17} | 2.6667 | 0.01812 | 88.40% | 31.27% |
| NA-base = 5×10^{17} | 2.6981 | 0.01796 | 88.24% | 31.19% |

Table 3. Figure-of-merits of the tandem cell for various top cell base doping concentration.

Table 2 presents the Figure-of-merits of the tandem cell for various top cell base thicknesses with doping concentration of $1 \times 10^{17} \text{ cm}^{-3}$, when the top cell emitter thickness is set to 100 nm with doping concentration of $1 \times 10^{18} \text{ cm}^{-3}$. Table 3 presents the Figure-of-merits of the

tandem cell for various top cell bases doping concentrations with thickness of 500 nm, when the top cell emitter thickness is set to 100 nm with doping concentration of $1 \times 10^{18} \text{ cm}^{-3}$. It is found that photocurrents strongly depend on top cell thickness, since the AM0 spectrum contains relatively more high-energy photons with energy greater than the GaInP top cell's energy gap, and photocurrents of triple-junction cells with a very thick top cell will generally be limited by the middle (GaInAs) cell. The tandem cell efficiency reaches the largest value (31.27%) with the top cell base thickness of 500 nm, because the photocurrents of the top and middle cells almost match each other. Table 3 shows that higher doping concentration at the top cell base leads to a considerable increase of the cell voltage and a less drop of cell photocurrent. It can be deduced from table 3 that doping concentration at the top cell base should be optimized between 5×10^{16} and $1 \times 10^{17} \text{ cm}^{-3}$ to obtain higher efficiency. In order to realize the values of the Figure-of-merits shown in table 2 and table 3, the external quantum efficiency of the top cell for various top cell base thicknesses and top cell base doping concentrations are presented in Figure6 (a) and Figure6 (b), respectively. It is found that the external quantum efficiency of the top cell increases with the increasing top cell base thickness (Figure6 (a)), while at short wavelengths, the efficiency increases with the increasing top cell base doping concentration, at large wavelengths, decreases (Figure6 (b)).

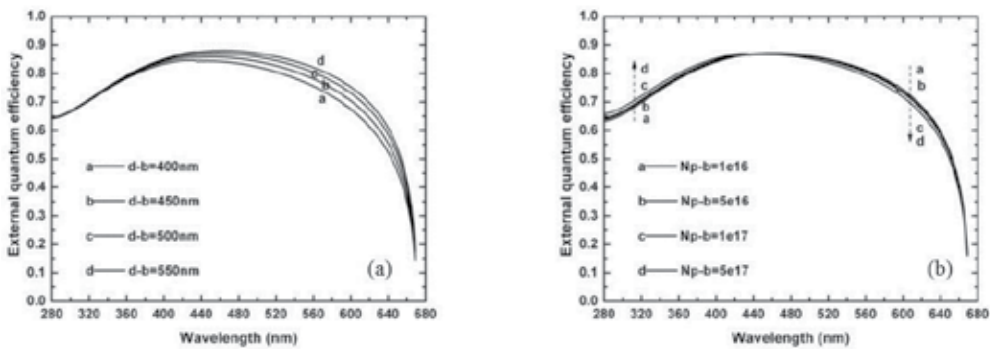


Figure 6. External quantum efficiency of the top cell for various top cell base thickness (a), and top cell base doping concentration (b).

| top cell emitter thickness d- emitter (nm) | open-circuit voltage Voc (V) | short-circuit current Jsc (A/cm ²) | fill factor | tandem cell efficiency |
|--|------------------------------|--|-------------|------------------------|
| d-emitter =50 nm | 2.6680 | 0.01848 | 88.62% | 31.98% |
| d-emitter =100 nm | 2.6667 | 0.01812 | 88.40% | 31.27% |
| d-emitter =150 nm | 2.6710 | 0.01737 | 89.09% | 30.25% |
| d-emitter =200 nm | 2.6707 | 0.01644 | 89.84% | 28.87% |

Table 4. Figure-of-merits of the tandem cell for various top cell emitter thickness.

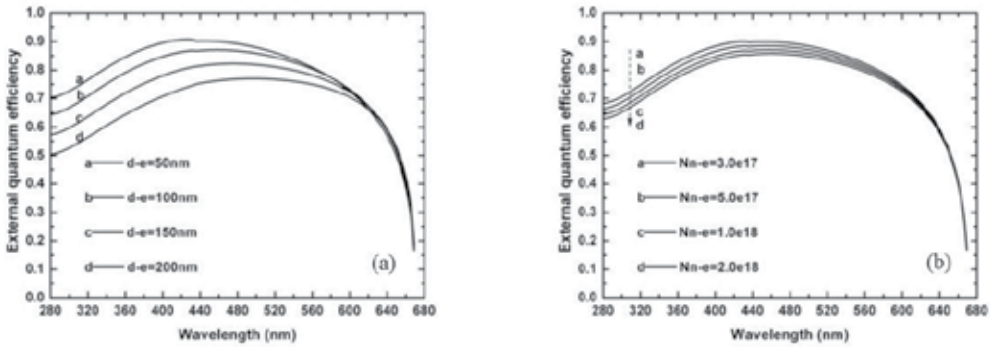


Figure 7. The external quantum efficiency of the top cell for various top cell emitter thickness (a), and top cell emitter doping concentration (b).

| top cell emitter doping concentration (1/cm ³) | open-circuit voltage Voc (V) | short-circuit current Jsc (A/cm ²) | fill factor | tandem cell efficiency |
|--|------------------------------|--|-------------|------------------------|
| ND -emitter =3x10 ¹⁷ | 2.6673 | 0.01816 | 89.30% | 31.66% |
| ND -emitter =5x10 ¹⁷ | 2.6674 | 0.01816 | 88.37% | 31.51% |
| N D-emitter =1x10 ¹⁸ | 2.6667 | 0.01812 | 88.40% | 31.27% |
| ND -emitter =2x10 ¹⁸ | 2.6652 | 0.01786 | 88.74% | 30.90% |

Table 5. Figure-of-merits of the tandem cell for various top cell emitters doping concentration.

3. Experimental procedure, results and discussions

3.1. The preparation of the triple junction GaInP/GaInAs/Ge epitaxial wafers

The Ga_{0.49}In_{0.51}P/Ga_{0.99}In_{0.01}As/Ge multi-junction solar cells were grown by the Veeco E475 MOCVD system on 6° off cut Germanium substrate. Standard growth conditions used were with growth pressure of 40 Torr, and rotation rate of 500 rpm. The precursors include trimethylindium (TMIn), trimethylgallium (TMGa), trimethylaluminium (TMAI), arsine, phosphine and diethyl-tellurium (DETe), diethyl-zink (DEZn). Top and middle sub-cells include the following layers: back-surface field (BSF) layer, base, emitter and window. The Ge-sub-cell consists of a base (substrate), a diffused emitter and a window. Sub-cells are connected in series by tunnel diodes, which in turn include highly doped thin (10–20 nm) layers. The growth temperature of 650 °C was applied to the layers consisting of the Ga_{0.99}In_{0.01}As buffer, middle cell layers, top cell layers and GaAs cap. AlGaAs was used as to the middle and top cell BSF, and AlInP as the window layer of InGaAs middle cell and GaInP top cell.

The Ge sub-cell is an important part of the structure of this cell, contributing 10% or more of the total cell efficiency [13]. The Ge junction is formed during III - V /Ge interface epitaxy. Group V elements such as P and As are n-type dopants in Ge, so the emitter of Ge junction was formed by diffusion of V elements during the deposition of III - V epilayers. In addition, the structure of Ge is different from the III - V materials such as GaAs and GaInP, the connection between Ge substrate and buffer layer or initial layer is important to the growth quality on buffer layer and the performance of Ge sub-cell. In this chapter, based on plenty of experiments, GaInP is selected as a suitable buffer material to be grown between the substrate and the active region of the device. Several researches on III - V materials grown on p-doped Ge substrate have indicated that the bottom Ge cell efficiency decreases as the thickness of the emitter increases, mainly owing to the lowering of the short circuit current. For this reason, GaInP is an optimized option with smaller diffusion length than GaAs. In addition, GaInP is also an appropriate material for the window layer of Ge junction.

The electrochemical capacitance-voltage results of GaInP initial layer grown on Ge indicate that the diffusion length of P is about 200 nm, when a thin Ge emitter for excellent performance of Ge sub-cell is fabricated. In the past, GaAs was employed as the middle cell material, and the 0.08% lattice-mismatch between GaAs and Ge was thought to be negligibly. To obtain enough current matched to the top cell, the middle cell was often designed to be 3~4 micrometers thick, but misfit-dislocations were generated in thick GaAs layers and deteriorated cell performance [5]. By adding about 1% indium into the GaAs cell layers, all cell layers are lattice-matched precisely to the Ge substrate. Application of InGaAs middle cell to lattice-match Ge substrates has demonstrated to be able to increase open-circuit voltage (Voc) due to lattice-matching and short-circuit current density (Jsc) due to the decrease of the energy gap in the middle cell.

The $\text{Ga}_{0.49}\text{In}_{0.51}\text{P}/\text{Ga}_{0.99}\text{In}_{0.01}\text{As}/\text{Ge}$ multi-junction solar cells for terrestrial concentrator application operate at high current densities higher than $10\text{A}/\text{cm}^2$. This brings specific challenges to the tunnel diode structures that are used for the series connection of the sub-cells. So the tunnel junction (TJ) growth is one of the most important issues affecting multi-junction solar cell performance. The problems of TJ growth are related to obtaining transparent and uniformly highly doped layer without any degradation of surface morphology [14]. The thickness of each side of the TJ junction has to be in the order of tens of nanometres, while the required doping has to be around $10^{19}\sim 10^{20}\text{ cm}^{-3}$. The reaching of the high doping level requires very different growth temperatures, in order to obtain an abrupt doping profile. In this experiment, the growth of tunnel junction was carried out at temperature of $600\text{ }^\circ\text{C}$ which is about $50\text{ }^\circ\text{C}$ lower than the growth temperature of other layers. DETe and CCl_4 were used as N-type dopant and P-type dopant respectively to fabricate small thickness, high doping AlGaAs/GaAs tunnel junctions.

GaInP lattice-matched to GaAs exhibits anomalous changes in the energy gap, depending on the growth conditions and the substrate misorientation [15]. These changes are the results of the spontaneous ordering during the growth of the cation-site elements (Ga and In) in planes parallel to the (111). One of changes is a lowering of the energy gap of the material, whose exact value depends on the degree of ordering. It appears to be the 100 meV reductions. The

$\text{Ga}_{0.49}\text{In}_{0.51}\text{P}/\text{Ga}_{0.99}\text{In}_{0.01}\text{As}/\text{Ge}$ multi-junction solar cells' performance depends on the energy gap of the GaInP top cell. The theoretical calculations for this combination of materials indicate that, to achieve maximum efficiencies, the energy gap of the GaInP top cell should be about 1.89 eV. The GaInP should be completely disordered. However, the MOCVD growth conditions that produce such a material have deleterious effects on the growth quality of GaInP, which determines the performance of the solar cell. To sum up, the growth of high quality GaInP with a maximizing degree of disorder is important for super high efficiency multi-junction solar cells. To fulfil this purpose, precise controls of the growth conditions including the growth temperature, growth rate and V/III ratio were carried out in our experiments. Based on the experimental results and theoretical calculations, the growth of GaInP was carried out at 640 °C, V/III ratio about 40, and growth rates of 0.6 nm/s.

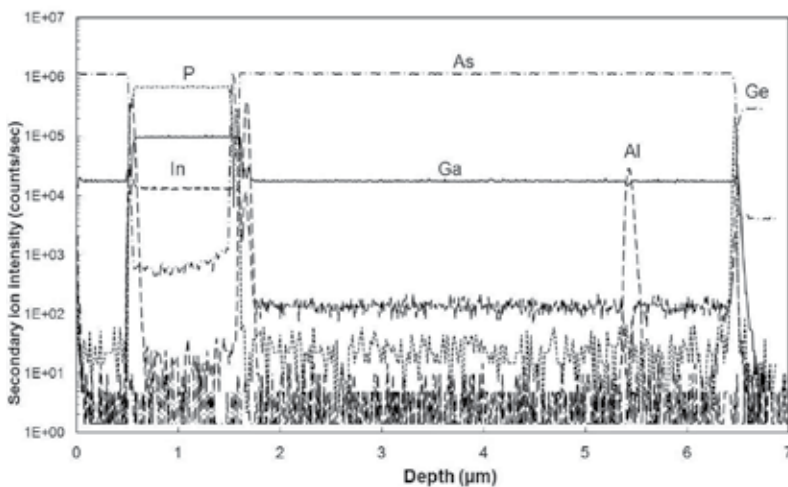


Figure 8. The SIMS spectrum of the $\text{Ga}_{0.49}\text{In}_{0.51}\text{P}/\text{Ga}_{0.99}\text{In}_{0.01}\text{As}/\text{Ge}$ multi-junction solar cells.

The SIMS spectrum of the $\text{Ga}_{0.49}\text{In}_{0.51}\text{P}/\text{Ga}_{0.99}\text{In}_{0.01}\text{As}/\text{Ge}$ multi-junction solar cells is calibrated and shown in Figure 8. With the elemental depth profile, we can clearly identify the cell structure and the doping level and the thickness of different functional layers.

3.2. The chip processing procedure and optimization

3.2.1. The process procedure of the multi-junction solar cell

The process designed for the concentrator multi-junction solar cells is as follows: the different electrode patterns on the front and back surfaces of the GaInP/ GaInAs/Ge epitaxial wafer are formed first, and then the wafer will be separated into independent cell chips by the methods of chemical etch and/or physical wheel-cutting. Figure 9 shows photos of the GaInP/ GaInAs/Ge epitaxial wafers and chips on wafer process stage. Figure 10 shows the principal process flow. The monolithic device structures of three sub-cells are grown on the

Ge substrate. The graphical front electrode (negative electrode) and the non-graphical back electrode (positive electrode) will then be deposited on the both surfaces of the epitaxial wafers with a series steps of lithography, electrode deposition, metal alloy, cap layer etching, AR coating and so on.

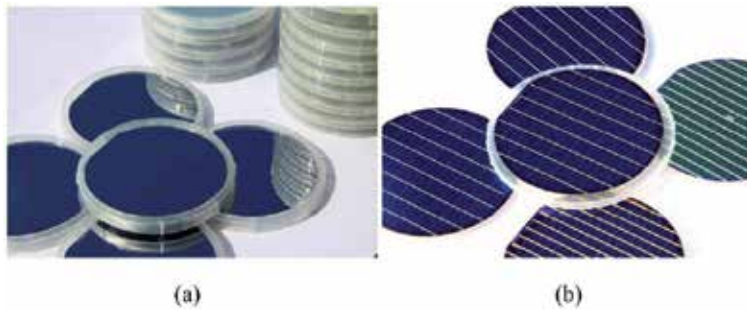


Figure 9. GaInP/ GaInAs/Ge epitaxial wafers (a), chips on wafers (b).

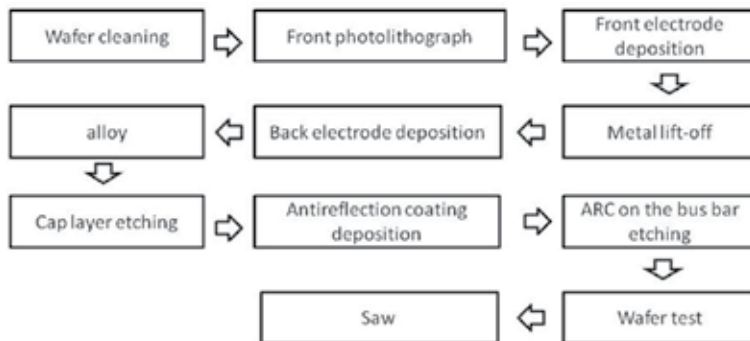


Figure 10. The principal chip process flow.

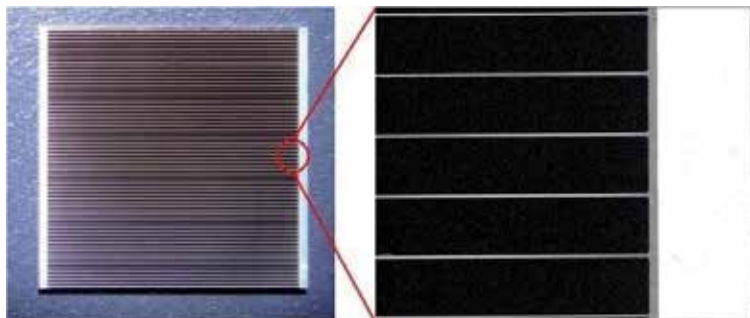


Figure 11. The detail of the graphical front electrode.

Figure 11 shows the isolated solar cell and details of the front electrode. Two busbars locate at the edge of the solar cell chip with some parallel gridlines between them. The multi-layer metal structure mainly includes ohmic contact layer, adhesion or barrier layer, conductive layer, and protective layer. The ohmic contact layer will faintly diffuse to the cap layer of the epitaxial wafer after an anneal process, which can decrease the contact resistance between the electrodes and the cap layer. When the photocurrents are generated in the cells, the gridlines will collect and then transfer the currents to the busbars. Finally the golden wires bonded on the busbars will export the currents to the external circuitry.

3.2.2. Research on the process technology optimization

3.2.2.1. Grid line design

Series resistance (r_s) is the main limiting factor to achieve a high performance for a multi-junction solar cell working under hundreds of suns concentration. Due to the complex constituent elements of series resistance, several aspects of the design and manufacture of the solar cells must be considered carefully. The gridline geometries and the metal structure of the triple junction solar cell are the most important factors to reduce the r_s . The main concerns are as follows: What is the best r_s value? Which steps during the whole manufacture process will affect the r_s value mostly?

It is known that there are many constituent elements contributed to the series resistance,

$$r_s = r_L + r_V + r_G + r_{FC} + r_{BC} \quad (22)$$

$$\frac{1}{r_L} = \frac{1}{r_E} + \frac{1}{r_W} \quad (23)$$

$$r_V = r_B + r_{Su} \quad (24)$$

where r_L is the resistance of the lateral current in the semiconductor structure, r_V is the resistance of the vertical current, r_G is the contribution of gridline, r_{BC} is the resistance of other symbols, and r_{FC} is resistance of the front contact. r_E and r_W are the contribution of emitter layer and window layer to the r_{El} respectively. r_B and r_{Su} are the contribution of base layer and substrate to the r_V respectively.

Traditionally the front metal grid of concentrator solar cells has been thickened up to 5~7 micrometers by electroplating. The higher ratio of the thickness to the width of the grid lines results in larger profile area. On the other hand, the resistance of the gridline metal (r_G) affects the series resistance of the solar cells greatly.

Due to the low thickness (100~150 nm) of the contact semiconductor layer, the lateral resistance in the semiconductor (r_L) also plays an important role in the constituent elements of series resistance. An effective method to reduce the r_L , is to decrease the space between the

neighbour gridlines, which can be described as the shadowing factor, F_s : a ratio of Area covered by metal to total area. As the shadowing factor increases, the area of the front contact will increase and the series resistance components related to the front contact, r_{FC} , decreases. The lateral current can be easier to collect through a shorter distance. Unfortunately, the shadow of the front grid line increases as the shadowing factor increasing, resulting in a reduction of the I_{sc} of the solar cell. Therefore, the balance between the lower lateral resistance and higher I_{sc} related to the shadowing factor should be considered carefully.

Experimental verification is carried out to obtain the optimum front grid design for 1000 suns concentration GaInP/GaInAs/Ge multi-junction solar cells. Typical values of the front contact resistance (r_{FC}) and the thickness of the grid line metal are $5 \times 10^{-5} \Omega \cdot \text{cm}^2$ and 7 micrometers, respectively. The front contact metal sheet resistance, r_{Msheet} , ranges from 3 to $5 \times 10^{-6} \Omega \cdot \text{cm}^2$. The space between the neighbour gridlines are in the range of 45 ~167 micrometers, respectively. All the F_s and WL values are referred to fingers of 7 micrometers thick in a $10 \times 10 \text{ mm}^2$ sized solar cell. It must be pointed that there is no antireflection coating on the surface of all the solar cells discussed here.

Figure 12 (a) shows the short-circuit current (I_{sc}), fill factor (FF) and efficiency (Eff) as a function of the shadowing factor. It is evident that with the wider space, the higher I_{sc} can be obtained, because more light can be absorbed by the solar cell. The FF increases obviously as the space increases. Therefore, we can draw a conclusion that the optimal front gridline design should result in higher I_{sc} and FF. As shown in Figure 12 (b), the highest $I_{sc} \times \text{FF}$ is found with an F_s of 5%, and the corresponding efficiency of 29.8% is also the highest one.

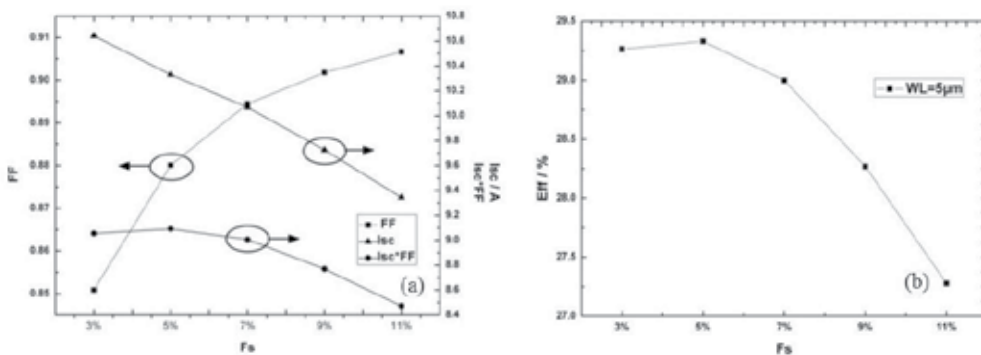


Figure 12. The short-circuit current (I_{sc}), fill factor (FF) and efficiency (Eff) as a function of the shadowing factor.

3.2.2.2. Antireflection Coating

Due to the high refractive indices of semiconductors, high reflection losses must be minimized by antireflection coatings (ARC) for GaInP/GaInAs/Ge multi-junction solar cells. This presents several challenges for the ARC design. Firstly, the wide wavelength range of sunlight requires an optimization of extreme broadband design and limits the material choice to

those with little or no absorption over the required wavelength range. For high concentrator multi-junction solar cells, the direct terrestrial sunlight spectrum (AM1.5D), defined for a zenith angle of 48.2° representing the average conditions of the United States, is split between each sub-cell in this triple junction design as shown in Figure 13. The bandwidth of absorption and internal quantum efficiency extends in both the UV and IR directions, ranging from 300~1800 nm. Secondly, for the concentrator multi-junction solar cells, light is incident upon the cell over a wide angular range, introducing an additional dimension for optimization. Thirdly, solar cells are required to operate for 20~30 years. Materials must not be modified or damaged by long-term exposure to UV light or large periodic changes in temperature and humidity. Furthermore, variations in the temperature-dependence of the refractive index of each layer will lead to a temperature-dependent transmission spectrum which may affect the performance of multi-junction solar cells. Finally, these ARC layers should be deposited inexpensively over large areas, together in a single coating chamber, and at low temperatures to minimize impact on the solar cell performance.

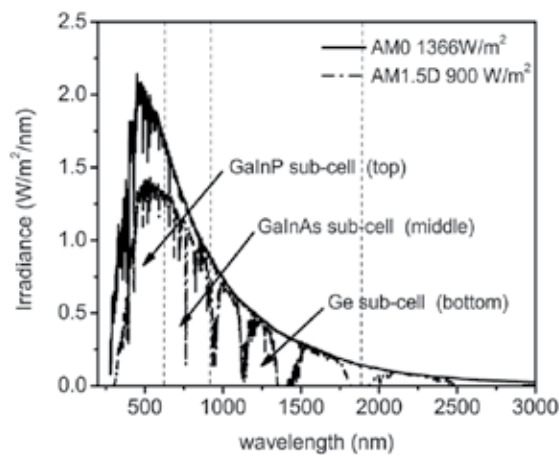


Figure 13. The wavelength versus irradiance spectrum.

In the triple junction solar cells, the window layer of the top cell, AlInP, was considered for the ARC designs, using a structure (air, ARC layer(s), AlInP) with direct normal incidence AM1.5D sunlight. Figure 14 shows the reflection spectra for two-layer material combinations commonly used for antireflection coatings. Both $\text{Al}_2\text{O}_3/\text{TiO}_2$ and $\text{SiO}_2/\text{TiO}_2$ offer coating solutions using practical deposition equipment. Commercially deposited $\text{Al}_2\text{O}_3/\text{TiO}_2$ coatings have shown a 30-35% improvement in the I_{sc} and a corresponding smaller increase to V_{oc} when compared with uncoated devices.

Figs. 15 shows the improvement in the external quantum efficiency (EQE) of the cells with $\text{Al}_2\text{O}_3/\text{TiO}_2$ coatings. It can be seen that an improvement in the EQE (AM1.5D) of the top and middle cells is from 65% to 88%. Figure 16 shows the improvement in the optical and electric-

cal properties of the samples above. It can be seen that the I_{sc} under 1000 suns is improved from 10.27 to 13.79 A, and the improvement in the I_{sc} is 34.3%; the V_{oc} also has a small increase of 0.03V. The FF shows an obvious decrease of 1.9% because of more ohmic loss with higher I_{sc} . The efficiency of the samples with Al_2O_3/TiO_2 coatings combination increases from 29.33% to 39.30%, a 34.0% improvement.

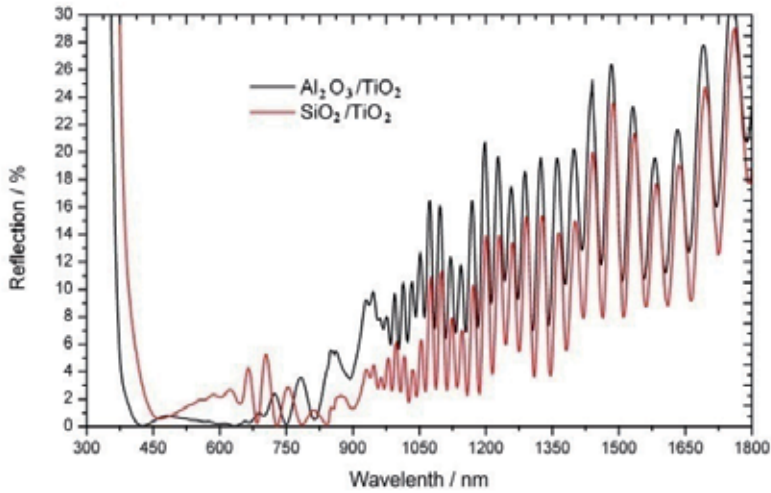


Figure 14. The reflection spectra of the solar cells with ARC.

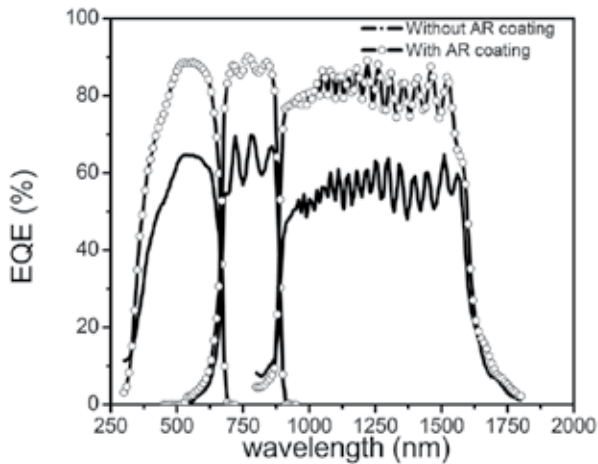


Figure 15. The EQE of the cells with and without ARC.

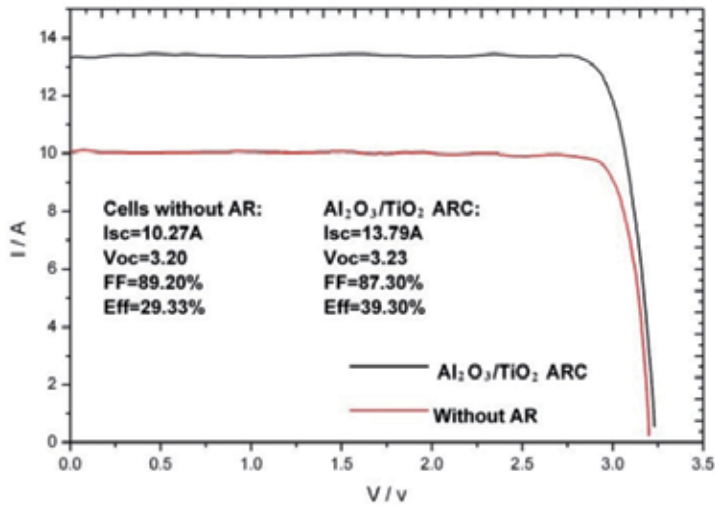


Figure 16. The optical and electrical properties of the cells with and without ARC.

4. The reliability of the multi-junction solar cell

4.1. Accelerated aging tests

Under high concentration of several hundreds or even thousands suns, multi-junction solar cells will suffer high temperature and high current density, which are challenging the reliability of these devices [16]. To obtain the approval from CPV customers, it is necessary to demonstrate the reliability of multi-junction solar cells operating under high concentration.

A new certification standard, namely the IEC62108, has been developed in which the procedure for qualifying CPV systems and assemblies is described. The IEC62108 is currently the only international standard on assessment of high concentration solar receivers and modules, which specifies the minimum requirements for the design qualification and the type approval of concentrator solar cells, and which gives the corresponding test procedures for each test sample, such as outdoor exposure test, electrical performance measurement, electrical test, irradiation test, and mechanical load test. After passing the IEC62108 certification, both the modules and assemblies can be suitable for long-term (25 years) operation in general open-air climates.

The purpose of the thermal cycling test is to determine the ability of the receivers to withstand thermal mismatch, fatigue, and other stresses caused by rapid, non-uniform or repeated changes of temperature. This test is vital to the reliability of concentrator solar cells, since generally these devices have to operate at high concentration of more than 1000 suns, high operation current density of more than 10A/cm², high operation temperature of more than 60 °C and large temperature difference between day and night.

In order to simulate the real operating conditions, IEC 62108 requires that during the process of thermal cycling test for concentrator solar cells carried out in the oven, a current should be flowing through the chips. Table 6 shows the three optional conditions. In principle, the temperature and the current injection time of cells are required to be accurately monitored during thermal cycling test. However, it is very difficult to monitor the real temperature of cells in real operating conditions, because a high electric current passing through the cells can lead to differences in temperature among the cells, the heat sink and the oven.

| Option | Maximum cell temperature | Total cycles | Applied current |
|--------|--------------------------|--------------|--|
| TCA-1 | 85 °C | 1000 | Apply 1.25×Isc when T > 25°C, cycle speed is 10 electrical/thermal |
| TCA-2 | 110 °C | 500 | Apply 1.25×Isc when T > 25°C, cycle speed is 10 electrical/thermal |
| TCA-3 | 65 °C | 2000 | Apply 1.25×Isc when T > 25°C, cycle speed is 10 electrical/thermal |

Table 6. The options of thermal cycling test from IEC 62108.

Using the thermal cycling test condition of TCA-1 from table 6, the cell temperature is controlled between -40 °C and 85 °C. A dwell time of 10 min of the high and low temperatures is required. The cycling period and frequency are 120 minutes and 12 cycles per day, respectively. In one thermal cycle, a specific current level of 7A is periodically on and off for 10 cycles, when the cell temperature is above 25 °C. In order to illustrate the changes of electrical performance of test samples, control samples are chosen and measured under the similar test condition. By this method, test condition variables are self-corrected, and the complex translation procedures are eliminated. Finally, the relative power P_r and relative power degradation P_{rd} are defined as follows:

$$P_r = \frac{P_m}{P_{mc}} \times 100\% \tag{25}$$

$$P_{rd} = \frac{P_{ri} - P_{rf}}{P_{ri}} \times 100\% \tag{26}$$

where P_m is the test sample's maximum power, P_{mc} is the control sample's maximum power measured at the similar condition as P_m , and P_{rf} and P_{ri} are the relative powers measured after and before the given test, respectively.

For comparison, eight San'an company's cells and eight B-company's cells were tested together. Tables 7 and 8 show the relative power degradation of San'an Company's and B-company's receiver samples after different numbers of thermal cycles, respectively. The

output powers gradually decrease with the increasing thermal cycles due to the samples' degradation. It is found that the relative power degradations of tested samples are within 10%. The degradation is believed to be responsible for the perimeter degradation [16, 17]. According to González et al., the arbitrary definition of device failure is a 10% of power loss, so the majority of test samples do not have failure, except the c B-company's receiver #56, the relative power degradation of which is from 12.85% after 560 thermal cycles to 14.89% after 1000 thermal cycles. Besides, from visual inspection on these samples, the DBCs soldered on alumina substrates are not peeled off after the 1000 thermal cycles, which indicates that it is suitable for long-term (~25 years) operation in general open-air climates.

| Serial sample | 0 cycle | 360 cycles | 560 cycles | 760 cycles | 1000 cycles |
|---------------|---------|------------|------------|------------|-------------|
| #182B5 | 0.00% | -2.47% | -4.00% | -5.56% | -8.02% |
| #183D1 | 0.00% | -0.14% | -3.19% | -3.88% | -5.44% |
| #182D5 | 0.00% | -3.66% | -4.78% | -5.82% | -8.21% |
| #183B1 | 0.00% | -2.48% | -4.83% | -6.33% | -8.25% |
| #182D1 | 0.00% | -4.62% | -5.38% | -6.21% | -7.95% |
| #183B6 | 0.00% | -5.85% | -6.08% | -5.84% | -7.09% |
| #183A4 | 0.00% | -5.02% | -5.70% | -6.97% | -7.96% |
| #183D5 | 0.00% | -5.47% | -5.83% | -6.06% | -7.37% |

Table 7. Relative power degradation of San'an Company's receiver samples after different numbers of thermal cycles.

| Serial sample | 0cycle | 360cycles | 560 cycles | 760 cycles | 1000 cycles |
|---------------|--------|-----------|------------|------------|-------------|
| #112 | 0.00% | -5.93% | -6.83% | -6.84% | -7.72% |
| #44 | 0.00% | -4.10% | -5.60% | -6.12% | -8.11% |
| #56 | 0.00% | -8.02% | -12.85% | -13.05% | -14.89% |
| #94 | 0.00% | -2.76% | -4.94% | -5.19% | -6.78% |
| #78 | 0.00% | -5.17% | -6.39% | -6.76% | -7.36% |
| #90 | 0.00% | -7.14% | -7.75% | -8.17% | -8.32% |
| #97 | 0.00% | -3.19% | -3.38% | -4.38% | -7.42% |
| #136 | 0.00% | -6.30% | -6.69% | -7.05% | -9.34% |

Table 8. Relative power degradation of B-company's receiver samples with different numbers of thermal cycles.

In conclusion, high concentration multi-junction solar cells are still at an early stage of technological development, and thus it is necessary to demonstrate the reliability of these solar cells before their industrialization. Accelerated aging test is a necessary tool to demonstrate the reliability of concentration photovoltaic solar cells, which is expected to be working for

no less than 25 years. According to the requirements from IEC 62108, this paper presents the reliability results from thermal cycling tests performed on San'an company's high concentration solar cells. We find that the light emitting intensity and the relative power degradation of San'an company's receivers are similar to that of B-company's receivers.

4.2. Discussion on outdoor power plant performance

Concentrated photovoltaic (CPV) system is usually located in sunny places for large-scale photovoltaic (PV) power station with installation capacity of 1-1000 megawatt (MW). It is composed of Fresnel lenses to concentrate, III-V multi-junction solar cells, polar axis type or pedestal type tracking system and integrated control method. By focusing sunlight onto high-efficiency solar cells, CPV is able to use fewer solar cells than traditional photovoltaic power. Since CPV has a high power-generating capacity with movable parts, easy to manufacture and to maintain, it is very suitable for a large scale PV power station.

According to the CPV Consortium, "CPV, with its higher efficiency delivers higher energy production per megawatt installed, provides the lowest cost of solar energy in high solar regions of the world. The technology is in its early stage with significant headroom for future innovation, and it has the ability to ramp to gigawatts of production very rapidly. Many of the limitations for PV in the past are overcome by advances in CPV technology." As of 2011, the global bases of installed CPV produced totally just 60 megawatts, according to the CPV Consortium. The organization predicts that capacity will rise to 275 megawatts by the end of 2012, 650 megawatts by the end of 2013, 1,100 megawatts by end of 2014 and 1,500 megawatts by the end of 2015.

World-widely, 40 MW Amonix power plants will be installed from 2012 on, at the same time 32.7 MW power plant located at Alamosa Colorado was measured during the week of March 2012. ISFOC (Institute of Concentration Photovoltaic Systems) main goal is to promote the CPV industrialization. For this purpose, ISFOC has made the installation of CPV Plants, up to 2.7 MW, all over the region of Castilla la Mancha. A lot of CPV power plants will be installed in near future without being introduced more. However, focusing on China, the relative long history of advanced CPV technology development, the years' experience of power plant operation, mature systems with high performance and reliability, the leading position of the western participants will set up a benchmark in the field and gain more attention and more shares from Chinese CPV market. For a few domestic CPV companies with installation records, further efforts are required to improve the performance and reliability of CPV products, to lower the cost by setting up complete supply chains in CPV industry, to facilitate the utilization of abundant solar resources from the north and west to the south and east via setting up transmission networks, so that a Chinese CPV market can be actually initiated, developed and matured.

The largest CPV power plant project in China was assembled at Golmud, Qinghai province by Suncore Photovoltaic Technology Co., Ltd, with the capacity of more than 50 MW. Suncore is a Sino-US joint venture established by San'an and Emcore. 1 MW of the project using 500 suns terrestrial system and 2MW using 1000 suns terrestrial system has been finished, as

shown in Figure 17. Conversion efficiency of 500 suns and 1000 suns terrestrial system can reach as high as 25% and 28.5%, respectively.



Figure 17. power plant installed at Golmud Qinghai province China.

The direct normal insolation (DNI) distribution of the local environment and the mapping of China were displayed Figure 18 (a) and (b). The I-V curves of 227 receivers using 500 suns terrestrial system module tested outdoor was shown in Figure 19. One can see that the efficiency could reach as high as 24.03% at the condition of much dust on the surface of the Fresnel lens, which affecting the light transmittance. Therefore, the actual efficiency should be high than this nominal value.

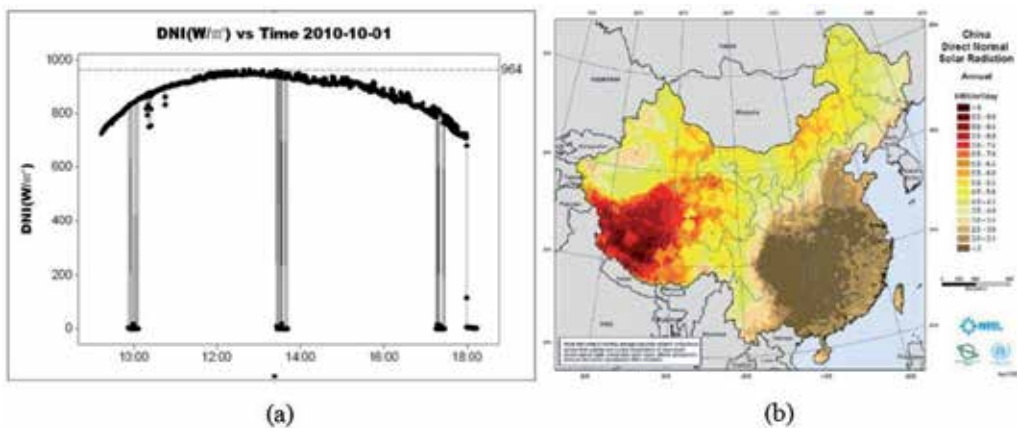


Figure 18. The DNI distribution of the whole day in Golmud (a), and the annual average direct normal insolation (DNI) GIS data at 40km resolution for China (b) from NREL.

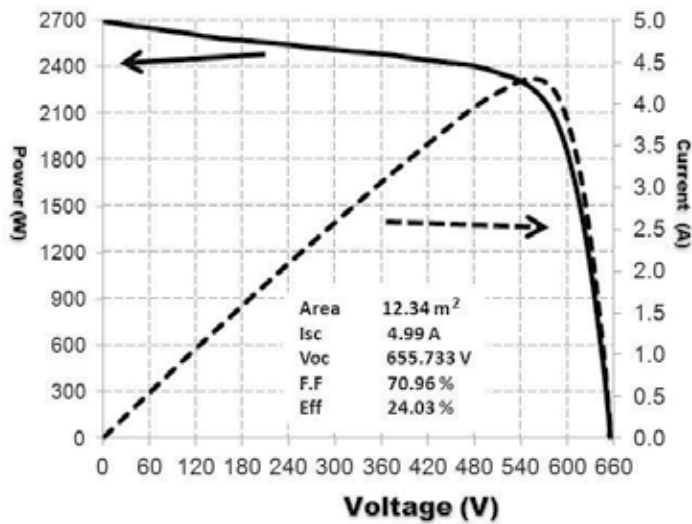


Figure 19. I-V curves of the 227 Receivers module tested outdoor.

Acknowledgements

This work was supported by a foundation from the National High Technology Research and Development Program (863 program) of China. (No. 2012AA051402).

Author details

Gui jiang Lin¹, Jingfeng Bi¹, Minghui Song¹, Jianqing Liu¹, Weiping Xiong¹ and Meichun Huang^{2*}

*Address all correspondence to: mchuang@xmu.edu.cn

1 Xiamen San'an Optoelectronics Co., Ltd., China

2 Department of Physics, Xiamen University, China

References

- [1] Green, M. A. (2005). *Third generation photovoltaics*, Berlin, Springer.

- [2] Luque, A., Martí, A., Stanley, C., Lo'pez, N., Cuadra, L., Zhou, D., & Mc Kee, A. (2004). General equivalent circuit for intermediate band devices: Potentials, currents and electroluminescence. *J. Appl. Phys.*, 96(03), 903-909.
- [3] King, R. R. (2008). Multi-junction solar cells: Record breakers. *Nature Photonics*, 2, 284-286.
- [4] King, R. R., Law, D. C., Edmondson, K. M., Fetzer, C. M., Kinsey, G. S., Yoon, H., Sherif, R. A., & Karam, N. H. (2007). 40% efficient metamorphic GaInP/GaInAs/Ge multi-junction solar cells. *Appl. Phys. Lett.*, 90(18), 3516-3518.
- [5] Yamaguchi, M., Takamoto, T., & Araki, K. (2006). Super high-efficiency multi-junction and concentrator solar cells. *Sol. Energy Mater. Sol. Cells*, 90-3068.
- [6] Daniel, C. L., King, R. R., Yoon, H. M., Archer, J., Boca, A., Fetzer, C. M., Mesropian, S., Isshiki, T., Haddad, M., Edmondson, K. M., Bhusari, D., Yen, J., Sherif, R. A., Atwater, H. A., & Karam, N. H. (2010). Future technology pathways of terrestrial III-V multi-junction solar cells for concentrator photovoltaic systems. *Solar Energy Materials & Solar Cells*, 94, 1314-1318.
- [7] Geisz, J. F., Kurtz, S., Wanlass, M. W., Ward, J. S., Duda, A., Friedman, D. J., Olson, J. M., Mc Mahon, W. E., Moriarty, T. E., & Kiehl, J. T. (2007). High-efficiency GaInP/GaAs/InGaAs triple-junction solar cells grown inverted with a metamorphic bottom junction. *Appl. Phys. Lett.*, 91(02), 3502-3504.
- [8] Guter, W., Schöne, J., Philipps, S. P., Steiner, M., Siefer, G., Wekkeli, A., Welser, E., Oliva, E., Bett, A. W., & Dimroth, F. (2009). Current-matched triple-junction solar cell reaching 41.1% conversion efficiency under concentrated sunlight. *Appl. Phys. Lett.*, 94(22), 3504-3506.
- [9] Fahrenbruch, A. L., & Bube, R. H. (1983). *Fundamentals of Solar Cells Photovoltaic Solar Energy Conversion*, New York, Academic Press.
- [10] Würfel, P. (2005). *Physics of solar cells: From principles to new concepts*. Verlag GmbH & Co KGaA, Weinheim, Wiley-VCH.
- [11] Olson, J. M., Ahrenkiel, R. K., Dunlavy, D. J., Keyes, B., & Kibbler, A. E. (1989). Ultra-low recombination velocity at Ga_{0.5}In_{0.5}P/GaAs heterointerfaces. *Appl. Phys. Lett.*, 55, 1208-1210.
- [12] Palik, E. D. (1991). *Handbook of Optical Constants of Solids II*, San Diego, USA, Academic Press.
- [13] Kalyuzhnyy, N. A., Gudovskikh, A. S., Evstropov, V. V., Lantratov, V. M., Mintairov, S. A., Timoshina, K. H., Shvarts, M. Z., & Andreev, V. M. (2010). Germanium Sub-cells for Multi-junction GaInP/GaInAs/Ge Solar Cells. *Semiconductors*, 44(11), 1520-1528.

- [14] Ebert, C., Pulwin, Z., Byrnes, D., Paranjpe, A., & Zhang, W. (2010). Tellurium doping of InGaP for tunnel junction applications in triple junction solar cells. *Journal of Crystal Growth*, 315, 61-63.
- [15] Garcia, I., Rey-Stolle, I., Algora, C., Stolz, W., & Volz, K. (2008). Influence of GaInP ordering on the electronic quality of concentrator solar cells. *Journal of Crystal Growth*, 310, 5209-5213.
- [16] González, J. R., Vázquez, M., Núñez, N., Algora, C., Rey-Stolle, I., & Galiana, B. (2009). Reliability analysis of temperature step-stress tests on III-V high concentration solar cells. *MICROELECTRONICS RELIABILITY*, 49, 673-680.
- [17] Algora, C. (2010). Reliability of III-V concentrator solar cells. *MICROELECTRONICS RELIABILITY*, 50, 1193-1198.

Use of Optoelectronic Plethysmography in Pulmonary Rehabilitation and Thoracic Surgery

Giulia Innocenti Bruni, Francesco Gigliotti and
Giorgio Scano

Additional information is available at the end of the chapter

<http://dx.doi.org/10.5772/53039>

1. Introduction

1.1. Methods

OEP system is an optoelectronic device able to track the three-dimensional co-ordinates of a number of reflecting markers placed non-invasively on the skin of the subject [1-4]. A variable number of markers (89 in the model used for respiratory acquisition in seated position) is placed on the thoraco-abdominal surface; each marker is a half plastic sphere coated with a reflective paper. Two TV Sensors 2008, cameras are needed to reconstruct the X-Y-Z co-ordinates of each marker, so for the seated position six cameras are required. Each camera is equipped with an infra-red ring flash. This source of illumination, which is not visible, is not disturbing and lets the system also operate in the dark. The infra-red beam, emitted by the flashes, is reflected by each marker and acquired by the cameras with a maximal sampling rate of 100 Hz. The signal is then processed by a PC board able to combine the signal coming from the cameras and to return, frame by frame, the three-dimensional co-ordinates of each marker. The process is simultaneously carried out for the six TV cameras needed for the seated respiratory model. Acquired data need a further operation called 'tracking' that is necessary to exclude possible phantom reflections and/or to reconstruct possible lost markers (this could happens sometimes during very fast manoeuvres such exercise); at this time the obtained files contain the X-Y-Z co-ordinates of each marker during the recorded manoeuvre, then data are stored on the PC hard disk. The spatial accuracy for each marker's position is about 0.2 mm [1]. Volumes for each compartment is calculated by constructing a triangulation over the surface obtained volume from the X-Y-Z co-ordinates of the markers and then using Gauss's theorem to convert the volume integral to an integral over this sur-

face [2]. The number and the position of used markers depends on the thoraco-abdominal model chosen. As proposed by Ward & Macklem [5] we use a three compartment chest wall model: the upper rib cage, lower rib cage and abdomen. Due to the fact that the upper portion of the rib cage is exposed to pleural pressure whereas the lower portion is affected by abdominal pressure, a model able to dynamically return changes in volume of each compartment and, as a sum, of the entire chest wall has been developed [2]. The number of used markers is 89, 42 placed on the front and 47 on the back of the subject.

To measure the volume of chest wall compartments from surface markers we define: 1) the boundaries of the upper rib cage as extending from the clavicles to a line extending transversely around the thorax at the level of the xiphoid process (corresponding to the top of the area of the apposition of the diaphragm to the rib cage at end expiratory lung volume in sitting posture, confirmed by percussion); 2) the boundaries of lower rib cage as extending from this line to the costal margin anteriorly down from the xiphosternum, and to the level of the lowest point of the lower costal margin posteriorly; and 3) the boundaries of abdomen as extending caudally from the lower rib cage to the level of the anterior superior iliac crest. The markers are placed circumferentially in seven horizontal rows between the clavicles and the anterior superior iliac spine. Along the horizontal rows the markers are arranged anteriorly and posteriorly in five vertical rows, and there is an additional bilateral row in the mid-axillary line. The anatomical landmarks for the horizontal rows are: 1) the clavicular line; 2) the manubrio-sternal joint; 3) the nipples (~ 5 ribs); 4) the xiphoid process; 5) the lower costal margin (10th rib in the midaxillary line); 6) umbilicus; 7) anterior superior iliac spine. The landmarks for the vertical rows are: 1) the midlines; 2) both anterior and posterior axillary lines; 3) the midpoint of the interval between the midline and the anterior axillary line, and the midpoint of the interval between the midline and the posterior axillary line; 4) the mid-axillary lines. An extra marker is added bilaterally at the midpoint between the xiphoid and the most lateral portion of the 10th rib to provide better detail of the costal margin; two markers are added in the region overlying the lung-apposed rib cage and in the corresponding posterior position. This marker configuration has previously been validated in normal subjects, along with a sensitivity analysis which assesses accuracy in estimating change in lung volume as a function of marker number and position [2]. When compared with the gold standard (water sealed spirometer) the accuracy in the volume change measurements of the 89 markers model is very high, showing volume differences smaller than 5% [2].

2. Exercise limitation and breathlessness in patients with Chronic Obstructive Pulmonary Disease (COPD)

Dynamic hyperinflation (DH) is supposed to be the most important factor limiting exercise and contributing to dyspnea by restrictive constraints to volume expansion in patients with COPD [6]. Indirect evidence of the importance of DH has been provided by studies that have demonstrated that pharmacological treatment [7,8], and lung volume reduction sur-

gery [9] explain in part the improvement in exercise performance and dyspnea by reducing DH in these patients. It has recently been found, however, that different patterns of chest wall kinematics may or may not be associated with different exercise performance in COPD patients [10,11]. There is little data available indicating that these patients may dynamically hyperinflate or deflate chest wall compartments during cycling while breathing air [10,12] or with oxygen supplementation [11]. As yet the contribution of reducing lung volume to dyspnea relief remains uncertain [11,13-15] in exercising COPD patients. It also remains to be determined whether changes in operational chest wall volumes substantially affect the response to endurance exercise rehabilitation programs. It should be remembered that (i) an increase in end-expiratory-volume of the chest wall constrains the potential for the tidal volume to increase; thus exacerbating the sensation of dyspnea; (ii) on the other hand, shifting abdominal volumes towards a lower operational point might not be able to reduce restrictive constraints on volume displacement if the rib cage dynamically hyperinflates. Arguably, rib cage hyperinflation would result in a higher volumetric load to the intercostal inspiratory muscles [16] and a higher sensory perception of dyspnea [17]; (iii) the possibility that abdominal deflation contributes *per se* to dyspnea should not be disregarded [16]. Evidence has indeed been provided that a decrease in abdominal volume resulting from increased abdominal muscle activity as soon as exercise starts even at minimal work rate [4] may contribute *per se* to increasing the work of breathing [10] and breathlessness [16], to reducing venous return and cardiac output [18], and to decreasing exercise capacity [4] in patients with COPD.

Dyspneic patients with COPD who are markedly hyperinflated are considered especially likely to display abnormalities in rib cage motion such as a paradoxical (inward) inspiratory movement of their lower rib cage [19-22]. Studies in healthy humans have led to the hypothesis that the primary mechanism of abnormal chest wall motion in patients with COPD is probably an abnormal alteration of forces applied to chest wall compartments [3,23] and an increase in airway resistance [24]. Chihara *et al.* [23] have speculated that when rib cage distortion is present, greater degree of recruitment of inspiratory rib cage muscles and greater predisposition to dyspnea for a given load and strength do occur. On the other hand, the role of hyperinflation on abnormal chest movement is questionable in healthy subjects [24]. Accordingly, it has recently been shown that paradoxical movement of the lower rib cage cannot be fully explained by static lung hyperinflation [19] or dynamic rib cage hyperinflation [25] in patients with COPD. By contrast, Aliverti *et al.* [26] have shown that lower rib cage paradox results in an early onset of dynamic hyperinflation as a likely explanation for the increased exertional breathlessness in these patients. Nonetheless, the link between changes in operational lung volumes and exertional breathlessness has not been definitely established in normoxic COPD patients [13,14,27].

Now the questions arise: does exercise reconditioning reduce rib cage distortion, and, if any, does rib cage distortion contribute to restoring exercise capacity and to relieving breathlessness? Does exercise reconditioning relieve dyspnea regardless of whether compartmental chest wall volumes are shifted toward upper or lower operational points?

3. How Optoelectronic Plethysmography (OEP) can help answer the above questions

The use of Optoelectronic Plethysmography (OEP) has allowed us to understand some of the mechanisms underlying the efficacy of rehabilitative treatment in patients with COPD. Rehabilitation interventions such as oxygen supplementation reduce ventilation and the rate of dynamic hyperinflation, but whether and to what extent reduction in lung volume contributes to dyspnea relief remains uncertain in these patients [13,14,27]. Innocenti Bruni *et al.* [11] tried to (i) determine whether and how hyperoxia would affect exercise dyspnea, chest wall dynamic hyperinflation, and rib cage distortion in normoxic COPD patients, and (ii) investigate whether these phenomena are interrelated. It was speculated that they are not, based on the following observations: (i) significant dyspnea relief and improvement in exercise endurance can occur even in the absence of an effect on dynamic lung hyperinflation [27]; (ii) externally imposed expiratory flow limitation is associated with no rib cage distortion during strenuous incremental exercise, with indexes of hyperinflation not being correlated with dyspnea [16]; (iii) end-expiratory-chest wall-volume may either increase or decrease during exercise in patients with COPD, with those who hyperinflate being as breathless as those who do not [10]; (iv) a similar level of dyspnea is associated with different increases in chest wall dynamic hyperinflation at the limits of exercise tolerance [28]. The volume of chest wall (V_{cw}) and its compartments: the upper rib cage (V_{rcp}), lower rib cage (V_{rca}), and abdomen (V_{ab}) were evaluated by OEP in 16 patients breathing either room air or 50% supplemental O_2 at 75% of peak exercise in randomized order; rib cage distortion was assessed by measuring the phase angle shift between V_{rcp} and V_{rca} . Ten patients increased end-expiratory V_{cw} ($V_{cw,ee}$) on air. In 7 *hyperinflators* and 3 *non-hyperinflators* the lower rib cage paradoxed inward during inspiration with a phase angle of 63.4° (30.7) compared with a normal phase angle of 16.1° (2.3) recorded in patients without rib cage distortion. Dyspnea by a modified Borg scale from zero (no dyspnea), to ten (maximum dyspnea) averaged 8.2 and 9 at end-exercise on air in patients with and without rib cage distortion, respectively. At iso-time during exercise with oxygen, dyspnea relief was associated with a decrease in ventilation regardless of whether patients distorted the rib cage, dynamically hyperinflated or deflated the chest wall. (Fig 1).

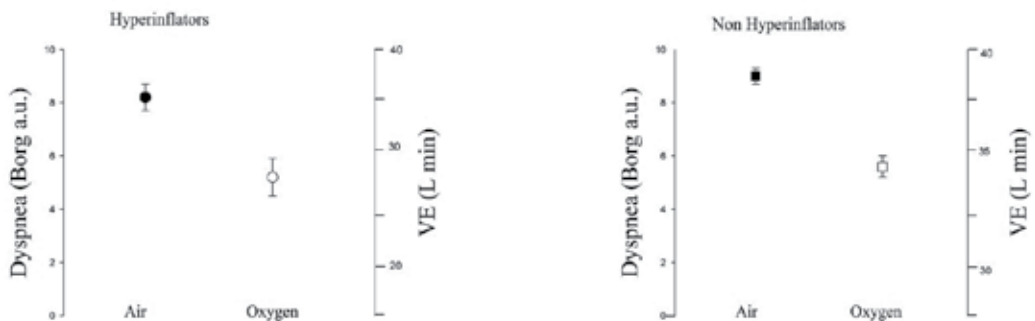


Figure 1. Oxygen supplementation decreases ventilation and dyspnea at isotime during constant load cycling exercise.

OEP allows us to demonstrate that dyspnea, chest wall dynamic hyperinflation, and rib cage distortion are not interrelated phenomena.

Georgiadou *et al.* [12] studied the effect of pulmonary rehabilitation on the regulation of total chest wall and compartmental volumes during exercise in patients with COPD. Twenty patients undertook high-intensity exercise 3 days week⁻¹ for 12 weeks. Before and after rehabilitation, the changes in chest wall (cw) volumes at the end of expiration (V_{cw,ee}) and inspiration (V_{cw,ei}) were computed by OEP during incremental exercise to the limit of tolerance (W_{peak}). Rehabilitation significantly improved W_{peak}. In the post-rehabilitation period and at identical work rates, significant reductions were observed in minute ventilation, breathing frequency and V_{cw,ee} and V_{cw,ei}. Inspiratory reserve volume was significantly increased. Volume reductions were attributed to significant changes in abdominal V_{cw,ee} and V_{cw,ei}. The improvement in W_{peak} was similar in patients who progressively hyperinflated during exercise and those who did not. The authors concluded that pulmonary rehabilitation lowers chest wall volumes during exercise by decreasing the abdominal volumes.

The study indicates that improvement in exercise capacity following rehabilitation is independent of the pattern of exercise-induced dynamic hyperinflation.

Preliminary laboratory data indicate that OEP substantially assists in clarifying the link between chest wall dynamic hyperinflation and breathlessness following pulmonary rehabilitation. The volume of the chest wall and its compartments were evaluated in 14 patients by OEP during constant load cycle exercise before and after pulmonary rehabilitation. Prior to rehabilitation exercise increased end-expiratory chest wall volumes in eight patients, but deflated the chest wall in six [11]. Rehabilitation increased exercise endurance. Relief in both dyspnea and leg effort at iso-time were associated with a decrease in ventilation regardless of whether patients hyperinflated or not. Also, the effect of pulmonary rehabilitation on rib cage distortion and dyspnea were independent of each other (Fig 2).

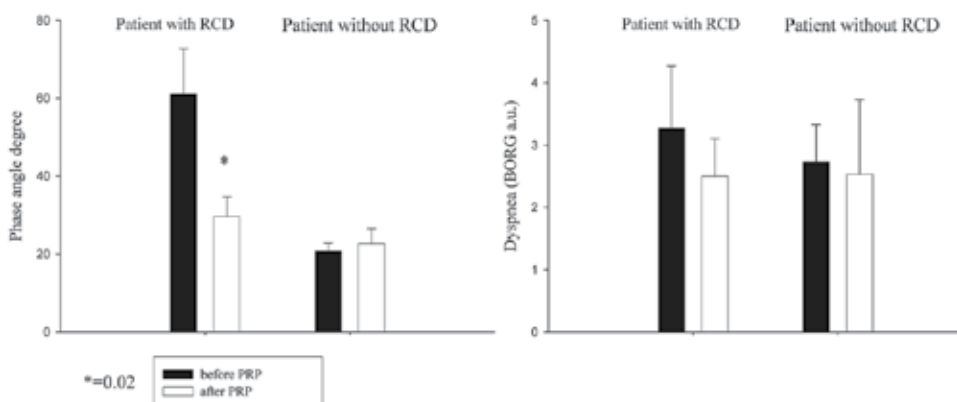


Figure 2. Effect of pulmonary rehabilitation (PRP) on phase angle and dyspnea in patients with and without ribcage distortion (RCD).

These data suggest that pulmonary rehabilitation reduces dyspnea regardless of rib cage distortion and dynamic chest wall hyperinflation.

Many COPD patients complain of severe dyspnea while performing simple daily-life activities using their arms. The increased demand during simple arm elevation may play a role in the development of dyspnea and in the limitation that is frequently reported by these patients when performing activities involving their arms [29,30]. Unsupported arm exercise training (UAET) is increasingly recognized as an important component of pulmonary rehabilitation in these patients [31]. Although some studies have demonstrated improvement in unsupported arm exercise after UAET [32-34], suggesting that the test can be sensitive to changes in arm exercise capacity, the impact of upper extremity training on arm exercise related-dyspnea and fatigue remains unclear [35-38] or undemonstrated [32,38-40]. Surprisingly, few studies [32,35,37-39] have investigated the effect of upper extremity training on ratings of perceived dyspnea by applying psychophysical methods, that is, the quantitative study of the relationship between stimuli and evoked conscious sensory responses. On this basis we have recently demonstrated that neither chest wall dynamic hyperinflation nor dyssynchronous breathing *per se* are the major contributors to dyspnea during unsupported arm exercise in COPD patients [25]. Using the same approach we have recently tried to document the impact of arm training on arm exercise-related perceptions. The finding that before rehabilitation patients stop arm exercise namely because of arm symptoms, makes a case for the excessive effort felt by subjects being elicited by arm/torso afferent information (from the muscles performing the excessive effort) conveyed to the motor-sensory cortex [25].

These findings may explain why even a very small decrease in ventilatory demand, reflective of a decrease in central motor output to ribcage/torso muscles, has a salutary effect on arm symptoms during arm training in patients with COPD [41].

OEP has also helped to clarify mechanisms by which some techniques of pulmonary rehabilitation such as breathing retraining, namely "pursed lip breathing" (PLB), act in reducing the sensation of dyspnea. Bianchi *et al.* [42] hypothesized that the effect of PLB on breathlessness relies on its deflationary effects on the chest wall. They found that patients exhibited a significant reduction in end-expiratory volume of the chest wall ($V_{cw,ee}$) and a significant increase in end-inspiratory volume of the chest wall in comparison with spontaneous breathing. In a stepwise multiple regression analysis, a decrease in end expiratory volume of the chest wall accounted for 27% of the variability in the Borg score.

These data indicate that by lengthening the expiratory time, PLB deflates the chest wall and reduces dyspnea.

In a further paper Bianchi *et al.* [43] identified the reasons why some patients benefit from PLB while others do not. The OEP analysis of chest wall kinematics shows why not all patients with COPD obtain symptom relief from PLB at rest. The most severely affected patients who deflate the chest wall during volitional PLB reported improvement in their sensation of breathlessness. This was not the case in the group who hyperinflated during PLB.

4. Comparing OEP with spirometric operational volumes

OEP may provide complementary information on operational volumes to that provided by spirometry. Vogiatzis *et al.* [28] found a good relationship between changes in inspiratory capacity (ΔIC_{pn}) and changes in end expiratory chest wall volume ($\Delta V_{cw,ee}$). By contrast we have not found any significant relationship between the two measurements (Fig 3).

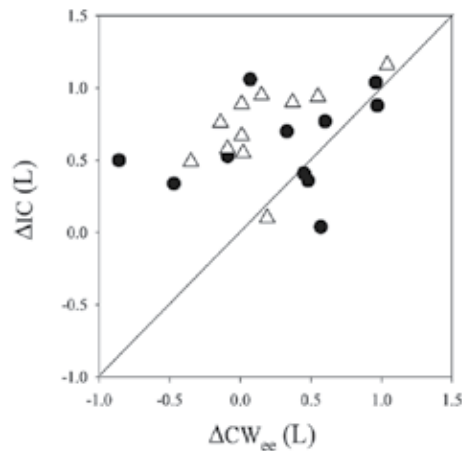


Figure 3. Plots of change in inspiratory capacity (IC) vs change in end-expiratory-chest-wall-volumes (CW_{ee}) from rest to end exercise, before (closed circles) and after (triangles) pulmonary rehabilitation. Continuous line is the identity line.

The decrease in IC_{pn} is much greater than the increase in $V_{cw,ee}$ in most patients. The reasons for this discrepancy are probably due to: i) error measurements with the pneumotachograph possibly linked to leakage and elevation of temperature in the system, and to spirometric drift resulting in spurious increments or decrements in volume measurements; ii) spirometry measures the volume of the gas entering or leaving the lungs at the mouth, while OEP measures the volume of the trunk which includes changes in gas volume, gas compression and blood volume shifts [16]. Arguably, activity of the abdominal muscles producing various amounts of gas compression and blood shifts might account for the prevalence of one method over the other. For instance, high gas compression and blood shift would result in a greater decrease in $V_{cw,ee}$ than an increase in the next IC_{pn} manoeuvre [44]. It has been postulated that OEP would not detect 89% of the reduction in inspiratory capacity measured with spirometry in some conditions [44].

5. OEP and reparative deformity of the rib cage

Pectus excavatum, the most common congenital chest wall deformity, is characterized by a depression of the anterior chest wall and sternum. Some patients will develop cardiopulmo-

nary symptoms for the first time as adolescents while others will experience a worsening of the symptoms they have endured for years. A minimally invasive technique for repair described by Nuss *et al.* [45,46] involves the placement of substernal concave bar(s) that will be rotated to elevate the sternum outward. The bar is left in place for 2-3 years while the anterior chest wall remodels. The chest wall is primarily involved when there are respiratory abnormalities, so the effect of repair should be assessed mainly by observing chest wall kinematics and possibly chest wall mechanics in pectus excavatum patients. A previous study carried out in adolescents with mild restrictive defect has shown that abnormalities in chest wall kinematics during maximal voluntary ventilation are not correlated with the computed tomography scan severity index, indicating the contribution of chest wall kinematics to clinical evaluation of pectus excavatum patients [47]. Should we wait 2-3 years before assessing repair effects (if any) on chest wall kinematics? Can the Nuss procedure influence timing, and kinematics of the chest wall and rib cage configuration in otherwise healthy subjects? Binazzi *et al.* [48] postulated that the repair effect based on increased chest wall end expiratory volume does not affect chest wall displacement and dynamic configuration of the rib cage. By using OEP they provided a quantitative description of chest wall kinematics before and 6 months after the Nuss procedure at rest and during maximal voluntary ventilation in 13 subjects with pectus excavatum. An average 11% increase in chest wall volume was accommodated within the upper rib cage and to a lesser extent within the abdomen and lower rib cage. Tidal volumes did not significantly change during the study period. The repair effect on chest wall kinematics did not correlate with the Haller index of deformity at baseline.

These data indicate that six months of the Nuss procedure do increase chest wall volume without affecting chest wall displacement and rib cage configuration.

6. Conclusion

In conclusion, we and others have shown that use of OEP can demonstrate the following: (i) dynamic hyperinflation of the chest wall may not necessarily be the principal reason for exercising limitation and breathlessness in COPD patients; (ii) pulmonary rehabilitation improves COPD patients' endurance and exercise-related perceptions regardless of changes in chest wall kinematics; (iii) in contrast with what is commonly believed, chest wall dynamic hyperinflation may have a salutary mechanical effect in patients with expiratory flow limitation and dynamic hyperinflation, who increase functional residual capacity because of achieving more tidal expiratory flow; (iv) OEP provides complementary information on operational volumes to that provided by spirometry.

Finally, there are very few reports on the use of OEP in pulmonary rehabilitation and thoracic surgery in patients with chronic respiratory disease other than COPD. We hope that the results presented here will stimulate new contributions on this topic.

Author details

Giulia Innocenti Bruni¹, Francesco Gigliotti¹ and Giorgio Scano^{1,2}

1 Section of Respiratory Rehabilitation, Fondazione Don C. Gnocchi, Florence, Italy

2 Department of Internal Medicine, Section of Immunology and Respiratory Medicine, University of Florence, Florence, Italy

References

- [1] Pedotti A, Ferrigno G. Opto-electronics based systems. In *Three-Dimensional Analysis of Human Movement, Human Kinetics*, 1st Ed.; Allard P, Stokes IA, Bianchi JP. Eds.; Human Kinetics Publishers: Champaign, USA, 1995; pp. 57-78.
- [2] Cala SJ, Kenyon C.M, Ferrigno G, Carnevali P, Aliverti A, Pedotti A, Macklem PT, Rochester DF. Chest wall and lung volume estimation by optical reflectance motion analysis. *Journal of applied Physiology*. 1996; 81:2680-2689.
- [3] Kenyon CM, Cala SJ, Yan S, et al. Rib cage mechanics during quiet breathing and exercise in humans. *Journal of Applied Physiology*. 1997;83:1242-55.
- [4] Aliverti A, Cala SJ, Duranti R, Ferrigno G, Kenyon CM, Pedotti A, Scano G, Sliwinski P, Macklem PT, Yan S. Human respiratory muscle action and control during exercise. *Journal of Applied Physiology* 1997;83:1256-1269
- [5] Ward ME, Ward JW, Macklem PT. Analysis of human chest wall motion using a two compartment rib-cage model. *Journal of Applied Physiology* . 1992; 72:1338-1347.
- [6] O' Donnell DE, Reville SM, Webb KA. Dynamic hyperinflation and exercise intolerance in COPD. *American Journal of Respiratory and Critic Care Medicine* 2001;164:770-777.
- [7] O'Donnell DE, Voduc N, Fitzpatrick M, Webb KA. Effect of salmeterol on the ventilatory response to exercise in chronic obstructive disease. *European Respiratory Journal* 2004;24:86-94.
- [8] Belman MJ, Botnick WC, Shin JW. Inhaled bronchodilators reduce dynamic hyperinflation during exercise in patients with chronic obstructive pulmonary disease. *American Journal of Respiratory and Critic Care Medicine* 1996;153:967-975.
- [9] Martinez FJ, de Oca MM, Whyte RI, Stetz J, Gay SE, Celli BR. Lung-volume reduction improves dyspnea, dynamic hyperinflation, and respiratory muscle function. *American Journal of Respiratory and Critic Care Medicine* 1997;155(6):1984-90.

- [10] Aliverti A, Stevenson N, Dellacà RL, Lo Mauro A, Pedotti A, Calverley PMA. Regional chest wall volumes during exercise in chronic obstructive pulmonary disease. *Thorax* 2004;59:210-216.
- [11] Innocenti Bruni G, Gigliotti F, Binazzi B, Romagnoli I, Duranti R, Scano G. Dyspnea, chest wall hyperinflation, rib cage distortion in exercising COPD patients. *Medicine and Science in Sport & Exercise* 2012. DOI:10.1249
- [12] Georgiadou O, Vogiatzis I, Stratakos G, Koutsoukou A, Golemati S, Aliverti A, Rousos C, Zakyntinos S. Effects of rehabilitation on chest wall volume regulation during exercise in COPD patients. *European Respiratory Journal* 2007; 29:284-291.
- [13] O'Donnell DE, Bain DJ, Webb K. Factors contributing to relief of exertional breathlessness during hyperoxia in chronic air flow limitation. *American Journal of Respiratory and Critic Care Medicine* 1997;155:530-535.
- [14] Somfay A, Porszasz J, Lee SM, Casaburi R. Dose-response effect of oxygen on hyperinflation and exercise endurance in non hypoxaemic COPD patients. *European Respiratory Journal* 2001;18:77-84.
- [15] Gigliotti F, Coli C, Bianchi R, Romagnoli I, Lanini B, Binazzi B, Scano G. Exercise training improves exertional dyspnea in patients with COPD: evidence of the role of mechanical factors. *Chest* 2003;123:1794-1802.
- [16] Iandelli I, Aliverti A, Kayser B, Dellacà R, Cala SJ, Duranti R, Kelly S, Scano G, Sliwinski P, Yan S, Macklem PT, Pedotti A. Determinants of exercise performance in normal men with externally imposed expiratory flow limitation. *Journal of Applied Physiology* 2002;92:1943-1952.
- [17] Ward ME, Eidelman D, Stubbing DG, Bellemare F, Macklem PT. Respiratory sensation and pattern of respiratory muscle activation during diaphragm fatigue. *Journal of Applied Physiology* 1988;65:2181-2189.
- [18] Potter WA, Olafsson S, Hyatt RE. Ventilatory mechanics and expiratory flow limitation during exercise in patients with obstructive lung disease. *Journal of Clinicl Investigation* 1971;50:910-919.
- [19] Binazzi B, Bianchi R, Romagnoli I, Lanini B, Stendardi L, Gigliotti F, Scano G. Chest wall kinematics and Hoover's sign. *Respiratory Physiology and Neurobiology*. 2008;160:325-333.
- [20] Garcia-Pachon, E. Paradoxical movement of the lateral rib margin (Hoover Sign) for detecting obstructive airway disease. *Chest*. 2002;122,651-655.
- [21] Gilmartin JJ, Gibson GJ. Abnormalities of chest wall motion in patients with chronic airflow obstruction. *Thorax*. 1984;39,264-271.

- [22] Gilmartin, JJ, Gibson GJ. Mechanisms of paradoxical rib cage motion in patients with chronic pulmonary disease. *American Review of Respiratory Diseases*. 1986;134:683–687.
- [23] Chihara K, Kenyon CM, Macklem PT. Human rib cage distortability. *Journal of Applied Physiology*. 1996;81:437-447.
- [24] Jubran A, Tobin MJ. The effect of hyperinflation on rib cage-abdominal motion. *American Review of Respiratory Diseases*. 1992;146:1378–1382.
- [25] Romagnoli I, Gigliotti F, Lanini B, Innocenti Bruni G, Coli C, Binazzi B, Stendardi L, Scano G. Chest wall kinematics and breathlessness during unsupported arm exercise in COPD patients. *Respiratory Physiology and Neurobiology* 2011;178:242-9.
- [26] Aliverti A, Quaranta M, Chakrabarti B, Albuquerque AL, Calverley PM. Paradoxical movement of the lower ribcage at rest and during exercise in COPD patients. *European Respiratory Journal* 2009;33:49-60.
- [27] Peters MM, Webb KA, O'Donnell DE. Combined physiological effects of bronchodilators and hyperoxia on exertional dyspnoea in normoxic COPD. *Thorax* 2006;61:559-67.
- [28] Vogiatzis I, Georgiadou O, Golemati S, Aliverti A, Kosmas E, Kastanakis E, Geladas N, Koutsoukou A, Nanas S, Zakynthinos S, Roussos C. Patterns of dynamic hyperinflation during exercise and recovery in patients with severe chronic obstructive pulmonary disease. *Thorax* 2005;60(9):723-9.
- [29] Tangri S, Wolf CR. The breathing pattern in chronic obstructive lung disease during the performance of some common daily activities. *Chest* 1973; 63:126-127.
- [30] Celli BR, Rassulo J, Make BJ. Dyssynchronous breathing during arm but not leg exercise in patients with chronic airflow obstruction. *New England Journal of Medicine*. 1986;314:1485-1490.
- [31] Ries AL, Bauldoff GS, Carlin BW, Casaburi R, Emery CF, Mahler DA, Make B, Rochester CL, Zuwallack R, Herrerias C. Pulmonary Rehabilitation: Joint ACCP/AACVPR Evidence-Based Clinical Practice Guidelines. *Chest* 2007;131:4S-42S.
- [32] Janaudis-Ferreira T, Hill K, Goldstein RS, Robles-Ribeiro P, Beauchamp MK, Dolmage TE, Wadell K, Brooks D. Resistance arm training in patients with COPD: a randomized controlled trial. *Chest* 2011;139:151-158.
- [33] McKeough ZJ, Alison JA, Bayfield MS, Bye PT. Supported and unsupported arm exercise capacity following lung volume reduction surgery: a pilot study. *Chronic Respiratory Disease* 2005;2:59-65.
- [34] Holland AE, Hill CJ, Nehez E, Ntoumenopoulos G. Does unsupported upper limb exercise training improve symptoms and quality of life for patients with chronic obstructive pulmonary disease? *J Cardiopulmonary Rehabilitation* 2004;24:422-427.

- [35] Ries AL, Ellis B, Hawkins RW. Upper extremity exercise training in chronic obstructive pulmonary disease. *Chest* 1988 ;93:688-692.
- [36] Neiderman MS, Clemente PH, Fein AM, Feinsilver SH, Robinson DA, Ilowite JS, et al. Benefits of a pulmonary rehabilitation program: improvements are independent of lung function. *Chest* 1991;99:7989-7804.
- [37] Martinez FJ, Vogel PD, Dupont DN, Stanopoulos I, Gray A, Beamis JF. Supported arm exercise vs unsupported arm exercise in the rehabilitation of patients with severe chronic airflow obstruction. *Chest* 1993;103(5):1397-402.
- [38] Costi S, Crisafulli E, Antoni FD, Beneventi C, Fabbri LM, Clini EM. Effects of unsupported upper extremity exercise training in patients with COPD: a randomized clinical trial. *Chest* 2009;136:87-395.
- [39] Couser JI Jr, Martinez FJ, Celli BR. Pulmonary rehabilitation that includes arm exercise reduces metabolic and ventilatory requirements for simple arm elevation. *Chest* 1993;103:37-41.
- [40] Lake FR, Henderson K, Briffa T, Openshaw J, Musk AW. Upper-limb and lower-limb exercise training in patients with chronic airflow obstruction. *Chest* 1990;97:1077-1082.
- [41] Romagnoli I, Scano G, Binazzi B, Coli C, Innocenti Bruni G, Stendardi L, Gigliotti F. Effect of arm training on unsupported arm exercise-related perception in COPD patients. Under revision in *Respiratory Physiology and Neurobiology*
- [42] Bianchi R, Gigliotti F, Romagnoli I, Lanini B, Castellani C, Grazzini M, Scano G. Chest wall kinematics and breathlessness during pursed-lip breathing in patients with COPD. *Chest* 2004;125(2):459-65.
- [43] Bianchi R, Gigliotti F, Romagnoli I, Lanini B, Castellani C, Binazzi B, Stendardi L, Grazzini M, Scano G. Patterns of chest wall kinematics during volitional pursed-lip breathing in COPD at rest. *Respiratory Medicine* 2007;101:1412-1418.
- [44] Macklem PT. Exercise in COPD: damned if you do and damned if you don't. *Thorax* 2005;60:887-888.
- [45] Nuss D, Kelly RE, Croitoru DP, Kats ME, A 10-year review of a minimally invasive technique for the correction of pectus excavatum. *Journal of Pediatric Surgery* 1998;33:545-552.
- [46] Nuss D, Minimally invasive surgical repair of pectus excavatum. *Seminars in Pediatric Surgery* 2008;17:209-217.
- [47] Binazzi B, Innocenti Bruni G, Coli C, Romagnoli I, Messineo A, Lo Piccolo R, Scano G, Gigliotti F. Chest wall kinematics in young subjects with pectus excavatum. *Respiratory Physiology and Neurobiology* 2012;180:211-217.
- [48] Binazzi B, Innocenti Bruni G, Gigliotti F, Coli C, Romagnoli I, Messineo A, Lo Piccolo R, Scano G. Effects of the Nuss procedure on chest wall kinematics in adolescents

with pectus excavatum. In press in *Respiratory Physiology and Neurobiology*. DOI:
10.1016/j.resp.2012.05.015



Edited by Sergei L. Pyshkin and John M. Ballato

Optoelectronics - Advanced Materials and Devices is a second edition following the initial Optoelectronics - Materials and Techniques book published in 2011 as part of the InTech collection of international works on optoelectronics. Optoelectronics, as the discipline devoted to the study and application of electronic devices that emit, detect, and otherwise control light, has widely proliferated globally and enabled many of today's modern conveniences. Because of this ubiquity, new applications and novel optical phenomena continue to drive innovation. Accordingly, as with the first book of the collection, this book covers recent achievements by specialists around the world. The growing number of countries participating in this endeavor including now Brazil, Canada, China, Egypt, France, Germany, India, Italy, Japan, Malaysia, Mexico, Moldova, Morocco, Netherlands, Portugal, Romania, Saudi Arabia, South Korea, Taiwan, Ukraine, USA, and Vietnam as well as joint participation of the US and Moldova scientists in edition of this book and writing one of its Chapters testify to the unifying effect of science. An interested reader will find in the book the description of properties and applications employing organic and inorganic materials, such as different polymers, oxides and semiconductors, as well as the methods of fabrication and analysis of operation and regions of application of modern optoelectronic devices.

Photo by kurga / iStock

IntechOpen

